Joule heating of green *Pinus radiata* logs for phytosanitary purposes: An in-depth investigation by experimentation and computational modelling

by

Nurzhan Nursultanov

A thesis submitted to the University of Canterbury in the partial fulfilment of
the requirements for the degree of Doctor of Philosophy
in Chemical and Process Engineering

2018

Abstract

Pinus radiata is one of New Zealand's main export products, and much of it is exported as whole green logs. Untreated logs may be infested by pests, which could be potentially harmful to the flora and fauna of an importing country. Therefore, in order to prevent pests from spreading, the logs must be treated. One of the main current wood treatment technologies is methyl bromide fumigation. The use of this chemical has been restricted due to its ozone depleting properties and, from October 2020, its release to the atmosphere will be prohibited in New Zealand. This research seeks to examine the technical feasibility of an alternative non-chemical method, Joule heating, to sterilize *P. radiata* green logs, using experimental and computational approaches.

The initial experiments started on green *P. radiata* boards and showed that for output power of 500 W with electric field limit of 5000 $V \cdot m^{-1}$ the average Joule heating rate of the pure sapwood was about 11 times higher than that of the heartwood boards. In transitional boards, with co-existing sapwood and heartwood parts, the heartwood was barely heated by the Joule heating effect, as the electric current flowed preferentially through the more conductive sapwood.

Later on, electrical conductivity of green *P. radiata* sapwood, with moisture content in the range of 100-200%, was studied over a 20-90°C temperature range. The results showed that the conductivity predominantly depends on temperature and grain orientation, and is independent of moisture content and basic density. The electrical conductivity in the longitudinal, radial, and tangential directions increased by factors of 3, 4, and 6, between 20 and 90°C, respectively. Using the linear mixed effect model, three empirical equations of electrical conductivity as a function of temperature and grain orientation were derived.

These equations were used in two computational fluid dynamics (CFD) models of Joule heating of export size *P. radiata* logs: three-dimensional (3D), built using ANSYS CFX, and one-dimensional (1D), custom built in MATLAB. In the 1D model, the sapwood of a log was assumed to be isotropic and its electrical conductivity was described by the derived equation of longitudinal electrical conductivity. In the 3D model, the sapwood was assumed to be either isotropic or anisotropic, described by all three derived electrical conductivity equations. These models

showed a close agreement; however, as the 1D model had a significantly shorter calculation time, it was used in the further verification and validation steps.

The 1D model was verified and validated using log-heating experiments and its accuracy was evaluated. Although the model cannot accurately predict local temperature distribution, it showed an acceptable agreement with the average global temperature distribution and the total electrical resistance, with the average error around 10%. The 1D model helped to control the heating process and was used to develop a heating sequence that allowed a more uniform temperature distribution within the treated logs. This study concluded that, using the CFD model and following the heating sequence, Joule heating can be successfully used in the phytosanitary treatment of export logs.

Acknowledgements

First and foremost, I would like to express my deepest gratitude to my primary supervisor, Dr. Bill Heffernan, for his continuous support during all these years of my PhD programme. His guidance, patience and understanding helped me to overcome many obstacles in my research and to finish this thesis. Seeing him doing experiments with us and his dedication to our project always inspired me to work harder.

I would like to thank my co-supervisors, Dr. Clemens Altaner and Professor Shusheng Pang, for their valuable feedback, advice, and their willingness to meet me on short notice. I am very grateful to them in every possible way.

I am also thankful to Dr. Justin Nijdam, who had been my supervisor for the first 1.5 years of the PhD programme. Within this short time, Justin helped me to develop the CFD modelling skills that allowed me to pursue my PhD programme and complete this thesis.

I would like to thank Associate Professor Elena Moltchanova from the Statistics Consulting Unit, University of Canterbury, for helpful comments in the statistical modelling.

My greatest appreciation and friendship goes to Mr. Ryan van Herel for his tremendous support during my struggles and frustration and for all that time he spent reviewing my thesis. Thank you, bro!

A special thanks to Mr. Steffen Fischer, a former postgraduate exchange student from Karlsruhe Institute of Technology, for his help in the earlier stage of the Joule heating project.

I would like to extend my thanks to the technicians of the Chemical & Process Engineering, Electrical & Computer Engineering, and Forestry departments for helping me with my experiments.

Furthermore, I would like to thank EPECentre for providing me with the scholarship and EPECentre's staff for their continuous support in my studies.

Last but not least, I would like to thank my parents, my wife and daughters, and my brothers. Thank you all for providing me with your support in all these years.

Contents

Glossaries

Latin Letters

A	area [m^2]
C_p	specific heat capacity [$J \cdot kg^{-1} \cdot °C^{-1}$]
I	electric current [A]
L	radiance [$W \cdot sr^{-1} \cdot m^{-2}$]
P	electrical power [W]
Q	thermal energy [J]
R	electrical resistance [Ω]
T	temperature [°C]
U	voltage [V]
V_g	green volume [m^3]
V_o	oven-dry volume [m^3]
V	volume [m^3]
W	work [J]
X	moisture content [%, $kg \cdot kg^{-1}$]
$\bar{S}$	heat source term [$W \cdot m^{-3}$]
$\boldsymbol{B}$	magnetic flux density [$V \cdot s \cdot m^{-2}$]
$\boldsymbol{D}$	electric displacement field [$C \cdot m^{-2}$]
$\boldsymbol{E}$	electric field [$V \cdot m^{-1}$]
$\boldsymbol{H}$	magnetic field strength [$A \cdot m^{-1}$]
$\boldsymbol{J}_e$	electric current density [$A \cdot m^{-2}$]
$\boldsymbol{J}_h$	heat flux [$W \cdot m^{-2}$]
$\boldsymbol{J}_m$	mass flux [$kg \cdot m^{-2} \cdot s^{-1}$]
$\hat{\boldsymbol{n}}$	unit normal vector
$\hbar_{vap}$	enthalpy of evaporation [$J \cdot kg^{-1}$]
$\hbar$	specific enthalpy [$J \cdot kg^{-1}$]

h	heat transfer coefficient [$\mathrm{W \cdot m^{-2} \cdot {}^{\circ}C^{-1}}$]
k	thermal conductivity [$\mathrm{W \cdot m^{-1} \cdot {}^{\circ}C^{-1}}$]
l	length [m]
m_g	green mass [kg]
m_o	oven-dry mass [kg]
m	mass [kg]
q	unit of charge [C]
r	radius [m]
t	time [s]

Greek Letters

α	thermal diffusivity [$m^2 \cdot s^{-1}$]
δ	error value
λ	temperature compensation coefficient [$\% \cdot °C^{-1}$]
μ	mean value
ρ_{el}	resistivity [$\Omega \cdot m$]
ρ_v	electric charge density [$C \cdot m^{-3}$]
ρ_g	green density [$kg \cdot m^{-3}$]
ρ_s	basic density [$kg \cdot m^{-3}$]
ρ	density [$kg \cdot m^{-3}$]
$\overline{\overline{\sigma}}$	second rank tensor of electrical conductivity [$S \cdot m^{-1}$]
σ	scalar electrical conductivity [$S \cdot m^{-1}$]
θ	slope
ε	emissivity

Acronyms

AIC	Akaike Information Criterion
ASE	Accelerated Solvent Extraction
CFD	Computational Fluid Dynamics
FDM	Finite Difference Method
FEM	Finite Element Method
FSP	Fibre Saturation Point
FVM	Finite Volume Method
PDE	Partial Differential Equation

Chapter 1

Introduction

1.1 General Overview

The New Zealand wood industry employs 20,000 people, generates $5 billion annual gross income, and is the third largest export earner for the country, accounting for 3% of New Zealand's GDP (Ministry of Primary Industry, 2012). Ninety percent of New Zealand's exotic trees (1.75 million hectares) are radiata pine (*Pinus radiata* D. Don) (Ministry of Primary Industry, 2012). According to a 2011 – 2012 'Facts and Figures' report provided by the New Zealand Forest Owners Association (2012), 49% of the total harvest volume is exported as green logs, and log exports increased by 38% from 2010 to 2011. In 2013, New Zealand exported over 13 million cubic meters of logs, of which approximately 11.4 and 1.5 million cubic meters were imported by China and India, respectively.

Tree species, like all living organisms, have their parasites. These parasites use wood as a source of nutrition, or for their habitat. Some of these parasites are bark beetles. They will remain inside harvested wood if it is not treated. Therefore, untreated green logs of New Zealand grown *P. radiata* with bark beetles, when exported, can potentially damage the flora and fauna of an importing country. For example, 52 exotic insects from Asia and 57 exotic insects from North America have already colonized European wood plants and, without phytosanitary treatment, the numbers of parasites will grow (Mattson et al., 2007). The consequences of poor wood sterilization are potentially catastrophic for New Zealand's export forestry industry, causing consequent harm to New Zealand's economy. Therefore, exported logs of New Zealand grown radiata pine must be treated prior to export and should be free of any pests.

1.2 Log Treatment Methods

One of the current phytosanitary treatments for many green logs is fumigation using methyl bromide. The major advantages of this treatment are fast penetration into an absorptive material

under normal conditions and rapid desorption after treatment (MAF Biosecurity New Zealand, 2009). Furthermore, this treatment is relatively cheap, as it requires simple equipment: a tarpaulin, methyl bromide gas bottles, and a water hose. The fumigation is performed on a pile of logs covered with a tarpaulin (Stakeholders in Methyl Bromide Reduction, 2018), as shown in Figure 1.1. A water hose is placed over the tarpaulin, around the pile and seals the

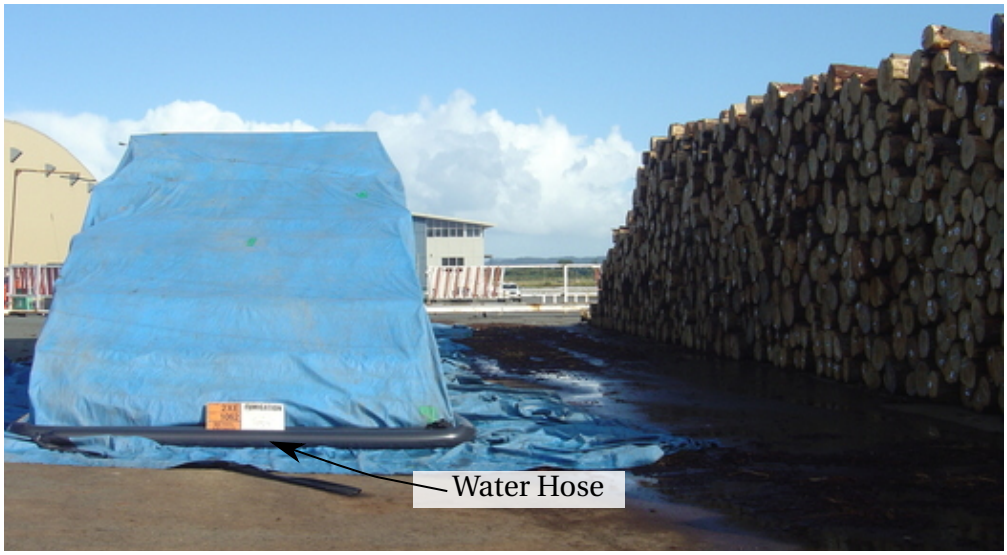

Figure 1.1. A photo of methyl bromide fumigation of export logs (PF Olsen Limited, 2011).

whole assembly on to the concrete wharf. The whole process is commonly completed within 24 hours (Stakeholders in Methyl Bromide Reduction, 2018). However, methyl bromide is not environmentally friendly due to its ozone-depleting properties, and since 2005 methyl bromide has been used only for quarantine and pre-shipment purposes (Ministry of the Environment, 2005). Furthermore, from October 2020, methyl bromide emissions must be recaptured (Ministry for Primary Industries, 2018), a requirement that will potentially increase the fumigation cost.

Because there are not many other industrial scale technologies to treat green export logs safely for the environment and for living organisms, the proposed green log treatment by the Joule heating method is under industry consideration. Joule heating, also known as electrical, resistive, and Ohmic heating, is the heat generation caused by the conduction of an electric current through a conductor (Ansari and Cho, 2010). The Joule heating effect is a known phenomenon, commonly observed when an electric clothes iron heats up. The main advantages of Joule heating are a relatively fast heating rate and nearly 100% energy conversion efficiency, from electrical into thermal energy. These advantages make this method more suitable for log export - many logs need to be treated in a relatively short time prior to shipment - than convective or

microwave heating. On the other hand, Joule heating causes hot and cold spot formation in wood (Fleischer and Downs, 1953) and it has not been thoroughly studied, with the previous work limited to the following four studies done by: Fleischer and Downs (1953), Lutz (1960), Perré (2004), and Heffernan (2009).

1.3 Objectives

The main focus of this research is to study Joule heating of green New Zealand grown *P. radiata*, including the technical feasibility of this method for sterilizing green export logs. The whole study is done using comprehensive experimental and computational analysis. The major objectives of this research are:

- To investigate Joule heating of green *P. radiata* using an electric power control system.
- To develop a computational model that can be used to optimize the Joule heating process.
- To establish a heat treatment process that would allow logs to reach the desired phytosanitary conditions.

These objectives are achieved by employing experimental testing and computational modelling. The scope of this thesis extends to determination of electrical conductivity of wood above 100% moisture content and studying non-uniform heating caused by knots, employing the developed three-dimensional knot heating model. However, this thesis does not aim to assess the economic feasibility of the Joule heating phytosanitary treatment, or to design a commercial full-scale treatment plant; these are suggested for future research.

This research was part of a larger project looking at alternative phytosanitary treatments. Concurrent work was carried out by Scion to determine the behaviour of pest insect species in *P. radiata*, which informed this research. The Scion work is also leading to the possibility of adding Joule heating to International Standards for Phytosanitary Measures No. 28 (ISPM 28) (IPPC, 2016b). The research in this thesis also fed into a Front-End-Loading study for building and operating an industrial plant to treat 2.1 million Japanese Agricultural Standard (JAS) m^3 of *P. radiata* logs per annum. Publications on these aspects of the overall project are in progress and will highlight the importance of the work reported in this thesis.

1.4 Thesis Outline

This thesis is split into the following chapters, each describing the principal milestones of this research:

Literature Review - Chapter 2 gives an extensive overview of wood structure, providing a background of the wood anatomy, knots, heartwood formation, and the main wood properties such as basic density and moisture content. A review of phytosanitary heat treatment conditions, the required temperature and duration, follows. Fundamentals of electrical engineering, with a discussion on non-uniform power dissipation, is included. The chapter is closed with a broad overview on the background of thermal and electrical properties of green wood, along with a discussion of computational modelling.

Joule Heating of Radiata Pine Boards - Chapter 3 describes the initial bench-top scale experiment of Joule heating of *P. radiata* boards. This experiment was designed to get fundamental understanding of Joule heating of green *P. radiata*. The work explained in this chapter determined the direction of the whole research presented in the following chapters.

Thermal Properties - A parallel work stream on the development of the computational model, discussed in Chapter 7, required to determine three wood properties: heat capacity and thermal conductivity, discussed in Chapter 4, and electrical conductivity, discussed in Chapter 5. Chapter 4 describes the comparison of two sets of two thermal equations for *P. radiata* - one for heat capacity and the other for thermal conductivity - derived previously by Pang et al. (1995) and Nijdam et al. (2000) to predict wood drying of *P. radiata*. The most accurate set of thermal equations was selected employing experimental testing and computational modelling, with a comprehensive explanation of the methods used.

Electrical Conductivity - In Chapter 5, electrical conductivity of wood is investigated using experimental testing. The goal of this study is to derive an equation (or multiple equations) of wood electrical conductivity that can be used in the computational model described in Chapter 7.

Computational Modelling and Verification - Chapter 6 shows all verification steps taken to ensure that the Joule heating model, discussed in Chapter 7, is error free. The model's output is compared with highly accurate solutions determined by analytical methods and previously published partial differential equations. Other verification principles are shown and discussed in this chapter.

Joule Heating of *P. radiata*: Industrial Application - In Chapter 7, the experimental testing of Joule heating of export size *P. radiata logs* and the dedicated three-dimensional and one-dimensional computational models are described. This chapter provides detailed images and method description, such as the implemented heating sequence to achieve phytosanitary conditions, followed by the experimental and computational results. A comparison of these results follows, with the conclusion of the model accuracy and of the Joule heating treatment efficacy.

Knot Heating - Chapter 8 describes the knot heating model, developed to show formation of hot and cold spots in a log during Joule heating. The work described in this chapter is preliminary and will require further study.

Conclusions, Recommendations and Future Work - Chapter 9 concludes the thesis, giving recommendations for further research.

Chapter 2

Literature Review

2.1 Wood Structure

P. radiata has a structure that is similar to most conifers (Harris, 1991c). The tree has an annulus of creamy white sapwood, which conducts sap upwards, and a pinkish, when freshly sawn, central inactive part, called heartwood. The heartwood, however, becomes light brown after drying. The sapwood contains live parenchyma cells, tracheids, and few extractives, whereas the heartwood contains dead parenchyma cells and tracheids, is dryer than the sapwood and is richer with extractives. On a cross sectional cut of a tree, earlywood and latewood bands can be observed. They are also called 'growth rings', because each annual growth ring consists of one earlywood and one latewood band. The earlywood bands, known as spring wood, are pale and formed at the beginning of spring, while the latewood bands, in contrast, are darker and formed in summer, and are therefore called summer wood. The whole trunk can be presented in a cylindrical coordinate system where the longitudinal direction is parallel to the axis of the stem, the radial direction is perpendicular to 'growth rings', and the tangential direction is tangential to 'growth rings' and perpendicular to the radial direction. A board sawn in the radial direction, perpendicular to the 'growth rings', is called a quarter-sawn board, while a board sawn in the tangential direction is called a flat-sawn board. A board containing both sapwood and heartwood is called transitional. The above features of *P. radiata* are presented in Figure 2.1.

2.1.1 Features of Stem

Wood and bark are products of cell division in the vascular cambium, which is a thin layer around the stem. This layer produces xylem and phloem cells that lie on the internal and external sides of the vascular cambium, respectively. The xylem cells, dividing inwards, form the wood, while the phloem cells, dividing outwards, produce the bark. To form different features of the wood structure, the vascular cambium of *P. radiata* has two types of initials: ray initials, which

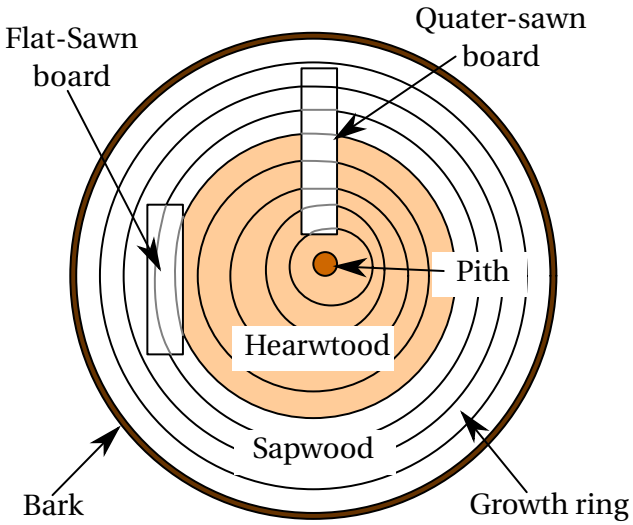

Figure 2.1. The cross section of a log.

give rise to horizontal features of the stem such as ray cells, and fusiform initials, which form the vertical system of the stem such as tracheids and epithelial cells of axial resin canals.

The tracheids are the main component of the wood structure, occupying more than 95% of the whole radiata pine's volume (Harris, 1991c). Their main purpose is to convey water and mineral salts as well as form structural support. The length of the axial tracheids may vary from 1 to 4 mm depending on their location within the wood structure (e.g. the tracheids close to the pith are the shortest, while the longest are in the outer wood) (Harris, 1991c). The tangential diameter of the axial tracheids varies from 20 to 55 µm. The average wall thickness of the axial tracheids is 3 µm, while the range of the wall thickness is 1.20 – 6.60 µm (Harris, 1991c). Two types of tracheids form the earlywood and latewood bands. The earlywood tracheids mainly conduct sap and water, while the latewood tracheids have mainly a stabilization purpose to support the crown. The earlywood and latewood tracheids are formed by the division of the same fusiform initials. The cell wall thicknesses of the earlywood tracheids and the latewood tracheids in corewood - the wood close to the pith - are 3 and 4 µm, respectively (Harris, 1991c). In the outerwood, near the bark, the thicknesses of earlywood and latewood tracheids walls are 4 and 5 µm, respectively. The earlywood tracheids are shorter than the latewood tracheids, but the radial diameter of the earlywood tracheids is several times larger than the radial diameter of the latewood tracheids, with the average radial diameters of the earlywood and latewood tracheids being 45 and 13 µm, respectively (Harris, 1991c). However, the tangential diameters of the earlywood and latewood tracheids are almost the same due to a limitation of tangential expansion of the fusiform initials

(Bamber and Burley, 1983; Harris, 1991c).

Radial tissue occupies less than 5% of the wood volume in most conifers; however, it plays a significant role in the tree, such as conduction of sap and nutrients, particularly during heartwood formation (Harris, 1991c). The radial wood rays are divided into two types (Harris, 1991c): 1) uniseriate (single row) or biseriate (double row) rays and 2) fusiform rays (a combination of a radial resin canal surrounded by epithelial cells, the latter secreting resin into the resin canal). The number of rays per millimetre in the transverse section (radial/tangential) varies from 4 – 9 with a mean value of 5.9, while in the tangential/longitudinal section, the number of rays is 4 – 8 with a mean value of 5.6 (Harris, 1991c).

The common feature of all pines is resin canals that lie longitudinally or radially, the latter ones as part of fusiform rays. The longitudinal and radial canals are interconnected, forming a network of canals which allow resin to flow to different parts of *P. radiata*, such as to a place of an injury or to the heartwood (Harris, 1991b). Normally the resin canals are 5 – 6 cells thick with a range of 4 – 8 cells. The resin canals are surrounded by epithelial cells. The parenchyma cells have a brick-like shape and function as storage and transportation in the wood. The most distinguishing feature of the parenchyma cells is that they do not die after maturation. The above features of *P. radiata* wood structure are presented in Figure 2.2.

2.1.2 Knots

Generally, *P. radiata* trees form from 1 to 5 nodes of branches each growing season and, occasionally, some develop zero or six nodes in an annual shoot (Chauhan et al., 2006; Kininmonth and Whiteside, 1991). According to Chauhan et al. (2006), 70% of *P. radiata*, from New Zealand's central North Island, forms from 3 to 4 nodes per year. The distance between two neighbouring nodes is called internode length (Figure 2.3). Depending on the number of formed nodes, the internode length in *P. radiata* logs varies significantly. For example, the internode length can reach 2 m in a uninodal (one node per year) *P. radiata* tree from the central North Island (Carson and Inglis, 1988; Jayawickrama et al., 1997). However, in a multinodal tree, the internode distance would be around 350 mm (Carson and Inglis, 1988; Jayawickrama et al., 1997). According to Grace et al. (1999), there are usually from 5 to 7 branches in a node. Within a node, branches grow in a spiral sequence, with a 2-3 mm vertical separation and a 137.5° azimuthal angle (Grace et al., 1998). In addition, the axis of branches is generally located at some vertical angle to the

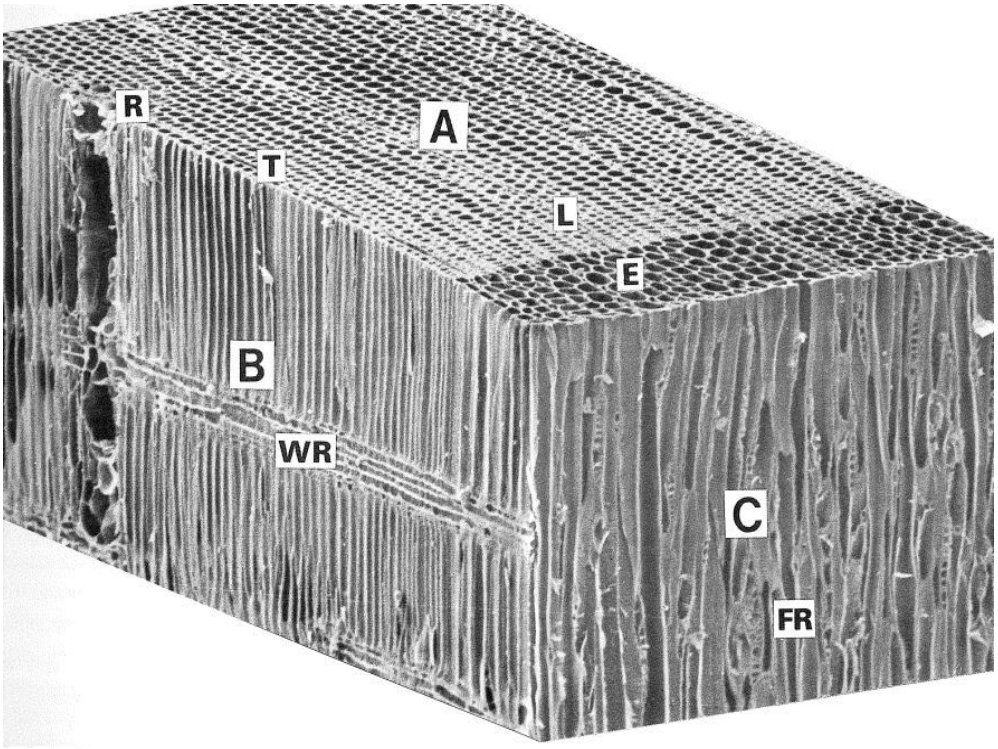

Face A (Transverse): **T** = cut ends of tracheids; **L** = latewood; **E** = earlywood; **R** = resin canal
Face B (Radial/longitudinal): **WR** = wood ray
Face C (Tangential/longitudinal): **FR** = fusiform ray

Figure 2.2. The scanning electron micrograph of *P. radiata.* Adapted from "Structure of wood and bark," by Harris. In J. A. Kininmonth and L. J. Whitehouse (Eds.), *Properties and Uses of New Zealand Radiata Pine,* p. 2.3. Copyright 1991 by Forest Research Institute.

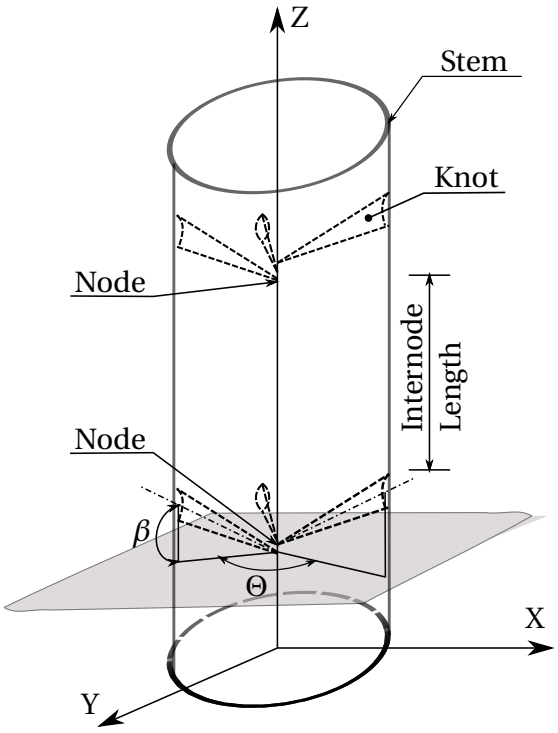

Figure 2.3. A schematic diagram of a stem section with knots, shown in Cartesian coordinates. *Note:* Θ and β are the azimuthal and vertical angles, respectively.

horizon (Samson, 1993; Xu, 2002).

When a branch is cut, its basal part left inside the tree is called a knot. Formed from the pith, knots have a conical shape (Hoadley, 2000), as depicted in Figure 2.3. In 30 year old New Zealand grown *P. radiata*, the diameter of knots varies from 25 to 80 mm, depending on growing conditions such as spacing between trees (Chauhan et al., 2006). If a branch was alive, the knot is connected to the surrounding wood and is called an intergrown or tight knot (Tsoumis, 1991), as shown in Figure 2.4a. Dead branches enclosed in a living stem result in encased or loose knots (Figure 2.4b). Knots vary in shape (round, oval and spike knots (Figure 2.4c), size (pin, small, medium, and large), and the quality of their wood (sound, unsound, and decayed) (Tsoumis, 1991). Knot wood is 25-100% denser than the surrounding wood (Keey et al., 2000) and, at 12% moisture content, the knot and clear wood densities of *P. radiata* are about 700 and 480 $\mathrm{kg \cdot m^{-3}}$, respectively (Xu, 2002). The denser the wood, the lower the moisture content and hence knots have generally lower moisture content than clear wood.

2.1.3 Cell Wall and Pits

The cell wall, present in plant cells, is a tough and rigid structure that prevents the cell from expanding when water fills wood cavities, and allows the cell to withstand osmotic pressure

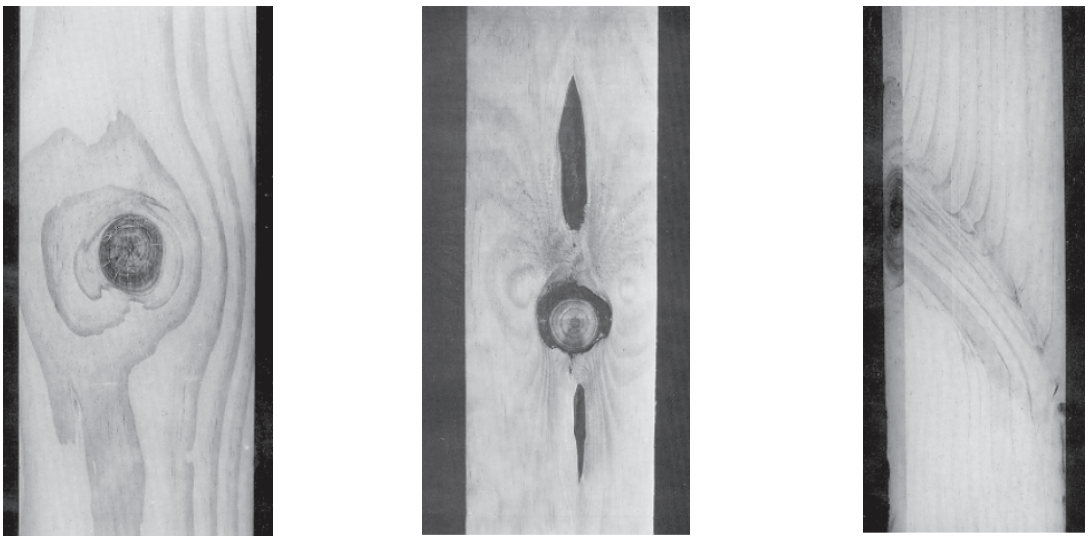

(a) (b) (c)

Figure 2.4. The knot types: (a) the intergrown knot, (b) the encased knot, and (c) the spike knot. *Note:* The dark features that surround the encased knot are bark pockets. Adapted from "Log Quality," by Kininmonth and Whiteside. In J. A. Kininmonth and L. J. Whitehouse (Eds.), *Properties and Uses of New Zealand Radiata Pine*, p. 5.7. Copyright 1991 by Forest Research Institute.

caused by a difference in concentration inside and outside of the cell. The cell wall is made of cellulose, hemicelluloses, and lignin. Cellulose, in the form of microfibrils, creates a framework for an amorphous mass of hemicelluloses and other carbohydrates (Harris, 1991c). Once a final dimension of each cell is formed, lignin encrust the structure, giving it rigidity (Harris, 1991c). In order to have enough tensile strength, the cell wall is made up of several component layers (Figure 2.5):

I A middle lamella (ML) is located between two cells in the intercellular region and is common to both cells (Harris, 1991c)

II The primary wall (P) is quite thin (0.1 μm) and therefore cannot be easily isolated from the middle lamella. Some studies combine the middle lamella with the primary wall and call them a compound middle lamella (Butterfield, 2006)

III The secondary wall lies next to the primary layer and has three different layers, S1, S2, and S3. These three layers are different from one another in thickness, orientation of microfibrils, and chemical composition (Butterfield, 2006).

The secondary walls of the living cells, called parenchyma, and the tracheids have pits. They allow water and dissolved nutrients to pass through (Harris, 1991c). However, not all pits are

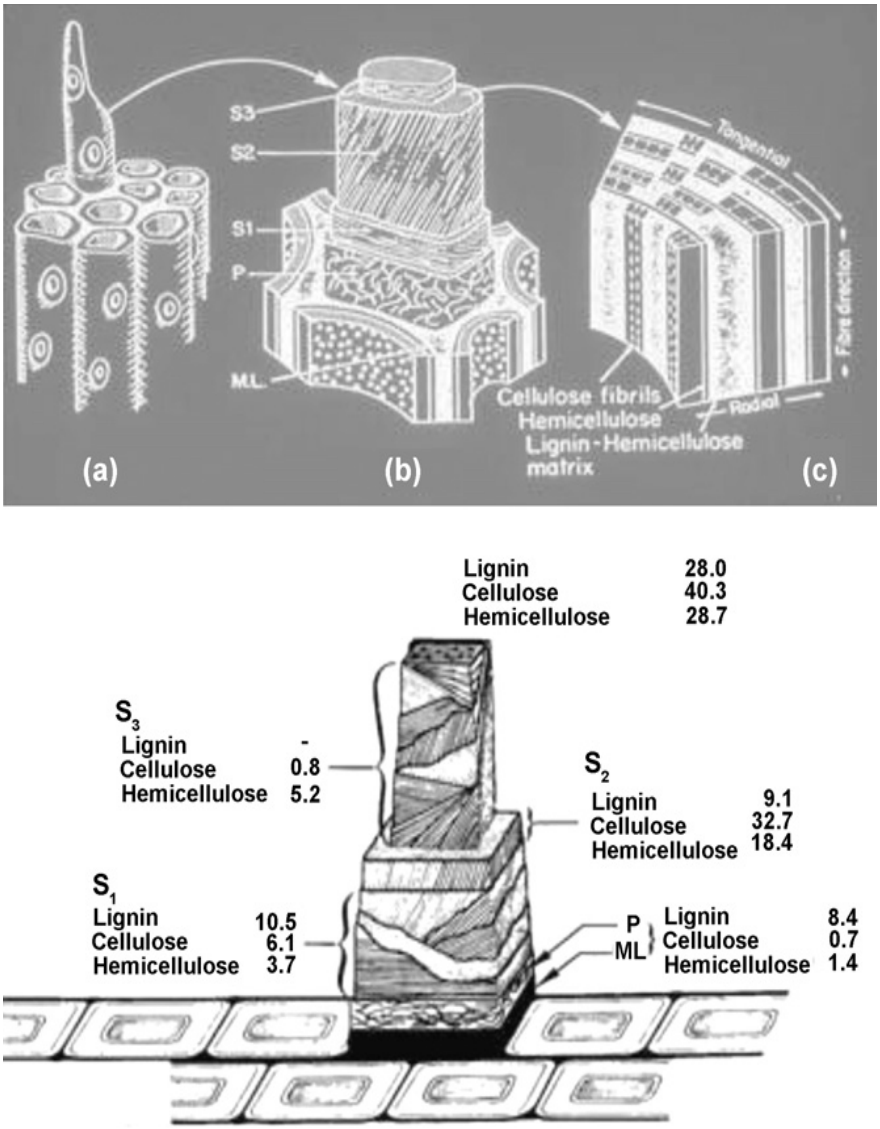

Figure 2.5. A schematic cell wall structure. Adapted from "Historical wood – structure and properties," by Nilsson and Rowell, 2012, *Journal of Cultural Heritage*, vol. 13, p. S6. Copyright 2012 by Elsevier Masson SAS.

the same. Harris (1991c) wrote that there are two types of pits, which connect different cell systems: either the parenchyma cells or the tracheids. The parenchyma cells have simple pits, while the tracheids have bordered pits where the secondary cell wall forms a pit chamber that does not exist in simple pits (Harris, 1991c). The pit chamber is split into two parts by a pit membrane. The thicker, circular central part of the pit membrane is called the torus, while the thinner part, surrounding the torus, is called the margo. An additional type of pit, called half-bordered, connects parenchyma cells with tracheids; these pits have a pit chamber only at one side of the margo. The structures of the pits in the earlywood tracheids and the latewood tracheids are different. The bordered pits in the earlywood tracheids prevent the spreading of air bubbles that can destroy the water column, which is full of water and nutrients during a growing season (Harris, 1991c). The big pit chambers inside the bordered pit of the earlywood tracheids allow the tori to tightly close the apertures and the bordered pits of the earlywood tracheids become aspirated. The aspirated, bordered pits prevent further spreading of air bubbles to the neighbouring tracheids, and minimize the risk associated with damaging the whole water conduction system. The aspiration of the bordered pits is an irreversible process common during wood drying and heartwood formation (Harris, 1991c). The bordered pits of the latewood tracheids have smaller chambers, making the tori less flexible and preventing the pits from becoming aspirated. These bordered pits can contain air bubbles and are therefore not involved in water conduction (Harris, 1991c). Figure 2.6 shows the schematic drawing of the different type of pits.

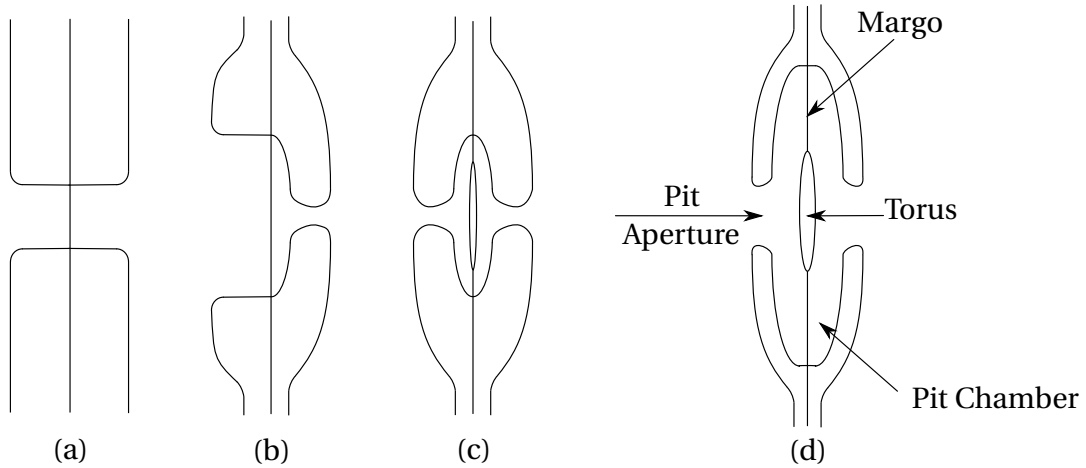

Figure 2.6. A schematic drawing of the pit types: (a) the simple pit, (b) the half-bordered pit, (c and d) the bordered pits of the latewood and earlywood tracheids, respectively.

2.1.4 Formation of Heartwood

Prior to the age of 12 – 14 years, *P. radiata* does not contain heartwood (Harris, 1991a). The first sign of the heartwood formation is the development of a dry-wood zone in the centre of a stem. The dry-zone formation starts with the aspiration of the bordered pits inside axial earlywood tracheids. In the area between the sapwood and the dry-wood zone, 50% of all earlywood tracheids become aspirated, disturbing the continuous conduction of sap. The percentage of aspirated tracheids progressively increases inwards from the dry-wood zone towards the pith, eventually reaching more than 95%. As a result, almost all tracheids inside the dry-wood zone become filled with gas (Harris, 1991a). The dry-wood zone is usually one half of a 'growth ring' wide. It spreads outwards during formation of heartwood. Located within the dry-wood zone, the heartwood of a living *P. radiata* tree contains 25 – 30% of the water present in sapwood. When the dry-zone is formed, the dry-zone's parenchyma cells produce additional resins, tannins and other organic substances such as pinosylvin, present in heartwood, and die shortly afterwards. The older the *P. radiata*, the greater the heartwood cross-section and the greater the extractives content (Bamber and Burley, 1983). In a typical thirty year old New Zealand grown *P. radiata*, the sapwood may occupy 80% of the whole wood volume (Bamber and Burley, 1983; Harris and Cown, 1991), and the extent of *P. radiata* sapwood varies from 12 to 25 cm in stems of 30 cm in diameter (Carrodus, 1972). However, the heartwood content varies within the stem at different heights, where the greatest heartwood content is at the bottom and the lowest at the top. Heartwood forms in a stem and branches (Figure 2.7).

2.1.5 Wood Properties Used in Joule Heating

Wood properties such as density, moisture and extractives content depend on tree species, the age, the geographical location and the climatic conditions. Density is often used to describe wood quality. Commonly, there are three main types of wood density: basic density, air-dry density, and green density. The air-dry density is the density of wood with a moisture content of around 12%, while the green density is the density of wood from a freshly felled tree. The limitation of these densities is their dependence on the wood moisture content and shrinkage. When wood is drying, its volume decreases due to the shrinkage, reaching the minimum volume at the oven-dry condition, with the moisture content of 0%. In contrast, basic density, derived from the oven-dry mass and green volume, is independent of the moisture content and shrinkage.

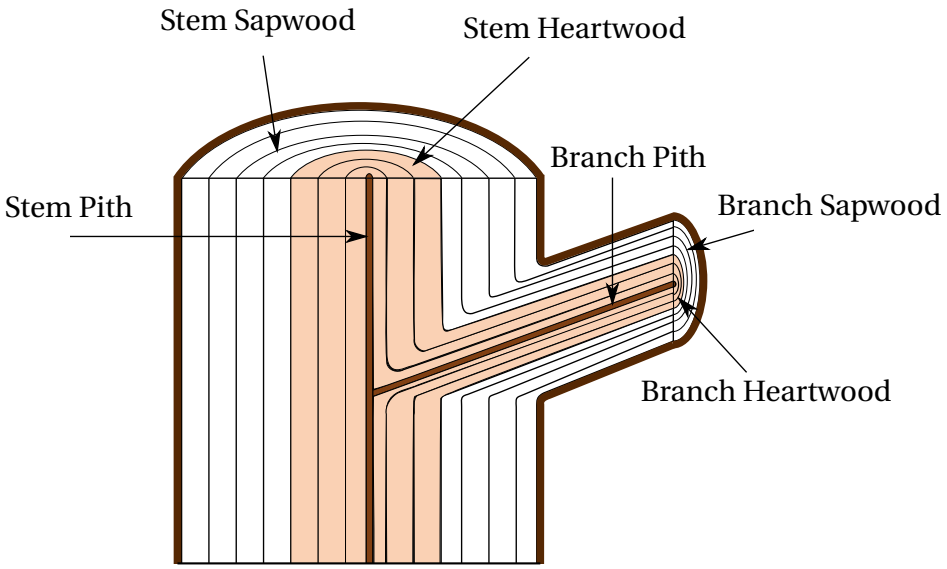

Figure 2.7. The schematic diagram of heartwood formation in a stem with a branch.

Therefore, this definition is a better basis for comparing wood samples, and used to develop relationships with other wood properties such as thermal conductivity (Harris and Cown, 1991). The basic density can be calculated as:

$$\rho_s = \frac{m_o}{V_g}, \tag{2.1}$$

where ρ_s is the basic density [kg$\cdot$m^{-3}], m_o is the mass of the oven-dry wood [kg], and V_g is the volume of the green, fully saturated wood [m^3]. The average basic density of *P. radiata's* earlywood is 350 and latewood is 550 kg$\cdot$m^{-3} (Harris and Cown, 1991). The basic density of *P. radiata's* sapwood varies in the range of 430 - 500 kg$\cdot$m^{-3}, while the basic density of the heartwood lies within 338 - 404 kg$\cdot$m^{-3} (Pang et al., 1995).

Moisture content, X, is the ratio of water mass with respect to the oven-dry mass of the wood, containing mainly cell walls and no moisture (Harris and Cown, 1991; Skaar, 1988), and can be determined as follows:

$$X = \frac{m_g - m_o}{m_o}, \tag{2.2}$$

where m_g is the mass of the green wood. There are various methods to determine moisture content (Skaar, 1988): gravimetric, distillation, Karl Fischer titration, nuclear magnetic resonance,

and electrical moisture meters. Although the distillation and Karl Fischer titration are the most accurate methods, they are time consuming and are not feasible for a large number of specimens. The nuclear magnetic resonance method requires sophisticated and expensive equipment. Electrical moisture meters give rapid readings and are relatively cheap, but only accurate below the fibre saturation point (FSP), at which wood fibres are fully saturated with bound water, without free water in wood cavities (Kininmonth, 1991). The FSP of *P. radiata* is about 30% of the dry mass (Pang and Herritsch, 2005). The gravimetric method, where the wet and oven-dry mass of the wood are measured, is the most common. The difference between the wet and dry mass values is assumed to be the mass of water. The method has acceptable accuracy, within 1% (Kininmonth, 1991), and requires only an oven and a balance. The main causes of error are 1) loss of volatile components such as resinous compounds of conifers and 2) residual bound water located within wood tissue, which can be difficult to drive off completely by heating (Kininmonth, 1991). As mentioned earlier, heartwood has lower moisture content than sapwood. The average moisture content of freshly harvested (green) New Zealand grown *P. radiata* is 45% in the heartwood and 150% in the sapwood (with a range from 100 to 200%) (Harris and Cown, 1991). At the green state, when wood fibres are filled with free water, the wood reaches full saturation.

Wood with high basic density has lower moisture content (Kininmonth, 1991). Dense wood, such as latewood, has a large ratio of wood mass per unit volume; hence, it does not have as much free volume for water. As a result, it will have a lower moisture content compared to the wood of low density at the same percentage of saturation. Knowing moisture content and basic density (ρ_s), green density (ρ_g) can be calculated as (Nijdam, 1998):

$$\rho_g = \rho_s(1 + X). \tag{2.3}$$

The wood contains organic (extractives) and inorganic (ash) compounds. These compounds affect properties of *P. radiata* such as odour and colour. In addition, dissolved in sap, some inorganic extractives affect wood electrical conductivity. The extractive content is usually expressed as a fraction of the oven-dry mass and can be described by the following equation (Harris and

Cown, 1991):

$$PEC = \frac{m_{ext}}{m_o} \times 100\%, \tag{2.4}$$

where PEC is the percentage of the extractives content, and m_{ext} is the mass of the extractives. Generally, different solvents such as water, ethanol, and acetone are used for extraction tests. A classical method of extraction is Soxhlet extraction (Uprichard, 1991; Walker, 2006). This method is slow and consumes a large volume of solvent. According to Thurbide and Hughes (2000), a Soxhlet apparatus, used in a standard test method of the Canadian Pulp and Paper Association, requires 5 hours of extraction time and consumes 150 mL of solvent per sample. Richter et al. (1996) suggest that an automated Soxhlet apparatus requires from 2 to 4 hours, consuming 50 – 100 mL of solvent per sample. Other methods such as Microwave-Assisted Extraction (MAE), Supercritical Fluid Extraction (SFE), and Accelerated Solvent Extraction (ASE) have been designed as alternative methods to the Soxhlet extraction (Janssen and Lou, 1999). These methods have been studied previously and compared with one another (Heemken et al., 1997; Richter et al., 1996; Saim et al., 1997; Thurbide and Hughes, 2000). Uprichard (1991) summarised all the findings about organic and inorganic content of *P. radiata*'s wood and the bark.

2.2 Phytosanitary Conditions

To use the Joule heating effect on the industrial scale for the phytosanitary treatment of green *P. radiata* logs, the required treatment conditions, usually governed by a phytosanitary standard, must be known. One of the most common standards in the wood treatment industry is the International Standard for Phytosanitary Measures No. 15 (ISPM 15). The purpose of the standard is to significantly reduce the hazards associated with pests spreading through global trade in raw wood packaging. All countries, which are signatories to the standard, are obliged to ensure that wood packaging is free of quarantine pests (IPPC, 2016a). ISPM 15 allows methyl bromide fumigation, although the use of methyl bromide has been restricted as it is an ozone-depleting chemical. Fields and White (2002) studied different alternatives to methyl bromide fumigation. However, heat sterilization is the only alternative method that has been accepted by ISPM 15. According to the standard, wood, including its core, must be heated to

the minimum temperature of 56°C for 30 minutes (IPPC, 2016a). To fulfil the heat sterilization requirement, the ISPM 15 proposes two heating methods: either conventional kiln heating, or dielectric heating such as using radio frequency or microwave heating.

Although a few cases did not show an absolute mortality at 56°C (Goebel et al., 2010; Nzokou et al., 2008), the temperature above 56°C proved to be fatal for most insects and their larvae (Dentener et al., 2001; Myers and Bailey, 2011; Uzunovic et al., 2013). Absolute mortality can be achieved by increasing the temperature and/or duration of the wood sterilization. Therefore, the higher the temperature and the longer the sterilization process, the more fatal the treatment is for insects. The use of the minimum required temperature, 56°C, for 30 minutes proposed by the ISPM 15 to sterilize New Zealand grown *P. radiata* green logs will be used as a starting point in this study.

Heat sterilization can be achieved using a conventional kiln dryer (Ananias et al., 2013; Cai and Oliveira, 2010; Lu et al., 2012) or radio frequency heating (Henin et al., 2008; Mõlder et al., 2013; Novotny et al., 2013; Uzunovic et al., 2013). Nzokou et al. (2008) compared conventional kiln heating with microwave heating. The kiln heating technique creates a more even temperature rise in the wood and avoids an uneven heat distribution that is common with microwave heating (Nzokou et al., 2008). However, the low heating rate of conventional kiln heating is the biggest disadvantage of this technique. Ananias et al. (2013) experimentally determined that an increase of a board's thickness from 16 to 37 mm extended the minimum required time to reach sterilizing conditions from 66 to 104 min in an industrial 100 m^3 kiln. Dentener et al. (2001) studied the time required to reach 45°C in logs by using the conventional kiln heating method, showing that 6, 10.5 and 13.5 h were required to sterilize logs of 10, 20, and 40 cm diameters respectively. Therefore, the thicker a wood board or the larger the diameter of a log, the longer is the time to reach the required temperature using conventional kilns.

The radio frequency heating method heats the wood mass much quicker than the conventional kiln method and ensures a relatively rapid temperature rise of the whole wood (Uzunovic et al., 2013). However, the main disadvantage of radio frequency heating is a relatively low energy conversion efficiency, which is around 65% at 2.45 GHz (Liu et al., 2011; Shim et al., 2010). On the other hand, the energy conversion efficiency in the Joule heating method is nearly 100%. The low energy conversion efficiency and relatively more sophisticated equipment requirements

make the radio frequency method more expensive than the Joule heating method (Perré, 2004). To minimise heat losses and to sustain the external surface temperature above 56°C, both these methods require conditioning chambers. However, the radio frequency plant must be properly shielded to protect humans from the potentially lethal radiation, significantly increasing the cost of the conditioning chamber.

To date, four research studies have investigated Joule heating of wood: three were entirely experimental (Fleischer and Downs, 1953; Lutz, 1960; Heffernan, 2009) and the other was purely based on computational modelling (Perré, 2004). Fleischer and Downs (1953), Lutz (1960), and Perré (2004) studied the applicability of Joule heating for veneer peeling - wood tends to be more easily peeled for veneer when it is heated to a certain temperature (Perré, 2004) -, while Heffernan (2009) tested the possibility of using Joule heating as a phytosanitary treatment method.

Fleischer and Downs (1953) positioned test logs vertically on a tray filled with salt water, the ground side, and attached a flat disc electrode to the other side of the log, the high voltage side. Lutz's (1960) report lacks a comprehensive description of the heating rig, such as the utilized electrode arrangement. Both of these studies did not control electric power and reported a relatively fast temperature rise, with non-uniform temperature distribution, where the average log temperature was higher than 50°C. In addition, Fleischer and Downs (1953) noticed a decrease of the total log resistance, and that internal checking developed in the logs. Potentially, the cause of checking in those logs was uncontrolled heating; such heating occurs at constantly increasing electric power, when the total log resistance decreases and the voltage is fixed, causing a constant rise of heat generation. This problem of uncontrolled heating was addressed by Heffernan (2009), who heated export size logs of plantation grown *P. radiata* for phytosanitary purposes. He developed an electric power controller, which reduced the applied voltage when the total log resistance decreased, keeping the electric power constant at 100 kW. Furthermore, Heffernan (2009) proposed a design of 1 MW machine that can be used on a wharf to treat export logs. This research showed promising results but required further study and development of tools such as a computational model to optimize the heating process and minimize the supplied energy. Trying to control electrical current distribution, Perré (2004) modelled several electrode arrangements, such as a pair of small flat disc electrodes attached just to the heartwood of the log, or a cylindrical electrode inserted into the heartwood. None of Perré's (2004) modelled

electrodes were tested experimentally. Perré (2004) predicted the formation of hot and cold spots within a similar temperature range to those measured by Heffernan (2009) and required by ISPM 15 (IPPC, 2016a). Although, according to these studies, the hot and cold spots make the use of Joule heating unsuitable for veneer peeling, the achieved temperature is within the range required for sterilization. In general, there is little reported literature related to wood sterilization by the Joule heating method. The technique, however, has been studied experimentally and computationally in other industries such as food processing (Ito et al., 2014).

2.3 Electrical Engineering Fundamentals

This section will cover the main electrical terminology and fundamentals of electrical engineering used in this research, as well as principles of electrical conductivity based on the literature by Rizzoni (2009) unless otherwise stated.

Electric current is defined as the flow rate of charge per unit time through a given surface, measured in coulombs per second [$C \cdot s^{-1}$] or amperes [A], as follows:

$$I = \frac{\Delta q}{\Delta t}, \tag{2.5}$$

where I is the electric current [A], q is the unit of charge [C], and t is time [s]. In order to move charges in an electrical circuit, the charges must use some energy. The total energy per unit charge is called electrical potential, or voltage, and is measured in Joules per coulomb [$J \cdot C^{-1}$] and called volts [V], derived as:

$$U = \frac{W}{\Delta q}, \tag{2.6}$$

where U is the voltage [V], W is the work [J].

When the electric current flows through a conductor, it experiences a certain amount of resistance, which varies based on the electrical properties of the conductor. The *resistance*, measured in ohms [Ω], is calculated using Ohm's law:

$$R = \frac{U}{I}, \tag{2.7}$$

where R is the resistance.

In addition to Equation 2.7, the resistance of a volume of material can be calculated, as follows:

$$R = \frac{\rho_{\text{el}} l}{A} = \frac{l}{\sigma A}, \tag{2.8}$$

where ρ_{el} is the electrical resistivity [$\Omega \cdot \text{m}$]; σ is the electrical conductivity [$\text{S} \cdot \text{m}^{-1}$], the reciprocal of the electrical resistivity; A is the cross-sectional area of the volume [m^2] normal to the flow of electrical current; and l is the length of the volume along the direction of current flow [m].

Work per unit time is called power, expressed as:

$$P = \frac{W}{\Delta t} = \frac{W}{\Delta q}\frac{\Delta q}{\Delta t} = U \cdot I = I^2 \cdot R = \frac{U^2}{R}, \tag{2.9}$$

where P is the power, measured in watts [W]. When 1 W of power is consumed for one hour of time, it is equal to 1 watt-hour [$\text{W} \cdot \text{h}$] of energy, which is equal to 3600 J.

Electrical elements such as resistors can be combined into electrical circuits, where the elements can be positioned in parallel and/or series (Figure 2.8). Equations 2.5 – 2.9 are used for individual electrical elements, but when electrical elements are part of an electrical circuit, laws such as Kirchhoff's circuit laws must be applied. Kirchhoff's current law states that the sum of all currents flowing into a node must be equal to the sum of currents flowing out of the node.

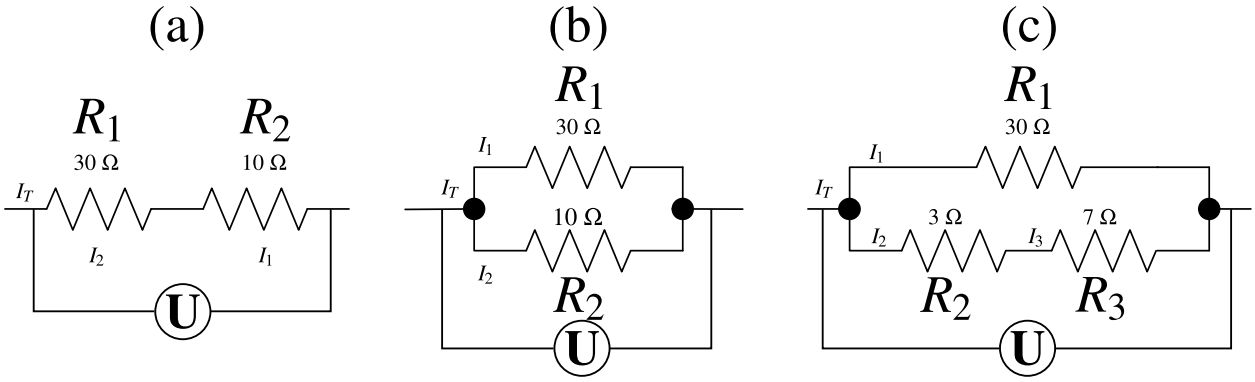

Figure 2.8. Positions of resistors within electrical circuits: (a) resistors in series, (b) parallel resistors, and (c) the bottom resistors (R_2 and R_3) are in series and the top resistor (R_1) is in parallel to the bottom ones.

Therefore, since there is only one pathway in Figure 2.8(a), the currents I_1 and I_2 flowing through the resistors R_1 and R_2, are equal to total current I_T, while the total resistance is equal

to the sum of R_1 and R_2. Based on Equation 2.9, the total power is equal to:

$$P = (10\ \Omega + 30\ \Omega) \cdot I_T^2 = 40\ \Omega \cdot I_T^2. \tag{2.10}$$

When resistors are in parallel as in Figure 2.8(b) then I_T is the sum of I_1 and I_2, and, since the voltage across the resistors is the same, then:

$$I_T = I_1 + I_2 = \frac{U}{30\ \Omega} + \frac{U}{10\ \Omega}, \tag{2.11}$$

and

$$3I_1 = I_2, \tag{2.12}$$

giving

$$\begin{aligned} P_1 &= 30\ \Omega \cdot (I_1)^2, \\ P_2 &= 10\ \Omega \cdot (3I_1)^2 = 90\ \Omega \cdot (I_1)^2. \end{aligned} \tag{2.13}$$

As a result, a resistor with lower resistance in a parallel connection has higher applied power. If both resistors have similar thermal properties, the resistor with lower resistance will have a higher temperature.

In Figure 2.8(c), the electrical currents I_2 and I_3 through the resistors R_2 and R_3 are equal as they are in series. Also, since the total resistance of R_2 and R_3 is 10 Ω and the resistance of R_1 is 30 Ω, the electrical current through R_1 is three times lower than through resistors R_2 and R_3. Thus, the power in all three resistors will be as follows:

$$\begin{aligned} P_1 &= 30\ \Omega \cdot (I_1)^2, \\ P_2 &= 3\ \Omega \cdot (3I_1)^2 = 27\ \Omega \cdot (I_1)^2, \\ P_3 &= 7\ \Omega \cdot (3I_1)^2 = 63\ \Omega \cdot (I_1)^2. \end{aligned} \tag{2.14}$$

In the previous result with two parallel resistors, the resistor with the lowest resistance has the highest applied power. However, in the case shown in Figure 2.8(c), the resistor with the lowest resistance has the lowest applied power. The total result is $P_3 > P_1 > P_2$; hence if all three resistors

have similar thermal properties $T_3 > T_1 > T_2$. However, unlike these simple cases with three resistors, the structure of wood is a complex three dimensional system of resistive elements with unique and temperature dependent values.

2.4 Electrical Conductivity of Green Wood

Electrical conductivity is the property of a material that quantifies how well the material conducts electrical current. Therefore, knowing spatial and local distribution of electrical conductivity allows estimation of specific power dissipation and hence prediction of temperature rise. According to Fleischer and Downs (1953), a lack of information about green wood's parameters such as its electrical properties leads to uncontrolled heating, which is a barrier to the Joule heating method being commercially developed on an industrial scale.

2.4.1 Effect of Temperature

Oven dried wood is an insulator, with an electrical conductivity of 10^{-15}–10^{-16} $\mathrm{S \cdot m^{-1}}$ (Glass and Zelinka, 2010), while green wood containing water with dissolved minerals in the sap, is an electrical conductor. In general, the effect of temperature on the electrical conductivity of aqueous solutions of salts such as potassium chloride is near linear, between 0 and 100°C (Haynes, 2014; McCleskey, 2011). The electrical conductivity of aqueous solutions can be calculated as follows (Bard and Faulkner, 2001):

$$\sigma = F \sum_i |z_i| u_i C_i, \tag{2.15}$$

where F is the Faraday constant, $|z_i|$ is the magnitude of the ionic charge, u_i is the mobility of the ions, and C_i is the concentration of the ions. The mobility of ions at the terminal velocity can be expressed as (Bard and Faulkner, 2001):

$$u_i = \frac{|z_i| e}{6\pi\eta r}, \tag{2.16}$$

where e is the electronic charge, η is the viscosity of the medium, and r is the radius of the ion. The viscosity of a liquid medium is inversely proportional to its temperature (Kleiber and Joh, 2010). Hence, an increase in the temperature decreases the viscosity of a liquid medium, consequently increasing the mobility of ions and the electrical conductivity of the whole solution.

Three parameters affect electrical conductivity of an ionic solution: the magnitude of the ionic charge, the concentration of the ions, and the temperature of the liquid medium. While the first two parameters are impractical to control, temperature control is necessary during the Joule heating of wood, to avoid boiling of the sap within timber undergoing treatment, and prevent any wood damage.

The electrical conductivity of wood is non-linearly dependent on temperature, indicating that wood properties have a significant effect on the relationship (Skaar, 1988). However, the effect of temperature and wood properties on the electrical conductivity have been predominantly studied below the FSP (Davidson, 1958; Forsén et al., 2000; Fredriksson et al., 2013; Skaar, 1988; Stamm, 1927).

2.4.2 Effect of Wood Properties

Wood Structure

Wood structure varies in the longitudinal, radial, and tangential directions, making the electrical conductivity directionally dependent, or anisotropic. Generally, the electrical conductivity in the longitudinal direction is much higher than the conductivities in the other directions; the radial electrical conductivity is slightly higher than the tangential conductivity (Stamm, 1927).

According to Kuroda and Tsutsumi (1982), the anisotropy of the electrical conductivity of *Cryptomeria japonica* depends on the moisture content. The authors found that the ratio of longitudinal to tangential conductivities decreased from about eight to two times, at the moisture content range of 1.5 to 8.5%, but then the ratio increased linearly to almost four times, at 8.5 to 20% of moisture content. The research done by Stamm (1960), who measured electrical conductivity of North American softwood and hardwood with a moisture content of 10-15%, showed similar results. The ratio of the longitudinal electrical conductivity to the radial conductivity, σ_L/σ_R, varied from 1.9 to 3.2, while the ratio of the longitudinal electrical conductivity to the tangential conductivity, σ_L/σ_T, varied from 2.1 to 3.9 (Stamm, 1960).

On the other hand, studying diffusion in wood, Burr and Stamm (1947) measured electrical conductivity of three softwood and six hardwood species, saturated with 0.1 N potassium chloride. The researchers initially dried their samples to a constant mass at 105 °C and then saturated the samples with the solution; the electrical conductivity was measured in three directions at 30°C. For sapwood, the ratio of σ_L/σ_R varied in the range of about 15-20 and σ_L/σ_T

varied in the range of 17-20. The average ratio of the radial to tangential conductivity, σ_R/σ_T, for softwood was around 1.1. The ratios of σ_L/σ_R and σ_L/σ_T of hardwood varied widely based on the type of wood, sapwood or heartwood, and wood species. The highest σ_L/σ_R and σ_L/σ_T ratios were 17 and 21, respectively, for heartwood of *Quercus rubra*. The lowest σ_L/σ_R and σ_L/σ_T ratios were 4 and 6, respectively, for heartwood of *Magnolia grandiflora*. The σ_R/σ_T varied from 1.2 to 2.4. However, Burr and Stamm's results may vary from actual green wood, where some cavities in the wood structure are empty.

Moisture Content and Density

In the range between 7% moisture content and the FSP, an increase of the moisture content by 1% increases the electrical conductivity up to four times (Skaar, 1988), reaching 10^{-3}–10^{-4} $\mathrm{S \cdot m^{-1}}$ at the FSP and increasing the conductivity by a factor of over 10^{10} from the oven-dry condition (Glass and Zelinka, 2010). However, the effect of the moisture content on the electrical conductivity above the FSP is less significant (Skaar, 1988; Stamm, 1929); from the FSP to the complete saturation of wood, the electrical conductivity increases by less than a hundredfold (Glass and Zelinka, 2010). Thus, the conduction of electrical charge depends primarily on the moisture content below the FSP (Brown et al., 1963; Forsén et al., 2000; Skaar, 1988; Stamm, 1927). Although a few studies were done above the FSP (Brischke et al., 2008; Stamm, 1929), they predominantly described the effect of moisture content at room temperature, without covering the temperature range required by phytosanitary treatment (above 56°C). The effect of wood density on electrical conductivity is inconsistent, as other factors such as lignin content have a more significant effect (Skaar, 1988).

2.5 Modelling Heat Transfer in Wood

2.5.1 Governing Equations

The drying process of wood, commonly conventional kiln drying, is explained by two partial differential equations (PDEs): a mass conservation equation (to describe moisture loss during the drying process) and an energy conservation equation (to describe heat transfer in the wood caused by external convection) (Perré and Turner, 1999; Plumb et al., 1985; Stanish et al., 1986). In contrast to wood drying, where wood loses almost all of its moisture, the moisture loss during food sterilization, using the Joule heating effect, is insignificant due to the use of a static heater

that prevents evaporation of the liquid medium; hence, the whole process is described by the equation of energy conservation and an electric charge conservation equation (De Alwis and Fryer, 1992; Marra et al., 2009; Salengke and Sastry, 2007; Zareifard et al., 2003). Perré (2004) modelled Joule heating of green wood, using three governing equations: the mass conservation equation, the energy conservation equation, and the electric charge conservation equation, but this model has not been experimentally verified and validated.

The main purpose of the Joule heating treatment is to ensure complete mortality of pests, with the minimum amount of introduced electrical energy, avoiding internal checking caused by overheating. Hence, the main objective of the treatment is to achieve the successful Joule heating treatment by reducing its duration, expected to be around 10 minutes, and avoiding a significant moisture loss during the treatment - evaporation consumes electrical energy and hence it should be minimised. These conditions allowed exclusion of the mass conservation equation and the evaporation term from the heat conservation equation. Additionally, in the Joule heating method, it is assumed that there is no heat transfer due to internal convection of water within the wood; hence the convection term in the heat transfer equation is equal to zero. Heat caused by the Joule heating effect is generated internally by an electrical power source. As a result, the process of heat sterilization of *P. radiata* green logs is governed by the equations of energy conservation and of electric charge conservation.

The energy conservation equation, without the convection term, is described as (Patankar, 1980):

$$\frac{\partial \rho_g \hbar}{\partial t} = \nabla \cdot (k \nabla T) + \bar{S}, \tag{2.17}$$

where ρ_g is the green density of wood [$\mathrm{kg \cdot m^{-3}}$], $\hbar$ is the specific enthalpy [$\mathrm{J \cdot kg^{-1}}$], T is the temperature [°C], k is the thermal conductivity of wood [$\mathrm{W \cdot m^{-1} \cdot °C^{-1}}$], and $\bar{S}$ is the heat source term [$\mathrm{W \cdot m^{-3}}$] representing electrical heating. For solids, incompressible fluids, and ideal gases:

$$C_p = \left(\frac{\nabla \hbar}{\nabla T} \right)_P, \tag{2.18}$$

where C_p is the specific heat capacity of wood [$\mathrm{J \cdot kg^{-1} \cdot °C^{-1}}$]. Hence, equation 2.17 can be

re-written in the following form:

$$\frac{\partial \rho_g C_p T}{\partial t} = \nabla \cdot (k \nabla T) + \bar{S}. \tag{2.19}$$

The governing equations for electric and magnetic fields are summarised in Maxwell's equations (Fleisch, 2008):

$$\nabla \cdot \boldsymbol{D} = \rho_{\mathrm{v}}, \tag{2.20}$$

$$\nabla \cdot \boldsymbol{B} = 0, \tag{2.21}$$

$$\nabla \times \boldsymbol{E} = -\frac{\partial \boldsymbol{B}}{\partial t}, \tag{2.22}$$

$$\nabla \times \boldsymbol{H} = \boldsymbol{J}_e + \frac{\partial \boldsymbol{D}}{\partial t}, \tag{2.23}$$

where $\boldsymbol{D}$ is the electric displacement field [$\mathrm{C \cdot m^{-2}}$], ρ_{v} is the electric charge density [$\mathrm{C \cdot m^{-3}}$], $\boldsymbol{B}$ is the magnetic flux density [$\mathrm{V \cdot s \cdot m^{-1}}$], or tesla [T], $\boldsymbol{E}$ is the electric field [$\mathrm{V \cdot m^{-1}}$], $\boldsymbol{H}$ is the magnetic field strength [$\mathrm{A \cdot m^{-1}}$], and $\boldsymbol{J}_e$ is the electric current density [$\mathrm{A \cdot m^{-2}}$]. From vector calculus, the divergence of the curl of any scalar field is equal to zero; hence taking divergence of both sides of Equation 2.23 and using Equation 2.20, the continuity of electric charge can be written as:

$$\nabla \cdot \boldsymbol{J}_e + \frac{\partial \rho_{\mathrm{v}}}{\partial t} = 0. \tag{2.24}$$

At a low frequency the electrical capacitance of wood can be assumed to be negligible, and the electric charge density in the wood volume is constant with time (Perré, 2004); therefore, Equation 2.24 can be expressed in a steady-state regime by the Laplace equation, described as

(De Alwis and Fryer, 1992; Marra et al., 2009; Perré, 2004; Sastry and Salengke, 1998):

$$\nabla \cdot (\boldsymbol{J}_e) = 0, \tag{2.25}$$

The electric current density is the product of electrical conductivity and electric field, written as:

$$\boldsymbol{J}_e = \sigma \boldsymbol{E}, \tag{2.26}$$

where σ is the electrical conductivity of wood [$\mathrm{S \cdot m^{-1}}$]. For an anisotropic material such as wood, the electrical conductivity is presented as a second rank tensor ($\overline{\overline{\sigma}}$) to link the vectors of the current density and electric field (Perré, 2004). If the electrical conductivity of wood depends on temperature, then the charge conservation equation and the energy conservation equation must be solved simultaneously (Marra et al., 2009). The electric field can be calculated as:

$$\boldsymbol{E} = \Delta U / l, \tag{2.27}$$

where U is the potential difference across the sample [V], and l is the length of the sample between attached electrodes [m]. If all the heat is assumed to be transferred into the wood, the source term in Equation 2.19 is determined by the following equation (Perré, 2004):

$$\bar{S} = \boldsymbol{J}_e \cdot \boldsymbol{E} = \sigma \boldsymbol{E}^2. \tag{2.28}$$

Alternatively, the source term can be written as:

$$\bar{S} = \frac{P}{V}, \tag{2.29}$$

where V is the volume of the conducting sample [$\mathrm{m^3}$]. Alternatively, the source term can be written as:

$$\bar{S} = \frac{(\Delta U)^2 \sigma A}{V l}. \tag{2.30}$$

2.5.2 Boundary and Initial Conditions

To solve the governing PDEs, initial and boundary conditions must be applied. The initial temperature of a sample is considered uniform and equal to the experimentally measured temperature prior to heating. Mathematically, this statement is expressed as:

$$T_i = T_{exp} \quad \text{at} \quad t = 0 \text{ s}, \tag{2.31}$$

where T_i is the initial temperature, and T_{exp} is the experimental temperature. Assuming no voltage is applied to the sample prior to heating, the electrical potential across the sample is equal to zero:

$$\Delta U_i = 0 \quad \text{at} \quad t = 0 \text{ s}. \tag{2.32}$$

At the electrically insulated surfaces, the boundary condition of the heat equation at the external surface of the sample is written as:

$$\boldsymbol{J}_h \cdot \widehat{\boldsymbol{n}} = h(T - T_a) \quad \text{at} \quad t > 0 \text{ s}, \tag{2.33}$$

where $\boldsymbol{J}_h$ is the heat flux [$\mathrm{W \cdot m^{-2}}$], $\widehat{\boldsymbol{n}}$ is the unit normal vector, h is the heat transfer coefficient [$\mathrm{W \cdot m^{-2} \cdot {}^{\circ}C^{-1}}$], T is the temperature of the sample's surface, and T_a is the ambient temperature, surrounding the sample. The boundary condition of the Laplace equation can be written as:

$$\boldsymbol{J}_e \cdot \widehat{\boldsymbol{n}} = 0 \quad \text{at} \quad t > 0 \text{ s}. \tag{2.34}$$

An additional boundary condition needs to be specified at the contact with electrodes (Perré, 2004)

$$\Delta U = U(t) \quad \text{at} \quad t > 0 \text{ s}, \tag{2.35}$$

where $U(t)$ is the voltage recorded across the sample. The experimental voltage can vary with time to control the generated heat and to avoid significant overheating.

2.6 Thermal Properties of Wood

There are two thermal constants in Equation 2.19 (k and Cp) that must be accurately assessed in order to correctly simulate heat transfer in *P. radiata*. According to Kollmann and Cote (1968), heat capacity depends substantially on moisture content of wood and can be described by:

$$C_p = \frac{XC_{p\,water} + C_{p\,(o.d.)\,wood}}{1+X}, \tag{2.36}$$

where $C_{p\,water}$ is the heat capacity of water, about 4180 [$J \cdot kg^{-1} \cdot °C^{-1}$] (Incropera and David, 2002), and $C_{p\,(o.d.)\,wood}$ is the average heat capacity of oven-dry wood which is about 1360 $J \cdot kg^{-1} \cdot °C^{-1}$ in the temperature interval from 0°C to 100°C (Desch and Dinwoodie, 1996; Stamm, 1964; Radmanović et al., 2014). Temperature has a significant effect on the heat capacity of wood (Dunlap, 1912; Koch, 1968), while density and the wood species have a less pronounced effect (Kollmann and Cote, 1968; Sonderegger et al., 2011). Hence, the dependence of mean heat capacity of 20 wood species on temperature can be expressed as (Sonderegger et al., 2011; Radmanović et al., 2014):

$$C_{p\,(o.d.)\,wood} = 1114 + 4.86T, \tag{2.37}$$

where T is temperature [°C]. However, this equation is only applicable for oven dry wood. According to Dupleix et al. (2013), in the green state, the heat capacity values of softwoods and hardwoods are different. Furthermore, Dupleix et al. (2013) derived empirical equations of heat capacity as a function of moisture content per the radial and tangential directions; that contradicts the earlier studies, where heat capacity was considered independent of the anisotropic structure (Kollmann and Cote, 1968; Sonderegger et al., 2011). Dupleix et al. (2013), however, did not explain the dependence of heat capacity on the grain orientation.

Thermal conductivity depends on density and grain orientation (Dupleix et al., 2013; Sonderegger et al., 2011). The average of the radial and tangential thermal conductivities of oven-dry Douglas fir is 0.10 $W \cdot m^{-1} \cdot °C^{-1}$, while the average longitudinal thermal conductivity is 0.28 $W \cdot m^{-1} \cdot °C^{-1}$ (Desch and Dinwoodie, 1996). Thermal conductivity also varies with moisture content. The value almost doubles when moisture content increases from 10 to 100%. Different equations of thermal conductivity and heat capacity have been found for wood in the different

studies (Table 2.1).

Table 2.1. Equations of thermal conductivity and heat capacity from other studies, as a function of temperature and/or wood parameters.

Literature	Predicting Equations [a]	Conditions
Dupleix et al. (2013)	$k^R = 0.002X + 0.130$ $k^T = 0.001X + 0.137$ ${C_p}^R = 0.0032X - 0.311$ ${C_p}^R = 0.0030X - 1.540$	Green Wood Spruce T = 20°C
Nijdam et al. (2000)	$k = \frac{(0.26+X)^{0.95}}{1+X}[0.0035X(T-273.15)+0.53]\times$ $(1.7\frac{\rho_s}{1000}+0.16)$ $C_p = \frac{(0.219+X)^{0.781}}{1+X}[8.5(T-273.15)+5300]$	*P. radiata* High Temp. Drying
Pang et al. (1995)	$k = \frac{\rho_s}{1000}(0.4+0.5X)+0.024$ $C_p = 4184\frac{X+0.324}{1+X}$	*P. radiata* High Temp. Drying
Perré and Turner (1999)	$k^T = 0.142 + 0.46X$ $k^R = 2k^T$ $k^L = 2k^T$ $\overline{\rho C_p} = \rho_s(1113 + 4.8T + 4185X)$	Soft Wood Low and High Temp. Drying
Yu et al. (2011)	$k = 01425 + 0.094X$	Larch $MC < 25\%$ [b]

[a] The indices R, T, and L denote the radial, tangential and longitudinal directions, respectively.
[b] Moisture content

Two studies, done by Nijdam et al. (2000) and by Pang et al. (1995), investigated drying of New Zealand grown radiata pine using computational and experimental approaches. Nijdam et al. (2000) used a heat capacity equation as a function of moisture content and temperature and an equation of thermal conductivity as a function of moisture content, temperature, and basic density. Pang et al. (1995), however, did not consider the effect of temperature on the wood's thermal properties. Haque (2007) simulated high temperature wood drying of *P. radiata* boards inside a kiln using the formulae for thermal conductivity and heat capacity published by Nijdam et al. (2000), Pang et al. (1995), and Haque and Langrish (2001). He found that the simulated average moisture content of wood during drying did not change significantly (less than 4.5%) using these different sets of formulae. Haque (2007), therefore, concluded that the effects of heat capacity and thermal conductivity on the overall drying rate were negligible. Olek et al. (2003) solved the PDE of heat conduction with the various thermal conductivities provided by

different authors in a validation exercise; it was found that the most inaccurate temperature prediction was obtained using a constant thermal conductivity. Including moisture content and temperature dependence for the thermal conductivity was found to improve the accuracy of the prediction.

2.7 Computational Modelling

There is no analytical solution to solve energy and electric charge conservation equations (Equation 2.17 and 2.25) that will adequately describe the complex process of electrical heating of green wood. Therefore, a numerical approximation needs to be implemented. A principal concept of the numerical approximation is to discretize a PDE into a set of linear equations. The numerical approximation has three main methods of discretization that are widely used in different engineering fields: the finite difference method (FDM), the finite volume method (FVM), and the finite element method (FEM). Any of these methods could be used for computational modelling of Joule heating in order to perform large numbers of simulations, with relatively low cost, in a short time (the speed and complexity of simulation being limited by the computer's performance). FDM, the oldest discretization method, is based on the Taylor series expansion and uses a grid to discretize the calculation domain and the grid's points to obtain results (Patankar, 1980). FEM is based on discretization of the calculation domain into triangular elements (Patankar, 1980) that gives flexibility to handle complex geometries, particularly common in structural mechanics, but it has difficulties in describing heat transfer and fluid flow, such as the upwind nature of convection (Patankar, 1980). FVM uses control volumes (a grid point is located within each control volume) to discretize the calculation domain, and a governing differential equation is integrated over each control volume (Patankar, 1980). FVM can handle more complex geometries than FDM in heat transfer and fluid flow problems (Peiró and Sherwin, 2005). Today, there is a varied range of commercial CFD codes that are based on FVM, such as ANSYS CFX. The main advantage of them is they have a user-friendly Graphic User Interface (GUI) and robust solver. Providing relatively fast and stable convergence, they produce accurate numerical results and solve different physical problems: fluid dynamics, structural mechanics, and electromagnetism. Generally, commercial CFD codes have a computer-aided design (CAD) geometry modeller and meshing tool, making the generation of complex three dimensional geometries easier. The main drawback of commercial codes, however, is their

relatively expensive licence, potentially economically unviable for projects with small budgets.

2.8 Summary

The literature review shows that there are four studies directly related to Joule heating of wood. Three of them used an entirely experimental approach (Fleischer and Downs, 1953; Lutz, 1960; Heffernan, 2009) and the other was based on computational analysis (Perré, 2004). Fleischer and Downs (1953) and Lutz (1960) did not control electric power, causing it to rise throughout the experiment, potentially resulting in internal checking. Hence, in this research, log heating will be controlled by reducing the applied voltage whenever electrical resistance of a log decreases, as described by Heffernan (2009). Perré (2004) assumed that electrical conductivity of green wood depends significantly on moisture content and is independent of temperature; however, this contradicts Stamm's (1929) work, which stated that, at moisture content above 100%, electrical conductivity of wood is independent of moisture content. In this research, electrical conductivity of green *P. radiata* will be measured experimentally, as it has not been well-studied, concentrating on the effect of temperature on electrical conductivity. Wood thermal properties, thermal conductivity and heat capacity, were measured experimentally in earlier studies and were expressed as a function of temperature and/or moisture content and basic density (Nijdam et al., 2000; Pang et al., 1995). Therefore, the goal of this part of the research is to find the most adequate heat capacity and thermal conductivity equations that can accurately predict heat transfer within *P. radiata*. In addition, there is no international phytosanitary standard applicable for logs treated using heat treatment. However, from ISPM 15 (IPPC, 2016a) and previous studies, the temperature of 56°C for 30 minutes is lethal for most wood pests and hence provides a sensible target.

Thus, the existing published knowledge, the gaps which have been filled and the successful combination of the two in this work can be stated as:

1. The log heating CFD model, to be developed in Chapter 7, will require green *P. radiata's* thermal conductivity, heat capacity, and electrical conductivity. Potentially, these variables will be expressed as a function of temperature and/or other wood parameters such as moisture content, basic density, and grain orientation.

2. Thermal conductivity and heat capacity have been reported in earlier studies, specifically

for *P. radiata*. Therefore, comparing those reported values, the best thermal properties which provide the most accurate prediction of heat diffusion in green *P. radiata*, will be selected for the log heating CFD model.

3. Electrical conductivity as a function of temperature, moisture content, basic density, and grain orientation has not been reported at moisture content much above fibre saturation for any timber and certainly not for *P. radiata*. The most closely related study, done by Stamm (1929, 1960), described the effect of moisture content on electrical conductivity of wood at a room temperature for *Pinus elliottii* and *Sequoia sempervirens*. Thus, in this research, electrical conductivity of green *P. radiata* will be determined using experimental testing and its correlation with temperature and wood properties will be assessed.

4. Up to date, a specific international phytosanitary standard designed for logs does not exist. Therefore, the experimental testing will be governed by the process conditions required by ISPM 15 - the minimum temperature of 56°C and the minimum time duration of 30 minutes. However, these conditions may be changed in this work if parallel research conducted by Scion leads to the adoption of a different heating standard for export logs.

Chapter 3

Joule Heating of Radiata Pine Boards

3.1 Introduction

In the previous studies by Fleischer and Downs (1953); Lutz (1960); Heffernan (2009), the authors used logs in their experiments and measured the log temperature using thermocouples and/or thermometers. In each study, formation of cold and hot spots within heated logs has been described. However, thermocouples and thermometers measure temperature at discrete points within a log, without giving full information of temperature distribution. In this study, flat boards of green *P. radiata* were heated using the Joule heating method and their temperatures were measured using a thermal imaging technique. This method revealed the internal temperature distribution, not normally observable, when a log is heated. The effects of moisture content and of basic density on the temperature rise of the boards were investigated. This chapter describes the methods and assumptions considered in the experiments, showing the obtained results with the discussions that guided the rest of the research.

3.2 Method

3.2.1 Sample Selection

The freshly sawn beams of *P. radiata* used for this research were provided by McVicar Timber Group Ltd, Christchurch, New Zealand. These boards were cut into pieces about 500 mm long and then stored inside plastic bags. To prevent wood from drying and maintain a constant vapour pressure inside the bags, a small amount of tap water was added to each bag. The bags were then sealed using duct tape, and put into a freezer at -18°C. Prior to the experiment, the external surfaces of the board, about 4 mm from the edge, were removed by trimming the surface on a table saw. A length of 12.5 mm was removed from each end of the board to make the total board's length 475 mm. Thereafter, using the table saw, the board was cut into thinner boards 10 mm

in thickness and then labelled, specifying the type of wood (pure sapwood, pure heartwood, and transitional, with co-existing sapwood and heartwood parts) and the face of the board that would be facing an infrared camera. The final dimensions of the boards used in the experiments were 475 mm long (always longitudinal), 100 mm wide (radial), and 10 mm thick (tangential). In order to ensure gentle de-frosting, the 10 mm thick boards were kept in a sealed plastic bag inside a fridge at 4°C for a day before Joule heating. The boards were always transported inside the bag to avoid moisture loss and were taken out of the bag just before an experiment. The total number of the studied boards were 19: nine transitional, six heartwood, and four sapwood boards.

3.2.2 Calibration of Infrared Camera and Measuring Wood Emissivity

The main benefit of the infrared camera for measuring board temperature during Joule heating is that it takes pictures of the whole board's surface, while thermocouples can measure the temperature of particular points on or inside the board. However, the infrared camera does not measure temperature inside the board and, if the board has a substantial thickness, there will be a temperature gradient within the board. On the other hand, the use of thermocouples is not practical, since it would be impossible to accurately determine local temperature distribution, including hot and cold spot formation. As a result, the temperature of the boards during Joule heating was measured using an infrared camera, manufactured by Wuhan Guide Infrared Co. Ltd., model EasIR-9.

To obtain accurate results from the infrared camera, the emissivity of the studied material must be known. The emissivity is the ratio of the emitted energy from the surface of the studied material to the emitted energy from an ideal black body at the same temperature (Cengel, 1998). There are different methods to determine emissivity, such as a non-contact thermometer, using a standard emitter with known emissivity at the same temperature as the studied material, or a contact thermometer, measuring the temperature of the studied material by a thermocouple and infrared camera. Both of these methods are approved by the American Society for Testing and Materials (ASTM) (ASTM E1933-14, 2014; Lopez et al., 2013; Madding, 1999). In this research, the first method with a reference emitter was used, where the reference material was a 3M Scotch Super 88 vinyl electrical tape (054007-06143), with a constant emissivity of 0.95 (Madding, 1999). This method assumes that the temperature of the reference material is equal to the temperature

of the tested material.

To measure emissivity more precisely, the temperature measurement was performed by two different infrared cameras: a Fluke infrared camera, model Ti20, as well as the Guide EasIR-9 infrared camera. Prior to using the cameras for the emissivity experiment, they were compared by taking pictures and video shots of a board's surface, fully coated by the electrical tape as shown in Figure 3.1a. The board was 100 mm long, 50 mm wide, and 10 mm thick. It had been

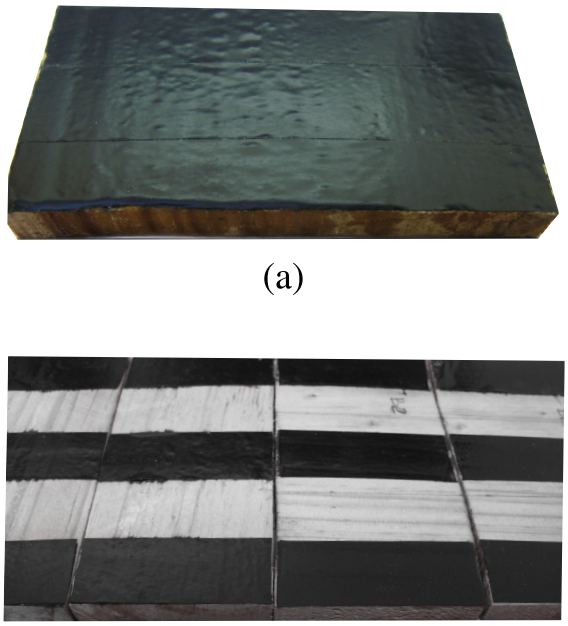

Figure 3.1. The samples used to calibrate the thermal camera and to determine the emissivity of *P. radiata*: (a) the fully coated surface of the board and (b) the partially coated boards.

put into the oven for 2 h at 80°C before the measurement. The thermal cameras were put 1 m away from the heated board for the measurement. Humidity and ambient temperature of the room, where the thermal pictures and videos were taken, were measured using a thermometer and a whirling hygrometer. The obtained data (48.5% RH and 19°C) and the emissivity value of the electrical tape were entered in the thermal cameras. When the board was taken out of the oven, it was positioned in front of the cameras, where the Guide camera made a video recording, and the Fluke thermal camera took infrared images every 30 s. In a single run of the experiment, the total duration of the Guide thermal video recording was 180 s, while the total number of measurements by Fluke camera was seven, recorded with a 30 second resolution. Overall, the experiment was repeated seven times.

After ensuring that the thermal cameras showed similar temperatures of the fully coated board,

four *P. radiata* boards 100 mm long, 50 mm wide, and 10 mm thick were used in the emissivity testing. Two of these boards were oven-dry wood, while the other two were green wood. The electrical tape was put on the surface of each board as shown in Figure 3.1b. These boards were then left inside the oven for 2 h at 80°C. A single board was taken out at a time. The board was positioned on a table in front of the cameras, and pictures and video recordings were taken. The experiment was repeated twice with each board, with the duration of each experiment being 120 s. The boards' cooling was measured every 30 s using the Fluke thermal camera and recorded by the Guide infrared camera. Madding (1999) advised to set an infrared camera to measure radiance - the radiant flux emitted, received, or reflected by a surface per unit projected area and per unit solid angle, $[\mathrm{W}\cdot\mathrm{sr}^{-1}\cdot\mathrm{m}^{-2}]$ (Wolfe, 1998), but neither the Fluke nor the Guide infrared camera supported a radiance mode. Hence, the temperature was measured in degrees Celsius and then, using the Sakuma Hattori equation (Equation 3.1), expressed in Planckian form (Fluke Corporation, 2011), the obtained temperature was converted into radiance, as follows:

$$L = \frac{C}{\exp\left[\frac{C_2}{A(T+273.15)+B}\right]-1}, \tag{3.1}$$

where L is radiance $[\mathrm{W}\cdot\mathrm{sr}^{-1}\cdot\mathrm{m}^{-2}]$, C_2 is the second radiation constant equal to 1.44×10^4 µm·K, T is the temperature [°C], C, A, and B are constants for the 8-14 µm band (Fluke's spectral range 7.5-14 µm and Guide's 8-14 µm) and equal to 1.000, 9.364 µm, and 178.4 µm·K, respectively.

Using the software provided with the cameras, the first image at the zero time (Figure 3.2a) of each experiment was extracted to a CSV file, where each pixel was represented as a temperature point (Figure 3.2b). Knowing the length and height of the board in pixels, the exact position of the tape and wood surfaces were determined. After the average temperature of the tape and wood surface were calculated, and using the following equation provided by Madding (1999), the emissivity of wood was obtained:

$$\varepsilon = \frac{L_T - L_B}{L_R - L_B}\varepsilon_R, \tag{3.2}$$

where ε is the emissivity, indices T, R, and B denote target material (the wood), reference material (the electrical tape), and background respectively.

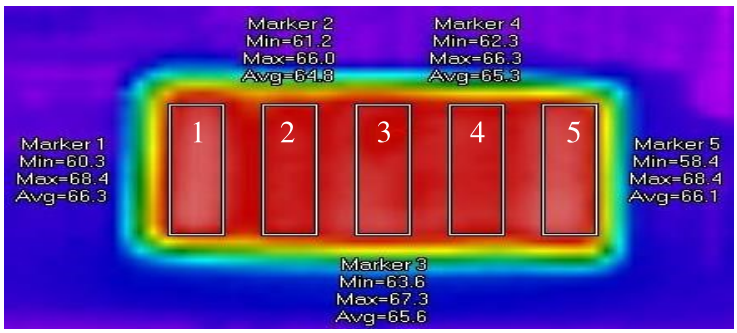

(a)

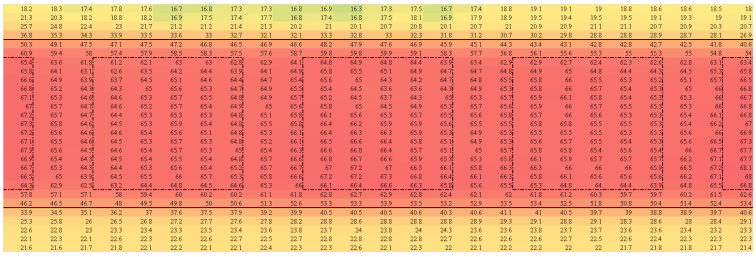

(b)

Figure 3.2. (a) The image obtained from the Fluke infrared camera, where markers 1, 3, and 5 represent the electrical tape and markers 2 and 4 represent wood, (b) the markers highlighted in the CSV file.

3.2.3 Experimental Set-Up and Procedure

Heating Process

Each board was weighed before and after the experiment to determine any loss of moisture during the Joule heating process. The boards' end faces (100mm×10mm) were covered with a special electrolyte conductive gel with high electrical conductivity to reduce contact resistance between the wood surface and the electrodes. Then, the boards were tightly clamped between the high voltage and low voltage electrodes by using spring pressure. Each electrode consisted of four aluminium segments placed in a vertical array (Figure 3.3). Once the boards were positioned into the Joule heating rig, a sinusoidal AC voltage (for these experiments the maximum electric field strength was around 5,000 $V \cdot m^{-1}$) at 400 Hz was supplied through a 12.5 : 1 set-up transformer by a programmable electrical source, Chroma 61504. Using an electrical controller to prevent runaway temperature rise, the supplied power was controlled, and if it reached 500 W, the voltage decreased automatically. Hence the power remained in a dead-band from 480 W to 520 W with the increase of the electric current (Figure 3.4). The electric current was measured at each segment of the electrodes as well as for the whole supply. The voltage across the board was measured and recorded using a power quality and energy analyser, Fluke 435 Series II, as

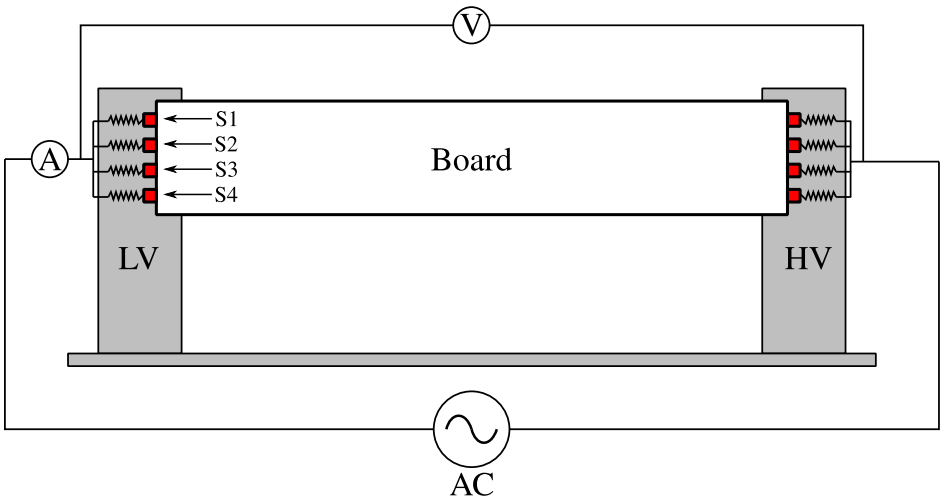

Figure 3.3. The schematic diagram of the experimental set-up of the flat-board experiment, where A, V, AC, LV, and HV denote an ammeter, a voltmeter, an electric source, low voltage and high voltage electrodes, respectively. Note: The four red parts attached to each end of the board are the electrodes' segments (S1-4).

well as a Pico data logger. The temperature rise of the boards was monitored using the Guide infrared camera, EasIR-9. The time of the experiment and the end of heating were measured by a stopwatch. In general, the experiments ended when supplied energy was about 35 W·h (126 kJ). However, to prevent pressure build up within the wood board, the maximum allowable surface temperature for the board was restricted to 90°C. The experiment was terminated if the indicated temperature exceeded this limit. After heating, the board was allowed to cool down and then put back into the plastic bag and sealed with duct tape. The sealed bag was then put into the fridge until further processing was required.

Processing Thermal Images

The video file with the recorded wood heating and cooling images was then uploaded to a PC. Using the Launch Guide IrAnalyser software (Wuhan Guide Infrared Co. Ltd), the thermal image at the end of heating was selected as a standard and analysed. Areas of similar surface temperature were identified and partitioned on each wood board (Figure 3.5a). If high temperature gradients appeared, such as those associated with localised hot and cold spot formation, partitioned areas were allowed to have some degree of uneven temperature distribution, to enable the rest of the blocks to have uniform temperature distributions. The target was to keep the deviation of temperature in a partitioned area of interest to within 10% of the mean value. In order to fulfil the target and calculate the standard deviation of the temperature within each area, the thermal image had to be exported into Excel, because the software only provides the

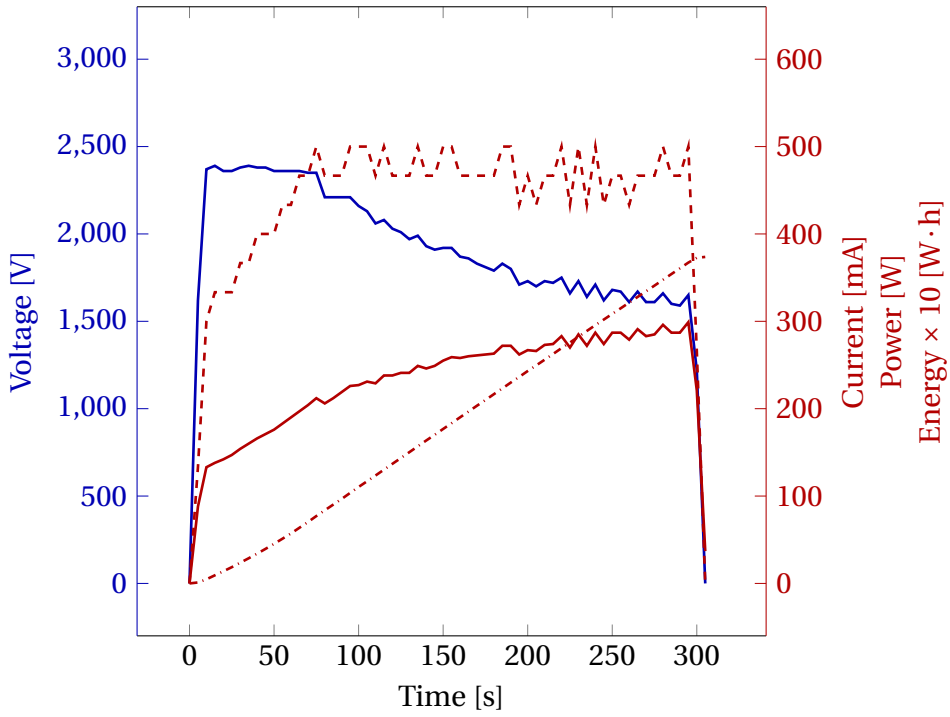

Figure 3.4. The electrical data of a typical flat-board's heating, where: the blue solid line denotes the voltage and the red solid, dashed, and dash-dotted lines denote the electric current, the power, and the energy, respectively.

minimum, average, and maximum values of temperature. When the temperature profile was converted to an Excel file, a distance of 6 mm from each end of the board was not considered, as these parts of the board were hidden from the camera behind the plastic supports of the test rig. Using the pixel coordinates provided by the software, the outlines of the partitioned areas were drawn in the Excel file, and then the pattern was transferred onto the surface of the board, and the board was sawn accordingly into blocks (Figure 3.5b – d).

Analysis of Wood Properties

All blocks were analysed for moisture content and basic density. To obtain accurate weight measurement, the edges were sanded to remove loose splinters from cutting. Each block was weighed with a 10 mg resolution to determine green mass. The green volume of each block was determined by the liquid displacement method, where the samples were submerged in a bucket of water placed on a tared balance. The mass shown on the tared balance represented the volume of water displaced by submerging the block, equal to the block's volume. Knowing the temperature of the water, the volume of displaced water was calculated using the obtained mass divided by the water density calculated using the Rackett equation (Kleiber and Joh, 2010;

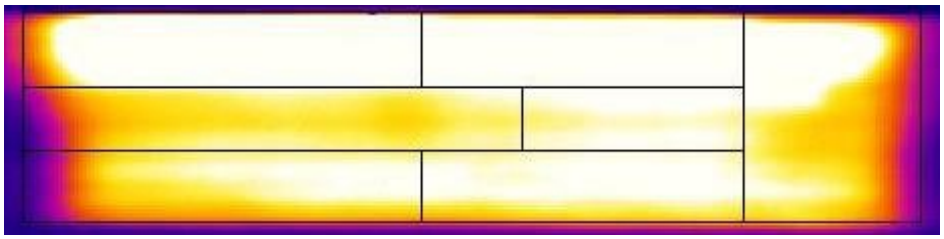

(a)

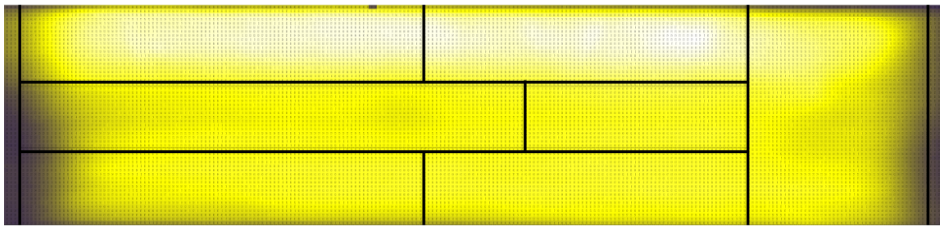

(b)

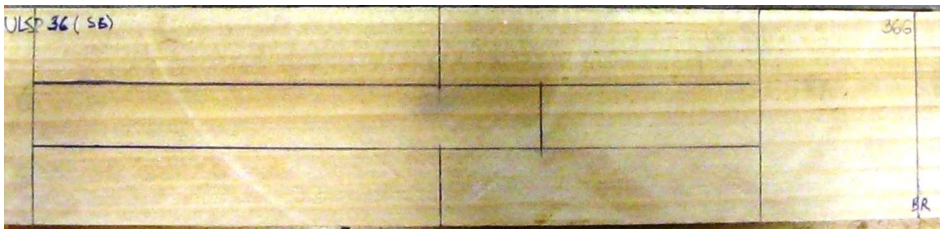

(c)

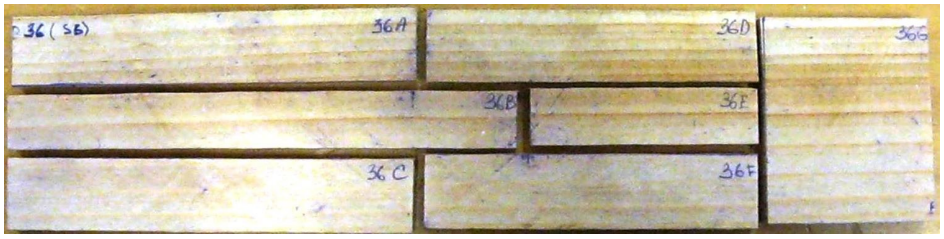

(d)

Figure 3.5. The principle of dividing the board into blocks based on temperature distribution: (a) the thermal image taken at the end of the Joule heating, (b) the formatted Excel file, (c) the pattern transferred on the boards' surface, and (d) the board cut following the pattern.

Poling et al., 2008):

$$\rho_{water} = \frac{A}{B^{1+\left(1-\frac{T+273.15}{C}\right)^{D}}}, \tag{3.3}$$

where A, B, C, and D are coefficients equal to 1.5053957, 0.03642, 617774, and 0.05871, respectively. Thereafter, the blocks were dried in an oven at 105°C until constant weight (ASTM D4442 - 16, 2016). Thereafter, the blocks were weighed at low relative humidity condition and their basic density and moisture content were determined, using Equation 2.1 and 2.2, respectively.

3.3 Results and Discussions

3.3.1 Calibration Results

The results from the Fluke and Guide infrared cameras, presented in Figure 3.6 and Appendix A.1, showed close agreement. The difference between the cameras with the mean value

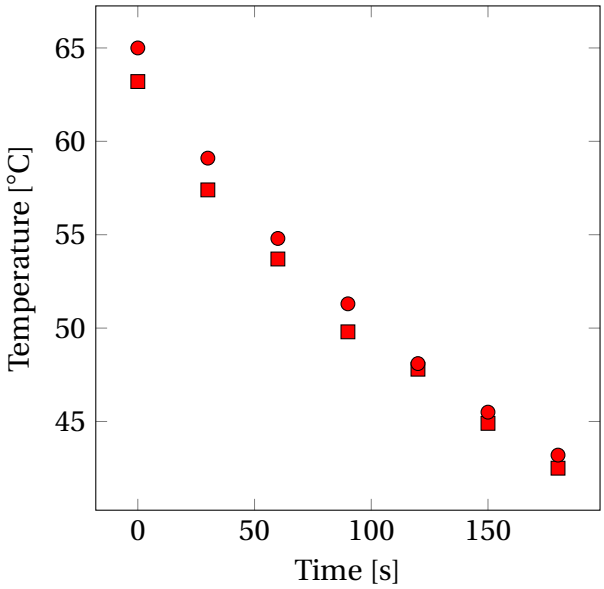

Figure 3.6. Temperature of the board's surface, fully coated by the electrical tape, measured by the Fluke and Guide infrared cameras, in the first test. The squares and circles represent results from the Fluke and Guide cameras, respectively.

of 1.0°C and standard deviation from the mean of ±0.7°C can be explained by the accuracy of both cameras, ±2°C or ±2%, whichever is greater, (Fluke Corporation, 2006; Wuhan Guide Infrared Co. Ltd., 2010), and some delay in pulling the trigger of the Fluke camera during the experiments. The difference was within the accuracy range of both cameras, so the cameras were used to determine the emissivity of *P. radiata*. Figure 3.7 shows a graph of temperature versus

apparent emissivity, where the apparent emissivity of wood decreases with temperature. Lopez

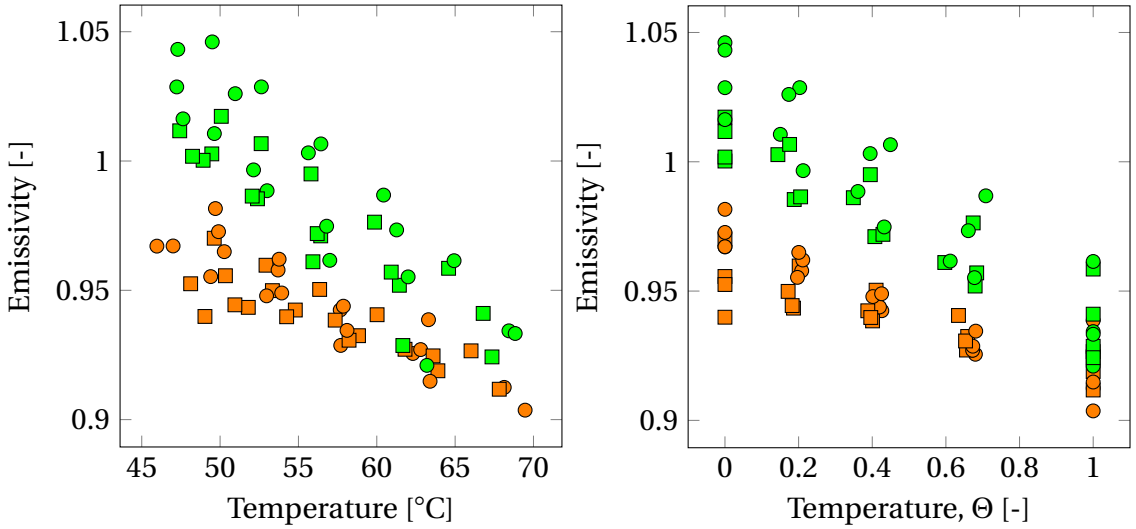

Figure 3.7. The correlation between the board's surface temperature and its emissivity (*left*) and rescaled, dimensionless temperature, Θ, of that surface versus the emissivity (*right*). The squares represent results obtained by the Guide camera, while the circles denote results using the Fluke camera. Green and orange are green wood and dry wood, respectively. Note: $\Theta = \frac{T - T_{min}}{T_{max} - T_{min}}$, where T is the temperature of the board, T_{max} and T_{min} are the maximum and minimum temperatures during recording.

et al. (2013) studied the apparent emissivity of wood from -25°C to 60°C and found a similar correlation. It should be noted, however, that the apparent emissivity of green boards at 50°C, measured using the Guide thermal imager, and some apparent emissivity values of green wood, measured by the Fluke camera, were greater than unity. The dry-wood emissivities were less than unity for both cameras.

In practice, however, an emissivity greater than unity is non-realistic. According to Equation 3.2, the apparent emissivity would be greater than unity if the wood temperature became hotter than the temperature of the tape. A reason for an apparent emissivity higher than unity is the tape possibly cooled down faster than the green wood surface, after the wood was removed from the oven. As the green wood has a greater heat capacity than dry-wood, the same effect did not occur in the dry-wood samples – i.e., the green wood samples contain more heat than dry-wood, at the same temperature, and cool down more slowly.

3.3.2 Joule Heating

The results of the Joule heating showed non-uniform temperature distribution inside the green *P. radiata* boards. Figure 3.8 shows different temperature rises of the blocks within one of the nine transitional boards (TB3). The blocks with slower temperature rise were from the

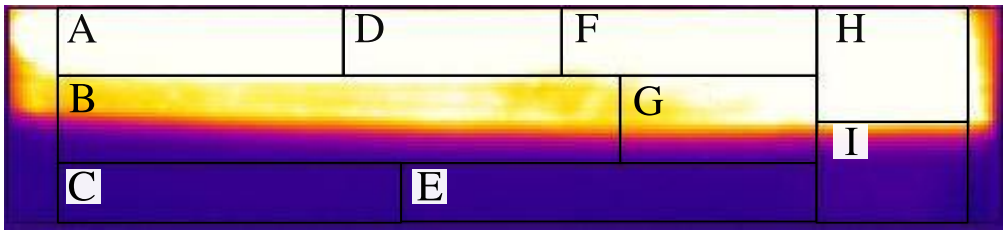

(a)

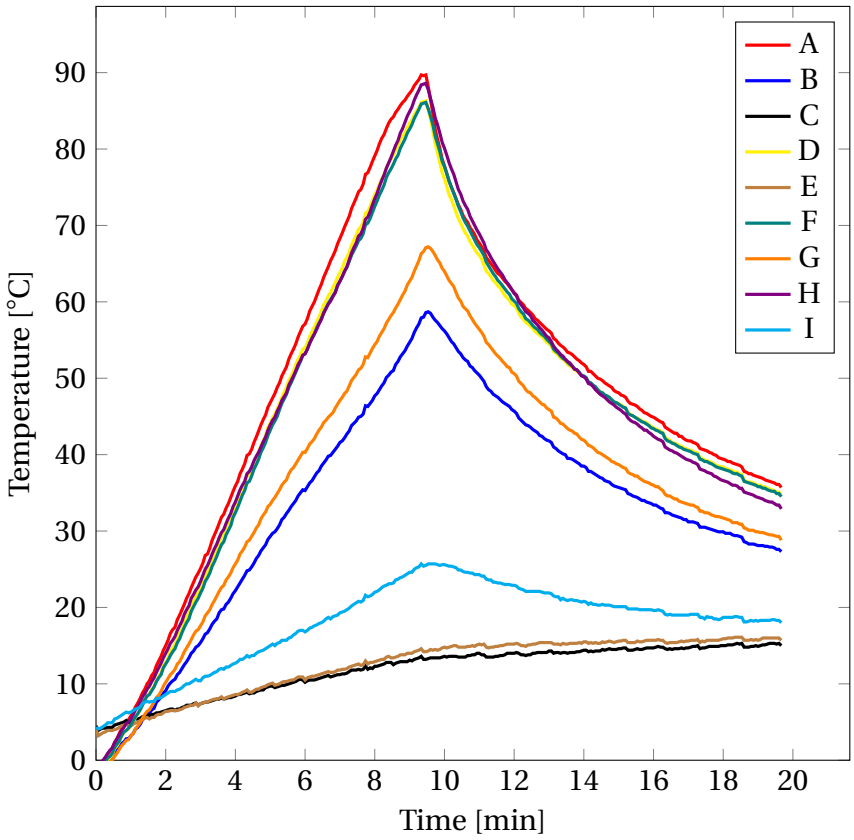

(b)

Figure 3.8. Transitional Board #3 (TB3): (a) the segmented thermal image taken at the end of heating and (b) the average temperatures of each segment throughout the experiment.

heartwood part of the transitional board, while the faster temperature rise was common to the blocks from the sapwood part. At the end of heating, the temperature difference between the sapwood and heartwood parts reached 70-80°C. Similar results were obtained for the other transitional boards (Appendix A.2.1).

The electrical data for TB3 (Figure 3.9), recorded by the Fluke 435, showed a constant voltage throughout the whole heating phase, as the electric power did not reach 500 W (similar results for the other transitional boards are given in Appendix A.2.2). The electrical current increased with

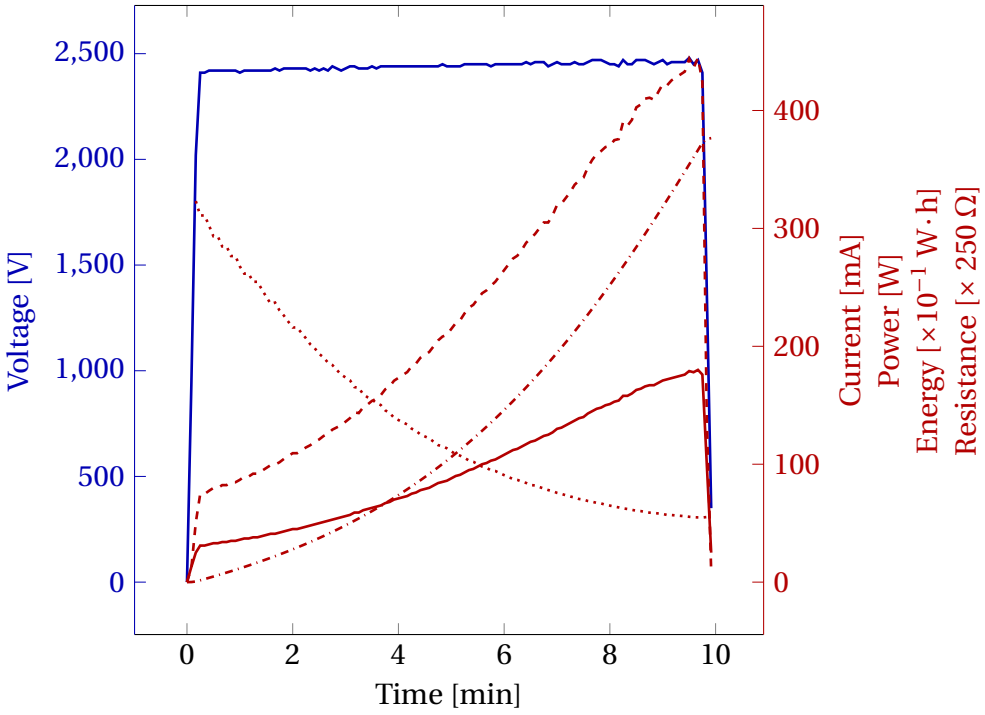

Figure 3.9. The electrical data of the TB3 transitional board during Joule heating. The blue solid line denotes the voltage and the red solid, dashed, dash-dotted, and dotted lines denote the electric current, the power, the energy, and the electrical resistance respectively.

temperature, indicating a strong effect of temperature on the electrical conductivity of wood (Skaar, 1988). Unlike metals, the electrical conductivity of which decreases with temperature, such behaviour is common to ionic solutions, where temperature increases the mobility of ions and hence improves the conductivity of a solution (Bard and Faulkner, 2001). Temperature rise and electrical data for sapwood boards (SB1-4) and heartwood boards (HB2-6) are also given in Appendices A.2.1 and A.2.2, respectively; the temperature recording of HB1 was corrupted.

During Joule heating of the sapwood boards, the electrical power controller reduced the voltage to keep the power in the dead-band, indicating the high electrical conductivity of these boards. Reduction of voltage was not observed during the heating of transitional or heartwood boards.

In general, the sapwood boards were the most electrically conductive, and, as a result, they heated faster than heartwood and transitional boards. For output power of 500 W with maximum electric field of 5000 $V \cdot m^{-1}$ the average Joule heating rate of the pure sapwood boards was about 11 $°C \cdot min^{-1}$, while the average heating rate of the heartwood boards was around 1 $°C \cdot min^{-1}$. The four segments of each electrode showed that, in the transitional boards, the electric current predominantly flowed through the sapwood part (Figure 3.10).

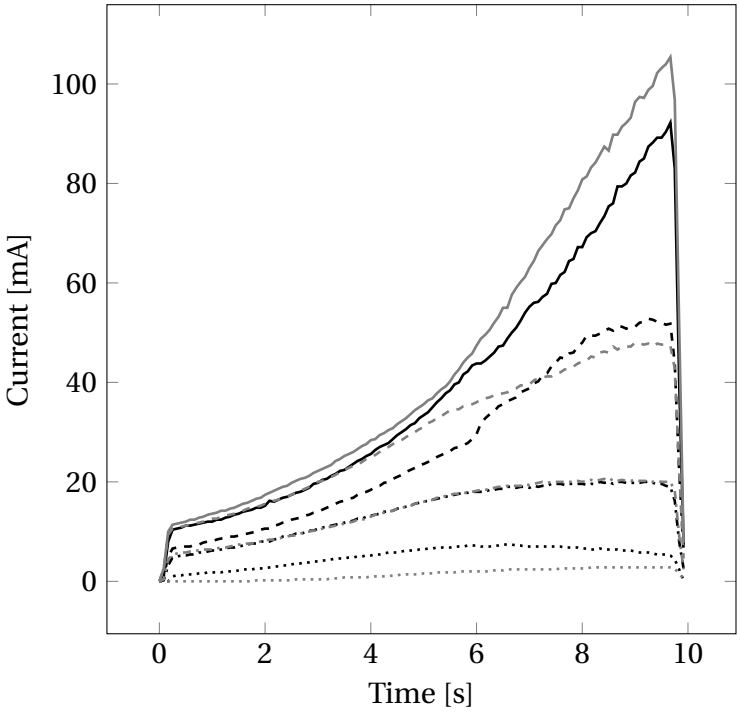

Figure 3.10. TB3. The electrical current flowed through each segment from the high voltage side (the black lines) to the low voltage side (the grey lines) side. The solid, dashed, dash-dotted, and dotted lines denote four segments from the top to bottom, respectively.

The pure heartwood boards showed relatively high resistance and were heated less than the sapwood and transitional boards. Since hot and cold spots did not develop on the surfaces of the heartwood boards, the whole surface of each pure heartwood board pointing at the thermal imager was considered to be one single block (Figure 3.11). The electrical resistance of the pure heartwood boards did not change notably over time and was significantly higher than the resistance of the other boards. Therefore, within a similar duration of Joule heating, the energy introduced to the heartwood boards was about an order of magnitude lower than that introduced to the transitional boards. To increase power dissipation within heartwood boards and enhance the Joule heating rate, the voltage across the heartwood boards should be increased. However, in a stem, the heartwood section co-exists with the sapwood. Thus, voltage applied to a log's

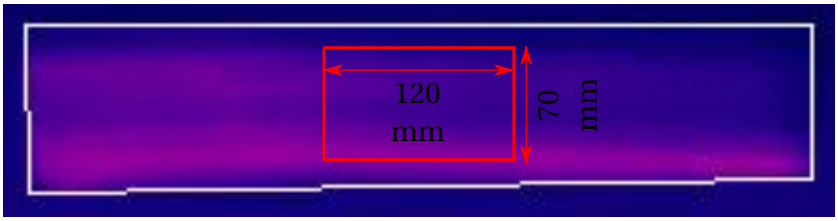

Figure 3.11. The thermal image of the typical heartwood board, taken at the end of heating. The white frame shows the approximate edges of the board and the red frame illustrates the part of the board used for the moisture content and basic density analysis. *Note:* The board's edges are not straight, as the camera was inadvertently under a small angle to the ground.

surface will drive an electric current through the sapwood section and an increase in the voltage will increase the power dissipation in the sapwood.

The average moisture content and basic density of the blocks cut from the heartwood, transitional, and sapwood boards are summarised in Table 3.1. The pure heartwood boards and

Table 3.1. The basic density (ρ_s) and moisture content (X) of the heartwood, transitional, and sapwood boards.

Wood Type	X [kg·kg^{-1}][a]	ρ_s [kg·m^{-3}][a]
Pure Heartwood	0.32±0.03	443±19
Transitional (Heartwood)	0.30±0.02	385±20
Transitional (Sapwood)	0.9±0.1	450±18
Transitional (Dry-Zone)	0.44±0.08	431±11
Pure Sapwood	1.2±0.1	467±26

[a] All the values are shown as the average value with the standard deviation (±) .

heartwood sections of the transitional boards had comparable moisture contents of about 32% and 30%, respectively. At these moisture contents, equal to *P. radiata's* FSP, most of wood's cavities are filled with air and vapour Harris (1991c). Air and vapour are poor conductors and hence they create barriers for an electric current flow, decreasing wood's electrical conductivity. The experimental results showed that, at approximately 15°C, electrical conductivity of the pure heartwood boards lay within a range of 0.001-0.002 S·m^{-1}. This is similar to the data stated by Skaar (1988), where electrical conductivities of wood at the FSP varies within a range of 0.001-0.0001 S·m^{-1}. Electrical conductivity of the transitional boards' heartwood sections cannot be calculated, as the exact cross-sectional area that conducted an electric current is unknown. Nonetheless, the transitional boards' heartwood electrical conductivity can be assumed to be similar to that of the pure heartwood boards.

Without the known cross-sectional area, electrical conductivity of the transitional board's sapwood and dry-zone (a relatively thin region between sapwood and heartwood) parts cannot be calculated. However, their moisture contents are higher than that of the heartwood and hence the electrical conductivity should be higher than the heartwood's electrical conductivity (Skaar, 1988; Stamm, 1929). The average moisture content of the pure sapwood boards was around 120%. At this moisture content, most of wood cavities are filled with sap, which is a much better conductor than air and vapour. This makes sapwood more electrically conductive than heartwood. The experimental results showed that, at around 15°C, the electrical conductivity of the pure sapwood boards was approximately 0.03 $S \cdot m^{-1}$, being 30 times higher than that of the pure heartwood boards. According to (Skaar, 1988), electrical conductivity increases by the maximum of hundred-folds from the FSP to complete saturation. The average electrical conductivity of the four sapwood boards increased to 0.075 $S \cdot m^{-1}$ at about 55°C.

In addition, all the transitional boards showed the abrupt temperature change between the heartwood and sapwood parts of the transitional boards, Figure 3.8 and Appendix A.2.1, indicating that the heat conduction across the dry-zone is low. Furthermore, the results showed that the heartwood parts of Boards TB1, TB2, and TB7 were heated much faster than those in the other transitional boards and the pure heartwood boards (Appendix A.2.1). However, the exact cause of this behaviour is unknown and hence it requires further studying.

Finally, using linear regression, moisture content and basic density of the blocks were correlated with the final temperature, determined at the end of Joule heating. Since the heartwood boards and the heartwood parts of the transitional boards were relatively non-conductive, only the pure sapwood boards and the sapwood sections of the transitional boards, with moisture content higher than 90%, were considered in the linear regression. To incorporate initial temperatures of each block and avoid boundary conditions created by ambient temperature variation during each experiment, a dimensionless temperature parameter was introduced to the regression, in addition to the absolute temperature value. The dimensionless temperature was calculated as:

$$\Theta = \frac{T_{j,i} - T_{j,i_0}}{T_{j_{max}} - T_{j_{min}}}, \tag{3.4}$$

where $T_{j,i}$ is the temperature of the block i within the board j after Joule heating, T_{j,i_0} is the

temperature of the block i at the zero time, $T_{j_{max}}$ and $T_{j_{min}}$ are the maximum and minimum temperature values observed within the board over the whole Joule heating period.

Figure 3.12 shows the effect of sapwood basic density on the sapwood final temperature. The

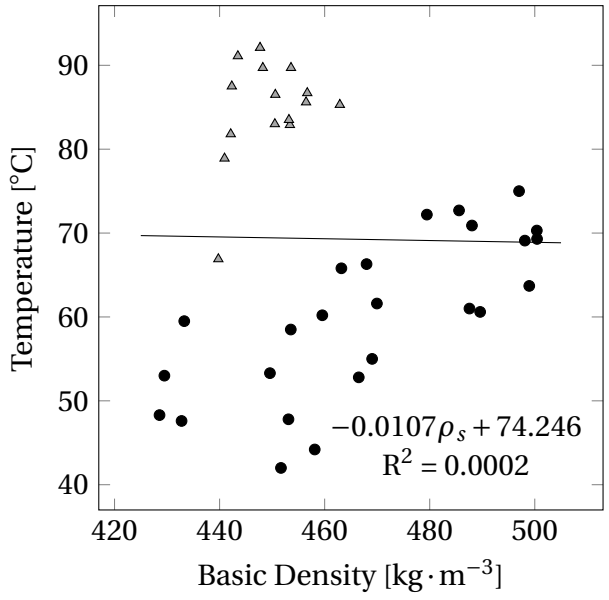

(a)

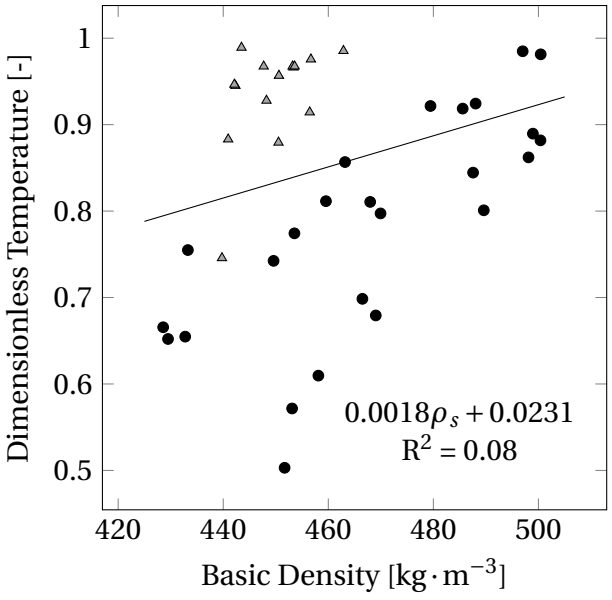

(b)

Figure 3.12. Effect of basic density on temperature of the blocks within the pure sapwood boards (circles) and within the sapwood section of the transitional boards (triangles). *Note:* The linear regression was based on the total number of samples.

slopes of the linear fits indicate an insignificant effect of basic density on temperature, which was not greatly improved after using the dimensionless temperature. On the other hand, the effect of moisture content on the blocks' temperature was more pronounced (Figure 3.13). The

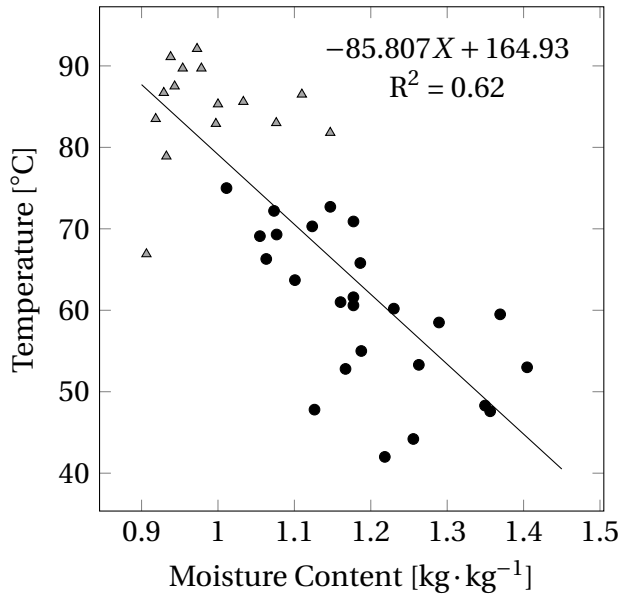

(a)

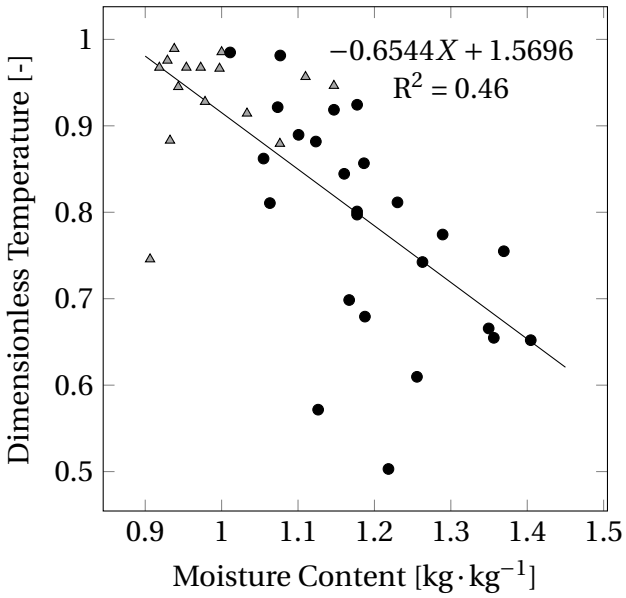

(b)

Figure 3.13. Effect of moisture content on temperature of the blocks within the pure sapwood boards (circles) and within the sapwood section of the transitional boards (triangles). *Note:* The linear regression was based on the total number of samples.

correlation showed that the lower the moisture content, the higher the final temperature, at the end of Joule heating. However, that was inapplicable for heartwood; having relatively low moisture content, heartwood is a poor conductor and cannot be readily Joule heated, unless separated from the sapwood and a much higher voltage applied to it. Therefore, the obtained correlations cannot be used to simply predict the temperature of the wood, and Joule heating of *P. radiata* needs to be further studied using a computational approach.

3.4 Conclusions

The experimental results showed that sapwood of green *P. radiata* could be heated to a temperature above 56°C and Joule heating can potentially be used for phytosanitary treatment. For output power of 500 W with maximum electric field of 5000 $V \cdot m^{-1}$, the Joule heating rate of pure sapwood boards of *P. radiata* was about 11 times higher than that of pure heartwood boards. However, the heating was non-uniform with formation of hot and cold spots in the sapwood. Electric current preferentially flows through sapwood, while the heartwood of radiata pine is a poor electrical conductor. In spite of poor conductivity of heartwood boards, they can be heated if the applied voltage is increased. However, in transitional boards, nearly all the current flows in the sapwood and, as both sapwood and heartwood portions experience the same applied voltage, the power dissipation in the heartwood is negligible. Thus, the heating of the heartwood portion of *P. radiata* transitional boards would be solely due to heat diffusion from the Joule heated sapwood. For this reason, Joule heating is potentially suited to the rapid heating of roundwood, pure sapwood sawn boards and pure heartwood sawn boards, but not to transitional boards. This will generally be true for all species where the different timber regions, such as sapwood and heartwood, have different electrical conductivities. Basic density of radiata pine's sapwood does not have a noticeable effect on the final sapwood temperature. Moisture content of sapwood, however, was correlated with temperature, where the lower the moisture content, the higher the final temperature. This correlation was inapplicable for heartwood; although the moisture content of heartwood was low, the experimentally achieved temperature of heartwood was low.

Chapter 4

Thermal Properties

4.1 Introduction

To solve the governing partial differential equation of heat conduction with the Joule heating effect (Equation 2.17), thermal conductivity (k) and heat capacity (C_p) of the heated medium must be known. Being a heterogeneous and anisotropic material, wood's thermal properties depend on the type of specimen, wood density, moisture content, grain orientation and temperature (Kollmann and Cote, 1968; Suleiman et al., 1999; Dupleix et al., 2013). Green wood structure is made of three main materials: water (bound in wood tissue and free water stored in tracheids), wood tissue (solid cell walls) and air (including water vapour). The air and dry wood tissue are good thermal insulators, with typical values of thermal conductivity and heat capacity shown in Table 4.1. Water, however, has a much higher thermal conductivity and heat capacity. Hence, because it contains free water in tracheids and bound water in the tissue, green wood's thermal properties become similar to water, but never reach the same values, even above 100% moisture content (Dupleix et al., 2013).

Thermal conductivity of wood can be measured using a hot plate (steady-state) method (MacLean, 1941; Skaar, 1988; Sonderegger et al., 2011) or a transient plane source (transient) method, Hot Disk, (Gustafsson, 1991; Suleiman et al., 1999; Yu et al., 2011). Dupleix et al. (2013)

Table 4.1. Thermal properties of air, dry wood, and water at about room temperature (Desch and Dinwoodie, 1996; Incropera and David, 2002; Stamm, 1964).

Materials	k [W·m^{-1}·°C^{-1}]	C_p [J·kg^{-1}·°C^{-1}]
Air	0.0238	1007
Wood [a]	0.231 - 0.418 ($\parallel$)[b] 0.0937 - 0.166 ($\perp$)[b]	1360
Water	0.606	4180

[a] For the basic density range of 350 - 700 kg·m^{-3}

[b] $\parallel$ and $\perp$ denote the parallel to grain and across grain directions

studied green wood thermal properties using both these methods and concluded that the transient method showed similar results to the proven, older, and slower technique. However, the disadvantage of the transient method was the effect of wood's heterogeneity on the result. To avoid the effect of boundary conditions on the transient measurement, the surface area of a sample must be much larger than the surface area of the Hot Disk sensor. Therefore, testing wood samples, the sensor cannot completely cover the surface of the sample and hence if there is a small change in the sensor's location it affects the result due to wood's heterogeneous structure (Dupleix et al., 2013). This means that the same block of green wood can show different results in subsequent tests and, to determine the average values of thermal properties for sapwood and heartwood, this method will require a large number of experiments. Furthermore, due to the anisotropic structure of wood, measuring thermal conductivity and heat capacity using Hot Disk method should be avoided (Hot Disk AB, 2007). Hence, heat capacity should be measured employing another method such as Differential Scanning Calorimetry.

The time required to cover the variation of thermal properties within a tree, covering the sapwood and heartwood sections, using two different methods would extend the duration of this research beyond the normal time-frame of a typical PhD programme. Therefore, it was decided to use developed equations of thermal conductivity and heat capacity from the published data (Table 2.1 of Chapter 2) that can adequately describe heat transfer within green New Zealand grown *P. radiata*. Due to variance of thermal properties between tree species, many of those equations are inaccurate in the prediction of thermal properties of green *P. radiata*. Two separate studies dealing with New Zealand grown *P. radiata* were found. The first study was done by Pang et al. (1995) and the second was done by Nijdam et al. (2000). In those studies, the researchers built computational models of drying green New Zealand grown *P. radiata* using a set of two equations (one for each thermal property) (Table 4.2).

The principal difference between the studies is that Nijdam et al. (2000) considered the effect of temperature on the thermal properties, while Pang et al. (1995) used the thermal properties independent of temperature. To choose the most appropriate equations, experimental and computational approaches were applied. In the experimental part of this study, blocks of sapwood and heartwood of green *P. radiata* were heated inside a water bath. Using temperature sensors, the temperature inside these blocks was recorded. Then, using CFD modelling, the

Table 4.2. Published equations of thermal conductivity and heat capacity for *P. radiata*.

Equation of Thermal Properties	Published by
$C_p = 4184\frac{X+0.324}{1+X}$	Pang et al. (1995)
$C_p = \frac{(0.219+X)^{0.781}}{1+X}(8.5(T-273.15)+5300)$	Nijdam et al. (2000)
$k = \frac{\rho_s}{1000}(0.4+0.5X)+0.024$	Pang et al. (1995)
$k = \frac{(0.26+X)^{0.95}}{1+X}[0.0035X(T-273.15)+0.53]\times (1.7\frac{\rho_s}{1000}+0.16)$	Nijdam et al. (2000)

experimental heating was simulated using Nijdam et al.'s (2000) and Pang et al.'s (1995) set of equations. The most accurate set of equations was selected for the modelling of Joule heating of *P. radiata* using the log heating (Chapter 7) or knot heating (Chapter 8) model.

In this thesis, to ensure credibility of all developed CFD models, each was verified and was validated if experimental data was available. In verification, each CFD model was tested using the following CFD quality criteria: independence of mesh and time-step resolution, convergence of iterative solutions, freedom of software bugs and operator errors caused by incorrectly specified input values. In validation, predicted CFD results were compared with available experimental results, to determine the accuracy of a CFD model. Chapters 6 and 7 describe the verification and validation of the overall log heating (major) CFD model, respectively, including thorough explanation of verification (with broader description of the above CFD quality criteria) and validation.

4.2 Methods

4.2.1 Experimental Testing

Sample Selection

The experimental work was done in two parts: (1) from June to August of 2015 and (2) January of 2016. Two sets of freshly sawn timber were provided by McVicar Timber Group Ltd, in June of 2015 and January of 2016. The first set contained two 100 × 100 × 3000 mm beams of sapwood *P. radiata* and one 100 × 100 × 3000 mm beam of heartwood *P. radiata*. The second set consisted of one 100 × 100 × 3000 mm beam of sapwood *P. radiata* and one 100 × 100 × 3000 mm beam of heartwood *P. radiata*. The beams were cut into shorter sections of 500 mm length and kept inside plastic bags with added tap water, to keep a constant vapour pressure inside the bags, preventing the blocks from drying. The bags were sealed with duct tape and put in a freezer at -20°C. Each of the sets had been in the freezer no longer than three months.

Several days prior to the experiment, one of the 500 mm sections was cut into smaller blocks of approximately rectangular parallelepiped shapes of different sizes, using bench and drop saws. These blocks were gently defrosted in a sealed plastic bag, with added tap water, inside a fridge at a temperature below 5°C. The lengths of the blocks' edges, as shown in Figure 4.1, were measured using digital and vernier callipers, with a resolution of 0.01 and 0.05 mm, respectively (Table B.1 of Appendix B). The blocks from the first set were measured by the digital calliper,

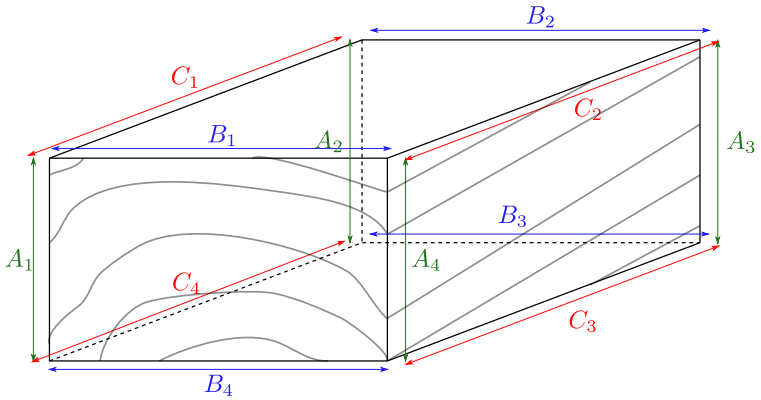

Figure 4.1. The dimensions of the blocks used in the Hot Water Bath experiment. *Note:* Edges A were assumed to be the heights. Edges B were the widths, and edges C were the lengths, always aligned with the longitudinal direction.)

while the other set was measured by the vernier calliper. In total, 52 blocks were used in the experiments, where 44 (26 sapwood and 18 heartwood) blocks were from the first set and eight

(four sapwood and four heartwood) blocks were from the second set. Blocks 3, 6, 8, 10, 39, 40, and 42 were predominantly sapwood but had a portion of heartwood (Figure 4.2). In the computational model, however, it was assumed that these blocks were entirely sapwood. Block

Figure 4.2. The portion of heartwood (HW) within Block 3.

16 was rejected due to a loss of temperature recordings, caused by a failure of the logging software. The average basic density and moisture content of the blocks are shown in Table 4.3.

Table 4.3. The average basic density (ρ_s) and moisture content (X) of the sapwood (SW) and heartwood (HW) blocks from green *P. radiata* timber.

Wood Type	ρ_s [kg·m^{-3}]	X [%]	Set
SW	440 (SD = 33)	151 (SD = 17)	I
HW	430 (SD = 11)	42 (SD = 4)	I
SW	485 (SD = 3)	163 (SD = 2)	II
HW	494 (SD = 3)	56 (SD = 9)	II

Experimental Procedure

Three platinum resistor sensors, PT-100, were used to measure temperature inside the blocks. They were connected to a data logger, PT-104, manufactured by Pico Technology. Platinum temperature sensors are more accurate than thermocouples, with the error of the sensors used being ±0.2°C (Pawson et al., 2018). The total error of the temperature recordings includes the errors of PT-104 data logger, self-heating, and stability; it varies from +0.459°C to −0.335°C; the total error is asymmetric, as the self-heating only contributes to the positive error (Pawson et al., 2018). To insert the temperature sensors into the blocks, three holes (T_1, T_2, T_3) were drilled using a pillar drill with a depth stopper. The diameter of the holes was 5 mm. The holes were drilled either parallel to the C edges (along the longitudinal direction), Type 1, if the lengths of the B edges were the longest (Figure 4.3a), or parallel to the B edges (across the longitudinal

direction), Type 2, if the lengths of the C edges were the longest (Figure 4.3b). The A edges were always the shortest. The second hole (T_2) was in the centre of the drilled face; all three holes lie on an axis of symmetry as shown in Figure 4.3. The distances (E and F) between the side holes and the nearest, shortest edges were measured using a ruler with a resolution of 0.5 mm. The depths of the drilled holes were measured using the callipers (Table B.2 of Appendix B), except for Blocks 8, 11, 12, 14, 15, 21 - 25, and 52, when a calliper was unavailable and the depths of the holes were estimated based on the length of the drill bit's penetration depth in the pillar drill, measured by the ruler.

The blocks were weighed with a 10 mg resolution prior to attaching temperature probes. Then, the blocks, with the inserted temperature probes, were submerged in a pre-heated water bath with a temperature controller and mixer, to create a continuous circulation of water around the blocks. An additional platinum temperature probe, T_4, was inserted into the water bath and placed on an external surface of the block (Figure 4.4). All temperature probes were connected to a data logger, Pico Technology PT-104, that logged the temperature readings every second. The experiment ended once the temperatures inside the block and water bath had equilibrated. Thereafter the volume of each block was measured using the water displacement method, and then each block was oven-dried at 105°C to calculate its moisture content and basic density. The blocks' properties and other parameters such as the duration of heating and the temperature of the water bath are summarised in Table B.3 of Appendix B.

4.2.2 CFD model

Mathematical Model

a) Governing Equation

While heated in the water bath, the moisture content of the blocks was considered to be constant throughout the experiment. This assumption allowed the omission of the mass conservation equation from the computational model. Also, it was assumed that there was no heat transfer due to internal convection of water within the wood, causing the convection term in the energy conservation equation to be equal to zero. Thus, a mathematical description of the model was presented by the heat conservation equation with the conduction term, written as:

$$\frac{\partial \rho_g C_p T}{\partial t} = \nabla \cdot (k \nabla T), \tag{4.1}$$

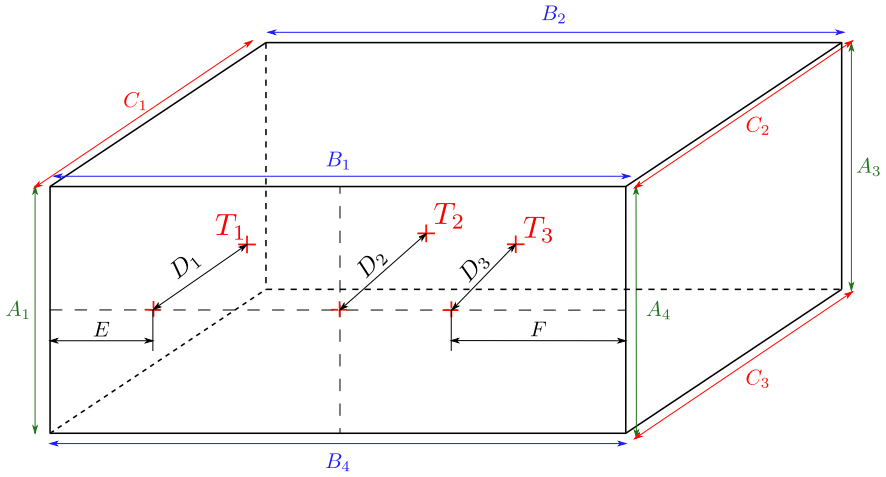

(a)

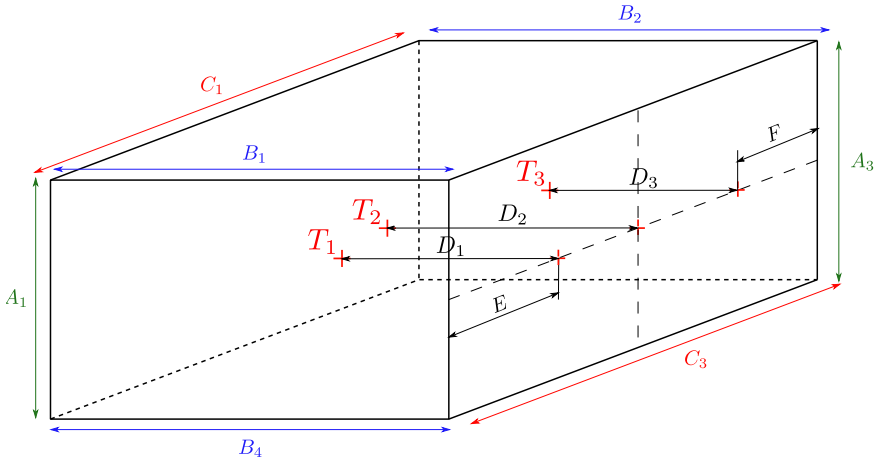

(b)

Figure 4.3. The dimensions of the drilled holes, where (a) is the Type 1 and (b) Type 2.

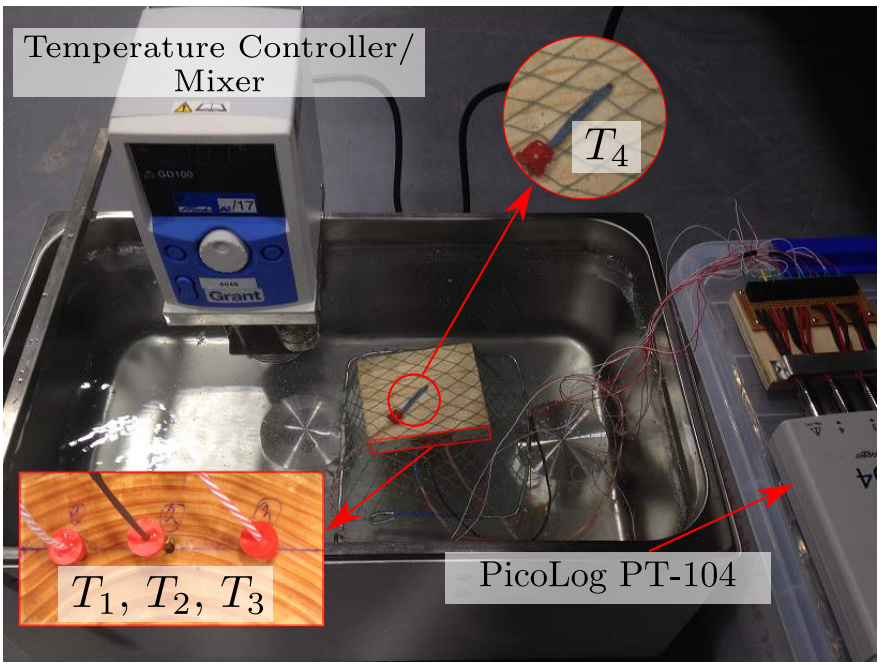

Figure 4.4. The complete experimental set-up of the water bath, with the submerged block and the positioned platinum temperature sensors. *Note:* The red pieces of plastic, attached to the temperature sensors' wires, worked as plugs and prevented water ingress into the drilled holes.

where C_p is the heat capacity [$\mathrm{J \cdot kg^{-1} \cdot °C^{-1}}$], T is the temperature [°C], k is the thermal conductivity [$\mathrm{W \cdot m^{-1} \cdot °C^{-1}}$], and ρ_g is the green density [$\mathrm{kg \cdot m^{-3}}$], calculated as:

$$\rho_g = \rho_s(1 + X), \tag{4.2}$$

where ρ_s is the basic density [$\mathrm{kg \cdot m^{-3}}$] and X is the moisture content [$\mathrm{kg \cdot kg^{-1}}$].

b) Boundary and Initial Conditions

Figure 4.5 shows a heat flow diagram of the block being heated inside the water bath. It was assumed that the initial temperature of the block was uniform, and equal to the mean of the initial readings of the inserted temperature probes (T_1, T_2, and T_3), calculated as:

$$T_i = \frac{(T_{0\_T_1} + T_{0\_T_2} + T_{0\_T_3})}{3}, \tag{4.3}$$

where T_i is the initial temperature of the block, and $T_{0\_T_1}$, $T_{0\_T_2}$, $T_{0\_T_3}$ are the initial temperatures recorded by the temperature sensors T_1, T_2, and T_3, respectively.

Each block was submerged to the middle of the water level. A mixer inside the water bath ensured a continuous water circulation around the blocks, while the heater maintained a constant

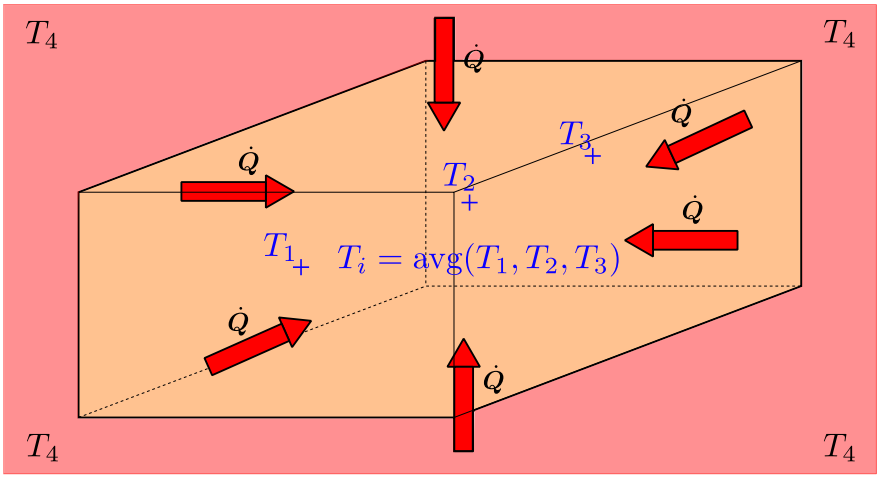

Figure 4.5. The heat flow diagram of the *P. radiata* block inside the water bath. *Note*: The red colour represents the water at temperature T_4 that is higher than the block's internal temperature. The red arrows show the direction of heat flux.

temperature. It was assumed that the mean temperature, measured by the fourth sensor, was uniform on each side of the block's external surface. As the sensor was located on the block's external surface, the boundary condition was considered as:

$$T_s = \frac{\sum_{N=1}^{\infty} T_4}{N} \quad \text{at} \quad t > 0\,\text{s}, \tag{4.4}$$

where T_s is the surface temperature of the block and N is the number of the temperature recordings made by the sensor T_4 throughout the experiment.

Computational Model

a) Building Geometry

As shown in Table B.1 of Appendix B, the lengths of the A, B, and C edges within each block varied, with the maximum length difference within a single block of 5.1, 2.6, and 1.81 mm, respectively. The average length difference within a single block for the A, B, and C edges were 2 mm (SD = 1 mm), 0.7 mm (SD = 0.6 mm), and 0.5 mm (SD = 0.5 mm), respectively. Thus, to build an exact geometry, coordinates of each of the blocks' vertices need to be used. However, ANSYS Design Modeller, the software used to build the blocks' geometries, does not support a technique of building 3D geometries by vertices; instead, it is necessary to build a 2D surface that is then extruded along a third direction, forcing at least two opposite faces of the 3D geometry to be parallel. Hence, building of the exact blocks' geometry was not practical in ANSYS Design Modeller, as none of the blocks' opposite faces were parallel to each other. The length of C edges

did not vary as significantly as the length of *A* and *B* edges within a single block. Thus, to build the blocks' geometries (Figure 4.1) in Design Modeller, it was decided to create a 2D surface, made of A and B edges, where the average length of two opposite edges were used (Figure 4.6a). It was assumed that the B edges were parallel to each other and perpendicular to one of the A

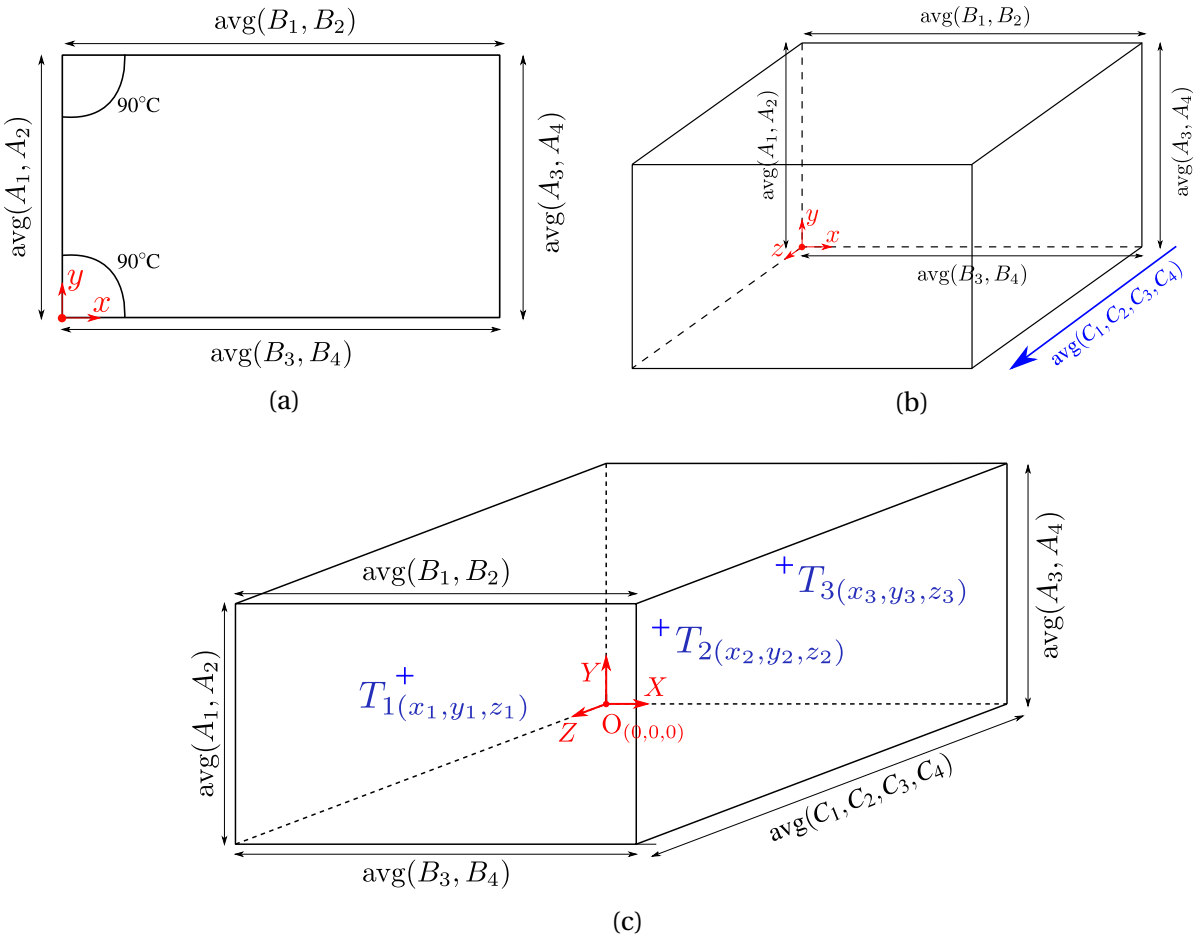

Figure 4.6. The top figures show the schematic diagram of building the blocks' geometry in ANSYS Design Modeller: (a) building the 2D surface and (b) extruding the 2D surface in the Z direction (along the blue arrow). The bottom figure (c) shows schematic position of the temperature sensors.

edges. The 2D surface was extruded by the average length of *C* edges (Figure 4.6b). As shown in Figure 4.6c, the positions of the temperature probes within the blocks were set using a 3D coordinate system; all the coordinates are summarized in Table B.4 of Appendix B.

b) Meshing Method

The geometry was meshed using the ANSYS Meshing Tool, with sweeping and edge size control methods. Each element of the mesh was a rectangular hexahedron (Figure 4.7). This meshing tool allows the user to specify either a number or size of mesh element. Since the blocks had different sizes, setting a number of elements would have created a denser mesh for smaller

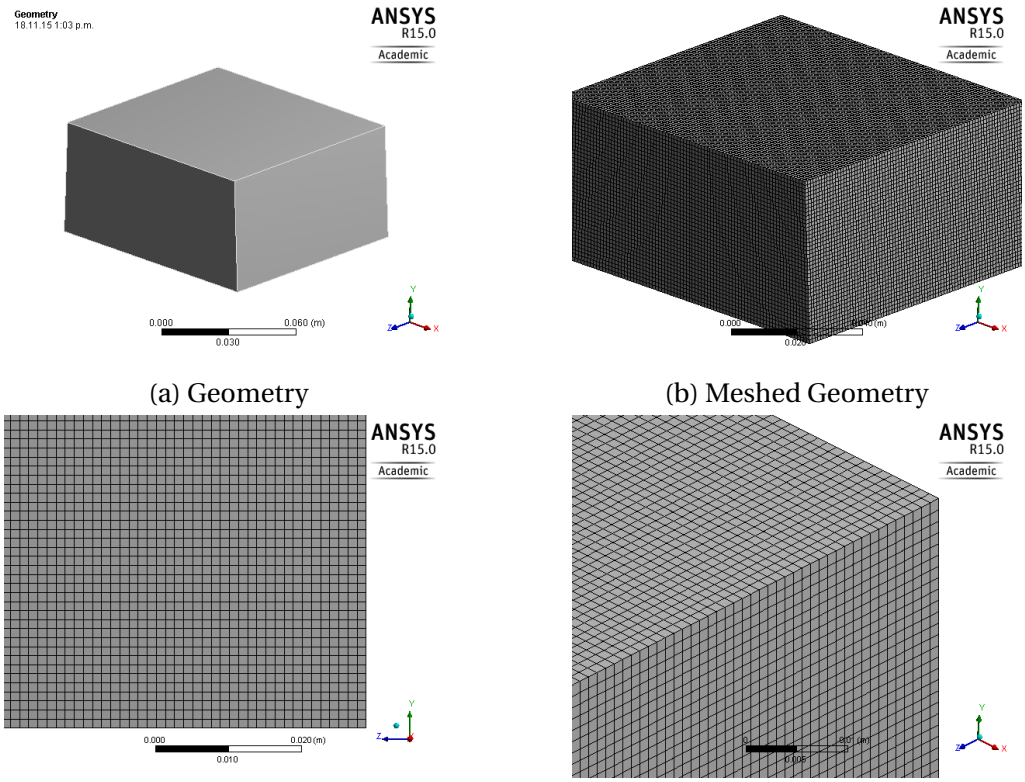

(a) Geometry

(b) Meshed Geometry

(c) ZY plane

(d) Meshed Corner

Figure 4.7. The geometry and mesh of a typical block used in the experiment.

blocks and a coarser mesh for larger blocks. Therefore, it was decided to specify a size of mesh that kept the mesh density independent of the blocks' dimensions.

c) Parameters of Computational Model

The governing equation, with the associated boundary and initial conditions, was solved using commercial CFD software, ANSYS CFX 17.0. The second order backward Euler scheme was used to discretize the equation, which led to a discrete system of linearized equations. This system was solved using an iterative solution algorithm provided by ANSYS CFX (ANSYS, Inc., 2013). The solution converged once the root mean square (RMS) of normalized equation residuals decreased to 10^{-6}. The convergence criteria was achieved in less than 20 iterations, at each time-step, using a double precision. The average time of a single simulation run was around three hours on an Intel Core i7-3770 @ 3.40 GHz, with 16 GB RAM, for the mesh element size of 1.25×10^{-3} m and 1000 time-steps. To automate 102 simulations, the model was built in ANSYS Workbench using a parametric study option. This option allowed one to change relatively quickly a model's parameters such as the size of the geometry, time of heating, wood properties, and mesh thickness, without changing the main code.

Mesh and Time-Step Independence

a) Mesh

A CFD solution depends on the mesh density and the size of time-steps. To achieve a mesh-independent solution, five mesh sizes were considered: 0.01, 5×10^{-3}, 2.5×10^{-3}, 1.25×10^{-3}, and 6.25×10^{-4} m; the size of mesh element was the same in all directions (X, Y, and Z). Hence, when the mesh was refined, the number of mesh elements increased by almost 8 times with each consecutive mesh. Table 4.4 shows the numbers of mesh elements and the corresponding size of mesh elements used in the mesh-independence study. Each simulation was done with

Table 4.4. The mesh element size and the corresponding number of elements used in the mesh independence study.

Size of Mesh Element [m]	Number of Mesh Elements
0.01	600
5×10^{-3}	4400
2.5×10^{-3}	34,440
1.25×10^{-3}	275,520
6.25×10^{-4}	2,190,720

1000 time-steps. The obtained results of the mesh-independence study were compared at each time-step using the following equation:

$$\delta = \frac{|T_{m.i.} - T_{f.m.}|}{T_{f.m.}} \cdot 100\%, \tag{4.5}$$

where $T_{m.i.}$ and $T_{f.m.}$ are the temperatures calculated in the cases with the tested mesh and with the finest mesh, respectively; δ is the calculated error at a single time-step. To select the most appropriate mesh, the maximum of determined error values was selected as:

$$\delta_{max} = max\,(\delta_1, ..., \delta_n)\,, \tag{4.6}$$

where n is the number of time-steps, equal to 1000 time-steps for the mesh-independence study. The mesh with the mesh size of 1.25×10^{-3} m provided a mesh-independent result and was used for the time-step independence study.

b) Time-Steps

Next, the minimum required time-step resolution was found. That was done by using four

time-steps resolutions: 500, 1000, 2000, and 4000 time-steps. In each simulation, the total time of heating was discretised into equally spaced time-points, the number of which depended on the selected time-step resolution (Figure 4.8). As the governing equation was solved at each time-step, the simulation based on 500 time-steps generated a result of 500 discrete solutions. Accordingly, results of 1000, 2000, and 4000 solutions have been generated using the 1000, 2000, and 4000 time-step resolutions. To compare these results, their number of solutions had to be equalized, meaning that the error had to be calculated at each of 500 actual, common time-points as:

$$\delta = \frac{|T_{ts.i.} - T_{ts.h.}|}{T_{ts.h.}} \cdot 100\%, \tag{4.7}$$

where $T_{ts.h.}$ and $T_{ts.i.}$ are the temperatures determined in the case with the highest number of time-steps and in the compared case, respectively. That resulted in an array of 500 error values for each time-step resolution. Using Equation 4.6, the time-step independence study showed that the resolution of 500 time-steps is sufficient to achieve temporal convergence.

4.2.3 Comparing Experimental and Computational Results

Two models, based either on Pang et al.'s (1995) or Nijdam et al.'s (2000) set of heat capacity and thermal conductivity equations, were compared in this study. The set of the equations that produced the most accurate results was selected for the simulation of the Joule heating effect in *P. radiata*, described in Chapter 7 and 8. The basis for comparison was the error value between predicted and experimental results.

To compare the simulated and experimental temperatures, the durations of the blocks' heating was divided into 500 equally spaced time-points - the number of time-points is equal to the number of time-steps, estimated using the time-step independence study -, written mathematically as:

$$t_s = \left\{0, t_{exp} \cdot \frac{1}{n}, ..., t_{exp} \cdot \frac{n}{n}\right\}, \tag{4.8}$$

where t_s is an array of 501 time values, n is the number of time-steps used in the simulation, and t_{exp} is the total time of heating during the experiment. The actual discretised time in a time-step was not an integer. However, as the experimental data was recorded each second; to

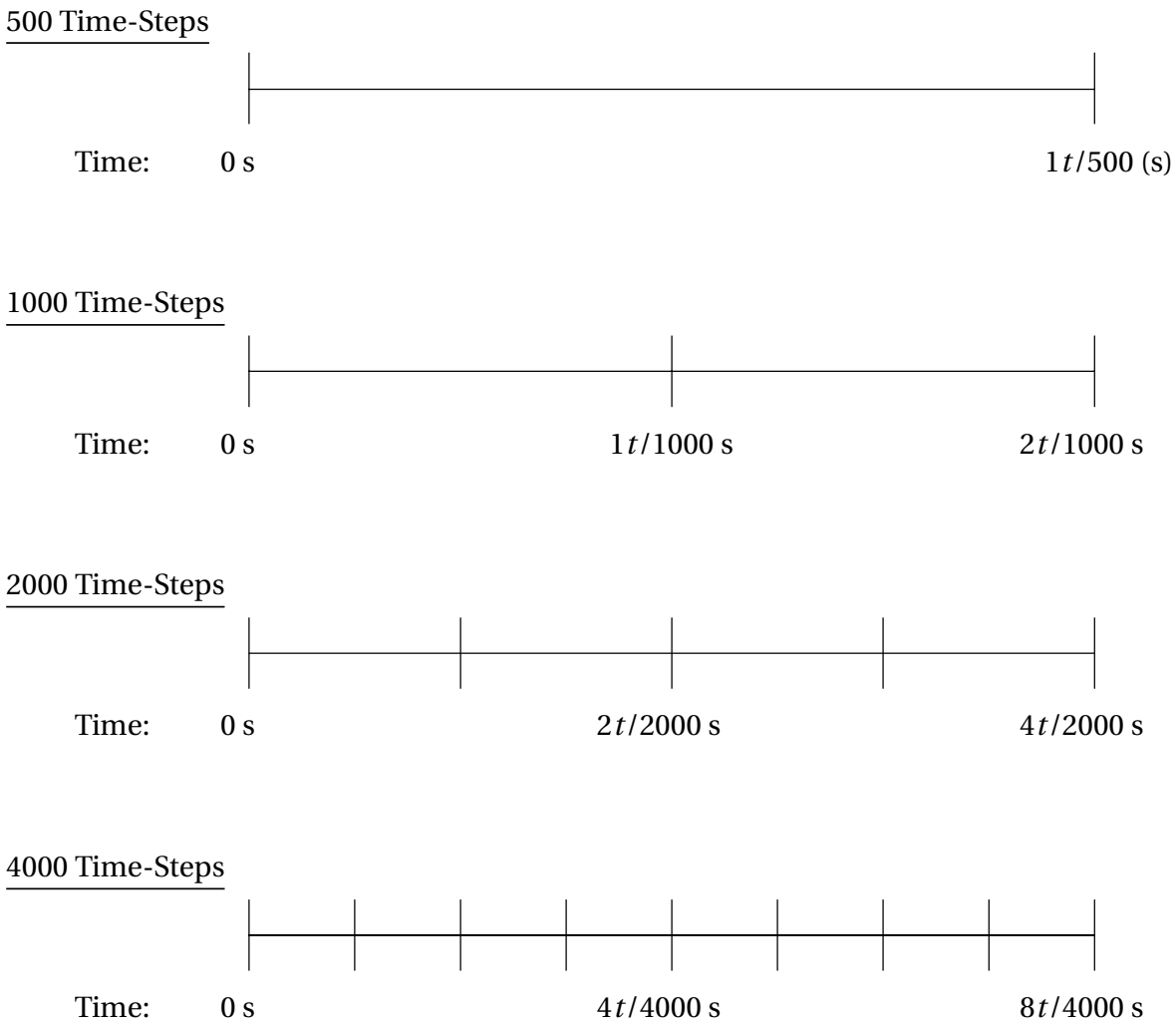

Figure 4.8. The schematic diagram of temporal discretization using different time-steps over the same period of time. To compare the temperature values and calculate the computational error, the temperature had to be estimated at common time-points for all resolutions. In this diagram, the common time-points are 0 s and $t/500$ s. *Note:* t is the total time of heating.

compare the predicted and experimental results, the time values in the obtained array (t_s) had to be integers. The experimental results showed that the maximum temperature rise in 1 second is lower than 0.4°C. This temperature rise lay within the error of temperature recording and hence it was assumed to be small. Thus, interpolation was unnecessary and the time values in the array (t_s) were rounded to the nearest integer. The experimental temperature was compared with the simulated data at those time-points by calculating error as:

$$\delta = T_{exp} - T_{sim}, \tag{4.9}$$

where T_{exp} and T_{sim} are the experimental and simulated temperatures, respectively. These errors, calculated at each time-point, were formed into an array of errors given as:

$$\delta_s = \{0, \delta_1, \delta_2, ..., \delta_n\}. \tag{4.10}$$

The first element of this array is zero, as the initial temperature in the model is equal to the temperature of the block at the beginning of the experiment. The sign of the error values was either positive, meaning that experimental temperature was higher than the predicted, or negative, when the predicted temperature was higher than the experimental. Thus, the closer the predicted value to the experimental value, the closer the error to zero.

The rate of heating varied throughout the experiment, as the blocks were heated until a complete temperature equilibrium between the blocks' internal temperature and the water bath's temperature was established (Figure 4.9). Thus, the highest heating rate was at the beginning of experiment, when the block's temperature was significantly lower than the temperature of water. During this time, generally the first 20 minutes of heating, both sets of equations showed the highest error (by absolute value). Therefore, to compare Pang et al.'s (1995) and Nijdam et al.'s (2000) equations, it was decided to use the highest error by absolute value, mathematically expressed as:

$$\delta_{ref} = max(|\delta_s|) = max(\{0, |\delta_1|, |\delta_2|, ..., |\delta_n|\}), \tag{4.11}$$

where δ_{ref} is the reference error value used for comparison of the models. Selecting the maximum error by absolute value and keeping the sign of the error values helped to identify the

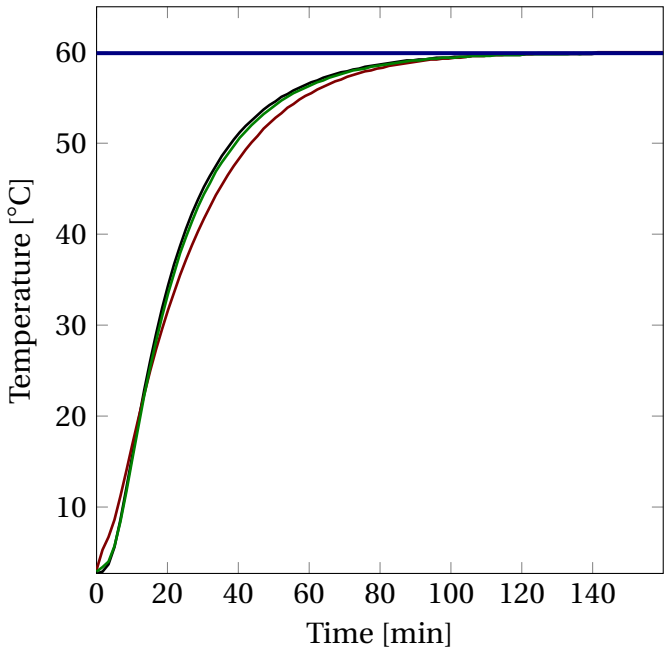

Figure 4.9. The experimental temperature rise of a typical *P. radiata* block recorded by T_1, T_2, and T_3 temperature probes, represented by the black, green, and red lines, respectively. The blue horizontal line is the average temperature of the water bath during the experiment.

accuracy of prediction, whether the selected set of thermal property equations overestimates or underestimates the blocks' temperature.

4.3 Results and Discussions

4.3.1 Mesh and Time-Step Independence Study

Mesh Independence

The mesh independence study started with the coarsest mesh size of 0.01 m, finally reaching the finest resolution of 6.25×10^{-4} m. Figure 4.10 shows the effect of mesh size on the calculated temperature values. The maximum difference between the coarsest and finest meshes was around 7°C. Figure 4.11a shows the effect of number of mesh elements on the maximum error. The solution achieved mesh-independence using the mesh of 275,520 mesh elements, which corresponds to the mesh element size of 1.25×10^{-3} m. This size of mesh element was used in the time-step independence study and to model each *P. radiata* block in 102 simulations.

Time-Step Independence

Figure 4.11b shows the effect of time-step resolution on the maximum computational error. The computational error lay below 0.2% and was only slightly improved with the increase of

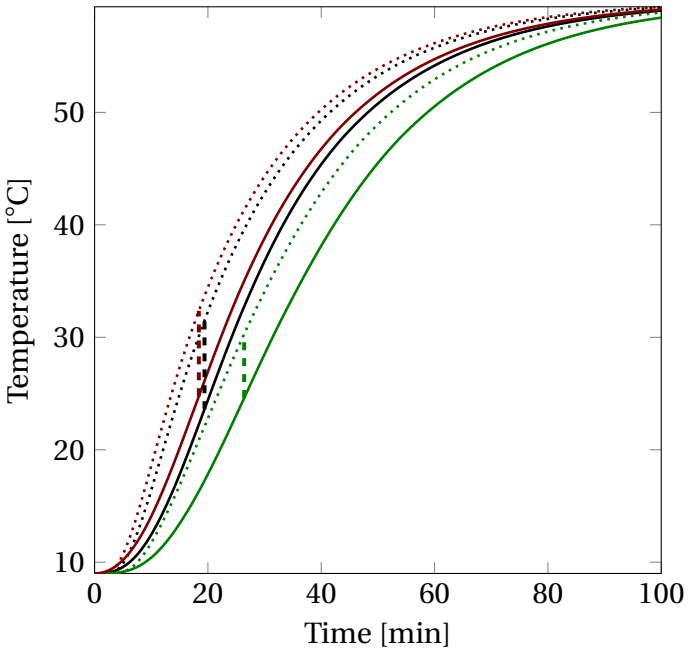

Figure 4.10. The simulated temperature rise of a typical *P. radiata* block recorded at T_1, T_2, and T_3 temperature probe locations, represented by the black, green, and red lines, respectively. The dotted and solid lines denote the results obtained using the mesh sizes of 0.01 and 6.25×10^{-4} m, respectively. The vertical dashed lines represent the highest difference between the results over the full period of heating.

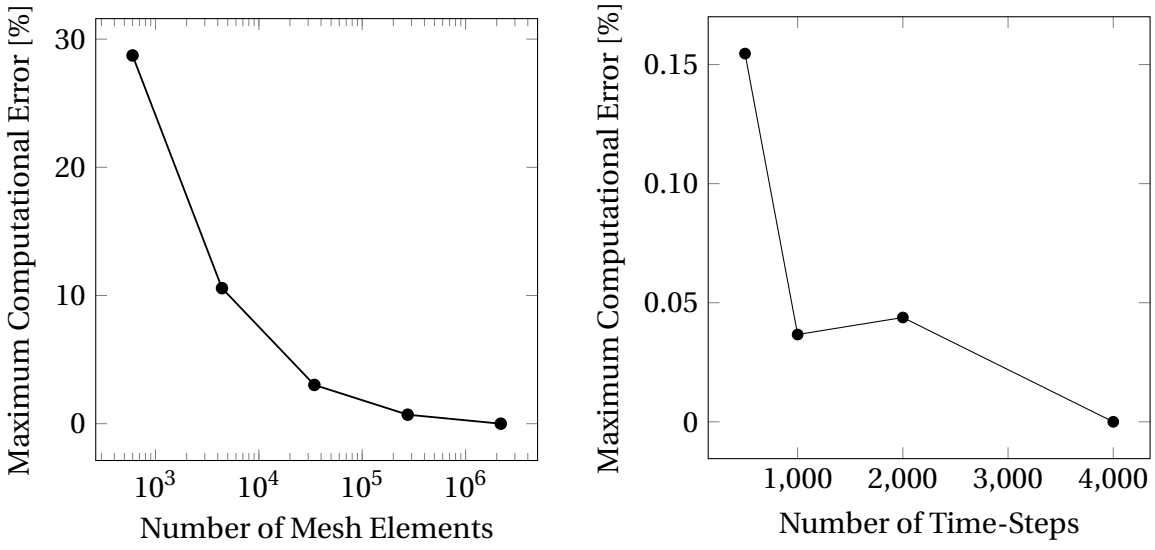

Figure 4.11. The effect of (a) mesh- and (b) time-step resolutions on the computational error.

time-steps resolution. Therefore, to compare the simulated results with the experimental values, it was decided to use 500 time-steps. This produced 501 transient temperature values in about three to four hours.

4.3.2 Experimental vs Computational Results

Figure 4.12(a-c) shows the difference between the experimental data of the temperature rise in a typical green *P. radiata* block, Block 7, and the calculated temperature, based on the equations shown in Table 4.2. Both equations predicted with acceptable accuracy the behaviour of the

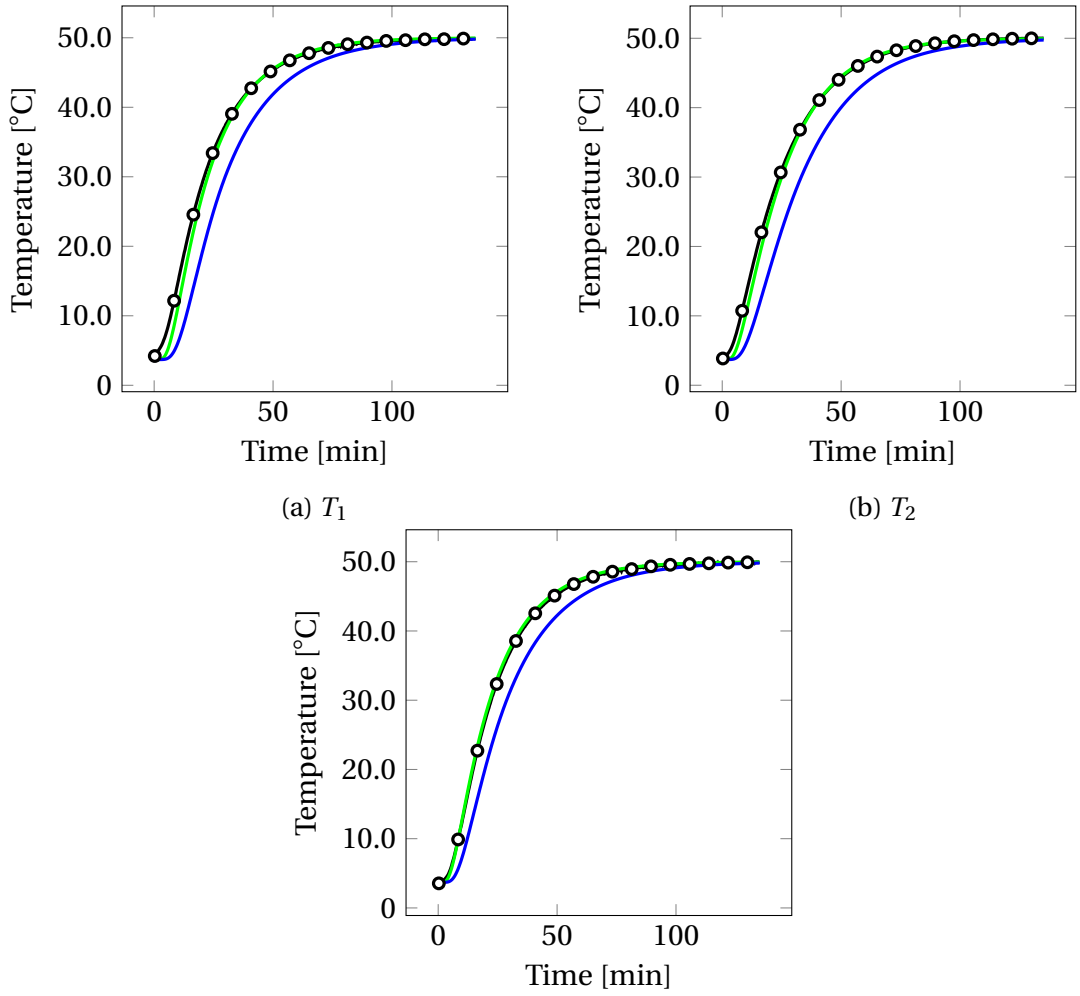

(a) T_1 (b) T_2

(c) T_3

Figure 4.12. The difference between the experimental and calculated temperatures of Block 7 at (a) T_1, (b) T_2, and (c) T_3. *Note*: The green and blue lines denote the results based on Pang et al. (1995)'s and Nijdam et al. (2000)'s equations, respectively. The black line with the white circular scatters represents the experimental data.

temperature rise in Block 7. The most significant difference was observed in the first 20 minutes of heating, when the rate of heating was the highest. In Block 7, using Pang et al. (1995)'s equations, the maximum temperature differences between the experimental and predicted values reached 3.6°C, 2.8°C, and -0.7°C at T_1 T_2, and T_3 temperature sensor locations, respectively. The maximum temperature differences between the experimental data and predicted temperature, calculated using Nijdam et al. (2000)'s equations, were 10.6°C, 9.4°C, and 7.1°C. Due to the

variation of thermal properties of *P. radiata*, the reference error varied between the blocks.

The variation of the reference error values over 51 blocks is shown in Figure 4.13 and summarised in Table B.5 of Appendix B. The temperature calculated using Nijdam et al.'s equations

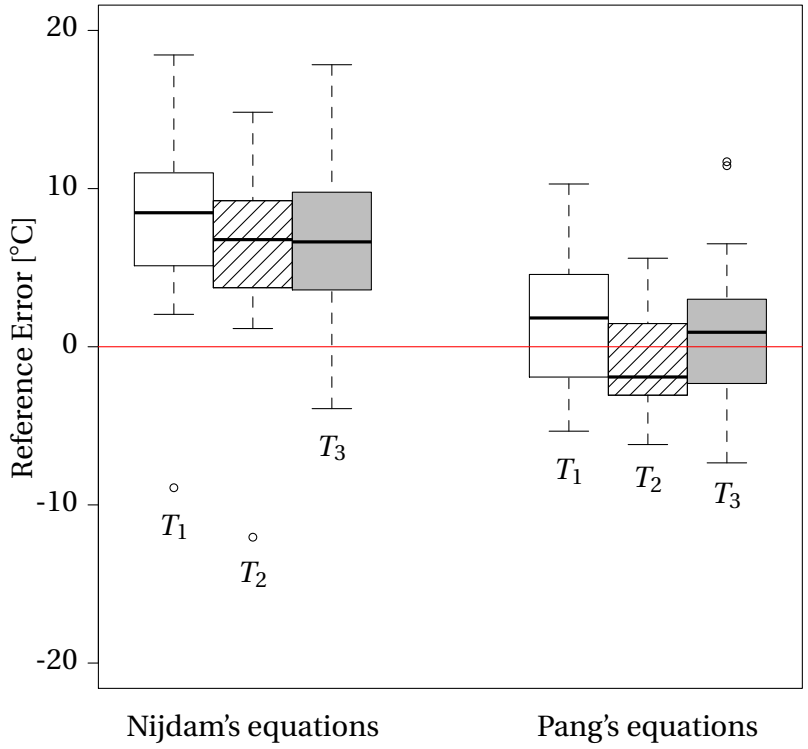

Figure 4.13. The box plots of differences between the measured and modelled temperatures. The latter were calculated using equations of heat capacity and thermal conductivity published by Pang et al. (1995) and Nijdam et al. (2000). T_1, T_2, and T_3 denote temperature sensor 1, 2, and 3, respectively.

was lower than measured, with the mean of the maximum temperature difference of 7.1°C. Overall, Pang et al. (1995)'s equations were more accurate, with the mean of the maximum temperature difference being 0.3°C. To conclude, due to the more accurate temperature prediction, Pang et al. (1995)'s equations were used in the computational modelling of the Joule heating effect in green *P. radiata*, described in Chapters 7 and 8.

Chapter 5

Electrical Conductivity

5.1 Introduction

Electrical conductivity determines the ability of a material to pass an electric current. Knowing the spatial and temporal distribution of conductivity helps to determine electric current due to an applied voltage and hence to determine the heating power - a product of the applied voltage and the electric current. The rate of electrical power dissipation is proportional to the rate of Joule heating. Thus, electrical conductivity should be known in order to control and predict Joule heating.

Wood's electrical conductivity, initially studied by Stamm (1927), has been well investigated below the FSP (Skaar, 1988). Below the FSP, moisture content has the most pronounced effect, increasing the electrical conductivity from 10^{-17} S·cm^{-1}, in dry wood, to about 10^{-6} S·cm^{-1}, at 25% moisture content. Temperature is the second parameter that has a significant effect on electrical conductivity; at 10% moisture content, a temperature rise from 20 to 80°C increases electrical conductivity of wood from almost 10^{-10} S·cm^{-1} to about 10^{-7} S·cm^{-1} (Skaar, 1988). Other parameters such as wood density, grain orientation, and wood's chemical composition have a less significant effect on electrical conductivity below the FSP (Skaar, 1988).

Although moisture content above the FSP has been studied using electrical moisture meters (Brischke et al., 2008; Chen et al., 2012; Fredriksson et al., 2013), the data of electrical conductivity above saturation is limited to several studies by Stamm (1929, 1964), Lin (1967), and Sharma et al. (1997), at around room temperature. Investigating electrical properties of slash pine (*Pinus elliottii*) and redwood (*Sequoia sempervirens*), Stamm found that the effect of moisture content in green wood is relatively small; the increase of slash pine's moisture content from 100 to 180% increased the electrical conductivity from 0.01 to 0.015 S·m^{-1}. Lin published similar values for 10 species of wood. Sharma, however, determined the longitudinal electrical conductivity of 10^{-3} S·m^{-1} for *Eucalyptus tereticornis*, *Grevillea robusta*, and *Hevea brasiliensis*, all grown

in India. Furthermore, Sharma studied the effect of grain orientation, where the transverse electrical conductivity varied in the range of 10^{-3} - 10^{-4} $S \cdot m^{-1}$. However, for the phytosanitary treatment by the Joule heating method, the effect of elevated temperature, 50-90°C, is of most interest, which has not been evaluated in the previous studies.

On the other hand, the electrical conductivity of the green *P. radiata* was determined from the experiment described in Chapter 3. Those boards reached a temperature above 56°C. Only the four sapwood boards were used to calculate electrical conductivity, because in the transitional boards, the exact cross-sectional area that conducted an electric current was unknown. During Joule heating, the temperature of the heartwood boards stayed below 25°C, with the electrical conductivity lying within a range of 0.001 to 0.002 $S \cdot m^{-1}$.

Thus, Figure 5.1 shows the dependence of each green *P. radiata* board's electrical conductivity on its average surface temperature calculated as:

$$T = \sum_{i=1}^{\infty} \frac{V_i}{V_t} T_i, \tag{5.1}$$

where i denotes the block within the board; V is the volume [m^3], with V_t as the total volume of the board; and T_i is the average temperature of the block. The electrical conductivity increased from 0.023 $S \cdot m^{-1}$, at 10°C, to about 0.075 $S \cdot m^{-1}$, at 55°C. Potentially, the heterogeneity of

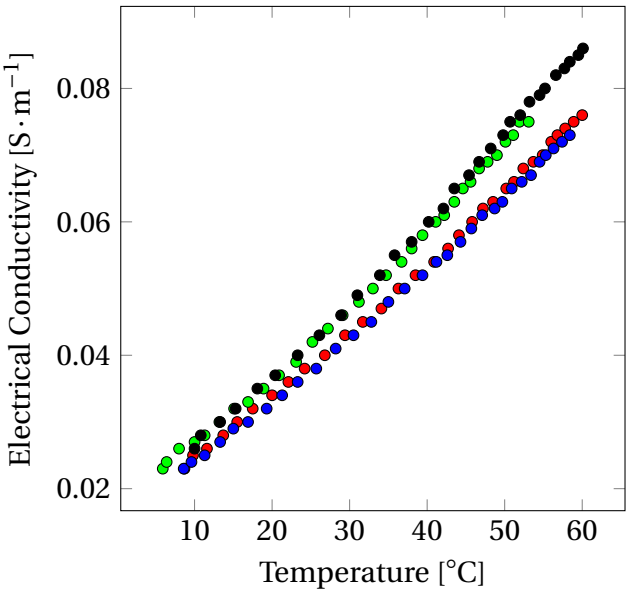

Figure 5.1. The effect of the average temperature of the studied *P. radiata* sapwood boards on the electrical conductivity, where the red, blue, green, and black circles denote SB1-4 (Appendix A.2), respectively.

the boards such as sloping grain might have affected the electrical conductivity, making their electrical conductivity different from that of clear wood, with straight grain. Hence, in this chapter, to determine electrical conductivity of clear wood, smaller samples (cubes of 3 cm side length), without obvious defects such as knots, sloping grain, and cracks, were used. Since heartwood of *P. radiata* is relatively non-conductive (Section 3.3.2), only sapwood was tested in this study. Effects of several parameters (moisture content, temperature, basic density, and grain orientation) on electrical conductivity were studied, and an equation of electrical conductivity as a function of key parameters was derived. The obtained equation was used to predict electrical conductivity of green *P. radiata* grown in different forests. Furthermore, comparing the obtained data with the conductivity of green *P. radiata* sapwood boards, the following two conjectures were tested in this study:

- As the Joule heating rate is much faster than that of convective heating, electrical heating can cause micro checking, affecting wood's structure and hence its electrical properties. Thus, electrical conductivity of green wood heated by the Joule heating effect would be different from the conductivity of the wood heated using another method such as convective heating.

- Electrical conductivity of wood is not scalable, meaning that electrical conductivity of small samples would be different from electrical conductivity of large samples such as logs, with a more heterogeneous structure.

Lastly, electrical conductivity of other wood species: *Eucalyptus nitens*, *Eucalyptus globoidea*, *Pseudotsuga menziesii*, and *S. sempervirens* was assessed in this study (Appendix C.1).

Some results shown in this chapter have been published in "Effect of temperature on electrical conductivity of green sapwood *Pinus radiata* (radiata pine)" by Nursultanov, Altaner, and Hefferman in 2017 at *Wood Science and Technology*, 51(4):795–809, doi:10.1007/s00226-017-0917-6.

5.2 Methods

5.2.1 Sample Preparations

All *P. radiata* samples were tested in three sets. *Set 1* was used to develop the statistical model of electrical conductivity. *Sets 2* and *3* were used to study the effect of forest location on the accuracy of the statistical model.

Set 1 was cut out of two 3-m-long flat-sawn beams of green *P. radiata*, with a 100×100 mm cross-sectional profile, sawn in McVicar Timber sawmill, Christchurch, New Zealand. These beams were cut from export size logs, with a small end diameter (SED) and a large end diameter (LED) between 350 and 450 mm and the heartwood LED and SED between 100 to 200 mm. The exact age of this wood and the forest where the tree had grown was unknown; presumably, the tree age was about 30 years - common practice in New Zealand is to harvest *P. radiata* trees at the age of 25-35 years (Harris, 1991b) -, and the forest was located somewhere in the Canterbury region of New Zealand. The beams were docked into shorter parts of 500 mm length by a drop saw and were sealed inside plastic bags. To reduce drying, those bags were stored inside a freezer at -20°C for less than three months, before being used. Prior to the experiment, one of those 500 mm blocks was cut along the length into strips with a cross-sectional profile of 30×30 mm, keeping the length of the blocks at 500 mm. These 500 mm strips were docked on a drop saw into cubes of 30 mm side length. Only the cubes with straight grain orientation were selected for further study. The cubes were sealed in a plastic bag and left inside a fridge overnight at 2°C, to defrost. Overall, in *Set 1*, 44, 24, and 24 cubes were used to measure electrical conductivity in the longitudinal, tangential, and radial directions, respectively. The cubes were cut from four 500 mm strips from different places within the 3 m freshly sawn beams.

Set 2 was cut out of a 3.3 m long log of green *P. radiata* harvested at Ashley forest, Canterbury, New Zealand. The LED and SED of the log were 390 and 360 mm, respectively; the heartwood LED and SED were 120 and 90 mm, respectively. The tree age, estimated by counting growth rings, was 27 years. The log was cut into three shorter logs of one metre length. Using a chain saw, one of the 1 m long logs was split along the length. Then, the halves of the log were cut on a table saw into one metre long strips, with 30×30 mm cross-sectional profile. Thereafter, these blocks were cut into cubes using a drop saw. The cubes with straight grain were selected for this study. The selected cubes had been inside a freezer at -20°C for less than two weeks prior to being processed. A day before each experiment, they were defrosted at a room temperature inside a sealed plastic bag. Overall, 33 cubes were tested in *Set 2*, where 19, 8, and 8 were used to measure electrical conductivity in the longitudinal, radial, and tangential directions, respectively. The mean basic density and moisture content of these cubes are shown in Table 5.1.

Set 3 was cut out of a 1 m long log of *P. radiata* harvested at Owen River forest, Nelson, New

Zealand; the age of this tree was around 10 years, estimated by counting growth rings. The log had a small heartwood section and some dry patches that spread along the length, as shown in Figure 5.2. Those patches indicated that the log started drying; testing of some cubes that were

Figure 5.2. The dry patches (paler colour) within the green *P. radiata*, harvested at Owen River forest.

cut out of those patches is described in Appendix C.2. However, to compare *Set 3* with the other sets, the cubes were cut out of the wet region. This set consisted of 40 cubes, of which 16, 12, and 12 were tested in the longitudinal, radial, and tangential directions, respectively. The mean basic density and moisture content of *Sets 1-3* are summarised in Table 5.1.

Table 5.1. The mean moisture content (MC) and basic density (BD) of *Sets 1-3*.

Set	MC [%]	BD [$kg \cdot m^{-3}$]
Set 1	173 ($SD = 10$)	416 ($SD = 14$)
Set 2	142 ($SD = 26$)	453 ($SD = 43$)
Set 3	206 ($SD = 6$)	355 ($SD = 7$)

5.2.2 Experimental Set-Up

The moisture content within the cubes during heating of samples was controlled with four custom built sealed boxes (Figure 5.3a). The main part of each box consisted of a sealed plastic enclosure with threaded cable glands; all the parts were designed to operate reliably up to 100°C. Two brass plate electrodes were mounted inside the boxes. Brass tubes were welded to the plates and put through the cable glands. The brass tubes were attached to an AC electric source, using crocodile clips. To improve the contact between the timber samples and the brass

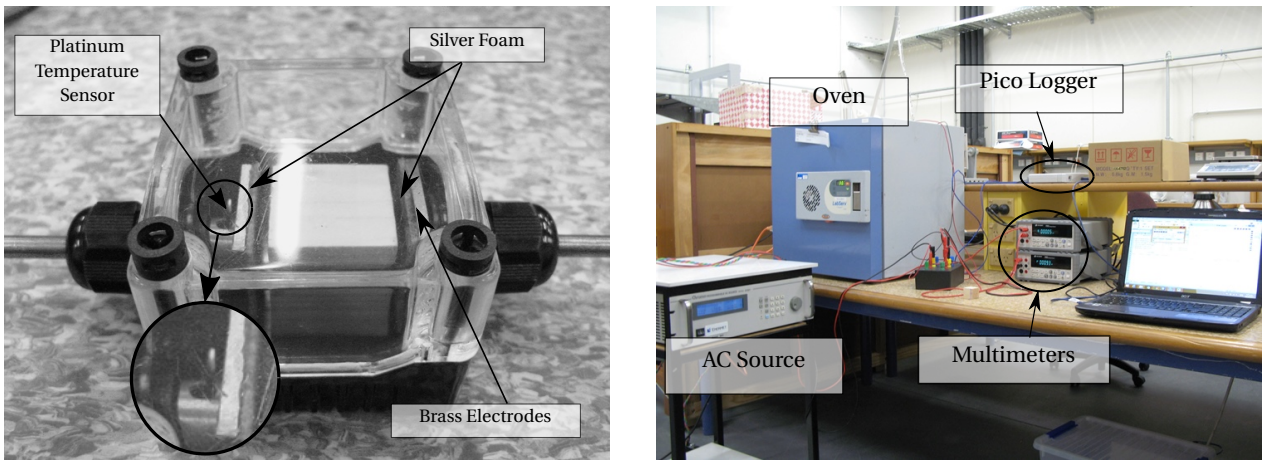

(a) Plastic Box (b) Complete Set-Up

Figure 5.3. The electrical conductivity testing rig.

electrodes, a self-adhesive electrically conductive silver foam (SOFT-SHIELD 4850 from Parker Chomerics) was stuck to the brass plates. Temperature of the boxes was maintained by an oven, with an integrated temperature controller. To measure the temperature of the sample, each box was equipped with a temperature sensor (PT-100) connected to a data logger (Pico Technology PT-104) that recorded the temperature every second. The complete set-up is shown in Figure 5.3b.

5.2.3 Experimental Procedure

Minimizing Contact Resistance

Prior to inserting the cubes into the boxes, their dimensions in all three directions were measured using a vernier calliper, with a resolution of 0.05 mm. The cubes were weighed with a resolution of 0.01 g. To pass an electrical current, wood, with its anisotropic electrical conductivity and rough surface, requires each point on the contact surface being attached to the electrodes; unlike metal materials that can rely on a single contact point on each electrode. A partial contact would increase the magnitude of contact resistance, overestimating the real electrical resistance of the wood. Appendix C.3 describes in detail the effect of contact resistance and the associated error, using axial electrical resistors.

In an ideal scenario, the contact resistance shall be reduced to zero, mathematically described as:

$$R_{exp} \underset{R_c \to 0}{=} 2 \cdot R_c + R_w, \tag{5.2}$$

where R is the electrical resistance [Ω]; exp denotes the resistance measured in the experiment; c refers to the electrical resistance of a single contact, arising due to air-gaps between the electrodes and sample surfaces; and w stands for the actual wood electrical resistance of the wood sample. Although silver foam can conform to the samples' contact surfaces, increasing the surface area of the contacts, the foam's porous structure leaves some air pockets on the contact surface. Therefore, to further improve the contacts, the surface of wood needs to be coated by a conducting material that fills those air pockets.

The first option was to use a high-conductive gel, saturated with sodium chloride. It filled the air pockets and reduced contact resistance. However, the ions of sodium chloride penetrated into the cubes, significantly enhancing their electrical conductivity. The penetration of sodium chloride into the cubes is described in Appendix C.4. Such penetration was not obvious during Joule heating of the boards described in Chapter 3, due to the boards' length of 475 mm. As such it was not considered to have significantly affected those results. That made the gel ideal for long samples with relatively rough contact surfaces such as logs. To avoid penetration of ions into cubes, it was decided to use a metal material. Free electrons, the carriers of electrical charge in metals, cannot escape from the structure and hence cannot enhance wood's electrical conductivity. Stamm (1960) used mercury to reduce contact resistance at a wood surface. However, unlike the gel, mercury does not adhere to a wood surface and hence it may not fill all the gaps. In addition, fumes of mercury are poisonous. In this research, two different materials were used to reduce contact resistance: a conductive silver epoxy and metal leaves (gold and silver). The leaves were around 0.1 μm thin. Thus, when applied over the contact surface, it was assumed that they replicated the irregularities of the contact surfaces.

To choose the most suitable material, cubes from *Set 1* were coated either by a silver epoxy (MG Chemicals 8330S-21G), a silver leaf or a 22 carat orange gold leaf, the latter two produced by Noris Blattgold GmbH. The gold and silver leaves, applied without an adhesive material to the wood, were considered weightless, while the mass of applied silver epoxy was measured. The number of cubes covered by each coating type for each direction is shown in Table 5.2. Due to the better performance of gold leaf, determined by testing *Set 1*, the entire second and third sets were coated by the gold leaf.

Table 5.2. Number of cubes from *Set 1* used per each direction and type of coating.

Type of Coating	Directions		
	L	R	T
Silver Epoxy	16	12	12
Gold Leaf	20	12	12
Silver Leaf [a]	8	-	-

[a] The silver leaf was not used in the radial and tangential directions due to the superior performance of the gold leaf.

Recording Data

The sealed boxes, with the cubes inside, were weighed and put into an oven that was at room temperature, around 23°C. A sinusoidal voltage of 50 V at 400 Hz was supplied to each box by a programmable AC voltage source (Chroma 61504). This frequency was selected to coincide with concurrent work on an experimental log-scale Joule heating apparatus. However, to avoid significant Joule heating, the duration of the excitation was 3 s, after which the electrical parameters such as voltage across the sample, measured by KEYSIGHT U3402A, electrical current through the sample, measured by KEYSIGHT U34461A, and the temperature inside the boxes were recorded. Knowing the voltages, electrical currents, and the cubes' dimensions, the resistance and conductivity of each cube were calculated, using Equations 2.7 and 2.8, respectively. Thereafter, the temperature in the oven was set to 30°C. After 35 minutes of heating at the set temperature - that is the minimum required equilibration period estimated by computer modelling as described below in this section - the next excitation was performed. The procedure was repeated every 10°C up to 90°C. After the last excitation, each sealed plastic box, with the cube inside, was weighed to determine the mass of moisture lost out of the plastic box. The cubes' green volume was measured using the water displacement test, followed by drying in a oven at 105°C until reaching a constant mass. The basic density and moisture contents of the cubes were calculated, using Equations 2.1 and 2.2, respectively.

Moisture Loss and Cube Temperature

During the experiment, the mass of the plastic boxes changed due to moisture loss from the cubes. The average moisture loss was 3×10^{-4} kg. The cubes lost some additional moisture to

the unoccupied volume inside the plastic boxes, calculated as:

$$V_f = V_{box} - V_g, \tag{5.3}$$

where V_f, V_{box}, and V_g are the unoccupied volume inside the box [m^3]; the internal volume of the plastic box, equal to 2.1×10^{-4} m^3; and the green volume of the sample, with the average value of 2.8×10^{-5} m^3, respectively. In the worst-case scenario, assuming the air in the box was dry prior to the experiment and reaching 100% of relative humidity at 90°C, the mass of vapour in the unoccupied volume can be determined as:

$$m_V = \frac{V_f}{\upsilon_{V@90°C}}, \tag{5.4}$$

where m_V is the mass of the vapour [kg] and $\upsilon_{V@90°C}$ is the specific volume of the saturated vapour at 90°C, equal to 2.3593 $m^3 \cdot kg^{-1}$ (Cengel and Boles, 2011). Thus, taking into account the mass of moisture lost out of the box during the experiment of 3×10^{-4} kg and the maximum mass of evaporated water trapped inside the box, calculated using Equation 5.4 to be about 8×10^{-5} kg, the total average loss of moisture from the cubes was around 3.8×10^{-4} kg, decreasing the average moisture content of the first set of cubes from 173% to 169%. According to Stamm (1929, 1964), the effect of moisture content on electrical conductivity is almost insignificant at these moisture contents, being less than the effect of a 1°C temperature change.

To ensure that the internal temperature of the cubes reached the target temperature at each temperature step, the heating process was modelled using computational fluid dynamics (CFD). The model was developed using a commercial software (ANSYS CFX 17.0), employing the Finite Volume Method (FVM). As the samples were located inside the plastic boxes, preventing significant drying of the samples, the mass conservation equation and heat diffusion due to internal convection of water were not considered. Therefore, the model was described by the following single governing equation of energy conservation which was solved using the Second Order Backward Euler scheme:

$$\frac{\partial \rho_g C_p T}{\partial t} = \nabla \cdot (k \nabla T). \tag{5.5}$$

The thermal properties of *P. radiata* used in the model are functions of moisture content and

basic density (Pang et al., 1995):

$$C_p = 4184\frac{X + 0.324}{1.0 + X}, \tag{5.6}$$

and

$$k = \frac{\rho_s}{1000}(0.4 + 0.5X) + 0.024. \tag{5.7}$$

The block's external surface temperature was assumed to be equal to the temperature inside the plastic box. Thus, the boundary conditions were expressed as:

$$T_s = T_{exp}(t), \tag{5.8}$$

where T_s is the temperature of the cube's external surface and $T_{exp}(t)$ is the temperature inside the plastic box, recorded during the experiment as a function of time, t. The cube's geometry was meshed using rectangular hexahedrons, created using the sweeping and edge size control methods. Using a mesh and time-step independence study (Appendix C.6), the final result was achieved using the uniform mesh of 64,000 mesh elements, built as an array of 40 × 40 × 40 elements, and 500 time-steps (Figure 5.4). Figure 5.5 displays the results of the CFD model,

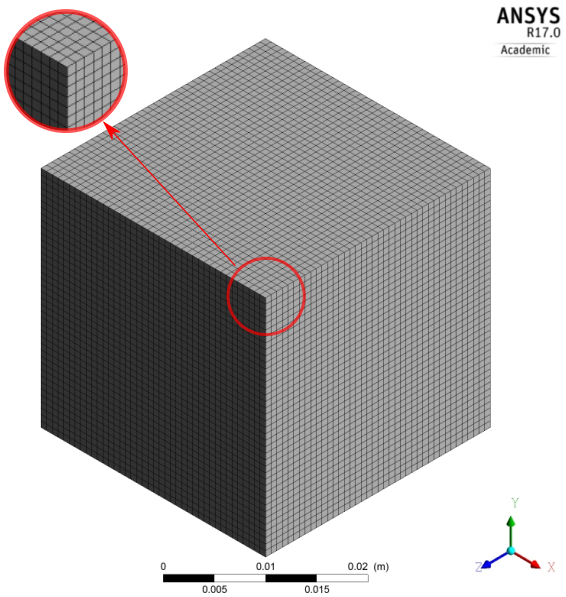

Figure 5.4. The uniform mesh of 64,000 mesh elements, used in the CFD model of heating green *P. radiata* cubes inside a plastic enclosure.

showing that around 35 minutes were required to reach each target temperature inside the cube under the applied conditions.

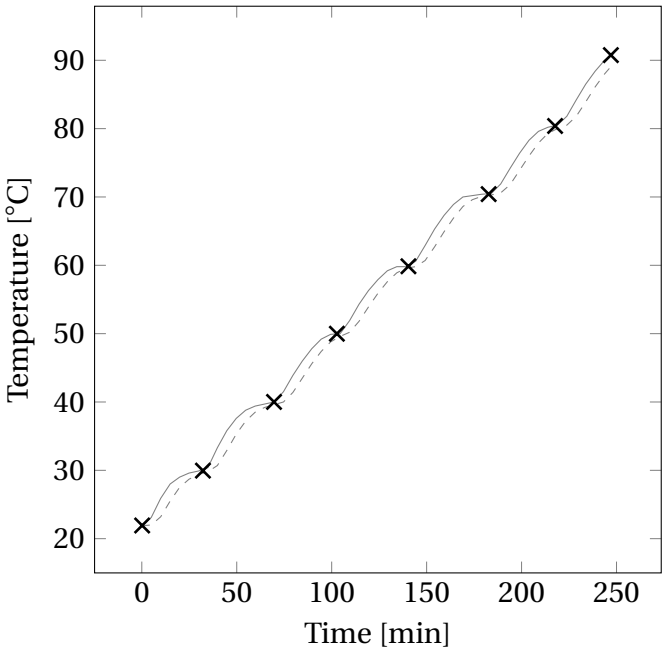

Figure 5.5. The modelled temperature of a test sample during the experiment. The solid and dashed lines represent the calculated cube's surface and internal temperatures (in the centre of the cube) respectively, while the crosses show the time when the actual electrical conductivity measurements were taken.

5.2.4 Statistical Modelling

Based on the experimental data, the four independent variables of temperature, moisture content, basic density, and the grain orientation were considered. Other wood parameters such as extractives of wood and electrical conductivity of the extractives' aqueous solutions were considered in an unpublished preliminary study; however, no correlation with Joule heating was found. To avoid multicollinearity - a phenomenon in which two or more independent variables are moderately or strongly correlated, causing inaccurate estimation of the predicted coefficients (Faraway, 2005) - in the model, initial data analysis using scatter plotting was performed. The variables that have a significant effect on the electrical conductivity were considered in the model. Then, using the statistical programming language, R 3.2.5 (R Core Team, 2016), with a user-created package, *lme4* (Bates et al., 2015), the fitted mixed effect regression model was developed. As the *lme4* package does not calculate p values, the *lmerTest* package (Kuznetsova et al., 2016) was used to calculate the p values.

5.3 Results

5.3.1 Statistical Modelling

The electrical conductivity of the first set of cubes was measured from 23°C to 90°C, in three principal (longitudinal, radial, and tangential) directions, with a total of 92 samples. These data are presented in the form of natural logarithm of electrical conductivity versus temperature in Figure 5.6. The wood was the most conductive in the longitudinal direction, with a mean value of electrical conductivity of 0.037 $S \cdot m^{-1}$, at 23°C, considering the data collected using the epoxy and leaves. This compares to 0.01 $S \cdot m^{-1}$ at 170% moisture content, measured by Stamm (1964) for slash pine in the longitudinal direction at room temperature. The electrical conductivities in the radial and tangential directions at the same temperature were 0.0037 and 0.0018 $S \cdot m^{-1}$, respectively. At room temperature, the average longitudinal electrical conductivity

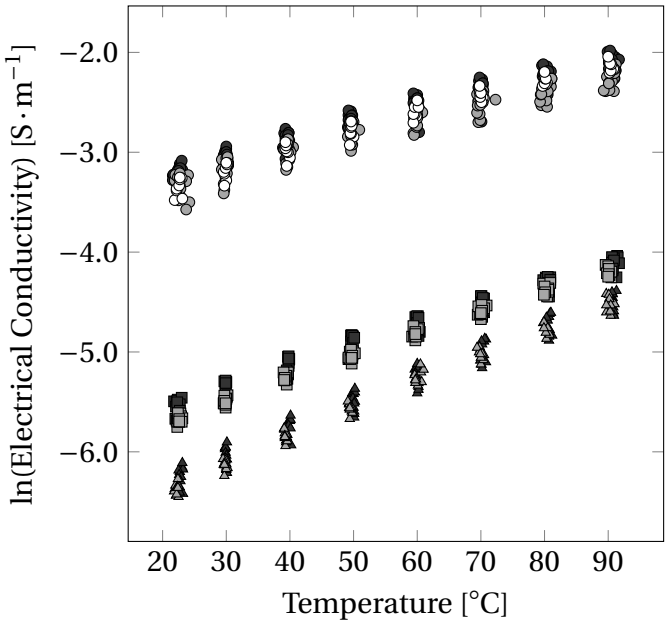

Figure 5.6. The natural logarithm of electrical conductivity of green *P. radiata* sapwood versus temperature. The circles, squares, and triangles denote the longitudinal, radial, tangential directions, respectively. The colours of scatters (black, grey, and white) represent the type of contact coating (gold leaves, silver epoxy, and silver leaves, respectively).

was approximately 10 and 20 times higher than the average radial and tangential conductivities, respectively (Figure 5.7). Similar ratio values between the longitudinal and transverse directions were provided by Burr and Stamm (1947), who measured electrical conductivity of softwood and hardwood, saturated with a solution of potassium chloride, at 30°C. However, the ratios between the longitudinal and transverse directions, measured by Sharma et al. (1997) at 70% moisture

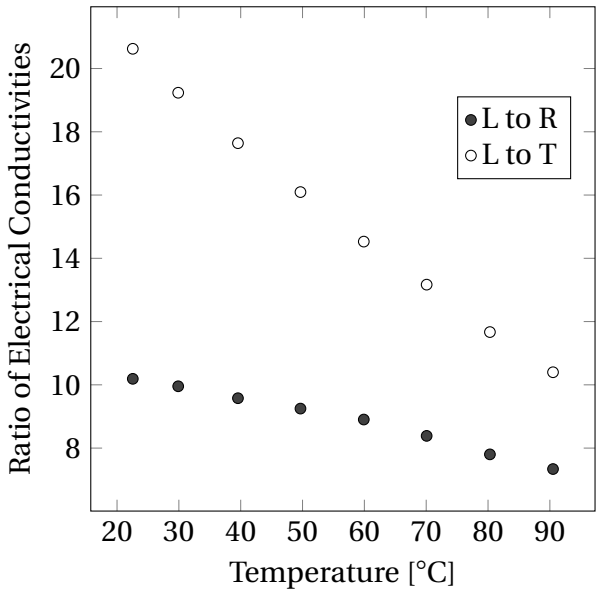

Figure 5.7. The effect of temperature on the ratios of the longitudinal electrical conductivity (L) to the radial (R) and tangential (T) electrical conductivities.

content, varied in a range of 5 to 10. In Figure 5.7, these ratios, however, decreased with the rise of temperature, and at around 90°C, they were about 7 for the longitudinal to radial ratio and 10 for the longitudinal to tangential ratio. The ratio of radial to tangential conductivity decreased from about 2, at room temperature, to 1.4, at 90°C. The most significant effect of the temperature rise was seen in the tangential direction, increasing the average conductivity by around 6 times between 20 and 90°C; the increase in the longitudinal and radial directions were about 3 and 4 times, respectively. The mean values of electrical conductivity at 90°C in the longitudinal, radial, and tangential directions were 0.12, 0.016, and 0.011 $S \cdot m^{-1}$, respectively.

The denser the wood tissue, the less water it can accommodate (Harris and Cown, 1991). To assess this relationship in the experimental data, a Pearson product-moment correlation coefficient was calculated. The experimental data showed a strong negative correlation between moisture content and basic density, with r = -.94, 95% CI [-.95, -.93], p value < .001, determined based on the total number of samples. To avoid multicollinearity behaviour, either the moisture content or the basic density (but not both) could be used in the statistical model. However, as stated by Skaar (1988), the effect of moisture content in green conditions was negligible in all directions (Figure 5.8), making the statistical model of electrical conductivity of green *P. radiata*'s sapwood a function only of temperature and direction.

Prior to deriving the model, the effect of the coating types was studied by comparing mean values of electrical conductivity in each direction. The sample mean of electrical conductivity

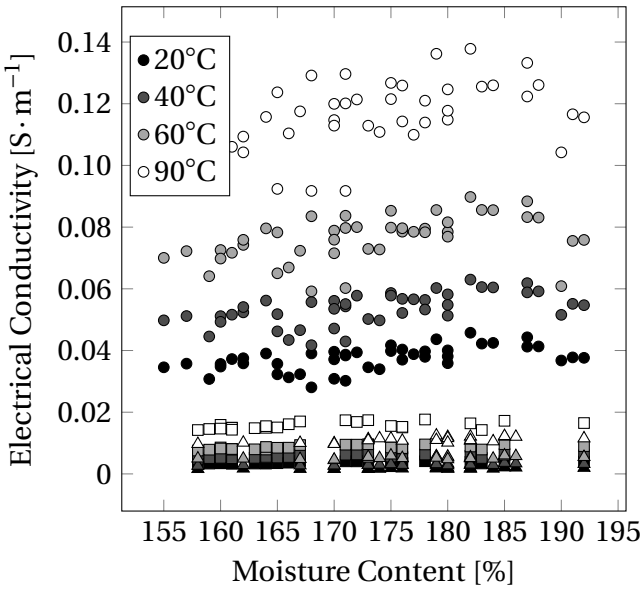

Figure 5.8. The effect of moisture content on the electrical conductivity in the longitudinal, radial, and tangential directions (the circle, square and triangle scatters, respectively) over the different temperature values.

obtained using the gold leaves was 10% higher than using the silver epoxy in the longitudinal and radial directions, and around 5% higher in the tangential direction. The results obtained using the silver leaves in the longitudinal direction were higher than the results obtained with the silver epoxy but lower than with the gold leaves. Thus, based on Equation 5.2, the data obtained by using the gold leaves was assumed the most accurate and was used to develop the statistical model.

Initially, several preliminary statistical models were developed:

$$\textit{Model 1:}\ \ln(\sigma) \sim (T) * D + (1|B), \tag{5.9}$$

$$\textit{Model 2:}\ \ln(\sigma) \sim \left[\beta_0 + \beta_1(T-55)\right] * D + (1|B), \tag{5.10}$$

$$\textit{Model 3:}\ \ln(\sigma) \sim \left[\beta_0 + \beta_1(T-55) + \beta_2(T-55)^2\right] * D + (1|B), \tag{5.11}$$

$$\textit{Model 4:}\ \ln(\sigma) \sim \left[\beta_0 + \beta_1(T-55) + \beta_2\frac{(T-55)^2}{1000}\right] * D + (1|B), \tag{5.12}$$

where β_i are the regression coefficients, with β_0 being the intercept; $(1|B)$ is the random effect term; $(T-55)$ is the mean centred temperature [°C]; and D is the direction, a factor variable.

These models were compared using the Akaike Information Criterion (AIC) - a statistical model selection method that compares models based on the maximum natural logarithm of the likelihood and the number of free parameters (Sakamoto et al., 1986; Bozdogan, 1987). The AIC values for *Models 1-4* were -690.8, -1081.4, -1267.8, and -1309.2; the most appropriate model has the lowest AIC value (Sakamoto et al., 1986) and hence *Model 4* was selected to describe electrical conductivity of green *P. radiata*. Using the estimated coefficients (Table 5.3), the following equations were derived:

$$\sigma_L = \exp\left[-2.60 + 0.017(T-55) - 0.073\frac{(T-55)^2}{1000}\right], \tag{5.13}$$

$$\sigma_R = \exp\left[-4.81 + 0.021(T-55) - 0.046\frac{(T-55)^2}{1000}\right], \tag{5.14}$$

$$\sigma_T = \exp\left[-5.37 + 0.026(T-55) - 0.046\frac{(T-55)^2}{1000}\right]. \tag{5.15}$$

Figure 5.9 shows the fitted model in all three directions with the data obtained using the gold leaf coating.

Table 5.3. Regression coefficients of the statistical model for electrical conductivity of green sapwood of *P. radiata*.

	Estimates	Std. Errors	t-value	p value
(Intercept)	-2.60	0.018	-143	< 2e-16
(T - 55)	0.017	0.00009	194	< 2e-16
(((T - 55)^2)/1000)	-0.073	0.004	-16.4	< 2e-16
DR	-2.21	0.030	-74.1	< 2e-16
DT	-2.77	0.030	-93.0	< 2e-16
(T - 55):DR	0.004	0.0001	29.4	< 2e-16
(T - 55):DT	0.009	0.0001	65.8	< 2e-16
(((T - 55)^2)/1000):DR	0.026	0.007	3.58	0.0004
(((T - 55)^2)/1000):DT	0.027	0.007	3.69	0.0003

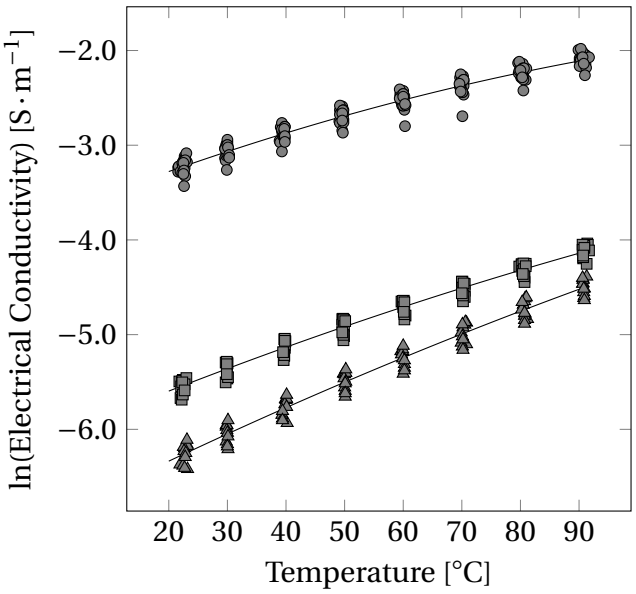

Figure 5.9. The mixed effect model (solid lines) fitted into the experimental data (obtained using gold leaf coating) of green *P. radiata*'s natural logarithm of electrical conductivity.

5.3.2 Electrical Conductivity of *Sets 1-3*

Figure 5.10 shows the effect of temperature on green *P. radiata's* electrical conductivity within three sets of samples, determined using the gold leaf coating. In the longitudinal and tangential directions, the lowest mean electrical conductivity was observed in *Set 2, P. radiata* from Ashley forest. *Set 1*, from McVicar Timber sawmill, had the lowest mean electrical conductivity in the radial direction; however, the difference was low, being less than 5% at 90°C, based on the highest radial electrical conductivity. *Set 3*, from Owen River forest, showed the highest electrical conductivity in the longitudinal and radial directions. In the longitudinal direction, its mean electrical conductivity was almost twice that of *Set 2*. This ratio difference stayed relatively constant over the whole temperature range. The difference between *Set 3* and *Set 1* was less pronounced and, in the longitudinal direction, it was less than 3%.

In addition, some of the samples from Ashley forest showed a sudden drop of electrical conductivity above 70°C (Figure 5.10a). After a thorough inspection of electrodes, this sudden drop of electrical conductivity was linked to corrosion of the electrodes. After replacing the silver foam and polishing the electrodes, this behaviour disappeared. As the condition of electrodes is crucial in this experiment, such behaviour can be used as an indicator of faulty electrodes in the future research.

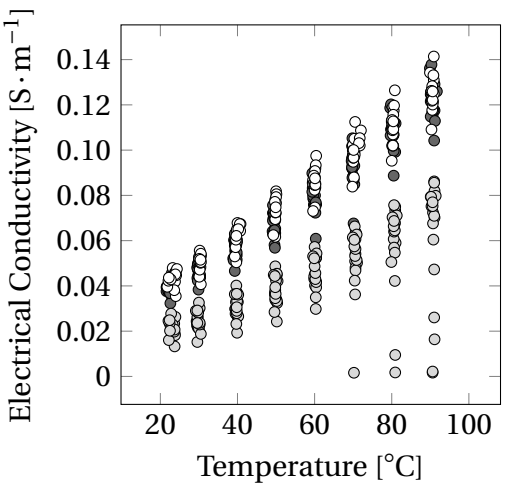

(a) Longitudinal

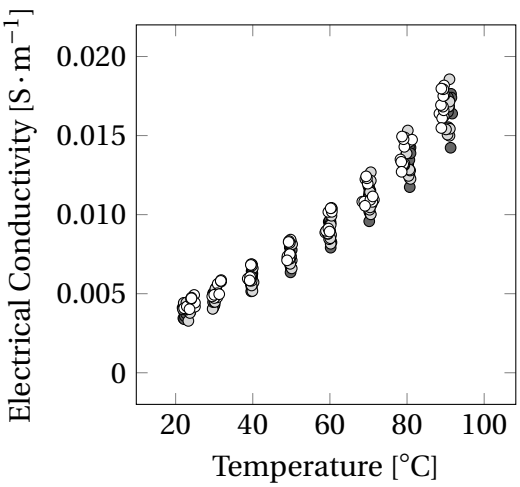

(b) Radial

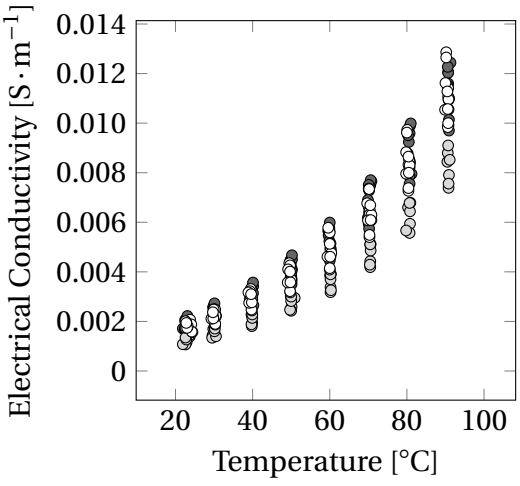

(c) Tangential

Figure 5.10. The effect of different *P. radiata* sapwood from three sites on electrical conductivity in all principal directions. The dark grey, light grey, and white colours denote *Set 1*, *Set 2*, and *Set 3*, respectively.

5.3.3 Electrical Conductivity of Cubes and Boards

The cubes' electrical conductivity was compared with the electrical conductivity of the flat boards of Chapter 3 in Figure 5.11. The electrical conductivity of the boards, being cut out of the beams provided by McVicar Timber sawmill, showed a close agreement with longitudinal electrical conductivity of *Set 1* and *Set 3*.

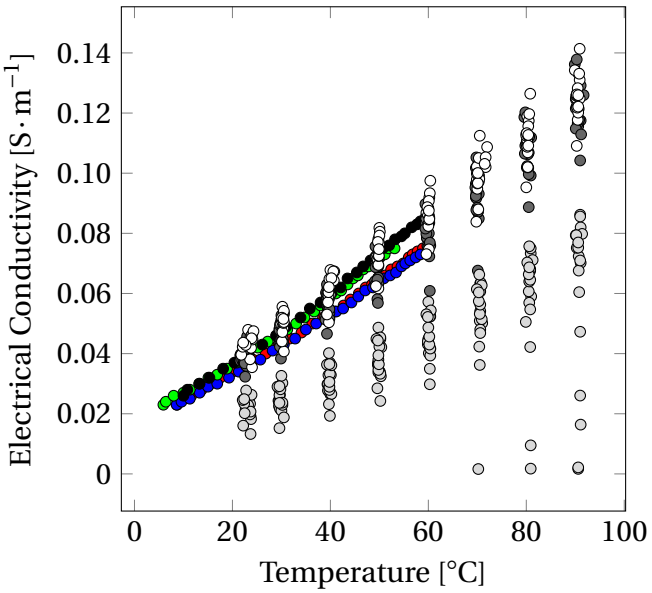

Figure 5.11. The effect of temperature on the electrical conductivity of cubes (the dark grey, light grey, and white circular scatters) and of four sapwood boards (the coloured circles).

5.4 Discussion

The carriers of electrical charge in aqueous solutions, such as wood sap, are ions. Three parameters affect the electrical conductivity of aqueous solutions: the magnitude of the ions' charge, the concentration of ions, and the mobility of ions (Bard and Faulkner, 2001). Potentially, the magnitude of the ions' charge and concentration of the ions are relatively constant within an energised sample at the centimetre scale. However, the mobility of ions strongly depends on temperature, where the higher the temperature, the more mobile the ions become (Bard and Faulkner, 2001). Moreover, the continuity or discontinuity of electrical conduction paths increases or decreases the electrical conductivity of green wood (Skaar, 1988).

Figure 5.10 shows the rise of electrical conductivity with the temperature in all grain directions. The result indicates that the increase of temperature increases the mobility of ions in the wood sap, resulting in an increase of electrical conductivity. As expected, the highest electrical conductivity was in the longitudinal direction, along which wood sap is conveyed and 95% of radiata pine's tissue is oriented (Harris, 1991b). In a freshly sawn tree, the longitudinal tissue, containing sap saturated earlywood tracheids, forms continuous water columns, which appear as direct electrical conduction paths (Sharma et al., 1997). On the other hand, there are few continuous paths in the radial direction - radial rays, occupying up to 5% of the wood volume, convey the sap (Bamber and Burley, 1983; Harris, 1991b) - and none in the tangential direction. Hence, the

radial electrical conductivity is slightly higher than the tangential conductivity. Thus, the higher the number of wood cavities in a given direction, the higher the conductivity of green sapwood in that direction.

Although there is no wood tissue aligned in the tangential direction, pits, all located in the radial walls, allow a tangential flow of sap. If pits conducted most of electric current through green sapwood, the tangential electrical conductivity would be much higher than the radial conductivity. However, the results showed that the effect of pits is insignificant. Stamm's (1929) experiments indicated the same behaviour. He oven-dried *S. sempervirens* samples and then re-saturated them with distilled water. Stamm (1929) found that electrical conductivity of the re-saturated samples was similar to that of green *S. sempervirens*. During drying, the pits in Stamm's (1929) samples had to be irreversibly aspirated; however, the aspiration did not affect the conduction of electric current, meaning that pits do not notably improve electrical conductivity. Furthermore, as pits in re-saturated wood were aspirated, the electric current flowed through the cell walls.

The effect of temperature on the electrical conductivity of salt solutions is near linear, in the range from 0 to 90°C (McCleskey, 2011; Haynes, 2014). However, based on the form of the statistical model (Equation 5.12), this correlation is non-linear for green wood. The effect of wood structure is less significant in the longitudinal direction, with the direct electrical conduction paths, and more significant in the transverse directions, where the conduction paths are indirect. In the radial direction, electric current must flow mainly through cell walls, with a small number of direct paths, presented by rays, while in the tangential direction, the current predominantly flows through cell walls. Without direct conductive paths, the conduction of current in the radial and tangential directions may rely on the diffusion rate of moisture, non-linearly correlated with temperature; according to Langrish and Walker (2006), a rise of temperature of wood from 25 to 100°C increases the diffusion rate of moisture up to 37 times. Moreover, the statistical analysis showed that the effect of temperature on electrical conductivity of green *P. radiata* sapwood is much more significant than moisture content. The derived Equations 5.13 - 5.15 incorporate the effects of temperature and direction on the electrical conductivity of green New Zealand *P. radiata*.

Figure 5.10 also shows variation of electrical conductivity between the sets of *P. radiata*. This

difference can be explained by variation of growing conditions such as temperature and level of rainfall, which affect trees' growth rate, resulting variation of wood properties between trees. However, it is unclear whether this variation was caused by tree-to-tree and/or site-to-site differences. Thus a larger data set from different trees should be collected. Furthermore, the results showed that the age of tree may not affect electrical conductivity significantly, as 10 year old radiata pine from Owen River forest (*Set 3*) behaved similarly to 30 year old *P. radiata* from McVicar Timber sawmill (*Set 1*). Further work should be done to verify the effect of tree age on electrical conductivity.

The statistical model does not require an adjustment to predict electrical conductivity of *P. radiata* from Owen river forest; however, to predict electrical conductivity of Ashley forest *P. radiata* the model must be modified. Due to a similar effect of temperature on electrical conductivity in each set - the ratio difference between the mean values of the sets' electrical conductivity was relatively constant from 20 to 90°C -, the modification of the model requires an additional coefficient, further called a *multiplier*, to adjust the predicted curve. For example, to predict electrical conductivity of Ashley forest's *P. radiata* in the longitudinal direction, the model needs to be multiplied by a factor of 0.62 (Figure 5.12). Thus, the multiplier can adjust

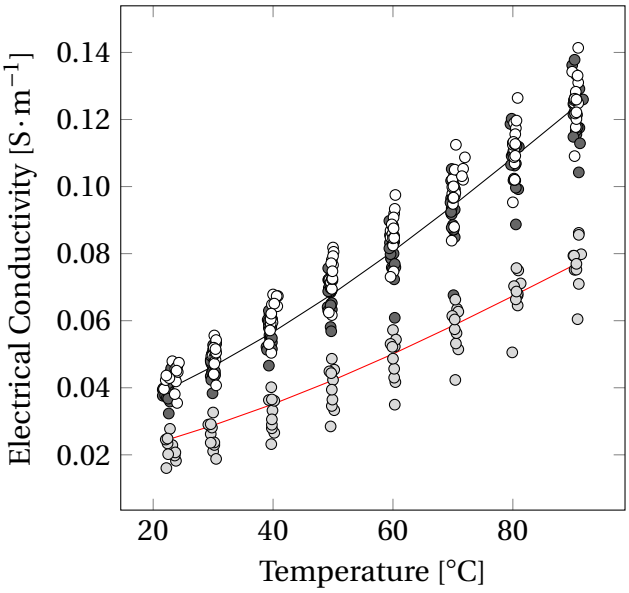

Figure 5.12. Adjusting the statistical model to predict longitudinal electrical conductivity of *Set 2*. The black and red solid lines denote the original and adjusted models. The white, light grey, and dark grey scatters represent *Sets 1-3*, respectively. *Note:* The electrical conductivity measurements affected by the electrode corrosion are not included in this graph.

the model, if initial experimental conductivity is known. In practice, this can be done by a short

excitation prior to Joule heating.

The boards, with the heterogeneous structure, and the cubes, with the relatively homogeneous structure, showed a good agreement (Figure 5.11). This contradicts the initial second conjecture of Section 5.1 and means that electrical conductivity in green sapwood is scalable, independent of a sample's dimensions. Furthermore, the type of heating does not affect electrical conductivity, as the boards were heated by Joule heating and the cubes were heated by convection-conduction. Therefore, if a log is preheated by convection and then heated by Joule heating, electrical conductivity can be predicted by the same model, assuming that the correct multiplier and temperature of the log are used in the model. As a result, the statistical model can be used to predict electrical conductivity of cubes, boards, and logs heated by different heating methods.

5.5 Conclusions

The obtained statistical model can be used to accurately simulate the Joule heating process in green sapwood of *P. radiata*. In such simulations, the model can be modified to account for the spatial and temporal distribution of electrical conductivity and hence specific power dissipation and resulting temperature rise. Comprised of three equations, one per grain direction, the model can be applied for simulation of Joule heating in samples of different shapes and sizes such as logs or sawn boards. The model is limited to the 100 - 200% moisture content range, common to New Zealand grown green *P. radiata* sapwood. Accurate estimation of green *P. radiata* sapwood's electrical conductivity requires only knowledge of wood temperature. The model can be adjusted by adding a multiplier that can be determined prior to an official Joule heating treatment, using a short excitation to estimate an initial electrical conductivity. The effects of moisture content and basic density on electrical conductivity, at moisture contents above 100%, are negligible, as stated by Stamm (1929), Lin (1967), and Sharma et al. (1997).

Chapter 6

Computational Modelling and Verification

6.1 Introduction

Simulations are widely used by engineers to study and collect data for different operations avoiding expensive and time-consuming experiments. The results of simulations enhance understanding of complex problems and help in decision making. This research used computational fluid dynamics (CFD) to develop a model of Joule heating of green *P. radiata* logs. CFD is an engineering tool commonly used to simulate fluid flow and/or heat transfer; it is generally employed in many engineering fields such as chemical and electrical engineering (Versteeg and Malalasekera, 2007).

If not used properly, CFD can provide non-physical results that can lead to faulty conclusions and then to problems in applications. Therefore, to reduce the error and ensure credibility of the CFD model, two main principles, verification and validation (V&V), are commonly applied (Oberkampf and Trucano, 2002). At the verification step, a model's output is compared with a highly accurate solution determined by analytical methods, benchmark ordinary differential equations (OED), or benchmark partial differential equations (PDE) (AIAA, 2002). Such comparisons are the most accurate method to quantitatively estimate the computational error.

There are four potential sources of error (AIAA, 2002). The first source of error is insufficient mesh and time-step resolution (spatial and temporal discretization convergence). Increasing the number of mesh elements (control volumes) and of time-steps should decrease the error asymptotically to zero, excluding rounding errors (AIAA, 2002). The second source is an iterative convergence error, only applicable if the solver of the CFD code is based on an iterative method of solving a system of discretised equations. Such CFD solvers generate a solution at each iteration, known as the iterative solution. The iterations stop when the iterative solution matches the exact

solution; in this case, the difference between the solutions, called the residual, is equal to zero. However, it is not generally practical to reach the exact solution; therefore, the numerical scheme will iteratively converge if the number of iterations at each time-step is sufficient to reduce the residuals to below an iterative convergence criterion, which depends on the simulated scenario and is specified by the user (AIAA, 2002). The third and fourth causes of error are mistakes (bugs) in the CFD code, created by the programmers, who developed the code, and errors made by the user (operator), respectively (Versteeg and Malalasekera, 2007). The verification procedure shall be repeated after each modification of CFD code (AIAA, 2002). The limitation of verification is that "highly accurate solutions" are only available for limited, particular cases that are commonly simpler than actual, real cases. Therefore, a CFD model needs to be simplified for the verification test.

Validation is a process that assesses the accuracy of a CFD model by comparing it with experimental data (AIAA, 2002). As verification, it generally starts with examining iterative convergence and performing a mesh and time-step independence study. Thereafter, the CFD results are compared with the experimental results. Thus, quality of the validation depends on accuracy of the experimental results. The last step of validation is to assess uncertainties of the model. However, it is often impractical for complex problems that involve multi engineering systems to strictly follow the procedure (AIAA, 2002). As a result, the validation procedure varies based on the simulated application. The CFD model of Joule heating of green *P. radiata* logs and its validation are discussed in Chapter 7. The purpose of this chapter, however, is to demonstrate the verification procedures that were used to build the CFD model for simulation of the Joule heating effect in wood.

6.2 Methods

6.2.1 Mathematical Formulation

Governing Equations

The proposed wood treatment based on the Joule heating effect is relatively fast and avoids significant moisture losses, allowing the governing equation of mass conservation to be omitted. It was assumed that there was no heat transfer due to internal convection of water and moisture evaporation within the wood in the Joule heating method; hence, the convection term in the

heat transfer equation was set to zero. Thus, the wood treatment was described by the heat conservation equation, written as :

$$\frac{\partial \rho_g C_p T}{\partial t} = \nabla \cdot (k \nabla T) + \bar{S}, \tag{6.1}$$

where ρ_g is the green density [$\mathrm{kg \cdot m^{-3}}$], C_p is the heat capacity [$\mathrm{J \cdot kg^{-1} \cdot °C^{-1}}$], T is the temperature [°C], t is the time [s], k is the thermal conductivity [$\mathrm{W \cdot m^{-1} \cdot °C^{-1}}$], and $\bar{S}$ is the heat source term [$\mathrm{W \cdot m^{-3}}$]. The conduction of an electrical current can be described by the governing conservation equation of electrical charge, described as:

$$\nabla \cdot (\boldsymbol{J}_e) = 0, \tag{6.2}$$

where $\boldsymbol{J}_e$ is the electric current density [$\mathrm{A \cdot m^{-2}}$], equal to:

$$\boldsymbol{J}_e = \sigma \boldsymbol{E}, \tag{6.3}$$

where σ is the electrical conductivity [$\mathrm{S \cdot m^{-1}}$], and $\boldsymbol{E}$ is the electric field [$\mathrm{V \cdot m^{-1}}$]. If the conducting material is anisotropic, such as wood, the electrical conductivity should be expressed as a second rank tensor ($\overline{\overline{\sigma}}$). The heat source term ($\bar{S}$) in Equation 6.1 can be calculated as (Perré, 2004):

$$\bar{S} = \boldsymbol{J}_e \cdot \boldsymbol{E} = \sigma \boldsymbol{E}^2. \tag{6.4}$$

The electric field ($\boldsymbol{E}$) is equal to:

$$\boldsymbol{E} = \frac{U}{l}, \tag{6.5}$$

where is U is the electric potential difference [V], across the length (l). In addition, according to the experimental results presented in Chapter 5, the electrical conductivity of green *P. radiata*

depends on temperature. Therefore, the governing equations are coupled and shall be solved simultaneously (Marra et al., 2009).

Boundary and Initial Conditions

To solve Equation 6.1, initial and boundary conditions need to be specified; Equation 6.2 is expressed in steady state form and hence requires only boundary conditions (Perré, 2004; Marra et al., 2009). Each verification case used in this study has unique boundary and initial conditions. In total, five verification cases were developed in this study:

Case 1: to verify constant power generation caused by the Joule heating effect inside a fully insulated geometry;

Case 2: to verify transient heat conduction and power generation using a known one dimensional analytical model;

Case 3: to verify the effect of non-uniform electrical conductivity;

Case 4: to verify anisotropic electrical conductivity;

Case 5: to verify hot and cold spot generation.

a) Case 1

This case was developed to verify the conversion of electrical energy into thermal energy. It was assumed that electrical energy was generated inside a 1 m^3 solid cube and 2303 V was applied across two opposite faces. Electrical conductivity of the cube was uniform and isotropic, equal to 0.05 $S \cdot m^{-1}$. The cube was thermally insulated and hence the generated heat stayed within the volume. The duration of heating was one hour. Heat capacity and density of the cube were 3500 $J \cdot kg^{-1} \cdot °C^{-1}$ and 1000 $kg \cdot m^{-3}$, respectively. According to Shim et al. (2010), during the Joule heating effect, the efficiency of energy conversion from electrical energy into thermal energy is close to 100%, assuming contact resistance is negligible. Therefore, based on these conditions, a temperature rise in the cubes was constant and uniform, analytically calculated as:

$$T_f = T_i + \frac{Q}{mC_p}, \tag{6.6}$$

where T_f and T_i are the final and initial temperature of the cube [°C], respectively; m is the mass of the cube [kg]; and Q is the heat [J] generated from electrical energy that can be expressed as:

$$Q = Pt. \tag{6.7}$$

Hence, 1 J is equal to 1 W·s. Using Equations 2.8 and 2.9, Equation 6.6 can be re-written as:

$$T_f = T_i + \frac{U^2 \sigma A t}{l m C_p}, \tag{6.8}$$

where l is the cube's length along which the electrical current flows, equal to 1 m; and A is the cross-sectional area of the cube, equal to 1 m^2. Thus, if the initial temperature of the cube was uniform and equal to 0°C, the final temperature of the cube after one hour of heating will be approximately 273°C.

The above initial and boundary conditions of *Case 1* can be summarised in the following form, common for CFD modelling:

$$T_i = 0\ ^\circ\text{C} \quad \text{at} \quad t = 0\ \text{s}, \tag{6.9}$$

and

$$\left.\begin{array}{ll} \boldsymbol{J}_h \cdot \hat{\boldsymbol{n}} = 0\ \text{W}\cdot\text{m}^{-2} & \text{at all external surfaces} \\ \boldsymbol{J}_e \cdot \hat{\boldsymbol{n}} = 0\ \text{A}\cdot\text{m}^{-2} & \text{at external surfaces} \\ U = 2303\ \text{V} & \text{at the high voltage electrode} \\ U = 0\ \text{V} & \text{at the low voltage electrode} \end{array}\right\} \quad \text{at} \quad t > 0\ \text{s}. \tag{6.10}$$

b) Case 2

During Joule heating of green wood, transient heat conduction occurs between the hot internal part and the cooler external surface. *Case 2* was developed to verify the CFD model using the analytical solution of one dimensional transient heat conduction for a slab with an internal constant heat source, such as the Joule heating effect. The slab had unique boundary and initial conditions, schematically shown in Figure 6.1.

It was assumed that the slab was infinitely tall and wide, with the initial temperature of 0°C.

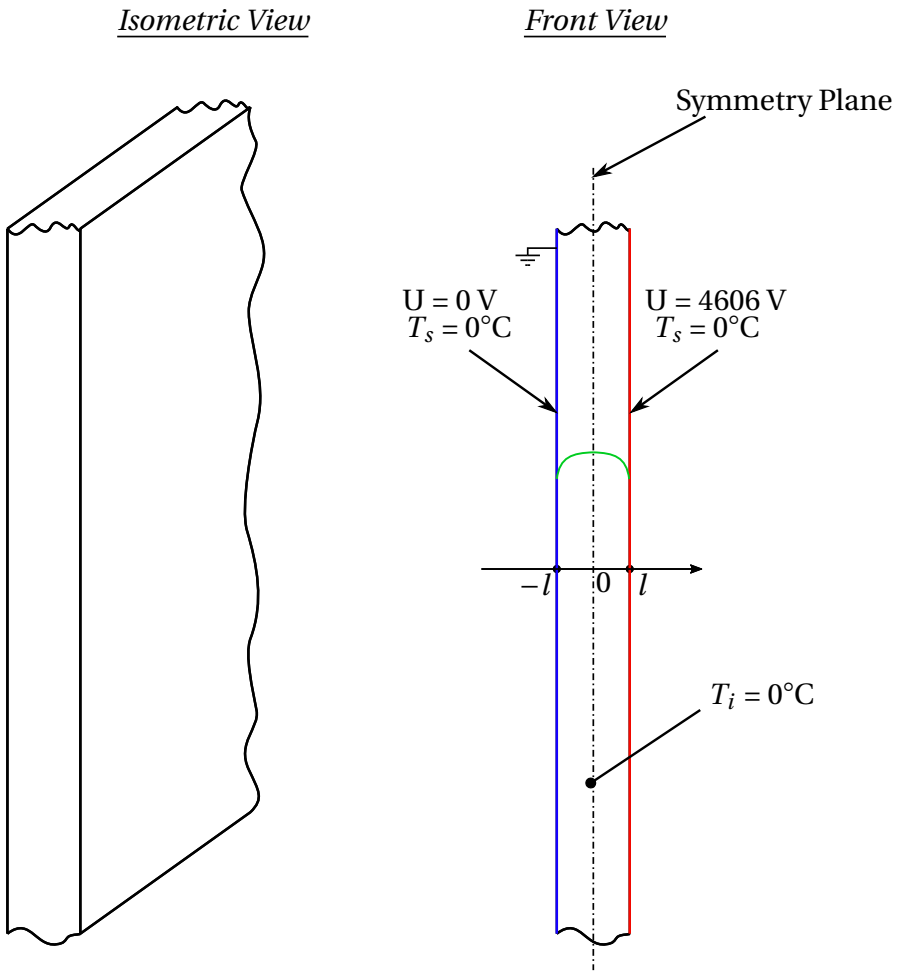

Figure 6.1. The schematic diagram of the slab with depicted boundary and initial conditions. *Note:* The red and blue lines denote the high-voltage and low-voltage sides. The green line schematically shows the expected temperature profile within the slab.

Two opposite faces of the slab were kept at constant temperature of 0°C. A constant rate of heat generation $\bar{S}$ was caused by the voltage drop of 4606 V across the slab. These conditions ensured one dimensional symmetrical heat conduction along the slab's thickness ($-l$ to l). As this case was symmetrical, the analytical solution provided the temperature profile from the symmetry plane to the face l. The solution is written as (Carslaw and Jaeger, 1959):

$$T = \frac{\bar{S}l^2}{2k}\left[1 - \frac{x^2}{l^2} - \frac{32}{\pi^3}\sum_{n=0}^{\infty}\frac{(-1)^n}{(2n+1)^3}\cos\frac{(2n+1)\pi x}{2l}\exp\left(\frac{-\alpha(2n+1)^2\,\pi^2 t}{4l^2}\right)\right], \tag{6.11}$$

where l is the distance from the symmetry plane to the face kept at 0°C [m]; α is the thermal diffusivity [$m^2 \cdot s^{-1}$]; t is the duration of Joule heating, equal to 1000 s; and x is the distance from the symmetry plane of the slab to a node of interest at which the temperature must be calculated. The node of interest should lie between the symmetry plane and the boundary face l. The thermal diffusivity (α) can be calculated as:

$$\alpha = \frac{k}{C_p \rho}. \tag{6.12}$$

As the slab was assumed to have uniform electrical conductivity (Table 6.1), the voltage drop (U) of 2303 V was uniform from the face l to the symmetry plane. The constant heat generation $\bar{S}$ is equal to:

$$\bar{S} = \sigma\left(\frac{U}{l}\right)^2. \tag{6.13}$$

Three temperature profiles were calculated, analytically, for three slabs' halves (*Case 2*) with the l distance set to: 0.475 m, 0.1 m, and 0.01 m.

Table 6.1. The properties of the slab used in *Case 2*.

Properties	Values	Units
Electrical Conductivity	0.034	$S \cdot m^{-1}$
Thermal Conductivity	10	$W \cdot m^{-1} \cdot °C^{-1}$
Heat Capacity	1000	$J \cdot kg^{-1} \cdot °C^{-1}$
Density	1000	$kg \cdot m^{-3}$

Unlike an analytical approach, computational calculations are based on geometries with finite dimensions. Figure 6.2 shows how the three dimensional geometry was used to solve the slab

heating problem with constant power generation by applying appropriate boundary conditions. This method allowed the use of a single three dimensional geometry of 0.475 m length (Z), 0.1 m

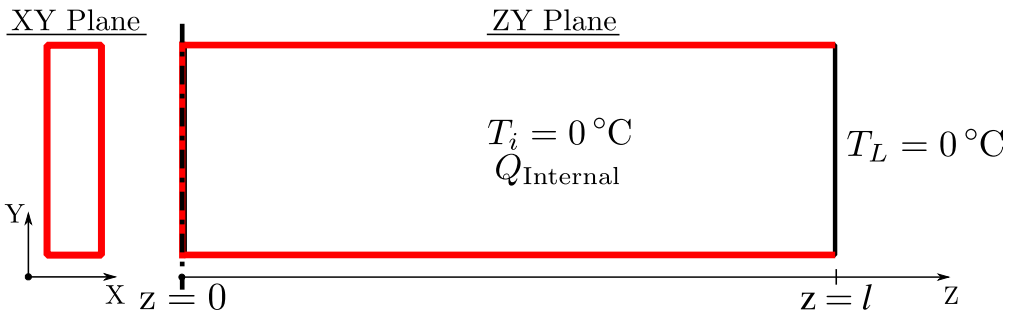

Figure 6.2. The example of 1D heat conduction in the Z direction, using the 3D geometry, where the red faces in the geometry are insulated. *Note*: The symmetry plane (the dash-dotted line) was assumed to be aligned with $z = 0$.

width (Y), and 0.01 m thickness (X) to obtain analytically calculated temperature profiles.

Three simulations were done. At the first simulation, the temperature profile was calculated along the Z direction. The constant voltage of 2303 V was applied through two electrodes across the length. One of the electrodes was attached to the face kept at 0°C, while the other electrode was attached to the opposite face, aligned with the symmetry plane. All faces of the geometry were thermally insulated, except the face that was at 0°C. Following this method, simulations were done in the other two directions: along the geometry's width (Y) and the thickness (X).

If heat conduction occurs in the Z direction, the above conditions can be re-written in the following form:

$$T_i = 0^\circ\mathrm{C} \quad \text{at} \quad t = 0 \text{ s}, \tag{6.14}$$

and

$$\left.\begin{aligned} T_L &= 0^\circ\mathrm{C} \quad \text{at } \mathrm{z_L} = 0.475 \text{ m} \\ \boldsymbol{J}_h \cdot \hat{\boldsymbol{n}} &= 0 \text{ W}\cdot\text{m}^{-2} \quad \text{at the line of symmetry (z = 0 m)} \\ \boldsymbol{J}_h \cdot \hat{\boldsymbol{n}} &= 0 \text{ W}\cdot\text{m}^{-2} \quad \text{at the other insulated sides} \\ \boldsymbol{J}_e \cdot \hat{\boldsymbol{n}} &= 0 \text{ A}\cdot\text{m}^{-2} \quad \text{at the insulated sides} \\ U &= 2303\,\text{V} \quad \text{at } \mathrm{z_L} = 0.475 \text{ m} \\ U &= 0\,\text{V} \quad \text{at } \mathrm{z_L} = 0 \text{ m} \end{aligned}\right\} \quad \text{at} \quad t > 0 \text{ s}. \tag{6.15}$$

However, if heat conducts in the X or Y direction, the length, along which the heat conduction occurs, will be either equal to 0.01 m or 0.1m, respectively.

c) Case 3

The aim of *Case 3* is to verify non-uniform electrical conductivity using a known analytical solution. In this case, three connected isotropic cubes of 0.05 m side-length were at the uniform temperature of 0°C prior to heating (Figure 6.3). Fifteen volts were applied across the whole

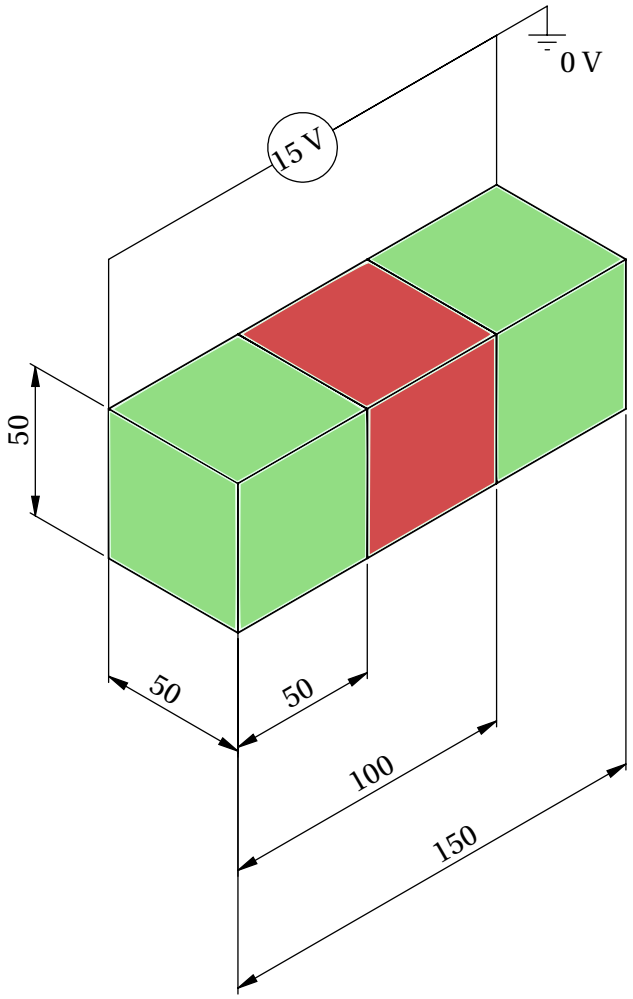

Figure 6.3. The schematic drawing of *Case 3*, where the electrical conductivity of the green and red cubes were 4 $S \cdot m^{-1}$ and 6 $S \cdot m^{-1}$, respectively. *Note:* The dimensions are in millimetres.

assembly, where the electrical conductivities of the central and side cubes were 6 and 4 $S \cdot m^{-1}$, respectively. The specified electrical conductivities were uniform within each cube. Other properties of density, thermal conductivity, and heat capacity were the same for all cubes and were equal to 1000 $kg \cdot m^{-3}$, 0.5 $W \cdot m^{-1} \cdot °C$, and 3500 $J \cdot kg^{-1} \cdot °C^{-1}$, respectively. The duration of the excitation was 1000 seconds.

If all the cubes' electrical conductivities were the same, 4 $S \cdot m^{-1}$, then the voltage drop along

the whole assembly's length would be linear. To prove that, let each cube be represented as an axial resistor with three cubes representing a system of series resistors (Figure 6.4). The resistance

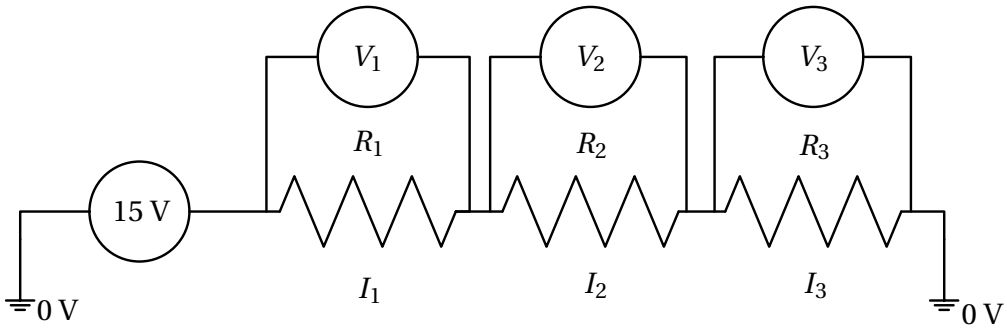

Figure 6.4. *Case 3* presented as three resistors in series.

of each resistor can be calculated using Equation 2.8 as:

$$R = \frac{l}{\sigma A}. \tag{6.16}$$

As the cubes have the same dimensions, their resistance values will be the same. According to Kirchhoff's law, electric current through each of the cubes is equal to the total current through the whole assembly, mathematically described as:

$$I = \frac{U}{R_1 + R_2 + R_3} = I_1 = I_2 = I_3. \tag{6.17}$$

Knowing electric current and resistance of each cube, the voltages across the cubes were calculated using Ohm's law:

$$U_i = R_i \cdot I_i, \tag{6.18}$$

where i denotes the number of the cube. Thus, if the dimensions, electrical conductivity, and electric current of each cube are the same, the voltage drop across each cube is the same and the electric field strength ($\mathrm{V \cdot m^{-1}}$) across the assembly is constant. However, if the electrical conductivity of the central cube increases from 4 to 6 $\mathrm{S \cdot m^{-1}}$ the voltage drop across the central cube will decrease. Figure 6.5 shows the change of the voltage drop across the central cube. In addition, power dissipation per unit volume, equal to the source term in Equation 6.1, within

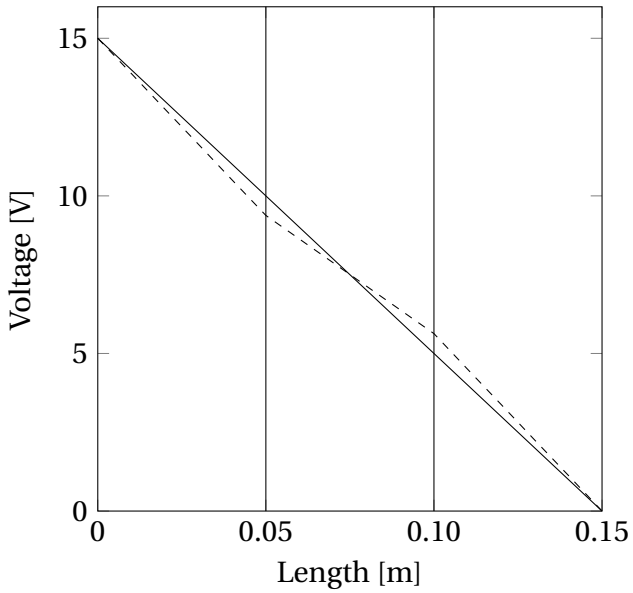

Figure 6.5. The analytical solution of *Case 3*. *Note:* The solid line represents the case where all the cubes have the same electrical conductivity of 4 $S \cdot m^{-1}$, and the dashed line denotes the case with the more conductive central cube of 6 $S \cdot m^{-1}$. The vertical solid lines denote the interfaces between the adjacent cubes.

each cube was calculated as:

$$P = \frac{UI}{V}, \tag{6.19}$$

where V is the volume of each cube [m^3].

To calculate *Case 3* using CFD modelling, each cube was presented as a separate domain with its own boundary and initial conditions. The external surfaces of the cubes were thermally insulated, while the interfaces between the cubes were considered as ideal thermal contacts (the thermal resistance is equal to zero). That meant: (1) two cubes with an adjacent interface had the same temperature at the interface; and (2) the interface could not accumulate energy and hence the heat flux on both sides of the contact surface was the same.

To explain the interface condition in detail, let one of the adjacent cubes be called Domain A and another be Domain B (Figure 6.6). Assuming that the heat transfer is one dimensional along the positive Z direction, then using Fourier's law of heat conduction, the heat flux can be described as:

$$\boldsymbol{J}_h \cdot \hat{\boldsymbol{n}} = -k\frac{\partial T}{\partial z}, \tag{6.20}$$

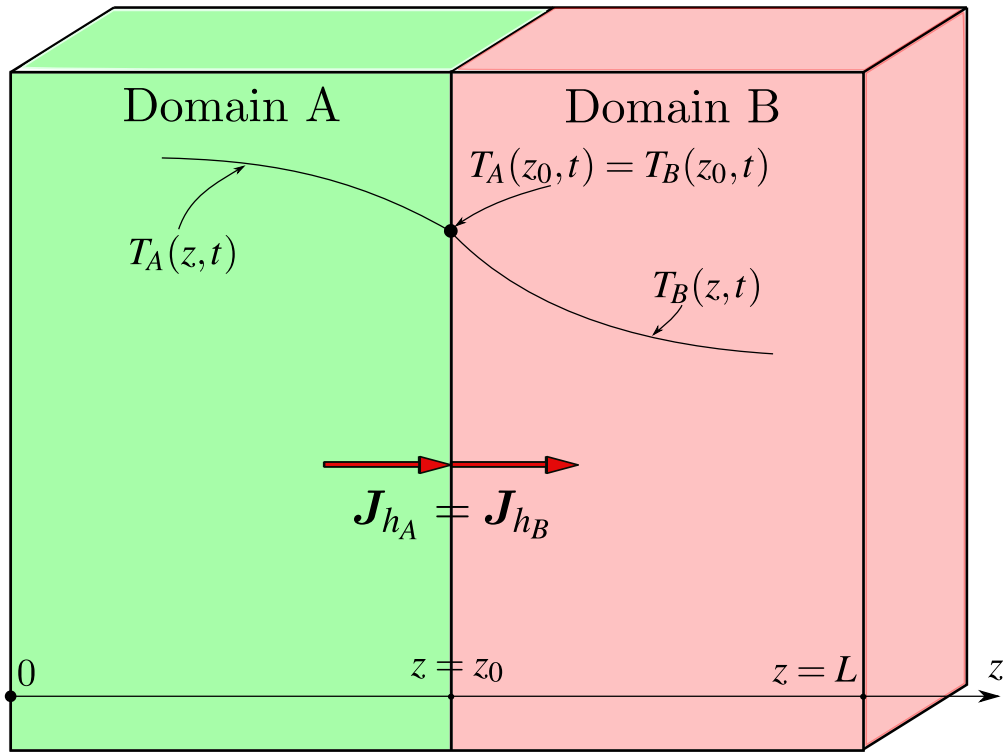

Figure 6.6. The interface boundary condition between two adjacent domains. *Note*: The red arrows are the direction of heat flux, perpendicular to the interface surface.

and the boundary conditions at the interface ($z = z_0$) can be expressed as follows (Cengel, 1998):

$$-k_A \frac{\partial T_A(z_0,t)}{\partial z} = -k_B \frac{\partial T_B(z_0,t)}{\partial z}. \tag{6.21}$$

Thus, summarizing the above, the initial condition for each domain in *Case 3* was

$$T_i = 0 \ ^\circ\text{C} \quad \text{at} \quad t = 0 \ \text{s}, \tag{6.22}$$

and the boundary conditions were

$$\left.\begin{aligned}
\boldsymbol{J}_h \cdot \hat{\boldsymbol{n}} &= 0 \ \text{W}\cdot\text{m}^{-2} \quad \text{at the external surfaces} \\
\boldsymbol{J}_e \cdot \hat{\boldsymbol{n}} &= 0 \ \text{A}\cdot\text{m}^{-2} \quad \text{at the external surfaces} \\
-k_i \frac{\partial T_i}{\partial z} &= -k_{i+1} \frac{\partial T_{i+1}}{\partial z} \quad \text{at the interface} \\
\boldsymbol{J}_{e_i} \cdot \hat{\boldsymbol{n}} &= \boldsymbol{J}_{e_{i+1}} \cdot \hat{\boldsymbol{n}} \quad \text{at the interface} \\
U_{LV} &= 0 \ \text{V} \quad \text{at the low voltage side} \\
U_{HV} &= 15 \ \text{V} \quad \text{at the high voltage side}
\end{aligned}\right\} \quad \text{at} \quad t > 0 \ \text{s}, \tag{6.23}$$

where i and $i+1$ denote the two adjacent cubes of interest. In *Case 3*, the planes of the interfaces are aligned with the XY plane and normal to the Z direction. Different mesh spacings were used in the CFD model to determine mesh-size independence of the solution and to test if there was continuity of temperature profiles over the cubes' interfaces, as non-physical discontinuities in temperature across an interface would indicate numerical issues (Appendix D.1).

d) Case 4

The experimental results, presented in Chapter 5, showed significant dependence of the *P. radiata* sapwood's electrical conductivity on fibre orientation. At about 20°C, the longitudinal conductivity was about 10 and 20 times higher than the radial and tangential conductivities, respectively. This affected conduction of electrical current in real, non-straight logs of a conical-section shape; electric current in these logs had to flow through a combination of transverse and axial directions. In CFD modelling, using isotropic electrical conductivity to predict this behaviour may have led to potentially non-physical results. Hence, to incorporate anisotropy, electrical conductivity in the governing equations needed to be expressed by a second rank tensor.

The graphical user interface (GUI) of the commercial software used for CFD modelling, ANSYS CFX, does not support anisotropic electrical conductivity. However, using additional code, written in the CFX Command Language (CCL), the anisotropic electrical conductivity was incorporated into the CFD model. The ANSYS technical support provided two sets of code: **Code 1** described the anisotropic electrical conductivity in the ANSYS CFX-Solver, and **Code 2** set the values of the anisotropic electrical conductivity in the X, Y, and Z directions (Appendix D.2). Designed to verify these codes, *Case 4* was based on two sub-cases: *Sub case 4.1* verified the code qualitatively and *Sub-case 4.2* verified it quantitatively. Thus, the aim of this verification was to test the solution of Equation 6.2, expressed in a steady state condition, with anisotropic electrical conductivity. To reduce the duration of the calculations, the heat conservation equation (Equation 6.1) was omitted and the simulations were performed at a steady state.

Sub-case 4.1

In this sub-case, a 1 m^3 cube, with anisotropic electrical conductivity, was energized from one of its sides (Figure 6.7). The three other sides of the cube, each normal to one of the principal directions, were grounded, and the remaining two sides were electrically insulated.

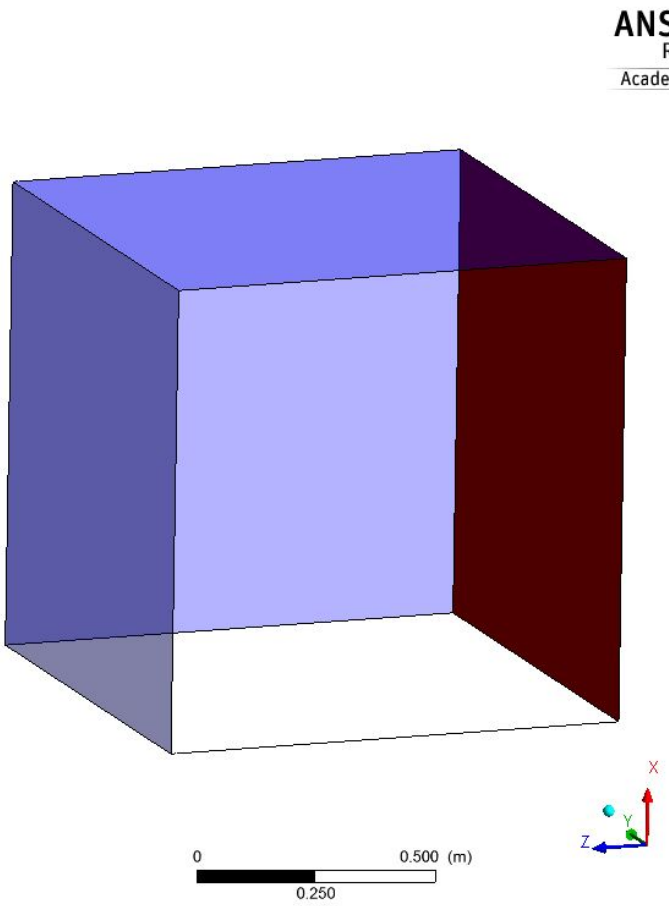

Figure 6.7. The schematic drawing of the 1 m^3 cube used for the *Sub-case 4.1* verification of anisotropic electrical conductivity. *Note*: The red, blue and transparent faces denote the high-voltage, low-voltage and insulated faces, respectively.

Varying with values of the directional components of the anisotropic electrical conductivity, the direction of the current flow was analysed. For example, if the directional components of electrical conductivity were 0.005 $S \cdot m^{-1}$ in the X and Y directions but 0.5 $S \cdot m^{-1}$ in the Z direction, the electric current would have to flow, preferentially, in the Z direction; as an electric current flows in the direction of the lowest resistance. Thus, in this verification test, four cases were tested (Table 6.2).

Table 6.2. Electrical conductivities used to verify the code of anisotropic electrical conductivity in Cartesian coordinates.

Conductivities	σ_X [$S \cdot m^{-1}$]	σ_Y [$S \cdot m^{-1}$]	σ_Z [$S \cdot m^{-1}$]
Scenario 1 ($\overline{\overline{\sigma}}_1$)	0.005	0.005	0.5
Scenario 2 ($\overline{\overline{\sigma}}_2$)	0.5	0.005	0.5
Scenario 3 ($\overline{\overline{\sigma}}_3$)	0.005	0.5	0.5
Scenario 4 ($\overline{\overline{\sigma}}_4$)	0.5	0.5	0.5

The boundary conditions of *Sub-case 4.1* can be summarised as follows:

$$\left.\begin{array}{ll} \boldsymbol{J}_e \cdot \hat{\boldsymbol{n}} = 0 \text{ A} \cdot \text{m}^{-2} & \text{at the insulated faces} \\ U = 0 \text{ V} & \text{at the low voltage sides} \\ U = 1000 \text{ V} & \text{at the high voltage side} \end{array}\right\} \quad \text{at} \quad t > 0 \text{ s}, \tag{6.24}$$

Sub-case 4.2

In this sub-case, two truncated cones, one inscribed into another (Figure 6.8), were used in the CFD model. The outer conical annulus was electrically conductive, with anisotropic electrical

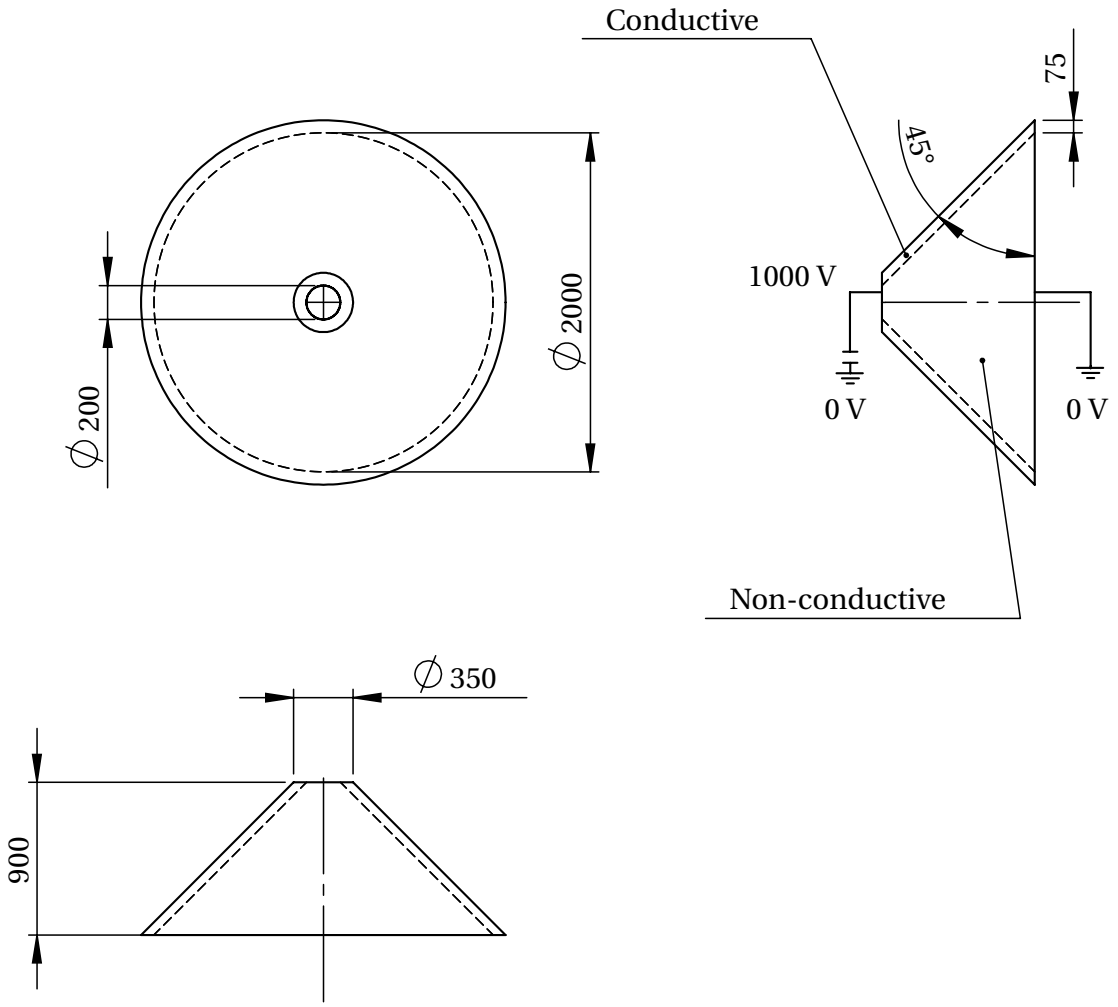

Figure 6.8. Geometry of the truncated cones *Note:* The solid and dashed cones imitated anisotropic sapwood and relatively non-conductive, isotropic heartwood.

conductivity set in cylindrical coordinates, while the inner cone was non-conductive. A constant voltage of 1000 volts was applied to the assembly at the small end, while the large end was grounded. The external surface was electrically insulated. The interface between the cones was assumed to be ideal - the resistance across the interface was equal to 0 Ω. Hence, the boundary

conditions were expressed by Equation 6.24.

Electrical conductivity of the inner cone was isotropic, equal to 10^{-10} S·m^{-1}. Anisotropic electrical conductivity of the outer conical annulus was set using additional code. The code used in *Sub-case 4.1* was unsuitable for anisotropic conductivity expressed in Cylindrical coordinates. As ANSYS CFX uses Cartesian coordinates in calculations, the new code of anisotropic electrical conductivity had to convert the Cylindrical components into Cartesian coordinates. The new code consisted of several pieces of software (Appendix D.3).

Five cases were developed to verify the model (Table 6.3). These cases were compared with a

Table 6.3. Electrical conductivities used to verify the code of anisotropic electrical conductivity in Cylindrical coordinates.

Conductivities	σ_r [S·m^{-1}]	σ_Θ [S·m^{-1}]	σ_{Axial} [S·m^{-1}]
Scenario 1 ($\overline{\overline{\sigma}}_1$)	0.5	0.01	1
Scenario 2 ($\overline{\overline{\sigma}}_2$)	2	0.01	1
Scenario 3 ($\overline{\overline{\sigma}}_3$)	0.01	0.01	1
Scenario 4 ($\overline{\overline{\sigma}}_4$)	100	0.01	1
Scenario 5 ($\overline{\overline{\sigma}}_5$)	1	0.01	1

case where both cones were isotropic. In this isotropic case, equipotential lines - contours of equal potential - lay perpendicular to the direction of electric current (Figure 6.9). The distance between neighbouring potential lines decreased towards the small end, as the resistance at the small end is higher than that at the large end due to the smaller cross-sectional area of the former. The higher the resistance, the higher the potential difference required to drive the electric current. Despite the decrease of the distance between the equipotential lines, if an electric current flows at a 45° slope in an isotropic medium, the distances between neighbouring equipotential lines in the axial and radial directions will be equal. In an anisotropic case, however, the axial and radial distances between equipotential lines are different. For example, if electrical conductivity in the radial direction is half that in the axial, then the ratio of the radial to axial distance between neighbouring equipotential lines will be one to two, as the potential difference in the radial direction must be twice that in the axial direction. Thus, comparing the distances between neighbouring equipotential lines allows one to quantify the computational error of the CFD model with anisotropic electrical conductivity.

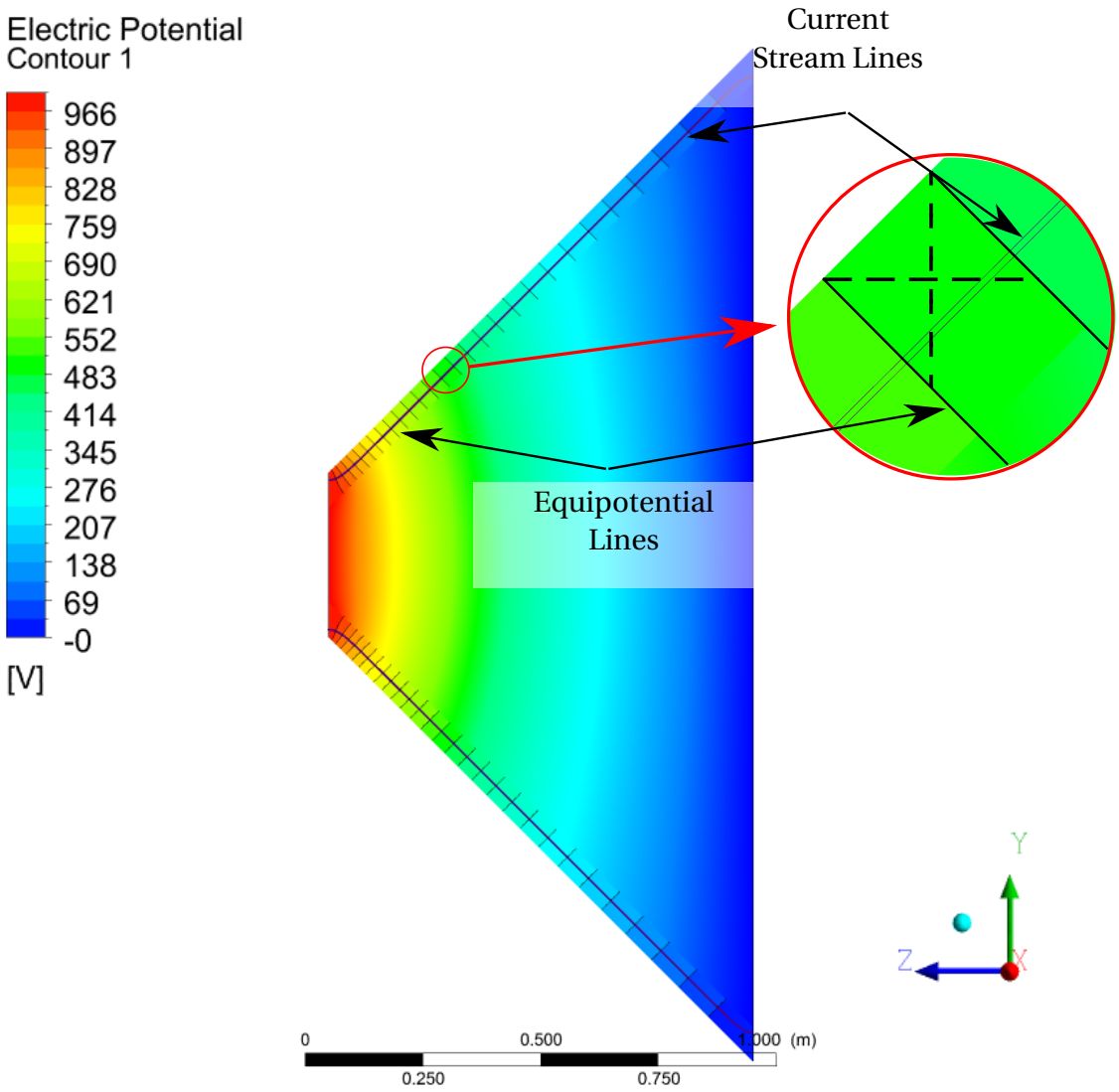

Figure 6.9. The equipotential and current stream lines laid along the isotropic outer conical section's length. The dashed lines show the distances between two neighbouring equipotential lines along the axial (horizontal) and radial (vertical) directions. *Note:* As ANSYS used Cartesian coordinates, the radial direction did not consistently align with the Y direction.

e) Case 5

This verification was based on a two dimensional non-uniform Joule heating problem solved by De Alwis and Fryer (1992), where a heterogeneous system - two solid blocks inserted into a viscous liquid medium (Figure 6.10) - was electrically heated. ANSYS CFX does not support flat

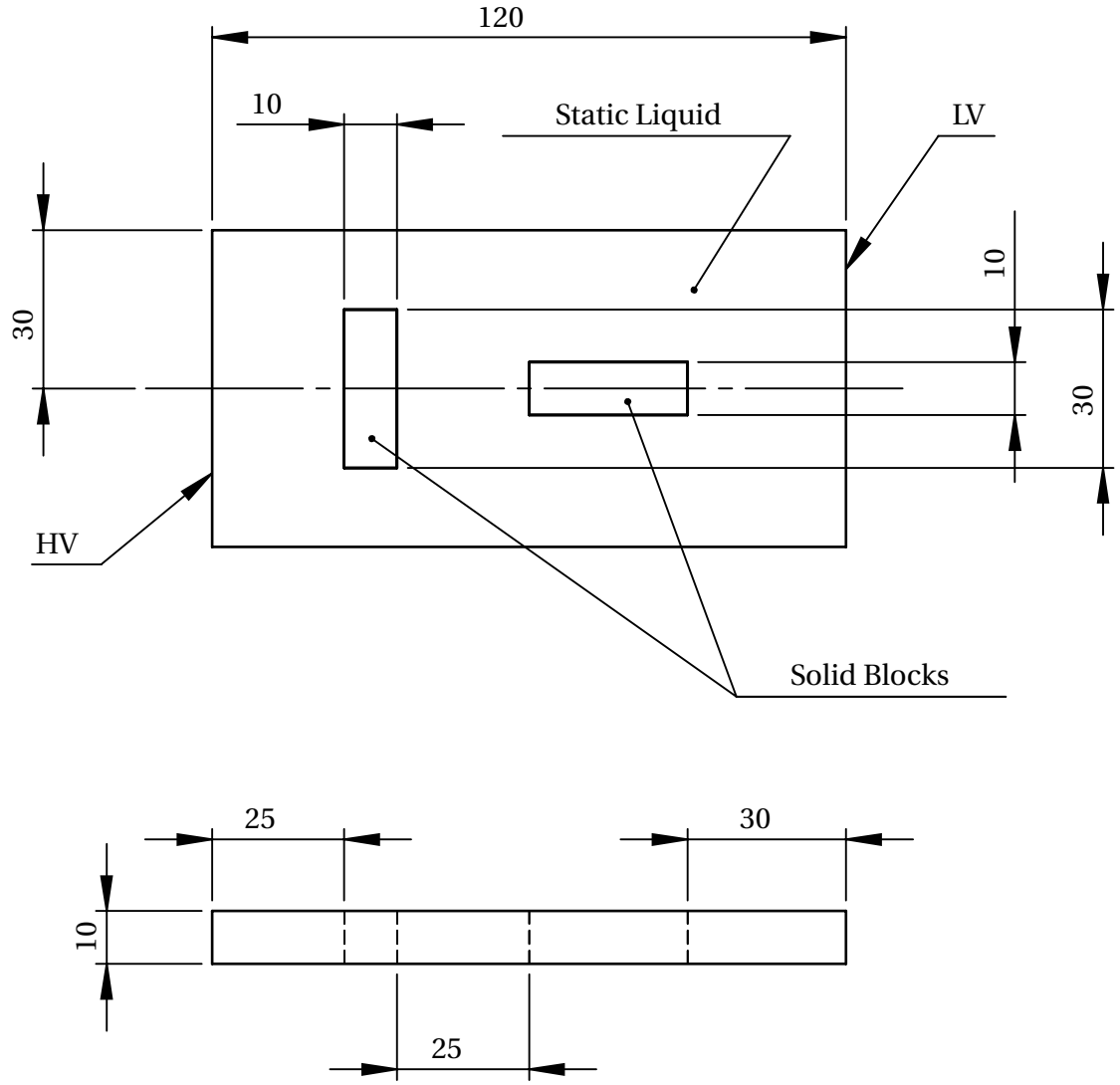

Figure 6.10. The geometry of the problem used in *Case 5*. The top scheme shows the 2D domain used by De Alwis and Fryer (1992) and the bottom scheme shows the thickness added to the domain in order to solve the problem in ANSYS CFX. *Note:* The values are in millimetres.

two dimensional geometries and hence a thickness of 10 mm was added to make the problem three dimensional. The viscous liquid was considered to be a static fluid. The solid blocks were made of the same material. In the first and second scenarios, the blocks were made of iron and dry wood, respectively. In each scenario, the assembly was at uniform temperature of 20°C prior to heating. It was then energised for 50 seconds by applying a constant voltage of 200 volts across the longest dimension. Thermal and electrical properties of the materials used in the verification

case are shown in Table 6.4.

Table 6.4. The properties of the materials used in *Case 5* (De Alwis and Fryer, 1992).

Properties	Liquid	Iron	Dry Wood
Electrical Conductivity [$S \cdot m^{-1}$]	0.763	1×10^{7}	1×10^{-7}
Density [$kg \cdot m^{-3}$]	1070	7650	530
Thermal Conductivity [$W \cdot m^{-1} \cdot °C^{-1}$]	1.97	22.6	0.14
Heat Capacity [$J \cdot kg^{-1} \cdot °C^{-1}$]	3372	460	1220

The boundary and initial conditions were summarised as follows:

$$T_i = 20 \text{ °C} \quad \text{at} \quad t = 0 \text{ s}, \tag{6.25}$$

and

$$\left.\begin{aligned} \boldsymbol{J}_h \cdot \hat{\boldsymbol{n}} &= 0 \text{ W} \cdot \text{m}^{-2} \quad \text{at the external surfaces} \\ \boldsymbol{J}_e \cdot \hat{\boldsymbol{n}} &= 0 \text{ A} \cdot \text{m}^{-2} \quad \text{at the external surfaces} \\ \boldsymbol{J}_{h_i} \cdot \hat{\boldsymbol{n}} &= \boldsymbol{J}_{h_{i+1}} \cdot \hat{\boldsymbol{n}} \quad \text{at the interface} \\ \boldsymbol{J}_{e_i} \cdot \hat{\boldsymbol{n}} &= \boldsymbol{J}_{e_{i+1}} \cdot \hat{\boldsymbol{n}} \quad \text{at the interface} \\ U_{LV} &= 0 \text{ V} \quad \text{at the low voltage side} \\ U_{HV} &= 200 \text{ V} \quad \text{at high voltage side} \end{aligned}\right\} \quad \text{at} \quad t > 0 \text{ s}, \tag{6.26}$$

where i and $i+1$ denote the contacting materials.

6.2.2 Computational Model

The computational model was implemented using the commercial CFD software ANSYS CFX 15.0, which is based on the finite volume method. The model utilised the second order backward Euler scheme to discretize the governing equations. The convergence criteria, the root mean square (RMS) residual level, for each simulated case was set to 10^{-6}. The convergence was achieved using double precision floating point arithmetic. The 3D geometries were built in ANSYS Design Modeller and meshed using the ANSYS meshing tool. The simulations were performed using local parallel computing on four cores of an Intel Core i7-3770 @ 3.40 GHz, with 16 GB RAM.

6.2.3 Mesh Spacings and Time-Steps

Generally, in the CFD models, hexahedral mesh elements are preferred over tetrahedral elements, due to easier control of the mesh structure and faster convergence (Patankar, 1980; Versteeg and Malalasekera, 2007). Each mesh element was considered as a control volume over which governing partial differential equations were integrated. To create a hexahedral mesh in the ANSYS Meshing tool, one of the faces of a simulated geometry was meshed using the edge sizing method. That created pattern was 'swept', using the sweeping method, through the whole geometry (Figure 6.11). The limitation of this method is in creating a hexahedral

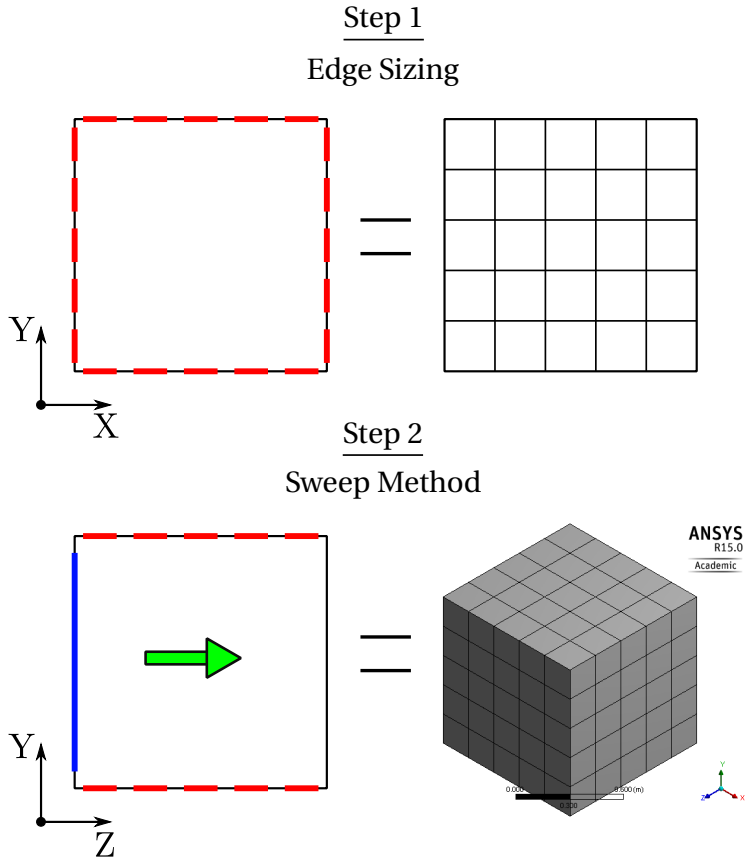

Figure 6.11. The method of meshing simple geometries using edge sizing and sweep methods. *Note*: The red bands indicate mesh elements, and the blue band shows the surface to be 'swept' in the direction of the green arrow.

mesh in geometries with complex shapes such as an exaggerated truncated cone. In that case, the geometry needs to be split into multiple simpler, 'sweepable' bodies. The figures of mesh types used in the verification are shown in Figure 6.12. To find the optimum numbers of mesh elements and time-steps, a time-step and mesh independence study was performed for each simulated case (Appendix D.1), except *Sub-case 4.1*. That case is non-physical, and it does not exist in the real world; as a grounded face cannot have a high voltage edge and a high voltage face

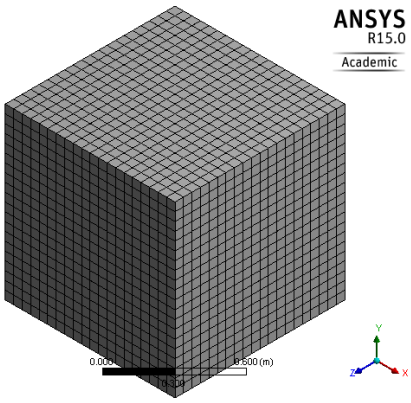

(a) *Case 1*/ *Case 4.1*

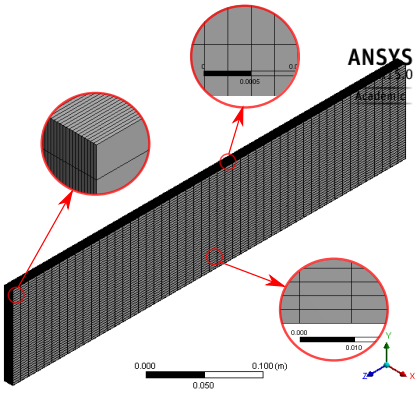

(b) *Case 2*

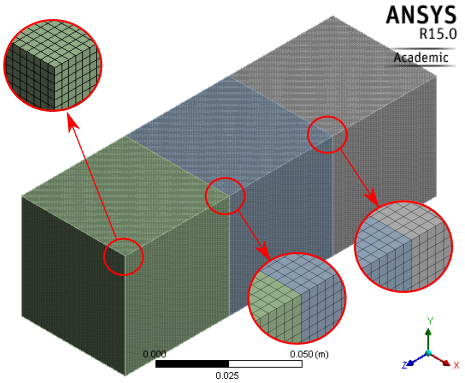

(c) *Case 3*

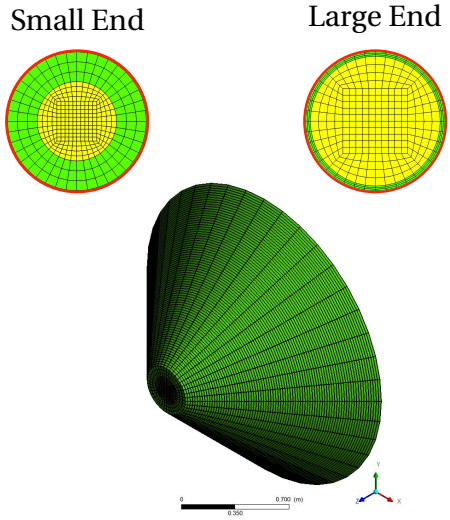

(d) *Case 4*

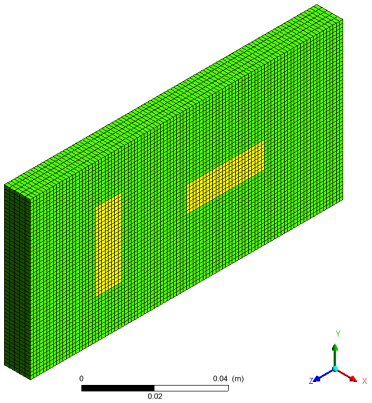

(e) *Case 5*

Figure 6.12. The meshed geometries used in the simulations. *Note*: The different colours of the geometries indicate domains within the assemblies.

cannot have a grounded edge. Therefore, the results of *Sub-case 4.1* do not have a quantitative meaning and hence a mesh independence study has not been performed.

6.3 Results and Discussion

Case 1

In this verification test, the CFD model was verified using the analytical solution of constant power generation within a thermally insulated cube, with uniform electrical and thermal properties. Equipotential lines, shown in Figure 6.13a, show uniform voltage drop along the cube's length. Temperature inside the cube was uniform, which means the boundaries were thermally

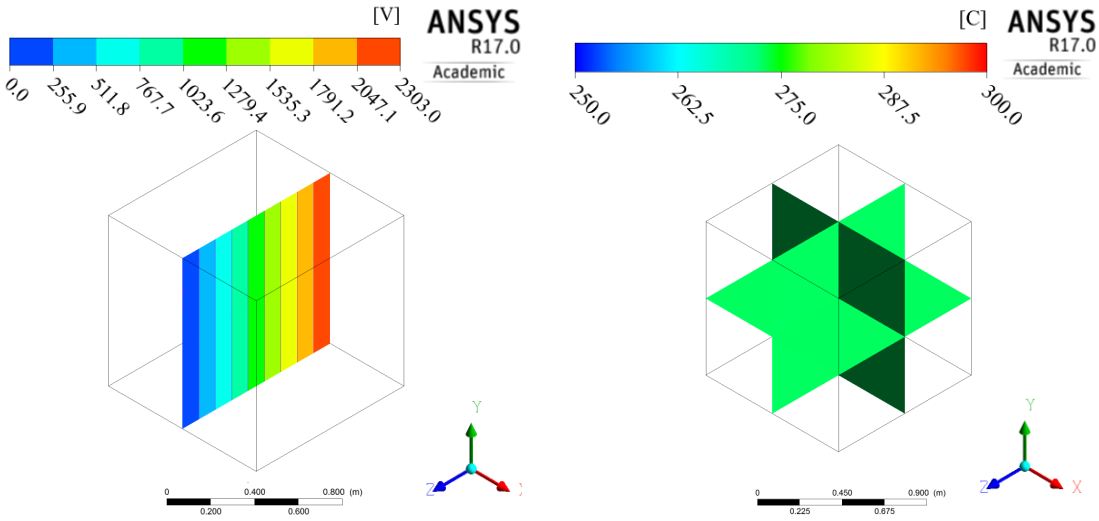

(a) (b)

Figure 6.13. *Case 1:* Equipotential lines and temperature profile within the cube's domain.

insulated (Figure 6.13b). According to the analytical solution, the temperature of the cube would reach about 273°C in one hour. The numerically and analytically calculated temperature values were in good agreement, with a relative error of less than 0.01% (Figure 6.14).

Case 2

Once the constant power generation was verified, the CFD model was used to simulate heat conduction within a slab with an internal volumetric heat source. Electrical conductivity of the slab was isotropic and uniform. Hence, the voltage drop across the slab was linear. Figure 6.15 shows electric potential lines that are the same distance apart. The distance between the lines would have changed, if the electrical conductivity of the slab varied within the domain, causing a non-linear voltage drop.

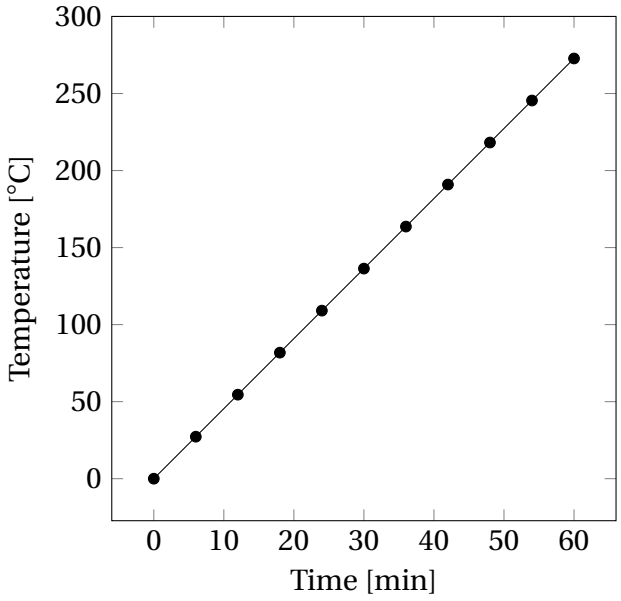

Figure 6.14. *Case 1:* The transient temperature rise of the insulated cube calculated computationally (circles) and analytically (line).

Compared with the analytical solutions (Figure 6.16), the CFD model accurately predicted the temperature profiles across the slab in all directions, with a relative error of around 0.1%. In addition, the obtained temperature distribution plots showed that the temperature varied only in a single direction (Figure 6.17), indicating that the problem was one dimensional and the boundary conditions were applied correctly.

Case 3

In this verification test, the CFD model simulated the Joule heating effect inside a thermally insulated assembly consisting of three cubes, where the central cube was the most electrically conductive, 6 $S \cdot m^{-1}$. Electrical conductivity of the other cubes was 4 $S \cdot m^{-1}$. The first step of verification was to compare the analytical voltage drop across the assembly with the simulated values (Figure 6.18). The CFD model showed a good agreement with the analytical solution, with a relative error of about 0.1%.

As the central block was more electrically conductive than the side cubes, it required a smaller voltage drop to pass the same electric current. Therefore, the voltage drop across the central cube was lower than in the outside cubes and hence the distance between the equipotential lines had to be larger at the central cube (Figure 6.19a). The power dissipation, calculated analytically, was equal to 50,625 and 33,750 $W \cdot m^{-3}$ for the side and central cubes, respectively. Figure 6.19b shows the same values calculated computationally. Solving simultaneously the governing equations,

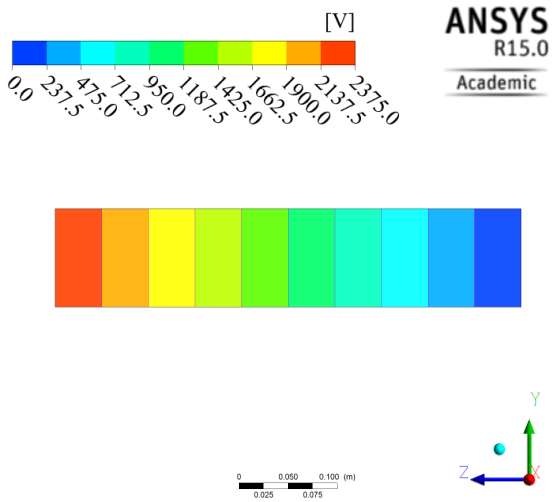

(a) First Simulation: Along Z direction (length)

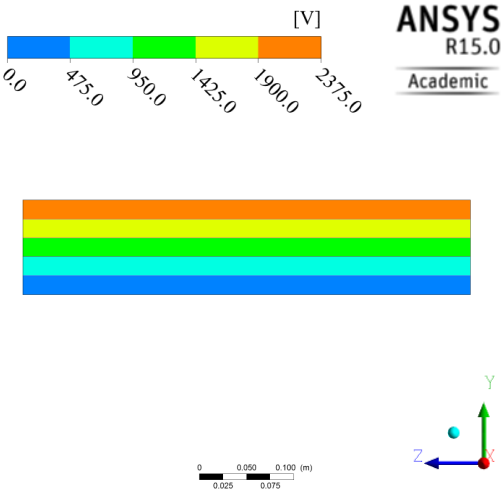

(b) Second Simulation: Along Y direction (width)

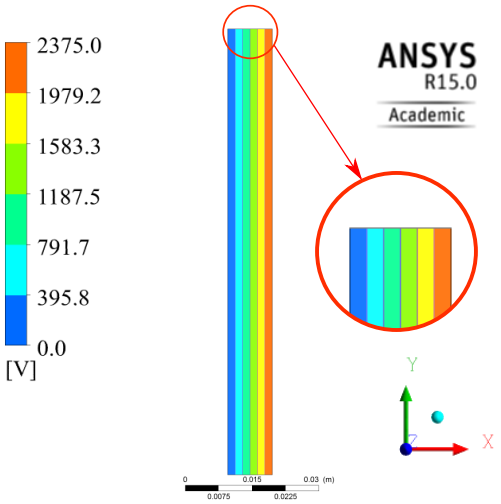

(c) Third Simulation: Along X direction (thickness)

Figure 6.15. *Case 2:* The equipotential lines across the slab, where (a) is the first simulation (one dimensional heat conduction along the length), (b) is the second simulation (one dimensional heat conduction along the width), and (c) is the third simulation (one dimensional heat conduction along the thickness).

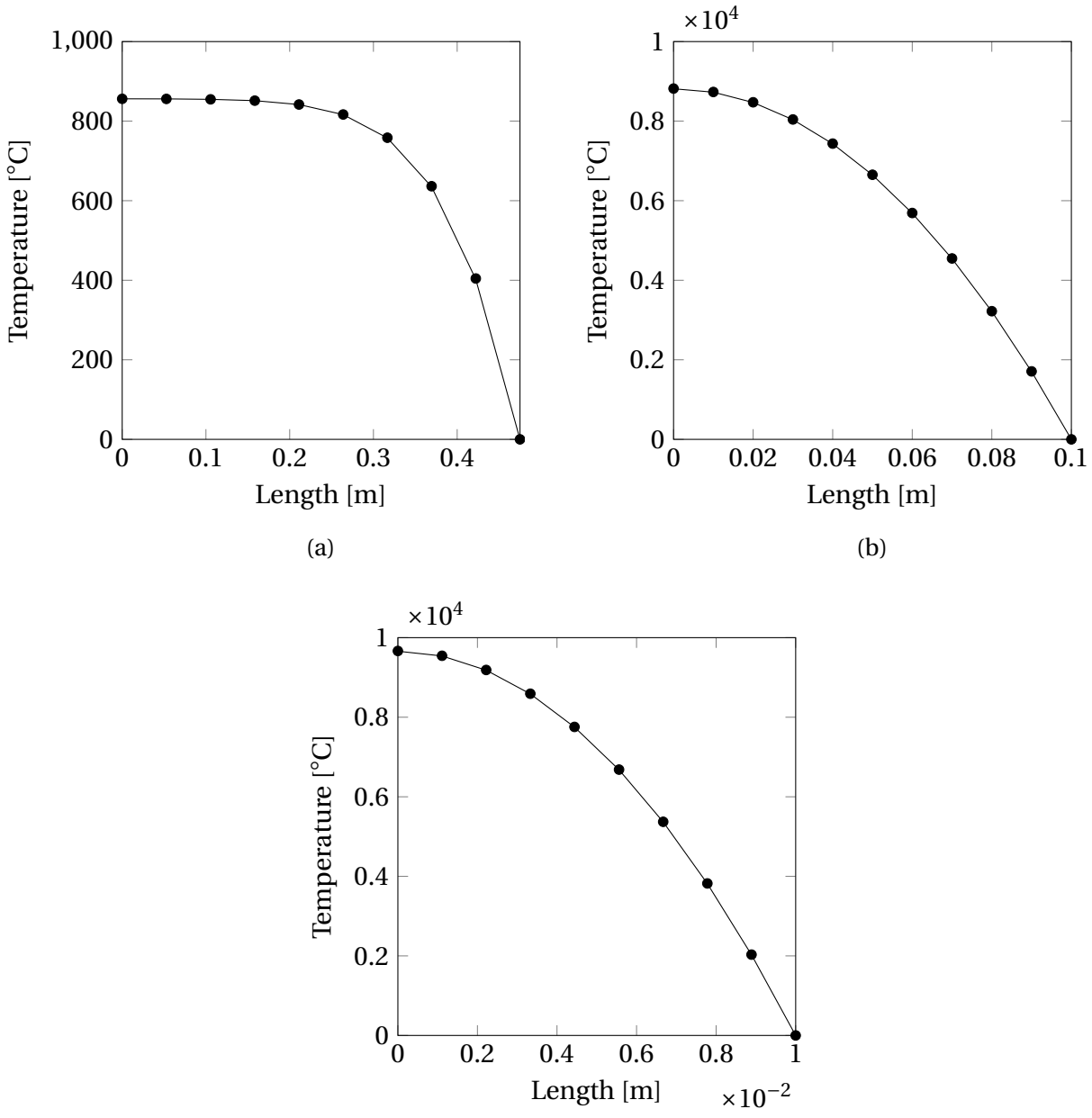

Figure 6.16. *Case 2:* The temperature profiles of the one dimensional heat conduction problem in the (a) Z, (d) Y, and (c) X directions, at $t = 1000$ s, calculated computationally (circles) and analytically (lines).

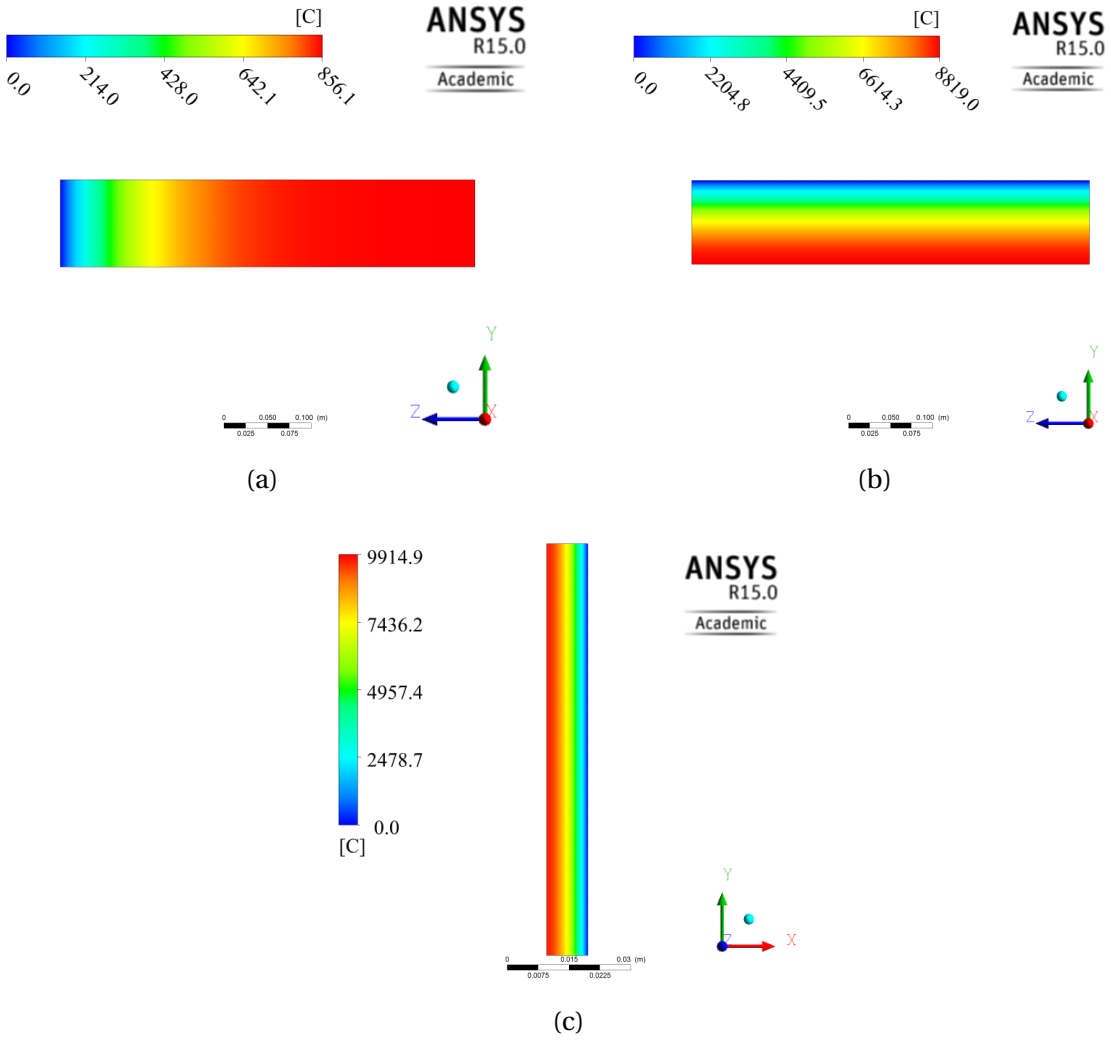

Figure 6.17. *Case 2:* The temperature distribution plots of one dimensional heat conduction problem in the (a) Z, (b) Y , and (c) X directions, at t = 1000 s.

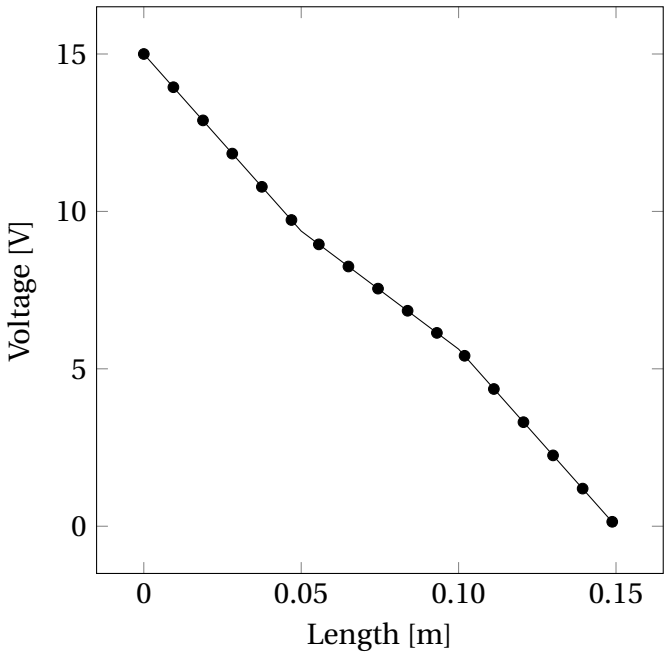

Figure 6.18. *Case 3:* The analytical solution of voltage drop across the three cube assembly (circles) vs the computational result (lines).

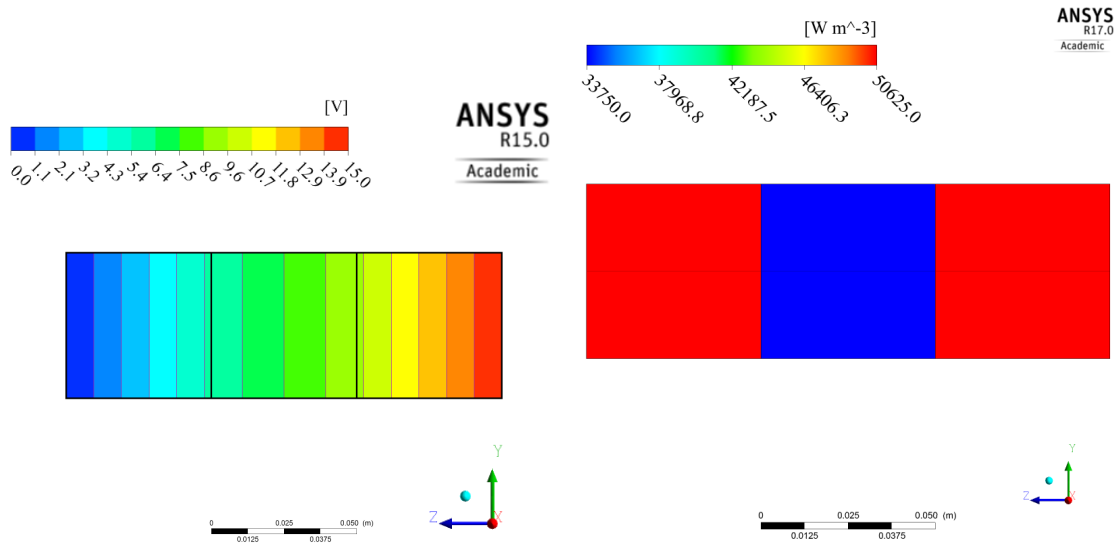

(a) (b)

Figure 6.19. *Case 3:* (a) the equipotential lines and (b) the power dissipation in the three cubes assembly.

the internal temperature profile within the assembly was calculated (Figure 6.20). The lowest voltage drop was across the central cube; therefore, the lowest generated power in the assembly was within the central cube, making it the coldest spot within the assembly.

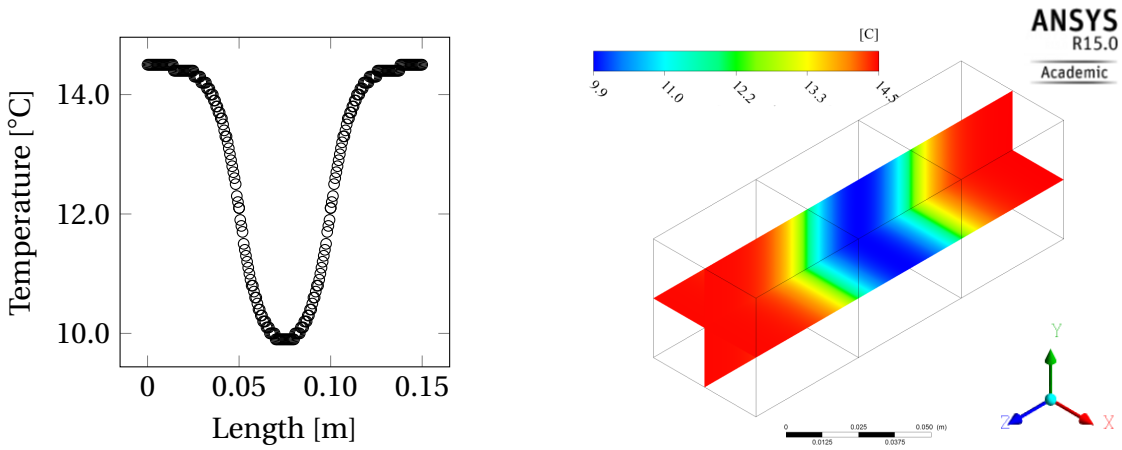

(a) (b)

Figure 6.20. *Case 3:* Temperature profile across the three cubes assembly (left) and temperature distribution plot (right), calculated at $t = 1000$ s.

Sub-case 4.1

In this verification, an anisotropic cube with three grounded sides (Figure 6.7) conducted an electric current; four scenarios of anisotropic electrical conductivity were considered. Figure 6.21 shows the first scenario, in which the cube was 100 times more conductive in the Z direction than that in the other directions. The streamlines showed the direction of the current flow, which was along the Z axis, as the cube was much more conductive in this direction. The equipotential lines showed voltage drop along the Z axis. However, as the other two faces were grounded, there was some potential difference in the X and Y directions and at the corners between the adjacent high voltage and grounded sides. The current density stream lines and equipotential lines obtained for the other scenarios are shown in Figure 6.22. Although scenario 4 is isotropic, most of the current flowed to the adjacent grounded faces and less current flowed to the opposite face. That can be explained by the length of the conducting paths along which the electric current flows; the longer those paths, the higher the resistance and the less the current flow. Thus the CFD model showed a good qualitative agreement with the theory in all scenarios of *Sub-case 4.1*.

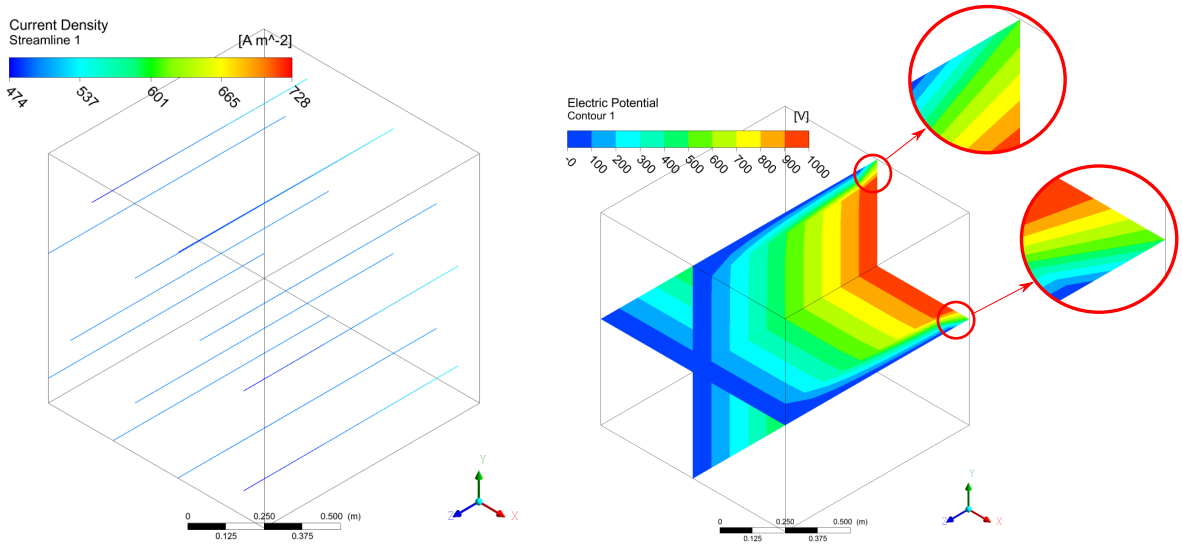

(a) (b)

Figure 6.21. Scenario 1 of *Sub-case 4.1*: (a) the current density stream lines and (b) the equipotential lines.

Sub-case 4.2

In contrast to the entirely qualitative verification of *Sub-case 4.1*, *Sub-case 4.2* was developed to qualitatively and quantitatively verify the CFD code with anisotropic electrical conductivity. In the first scenario of *Sub-case 4.2*, electrical conductivity in the radial direction was half that in the axial direction. Theoretically, in this scenario with a slope of the cone's external sides at 45°, the distance between two neighbouring equipotential lines in the radial directions should be half that in the axial direction, as twice the voltage drop is required in the radial direction. Reciprocally, in Scenario 2, the distance in the radial direction will be twice that in the axial direction if electrical conductivity in the radial direction is twice that in the axial direction. The CFD model showed accurate results for both these scenarios (Figure 6.23a and b). However, when electrical conductivity was 100 times lower in the radial direction than that in the axial direction, as considered in the third scenario of *Sub-case 4.2*, the equipotential lines were approximately parallel to the axial direction (Figure 6.23c). Figure 6.23d shows the case where electrical conductivity in the radial direction was hundredfold higher than that in the axial direction, and the equipotential lines were about parallel to the radial direction.

In the last scenario of *Sub-case 4.2*, electrical conductivity in the radial and axial directions was the same but was much higher than in the tangential direction. Figure 6.24 shows the same

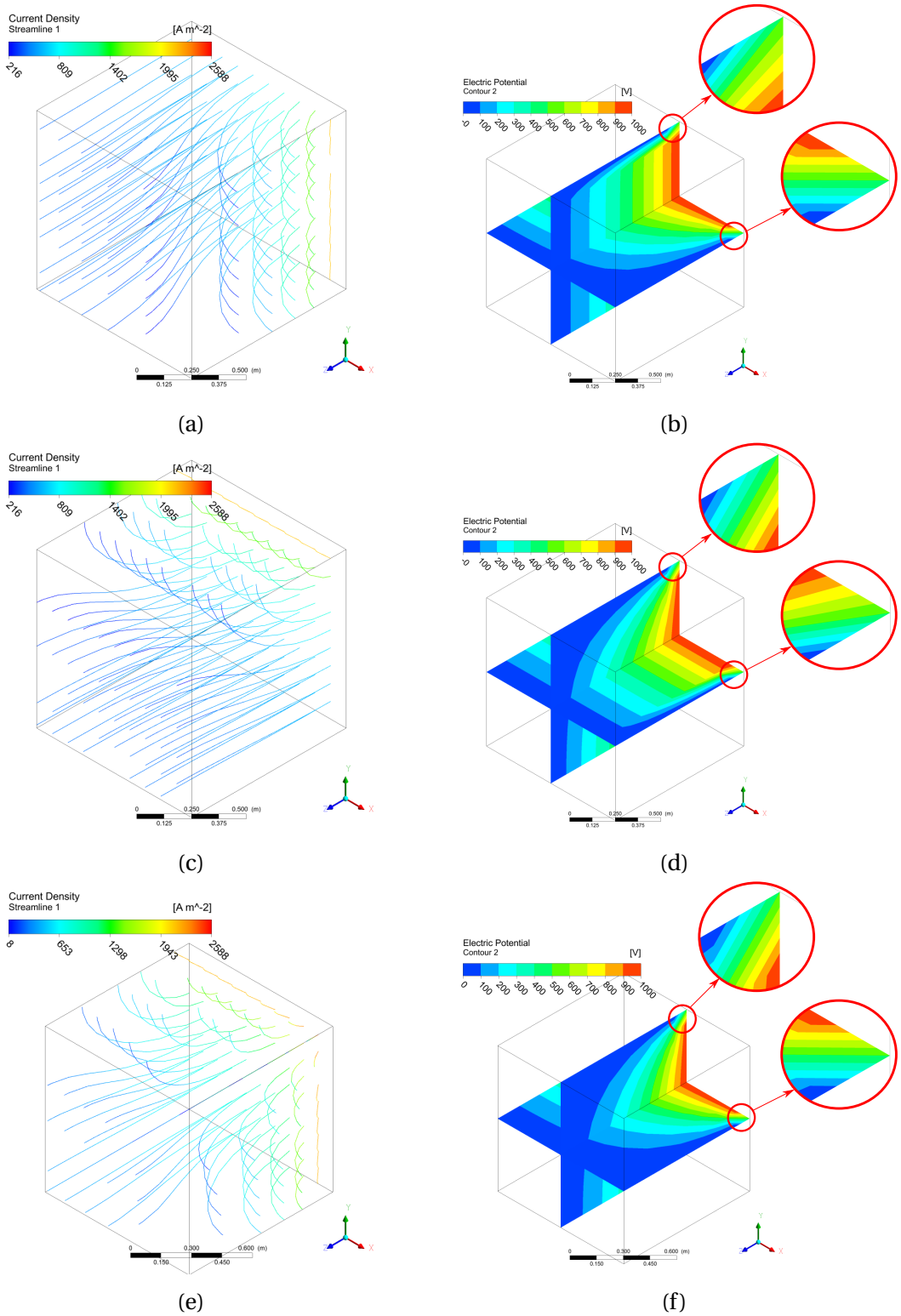

(a) (b) (c) (d) (e) (f)

Figure 6.22. *Sub-case 4.1*: the current density stream lines (*left*) and the equipotential lines (*right*). *Note:* The rows of the figures from the *top* to *bottom*: Scenarios 2, 3, and 4.

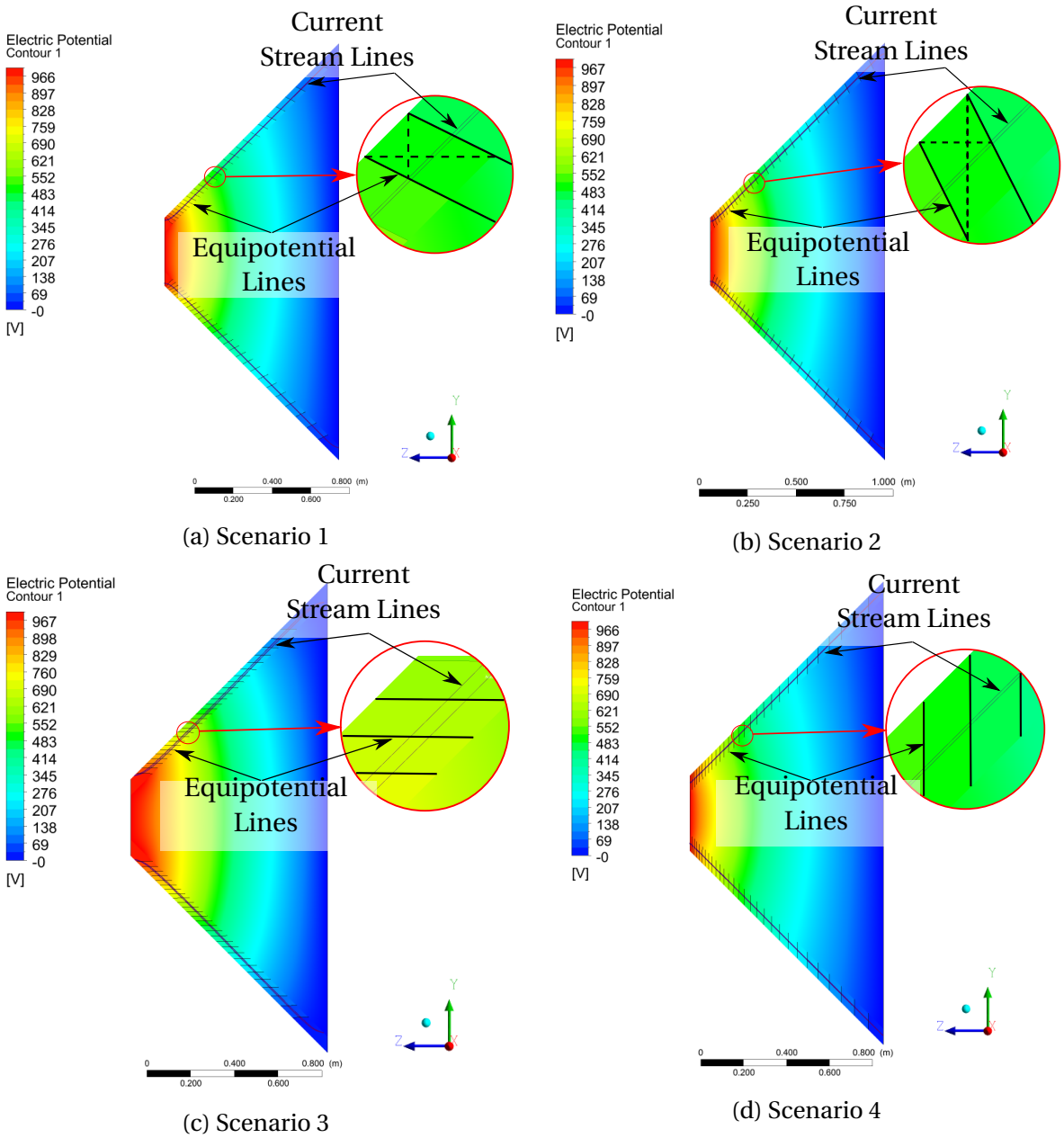

(a) Scenario 1

(b) Scenario 2

(c) Scenario 3

(d) Scenario 4

Figure 6.23. *Sub-case 4.2*: The equipotential and current lines laid along the external annulus's length. The dashed lines show the distances between two neighbouring equipotential lines along the axial (horizontal) and radial (vertical) directions. *Note:* As ANSYS uses Cartesian coordinates, the radial direction did not consistently align with the Y direction.

distance between neighbouring equipotential lines in the radial and axial directions, similar to the isotropic scenario, shown in Figure 6.9. That can be explained by the external annulus's

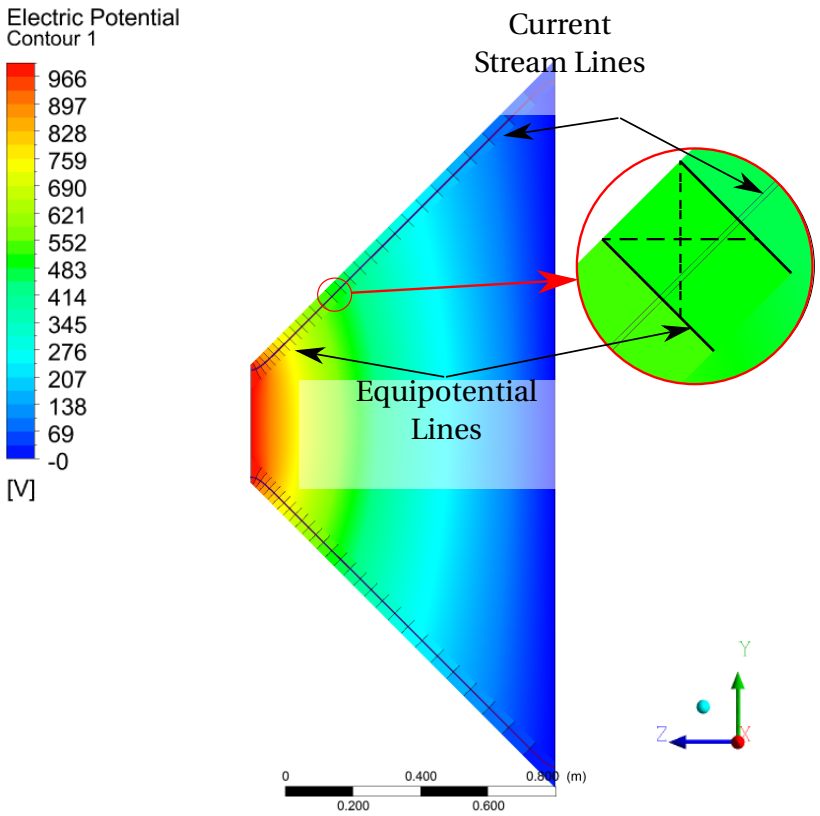

Figure 6.24. Scenario 5 of *Sub-case 4.2*: The equipotential and current stream lines. The dashed lines show the distances between two neighbouring equipotential lines along the axial (horizontal) and radial (vertical) directions. *Note:* As ANSYS uses Cartesian coordinates, the radial direction did not consistently align with the Y direction.

uniform structure. If the conical annulus had a non-conductive internal part, the current would have to flow around it in the tangential direction.

Case 5

Figure 6.25 shows equipotential lines across the assembly in two scenarios of *Case 5*; in the first and second scenarios, two iron and two dry wood blocks were inserted in a static fluid medium, respectively. The electric field distribution predicted by the CFD model was in good agreement with the results published by De Alwis and Fryer (1992). In the first scenario, the voltage drop across the iron blocks was negligible, as electrical conductivity of the blocks was much higher than that of the static liquid. Hence, at those blocks, the equipotential lines lay much further apart from each other. Being more conductive, the iron blocks attracted most of the electric current flow. On the other hand, when the iron blocks were replaced by the dry wood,

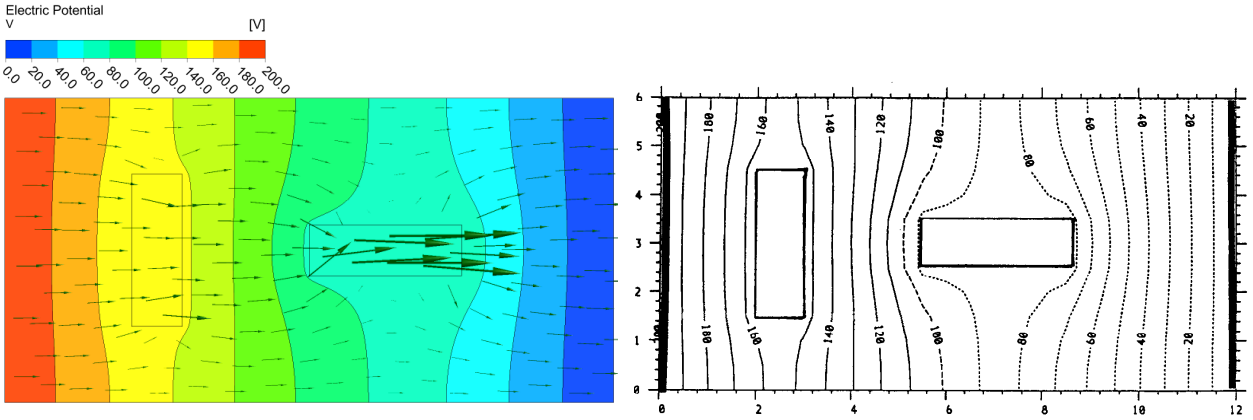

(a) Iron Blocks

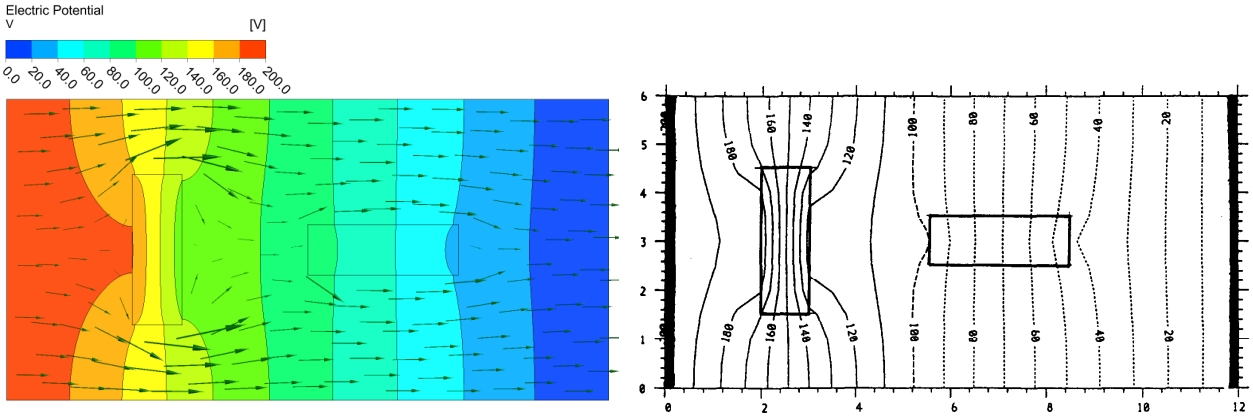

(b) Wood Blocks

Figure 6.25. The plots of equipotential lines within the heterogeneous assembly of *Case 5*. *Note:* The green arrows show the direction and magnitude of the electric current density. The plots on the right are adapted from "Operability of the Ohmic Heating Process: Electrical Conductivity Effects," by De Alwis and Fryer, 1992, *Journal of Food Engineering*, vol. 15, p. 36 & 38. Copyright 1991 by Elsevier Science Publishers Ltd, England.

the electric current flowed around the blocks through the liquid medium. A higher voltage drop was required to drive the current near the wood blocks and hence the equipotential lines were denser there.

Knowing the distribution of the electric field and current density, the power dissipation within the assembly was calculated (Figure 6.26). Qualitatively, the CFD model showed a good agreement with the results published by De Alwis and Fryer (1992). The highest power dissipation was in the liquid medium, at the interface between the materials. In the first scenario, with the inserted iron blocks, the highest power dissipation was near the ends of the horizontal block. The electric current had to flow through a relatively small cross-sectional area, equal to the width of the block; that required a higher voltage drop, resulting in the high power dissipation at the block's ends. In the second scenario, with the dry wood blocks, the highest power dissipation was near the ends of the vertical block. The current had to flow around the block through a relatively small cross-sectional area located between the block and external edge of the domain. Thus, the high current and voltage drop across that region created the high power dissipation.

However, the values of power dissipation calculated in this study were around 1000 times higher than those published by De Alwis and Fryer (1992). Potentially, that can be explained by the method that was used by De Alwis and Fryer (1992) to calculate the power dissipation values. They used a 2D model to determine heat generation, expressing the heat generation term per unit area ($W \cdot m^{-2}$), while their results were given in $W \cdot m^{-3}$. The researchers did not explicitly explain the conversion from $W \cdot m^{-2}$ to $W \cdot m^{-3}$. Instead, De Alwis and Fryer (1992) must have calculated two dimensional power dissipation assuming a thickness of their 2D geometry, equal to 0.001 m. To check this assumption, the temperature distribution within the assembly was compared with that calculated by De Alwis and Fryer (1992). As the simulated problem did not consider cooling of the assembly or other heating mechanisms apart from the Joule heating method, a significant difference in power dissipation would have created a noticeable difference in the predicted temperature values with De Alwis and Fryer's (1992) results. Figure 6.27 shows good agreement between temperature contours calculated in this study and those published by De Alwis and Fryer (1992). That indicated that the power dissipation was calculated correctly and proves the assumption that De Alwis and Fryer assumed a 0.001 m thickness for their 2D assembly to determined the power dissipation. The principal difference

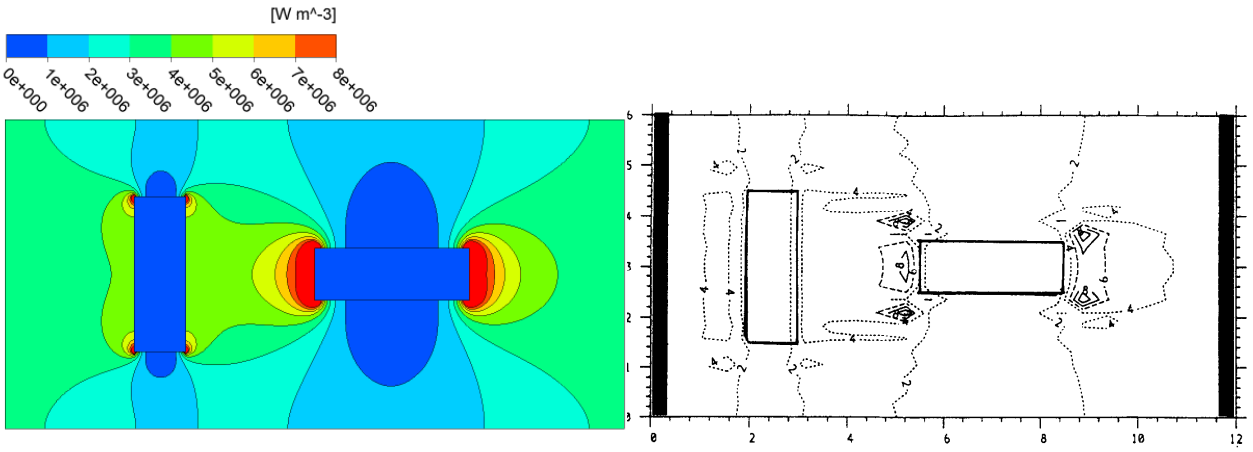

(a) Iron Blocks

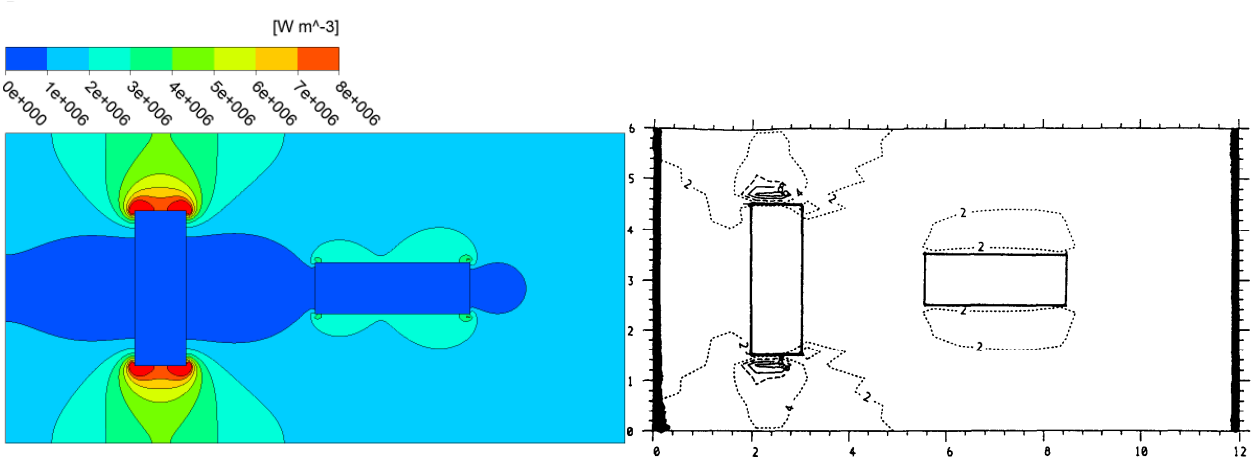

(b) Wood Blocks

Figure 6.26. The power contour plots within the heterogeneous assembly of *Case 5*. The right-hand plots are in $kW \cdot m^{-3}$, adapted from "Operability of the Ohmic Heating Process: Electrical Conductivity Effects," by De Alwis and Fryer, 1992, *Journal of Food Engineering*, vol. 15, p. 36 & 38. Copyright 1991 by Elsevier Science Publishers Ltd, England.

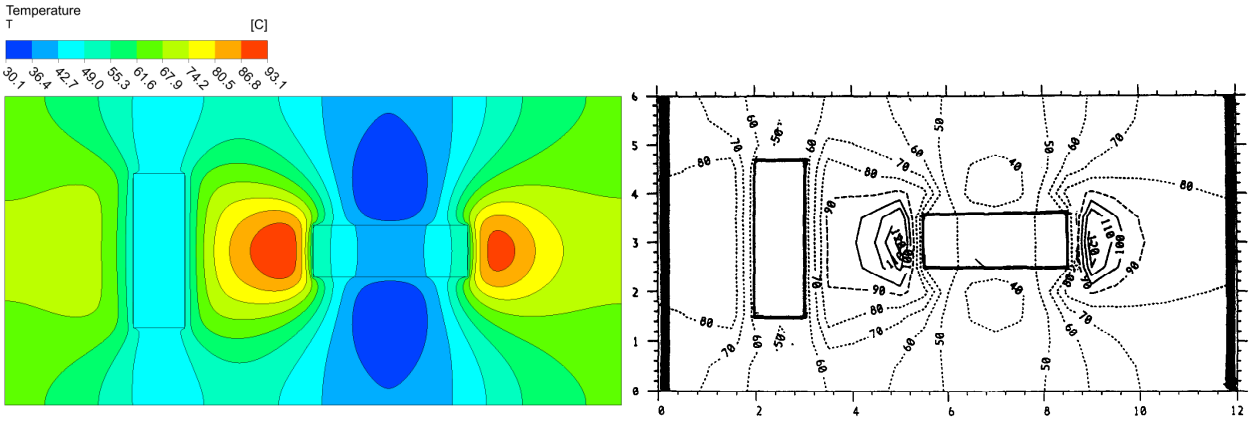

(a) Iron Blocks

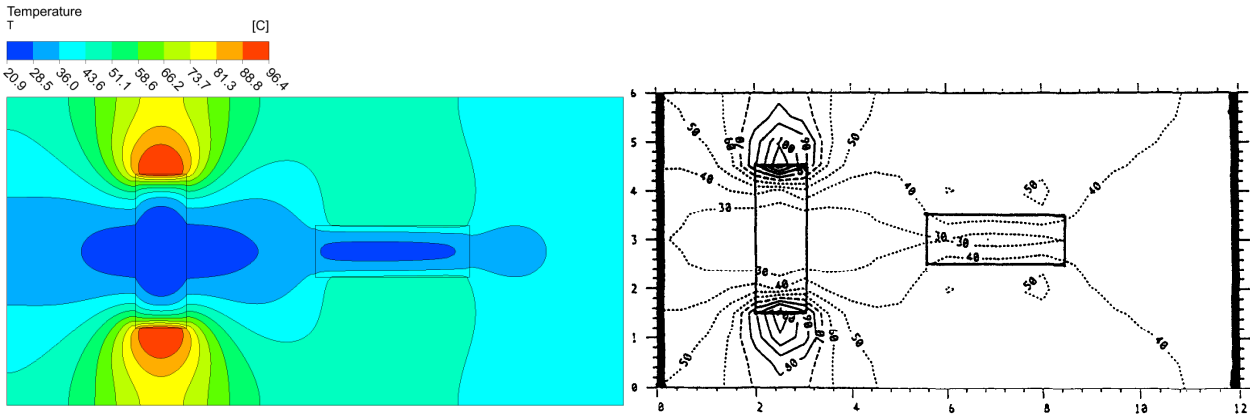

(b) Wood Blocks

Figure 6.27. The plots of temperature distribution after 50 s of Joule heating within the heterogeneous assembly of *Case 5*. The plots on the right are adapted from "Operability of the Ohmic Heating Process: Electrical Conductivity Effects," by De Alwis and Fryer, 1992, *Journal of Food Engineering*, vol. 15, p. 37 & 39. Copyright 1991 by Elsevier Science Publishers Ltd, England.

between the results was the resolution of the plots: De Alwis and Fryer used 576 mesh elements for their 2D problem, while in this research, the 2D plane was discretised into approximately 20,000 mesh elements, with the total number of elements in the 3D geometry equal to 184,320. Hence, a higher resolution and accuracy of the results was achieved in this work.

6.4 Conclusions

The CFD model showed a good agreement with the analytical solutions, taking into account heat losses and internal heat generation. Using the additional code for anisotropic electrical conductivity, the model appropriately described the physics of the Joule heating effect in anisotropic materials. The additional code can be modified to set anisotropic electrical conductivity in Cylindrical coordinates. Finally, the developed CFD model can be used for simulations of hot and cold spots within a heterogeneous medium. Therefore, the model can be used to simulate the Joule heating of *P. radiata* logs described in Chapter 7.

Chapter 7

Joule Heating of *P. radiata*: Industrial Application

7.1 Introduction

One of the main objectives of this PhD research is to develop a CFD model of Joule heating of green *P. radiata* logs that can be used prior to the Joule heating treatment to predict the temperature rise of the log. This chapter describes the method of developing two CFD models that can be used on the lab or industrial scale. The first model is a 1D model, custom built in MATLAB, and the second model is a complex 3D model, developed in ANSYS CFX. These models were compared and the best model has been validated using experimental data.

Fleischer and Downs (1953) pioneered wood heating using the Joule heating effect for a veneer peeling process. They tested some common North American hardwood and softwood species. However, their experimental data cannot be used for the validation due to a lack of the detailed results, caused by "the exploratory nature of the experiments", and due to the different species used by Fleischer and Downs (1953). The results of board heating experiments, described in Chapter 3, could have been used for the validation of the model. However, the boards' size, the shape, and the heating conditions would be different from a real scale application, where the treated sample will be an export size log. According to the results of the verification procedure, described in Chapter 6, electrical heating would depend on the shape and size of the Joule heated body. Hence, the validation has not been done based on the boards heating experiment. Rather, it was decided to validate the log heating model using an additional set of experiments using five green export-size logs. This chapter discusses the methods and the assumptions considered in the experimental part, with discussion of the model's accuracy.

7.2 Methods

7.2.1 Sample Preparation

Five green *P. radiata* logs from Chaney's forest, Canterbury, New Zealand, were selected in this study. They were approximately 3.3-m-long, with the average large-end diameter (LED) and small-end diameters (SED) of around 380 and 340 mm, respectively. The average heartwood LED and SED were approximately 200 and 170 mm, respectively. Once delivered to the High Voltage lab's premises, at the University of Canterbury, Christchurch, New Zealand, the logs' ends were coated with a psyllium husk gel. That prevented the logs' ends from fast drying, avoiding checking at the ends. Then, the logs were kept under a sheet of tarpaulin until being used in the experiment.

7.2.2 Experimental Procedure

Pre-Heating

Prior to the experiment, each log's dimensions were measured. The logs' LED and SED were estimated based on a circular perimeter of each end, which was measured using a string and a measuring tape, with a resolution 0.5 mm. The heartwood LED and SED were measured by a ruler, with a resolution of 0.5 mm. The length of the logs was measured by a measuring tape, with a resolution 0.5 mm.

To estimate the amount of energy required to heat each log, its initial temperature was determined by a resistive temperature sensor (PT100 type) inserted to the centre of the log through a hole of 5 mm diameter. This hole was drilled at the log ends through the pith. As the drilling caused heat generation that affected temperature readings, some time was allowed to reach a steady-state value, assumed to be equal to the initial temperature of the whole log. Thereafter, the sensor was taken out and the log was installed on two fibre glass supports inside the rig between two electrodes. To measure transient moisture loss from the logs, the two fibre glass supports were positioned on top of four load cells, one per each of their two legs (Figure 7.1). However, the performance of the load cells was affected by the temperature sensitivity and the mechanical set-up configuration, which resulted in inaccurate mass readings.

A poor contact between the electrodes and the log could have created high contact resistance. Two main reasons for a poor contact are: air pockets at the interface, caused by a rough cut,

(a) (b)

Figure 7.1. (a) the load cell and (b) the two positioned load cells under the fibre glass support .

and dry ends of the log (Fleischer and Downs, 1953; Lutz, 1960); although the ends were initially covered with high conductive gel, they were dry prior to the experiment. As expected the gel prevented significant cracking and the ends were free of noticeable cracks. High contact resistance would have created high power dissipation in the electrode region, damaging the electrodes and the log's ends. To reduce contact resistance, an open-cell polyurethane foam pad, loaded with a high-conductivity gel, was inserted in-between the electrodes and the log. The foam conformed to the uneven surface of the ends, while the gel filled air pockets and wetted the contact surface. The gel was made of psyllium husk and was a saturated aqueous sodium chloride solution. To further improve the contacts, the electrodes were driven by 63 mm diameter pneumatic rams, one per electrode, operating at 3 bar pressure, compressing the foam pads with a force of about 950 N at each end.

The whole rig, with the clamped log, was positioned inside a chamber that stopped excessive heat and moisture losses out of the log. In addition, the chamber ensured that the log's external surface stayed heated above 56°C. Ideally, if the chamber was completely insulated and its volume was only slightly larger than that of the log, then the temperature inside the chamber would have risen entirely due to the heat dissipation from the Joule heated log. However, the volume of the chamber was about 60 times larger than that of the log and the chamber's thermal insulation was insufficient to retain the dissipated heat from the log. Therefore, the chamber's temperature of 60°C had been reached and maintained over the whole experiment using an external electrical heat blower with a rating of up to 19 kW, using on-off control. Circulating

hot air through the chamber, the temperature of 60°C was reached within 30-45 minutes. In addition, to reduce moisture loss from the log during the experiment, the humidity of the chamber was increased by a steam generator. The temperature and humidity were monitored by four temperature and four humidity sensors.

Heating

Each electrode consisted of 30 segments that were attached to 30 dedicated power-control boards. This arrangement allowed the electric current flowing through each segment on the electrodes to be separately monitored (Figure 7.2). Electric current flowing through each segment,

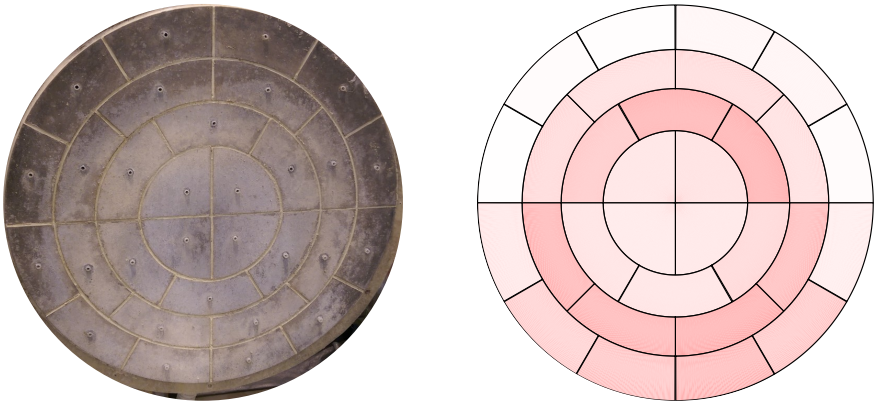

Figure 7.2. The electrode's face made of 30 segments (*left*) and the pattern of the electric current flowing through the face (*right*). *Note:* The holes in the centre of each segment allow high conductivity gel to be pumped through the electrode. The deeper the shade of red, the higher the current in the segment.

the total current, and the voltage across the log were measured and logged, with 10 seconds resolution, using custom built programs in LabVIEW software. Additional current and voltage measurements were made using a Fluke 435 power quality meter, which logged the data with five seconds resolution on the primary side of two electrical transformers.

Fleischer and Downs (1953) did not limit electrical power in their experiments, causing uncontrolled Joule heating. Potentially, this was one of the main reasons of end checking observed by Fleischer and Downs (1953). In this research, however, the power was limited to 100 kW by reducing sinusoidal voltage at 50 Hz whenever the power exceeded an upper limit, using dead-band control. Thus, the Joule heating rates in this research were different from those observed in Fleischer and Downs (1953)'s (1953) work and hence a direct comparison of temperature between the studies was avoided. In addition, to prevent local overheating due to hot spot formation, the total electrical energy supplied to the log was divided into three excitations. The

time between the excitations was called relaxation, during which the temperatures of hot and cold spots within the log were allowed to equilibrate. According to the computational model of non-uniform heating, described in Chapter 6, inserting temperature sensors into the log can distort the electric current flow causing formation of cold and hot spots; consequently, that would have affected accuracy of the temperature measurements. Thus, there were no holes drilled into the log, except the hole that was used to determine the initial temperature of the log. Therefore, there was no temperature recording until the end of the last excitation and hence the actual temperature of the log was unknown during the heating stage.

Post-Heating

According to Pawson et al. (2018), penetration of wood beetles into a healthy tree will be unlikely if the time from the harvest to the treatment prior to export is relatively short. However, if this time is about 20 weeks, the depth of heat treatment penetration into the log must be at least 32 mm. Therefore, after the last excitation, the temperature of the log was measured at the depth of 32 mm using 10 wireless resistive temperature detectors (PT100 type), called RTDs 1-10, inserted into the log as two rings of five sensors, as shown in Figure 7.3. Four additional

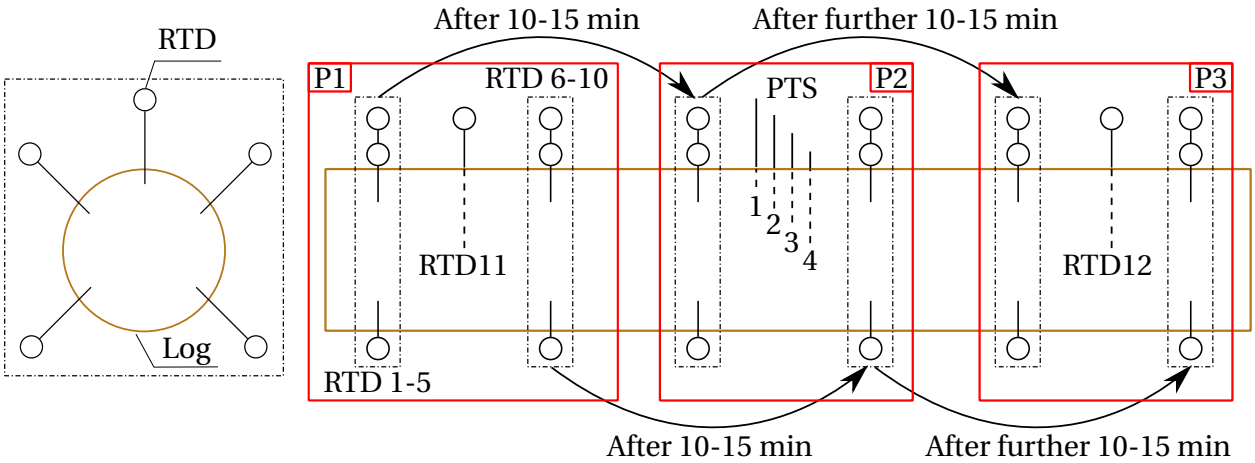

Figure 7.3. The positions of temperature sensors within the log (*the brown contours*), where RTDs and PTSs denote the wireless resistive temperature sensors and the temperature sensors connected to the Pico Technology logger, respectively. P1, P2, and P3 denote positions of RTDs 1-10.

temperature sensors (PT100 type), called PTSs 1-4, connected to a logger (Pico Technology PT104), were inserted at the middle of the log a centimetre apart from each other (Figure 7.4); PTS 1, 2, 3, and 4 were inserted to the depths of 32, 62, 92, and 122 mm, respectively. In addition, RTDs 11 and 12 were inserted to the depth of about 150 mm at each end of the log. One of them

Figure 7.4. PTSs 1-4 connected to the Pico Technology logger.

was inserted into middle of the log's left half and the other to the middle of the right half. After 10-15 minutes, RTDs 1-10, inserted into the left part of the log, Position 1 (P1), were shifted to the middle of the log, Position 2 (P2). Finally, after further 10-15 minutes the temperature sensors were shifted to the right end of the log, Position 3 (P3) (Figure 7.5). Predominantly, the temperature sensors were inserted into knot-free parts of the log. The heat blower was left on, maintaining the chamber temperature for about one hour after the last excitation. All the temperature sensors were left inside the log overnight to record its cooling.

Calculating Electrical Conductivity

As the electric current preferentially flowed through the sapwood, the log's electrical conductivity was governed by electrical conductivity of the sapwood. Hence, to assess the effect of temperature on the log's electrical conductivity, the sapwood temperature had to be determined. As mentioned previously, temperature within the log was not measured during the experiment. Therefore, a correlation of the log's electrical conductivity with temperature was based on two temperature points: the sapwood's initial temperature, determined prior to heating, and the final temperature, estimated after the last excitation (at the beginning of the post-heating period). Although, the initial temperature was recorded in the heartwood of the log, it was assumed to be relatively uniform throughout the log. On the other hand, after the last excitation, the final sapwood temperature was non-uniform - there was heat dissipation to the ambient and heat

Figure 7.5. RTDs 1-10 inserted in two rings into the left side of the log at P1 *(top)* and, about 30 minutes later, inserted into the right side of the log at P3 *(bottom)*.

conduction into the heartwood. Hence, electrical conductivity was correlated with the sapwood's mean temperature, which was calculated based on the temperature values measured by those PTSs inserted exclusively into the sapwood. The main assumption in the calculation of the final sapwood temperature is that the log had not cooled significantly between the end of the last excitation and the beginning of the temperature logging by PTSs. The logs' electrical conductivity was compared with the electrical conductivity equation for the longitudinal direction (Equation 5.13), the cubes' electrical conductivity (*Set 1*), discussed in Chapter 5, and the electrical conductivity of *Betula alleghaniensis*, determined by Fleischer and Downs (1953).

Calculating Local Resistance

During the experiments, measuring electric current and voltage allowed calculation of the log's total electrical resistance, which decreased with the log's increasing temperature. However, temperature within the log was non-uniform and varied due to the heterogeneous structure of wood. As electrical resistance of wood depends on temperature, the local resistance within the log was dependent on hot and cold spot formation. It is impractical to measure local resistance in wood, as the cross-sectional area and the length of the conducting path within the log are unknown. In spite of this, the local internal resistance of the logs was estimated computationally using experimental temperature values recorded by the PTSs inserted into the sapwood.

To determine local resistance, it was assumed that the tip of the temperature sensors was located inside a concentric cylinder as shown in Figure 7.6. The thickness of the concentric cylinder was assumed to be 4 mm, the same as the diameter of PTSs. The temperature within the cylinder was assumed to be uniform and equal to the initial temperature values, recorded after the last excitation, at the beginning of the post-heating period. Thus, using these four experimental temperatures in Equation 5.13 to determine electrical conductivity of the cylinder, the local resistance of each cylinder can be calculated as:

$$R = \frac{l}{\sigma(T) A_{cr}}, \tag{7.1}$$

where l is the length of the concentric cylinder, equal to the length of the log; A_{cr} is the cross-sectional area of each concentric cylinder; and $\sigma(T)$ is the electrical conductivity of each concentric cylinder. The electrical conductivity of the heartwood was regarded as spatially and

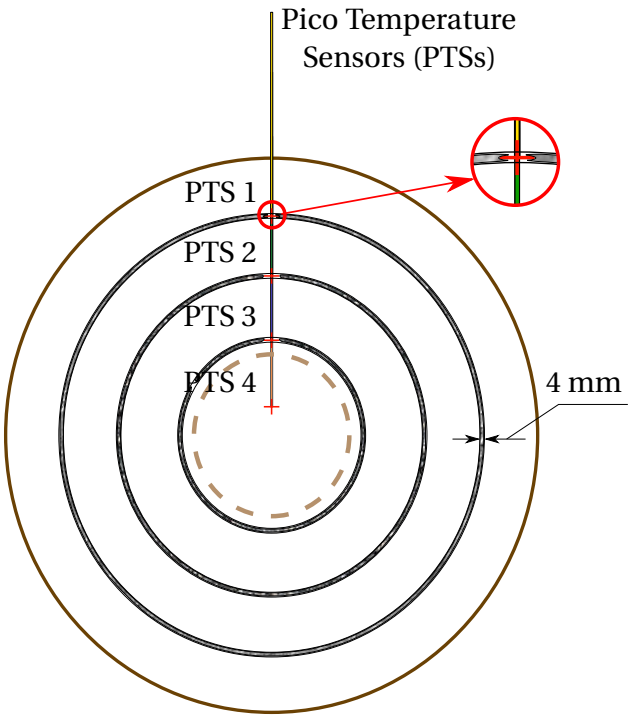

Figure 7.6. The schematic position of PTSs 1-4 within the log. The red crosses indicate the depth, to which each sensor was inserted. The shaded concentric rings denote the cross-sectional surfaces of the conducting cylinder. The dashed, light-brown ring represents the heartwood. *Note:* The sizes and proportions are not to scale.

temporally constant and negligible; hence, the local resistance of the heartwood was not calculated.

7.2.3 Mathematical Formulation

Governing Equations

As the experiment was relatively short, less than 30 minutes in duration, and the humidity inside the chamber was enhanced by a steam generator, it was assumed that there was no significant moisture loss. Therefore, the mass conservation equation and the evaporation source term in the heat balance equation were excluded from the model. The heat transfer inside the log was assumed to be entirely due to conduction, allowing the process of Joule heating described by Equations 2.19 and 2.25 to be written as:

$$\frac{\partial \rho_g C_p T}{\partial t} = \nabla \cdot (k \nabla T) + \bar{S}, \tag{7.2}$$

and

$$\nabla \cdot (\boldsymbol{J}_e) = 0, \tag{7.3}$$

respectively. To model relaxation, the source term ($\bar{S}$) in the heat conservation equation (Equation 7.2) was set to zero. The governing equations were solved within each control volume of the sapwood and heartwood domains.

It was assumed that the logs' ends and the heartwood had a circular shape. Furthermore, unlike a real log, in which the log centre does not align with the heartwood's centre (Figure 7.7), in the model the centres of the log and of the heartwood were assumed to be aligned. This assumption led to some difference between the actual position of the sapwood-heartwood interface and that assumed in the model.

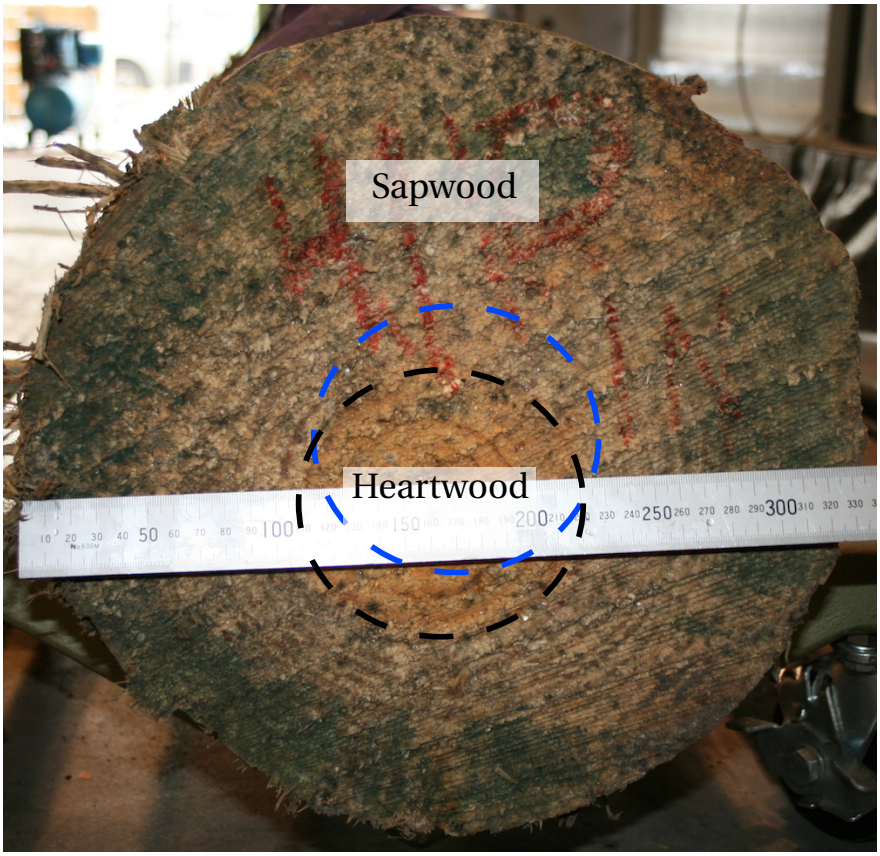

Figure 7.7. One of Log 5's ends with the off-centred heartwood (black dashed line). The blue dashed line denotes the contour of the heartwood if its centre aligned with the log's centre.

The thermal properties of *P. radiata's* sapwood and heartwood were described by the following

equations (Pang et al., 1995):

$$C_p = 4184\frac{X+0.324}{1+X}, \tag{7.4}$$

and

$$k = \frac{\rho_s}{1000}(0.4+0.5X)+0.024, \tag{7.5}$$

where X is the moisture content [kg·kg^{-1}], and ρ_s is the basic density [kg·m^{-3}]. As the modelling was done prior to the experiment, moisture contents and basic densities of the sapwood and heartwood had to be approximated to the published average values (Table 7.1).

Table 7.1. The average moisture contents and basic density of green *P. radiata* (Harris and Cown, 1991; Pang et al., 1995).

Wood Type	X [kg·kg^{-1}]	ρ_s [kg·m^{-3}]
Sapwood	1.5	450
Heartwood	0.45	400

In the experimental part, the contact resistance was reduced by inserting an open-cell polyurethane foam loaded with conductive gel in-between the log and electrodes. Thus, the contact resistance was assume to be equal to zero and hence power was dissipated only inside the log. In the model, this assumption can be expressed as:

$$\bar{S} = \boldsymbol{J}_e \cdot \boldsymbol{E}, \tag{7.6}$$

where

$$\boldsymbol{J}_e = \sigma \boldsymbol{E}. \tag{7.7}$$

Perré's (2004) model assumed that electrical conductivity of wood solely depends on the moisture content, but not on temperature. However, according to Nursultanov et al. (2017), conductivity of green *P. radiata's* sapwood, above 100% moisture content, is independent of moisture content and basic density but significantly depends on temperature and the grain orientation. Thus, electrical conductivity of green *P. radiata's* sapwood was expressed by Equations 5.13-5.15,

written as (Nursultanov et al., 2017):

$$\sigma_L = \exp\left[-2.60 + 0.017(T-55) - 0.073\frac{(T-55)^2}{1000}\right], \tag{7.8}$$

$$\sigma_R = \exp\left[-4.81 + 0.021(T-55) - 0.046\frac{(T-55)^2}{1000}\right], \tag{7.9}$$

$$\sigma_T = \exp\left[-5.37 + 0.026(T-55) - 0.046\frac{(T-55)^2}{1000}\right], \tag{7.10}$$

where σ_L, σ_R, and σ_T are the longitudinal, radial, and tangential conductivities, respectively. This principle difference in wood electrical conductivity between Perré's (2004) and the current model prevents a direct comparison of the estimated temperatures.

Solely based on the longitudinal direction of electrical conduction, the 1D model cannot simulate Joule heating of wood with anisotropic electrical conductivity and hence its calculation was entirely based on Equation 7.8. On the other hand, the 3D model simulated Joule heating considering the anisotropic structure of sapwood by employing Equations 7.8-7.10. To use these equations, electrical conductivity in Equation 7.7 had to be expressed as a second rank tensor ($\overline{\overline{\sigma}}$). To study the effect of anisotropy on temperature prediction, the 3D model simulated an additional case with isotropic sapwood solely based on Equation 7.8. In all models, electrical conductivity of heartwood was considered constant and equal to 0.001 $\mathrm{S \cdot m^{-1}}$, the same as sapwood's electrical conductivity at 30% moisture content, at the temperature range of 20-40°C (Appendix C.2), and similar to the heartwood boards, described in Chapter 3. In addition, the log's ends could have had higher electrical conductivity due to penetration of sodium chloride from the the gel, similar to penetration of sodium chloride into the *P. radiata* cubes, discussed in Appendix C.4. Potentially, high conductivity of the ends will reduce the electric potential drop across that region, significantly reducing the power dissipation and the temperature rise. However, in the developed models, it was assumed that penetration of sodium chloride is negligible - additional study is required to determine the depth of salt penetration inside logs - and hence testing of this assumption has been left for future research.

Initial and Boundary Conditions

Although the chamber had been pre-heated up to 60°C for around 30-45 minutes prior to the first excitation, the log's internal temperature did not change significantly, due to the sapwood's relatively low thermal conductivity, the high heat capacity, and the large volume. Therefore, the log's initial temperature was assumed to be uniform and equal to the temperature measured at the pre-heating stage. Thus, the initial condition can be expressed by the following equation:

$$T_i = T_0, \tag{7.11}$$

where T_i is the initial temperature and T_0 is the experimental temperature of log, measured in the centre prior to heating.

The log was surrounded by hot air at 60°C that continuously circulated within the chamber. When the log's external temperature was below 60°C, it was heated by the air; however, when its external temperature rose above 60°C, the log lost heat to the air. That cooling and heating was due to combined natural and forced convection. In addition, the log lost heat due to thermal radiation, moisture evaporation, and conduction of heat to the electrodes. Hence, the total heat loss at the surface can be expressed as:

$$\boldsymbol{J}_{h_t} = \boldsymbol{J}_{h_{conv}} + \boldsymbol{J}_{h_{rad}} + \boldsymbol{J}_{h_{cond}} + \boldsymbol{J}_m \bar{h}_{vap}, \tag{7.12}$$

where $\boldsymbol{J}_{h_t}$, $\boldsymbol{J}_{h_{conv}}$, $\boldsymbol{J}_{h_{rad}}$, and $\boldsymbol{J}_{h_{cond}}$ are the total heat flux, the convective heat flux, the thermal radiative heat flux, and conductive heat flux, respectively [$\mathrm{W \cdot m^{-2}}$]; $\boldsymbol{J}_m$ is the mass flux of free water [$\mathrm{kg \cdot m^{-2} \cdot s^{-1}}$]; and $\bar{h}_{vap}$ is the enthalpy of vaporisation [$\mathrm{J \cdot kg^{-1}}$].

In the experimental part, the tested logs were weighed inaccurately and hence the mass of evaporated moisture was unknown. However, as the average duration of the Joule treatment was about 30 minutes, with approximately 3 min of actual Joule heating per excitation, it was assumed that the moisture loss was negligible and hence the heat loss caused by evaporation was not considered in the model. The conductive heat loss to electrodes was assumed to be insignificant, as the thermal conductivity of wood was much lower than that of the aluminium electrodes. Furthermore, the contact surface with the electrodes was small, about 5% of the log's total external surface. As most of the log surface was in contact with air, its heating and cooling

was expressed by the convective boundary condition, written as:

$$\boldsymbol{J}_{h_{conv}} = h(T_s - T_a), \tag{7.13}$$

where h is the convective heat transfer coefficient [$\mathrm{W \cdot m^{-2} \cdot {}^{\circ}C^{-1}}$], and T_a and T_s are the air temperature inside the chamber and of the log's external surface, respectively. Finally, the radiative flux was described as (Moran et al., 2003):

$$\boldsymbol{J}_{h_{rad}} = h_{rad}(T_s - T_{sur}), \tag{7.14}$$

where T_{sur} is the temperature of the surrounding, along with T_s expressed in Kelvin [K], and h_{rad} is the radiative heat transfer coefficient expressed as:

$$h_{rad} = \varepsilon c(T_s + T_{sur})(T_s^2 + T_{sur}^2), \tag{7.15}$$

where ε is the emissivity of the log, assumed to be about 0.93 (Section 3.3.1 of Chapter 3), and c is the Stefan-Boltzmann constant, equal to $5.67 \times 10^{-8}\ \mathrm{W \cdot m^{-2} \cdot K^{-4}}$.

The convective heat transfer coefficient (h) in Equation 7.13 can be determined using two methods: fitting a model into the experimental data (Nijdam et al., 2000), or calculated, using published empirical equations (Incropera and David, 2002). In the second method, however, these empirical equations require the experimentally determined surface temperature and velocity of the hot air near the log's surface (Tremblay et al., 2000). Due to the complexity of the experimental set-up and hazards related to high voltage and current, the surface temperature and velocity were not measured. An alternative approach is performing a sensitivity analysis with several heat transfer coefficients. In this research, a sensitivity analysis was done, with the coefficients of 15, 25, 35, and 50 $\mathrm{W \cdot m^{-2} \cdot {}^{\circ}C^{-1}}$. These are common values to wood drying CFD models (Tremblay et al., 2000). The additional heat transfer coefficient of 100 $\mathrm{W \cdot m^{-2} \cdot {}^{\circ}C^{-1}}$ was used to model the worst case scenario.

The radiative heat flux was not determined, as the log's experimental surface temperature was unknown. Since a sensitivity analysis of the heat transfer coefficient was done in this study, it was decided to omit radiative heat loss in the model. Some high heat transfer coefficients, particularly 100 $\mathrm{W \cdot m^{-2} \cdot {}^{\circ}C^{-1}}$, provided a case where the radiative heat loss was less significant

than convective cooling. To prove that, it was assumed that the surface temperature of the log was 100°C. The temperature of the surrounding, the inner wall temperature of the chamber, and hot air were assumed to be about 60°C. Solving Equations 7.13 and 7.14, the heat flux due to convection and radiation were 4000 and 373 $\mathrm{W \cdot m^{-2}}$, respectively. In this case, the effect of radiative heat loss was less than 10% of the total combined effect of convection and radiation. Therefore, modelling heat loss with 100 $\mathrm{W \cdot m^{-2} \cdot {}^{\circ}C^{-1}}$ was assumed to cover both effects in a single boundary condition.

Knowing the magnitude of the heat flux flowing through the boundary faces allows one to calculate the thermal energy absorbed or released during the Joule heating treatment. For example, the amount of thermal energy absorbed by the sapwood from the air can be calculated as:

$$Q = \boldsymbol{J}_{h_b} A t, \tag{7.16}$$

where A is the external surface area of the log through which the flux flows; and $\boldsymbol{J}_{h_b}$ is the heat flux flowing though the boundary, in this case determined from Equation 7.13. In the 1D model, the external surface area (A) was assumed to be equal to the circumference of the log multiplied by its length.

The log's ends were considered to be thermally insulated; mathematically, that was written as:

$$\boldsymbol{J}_h \cdot \widehat{\boldsymbol{n}} = 0. \tag{7.17}$$

However, the electrical boundary condition at the low voltage end was:

$$U = 0 \text{ V}, \tag{7.18}$$

and at the high voltage end was:

$$U = \sqrt{P R_T}, \tag{7.19}$$

where P is the electrical power, equal to 100 kW; and R_T is the total log resistance [Ω]. This boundary condition at the high voltage side takes into account the decrease of the log's resistance

during Joule heating due to the increase in its temperature. Using Equation 7.8, the resistance was calculated at each control volume assuming that it is a concentric cylinder of the log's length. Knowing the width of each control volume, equal to the thickness of those concentric rings, the cross-sectional area of each ring was calculated. As most of the electrical current flows through the much more conductive sapwood, the resistance of the log is governed by the resistance of the sapwood. Hence, the total resistance of the sapwood was assumed to be equal to that of the log, mathematically expressed as:

$$R_T = R_{SW} = \left(\sum_{n=1}^{N_{CV}} \frac{1}{R_n} \right)^{-1}, \tag{7.20}$$

where R_{SW} denote the sapwood resistance and N_{CV} is the total number of control volumes (concentric rings) within the sapwood.

Local Predicted Resistance and Current Density

To compare the local resistances calculated based on the experimental temperature with those estimated based on the predicted temperature, the predicted local resistance of each of the 4 mm thick concentric cylinders was calculated as:

$$R_{\mathrm{C}} = \left(\sum_{n=1}^{N_{CV_{\mathrm{C}}}} \frac{1}{R_n} \right)^{-1}, \tag{7.21}$$

where R_{C} is the resistance of each 4 mm thick concentric cylinder; $N_{CV_{\mathrm{C}}}$ is the number of modelled control volumes, within the concentric cylinder of 4 mm thickness; and R_n is the resistance of each modelled control volume estimated based on the predicted temperature.

Finally, knowing the electrical resistance of each control volume and the voltage applied to the log allows us to calculate electric current flowing through each control volume, described as:

$$I_n = \frac{U}{R_n}, \tag{7.22}$$

where I_n and R_n are the electric current flowing through the control volume and its electrical resistance, respectively. Dividing the electric current values by the cross-sectional area of each control volume results in the local electric current density.

Total Energy and Duration of Excitation

As the CFD model was designed to predict the temperature of green *P. radiata* logs during Joule heating, it had to determine the amount of energy required to heat a log to the required target temperature. In this research, the target temperature had to be above 56°C to achieve the phytosanitary conditions. Taking into account cold and hot spots formation, observed during board heating (Chapter 3), the target temperature was assumed to be 75°C. The sapwood of green *P. radiata* is much more conductive than the heartwood; therefore, it was assumed that all heat from Joule heating would be generated inside the sapwood. The total required energy was calculated as:

$$Q = m_{SW} C_{p_{SW}} (75 - T_i), \tag{7.23}$$

where m_{SW} is the mass of the sapwood, estimated as:

$$m_{SW} = \rho_{g\,SW} (V_L - V_{HW}), \tag{7.24}$$

where V is the green volume [m^3]; the L, SW, and HW indices denote the log, sapwood, and heartwood, respectively; and ρ_g is the green density, equal to:

$$\rho_{g\,SW} = \rho_{s\,SW} (1 + X_{SW}) \tag{7.25}$$

These volumes were estimated using the measured dimensions of the log. As each experiment consisted of three excitations, the amount of energy per single excitation (Q_e) was equal to:

$$Q_e = \frac{Q}{3}, \tag{7.26}$$

where the duration of an excitation (t_e) was calculated as:

$$t_e = \frac{Q_e}{P}. \tag{7.27}$$

In the simulations done prior to heating, the relaxation period (t_r) was assumed to be 10 minutes. However, in the experiments, the relaxation time slightly varied, with the mean duration of

11 minutes. Therefore, to compare the experimental and predicted results, the model was re-run using the experimental relaxation periods. In addition, the model predicted the first 30 minutes of the log's equilibration period, after the last excitation, when the temperature inside the chamber had been maintained at about 60°C. This allowed comparison of the calculated temperature of the log, at the depths of PTSs 1-4, with the experimental results (Figure 7.6).

7.2.4 Computational Model

Ideally, a CFD model should be used prior to the Joule heating treatment to determine the amount of required power and the temperature rise. Therefore, the CFD model had to be relatively accurate, user friendly, fast, robust, financially viable and computationally efficient. Many commercial CFD programs generate accurate solutions in complex, multi-physical 3D problems. However, their licence can be expensive for projects with a limited budget. They often require a certain level of expertise in CFD modelling such as creating geometries and making a proper mesh. Furthermore, some commercial codes such as ANSYS CFX require a meshed 3D geometry to solve a 1D problem, that increases the time of calculations due to a large number of mesh elements in the 3D domain. On the other hand, self-developed codes can be implemented using free or relatively inexpensive programming languages. Hence, such codes are comparatively cheap but they require extensive knowledge of computer programming and numerical calculations. Unlike commercial codes that need to specify many input parameters, custom built codes can be designed for a specific application and would require only limited input parameters. Such CFD codes would be suitable for operators without comprehensive knowledge of CFD modelling, but they cannot be easily adjusted to suit other applications.

In this study, two models based on the finite volume method were built and compared: a 3D model using a commercial CFD software, ANSYS CFX 17.0, and a self-developed 1D model, built in MATLAB. Both models are based on the assumption that the simulated log is uniform and does not have heterogeneous features such as knots or encased bark. This assumption was necessary, as a model with the exact geometry of any given log is impractical to build. Firstly, the exact model would require precise positions of all heterogeneous features within the log, which are often unknown for internal, encased knots and bark. Secondly, the exact model would take considerable calculation time, which makes it unsuitable for simulation prior to each Joule heating treatment. Thus, modelling the homogeneous structure of the log, the 1D and 3D

models simulated the whole experiment (three excitation, two relaxations, and 30 minutes of equilibration) in a single simulation run. The comparison of the 1D and 3D models was done based on Joule heating of Log 1 using a 25 $W \cdot m^{-2} \cdot °C^{-1}$ heat transfer coefficient.

One Dimensional Model

The 1D model was based on the assumption that a temperature gradient within the Joule heated log existed exclusively in the radial direction. The governing equation of heat conservation was solved using the fully implicit scheme, described by Patankar (1980) and Versteeg and Malalasekera (2007). The log's conical shape was assumed to be a cylinder with the diameter equal to the log's SED. The model consisted of two domains: sapwood and heartwood. The diameter of the heartwood domain was equal to the experimentally determined heartwood SED. To discretize the governing heat equation at the interface between the sapwood and the heartwood, a harmonic mean of the thermal conductivities was used (Majumdar, 2006; Patankar, 1980). The complete discretization of the 1D governing heat equation expressed in Cylindrical coordinates is discussed in Appendix E.1. The governing conservation equation of electric charge was not solved in the 1D model, as the applied voltage was constant (and zero) in the radial direction.

Three Dimensional Model

In the 3D model, the governing equations were discretised using the second-order backward Euler scheme. To solve the system of discretised equations, ANSYS CFX uses an iterative solving method. The iteration stops once a convergence criterion is achieved. In this model, the convergence criterion was the root mean square of residuals set to 10^{-6}. The convergence criterion for most time steps was achieved within 20 iterations, using the finest mesh and the narrowest time-step with double precision floating point arithmetic. The 3D geometry was built using ANSYS Design Modeller and was meshed employing the ANSYS meshing tool. The simulations were performed using local parallel computing on four cores of an Intel Core i7-3770 @ 3.40 GHz, with 16 GB RAM. The 3D model was used to build three cases. In *Case 1*, the log had isotropic sapwood and a cylindrical shape, with a diameter equal to the log's SED; this case is identical to the 1D model and was designed to verify the self-developed 1D model. In *Case 2*, the sapwood of the log was isotropic and the log's geometry was built based on the real log's dimensions. In *Case 3*, the sapwood was anisotropic with the geometry built based on the real

log's dimensions.

7.2.5 Mesh and Time-Step Independence

As computational error decreases asymptotically to zero with increasing the number of mesh elements and of time-steps (AIAA, 2002), it was assumed that the results obtained using the highest mesh and time-step resolutions are the most accurate. Following the method described in Section 4.2.2, the maximum computational error was calculated for the temperature recorded at the depths of 32 mm, 62 mm, 92 mm, and 122 mm into Log 1.

Mesh

The mesh independence study was done for the 1D and 3D models with three types of mesh resolution: coarse, medium, and fine. The coarse mesh for the 1D model was made of 1000 control volumes. The total number of control volumes for the 1D model's medium and fine meshes were 2000 and 4000, respectively. As the thickness of heartwood and sapwood were different the number of control volumes within each domain were calculated as follows:

$$N_{CV_{HW}} = \frac{r_{HW}}{r_{Log}} N_{CV}, \tag{7.28}$$

and

$$N_{CV_{SW}} = \frac{d_{SW}}{r_{Log}} N_{CV}, \tag{7.29}$$

where N_{CV} is the total number of the control volumes; $N_{CV_{HW}}$ and $N_{CV_{SW}}$ are the number of control volumes in the sapwood and heartwood domains, respectively; r_{HW}, d_{SW}, and r_{Log} are the heartwood's radius, the sapwood's thickness, and the log's radius at the small end, respectively (Figure 7.8a). As a number of control volumes is an integer value, $N_{CV_{HW}}$ and $N_{CV_{SW}}$ were rounded to the closest integer values. The effect of mesh resolution on computational error was measured by comparing temperature values estimated using different mesh resolutions at the location of PTSs 1-4. Although in the experiments PTSs 1-4 were in a line longitudinally, one centimetre apart (Figure 7.4), in the 1D model the PTSs were all on the same radial line.

In the 3D model, the geometry was built and meshed following the method described in Section 6.2.3 (Figure 7.8b). The mesh independence was performed for each of the 3D cases,

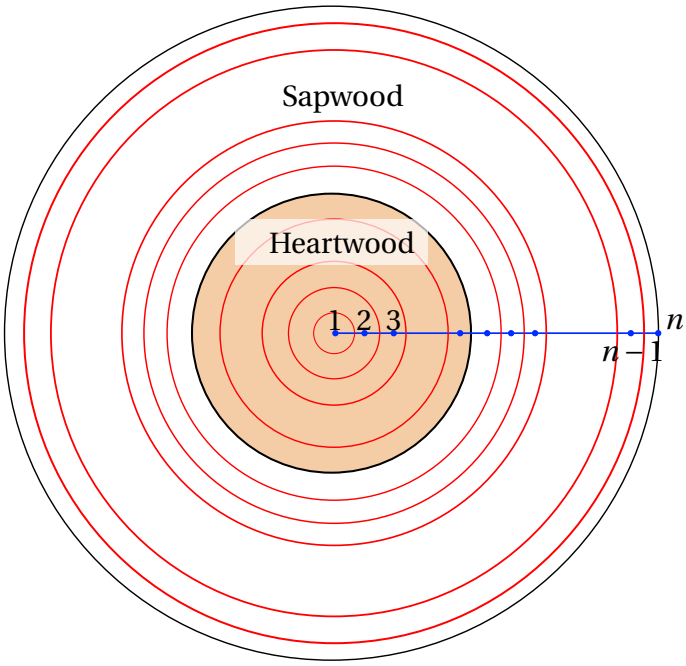

(a)

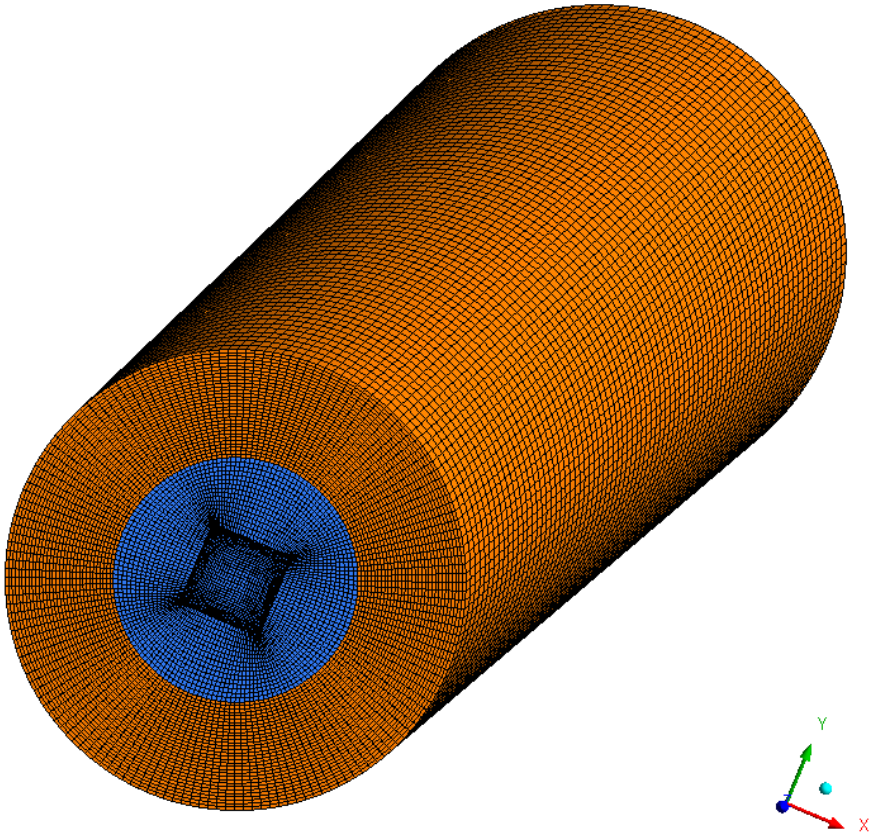

(b)

Figure 7.8. (a) a schematic diagram of a mesh (grid) used in the 1D model and (b) a typical mesh used in the 3D model. *Note:* In (a), n is the total number of control volumes, equal to $N_{CV_{HW}} + N_{CV_{SW}}$. In (b), the orange and blue colours denote sapwood and heartwood, respectively.

using three resolutions of 11,600, 92,800, and 742,400 mesh elements. The location of the PTSs in the 3D geometry imitated the actual position of the sensors within the log, where they were a centimetre apart from each other. The middle of the log was half way between TPSs 2 and 3.

Time-Steps

In the time-step independence study of the 1D and 3D models, three time-step resolutions were considered: 500, 1000, and 2000 steps per each simulated period (excitation, relaxation, and equilibration). As the model simulated all these periods in a single run, the total number of time-steps in the whole simulation were either 3000 6000, or 12,000 time-steps. However, in the time-step independence study of 3D *Case 3*, the resolutions per simulated period were 1000, 2000, and 4000 time-steps and hence the total number of time-steps were 6000, 12,000, and 24,000, respectively.

Furthermore, in the mesh and time-step independence study of 3D *Cases 1-3*, the accuracy of solving the electric charge conservation equation was assessed. To assess the computational error, the effect of mesh and time-step resolutions on the balance of electric current - the amount of electric current entering the log must be equal to the current leaving the log - was studied.

7.3 Results and Discussion

7.3.1 Experimental Results

Electrical Data

Table 7.2 shows the amount of energy introduced to each log by the Joule heating process, the volumes of the whole logs and their sapwood portions, and the initial temperature. The amount

Table 7.2. Supplied electrical energy and the log parameters.

Logs	Energy [kW·h]	V_L [m^3]	V_{SW} [m^3]	T_i [°C]
Log 1	12.1	0.28	0.20	10
Log 2	14.4	0.34	0.24	12
Log 3	17.9	0.41	0.29	10
Log 4	12.9	0.28	0.20	10
Log 5	17.8	0.35	0.30	16

of supplied electrical energy depends on the size of sapwood; the larger the sapwood, the higher the required energy. Based on the results from Logs 1-5, 1 m^3 of logs, with the average sapwood

to log volume ratio of 0.75, require approximately 40 kW·h. This value, however, depends on the initial temperature of the log, where the colder the log, the more energy it requires to reach the phytosanitary temperature condition. Therefore, energy consumption in summer, when beetles are active, can be much lower than in winter, when beetles are significantly less active and the treatment may not be required.

Each log was energised in three excitations. The duration of each excitation was around three minutes and was limited by the maximum available electrical power of 100 kW (Figure 7.9). An electric potential difference was created across the log between the segmented electrodes. These electrodes allowed determination of the current distribution at each of the log's end (Figure 7.10). According to the current distribution results, there were three distinguishable regions: an external relatively non-conductive ring, a relatively conductive middle ring, and a relatively non-conductive central circular region. These regions were present at each excitation and the patterns of current distribution stayed relatively constant through all excitations.

The external non-conductive ring of the segments carried a small amount of the electric current. That can be explained by a non-direct contact between the external segments and the log, as the diameter of the logs was smaller than that of the electrodes. However, there was an indirect contact between the external segments and the logs' ends, due to the small current flow from the external segments into the log through the foam soaked with the high conductive gel. Next to the relatively non-conductive external ring, there was a much more conductive ring of segments that carried most of the electric current. This ring of segments was in direct contact with the sapwood section and hence these segments carried most of the current. The third region was located at the centre of the second conductive ring and carried a small amount of current. This region was in contact with the heartwood. However, as the first ring of electrodes, the third region had an indirect contact with the sapwood through the gel-soaked foam. These results show that segmented electrodes allow determination of a log's overall and heartwood diameters, without measuring them by a tape and/or a ruler. Using segmented electrodes could be more beneficial than other methods dependent on the visual difference between sapwood and heartwood, as heartwood sometimes is hard to identify by visual means, particularly when the ends were covered in mud. However, in this experiment, due to the relatively large size of the segments, there was not enough resolution to precisely identify the border between heartwood

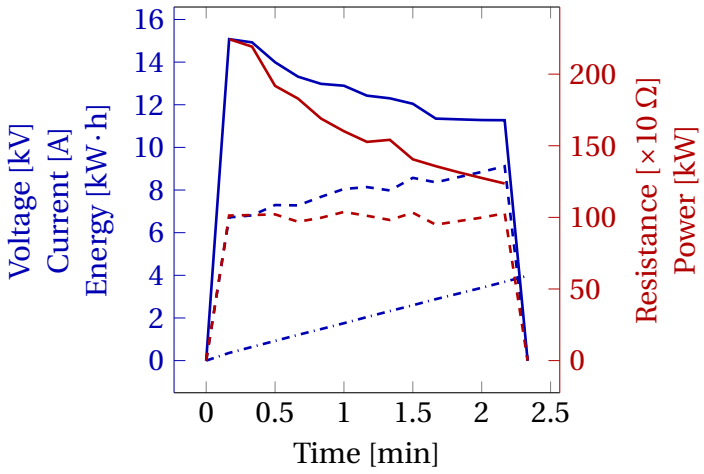

(a) First Excitation

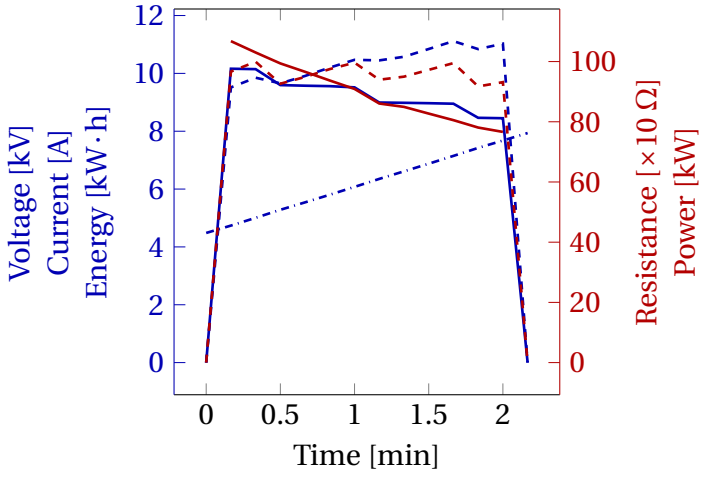

(b) Second Excitation

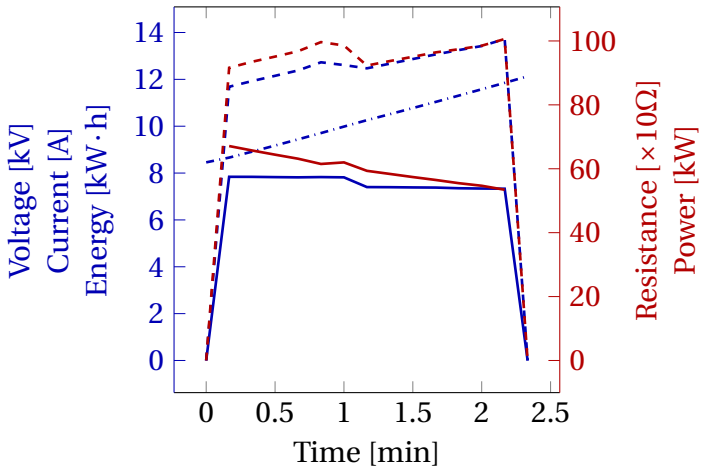

(c) Third Excitation

Figure 7.9. The electrical data of Log 1. The blue solid, dashed, and dash-dotted lines denote the voltage, the current, and the energy, respectively. The red solid and dashed lines denote the electrical resistance and the power, respectively.

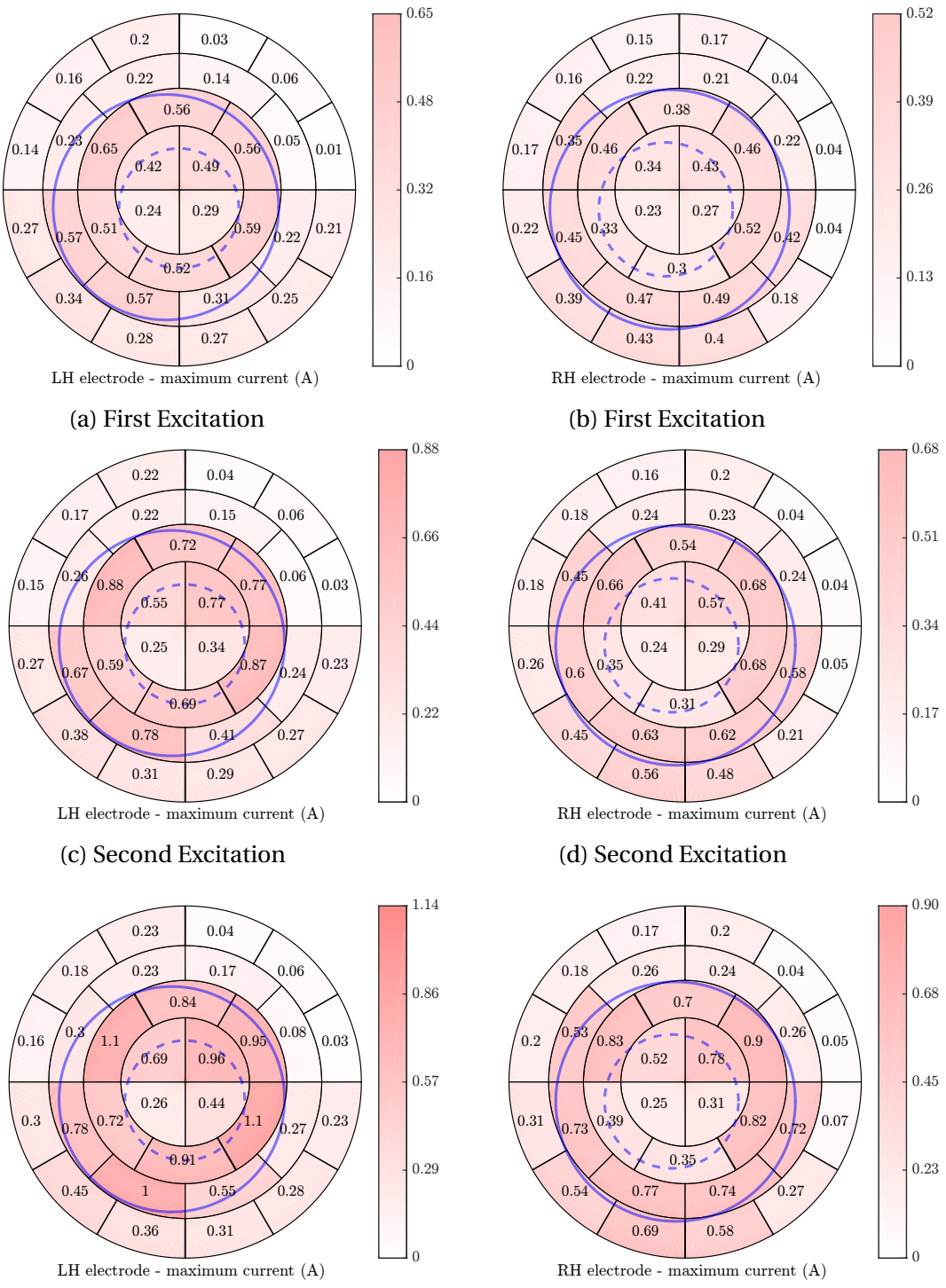

(a) First Excitation

(b) First Excitation

(c) Second Excitation

(d) Second Excitation

(e) Third Excitation

(f) Third Excitation

Figure 7.10. The current distribution at the left-hand electrode (LH) (*left*) and the right-hand electrode (RH) (*right*) of Log 1. *Note:* The blue solid and dashed lines denote approximately the size of the log and its heartwood. The values are in amperes.

and sapwood, and the actual size of the logs (Table 7.3). The electrical data of Logs 2-5 is shown in Appendices E.2 and E.3.

Table 7.3. The sizes of the tested logs.

Parameter [m][a]	Log 1	Log 2	Log 3	Log 4	Log 5
Log LED	0.34	0.38	0.42	0.35	0.40
HW LED	0.19	0.21	0.22	0.19	0.15
Log SED	0.32	0.35	0.37	0.31	0.34
HW SED	0.17	0.18	0.2	0.16	0.11
L	3.26	3.3	3.3	3.29	3.3
r_L	0.16	0.18	0.2	0.16	0.18
d_{SW}	0.07	0.08	0.09	0.07	0.12
r_{HW}	0.09	0.10	0.11	0.09	0.06

[a] LED and SED are the large end and small end diameters, respectively. r_L, d_{SW}, and r_{HW} are the calculated log's radius, sapwood thickness, and heartwood radius at the middle of the log, respectively. These values were calculated assuming that the log's and heartwood's cross-sections were circles and their centres at both ends were aligned.

Temperature Data

a) 'External' Temperature (32 mm depth)

Figure 7.11 shows the recorded temperature change of Log 1, measured using RTDs 1-10. These temperature sensors were inserted 32 mm into the log at P1, P2, and P3 positions (Figure 7.4). All the measured points within Log 1 were heated above 60°C. That would be lethal for most, if not all, wood beetles, their larvae, pupae, and eggs (Dentener et al., 2001; Myers and Bailey, 2011; Pawson et al., 2018; Uzunovic et al., 2013). This temperature was maintained above 60°C for more than 90 minutes, three times longer than that required by ISPM15. Similar results were achieved testing Logs 2-5, shown in Appendix E.4; the lowest temperature of 59.8°C recorded at the 32 mm depth was observed in Log 5 at P1, recorded by RTD 6. After inspection, it was found that the temperature was measured inside a large knot (Figure 7.12). This result indicated that knots can be potentially colder than the rest of the log and hence more temperature measurements near and inside knots should be conducted in the future. In this PhD research, knot heating has been modelled and the results are discussed in Chapter 8.

Generally, the temperature recorded at P1 was higher than that at P2, while the temperature at P3 was the lowest (Figure 7.13). That could have been caused by gradual cooling of the logs; the temperature values recorded at P3 were determined about 25 minutes after the last excitation.

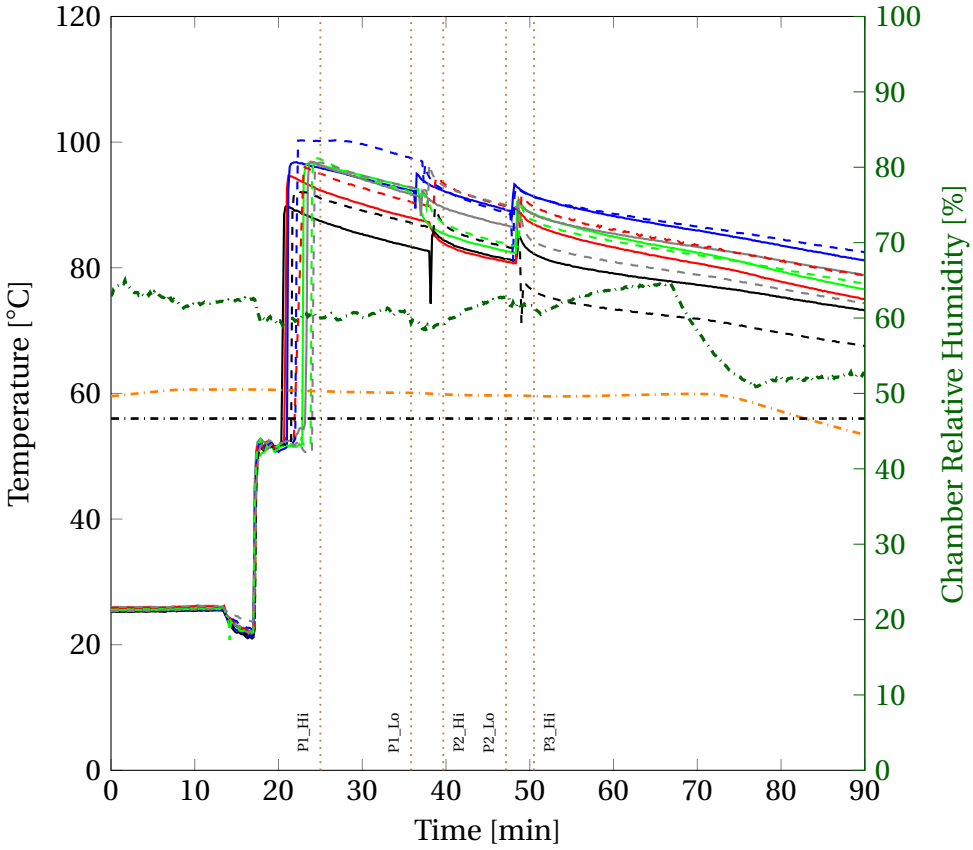

Figure 7.11. The external temperature (32 mm depth) of Log 1 during first 90 minutes after the last excitation ($t = 0$), measured by RTDs 1-10. The solid and dashed lines denote the temperature recorded by RTDs 1-5 and RTDs 6-10, respectively. The black and orange dash-dotted lines denote the ISPM15 temperature of 56°C and the chamber temperature, respectively. The dark green dash-dotted line represents the relative humidity in the chamber. *Note:* P1_Hi is the beginning of temperature recording at P1, P1_Lo is the end of temperature recording of temperature at P1. P2_Hi is the beginning of temperature recording at P2, P2_Lo is the end of temperature recording of temperature at P2. P3_Hi is the beginning of temperature recording at P3.

However, significant cooling was avoided, as the heat blower had maintained the chamber's temperature at approximately 60°C. Thus, if there is a temperature variation along a treated log, caused by the log's conical shape, it should determined by simultaneously positioning temperature sensors in the longitudinal direction (rather than in the circular pattern employed here).

(b) Internal temperature

The internal log temperature was measured by six temperature sensors: RTDs 11 and 12, and PTSs 1-4, inserted to four different depths. According to Table 7.3, the thickness of the sapwood in the middle of the logs varied from 70 to 120 mm. Therefore, PTSs 1 and 2 measured temperature within sapwood, while RTDs 11 and 12 recorded temperature of the heartwood. Depending on

Figure 7.12. The knot that had a temperature below 60°C after the experiment.

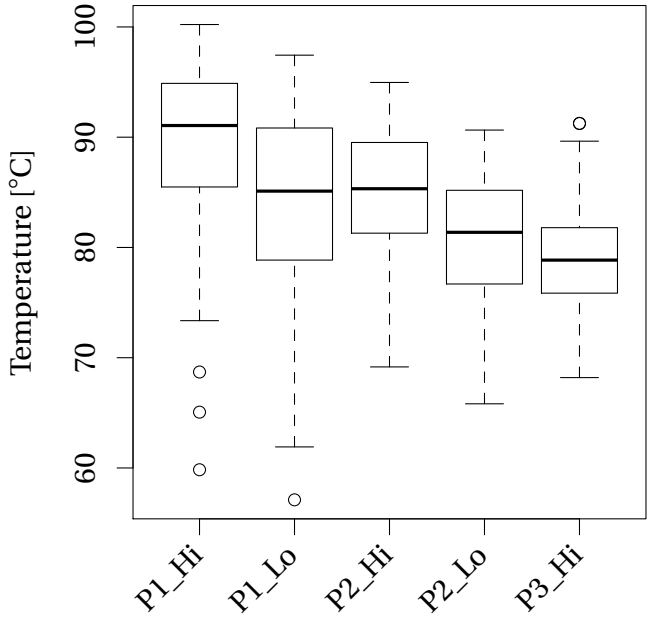

Figure 7.13. The box plot of "Hi" and "Lo" temperature values, measure by RTDs 1-10, at P1, P2, and P3. *Note:* Hi and Lo denote the beginning and the end of the temperature recording, respectively, at P1, P2, and P3.

the thickness of sapwood, PTSs 3 and 4 were inserted either into sapwood, heartwood, or the transitional zone.

Figure 7.14 shows the internal temperature of Log 1, where the highest temperature was measured by PTS 1, inserted to the depth of 32 mm. The recorded value was similar to those measured by RTDs 1-10. The lowest temperature of the log was recorded by RTDs 11 and 12, inserted to the average depth of 150 mm. Similar results were observed in other logs (Appendix E.5),

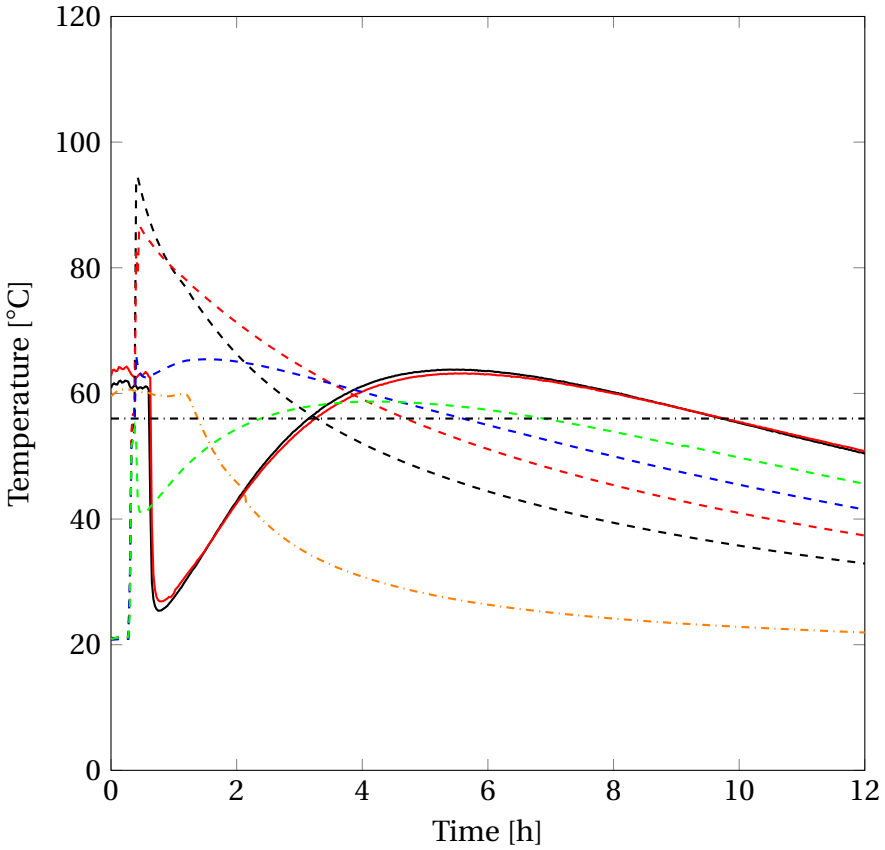

Figure 7.14. The internal temperature of Log 1 during 12 hours of cooling, after the last excitation, measured by RTDs 11 and 12 (the black and red solid lines, respectively), and PTSs 1 (32 mm depth), 2 (62 mm depth), 3 (92 mm depth), and 4 (122 mm depth), shown as the black, red, blue, and green dashed lines, respectively. The black and orange dash-dotted lines denote ISPM15 temperature of 56°C and the chamber's temperature, respectively.

except Log 4, where PTS 4 inserted into 122 mm was colder than RTD 12 inserted 145 mm into the log. That can be potentially explained by hot water permeating from the sapwood into the drilled hole of RTD 12. Nonetheless, the temperature of heartwood was much lower than that of sapwood. The temperature of PTSs 2-4 varied depending on the thickness of sapwood. Overall, the thicker the sapwood, the larger the heated volume and the higher the required energy. In addition, the internal temperature, measured by RTDs 11 and 12, reached the range of 40-60°C approximately 4.5 hours after the last excitation. This means that the centre of a log can be heated to phytosanitary temperature conditions. However, the amount of required energy and time to heat heartwood will depend on its size, where the smaller the heartwood, the lower the additional energy and the faster the heartwood's temperature rise. Furthermore, the larger the sapwood section within the log, the higher the total required energy.

Electrical Conductivity

The total log resistance dropped from the range of 1.5-2.5 kΩ to about 0.5 kΩ, meaning that the logs became 3-5 times more conductive at the end of the last excitation. The segmented electrodes showed that the most of electric current flowed through the sapwood. According to Figure 7.10 and Appendix E.3, the ratio of apparent electric current flowing though the sapwood to that flowing through the heartwood increased from about two, at the first excitation, to about four times, at the last excitation. Hence, as most of the electric current flowed through the sapwood, the decrease of the total log resistance was predominantly caused by the decrease of the sapwood's resistance. Therefore, to compare the log electrical conductivity with the previously tested cubes (Chapter 5), the sapwood's initial temperature and the average temperature at the end of the final excitation were used. Figure 7.15 shows the effect of the log's sapwood temperature on the electrical conductivity, which was compared with the electrical conductivity of the cubes from *Set 1* (Section 5.3), the conductivity of *B. alleghaniensis*, measured by Fleischer and Downs (1953), and the obtained statistical model, Equation 5.13. The conductivity

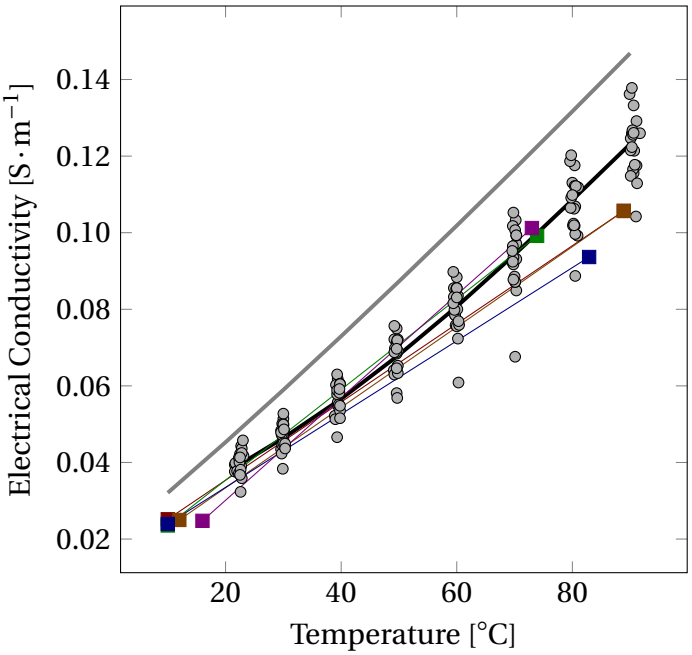

Figure 7.15. The effect of temperature on the electrical conductivity of logs (squares) and cubes of *Set 1* (grey dots). *Note:* The black line denotes the electrical conductivity equation for the longitudinal direction derived in Chapter 5. The grey line represents electrical conductivity of *B. alleghaniensis* measured by Fleischer and Downs (1953). The red, orange, green, blue, and violet square scatters represent Logs 1-5, respectively.

of *B. alleghaniensis* was approximately 25% higher than that of the logs; this can be explained

by the difference in the wood structure of *P.radiata* and *B. alleghaniensis*. However, the dependence of the logs' conductivity on temperature is comparable with the earlier results and hence Equation 5.13 was used in the CFD model, with the multiplier being equal to 1.

7.3.2 Results of Mesh and Time-Step Independence Study

1D Model

Figure 7.16 shows the effect of mesh and time-step resolutions on the computational error of temperature. Although the computational error decreases with the number of control volumes,

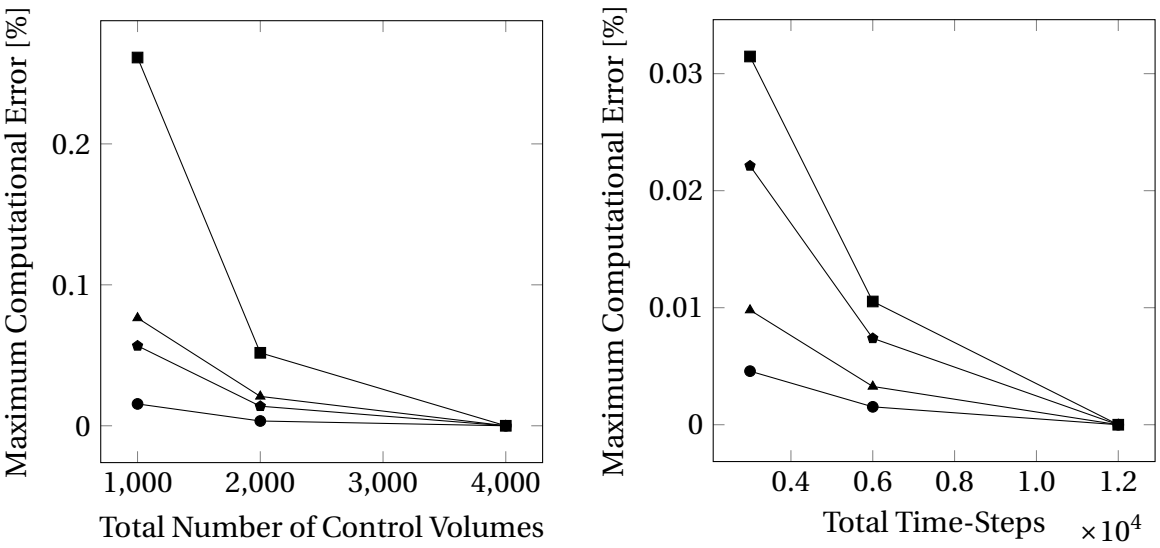

Figure 7.16. The results of (a) mesh and (b) time-step independence studies for the 1D model. *Note:* The circular, triangular, square, and pentagonal scatters denote PTS 1, 2, 3 and 4, respectively.

the error was always below 0.25%. The time-step resolution makes the similar pattern, with the error staying below 0.03%. Thus, the obtained results showed independence of mesh and time-step resolutions. However, as the duration of the calculation was relatively short (less than two minutes), it was acceptable to use the highest mesh and time-step resolutions, which were 4000 control volumes and 12,000 total time-steps, respectively.

3D Model

In the 3D model, the effects of mesh resolution were more pronounced (Figure 7.17). In particular, the maximum computational error of temperature measured at PTS 3, located near the sapwood-heartwood interface, decreased from about 13% to below 5% by changing the mesh from the coarse to medium resolution. Such dependence of temperature error on mesh

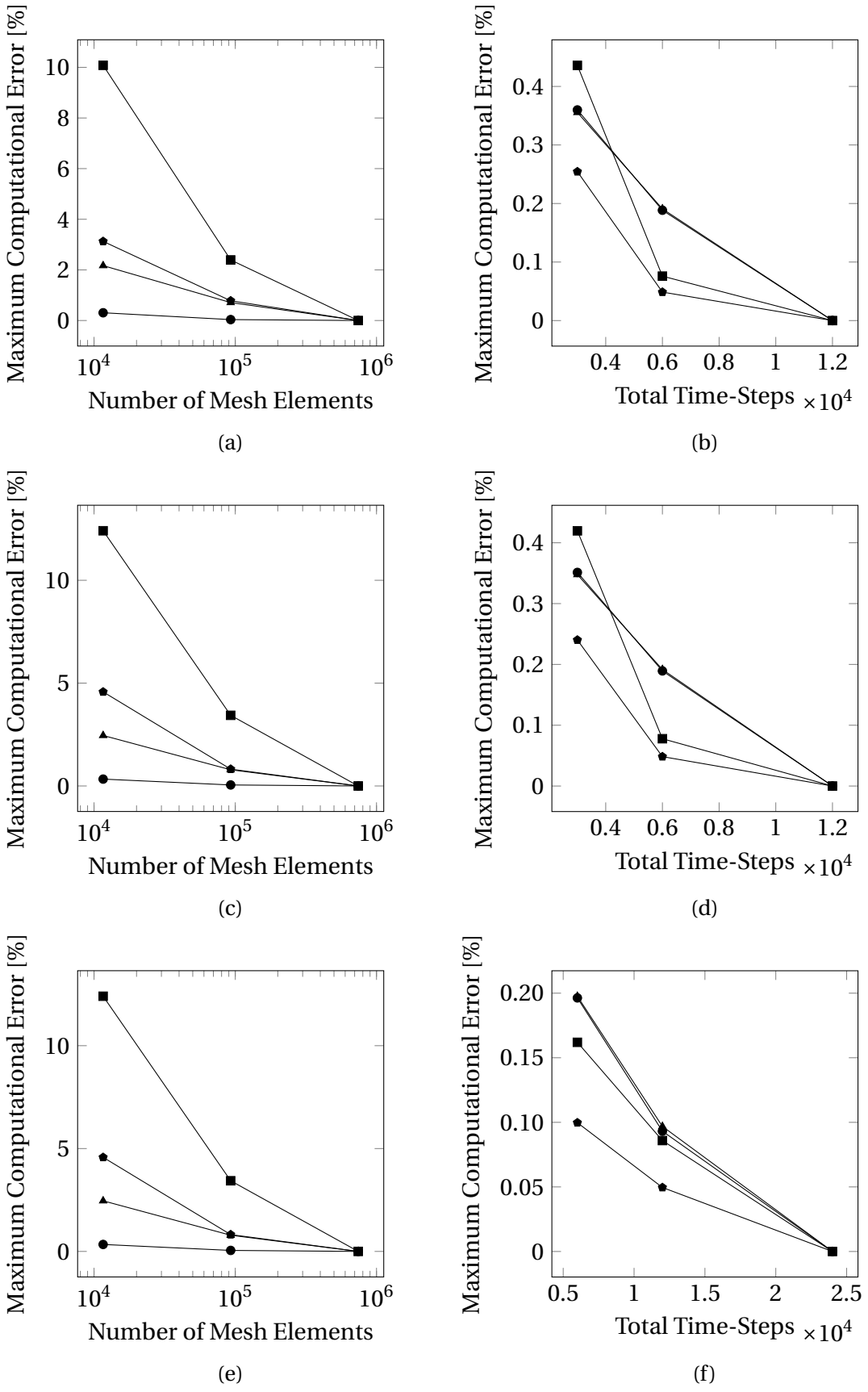

Figure 7.17. The effect of mesh (*left*) and time-step (*right*) resolutions on the maximum computational error for the 3D model. *Note:* The circular, triangular, square, and pentagonal scatters denote PTS 1, 2, 3 and 4, respectively. The top, middle, and bottom graphs denote *Cases 1, 2,* and *3*, respectively.

resolution at PTS 3 can be explained by close location of the temperature measuring point to the sapwood-heartwood interface. This region requires a higher number of mesh elements to accurately predict the existing temperature gradient. In the time-step independence study of *Cases 1* and *2*, an increase of the total number of time-steps from 3000 to 6000 reduced the computational error of temperature measured at PTS 3 from approximately 0.4% to about 0.1%. In *Case 3*, the initial computational error decreased from 0.2% to 0.1%; the average of four error values dropped to about 0.08% using 12,000 time-steps. In addition, the effect of mesh and time-step resolutions on the balance of electric current was insignificant, with the error lying within the range of 0.013-0.015 A for *Cases 1 and 2*, and within 0.01-0.02 A for *Case 3*. Thus, to obtain accurate solutions in the shortest possible time (within 12 hours), the finest mesh resolution (742,400 mesh elements) and the lowest number of the total time-steps (3000 for *Cases 1 and 2* and 6000 for *Case 3*) were used to compare the final 3D model results with the 1D model.

7.3.3 1D Model vs 3D Model

Figure 7.18 shows the calculated voltage and the electric current using the 1D model and the results of *Cases 1-3* simulated using the 3D model. The electric current calculated by the 3D

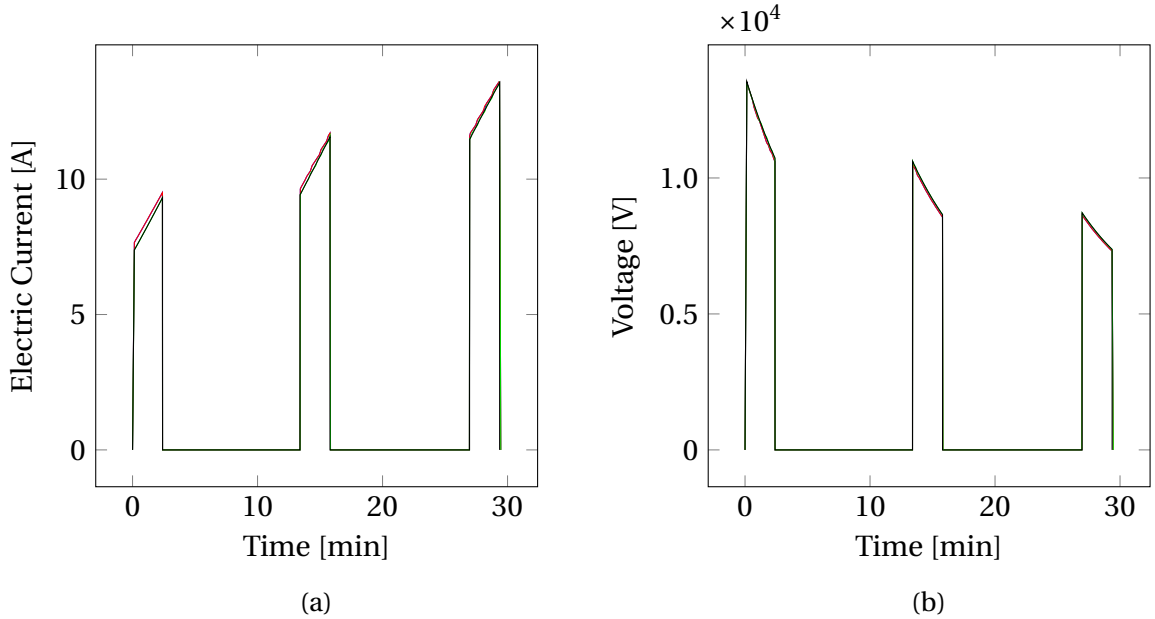

Figure 7.18. The predicted electric current and voltage of Log 1 calculated by the 1D and 3D models. *Note:* The black line denotes the 1D model, while the blue, red, and green lines represent the results of 3D model *Cases 1, 2*, and *3*, respectively.

model in *Case 2* and *3* was slightly higher than that calculated in *Case 1* and by the 1D model.

Hence, as the electrical power was fixed at 100 kW, the voltage across the log in *Cases 2* and *3* was lower than that calculated in *Case 1* and the 1D model. These differences, however, were negligible, about 3.5% and 1.8% for electric current and voltage, respectively.

The constant power generation caused a temperature rise within the log, depicted in Figure 7.19. Calculating temperature at PTSs 1-4, the highest temperature within the log was

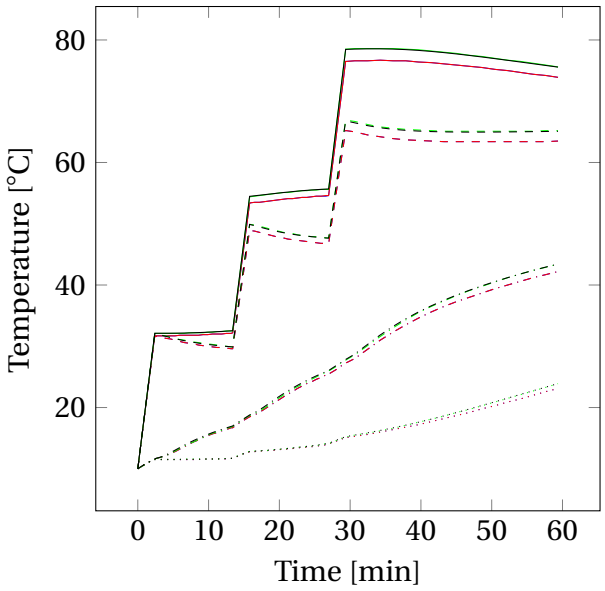

Figure 7.19. The predicted temperature of Log 1 at PTSs 1-4 calculated by the 1D and 3D models. *Note:* The black lines denote the 1D model, while the green, red, and blue lines represent the results of 3D model *Cases 1, 2*, and *3*, respectively. The solid, dashed, dash-dotted, and dotted lines represent PTS 1-4, respectively.

estimated at PTS 1 and the coldest temperature at PTS 4. Such behaviour was observed in the experimental results (Figure 7.14). At the end of the third excitation, the temperature of Log 1 determined in *Case 2* and *3* was 2°C lower than that calculated in *Case 1* and by the 1D model.

All the simulated cases showed a similar global temperature distribution in the radial direction; at the end of the last excitation, the global hot spot was within the sapwood, near the log's surface, and the global cold spot was in the centre of the log. In the 1D model, this temperature distribution profile was assumed to be constant along the log's length, the same as in *Case 1* (Figure 7.20a). However, in *Case 2* and *3*, the temperature varied along the log in a range of 2-5°C, where the hottest part was near the small end (Figure 7.20b). This temperature variation can be explained by the change of the log's diameter, due to the conical shape of Log 1. At the small end, the relatively small cross-sectional area caused a local rise of current density, consequently resulting in higher power dissipation. In the experiments, there was a difference between P1, P2, and P3 temperature values; however, as discussed earlier, that was probably caused by the log's

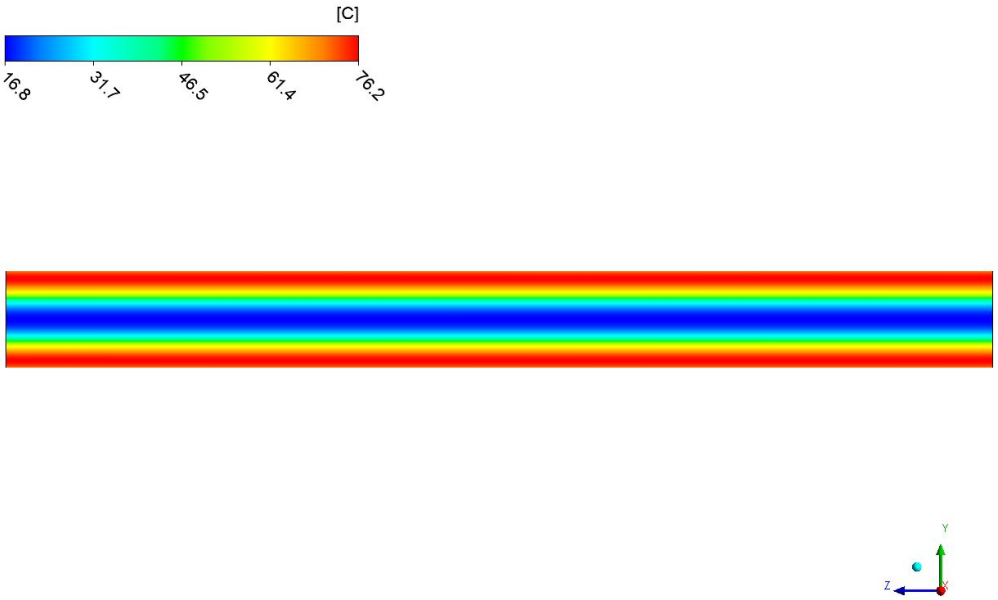

(a) 1D model and *Case 1*

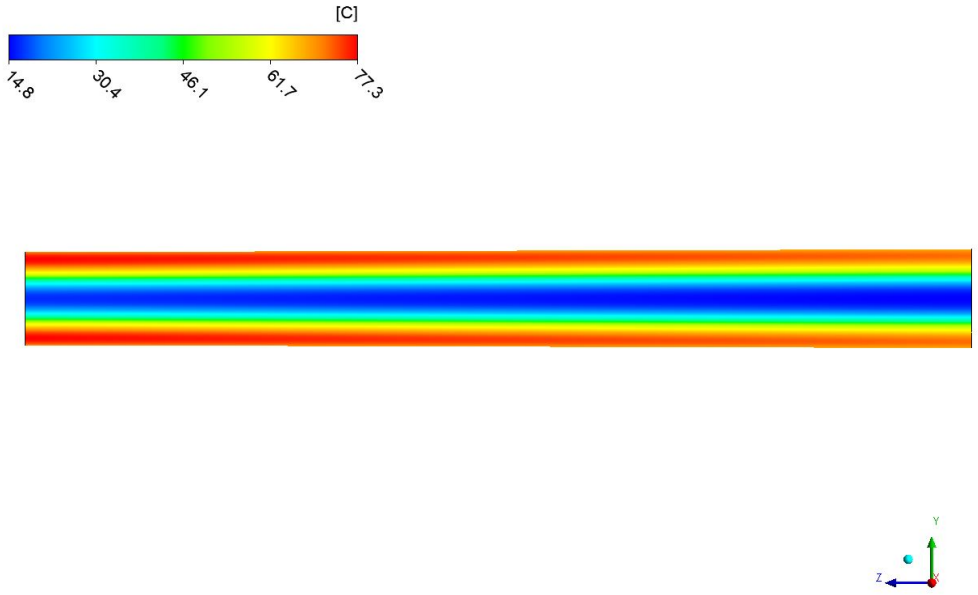

(b) *Cases 2* and *3*

Figure 7.20. The predicted temperature profiles along Log 1 after 30 minutes of equilibration.

cooling during the equilibration period. Hence, to test this supposition, temperature should be measured simultaneously along the log's length in future experiments.

Figure 7.21 shows the temperature profile along the radius of Log 1 after 30 minutes of equilibration, at 60°C, calculated by the 1D and 3D models. The 1D model showed a close agreement

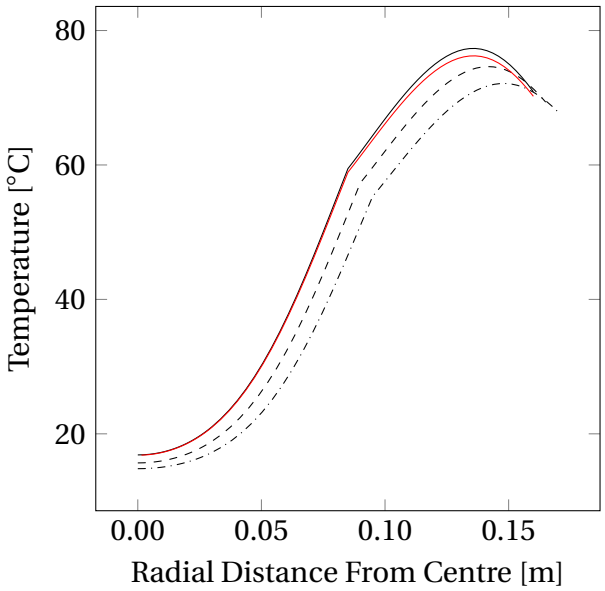

Figure 7.21. The radial temperature profile in the cylindrical and conical logs. *Note:* The black solid, dashed, and dash-dotted lines denote temperature profiles at the small end, the middle, and the large end of the conical log, respectively. The red solid line represents temperature profile within the cylindrical log, modelled in *Case 1* and by the 1D model.

with *Case 1*, which indicates that the custom-build CFD code is bug-free and generates comparable results to the commercial CFD code. Furthermore, the 1D model showed similar results as *Cases 2* and *3* of the 3D model and required less computational power, significantly reducing the calculation time. Thus, due to the above advantages of the 1D model, it was selected for the sensitivity analysis of the heat transfer coefficient and was validated based on the experimental results of Logs 1-5.

7.3.4 Sensitivity Analysis of Heat Transfer Coefficient

The 1D model simulated Log 1's treatment using five heat transfer coefficients (Figure 7.22). Due to the relatively low thermal conductivity, high heat capacity of sapwood, and the short duration of the treatment, the effect of the heat transfer coefficient on the log's temperature profile is significant within 3 cm depth into the log. Although a higher heat transfer coefficient caused faster cooling when the log's surface was hotter than the ambient air, at the end of the

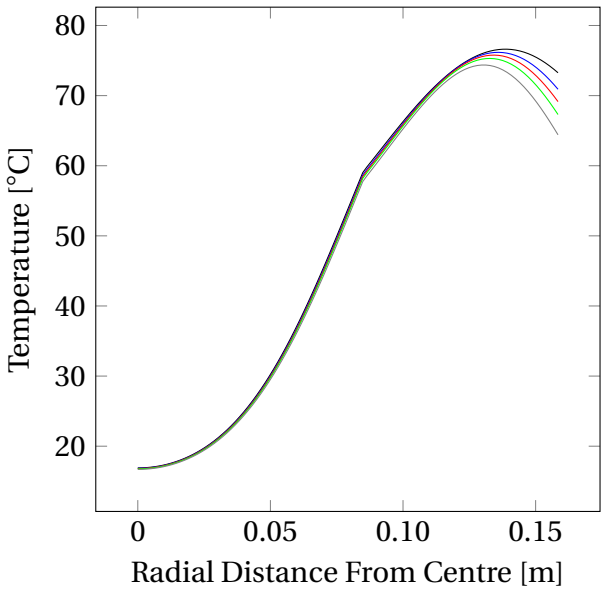

Figure 7.22. The effect of the heat transfer coefficient on the temperature profile of Log 1, determined 30 minutes after the last excitation. *Note:* The black, blue, red, green, and grey lines denote the heat transfer coefficients of 15, 25, 35, 50, and 100 $W \cdot m^{-2} \cdot °C^{-1}$, respectively.

last excitation period, the temperature at PT1 calculated using 100 $W \cdot m^{-2} \cdot °C^{-1}$ was higher than that estimated using 15 $W \cdot m^{-2} \cdot °C^{-1}$, as shown in Figure 7.23.

At the beginning of treatment, when the surface temperature of the log is below 60°C, the log's surface is heated by convective heating. The higher the heat transfer coefficient, the faster the convective heating. Hence, in the first excitation and relaxation, the surface temperature calculated with 100 $W \cdot m^{-2} \cdot °C^{-1}$ is higher than that determined using 15 $W \cdot m^{-2} \cdot °C^{-1}$. As electrical conductivity is correlated with temperature, a high heat transfer coefficient increases the power dissipation near the log surface. However, a high convective heating causes a higher temperature gradient within the sapwood, leading to lower power dissipation further below the surface. As a result, the temperatures of PTSs 2-4 at the end of the last excitation estimated using 100 $W \cdot m^{-2} \cdot °C^{-1}$ were lower than those calculated with the lower heat transfer coefficients. Thus, if the treated log had a uniform structure and its external surface solely had to be treated, the convective heating should be increased, for instance by enhancing the hot air flow around the log. On the other hand, to achieve more uniform temperature radially in sapwood, the convective heating should be reduced.

In the 1D model, at the end of the last excitation, the heat flowed from the global hot spot in two directions. The first direction was towards the log's external surface and the second direction was towards the centre, the global cold spot. In the experimental conditions, however, formation

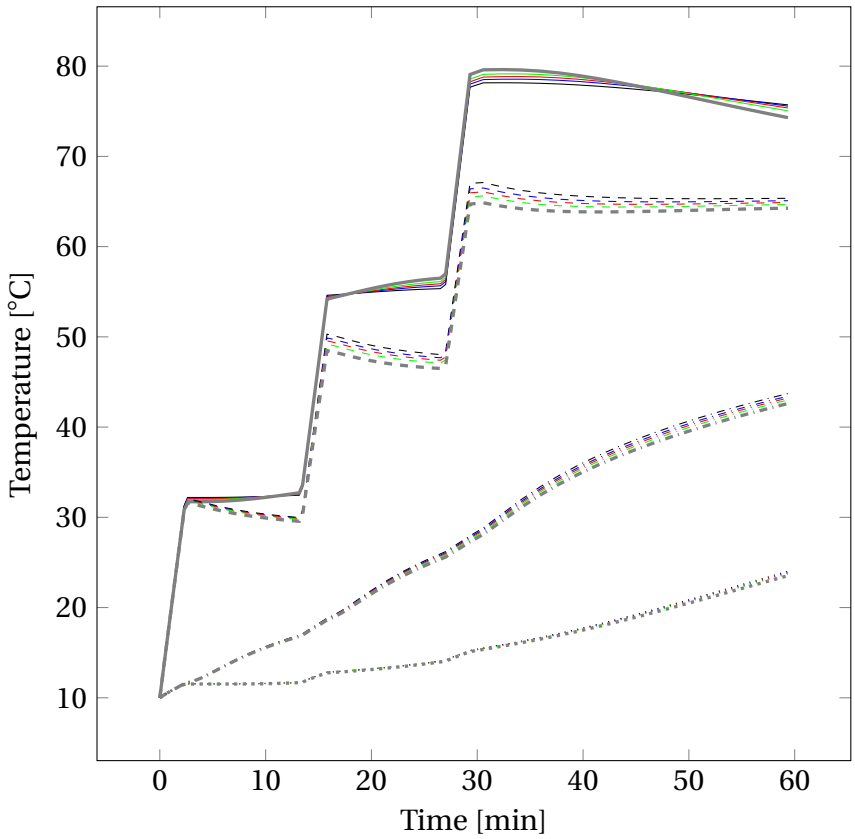

Figure 7.23. The effect of the heat transfer coefficient on the temperature of Log 1 at PTSs 1-4 (the solid, dashed, dash-dotted, and dotted lines, respectively). *Note:* The black, blue, red, green, and grey lines denote the heat transfer coefficient equal to 15, 25, 35, 50, and 100 $W \cdot m^{-2} \cdot °C^{-1}$, respectively.

of local hot and cold spots affected the cooling rate that was recorded at discrete points using inserted temperature sensors. In addition, the log cooled due to moisture evaporation, which was not included in the model as the duration of the Joule heating treatment was relatively short. Therefore, the experimental cooling rate after the last excitation of the logs was different from the predicted data. Nonetheless, the 1D model showed that the effect of the heat transfer coefficient was small due to relatively short duration of the heat treatment; therefore, the heat transfer coefficient was assumed to be 25 $W \cdot m^{-2} \cdot °C^{-1}$ - about the average value used in wood drying models (Tremblay et al., 2000) - in the simulations of Logs 2-4 (Appendix E.6).

7.3.5 Experimental vs Computational Results

Temperature

As the temperature sensors were inserted into the logs at the post-heating stage, the logs' experimental temperature rise had not been measured during heating. Therefore, the simulated transient temperature rise, from the beginning of heating until the end of the last excitation, was

not compared to experimental data. However, the temperature measured after the last excitation showed the final temperature of the logs at the beginning of the equilibration period. Table 7.4 shows the experimental and predicted temperature values measured after the last excitation.

Table 7.4. The experimental and predicted temperature values measured at the different depths after the third (final) excitation.

Log	Experimental Temperature [°C]				Calculated Temperature [°C]			
	32 mm [a]	62 mm	92 mm	122 mm	32 mm	62 mm	92 mm	122 mm
Log 1	95±4	87	64	41	78	67	28	15
Log 2	93±4	77	55	36	77	69	37	19
Log 3	90±6	81	56	34	88	79	45	19
Log 4	90±3	81	61	39	82	70	29	16
Log 5	78±11	80	59	49	86	83	79	48
Average	88±8	81±3	59±3	40±6	82±5	74±7	44±21	23±14

[a] The temperature of the logs at the 32 mm depth is shown as the average value with the standard deviation (±), based on the results obtained from RTDs 1-10 (at P1) and PTS 1.

Generally, the experimental temperature was higher than the calculated values. At the depth of 32 mm, the experimental results exceeded the predicted temperatures by 5°C to 17°C. This difference increased to about 20°C at the 122 mm depth. Log 5, however, showed a different trend; its average experimental temperature at the 32 mm depth was about 8°C lower than the predicted average temperature. Furthermore, its experimental average temperature was 12°C lower than that measured in the other logs. The difference was linked to the relatively low temperature measured at the site of a large knot.

Measuring temperature within the knot of Log 5 decreased the average value and increased the standard deviation. Hence, the predicted temperature at 32 mm into Log 5 lay within the standard deviation from the experimental mean value. However, the temperature measurements at 32 mm into Logs 1-4 had much lower standard deviations, which can be explained by the fact that the temperature was measured predominantly at knot-free areas. Therefore, the local cold spot temperature of Logs 1-4, potentially caused by knots, has not been measured. As a result, their experimental average temperatures had lower standard deviation and were much higher than the predicted values. That leads to the conclusion that, in future research, the temperature of a log should be measured both inside knots and at knot-free areas to determine the actual temperature variation within a log.

The temperature at the other depths were measured at a single, discrete point and hence

the variation of the temperature values at those depths is unknown. The comparison with the calculated values showed that the prediction underestimated the logs' temperatures. However, the recorded experimental temperature may not represent the average value measured in clear wood, because it could have been affected by local hot spots. Furthermore, the increase of temperature difference at the depth of 92 and 122 mm can be explained by hot water penetration from the sapwood during drilling. Hot water may have increased the actual temperature of the heartwood. Lastly, as, in the model, the log's and heartwood's centres were aligned, while in real logs the heartwood can be off-centred (Figure 7.7); the difference between the predicted and experimental temperatures measured at the 92 mm and 122 mm depths was potentially caused by the inaccurate assumed location of the sapwood-heartwood interface. Hence, to compare the experimental and predicted temperatures of a log at different depths more data within a single log should be collected in the future. Ideally, instead of measuring temperature at single points, a temperature distribution within the log should be measured. That can be achieved by cutting the logs inside the chamber after the last excitation and measuring temperature of the offcuts using a thermal camera. Otherwise, more experiments should be performed to collect a more extensive data set for comparison with the 1D model.

In addition, the difference between the predicted and experimental temperatures could have been caused overestimating the required energy introduced into the logs. Being stored at normal ambient conditions, the logs were gradually drying. Hence, at the test day, the real moisture content could have been lower than that assumed in the model, which was based on average values given by Pang et al. (1995). A loss of moisture would affect the heat capacity, described by Equation 7.4, where the lower the moisture content, the lower the heat capacity. As the heat capacity was used to calculate the required energy (Equation 7.23), the latter should decrease with drying. In the simulations of Logs 1-5, a constant sapwood moisture content was assumed to be 150%. However, if the logs' real sapwood moisture content had been lower than 150%, the model would have overestimated the required energy introduced into the logs, resulting in higher experimental temperature. Testing this conjecture is described in Appendix E.7.1, using an additional log (Log 6) from the subsequent experiment. The results of this work are encouraging and indicate how mass measurement can be used to improve the process.

Resistance

Although there is a pronounced difference between the locally measured experimental temperature and the predicted average temperature, the 1D model showed an acceptable agreement with the total experimental resistance (Figure 7.24 and Appendix E.8). Generally, the error of

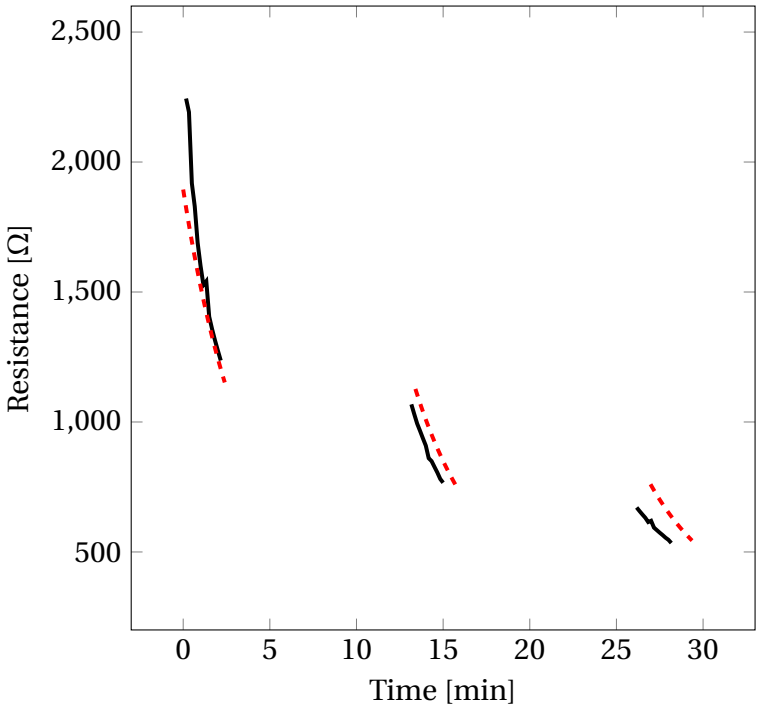

Figure 7.24. The total experimental electrical resistance (black solid line) and the predicted resistance of Log 1 using the 1D model (dashed red line).

the calculated total resistance was approximately 10%, with a higher initial error (around 20%) being observed at the beginning of the first excitation. Currently, this high initial error cannot be explained and hence it should be investigated in future work.

As the resistance is highly temperature dependent, it can be assumed that the average experimental temperature of the sapwood was comparable to the predicted temperature, regardless of local hot and cold spot formation. Hence, measuring the resistance can be used as a feedback parameter to control the process. For example, knowing the total resistance will allow assessment of the magnitude of the average temperature, without drilling holes in the log. In addition, a significant difference from the predicted resistance values would indicate faults in the operation such as excessive power dissipation at the contacts. However, total experimental resistance cannot be used to assess the log's internal temperature distribution, as different temperature profiles can result in the same total resistance. For example, Figure 7.25 shows the electrical resistance profiles calculated using experimental and predicted temperature values measured

within the sapwood of Log 1 at the end of the last excitation. As the experimental temperature of

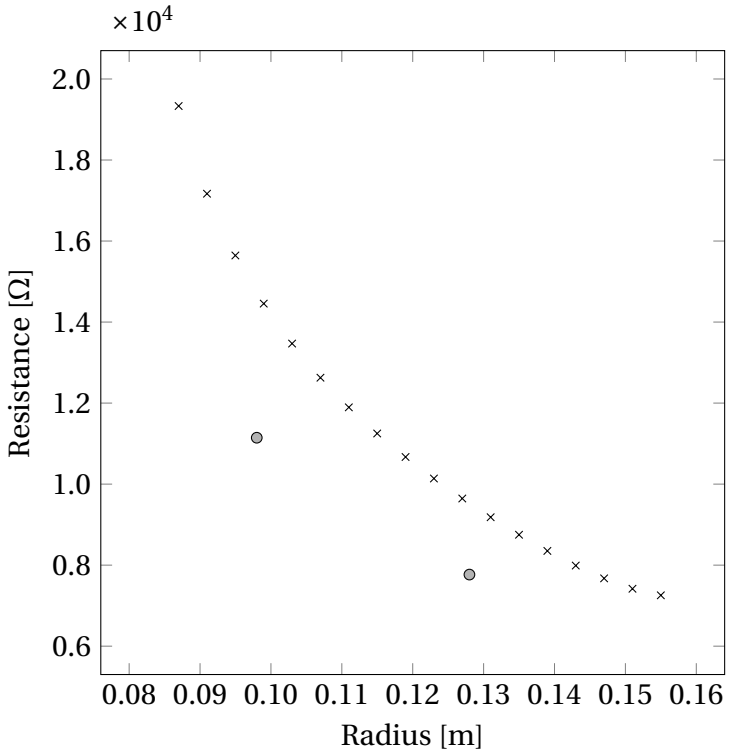

Figure 7.25. The local resistance calculated using experimental temperatures (PTSs 1 and 2) (circles) within the sapwood of Log 1 determined at the end of the last excitation. The crosses represent the predicted resistance profile.

Log 1 was higher than that predicted by the 1D model (Table 7.4), the local calculated resistances based on the experimental temperature were lower than those calculated based on the predicted temperature values. The difference between the experimental and predicted local electrical resistances varied from 20 to 30% and was proportional to the temperature difference.

The experimental local resistance, however, could have been different if it was possible to measure it directly. In general, wood's structure is more complex than the assumption that wood is made of concentric rings of uniform thermal and electrical properties. Therefore, the calculated local experimental resistance is an approximation of the real value. In this research, knowledge of real local resistance is unnecessary, as modelling a detailed log structure in a CFD model is not practical; therefore, the model will be always relatively inaccurate in the prediction of the real local resistance or temperature distribution. Instead, the model aims to accurately predict the log's total resistance (Figure 7.24 and Appendix E.8) and the average temperature. Appendix E.9 shows the local electrical resistance of Logs 2-5, where the most accurate prediction of local resistance was observed in Log 3, with the error below 5%. It also shows that the error can be either positive or negative.

7.3.6 Current Density and Internal Temperature Profiles

Figure 7.26 shows the calculated current density distribution in Log 1 based on the predicted internal temperature distribution. The model predicted that the area of the highest current density moved towards the heartwood, with each subsequent excitation. That can be explained by the shift of the global hot spot (Figure 7.27). At the first excitation, the log was heated by the 60°C hot air, causing its external surface to be the hottest region. However, from the end of the second excitation, the log's external temperature became hotter than the temperature of the air and hence it started losing heat to the air. As a result, the global hot spot shifted closer to the centre of the sapwood.

The higher the temperature, the higher the conductivity and the higher the electric current density. As the electric current density is proportional to the power, or heat dissipation density, the hottest region gets hotter faster during an excitation. During the relaxation, the difference between the hot and cold spots will reduce, making the temperature rise during a subsequent excitation relatively more uniform. Therefore, to avoid local overheating, the relaxation periods must be considered during the Joule heating treatment. Furthermore, regulating the external temperature conditions around the log, the heating rate of the sapwood's different parts can be controlled. For example, if an importing country accepts logs with a heat treatment depth of 32 mm, then during the treatment, the chamber's temperature around the logs should be high. That will create a global hot spot at the external surface, ensuring higher power dissipation in that region. On the other hand, in veneer peeling, where the whole log should be heated above 60°C (Perré, 2004), colder ambient temperature is required. Cooling the log from outside will develop an internal temperature gradient, with a global hot spot close to the log's heartwood. Hence, during the subsequent excitation, the greatest heat dissipation density will be near to the heartwood; the shorter the distance between the global hot spot and the heartwood, the faster the heartwood's temperature rise. The distribution of electric current density and temperature within Logs 2-5 are shown in Appendices E.10 and E.11, respectively.

7.3.7 Calculated Energy Transfer

Figure 7.28 shows the calculated amount of energy converted into heat due to the Joule heating effect in Log 1. Most of the supplied electrical energy of 12 kW·h (43.2×10^6 J) was converted into heat within the sapwood. Less than 1%, 0.085 kW·h or 30.6×10^4 J, was converted to heat

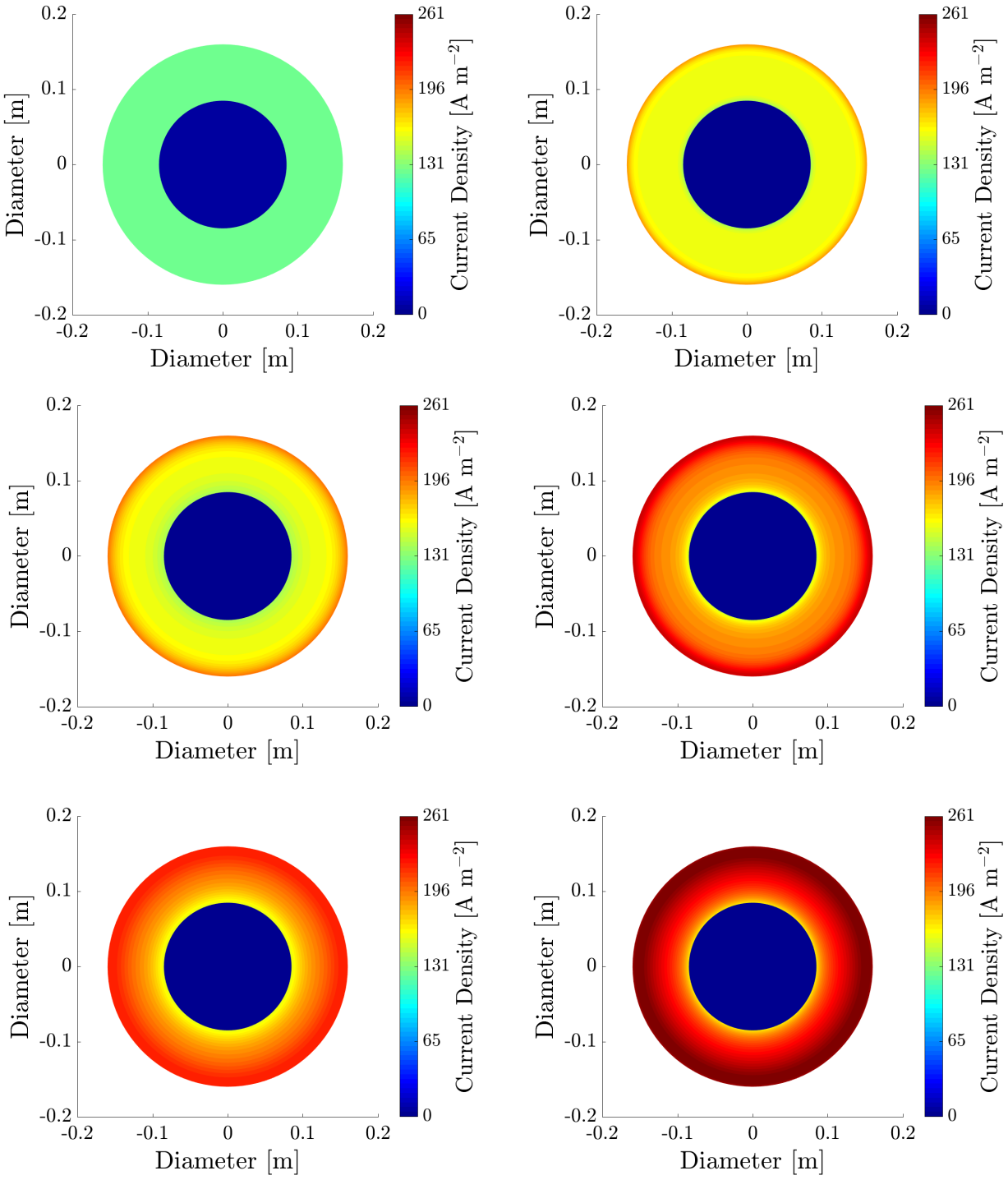

Figure 7.26. The predicted current density distribution within Log 1 at the beginning (*left*) and the end (*right*) of each excitation. The top, middle, and bottom figures are the results from the 1st, 2nd, and 3rd excitation, respectively.

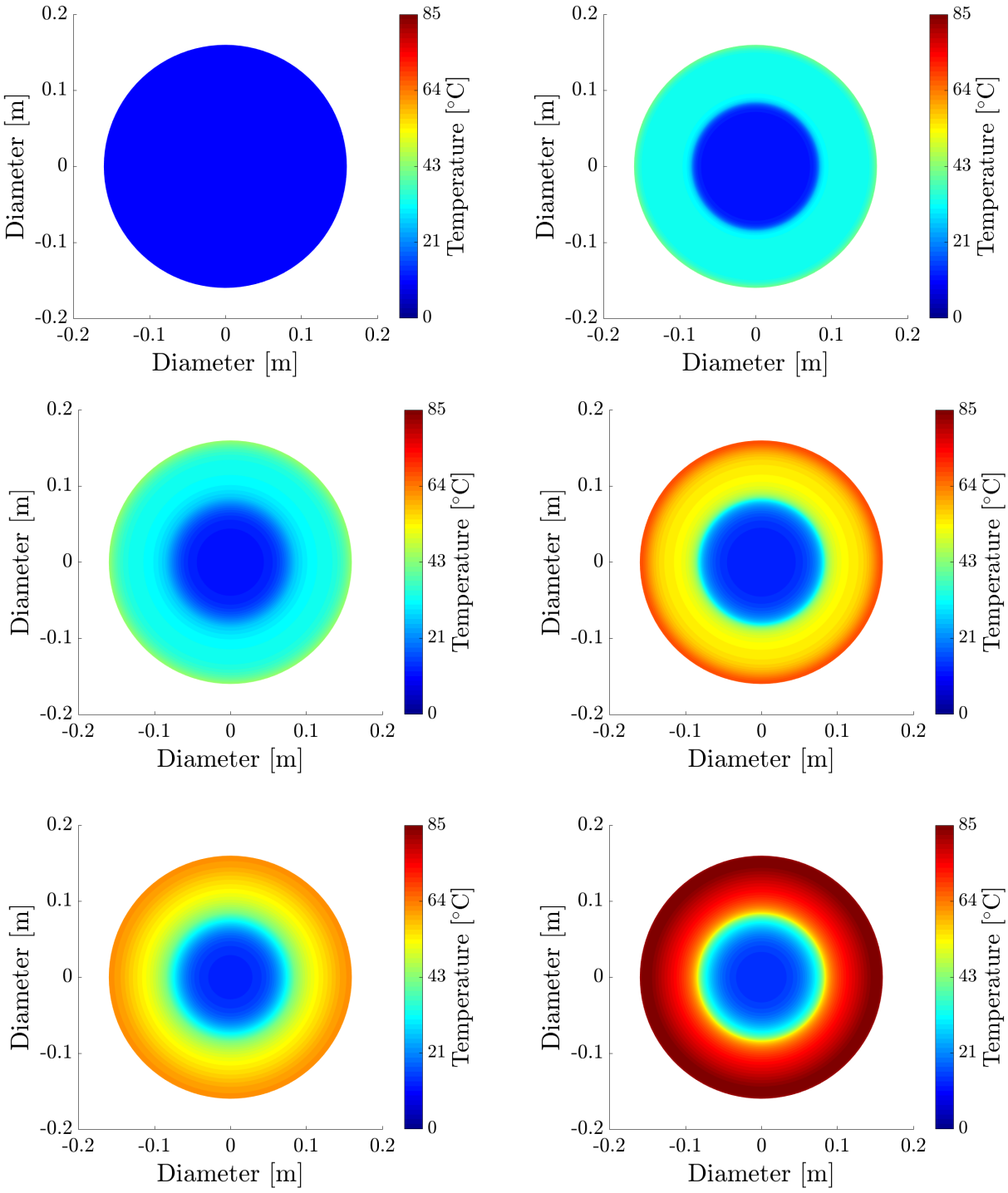

Figure 7.27. The predicted temperature distribution within Log 1 at the beginning (*left*) and the end (*right*) of each excitation. The top, middle, and bottom figures are the results from the 1st, 2nd, and 3rd excitation, respectively.

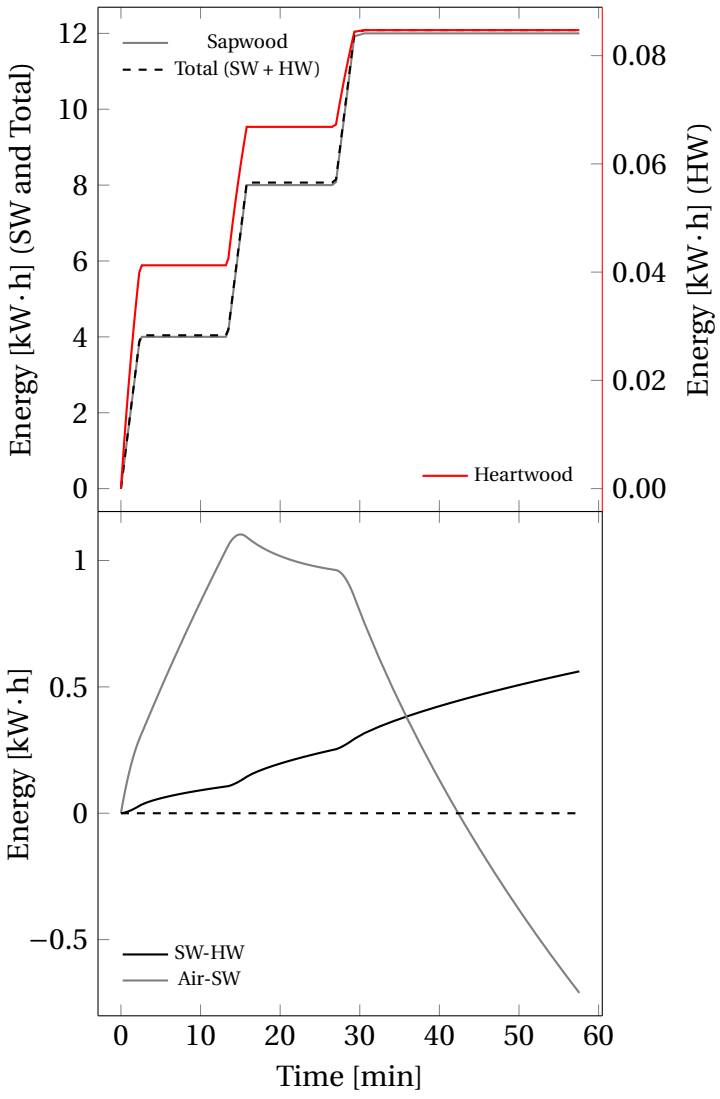

Figure 7.28. The amount of energy generated within Log 1 due to the Joule heating effect (*top*), within the heartwood and the sapwood . The heat diffusion (*bottom*) between the surrounding air and the sapwood, Air-SW, and heat conduction from the sapwood to the heartwood, SW-HW.

in the heartwood by the Joule heating effect. While the log's external temperature was lower than that inside the chamber, the log's sapwood absorbed about 1 kW·h (36×10^5 J) of heat from the air. However, during the second excitation, the surface temperature of the log rose above 60°C and hence the log started losing heat. Most of the heat was released after the last excitation, when the temperature of the log was the highest. If the chamber was well insulated the heat loss from the log would increase the temperature inside the chamber; however, the chamber's temperature remained around 60°C during the treatments. Overall, the heat released to the environment was 0.5-1.5 kW·h higher than the heat gained by the logs at the beginning of the treatment, when the log surface temperature was below 60°C. Therefore, if the efficiency of the chamber's thermal insulation was sufficiently high, heating the air inside the chamber would be unnecessary after an initial pre-heating period. Finally, the sapwood conducted approximately 0.5 kW·h to the heartwood over 60 minutes of treatment. This amount of heat would continue to rise until the temperature at the interface between the sapwood and the heartwood was equal to the heartwood's internal temperature. Logs 2-5 showed similar results, shown in Appendix E.12.

7.4 Conclusions

The developed CFD models can be used prior to the treatment, to estimate the amount of energy required to reach a phytosanitary condition for a green *P. radiata* log and to predict the log's average temperature and its total resistance. The latter can be measured experimentally and be used as a feedback parameter during the operation. Comparison of the total experimental and predicted resistances can provide information about the log's average temperature, without drilling holes in the log, and indicate potential faults during operation such as a poor contact between the log and the electrodes.

The 1D and 3D models show comparable results, but the relatively short calculation time of the 1D model makes it more suitable for industrial applications. None of the developed models, however, can be used to simulate local hot and cold spot formation, caused by knots or other heterogeneous features. Such modelling will require building the exact geometry of a treated log, which is impractical and unnecessary for an industrial operation, where the simulations must be done in a 'relatively' short time prior to the treatment. The model needs to be further validated, as the variation of wood properties within a single species requires the performance of a larger number of experiments.

Chapter 8

Knot Heating

8.1 Introduction

The Joule heating effect results in hot and cold spot formation within green *P. radiata's* sapwood. This phenomenon was initially reported, for other species, by Fleischer and Downs (1953). However, they have not explicitly studied non-uniform heating and hence they have not identified the causes of cold and hot spot formation. Perré (2004) modelled Joule heating of green logs but did not include heterogeneous features such as knots in his model. The same approach was used in the CFD models developed in this research (Chapter 7). These models provided relatively fast and accurate simulations of Joule heating of green *P. radiata* logs. In particular, the predicted total electrical resistance and the average temperature showed good agreement with the experimental data. However, the developed CFD models cannot simulate formation of local hot and cold spots. Hence there will always be a difference between the predicted and non-averaged experimental values. Although it is unnecessary to build an exact CFD model to control the Joule heating process, the local non-uniform heating behaviour must be studied to identify potential locations and magnitudes of cold and hot spots.

The experimental part of this research showed that temperature measured inside a knot in Log 5 is lower than that recorded at knot-free regions (Chapter 7). However, as temperature was measured predominantly at knot-free regions, it was unclear whether that relatively low temperature observed at the knot was a single case or a common behaviour. Hence, this phenomenon must be further studied using experimental and/or computational approaches. A thorough experimental and computational study would extend duration of this research beyond the normal time-frame of a typical PhD programme. Hence, it was decided to create a simplified 3D knot-heating model that can be used as a reference in the future research. This chapter will describe the method of building the 3D knot-heating model and will cover the employed verification procedure. No validation has been done for the knot-heating model and hence it

will require to be validated in the future research.

8.2 Methods

8.2.1 Geometry

Assumed Condition

In the knot-heating model, it was assumed that a 3-m-long green *P. radiata* log was treated using the Joule heating effect. The log and its heartwood section had a cylindrical shape, with the diameters of 380 and 200 mm, respectively (Figure 8.1). The centre of the log aligned with

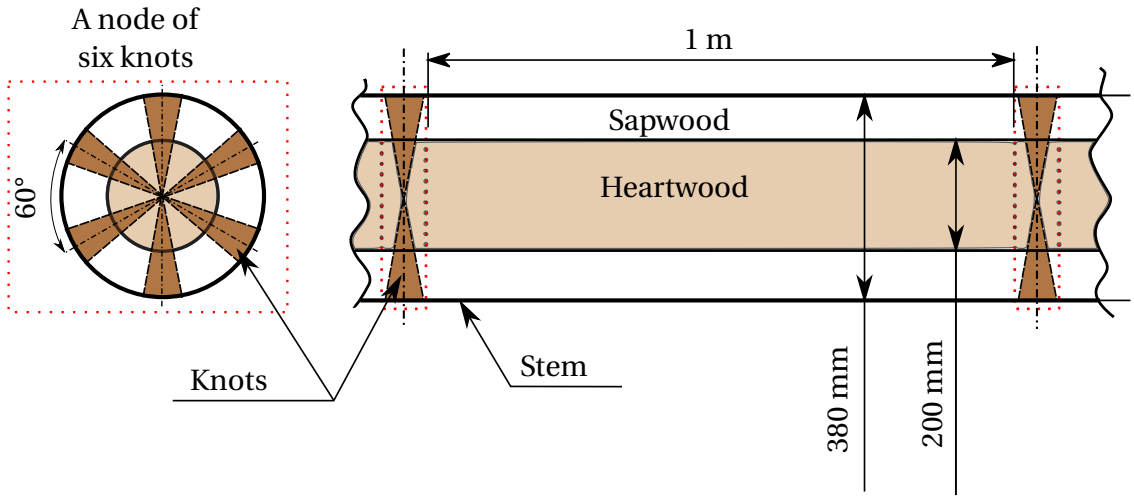

Figure 8.1. The schematic diagram of modelled internode length.

the heartwood's centre. The log was cut from a tree with the constant internode length of 1 m. A node consisted of six knots. All knots within a node lay on the same circumference and were the same distance apart; hence, the azimuthal angle was assumed to be 60°. All knots were perpendicular to the stem - that means branches on the tree grew horizontally. All six knots within a node aligned with the other six knots in the neighbouring node. The shape of each knot was assumed to be a perfect cone, with a base diameter of 70 mm. Knots did not affect the log's grain orientation and hence there was no sloping grain around the them. Generally, heartwood develops inside a branch, in a similar fashion as it develops in a stem (Figure 2.7). However, to simplify the computational model, it was assumed that the knots' part, located within the log's sapwood, did not develop heartwood. Furthermore, it was assumed that, prior to the treatment, the whole log was at a uniform temperature of 10°C. The total electrical power dissipated in the 3 m long log was 100 kW.

CFD Geometry

Repeatability of the nodes and the symmetrical position of the knots in a node allowed a simple geometry to be defined, as shown in Figure 8.2a. The geometry consisted of four domains: the

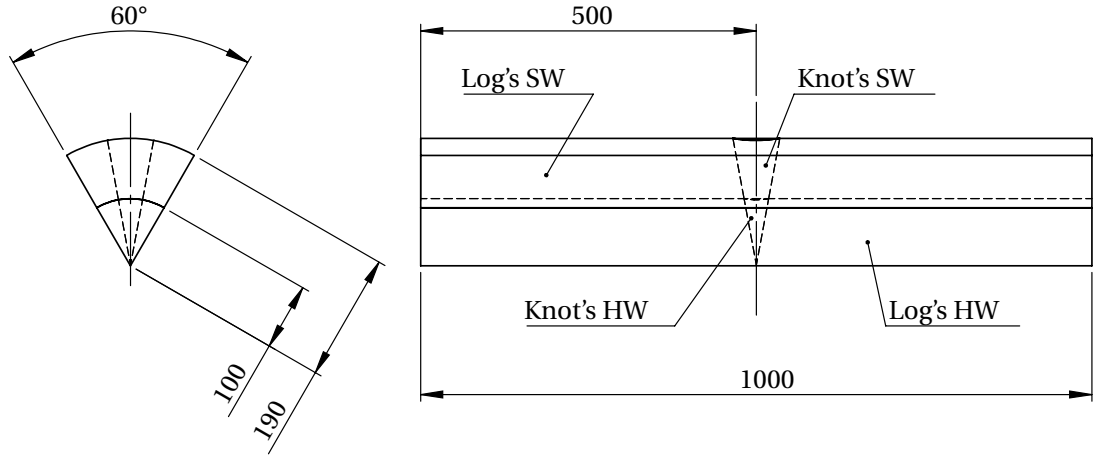

(a)

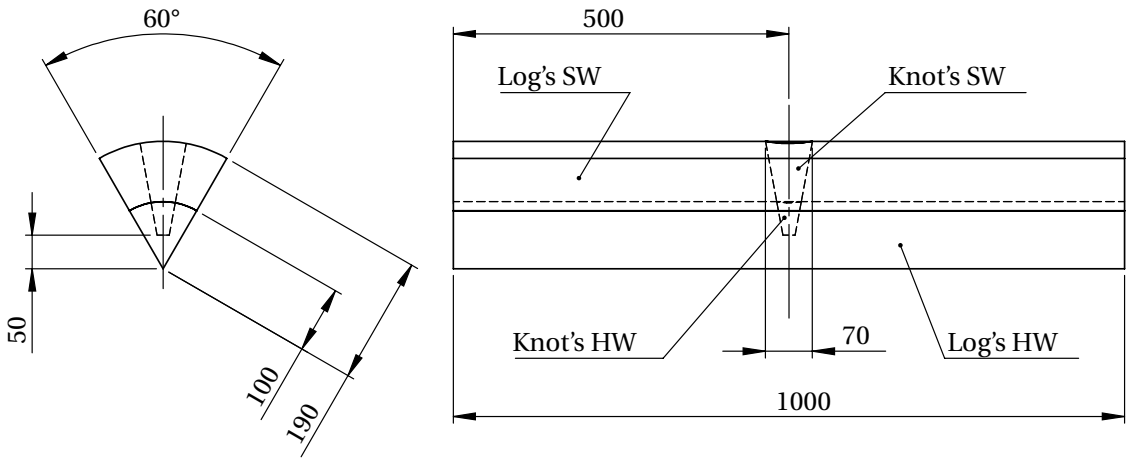

(b)

Figure 8.2. The simplified geometry of the knot-heating model: (a) the initial geometry and (b) the final geometry used in the model. *Note:* All dimensions are in millimetres. SW and HW denote sapwood and heartwood, respectively

log's sapwood, the knot's sapwood, the log's heartwood, and the knot's heartwood. Each domain had uniform thermal and electrical properties. Such geometry allowed a significant reduction in computation time by decreasing the total number of mesh elements. However, the geometry had a problem - the knot's tip was sharp and affected the meshing process, resulting in a poor quality of mesh elements near the tip, consequently affecting the calculation. Hence, it was decided to truncate the conical knot by cutting 50 mm from the tip (Figure 8.2b). It was believed that the truncation would not affect the simulation, as the vast majority of the electric current would flow through the sapwood. In addition, due to complexity of this geometry and associated

difficulties with meshing, this geometry was used to model a verification case of constant power generation, similar to *Case 1* described in Section 6.2. This verification model with an available analytical solution was used to verify the meshing method and to ensure that the computational calculation was error free.

8.2.2 Computational Model

To model this 3D problem, a commercial CFD program, ANSYS CFX (version 17.0), was used. The governing equations of heat conservation and of electrical charge conservation were discretised using the second-order backward Euler scheme. In this model, the convergence criterion was the root mean square of residuals set to 10^{-6}. The convergence criterion for most of time steps was achieved within 20 iterations, using double precision floating point arithmetic. The 3D geometry was built using the ANSYS Design Modeller software and was meshed employing the ANSYS meshing tool. The simulations were performed using local parallel computing on four cores of an Intel Core i7-3770 @ 3.40 GHz, with 16 GB RAM.

8.2.3 Mathematical Formulation

Constant Power Generation Model

a) Governing Equations

In the constant power generation model, it was assumed that a body of the same geometry as in Figure 8.2b was heated by the Joule heating effect. The whole assembly was fully insulated and had uniform thermal and electrical properties (Table 8.1). Under these conditions, the heat

Table 8.1. The parameters assumed in the power generation model

Parameter	Value
Heat Capacity (C_p) [$\mathrm{J \cdot kg^{-1} \cdot °C^{-1}}$]	3052
Electrical Conductivity (σ) [$\mathrm{S \cdot m^{-1}}$]	0.001
Density (ρ) [$\mathrm{kg \cdot m^{-3}}$]	1125
Electrical Power (P) [kW]	100
Heating Duration (Δt) [s]	100

generated inside this geometry was uniform, without heat losses to the ambient. Mathematically, this model was expressed as:

$$\frac{\partial \rho C_p T}{\partial t} = \bar{S}, \tag{8.1}$$

where the heat source ($\bar{S}$) was calculated as:

$$\bar{S} = \boldsymbol{J}_e \cdot \boldsymbol{E}. \tag{8.2}$$

To determine electric field ($\boldsymbol{E}$) and current density ($\boldsymbol{J}_e$) distribution in the body, the model solved the conservation equation of electric charge, written as:

$$\nabla \cdot (\boldsymbol{J}_e) = 0, \tag{8.3}$$

where the current density ($\boldsymbol{J}_e$) was equal to:

$$\boldsymbol{J}_e = \sigma \boldsymbol{E} = \sigma \frac{U}{l_L}. \tag{8.4}$$

b) Boundary and Initial Conditions

To solve the governing equations, unique boundary and initial conditions had to be applied. Prior to heating, the body was at a uniform initial temperature of 10°C, mathematically expressed as:

$$T_i = 10^{\circ}\text{C}. \tag{8.5}$$

As the whole geometry was insulated, then there were no heat losses to the ambient environment and hence the experimental thermal boundary conditions were as follows:

$$\boldsymbol{J}_h \cdot \hat{\boldsymbol{n}} = 0. \tag{8.6}$$

The interfaces between the adjacent domains were assumed to be ideal, meaning that the heat flux on both sides of each interface is equal. That was described as:

$$\boldsymbol{J}_{h_i} \cdot \hat{\boldsymbol{n}} = \boldsymbol{J}_{h_{i+1}} \cdot \hat{\boldsymbol{n}} \tag{8.7}$$

where the indices i and $i+1$ denote the first and second of two adjacent domains. The interface

boundary conditions for the electric charge equations were written as:

$$\boldsymbol{J}_{e_i} \cdot \hat{\boldsymbol{n}} = \boldsymbol{J}_{e_{i+1}} \cdot \hat{\boldsymbol{n}}, \tag{8.8}$$

which means the interface resistance was equal to zero. One of the geometry's faces was grounded (Figure 8.3):

$$U = 0 \text{ V}, \tag{8.9}$$

and the opposite face, as shown in Figure 8.3, was at high voltage, determined as follows:

$$U = \sqrt{PR}, \tag{8.10}$$

where R is the total resistance of the whole body, calculated as:

$$R = \frac{l_s}{\sigma A}, \tag{8.11}$$

where l_s the length of the log segment, equal to 1 m. The cross-sectional area (A) of the body is equal to:

$$A = \frac{\pi r_L^2}{6}, \tag{8.12}$$

where r_L is the radius of the log, equal to 190 mm.

c) Analytical Solution

In addition, Equation 8.1 was solved analytically as:

$$T_f = T_i + \frac{\bar{S}\Delta t}{\rho C_p}. \tag{8.13}$$

The heat source ($\bar{S}$) was calculated alternatively as:

$$\bar{S} = \frac{P_s}{V}, \tag{8.14}$$

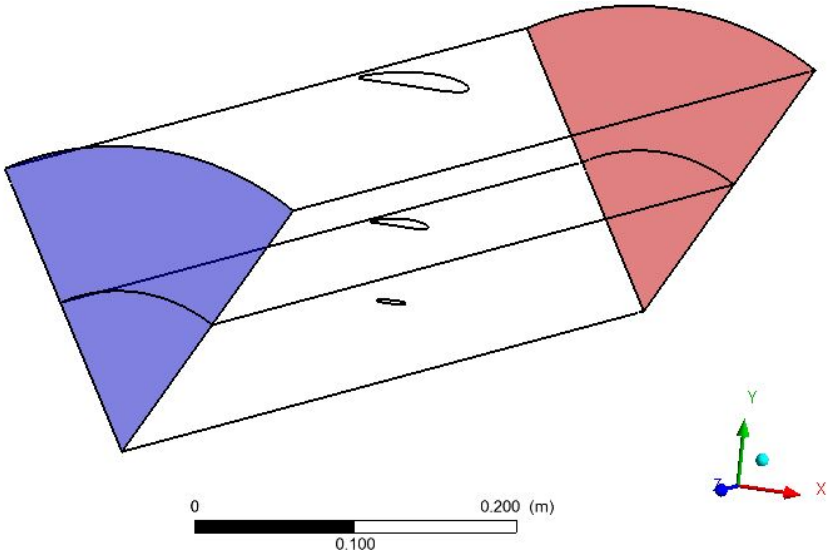

Figure 8.3. The grounded (*blue*) and high-voltage (*red*) boundaries. *Note:* The external colourless faces represent electrically insulated boundaries.

where V is the body's volume, equal to:

$$V = \frac{\pi r_L^2}{6} l_s, \tag{8.15}$$

and where P_s is the electrical power for the log segment, determined as:

$$P_s = \frac{P}{6 l_s}, \tag{8.16}$$

where P is the total electrical power, equal to 100 kW for a 3-m-long log. Hence, solving Equation 8.1, the temperature of the homogeneous body should be approximately 164.1°C after 100 s of Joule heating using about 5.5 kW of electrical power. In addition, the voltage drop across this uniform geometry was estimated by knowing electrical resistance, calculated using Equation 8.11, and electrical power. Comparing the obtained computational and analytical results allowed assessment of the CFD model's computational error.

Knot Heating Model

a) Governing Equations

In the knot-heating model, it was assumed that the internal heat transfer within the log and

the knot was due to conduction, governed by the following equation:

$$\frac{\partial \rho_g C_p T}{\partial t} = \nabla \cdot (k \nabla T) + \bar{S}. \tag{8.17}$$

In addition, to model current density distribution within the assembly and to calculate the heat source term ($\bar{S}$), Equations 8.2 and 8.3 were solved computationally.

b) Boundary and Initial Conditions

As the whole assembly was assumed to be at 10°C, the initial condition was expressed by Equation 8.5. The top face of the log, including the knot's top face, was exposed to the ambient environment. This was described by a convective boundary condition as follows (Figure 8.4):

$$\boldsymbol{J}_h \cdot \hat{\boldsymbol{n}} = h(T_s - T_a), \tag{8.18}$$

where T_a is the chamber temperature of 60°C, and T_s is the surface temperature of the log. The heat transfer coefficient (h) was equal to 25 $\mathrm{W \cdot m^{-2} \cdot {}^{\circ}C^{-1}}$. As the external face was in contact with air, there was no current flow across it. Hence, the current density was equal to zero:

$$\boldsymbol{J}_e \cdot \hat{\boldsymbol{n}} = 0. \tag{8.19}$$

The symmetry planes assumed that the solution on both sides of the plane was symmetrical. Therefore, the flux across the symmetry plane was equal to zero and the boundary conditions were described by Equations 8.6 and 8.19. The electrical boundary conditions at the high-voltage and ground sides were expressed by Equations 8.10 and 8.9, respectively. The contact surfaces were thermally insulated and hence heat flux across the contact surface was equal to zero, described by Equation 8.6.

c) Other Parameters in Knot Heating Model

The total energy required by the log segment was calculated using Equation 7.23, written as:

$$Q = m_{SW} C_{pSW} \left(T_f - T_i\right), \tag{8.20}$$

where m_{SW} is the total green mass of the log segment's sapwood; and T_f and T_i are the initial

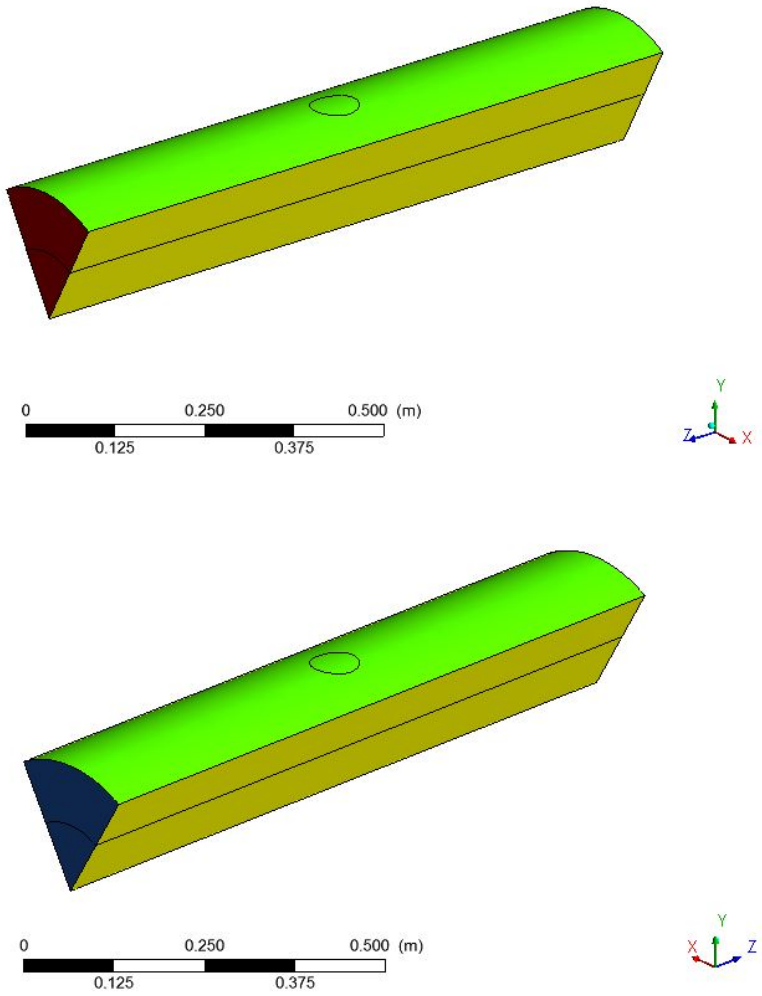

Figure 8.4. The boundary conditions in the knot-heating model, shown from different ends of the log. The red and blue faces denote the thermally insulated high-voltage and low-voltage sides, respectively. The yellow faces represent symmetry planes, while the green (top) surface is the convective boundary. The black lines are the contours of the domains.

and final temperature of the same part, equal to 75°C and 10°C, respectively. The mass of the sapwood was calculated using the following equation:

$$m_{SW} = \rho_{sSW}(1 + X_{SW})V_{SW}. \tag{8.21}$$

The sapwood's basic density (ρ_{sSW}) and moisture content (X_{SW}) were assumed to be 450 kg$\cdot$m^{-3} and 1.5, respectively (Pang et al., 1995). On the other hand, the heartwood's basic density and moisture content were 400 kg$\cdot$m^{-3} and 0.45, respectively (Pang et al., 1995). The sapwood's

volume (V_{SW}) was estimated as:

$$V_{SW} = V_L - V_{HW} = \frac{\pi}{6}\left(r_L^2 - r_{HW}^2\right) l_s. \tag{8.22}$$

Heat capacity (C_p) and thermal conductivity (k) of the sapwood and the heartwood were calculated using the following equations (Pang et al., 1995):

$$C_p = 4184\frac{X + 0.324}{1 + X}, \tag{8.23}$$

and

$$k = \frac{\rho_s}{1000}(0.4 + 0.5X) + 0.024. \tag{8.24}$$

The total energy was divided into three excitations and the duration of each excitation was calculated as:

$$t_e = \frac{Q}{3P_s} \tag{8.25}$$

The model simulated the whole treatment, including three excitations, two relaxation periods of 10 minutes and the final equilibration period of 30 minutes, in a single run.

d) Electrical Conductivity in Knot Heating Model

Being attached to the log's ends, the electrodes caused current flow through the log between the high-voltage end and the low-voltage end. Therefore, the main electrically conductive path aligned with the log's longitudinal direction (Figure 8.5). However, the knot's longitudinal

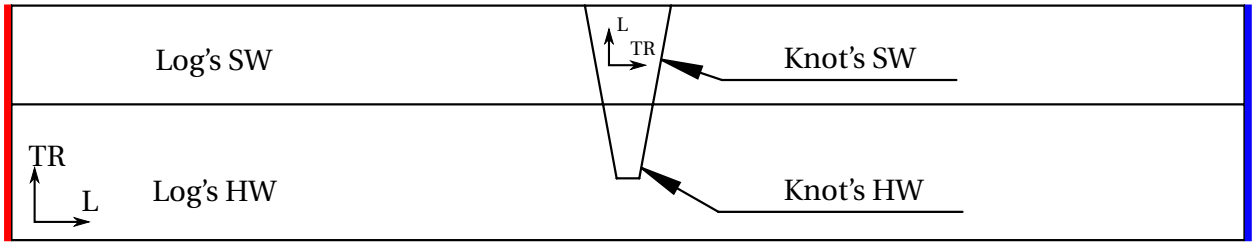

Figure 8.5. The schematic diagram of grain orientation in the knot and the surrounding wood. The L and TR denote the longitudinal and transverse directions. *Note:* The electric current flowed along the log's longitudinal direction from the high-voltage (red) to low-voltage face (blue).

direction lay perpendicularly to the current flow and did not contribute to the current conduction. On the other hand, the log's longitudinal direction aligned with the knot's transverse directions, i.e. radial and/or tangential directions. However, assuming that electrical conductivity of knots (branches) was similar to that of logs, the knot's transverse electrical conductivity had to be about 10 times lower than the log's longitudinal conductivity. Therefore, the electric current had to flow predominantly through the log's sapwood and diverge around the knot. Near the knot, the electric current had to flow through the transverse directions of the log's sapwood. Thus, anisotropic electrical conductivity of the log's sapwood had to be considered and was expressed by the following equations (Nursultanov et al., 2017):

$$\sigma_L = \exp\left[-2.60 + 0.017(T-55) - 0.073\frac{(T-55)^2}{1000}\right], \tag{8.26}$$

$$\sigma_R = \exp\left[-4.81 + 0.021(T-55) - 0.046\frac{(T-55)^2}{1000}\right], \tag{8.27}$$

$$\sigma_T = \exp\left[-5.37 + 0.026(T-55) - 0.046\frac{(T-55)^2}{1000}\right]. \tag{8.28}$$

To use these equations in the ANSYS CFX model, two additional blocks of code, described in Appendix D.3, were used. As there is no electric field to drive current in the knot's longitudinal direction and the radial and tangential electrical conductivities of green *P. radiata* sapwood are comparable, the knot's sapwood electrical conductivity could be considered isotropic and be described either by the radial (Eq. 8.27) or tangential (Eq. 8.28) electrical conductivity equation. In this model, the electrical conductivity of the knot's sapwood was expressed by Equation 8.27 of green *P. radiata* sapwood's radial electrical conductivity. The electrical conductivity of the knot's and log's heartwood was 0.001 $\mathrm{S \cdot m^{-1}}$.

8.2.4 Mesh and Time-Step Independence

The mesh and time-step independence study was performed using the method described in Section 4.2.2. In the constant power generation case, the temperature rise within the geometry had to be constant and uniform, as the body was assumed to be homogeneous. However, the preliminary simulation showed a local temperature variation within the body (Figure 8.6). Using

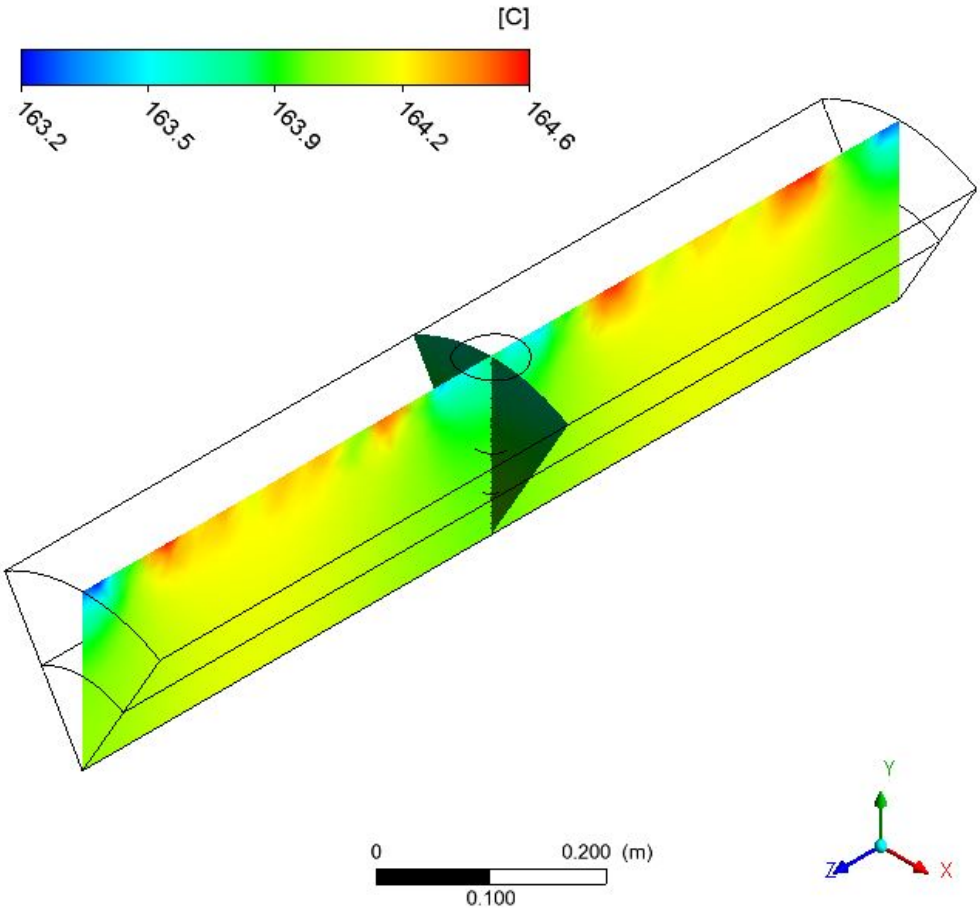

Figure 8.6. Local temperature distribution within the uniform geometry caused by the unstructured mesh, at t = 100 s.

the lowest mesh and time-step resolution, the temperature varied from 163.2°C to 164.6°C, with the volume average temperature of about 164.1°C. That was a variation of less than 1% of the volume average temperature and was an artefact of using the unstructured mesh. Although the variation was small, to minimise this behaviour, the maximum computational error was calculated based on the volume averaged temperature.

In the knot heating problem, the results obtained with the highest mesh and time-step resolution were compared with those determined using lower resolutions. For this comparison, temperature values at three points in the assembly were selected (Figure 8.7). Computational error was calculated for each of these temperature points following the method described in Section 4.2.2.

Mesh

The geometry had several complex regions such as the area around the knot and the sharp edge representing the pith. In order to mesh this geometry using the structural meshing technique,

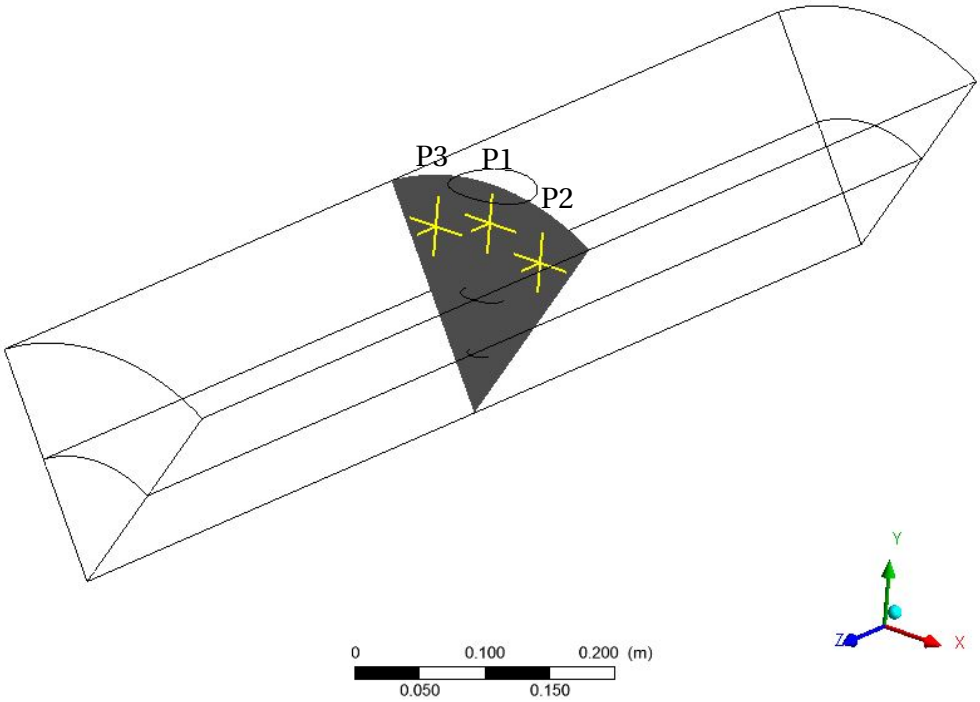

Figure 8.7. Positions (P1, P2, and P3) within the log segment geometry used to determine temperature values for the mesh and time-step independence study.

described in Section 6.2.3, the whole assembly should have been divided into many “sweepable" blocks. Building a multi-block structure is a complicated process which requires numerous attempts. Therefore, to reduce time spent on meshing, the mesh (Figure 8.8a) was built using an unstructured meshing method. Being automatic, this meshing method allowed quick building of the unstructured mesh without manually splitting the geometry into blocks. Versteeg and Malalasekera (2007) described advantages of unstructured meshing and the associated discretization methods. However, unstructured meshing has poorer control of the mesh resolution than the structural meshing method. In addition, to ensure accurate discretization of the governing equations at the interfaces, the mesh had to be conformal. This means that each mesh element at one side of an interface shares two of its vertices with the adjacent element on the opposite side, as depicted in Figures 8.8b-d. In the mesh independence study, three mesh resolutions were used: a coarse mesh of 8.5×10^4 elements, a medium mesh of 3.1×10^5 elements, and a fine mesh of 6.5×10^5 elements. These resolutions were used in both the constant power generation and knot-heating models.

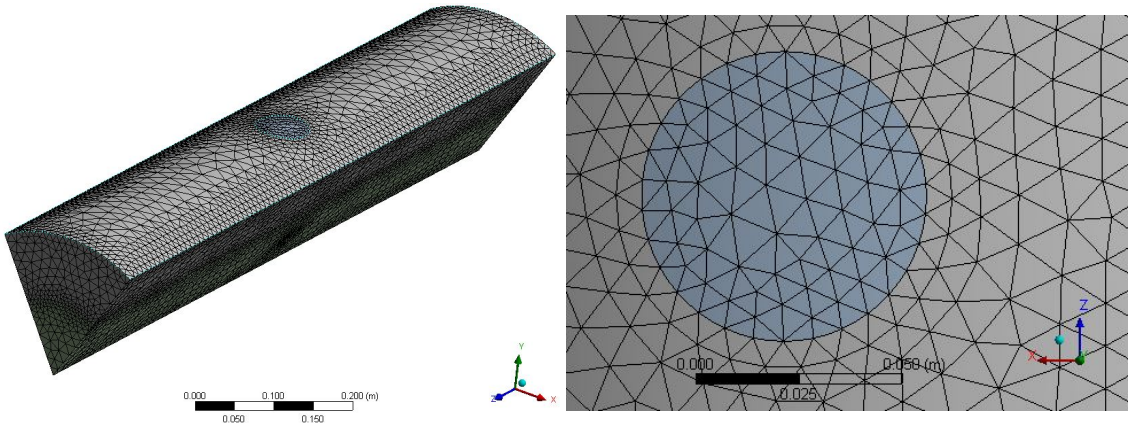

(a) Isometric View

(b) Top View (Knot)

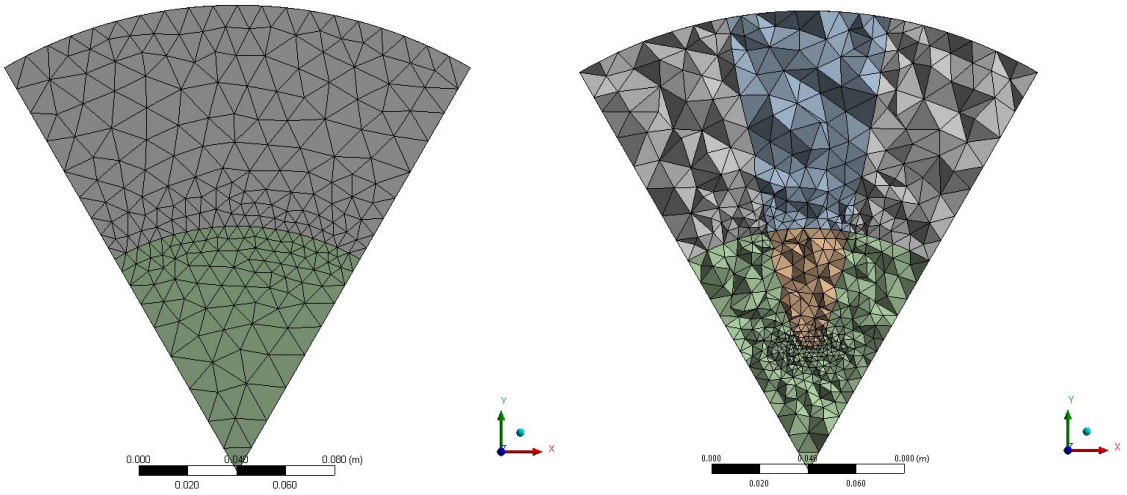

(c) Front View

(d) Middle Cross-Sectional Cut

Figure 8.8. The unstructured mesh used in the constant power generation and knot-heating models.

Time-Steps

Three time-step resolutions of 500, 1000, and 2000 time-steps were used in this study. The constant power generation case modelled a temperature rise within 100 seconds of Joule heating. This simulation had a single modelled period and hence the total number of time-steps were 500, 1000, and 2000 time-steps. However, the knot heating model simulated six modelled periods of the Joule heating treatment: three excitations, two relaxations of 10 minutes each, and 30 minutes of the equilibration period, within a single simulation run. Each of these periods was discretised into 500, 1000, and 2000 time-steps, except the equilibration period of 30 minutes. Being three times longer than the relaxation periods, the 30 min cooling period was discretised into 1500, 3000, and 6000 time-steps. A small time-step in the equilibration period helped with convergence of the computational solution during the transition from the third excitation to the

equilibration period. Therefore, the total numbers of time-steps in the knot-heating model were 4000, 8000, and 16,000.

8.3 Results and Discussion

8.3.1 Results of Mesh and Time-Step Independence Study

Constant Power Generation Case

There was no significant effect of mesh and time-step resolutions on the maximum computational error (Figure 8.9a and b). The error was much lower than 1% using the lowest resolution -

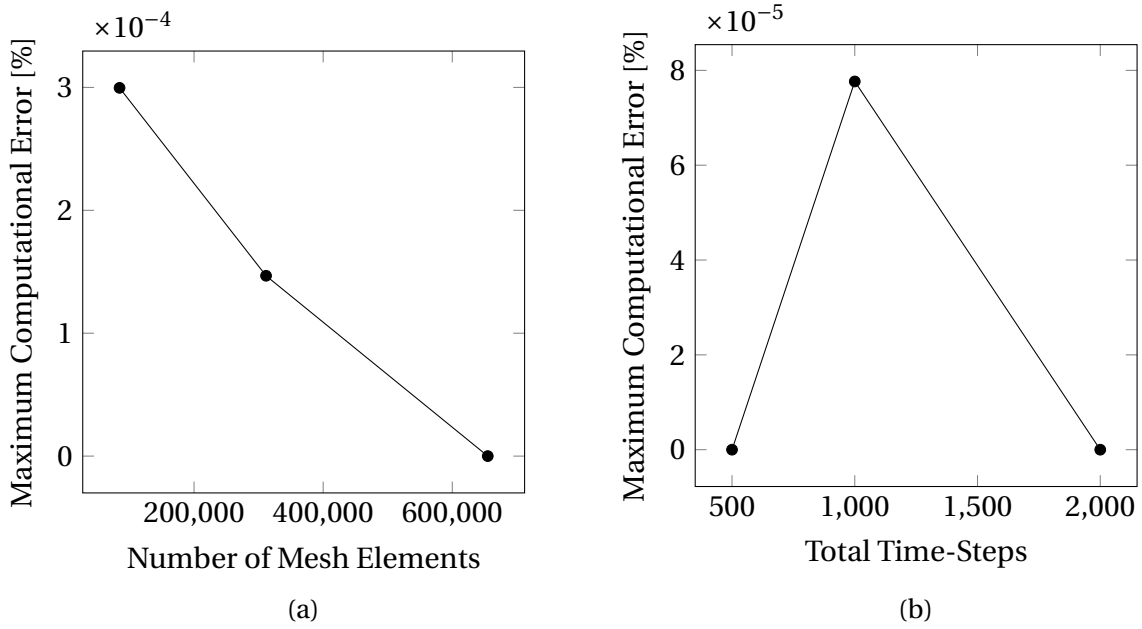

Figure 8.9. The effect of (a) mesh and (b) time-step resolutions on the computational error in the constant power generation model.

8.5×10^4 mesh elements and 500 time-steps. Providing a relatively accurate result, this resolution ensured the shortest calculation time and hence it was optimal to generate a final result.

Knot Heating Model

In the knot heating model, the mesh and time-step independence study was done based on temperature measured at three points defined in Figure 8.7. Figure 8.10 shows effect of mesh and time-step resolutions on the maximum computational error. The effect of time-step resolution was insignificant, with the maximum computational error being below 1% (Figure 8.10b). However, increasing the mesh resolution from coarse to medium reduced the computational error from about 8% to about 1% of the temperature measured at P1 (Figure 8.10a). The effect of mesh resolution on the error of temperature measured at P2 and P3 was less

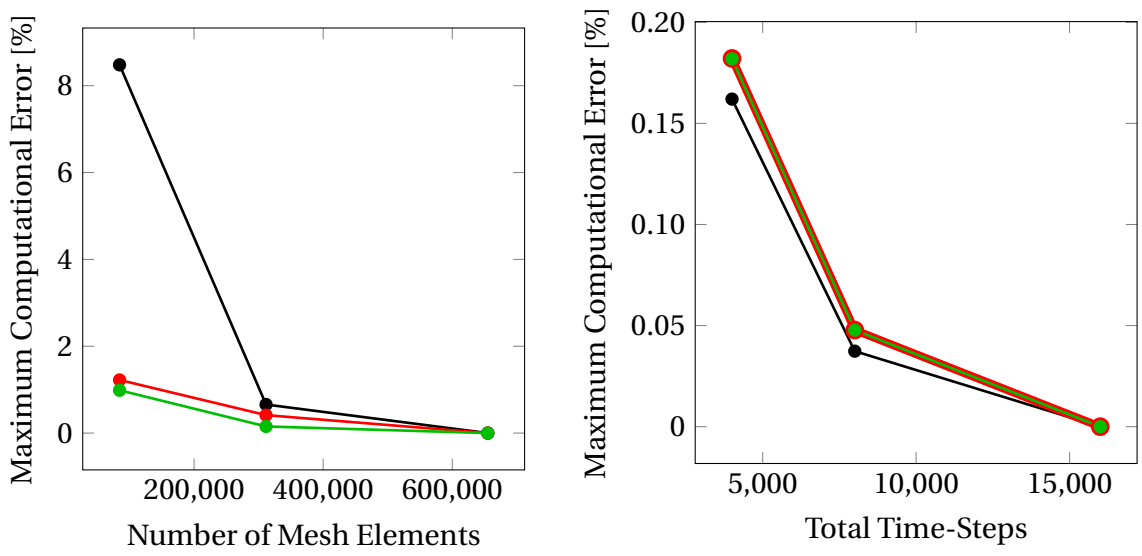

Figure 8.10. The effect of (a) mesh and the (b) time-step resolutions on the maximum computational error at P1 (black), P2 (red), and P3 (green) in the knot-heating model.

pronounced. According to the mesh and time-step independence, the optimal mesh and time-step resolution for the knot-heating model was 3.1×10^5 mesh elements and 4000 total time-steps.

8.3.2 Verification: Constant Power Generation

Besides slightly non-uniform temperature distribution caused by the unstructured mesh (Figure 8.6), there were no global temperature gradients within the geometry, as depicted in Figure 8.11a. That confirmed that the insulated boundary conditions were specified correctly. As each part of the geometry had the same electrical conductivity of 0.001 $S \cdot cm^{-1}$, the voltage drop across the body was uniform and hence the electric equipotential lines were equally spaced and parallel to each other (Figure 8.11b). Finally, Figure 8.12 shows the comparison of the analytically and computationally predicted temperatures, where the computational results were in a good agreement with the analytical solution.

8.3.3 Non-uniform Heating: Effect of Knot

Power Dissipation

As the electrical conductivity of the knot was lower than that of the sapwood, most of the electric current had to flow around the knot (Figure 8.13). The distance between equipotential

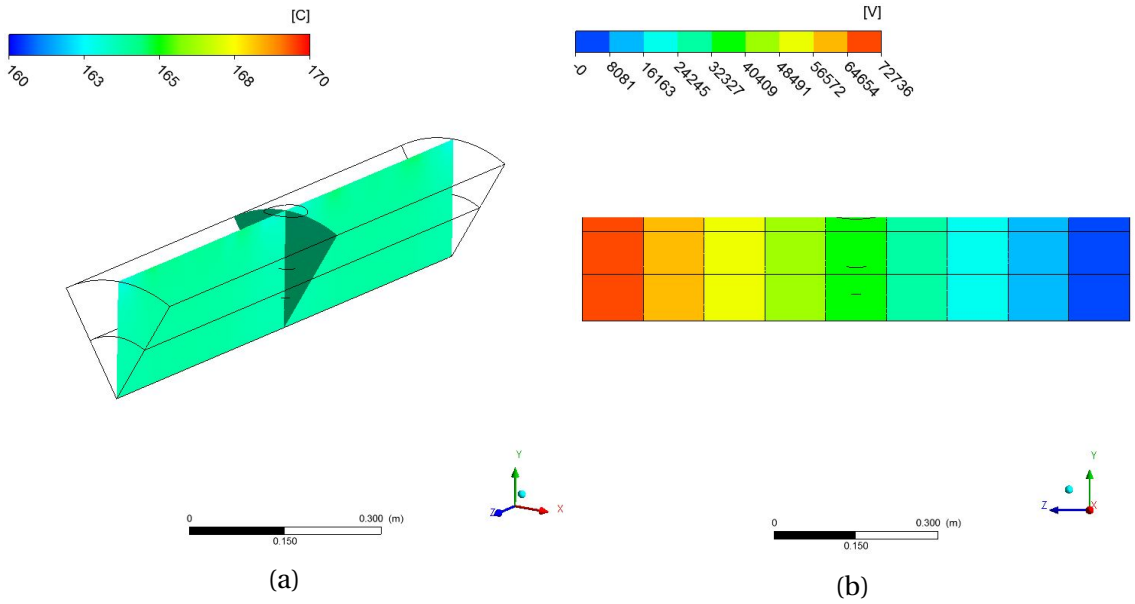

Figure 8.11. The constant power generation case: (a) the global temperature distribution and (b) the equipotential lines across the geometry.

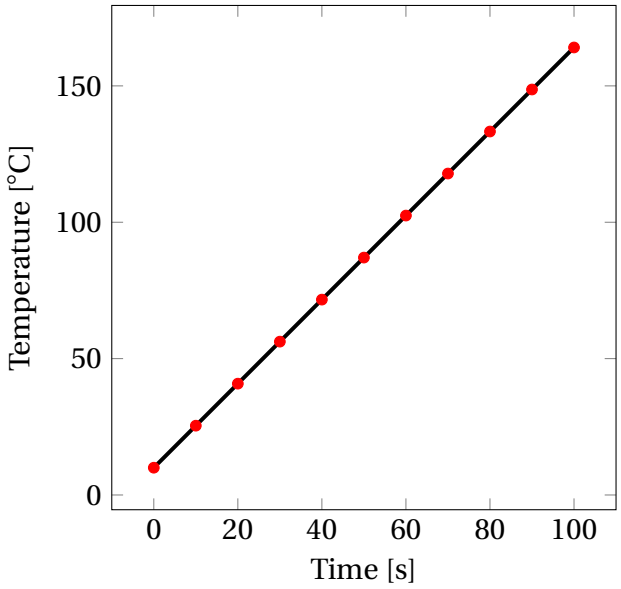

Figure 8.12. The analytically calculated temperature (solid black line) and the computationally estimated volume average temperature (red circles) of the uniform body.

lines decreased across the knot, indicating that a higher electric potential difference developed over this highly resistive region, as shown in Figure 8.14. As a result, the region of the highest power dissipation occurred in the sapwood, particularly at the interface with the knot, as depicted in Figure 8.15a. This region was the hottest spot. The power dissipation within the knot was an order of magnitude lower than that at the hot spot and hence the rate of Joule heating of the knot was lower. In addition, there were two spots with relatively low power dissipation in the sapwood - at the front and behind the knot (Figure 8.15b). The power dissipation at these spots

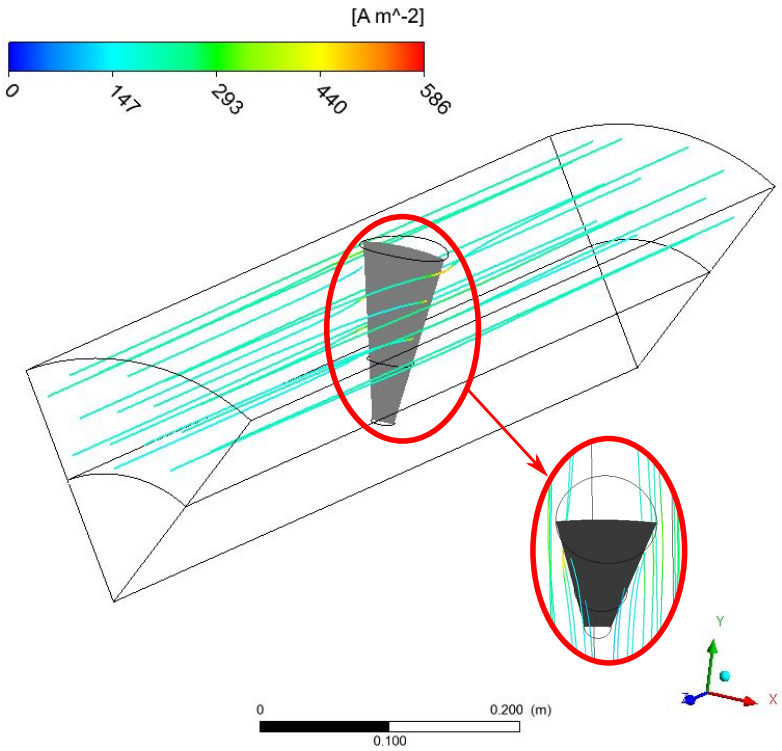

Figure 8.13. The current density streamlines flowing through the log segment at the end of the 3rd excitation. *Note:* The grey plane represents the cross-sectional shape of the knot.

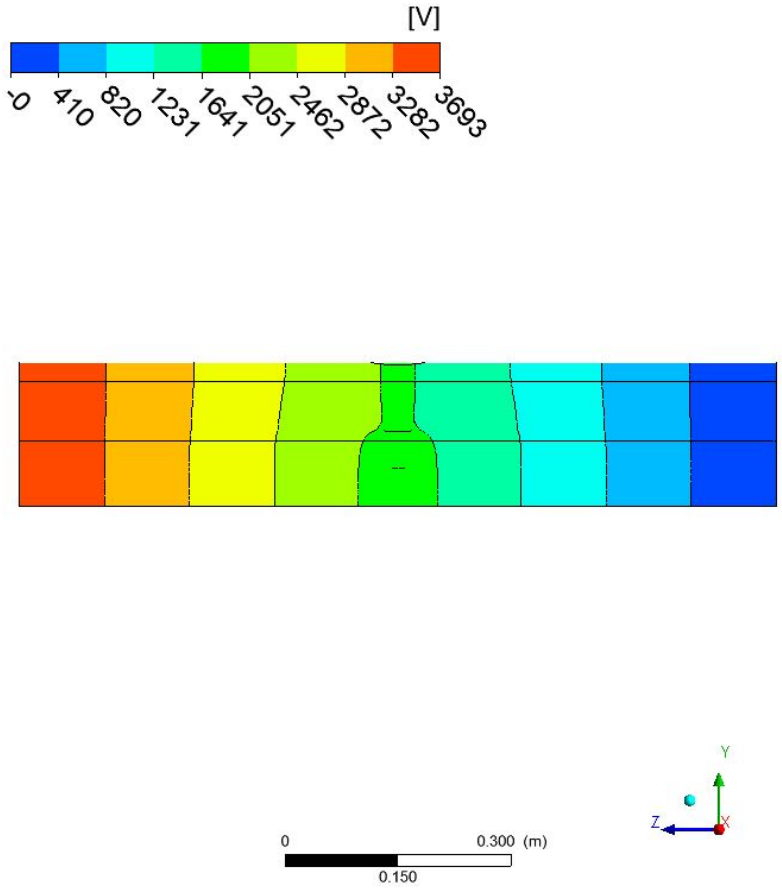

Figure 8.14. The equipotential lines across the whole assembly.

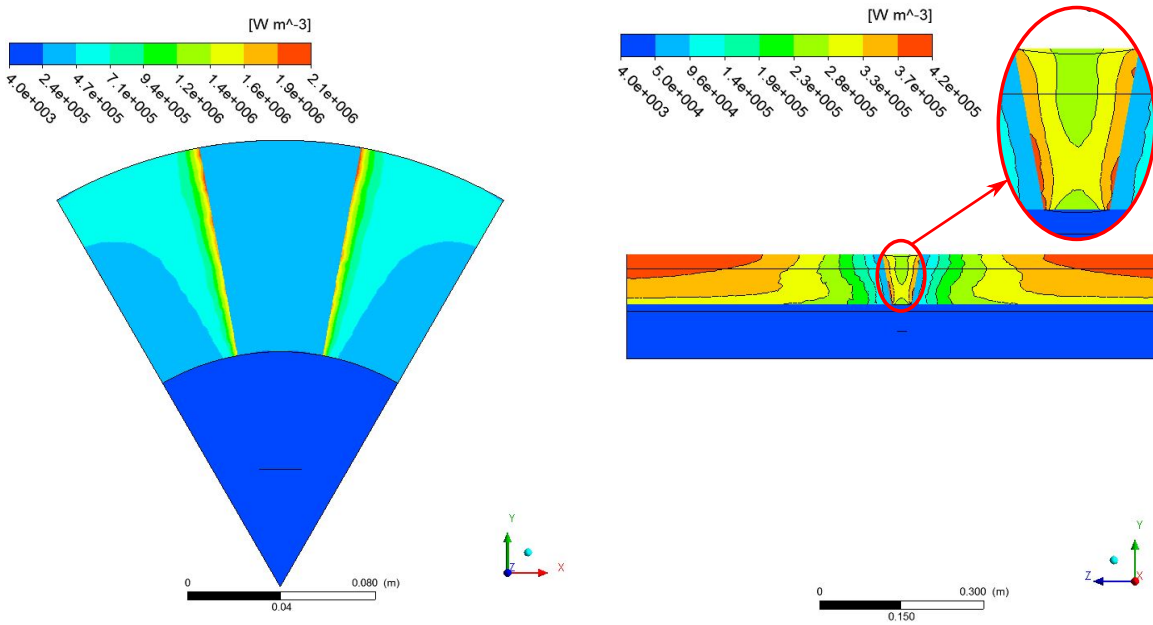

(a) Middle Cross-Sectional Cut

(b) Side

Figure 8.15. The power dissipation within the log and the knot at the end of the 3rd excitation.

was about half that inside the knot. Finally, the region of the lowest power dissipation within the whole assembly was the log's and knot's heartwood parts. They were barely heated by the Joule heating effect.

Temperature

At the end of the last excitation, the volume average temperature of the log's sapwood was about 70°C. The region with the highest dissipated power was heated to about 124°C (Figure 8.16a). The lowest temperature in the log's sapwood was approximately 52°C, located at the front and behind the knot (Figure 8.16b). The volume average temperature of the knot was 77°C, with the minimum and maximum temperatures of 54°C and 117°C, respectively. The temperature of the knot's sapwood varied from 61°C to 84°C. The volume average temperature of the knot's and the log's heartwood regions were approximately 45°C and 33°C, respectively. The volume average temperature of the knot's heartwood was relatively high, because its conical tip was truncated and hence the pith's temperature was not considered. Temperature distribution plots determined at other time points are shown in Appendix F.

Most of the estimated values are similar to those observed in the experiments, described in Chapters 3 and 7. However, the hot spot's predicted temperature was abnormally high. It is believed that such high temperature is impossible to achieve in green *P. radiata* using Joule heating under the considered boundary conditions. Assuming sap is pure water, to reach

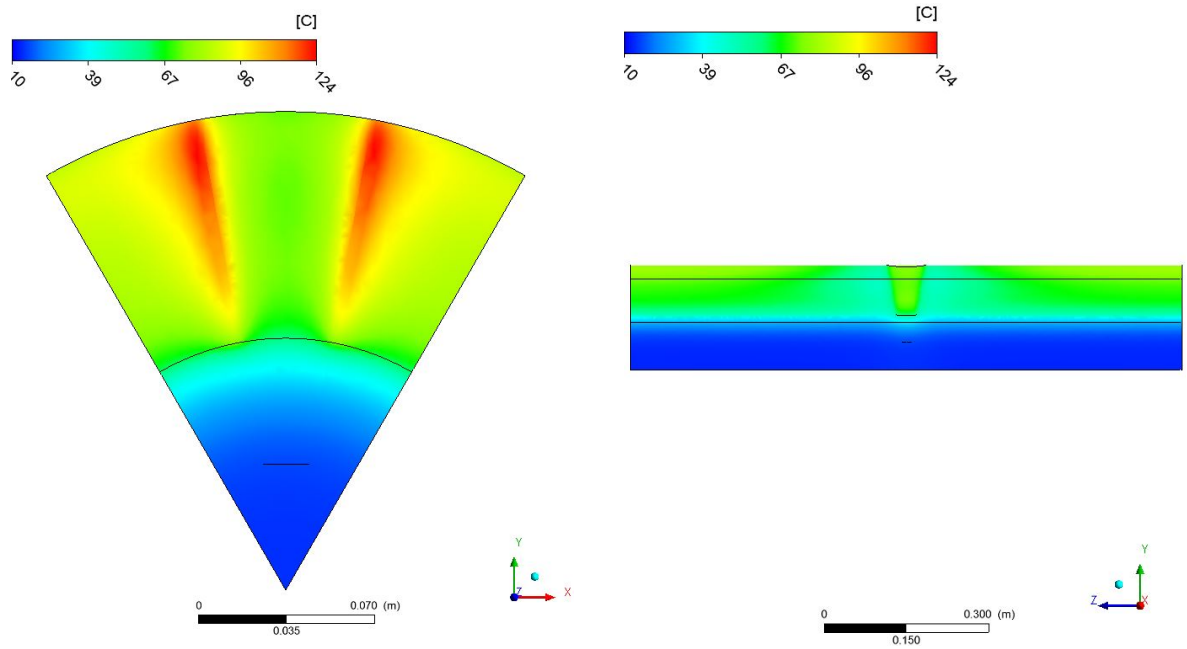

(a) Middle Cross-Sectional Cut

(b) Side

Figure 8.16. The temperature distribution within the log and the knot at the end of the 3rd excitation.

temperature of 124°C, the wood cavities had to be pressurised to about 2.3 bar (Cengel and Boles, 2011). According to Keey et al. (2000), some overpressure is possible in various species, but it is less likely in softwoods with high permeability such as *P. radiata*. Furthermore, above the boiling point of sap, generated vapour does not conduct electric current, making wood substantially less conductive. Therefore, above the boiling point, the Joule heating effect will not exist or will be negligible; the latter will occur, if free water in wood cavities is evaporated, but cell walls remain saturated with bound water, similar to wood at the FSP or heartwood. As sap is a water solution with dissolved minerals and other nutrients, its boiling point could be higher or lower than that of water (100°C at the normal atmospheric pressure). The present model does not take into account the effect of evaporation. However, the model can be modified by setting a temperature limit in the electrical conductivity equations (Eq. 8.26-8.28) using a conditional "if" statement. For example, if the temperature of green sapwood gets above the sap's boiling point (say above 100°C) the electrical conductivity of wood reduces to zero or 0.001 $S \cdot m^{-1}$ - the electrical conductivity of green *P. radiata* sapwood at the FSP.

The obtained results could not be verified with published data. Fleischer and Downs (1953) observed non-uniform heating in green wood, but they did not investigate this behaviour. Perré (2004) did not assume heterogeneity of the sapwood and heartwood regions and hence he did

not model local hot and cold spot formation. Although some non-uniform heating was observed during the board heating experiments, discussed in Chapter 3, the selected boards were knot-free. Thus, in future work, the developed model should be verified and then validated using properly designed experiments. Furthermore, non-uniform heating observed in the Joule heated boards indicated that there are other features, apart from knots, that cause non-uniform heating in green wood. Therefore, other causes of non-uniform heating should be studied in future research, for example using pruned logs. Without knots in the sapwood, these logs can be expected to heat more uniformly by the Joule heating effect, but will still include some heterogeneity.

8.4 Conclusions

The developed model is a tool that can be used to study hot and cold spot formation caused by the Joule heating effect within non-uniform green wood. The model showed that knots are one of the causes of non-uniform electrical heating. Knots cause distortion of electric current and voltage distribution, resulting in non-uniform heating. Hence, the proposed Joule heating phytosanitary treatment cannot guarantee complete mortality of pests in absolutely all logs – there will be some logs that cannot be treated by the Joule heating method. Such limitations cannot be identified by the present model, as it should be further improved, e.g. by taking into account the effect of evaporation and the consequent drop of electrical conductivity. If improved, the model can be used to determine those limitations of the Joule heating phytosanitary treatment such as the maximum allowable number of knots in a log and the maximum allowed size of knots. Future research needs experimental testing to verify and validate the developed model.

Chapter 9

Conclusions, Recommendations and Future Work

9.1 Conclusions

In this thesis, Joule heating of green *P. radiata* was studied systematically using computational and experimental approaches. Initially, the Joule heating effect was studied using three types of *P. radiata* boards: pure sapwood, pure heartwood, and transitional, with co-existing sapwood and heartwood parts. Thereafter, thermal and electrical properties of the log were studied using smaller samples, with a more uniform structure. Using these properties, the CFD model of Joule heating of *P. radiata* logs was developed. The modelled results were compared with experimental data collected in the log heating experiment. The model was used to simulate non-uniform heating caused by knots within the treated log.

The main findings of this research can be summarised as:

- Export size logs can be treated using the Joule heating method, if infested parts of a log are heated up to the temperature of 56°C for the minimum duration of 30 minutes. Depending on wood pest species, the infested log parts can be located close to the log surface or near the log centre. This infestation depth would govern the treatment duration, the number of excitations and relaxations, and the amount of required energy.

- The developed log heating 1D and 3D CFD models can be used to determine the amount of required energy, and to predict the log's internal temperature profile and the log's total electrical resistance. These CFD models allow the number of excitations and relaxations to be altered, to determine the shortest and most efficient treatment method. The model shows a good agreement with the average experimental temperature and the total resistance of

the log, with the average error in predicted resistance of approximately 10%. However, the model cannot be used to determine local variation of temperature and resistance, caused by different heterogeneous features such as knots.

- The developed heating procedure of three excitations with 10 minute relaxations ensures that at least the outer 32 mm annulus of the log reaches required phytosanitary conditions. The whole process should be carried out inside a chamber, to reduce heat losses from the log and to ensure that the log surface remains at the phytosanitary conditions.

- For input power limited to 500 W with electric field limited to 5000 $\mathrm{V \cdot m^{-1}}$, the Joule heating rate of pure sapwood boards of *P. radiata* was about 11 times higher than that of pure heartwood boards. Thus, if a sample contains sapwood and heartwood parts, as are present in export-size logs, the latter will not be heated electrically, as most of the electric current will flow through the sapwood. In other wood species with conductive heartwood and transitional zones such as *S. sempervirens*, Joule heating will occur within a whole treated log. However, the Joule heating rate of these zones will vary proportionally to their electrical conductivity, based on the following equation:

$$P = \frac{U^2}{R} = \frac{U^2 A}{\rho_{\mathrm{el}} l} = \frac{U^2 \sigma A}{l}.$$

- Within a 100-200% moisture content range, electrical conductivity of green *P. radiata* sapwood significantly depends on temperature and grain directions, and is independent of moisture content and basic density. The longitudinal conductivity is about one order of magnitude higher than the radial and tangential conductivities. The effect of temperature on electrical conductivity is near linear in the longitudinal direction and is non-linear in the other directions. The developed statistical model links electrical conductivity with temperature and grain orientation and hence can be used to accurately simulate the Joule heating process in *P. radiata* samples of different shape. However, this model is limited to the moisture content range of 100-200%.

9.2 Recommendations and Future Work

Based on the knowledge and experience obtained during this research, the following recommendations for future work can be made:

- The aim of this research was to determine technical feasibility of the Joule heating treatment for phytosanitary measures. However, an economic feasibility of the Joule heating method and a design of a commercial full-scale operating plant lie beyond the scope of this thesis; preliminary work, yet to be publicly reported, has been carried out and further research is recommended.

- The main challenge in Joule heating of green wood is to ensure uniform heating, avoiding significant temperature difference between hot and cold spots. According to the knot heating model, knots create distortion of electric current flow and cause cold and hot spot formation. Hence, there will be some logs that cannot be treated by the proposed Joule heating method. Limits such as the maximum allowable number of knots and/or the maximum allowed knot size will define applicability of the Joule heating method to treat each export log. To determine such limitations in future research, an experiment with many different types of logs should be done, including logs with an extremely high number of knots and without knots. This experimental work must be supported by a verified and validated knot heating model.

- In the knot-heating simulation, the hot spot temperature was unrealistically high. This was explained by not including an evaporation effect and hence allowing sap to be electrically conductive at unrealistically high temperatures. However, in real world conditions, vapour is not electrically conductive. Therefore, incorporating this effect in the model will allow electrical conductivity to drop to zero, or a near zero value, whenever the hot spot temperature exceeds the sap's boiling point. This modification of the knot-heating model is suggested for future work.

- Although the CFD models showed a relatively good agreement with the experimental data, the models should be further validated using a larger number of logs. This can be possible if a pilot-scale log treatment plant with continuous operation is available. Thus, further

validation of the 1D model and developing such a pilot-scale plant are proposed for future work.

- The predicted total initial resistance of treated logs was noticeably lower than the experimental initial resistance. Although this difference decreased to about 10% shortly after the beginning of the first excitation, this behaviour was not explained in this research and hence it should be investigated in future work.

- Depending on the initial moisture content of a log and the time it spends prior to the Joule heating treatment, its sapwood's apparent moisture content can be different from the average published data. This difference can cause over- or under-heating of logs. For example, testing Log 6 in the subsequent test showed that apparent moisture content was much lower than that assumed in the model, resulting in about 4 kW·h of excess energy. To optimize the calculation of the required energy, an estimate of the most likely moisture content should be made, based on the actual log mass and dimensions. To this end, further experiments, of the type carried out for Log 6, need to be calculated.

- The samples of *Set 2* (from Ashley forest) had lower electrical conductivity than those of *Sets 1* and *3* (McVicar timber sawmill and from Owen River forest, respectively). It was unclear whether this variation was caused by a tree-to-tree and/or site-to-site difference. Hence, it is recommended to further evaluate this variation by collecting a larger data set from different *P. radiata* trees and forests. If there is a variation in electrical conductivity among New Zealand forests, a unique multiplier for forest provenance can be set for each of them; thus the developed statistical model can be updated.

References

AIAA (1998(2002)). Guide for the verification and validation of computational fluid dynamics simulations. AIAA G-077-1998.

Ananias, R. A., Venegas, R., Salvo, L., and Elustondo, D. (2013). Kiln schedule certification for industrial drying of radiata pine. *Wood and Fiber Science*, 45(1):98–104.

Ansari, M. Z. and Cho, C. (2010). An analytical model of joule heating in piezoresistive microcantilevers. *Sensors*, 10(11):9668–9686.

ANSYS, Inc. (2013). *ANSYS CFX-Solver theory guide*. Canonsburg, PA, 15.0 edition.

ASTM D4442 - 16 (2016). Direct moisture content measurement of wood and wood-based materials.

ASTM E1933-14 (2014). Measuring and compensating for emissivity using infrared imaging radiometers.

Bamber, R. K. and Burley, J. (1983). *The wood properties of radiata pine*. Commonwealth Agricultural Bureaux.

Bard, A. J. and Faulkner, L. R. (2001). *Electrochemical methods: fundamentals and applications*. John Wiley, New York, 2nd edition.

Bates, D., Mächler, M., Bolker, B., and Walker, S. (2015). Fitting linear mixed-effects models using lme4. *Journal of Statistical Software*, 67(1):1–48.

Bozdogan, H. (1987). Model selection and akaike's information criterion (aic): The general theory and its analytical extensions. *Psychometrika*, 52(3):345–370.

Brischke, C., Rapp, A. O., and Bayerbach, R. (2008). Measurement system for long-term recording of wood moisture content with internal conductively glued electrodes. *Building and Environment*, 43(10):1566–1574.

Brown, J., Davidson, R., and Skaar, C. (1963). Mechanism of electrical conduction in wood. *For. Prod. J*, 13(10):455–459.

Burr, H. K. and Stamm, A. J. (1947). Diffusion in wood. *The Journal of Physical Chemistry*, 51(1):240–261.

Butterfield, B. (2006). The structure of wood: form and function. In Walker, J. C. F., editor, *Primary wood processing*, pages 1–22. Springer, Dordrecht, The Netherlands.

Cai, L. and Oliveira, L. C. (2010). Heating performance of frozen lodgepole pine lumber. *Wood and Fiber Science*, 42(4):467–473.

Carrodus, B. B. (1972). Variability in the proportion of heartwood formed in woody stems. *New Phytologist*, 71(4):713–718.

Carslaw, H. S. and Jaeger, J. C. (1959). *Conduction of heat in solids*. Oxford: Clarendon Press, 2nd edition.

Carson, M. and Inglis, C. (1988). Genotype and location effects on internode length of *Pinus radiata* in New Zealand. *New Zealand Journal of Forestry Science*, 18(3):267–279.

Cengel, Y. A. (1998). *Heat transfer: A practical approach*. WCB McGraw-Hill, Boston.

Cengel, Y. A. and Boles, M. A. (2011). *Thermodynamics: An Engineering Approach*. McGraw-Hill, New York, 7th edition.

Chauhan, S., Donnelly, R., Huang, C.-l., Nakada, R., Yafang, Y., and Walker, J. C. F. (2006). Wood quality: In context. In Walker, J. C. F., editor, *Primary wood processing*, pages 121–158. Springer, Dordrecht.

Chen, Z., White, M., and Wu, Y. (2012). Vacuum-steam phytosanitation of hardwood pallets and pallet stringers. *Forest Products Journal*, 62(5):378–382.

Davidson, R. (1958). The effect of temperature on the electrical resistance of wood. *For. Prod. J*, 8(5):160–164.

De Alwis, A. and Fryer, P. (1992). Operability of the ohmic heating process: Electrical conductivity effects. *Journal of Food Engineering*, 15(1):21–48.

Dentener, P. R., Lewthwaite, S. E., Rogers, D. J., Meier, X., Whiting, D. C., and McDonald, R. M. (2001). Heat treatments for control of huhu beetle (*Prionoplus reticularis*) larvae in logs. *New Zealand Journal of Forestry Science*, 31(2):273–286.

Desch, H. E. and Dinwoodie, J. M. (1996). *Timber : structure, properties, conversion, and use*. Food Products Press, New York, 7th edition.

Dunlap, F. (1912). *The specific heat of wood*, volume 110 of *Forest Service - Bulletin*. U.S. Dept. of Agriculture.

Dupleix, A., Kusiak, A., Hughes, M., and Rossi, F. (2013). Measuring the thermal properties of green wood by the transient plane source (TPS) technique. *Holzforschung*, 67(4):437–445.

Faraway, J. J. (2005). *Linear models with R*, volume 63. Chapman & Hall/CRC, Boca Raton, FL.

Fields, P. G. and White, N. D. G. (2002). Alternatives to methyl bromide treatments for stored-product and quarantine insects. Annual Review of Entomology.

Fischer, S. (2014). Dependence on wood properties of log strerilization by Joule heating. Master's thesis, Karlsruhe Institute of Technology, Karlsruhe, Germany.

Fleisch, D. (2008). *A student's guide to Maxwell's equations*. Cambridge University Press.

Fleischer, H. O. and Downs, L. E. (1953). Heating veneer logs electrically. Technical report, United States Department of Agriculture, Forest Service, Forest Products Laboratory.

Fluke Corporation (2006). *User manual: Ti20 thermal imager*.

Fluke Corporation (2011). Quick reference to infrared thermometer calibration. http://support.fluke.com/hart-sales/Download/Asset/4100366_6203_ENG_A_W.PDF.

Forsén, H., Tarvainen, V., et al. (2000). *Accuracy and functionality of hand held wood moisture content meters*. Technical Research Centre of Finland (VTT), Finland.

Fredriksson, M., Wadsö, L., and Johansson, P. (2013). Small resistive wood moisture sensors: A method for moisture content determination in wood structures. *European Journal of Wood and Wood Products*, 71(4):515–524.

Glass, S. V. and Zelinka, S. L. (2010). Moisture relations and physical properties of wood. In *Wood Handbook - Wood as an Engineering Material. General Technical Report FPL-GTR-190*, pages 4.1–4.19. Department of Agriculture, Forest Service, Forest Products Laboratory, Madison,WI: U.S.

Goebel, P. C., Bumgardner, M. S., Herms, D. A., and Sabula, A. (2010). Failure to phytosanitize ash firewood infested with emerald ash borer in a small dry kiln using ispm-15 standards. *Journal of Economic Entomology*, 103(3):597–602.

Grace, J., Blundell, W., and Pont, D. (1998). Branch development in pinus radiata-model outline and data collection. *New Zealand Journal of Forestry Science*, 28:182–194.

Grace, J., Pont, D., Goulding, C., and Rawley, B. (1999). Modelling branch development for forest management. *New Zealand Journal of Forestry Science*, 29(3):391–408.

Gustafsson, S. E. (1991). Transient plane source techniques for thermal conductivity and thermal diffusivity measurements of solid materials. *Review of Scientific Instruments*, 62(3):797–804.

Haque, M. N. (2007). Simulation of temperature and moisture content profiles in a *Pinus radiata* board during high-temperature drying. *Drying Technology*, 25(4):547–555.

Haque, M. N. and Langrish, T. A. G. (2001). Stack-wide effects in the modeling of solar kilns for drying timber. *Drying Technology*, 19(1):99–114.

Harris, J. M. (1991a). Formation of wood and bark. In Kininmonth, J. A. and Whitehouse, L. J., editors, *Properties and uses of New Zealand radiata pine*, pages 3.1–3.18. Ministry of Forestry, Forest Research Institute with assistance from the New Zealand Lottery Grants Board, Rotorua, New Zealand.

Harris, J. M. (1991b). Radiata pine in New Zealand. In Kininmonth, J. A. and Whitehouse, L. J., editors, *Properties and uses of New Zealand radiata pine*, pages 1.1–1.7. Ministry of Forestry, Forest Research Institute with assistance from the New Zealand Lottery Grants Board, Rotorua, New Zealand.

Harris, J. M. (1991c). Structure of wood and bark. In Kininmonth, J. A. and Whitehouse, L. J., editors, *Properties and uses of New Zealand radiata pine*, pages 2.1–2.16. Ministry of Forestry,

Forest Research Institute with assistance from the New Zealand Lottery Grants Board, Rotorua, New Zealand.

Harris, J. M. and Cown, D. J. (1991). Basic wood properties. In Kininmonth, J. A. and Whitehouse, L. J., editors, *Properties and uses of New Zealand radiata pine*, pages 6.1–6.28. Ministry of Forestry, Forest Research Institute with assistance from the New Zealand Lottery Grants Board, Rotorua, New Zealand.

Haynes, W. M. (2014). *CRC handbook of chemistry and physics*. CRC press.

Heemken, O. P., Theobald, N., and Wenclawiak, B. W. (1997). Comparison of ASE and SFE with Soxhlet, Sonication, and Methanolic Saponification extractions for the determination of organic micropollutants in marine particulate matter. *Analytical Chemistry*, 69(11):2171–2180.

Heffernan, B. (2009). Joule heating of export logs. Technical report, New Zealand Ministry of Agriculture and Forestry.

Henin, J. M., Charron, S., Luypaert, P. J., Jourez, B., and Hébert, J. (2008). Strategy to control the effectiveness of microwave treatment of wood in the framework of the implementation of ISPM 15. *Forest Products Journal*, 58(12):75–81.

Hoadley, R. B. (2000). *Understanding wood: A craftsman's guide to wood technology*. Taunton Press.

Hot Disk AB (2007). *Instruction manual: Hot Disk Thermal Constant Analyser Ver. 5.9*. Hot Disk AB,.

Incropera, F. P. and David, P. D. (2002). *Fundamentals of heat and mass transfer*. John Wiley & Sons Inc., USA.

Invensys Foxboro (2015). Conductivity ordering guide. http://myweb.wit.edu/sandinic/Research/conductivity%20v%20concentration.pdf.

IPPC (2016a). International standards for phytosanitary measures (ISPM 15). https://www.ippc.int/static/media/files/publication/en/2016/06/ISPM_15_2013_En_2016-06-07.pdf. Accessed: 28.06.2017.

IPPC (2016b). ISPM 28 phytosanitary treatments for regulated pests. https://www.ippc.int/static/media/files/publication/en/2016/01/ISPM_28_2007_WithoutApp1_En_2015-12-22_PostCPM10_InkAmReformatted.pdf. Accessed: 16.06.2018.

Ito, R., Fukuoka, M., and Hamada-Sato, N. (2014). Innovative food processing technology using ohmic heating and aseptic packaging for meat. *Meat Science*, 96(1):675–681.

Janssen, H.-G. and Lou, X. (1999). Supercritical fluid extraction in organic analysis. In Handley, A. J., editor, *Extraction Methods in Organic Analysis*, chapter 5, pages 101–145. Sheffield Academic Press Ltd., Sehffeild, England.

Jayawickrama, K., Shelbourne, C., and Carson, M. (1997). New Zealand's long internode breed of *Pinus radiata*. *New Zealand Journal of Forestry Science*, 27(2):126–141.

Keey, R. B., Langrish, T. A. G., and Walker, J. C. F. (2000). *Kiln-drying of lumber*. Wood Science. Springer, Verlag Berlin Heidelberg.

Kininmonth, J. A. (1991). Wood-water relationships. In Kininmonth, J. A. and Whitehouse, L. J., editors, *Properties and uses of New Zealand radiata pine*, pages 7.1–7.23. Ministry of Forestry, Forest Research Institute with assistance from the New Zealand Lottery Grants Board, Rotorua, New Zealand.

Kininmonth, J. A. and Whiteside, I. D. (1991). Log quality. In Kininmonth, J. A. and Whitehouse, L. J., editors, *Properties and uses of New Zealand radiata pine*, pages 5.1–5.21. Ministry of Forestry, Forest Research Institute with assistance from the New Zealand Lottery Grants Board, Rotorua, New Zealand.

Kleiber, M. and Joh, R. (2010). D1 calculation methods for thermophysical properties. In *VDI heat atlas*, pages 119–152. Springer Berlin Heidelberg, Berlin, Heidelberg, 10 edition.

Koch, P. (1968). Specific heat of ovendry spruce pine wood and bark. *Wood Science*, 1(4):203–214.

Kollmann, F. F. and Cote, W. A. J. (1968). *Principles of wood science and technology. Vol. I. Solid wood*. Springer-Verlag.

Kuroda, N. and Tsutsumi, J. (1982). Anisotropic behaviour of electrical conduction in wood. *Mokuzai Gakkaishi*, 28:25–30.

Kuznetsova, A., Bruun Brockhoff, P., and Haubo Bojesen Christensen, R. (2016). *lmerTest: tests in Linear Mixed Effects Models*. R package version 2.0-32.

Langrish, T. and Walker, J. C. F. (2006). Drying of timber. In Walker, J. C. F., editor, *Primary wood processing*, pages 251–295. Springer, Dordrecht.

Lin, R. (1967). Review of the dielectric properties of wood and cellulose. *Forest Products Journal*, 17(7):61.

Liu, H., Wang, Z., and Xu, P. (2011). Mass diffusivities of radiata pine in superheated steam drying. In *2010 International Conference on Advances in Materials and Manufacturing Processes, ICAMMP 2010, November 6, 2010 - November 8, 2010*, volume 146-147 of *Advanced Materials Research*, pages 357–360, Shenzhen, China. Trans Tech Publications.

Lopez, G., Basterra, L., Acuna, L., and Casado, M. (2013). Determination of the emissivity of wood for inspection by infrared thermography. *Journal of Nondestructive Evaluation*, 32(2):172–176.

Lu, J., Jiang, J., Wu, Y., and Li, X. (2012). Modeling the heat transfer during log heating. *Drying Technology*, 30(14):1541–1547.

Lutz, J. F. (1960). Heating veneer bolts to improve quality of Douglas-fir plywood. Technical report, United States Department of Agriculture, Forest Service, Forest Products Laboratory.

MacLean, J. (1941). Thermal conductivity of wood. *Heating, Piping, and Air Conditioning*, 101(6):380–391.

Madding, R. P. (1999). Emissivity measurement and temperature correction accuracy considerations. In LeMieux, D. and Snell, J., editors, *Thermosense XXI, SPIE-International Society for Optical Engineering*, pages 393–401.

MAF Biosecurity New Zealand (2009). Methyl bromide information. http://www.biosecurity.govt.nz/files/regs/treat/methyl-bromide-info.pdf. Accessed: 15.02.2014.

Majumdar, P. (2006). *Computational methods for heat and mass transfer*. Taylor & Francis, New York.

Marra, F., Zell, M., Lyng, J., Morgan, D., and Cronin, D. (2009). Analysis of heat transfer during ohmic processing of a solid food. *Journal of Food Engineering*, 91(1):56–63.

Mattson, W., Vanhanen, H., Veteli, T., Sivonen, S., and Niemelä, P. (2007). Few immigrant phytophagous insects on woody plants in europe: Legacy of the european crucible? *Biological Invasions*, 9(8):957–974.

McCleskey, R. B. (2011). Electrical conductivity of electrolytes found in natural waters from (5 to 90) °C. *Journal of Chemical & Engineering Data*, 56(2):317–327.

Ministry for Primary Industries (2018). Methyl bromide 2020 deadline. https://www.mpi.govt.nz/exporting/forest-products/wood-and-wood-products/methyl-bromide-2020-deadline/. Accessed: 19.05.2018.

Ministry of Primary Industry (2012). What forestry means to New Zealand. http://www.mpi.govt.nz/news-and-resources/statistics-and-forecasting/forestry/. Accessed: 05.12.2013.

Ministry of the Environment (2005). Methyl bromide. http://www.mfe.govt.nz/more/hazards/risks-ozone-depleting-substances/methyl-bromide. Accessed: 28.06.2017.

Moran, M. J., Shapiro, H. N., Munson, B. R., and DeWitt, D. P. (2003). *Introduction to thermal systems engineering: thermodynamics, fluid mechanics, and heat transfer*. John Wiley & Sons, Inc.

Myers, S. W. and Bailey, S. M. (2011). Evaluation of a heat treatment schedule for the Asian longhorned beetle, *Anoplophora glabripennis* (Coleoptera: Cerambycidae). *Forest Products Journal*, 61(1):46–49.

Mõlder, H., Järvik, J., Pilt, K., Märss, M., and Reiska, R. (2013). Microwave treatment against the attack of wood boring in timber structures. *Agronomy Research*, 11(2):497–504.

New Zealand Forest Owners Association (2012). Facts and figures. http://www.nzfoa.org.nz/images/stories/pdfs/nzf8135_factsfigures.pdf. Accessed: 05.12.2013.

Nijdam, J. (1998). *Reducing moisture-content variations in kiln-dried timber*. PhD thesis, The University of Canterbury.

Nijdam, J. J., Langrish, T. A. G., and Keey, R. B. (2000). A high-temperature drying model for softwood timber. *Chemical Engineering Science*, 55(18):3585–3598.

Nilsson, T. and Rowell, R. (2012). Historical wood – structure and properties. *Journal of Cultural Heritage*, 13(3, Supplement):S5–S9.

Novotny, M., Skramlik, J., Suhajda, K., and Tichomirov, V. (2013). Sterilization of biotic pests by microwave radiation. *Procedia Engineering*, 57:1094–1099.

Nursultanov, N., Altaner, C., and Heffernan, W. J. B. (2017). Effect of temperature on electrical conductivity of green sapwood of *Pinus radiata* (radiata pine). *Wood Science and Technology*, 51(4):795–809.

Nzokou, P., Tourtellot, S., and Kamdem, D. P. (2008). Kiln and microwave heat treatment of logs infested by the emerald ash borer (*Agrilus planipennis Fairmaire*) (Coleoptera: Buprestidae). *Forest Products Journal*, 58(7-8):68–72.

Oberkampf, W. L. and Trucano, T. G. (2002). Verification and validation in computational fluid dynamics. *Progress in Aerospace Sciences*, 38(3):209–272.

Olek, W., Weres, J., and Guzenda, R. (2003). Effects of thermal conductivity data on accuracy of modeling heat transfer in wood. *Holzforschung*, 57(3):317–325.

Pang, S. and Herritsch, A. (2005). Physical properties of earlywood and latewood of *Pinus radiata* D. Don: Anisotropic shrinkage, equilibrium moisture content and fibre saturation point. *Holzforschung*, 59(6):654–661.

Pang, S., Keey, R. B., and Langrish, T. A. G. (1995). Modelling the temperature profiles within boards during the high-temperature drying of *Pinus radiata* timber: the influence of airflow reversals. *International Journal of Heat and Mass Transfer*, 38(2):189–205.

Patankar, S. (1980). *Numerical heat transfer and fluid flow*. CRC Press.

Pawson, S., Bader, M., Brockerhoff, E., Heffernan, B., Kerr, J., and O'Connor, B. (2018). Quantifying the thermal tolerance of wood borers and bark beetles for the development of phytosanitary treatments of pine logs. Manuscript submitted for publication.

Peiró, J. and Sherwin, S. (2005). Finite difference, finite element and finite volume methods for partial differential equations. In *Handbook of Materials Modeling*, chapter 8.2, pages 2415–2446. Springer.

Perré, P. (2004). Electrical heating of green logs using Joule's effect: A comprehensive computational model used to find a suitable electrode design. *Wood Science and Technology*, 38(6):429–449.

Perré, P. and Turner, I. W. (1996). The use of macroscopic equations to simulate heat and mass transfer in porous media: some possibilities illustrated by a wide range of configurations that emphasise the role of internal pressure. In Turner, I. W. and Mujumdar, A. S., editors, *Mathematical Modeling and Numerical Techniques in Drying Technology*, pages 83–156. Marcel Dekker Inc., USA.

Perré, P. and Turner, I. W. (1999). A 3-d version of transpore: A comprehensive heat and mass transfer computational model for simulating the drying of porous media. *International Journal of Heat and Mass Transfer*, 42(24):4501–4521.

PF Olsen Limited (2011). Wood matters - june 2011. https://nz.pfolsen.com/market-info-news/wood-matters/2011/june/. Accessed: 19.05.2018.

Plumb, O. A., Spolek, G. A., and Olmstead, B. A. (1985). Heat and mass transfer in wood during drying. *International Journal of Heat and Mass Transfer*, 28(9):1669–1678.

Poling, B. E., Thomson, G. H., Friend, D. G., Rowley, R. L., and Wilding, W. V. (2008). Physical and chemical data. In Green, D. W. and Perry, R. H., editors, *Perry's chemical engineers' handbook*, pages 2.1 – 2.517. McGraw-Hill, U.S.A., 8 edition.

R Core Team (2016). *R: a language and environment for statistical computing*. R Foundation for Statistical Computing, Vienna, Austria.

Radmanović, K., Đukić, I., and Pervan, S. (2014). Specific heat capacity of wood. *Drvna Industrija*, 65(2):151–157.

Richter, B. E., Jones, B. A., Ezzell, J. L., Porter, N. L., Avdalovic, N., and Pohl, C. (1996). Accelerated

solvent extraction: A technique for sample preparation. *Analytical Chemistry*, 68(6):1033–1039.

Rizzoni, G. (2009). *Fundamentals of electrical engineering*. McGraw-Hill.

Saim, N., Dean, J. R., Abdullah, M. P., and Zakaria, Z. (1997). Extraction of polycyclic aromatic hydrocarbons from contaminated soil using soxhlet extraction, pressurised and atmospheric microwave-assisted extraction, supercritical fluid extraction and accelerated solvent extraction. *Journal of Chromatography A*, 791(1–2):361–366.

Sakamoto, Y., Ishiguro, M., and Kitagawa, G. (1986). *Akaike information criterion statistics*. Dordrecht, The Netherlands: D. Reidel.

Salengke, S. and Sastry, S. (2007). Experimental investigation of ohmic heating of solid–liquid mixtures under worst-case heating scenarios. *Journal of Food Engineering*, 83(3):324–336.

Samson, M. (1993). Modelling of knots in logs. *Wood Science and Technology*, 27(6):429–437.

Sastry, S. K. and Salengke, S. (1998). Ohmic heating of solid-liquid mixtures: a comparison of mathematical models under worst-case heating conditions. *Journal of Food Process Engineering*, 21(6):441–458.

Sharma, S., Shukla, S., and Kamala, B. (1997). Studies on DC electrical resistivity of plantation grown timbers. *Holz als Roh-und Werkstoff*, 55(6):391–394.

Shim, J., Lee, S. H., and Jun, S. (2010). Modeling of ohmic heating patterns of multiphase food products using computational fluid dynamics codes. *Journal of Food Engineering*, 99(2):136–141.

Skaar, C. (1988). *Wood-water relations*. Springer-Verlag.

Sonderegger, W., Hering, S., and Niemz, P. (2011). Thermal behaviour of norway spruce and european beech in and between the principal anatomical directions. *Holzforschung*, 65(3):369–375.

Stakeholders in Methyl Bromide Reduction (2018). FAQs: phytosanitary fumigation for export logs and timber products. http://www.stimbr.org.nz/methyl-bromide-faqs.html. Accessed: 19.05.2018.

Stamm, A. J. (1927). The electrical resistance of wood as a measure of its moisture content. *Industrial & Engineering Chemistry*, 19(9):1021–1025.

Stamm, A. J. (1929). The fiber-saturation point of wood as obtained from electrical conductivity measurements. *Industrial & Engineering Chemistry Analytical Edition*, 1(2):94–97.

Stamm, A. J. (1960). Bound-water diffusion into wood in across-the-fibre directions. *Forest Products Journal*, 10(10):524–8.

Stamm, A. J. (1964). *Wood and cellulose science*. Ronald Press Co., New York.

Stanish, M. A., Schajer, G. S., and Kayihan, F. (1986). Mathematical model of drying for hygroscopic porous media. *AIChE Journal*, 32(8):1301–1311.

Suleiman, B. M., Larfeldt, J., Leckner, B., and Gustavsson, M. (1999). Thermal conductivity and diffusivity of wood. *Wood Science and Technology*, 33(6):465–473.

Thurbide, K. B. and Hughes, D. M. (2000). A rapid method for determining the extractives content of wood pulp. *Industrial & Engineering Chemistry Research*, 39(8):3112–3115.

Tremblay, C., Cloutier, A., and Fortin, Y. (2000). Experimental determination of the convective heat and mass transfer coefficients for wood drying. *Wood Science and Technology*, 34(3):253–276.

Tsoumis, G. (1991). *Science and technology of wood: structure, properties, utilization*. Van Nostrand Reinhold, New York.

Uprichard, J. M. (1991). Chemistry of wood and bark. In Kininmonth, J. A. and Whitehouse, L. J., editors, *Properties and uses of New Zealand radiata pine*, volume 1, pages 4.1–4.45. N.Z. Ministry of Forestry, Forest Research Institute with assistance from the New Zealand Lottery Grants Board, Rotorua, New Zealand.

Uzunovic, A., Gething, B., Coelho, A., Dale, A., Janowiak, J. J., Mack, R., and Hoover, K. (2013). Lethal temperature for pinewood nematode, *Bursaphelenchus xylophilus*, in infested wood using radio frequency (RF) energy. *Journal of Wood Science*, 59(2):160–170.

Versteeg, H. K. and Malalasekera, W. (2007). *An introduction to computational fluid dynamics: the finite volume method*. Pearson Education Limited.

Walker, J. C. F. (2006). Basic wood chemistry and cell wall ultrastructure. In Walker, J. C. F., editor, *Primary wood processing*, chapter 2, pages 23–67. Springer.

White, D., Beadle, C., Worledge, D., Honeysett, J., and Cherry, M. (1998). The influence of drought on the relationship between leaf and conducting sapwood area in eucalyptus globulus and eucalyptus nitens. *Trees*, 12(7):406–414.

Wolfe, W. L. (1998). *Introduction to radiometry*, volume TT29. SPIE Press.

Wuhan Guide Infrared Co. Ltd. (2010). *User manual: Guide EasIR-9 thermal camera*.

Xu, P. (2002). Estimating the influence of knots on the local longitudinal stiffness in radiata pine structural timber. *Wood Science and Technology*, 36(6):501–509.

YSI Inc. (2008). *Operations manual EcoSense EC300*.

Yu, Z. T., Hu, Y. C., Xu, X., Fan, L. W., and Cen, K. F. (2011). Experimental measurements of thermal conductivity of wood species in china: Effects of density, temperature, and moisture content. *Forest Products Journal*, 61(2):130–135.

Zareifard, M. R., Ramaswamy, H. S., Trigui, M., and Marcotte, M. (2003). Ohmic heating behaviour and electrical conductivity of two-phase food systems. *Innovative Food Science & Emerging Technologies*, 4(1):45–55.

Appendices

Appendix A

A.1 Temperature of Fully Coated Board

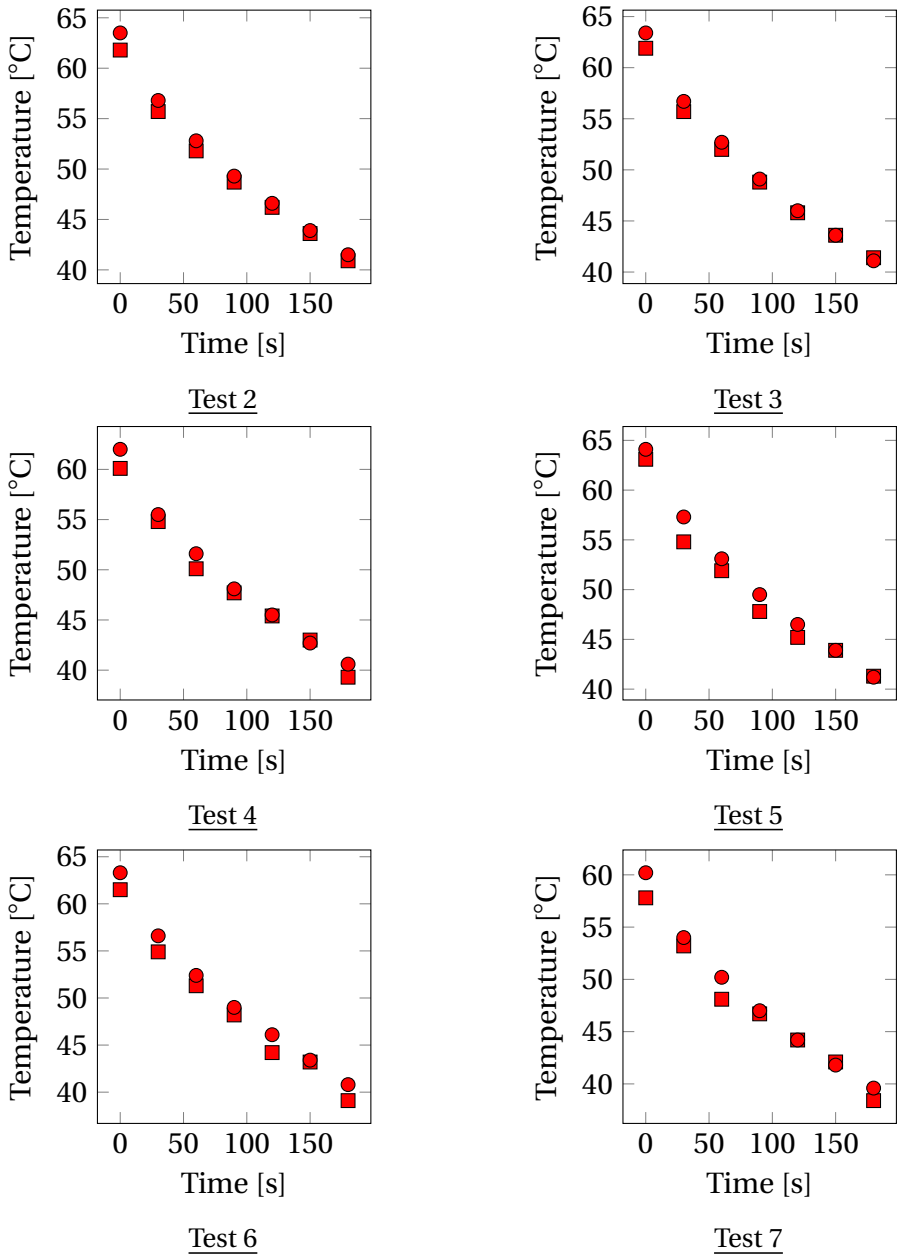

Figure A.1. The cooling curves of the fully coated board, measured by the Fluke (squares) and Guide (circles) infrared cameras.

A.2 Joule Heating Result - *P. radiata* Boards

A.2.1 Temperature

Transitional Boards (TB)

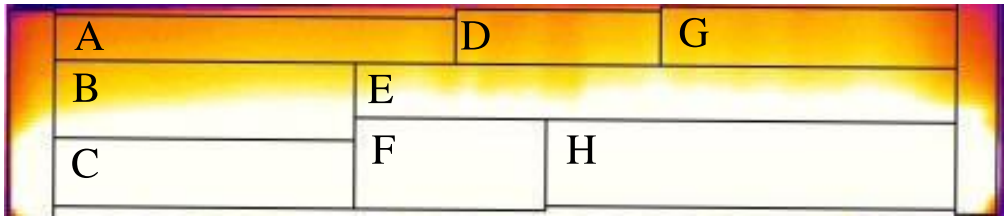

(a)

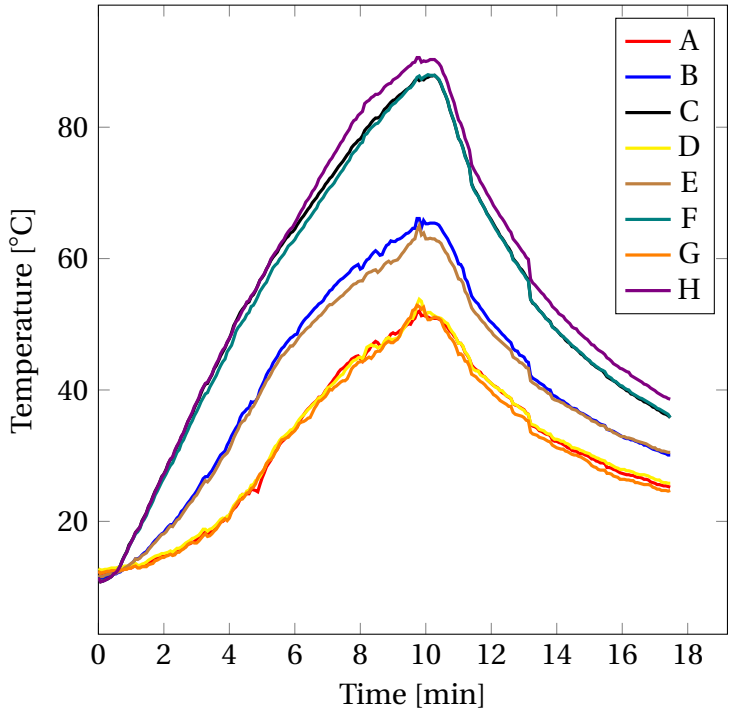

(b)

Figure A.2. Transitional Board #1 (TB1): (a) the segmented thermal image taken at the end of Joule heating and (b) the average temperatures of each segment throughout the experiment.

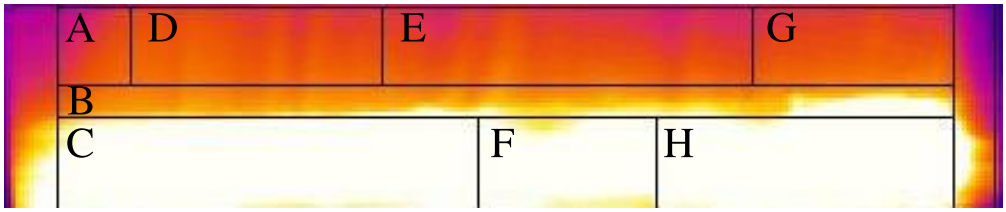

(a)

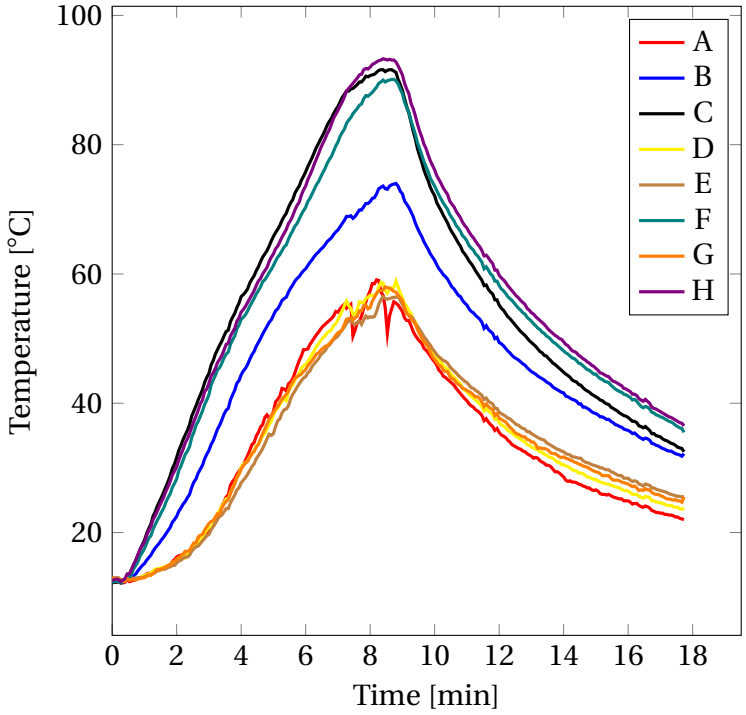

(b)

Figure A.3. Transitional Board #2 (TB2): (a) the segmented thermal image taken at the end of Joule heating and (b) the average temperatures of each segment throughout the experiment.

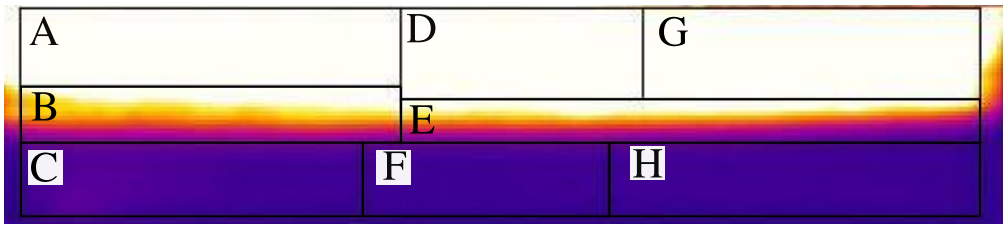

(a)

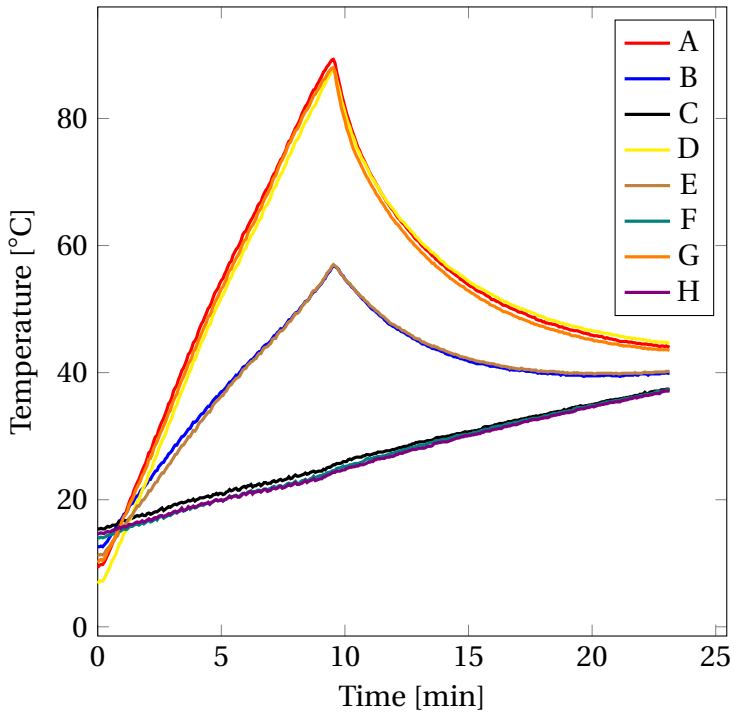

(b)

Figure A.4. Transitional Board #4 (TB4): (a) the segmented thermal image taken at the end of Joule heating and (b) the average temperatures of each segment throughout the experiment.

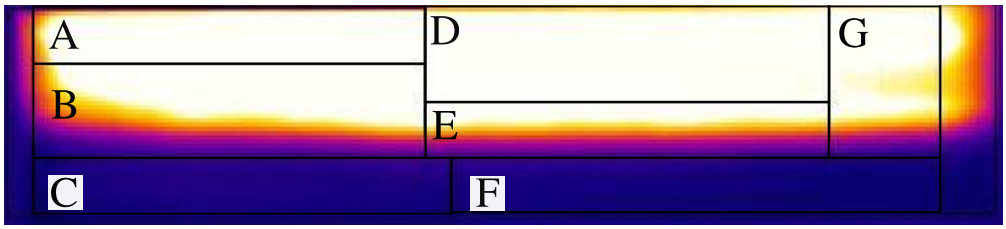

(a)

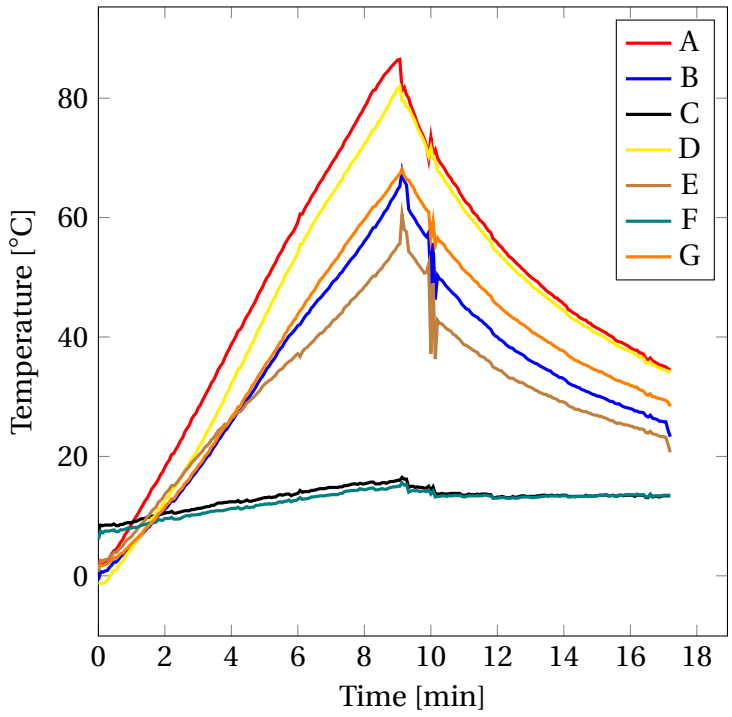

(b)

Figure A.5. Transitional Board #5 (TB5): (a) the segmented thermal image taken at the end of Joule heating and (b) the average temperatures of each segment throughout the experiment. *Note:* During thermal video recording of this board, the Guide infrared camera terminated the recoding, after about 10 minutes from the beginning of heating. To continue the recording, a memory card inside the camera was reinserted. This interruption was approximately a minute long. While reinserting the card, the camera was slightly shifted from its actual position. Therefore, when the recording continued, the pixel coordinates of the board had been changed; that affected the average temperature of each segment.

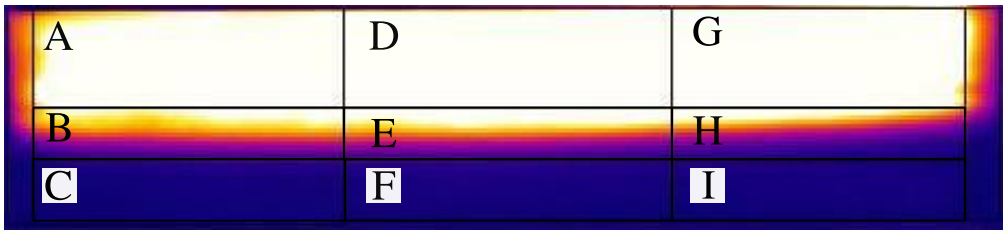

(a)

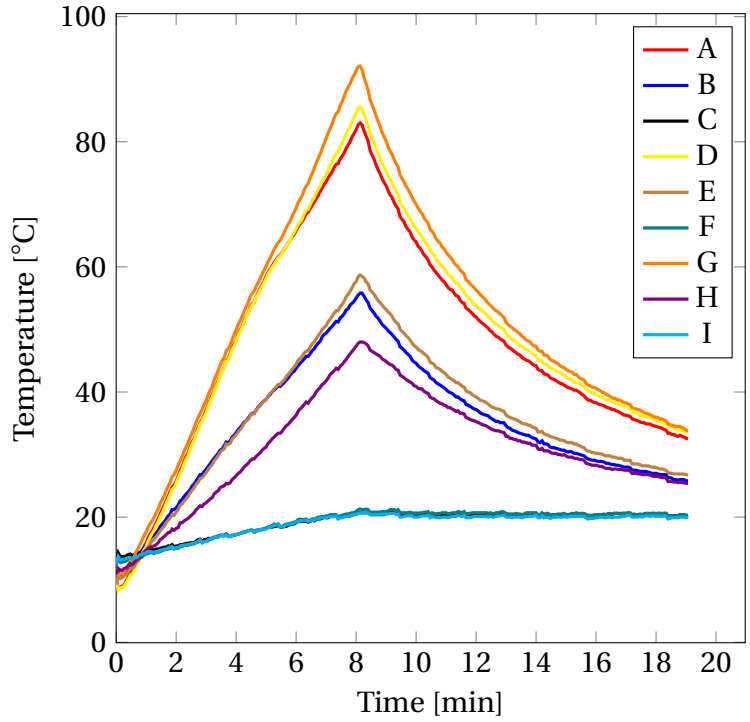

(b)

Figure A.6. Transitional Board #6 (TB6): (a) the segmented thermal image taken at the end of Joule heating and (b) the average temperatures of each segment throughout the experiment.

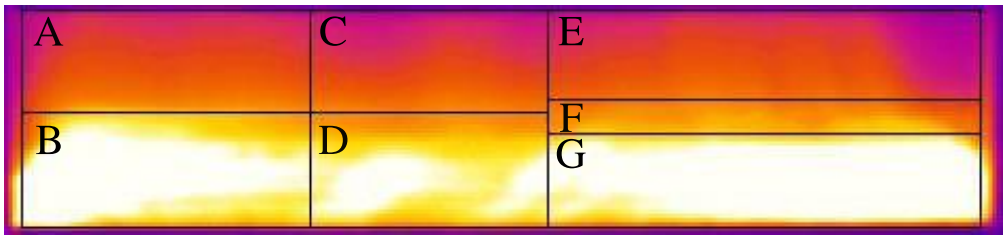

(a)

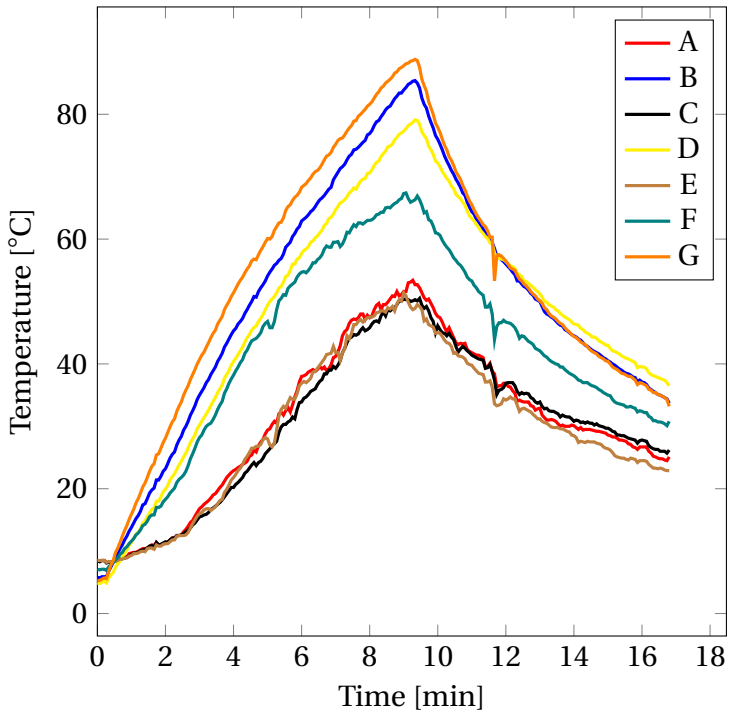

(b)

Figure A.7. Transitional Board #7 (TB7): (a) the segmented thermal image taken at the end of Joule heating and (b) the average temperatures of each segment throughout the experiment.

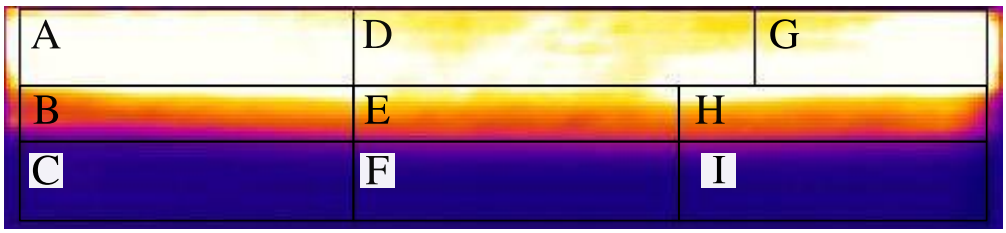

(a)

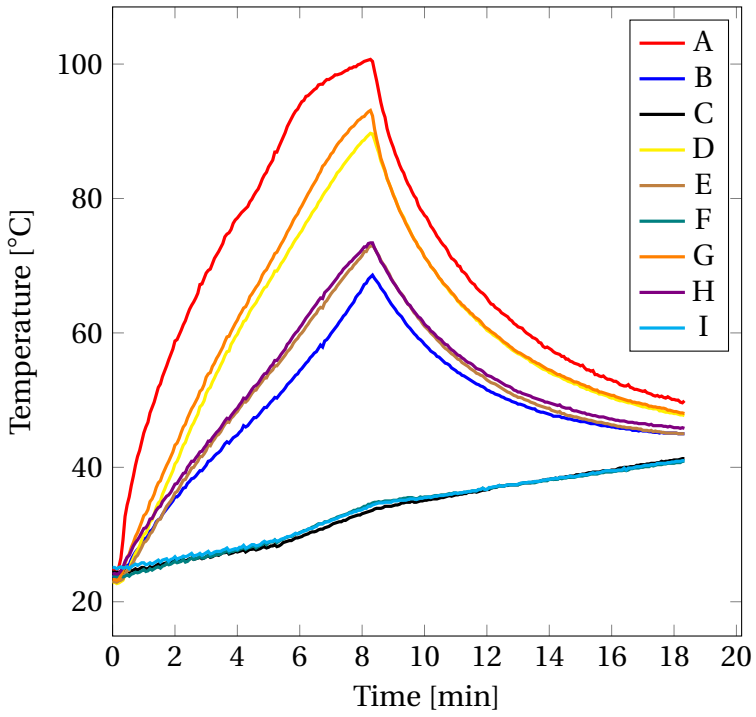

(b)

Figure A.8. Transitional Board #8 (TB8): (a) the segmented thermal image taken at the end of Joule heating and (b) the average temperatures of each segment throughout the experiment.

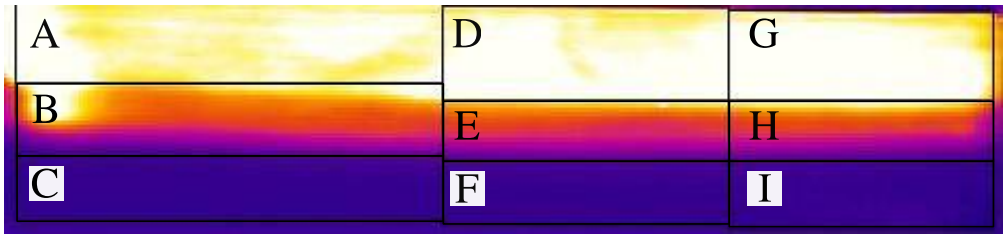

(a)

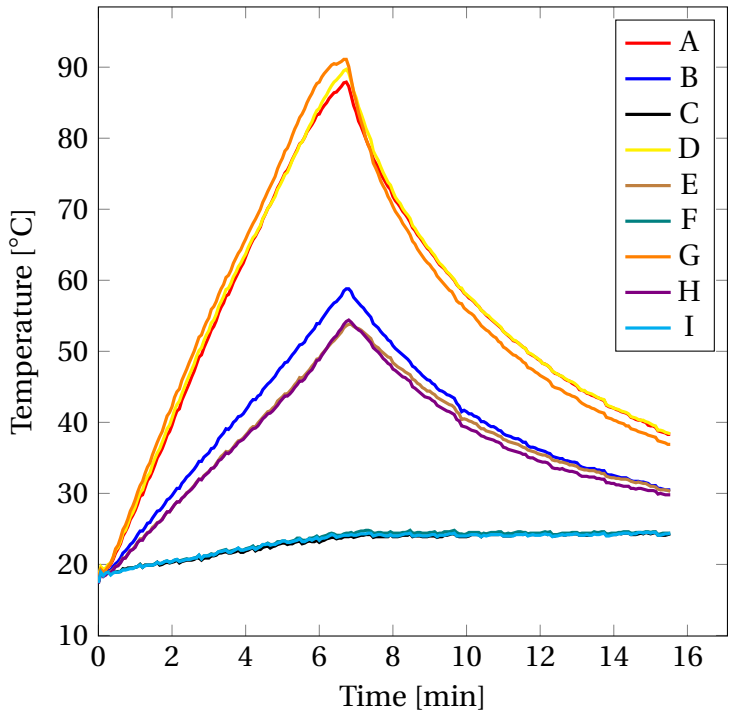

(b)

Figure A.9. Transitional Board #9 (TB9): (a) the segmented thermal image taken at the end of Joule heating and (b) the average temperatures of each segment throughout the experiment.

Sapwood Boards (SB)

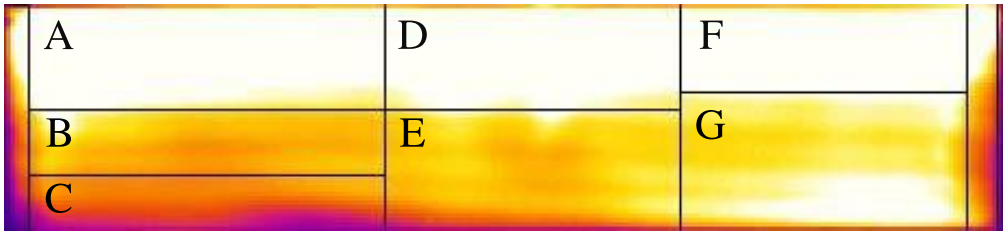

(a)

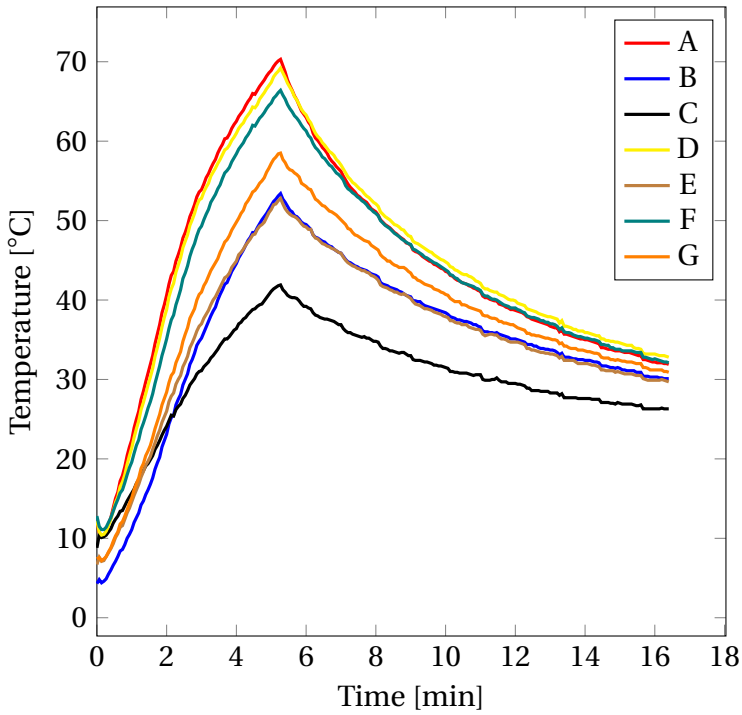

(b)

Figure A.10. Sapwood Board #1 (SB1): (a) the segmented thermal image taken at the end of Joule heating and (b) the average temperatures of each segment throughout the experiment.

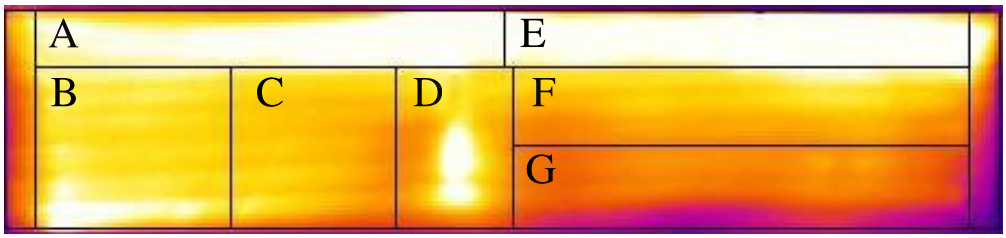

(a)

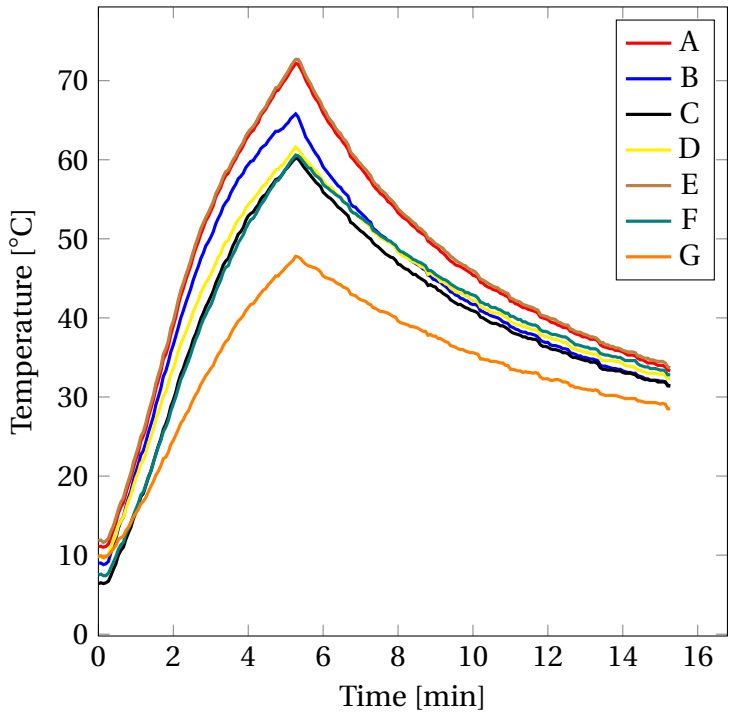

(b)

Figure A.11. Sapwood Board #2 (SB2): (a) the segmented thermal image taken at the end of Joule heating and (b) the average temperatures of each segment throughout the experiment.

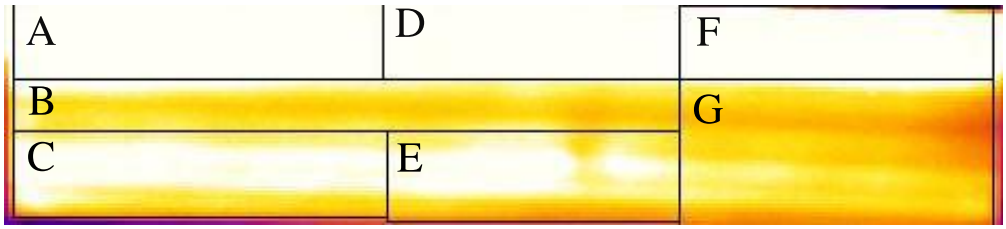

(a)

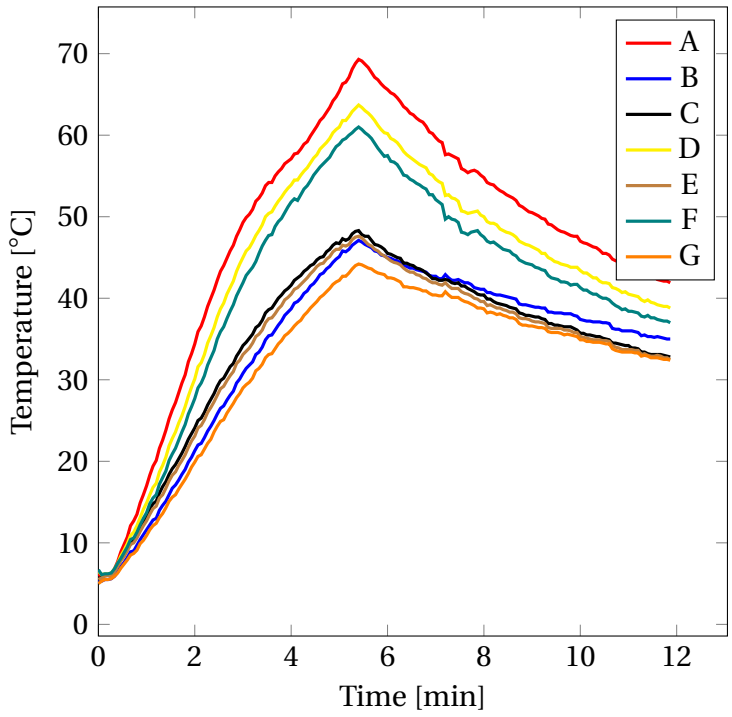

(b)

Figure A.12. Sapwood Board #3 (SB3): (a) the segmented thermal image taken at the end of Joule heating and (b) the average temperatures of each segment throughout the experiment.

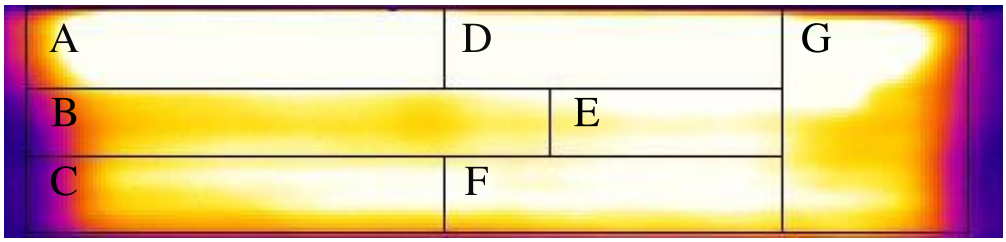

(a)

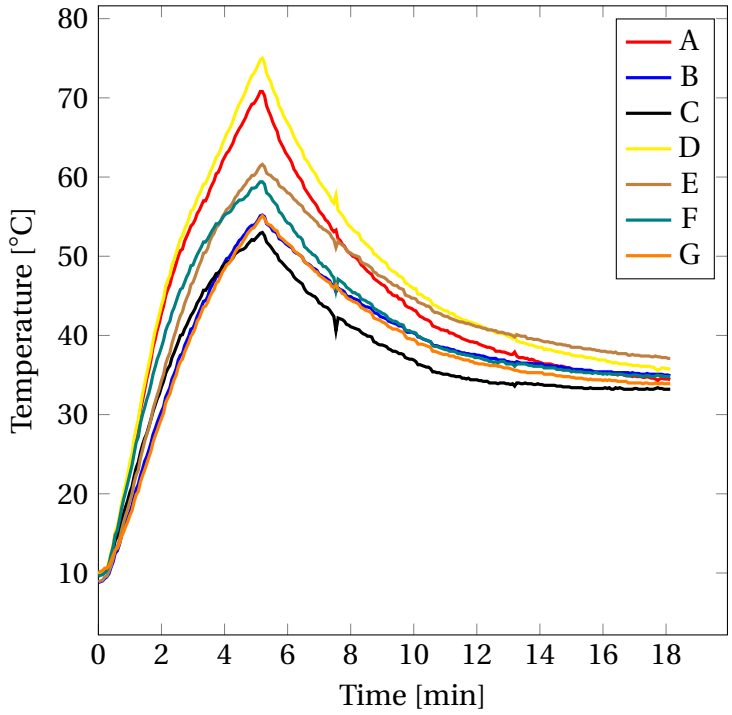

(b)

Figure A.13. Sapwood Board #4 (SB4): (a) the segmented thermal image taken at the end of Joule heating and (b) the average temperatures of each segment throughout the experiment.

Heartwood Boards (HB)

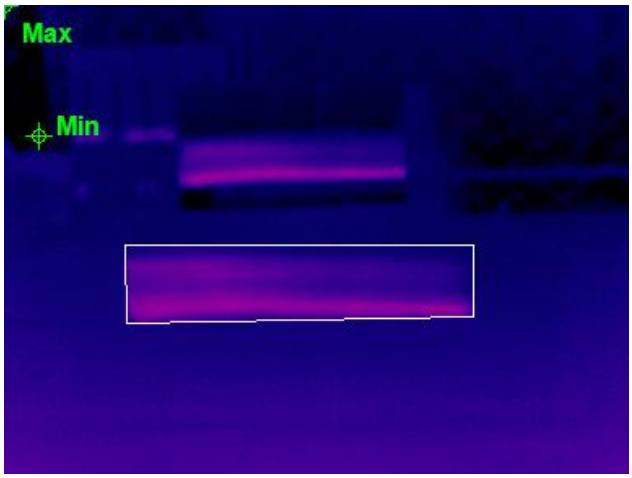

(a)

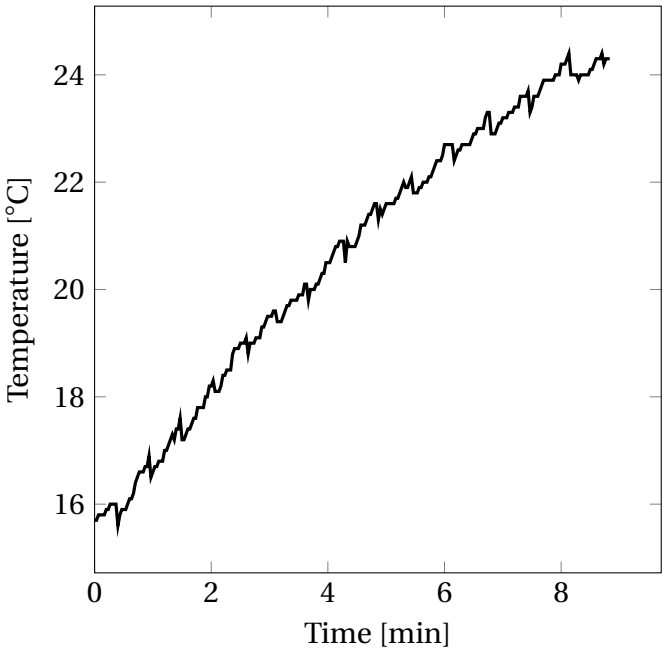

(b)

Figure A.14. Heartwood Board #2 (HB2): (a) the thermal image taken at the end of Joule heating and (b) the average temperatures of the heartwood board, determined within the white frame, throughout the experiment.

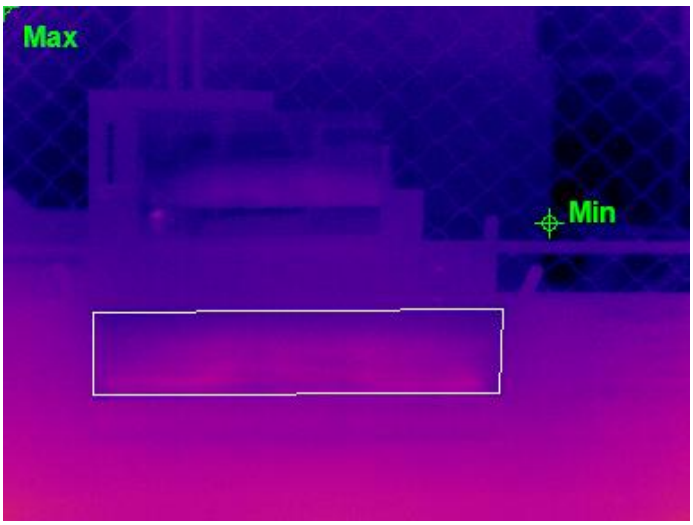

(a)

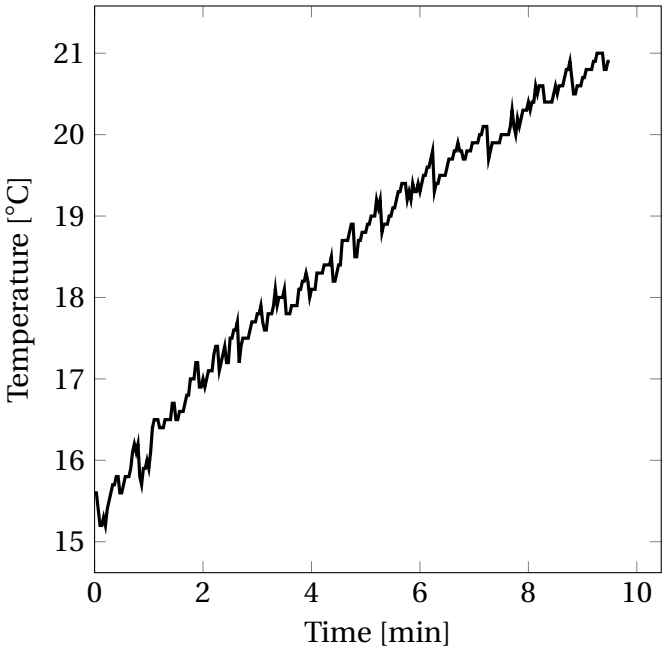

(b)

Figure A.15. Heartwood Board #3 (HB3): (a) the thermal image taken at the end of Joule heating and (b) the average temperatures of the heartwood board, determined within the white frame, throughout the experiment.

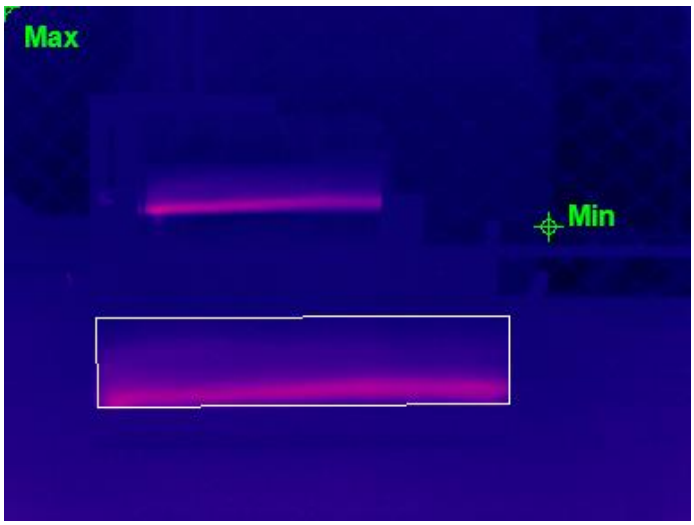

(a)

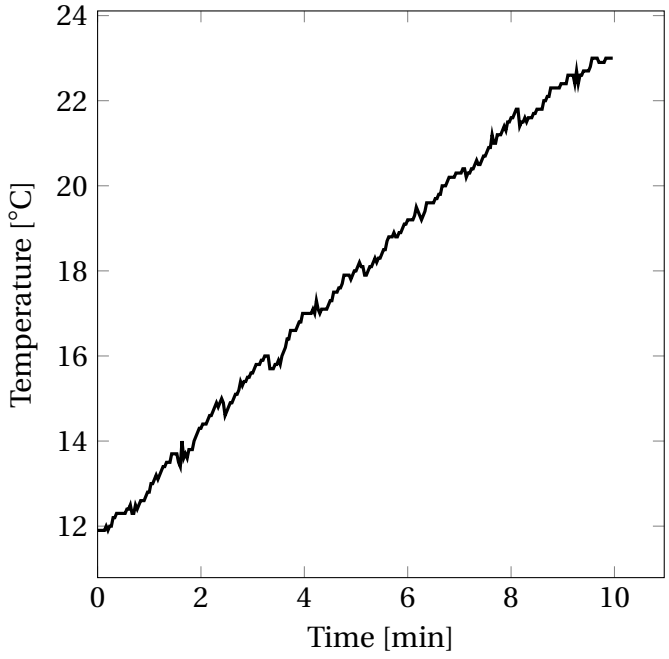

(b)

Figure A.16. Heartwood Board #4 (HB4): (a) the thermal image taken at the end of Joule heating and (b) the average temperatures of the heartwood board, determined within the white frame, throughout the experiment.

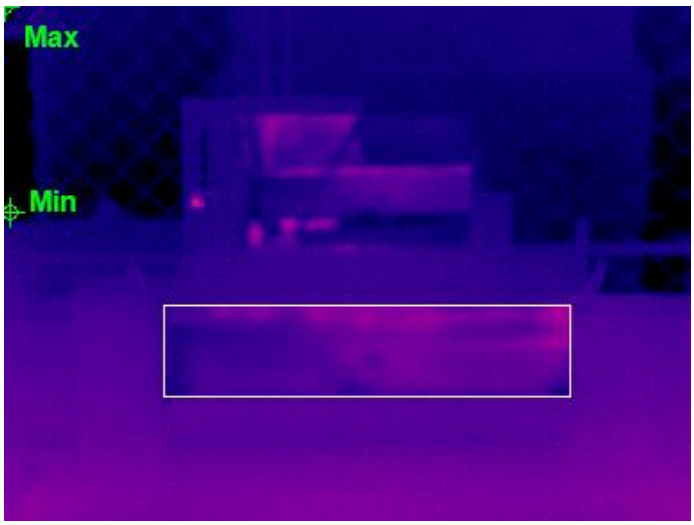

(a)

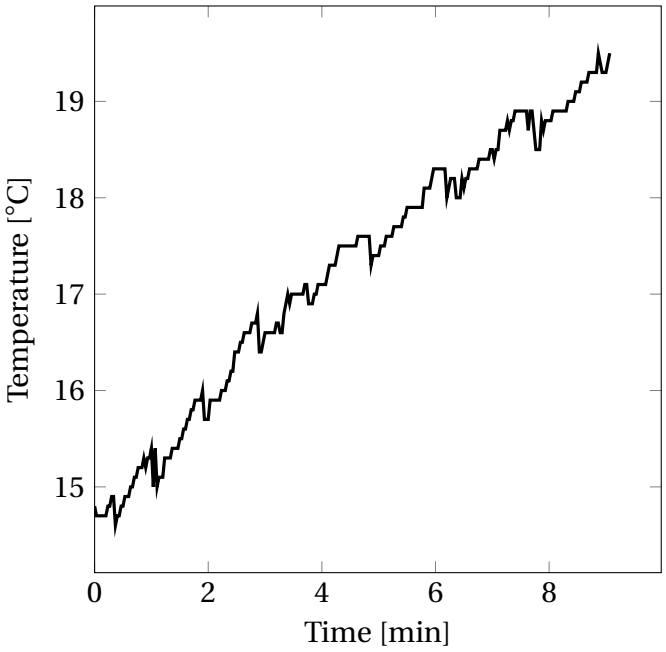

(b)

Figure A.17. Heartwood Board #5 (HB5): (a) the thermal image taken at the end of Joule heating and (b) the average temperatures of the heartwood board, determined within the white frame, throughout the experiment.

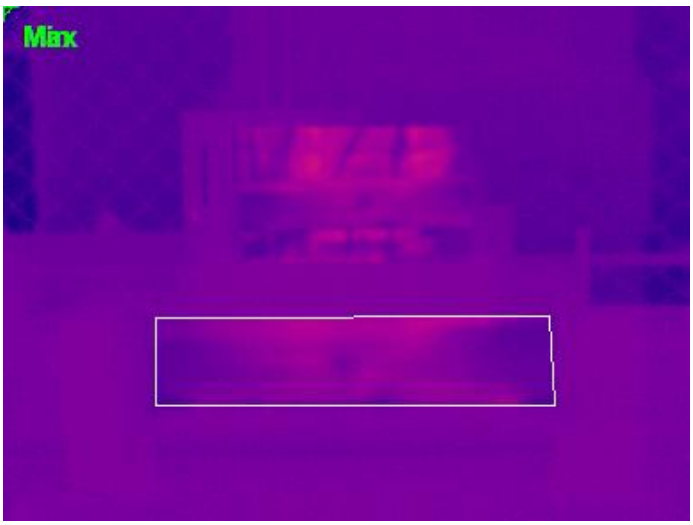

(a)

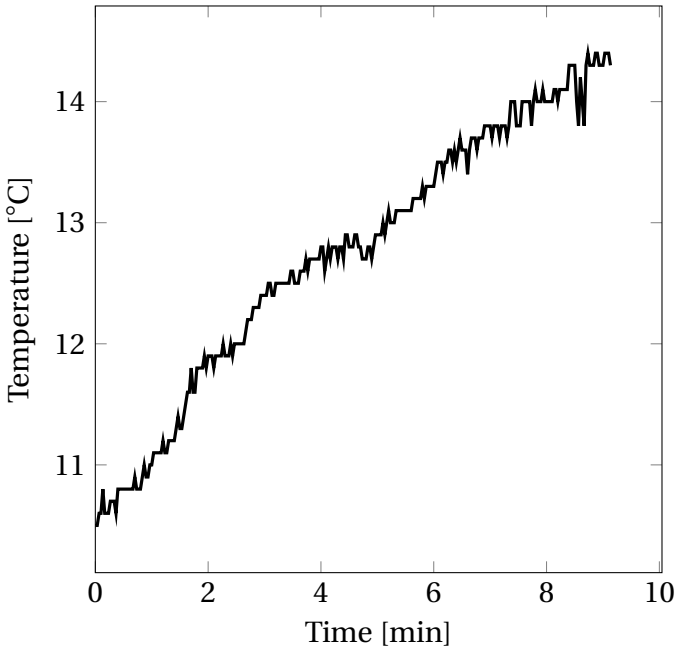

(b)

Figure A.18. Heartwood Board #6 (H6): (a) the thermal image taken at the end of Joule heating and (b) the average temperatures of the heartwood board, determined within the white frame, throughout the experiment.

A.2.2 Electrical Data

Transitional Boards (TB)

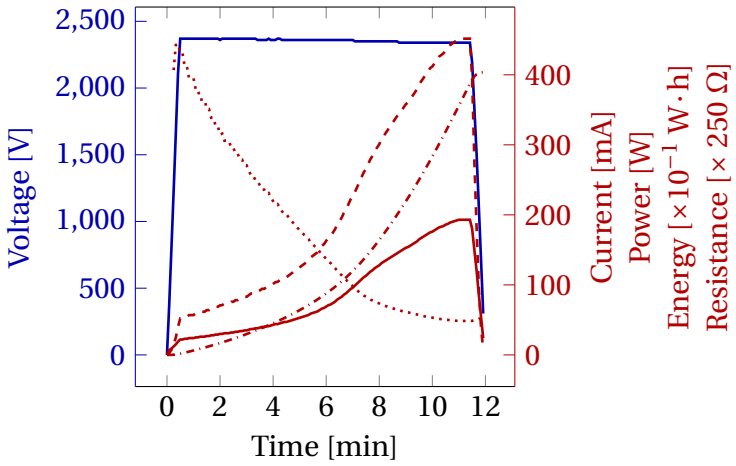

Figure A.19. The electrical data of TB1's heating, where: the blue solid line denotes the voltage and the red solid, dashed, dash-dotted, and dotted lines denote the electric current, the power, the energy, and the electrical resistance, respectively.

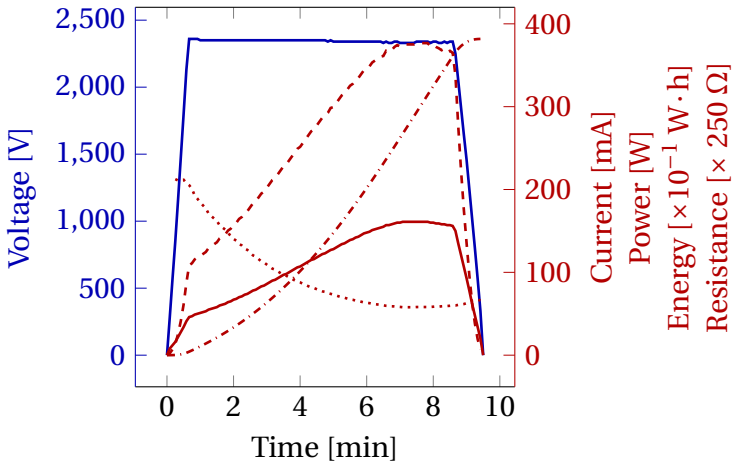

Figure A.20. The electrical data of TB2's heating, where: the blue solid line denotes the voltage and the red solid, dashed, dash-dotted, and dotted lines denote the electric current, the power, the energy, and the electrical resistance, respectively.

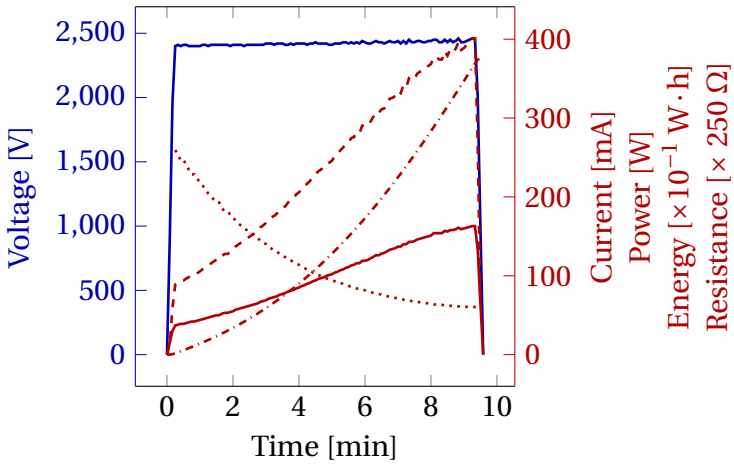

Figure A.21. TB4. The electrical data of TB4's heating, where: the blue solid line denotes the voltage and the red solid, dashed, dash-dotted, and dotted lines denote the electric current, the power, the energy, and the electrical resistance, respectively.

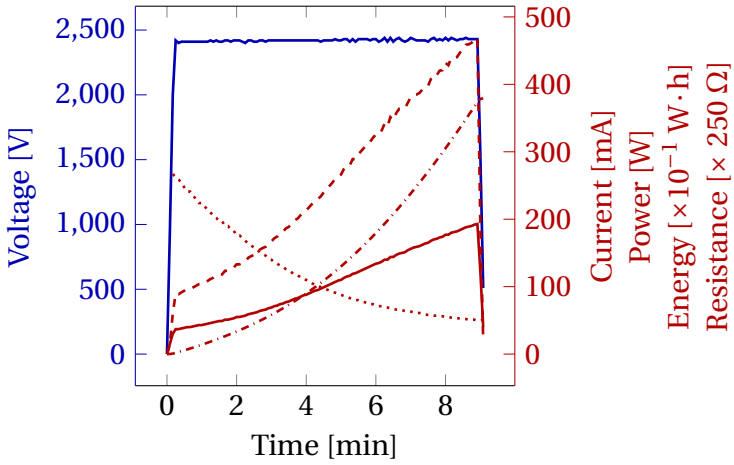

Figure A.22. TB5. The electrical data of TB5's heating, where: the blue solid line denotes the voltage and the red solid, dashed, dash-dotted, and dotted lines denote the electric current, the power, the energy, and the electrical resistance, respectively.

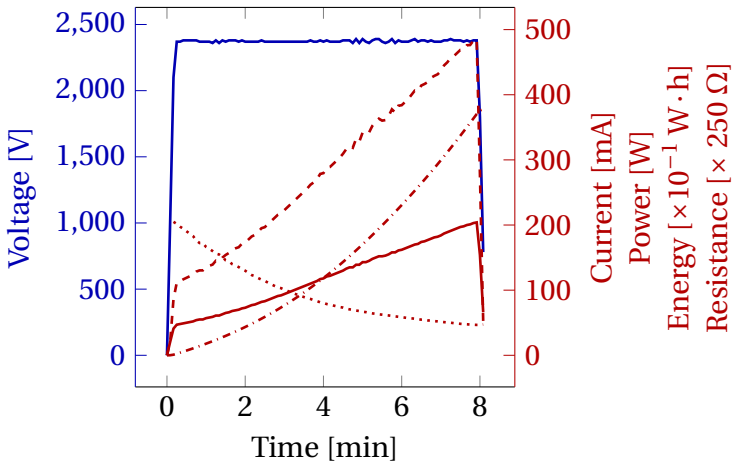

Figure A.23. TB6. The electrical data of TB6's heating, where: the blue solid line denotes the voltage and the red solid, dashed, dash-dotted, and dotted lines denote the electric current, the power, the energy, and the electrical resistance, respectively.

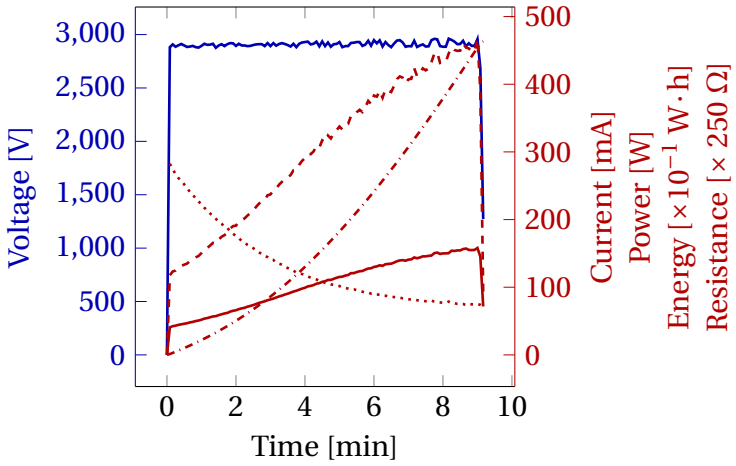

Figure A.24. TB7. The electrical data of TB7's heating, where: the blue solid line denotes the voltage and the red solid, dashed, dash-dotted, and dotted lines denote the electric current, the power, the energy, and the electrical resistance, respectively.

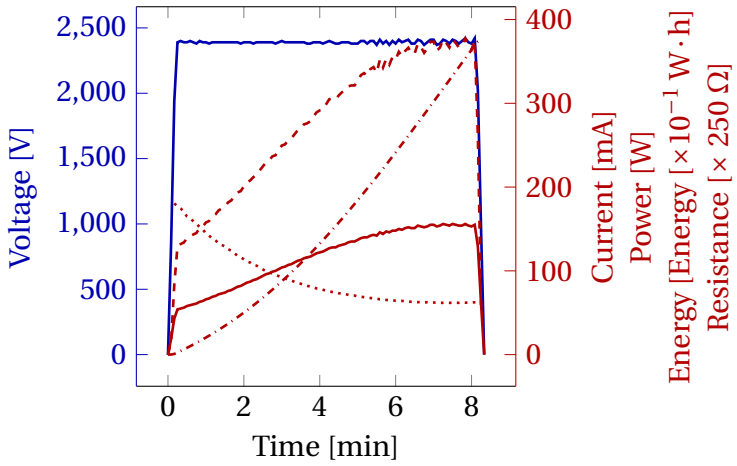

Figure A.25. TB8. The electrical data of TB8's heating, where: the blue solid line denotes the voltage and the red solid, dashed, dash-dotted, and dotted lines denote the electric current, the power, the energy, and the electrical resistance, respectively.

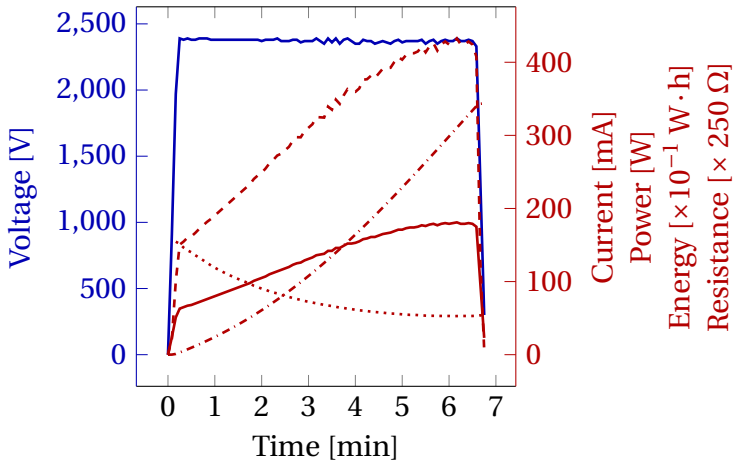

Figure A.26. TB9. The electrical data of TB9's heating, where: the blue solid line denotes the voltage and the red solid, dashed, dash-dotted, and dotted lines denote the electric current, the power, the energy, and the electrical resistance, respectively.

Sapwood Boards (SB)

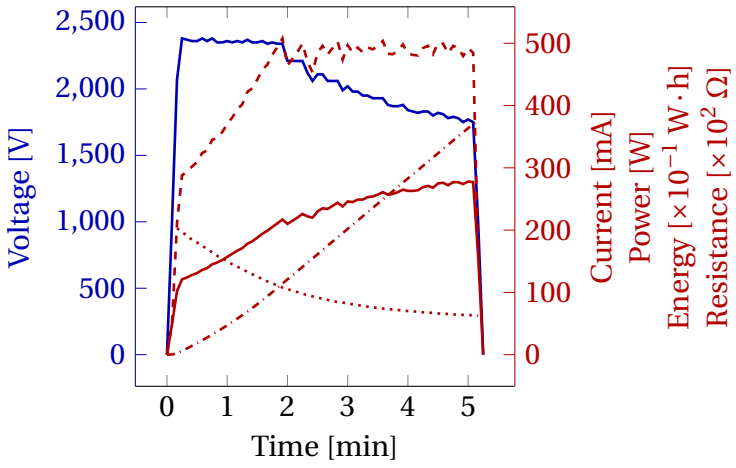

Figure A.27. SB1. The electrical data of SB1's heating, where: the blue solid line denotes the voltage and the red solid, dashed, dash-dotted, and dotted lines denote the electric current, the power, the energy, and the electrical resistance, respectively.

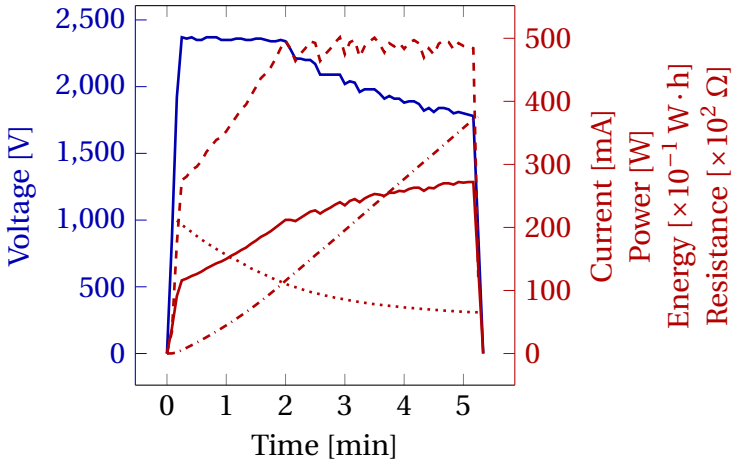

Figure A.28. SB2. The electrical data of SB2's heating, where: the blue solid line denotes the voltage and the red solid, dashed, dash-dotted, and dotted lines denote the electric current, the power, the energy, and the electrical resistance, respectively.

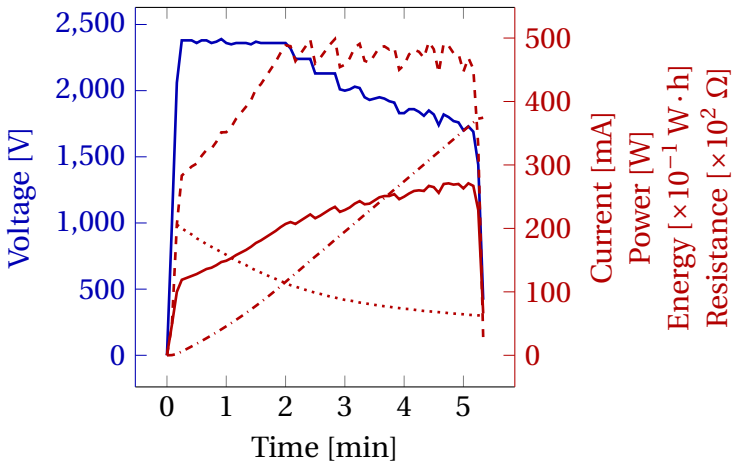

Figure A.29. SB3. The electrical data of SB3's heating, where: the blue solid line denotes the voltage and the red solid, dashed, dash-dotted, and dotted lines denote the electric current, the power, the energy, and the electrical resistance, respectively.

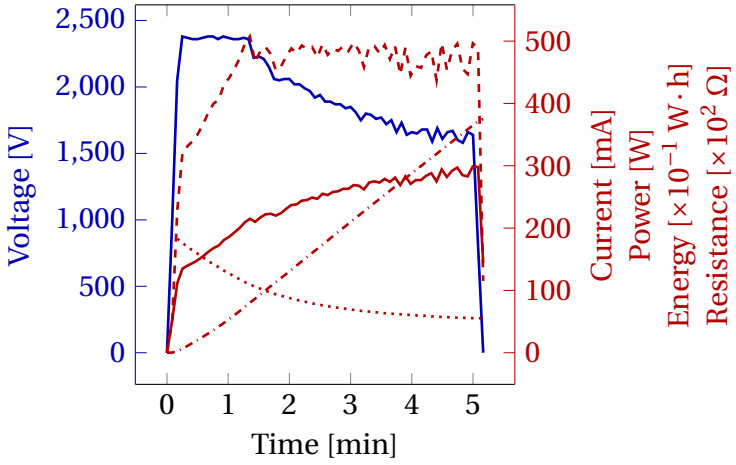

Figure A.30. SB4. The electrical data of SB4's heating, where: the blue solid line denotes the voltage and the red solid, dashed, dash-dotted, and dotted lines denote the electric current, the power, the energy, and the electrical resistance, respectively.

Heartwood boards (HB)

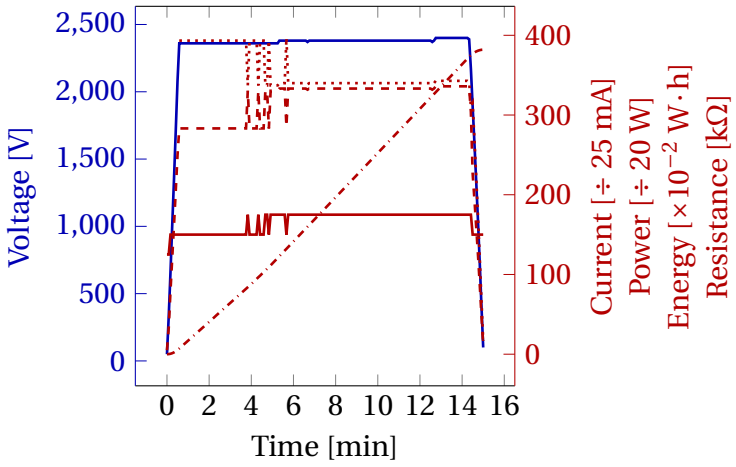

Figure A.31. HB1. The electrical data of HB1's heating, where: the blue solid line denotes the voltage and the red solid, dashed, dash-dotted, and dotted lines denote the electric current, the power, the energy, and the electrical resistance, respectively.

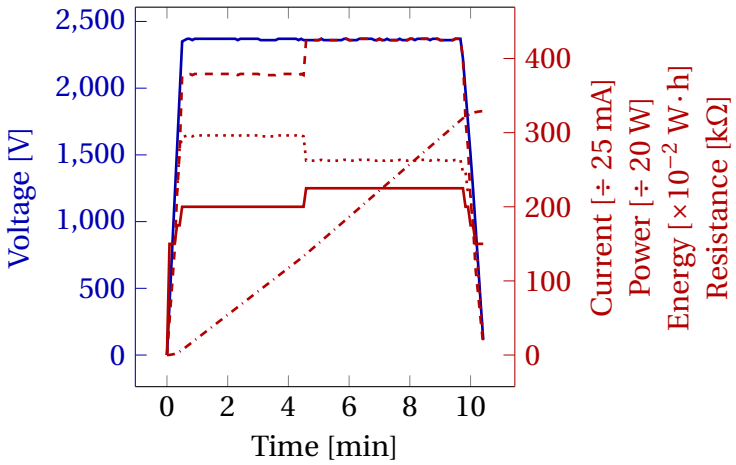

Figure A.32. HB2. The electrical data of HB2's heating, where: the blue solid line denotes the voltage and the red solid, dashed, dash-dotted, and dotted lines denote the electric current, the power, the energy, and the electrical resistance, respectively.

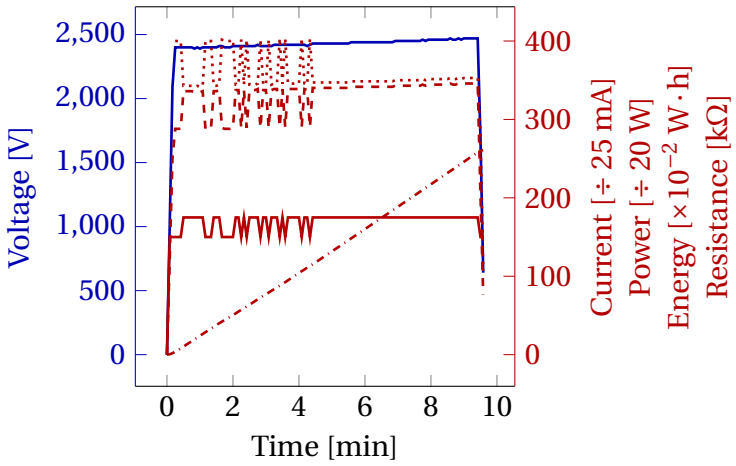

Figure A.33. HB3. The electrical data of HB3's heating, where: the blue solid line denotes the voltage and the red solid, dashed, dash-dotted, and dotted lines denote the electric current, the power, the energy, and the electrical resistance, respectively.

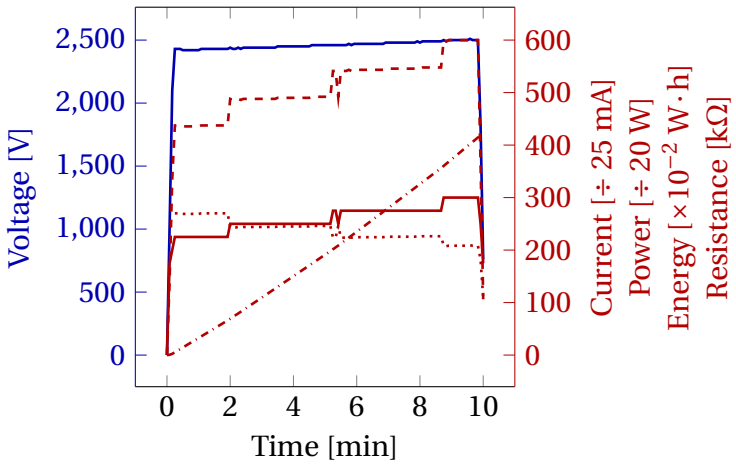

Figure A.34. HB4. The electrical data of HB4's heating, where: the blue solid line denotes the voltage and the red solid, dashed, dash-dotted, and dotted lines denote the electric current, the power, the energy, and the electrical resistance, respectively.

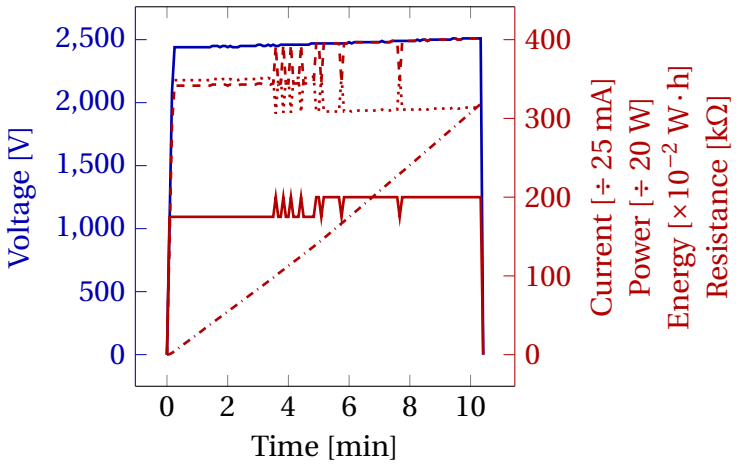

Figure A.35. HB5. The electrical data of HB5's heating, where: the blue solid line denotes the voltage and the red solid, dashed, dash-dotted, and dotted lines denote the electric current, the power, the energy, and the electrical resistance, respectively.

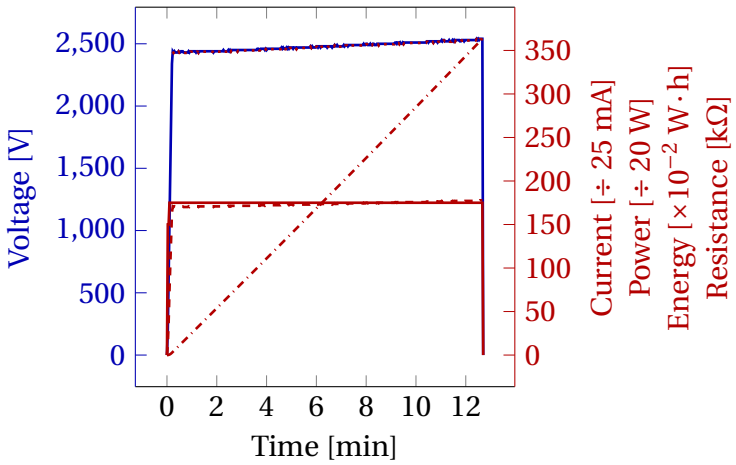

Figure A.36. HB6. The electrical data of HB6's heating, where: the blue solid line denotes the voltage and the red solid, dashed, dash-dotted, and dotted lines denote the electric current, the power, the energy, and the electrical resistance, respectively.

Appendix B

B.1 Blocks' Dimensions and Other Parameters

Table B.1. Dimensions of the blocks.

Blocks	A_1 [mm]	A_2 [mm]	A_3 [mm]	A_4 [mm]	B_1 [mm]	B_2 [mm]	B_3 [mm]	B_4 [mm]	C_1 [mm]	C_2 [mm]	C_3 [mm]	C_4 [mm]
B1	52.2	51.8	51.9	52.1	104.4	104.3	103.5	103.0	100.3	100.1	100.1	99.8
B2	52.4	52.0	49.7	52.2	104.2	104.5	104.2	103.7	95.0	95.2	94.9	95.1
B3	47.6	49.1	51.6	50.0	102.8	102.8	103.3	103.1	97.7	97.5	97.6	97.4
B4	49.8	51.9	53.7	51.9	103.0	103.6	103.0	103.3	97.3	97.5	97.8	97.5
B5	47.3	47.3	50.0	50.1	102.9	103.2	102.7	103.2	95.3	95.6	95.4	95.8
B6	51.2	51.3	54.1	54.7	103.1	102.8	103.1	102.9	95.9	96.1	96.1	95.7
B7	53.8	52.1	48.7	50.9	103.0	103.4	103.5	103.8	99.4	99.3	99.6	99.8
B8	48.1	49.6	52.0	51.1	103.3	103.1	103.7	103.7	99.3	99.1	99.4	99.5
B9	51.5	50.0	50.5	51.0	102.6	102.7	102.7	103.0	107.1	105.7	105.4	106.8
B10	50.2	52.4	51.6	50.7	102.4	102.8	102.9	102.8	105.4	103.9	104.1	105.3
B11	82.0	81.5	81.8	81.6	41.7	39.7	39.5	41.5	103.4	102.0	101.6	102.7
B12	81.4	81.1	81.4	80.8	40.8	41.3	41.8	41.1	102.7	101.5	101.1	102.3
B13	39.0	40.2	39.2	37.6	84.6	85.0	84.7	84.9	102.8	102.5	102.6	102.7
B14	38.8	39.0	39.7	40.0	83.9	84.4	83.7	84.3	102.8	102.8	102.4	102.6
B15	42.3	42.4	42.2	42.1	81.6	81.2	81.4	81.3	102.5	102.7	102.6	102.6
B17	34.4	37.3	37.8	35.2	83.9	84.2	83.6	84.0	102.8	102.6	102.4	102.8
B18	43.4	41.7	41.0	42.6	84.5	84.4	84.2	84.4	102.8	102.4	102.5	102.6
B19	39.0	38.8	39.2	39.5	81.5	81.3	81.3	80.9	102.2	102.4	102.7	102.4
B20	43.4	41.9	41.5	42.2	81.4	80.8	81.3	80.2	102.5	102.8	102.7	102.8
B21	36.3	36.1	35.3	35.9	83.7	84.4	83.8	84.1	103.0	102.7	102.5	102.8
B22	41.4	42.6	43.3	41.8	84.4	84.5	84.3	84.4	102.7	102.4	102.5	102.6

B23	38.3	39.3	39.4	39.9	81.6	81.2	81.5	81.1	102.6	102.8	102.9	102.6
B24	43.1	41.6	41.2	42.8	81.0	80.6	80.7	80.5	102.6	102.8	102.7	102.7
B25	39.0	35.9	35.7	38.2	85.1	82.6	84.5	84.6	102.6	102.4	102.4	102.6
B26	39.4	43.2	43.1	39.5	89.6	85.2	84.0	84.6	102.6	102.6	102.4	102.7
B27	34.6	35.0	36.7	36.8	83.7	84.1	83.7	84.2	103.0	102.9	102.6	102.8
B28	42.9	43.9	41.4	40.7	84.3	84.4	84.5	84.6	102.8	102.6	102.6	102.7
B29	41.4	41.6	40.4	40.9	89.4	89.7	90.0	90.5	106.5	106.4	106.4	106.6
B30	40.7	39.9	39.6	40.7	90.8	91.1	91.2	91.4	107.5	106.3	106.6	106.6
B31	40.7	39.9	40.0	41.2	91.1	90.6	90.5	82.0	106.6	106.5	106.5	106.6
B32	41.5	40.6	40.6	41.3	89.3	89.2	88.7	88.3	106.7	106.6	106.5	106.4
B33	62.6	60.9	60.7	62.6	89.4	89.6	89.5	89.8	106.4	106.5	106.6	106.6
B34	60.5	62.0	62.6	60.8	89.3	89.2	89.7	88.8	105.7	105.7	105.8	105.6
B35	28.9	29.4	30.5	29.0	89.2	89.2	89.2	89.4	106.2	106.4	106.5	106.5
B36	30.6	28.8	28.5	31.4	89.3	89.3	89.4	89.5	106.5	106.4	106.6	106.6
B37	28.8	29.0	29.5	28.9	89.1	89.2	89.4	89.4	106.4	106.9	106.7	106.3
B38	28.7	29.5	29.7	29.1	89.3	89.3	89.4	89.2	106.2	106.8	106.5	106.2
B39	47.4	47.0	47.0	48.0	102.6	102.8	102.8	102.8	94.8	94.6	94.6	94.5
B40	47.9	47.4	46.8	47.9	82.4	80.3	80.9	82.9	102.7	102.5	103.0	103.0
B41	47.6	47.5	47.5	47.5	83.2	83.7	83.6	82.9	103.3	103.5	103.0	103.2
B42	48.2	47.8	48.1	48.5	82.0	83.4	84.4	83.1	103.3	103.9	103.3	103.5
B43	48.3	48.2	48.7	48.4	60.8	61.2	61.5	61.7	92.9	92.4	93.5	94.1
B44	48.2	48.8	48.6	48.5	83.1	82.0	81.4	82.3	102.3	102.8	102.6	102.9
B45	51.6	52.1	51.7	51.6	104.4	104.2	104.6	104.3	101.0	101.1	101.1	101.1
B46	52.2	52.1	52.0	51.7	104.4	104.1	104.1	103.9	100.8	100.9	100.9	100.6
B47	51.7	52.1	52.3	52.3	104.1	104.2	104.0	103.9	101.6	101.4	101.6	101.6
B48	51.6	51.8	51.7	51.8	104.5	104.5	104.5	104.6	100.7	100.5	101.0	101.1
B49	56.4	54.5	54.5	56.6	101.0	101.0	101.2	100.6	107.2	107.2	107.0	107.0
B50	51.4	55.0	55.0	55.8	100.0	99.9	99.0	100.0	107.2	106.0	106.4	106.8
B51	56.6	55.0	55.0	56.2	100.0	100.2	101.0	101.0	108.0	107.1	107.1	107.7
B52	56.2	55.7	56.1	55.4	100.1	99.8	100.0	100.2	107.0	107.5	107.2	107.1

Table B.2. The position and depth of the holes, and the block type.

Blocks	D_1 [mm]	D_2 [mm]	D_3 [mm]	E [mm]	F [mm]	Type
B1	51.5	41.2	50.6	20	20	1
B2	30.1	50.4	49.8	20	10	1
B3	48.7	27.5	38.0	20	20	1
B4	39.7	50.2	29.1	10	15	1
B5	40.2	39.9	44.0	15	15	1
B6	48.9	39.6	30.9	10	10	1
B7	30.1	30.7	40.2	30	25	1
B8	50	40	50	30	10	1
B9	40.7	40.1	40.7	35	10	1
B10	39.8	40.4	40.9	35	10	1
B11	50	50	50	10	20	2
B12	50	50	50	10	20	2
B13	35.3	34.8	37.2	10	10	2
B14	35	35	35	10	10	2
B15	40	40	40	40	40	2
B17	35.9	35.9	35.7	20	30	2
B18	36	36	36.2	20	30	2
B19	40.3	40.3	40.2	20	20	2
B20	39.8	39.9	39.2	10	10	2
B21	35	35	35	25	15	2
B22	35	35	35	25	15	2
B23	40	40	40	20	20	2
B24	40	40	40	20	20	2
B25	40	40	40	30	15	2
B26	40.0	39.4	39.3	15	40	2

B27	39.2	39.3	39.7	20	20	2
B28	39.6	40.2	40.4	20	20	2
B29	36.5	37.3	37.4	20	35	2
B30	35.2	36.5	36.5	20	35	2
B31	41.4	41.6	40.7	30	10	2
B32	40.8	40.4	40.9	30	10	2
B33	49.0	49.4	50.4	25	28	2
B34	50.4	50.7	51.8	27	13	2
B35	40.0	39.9	39.9	30	15	2
B36	41.0	40.6	39.4	30	15	2
B37	40.2	40.1	40.0	30	15	2
B38	40.4	40.2	40.5	30	15	2
B39	51.2	51.5	49.9	26	13	1
B40	50.8	49.9	49.2	26	13	2
B41	49.7	50.0	50.6	26	13	2
B42	49.1	50.4	50.7	26	13	2
B43	41.0	40.4	40.1	25	25	2
B44	38.6	35.1	35.2	20	20	2
B45	64.7	65.5	65.2	20	20	1
B46	43.3	44.4	44.4	30	30	1
B47	37.8	38.3	38.7	15	25	1
B48	48.9	48.7	48.5	40	10	1
B49	48.0	47.9	43.5	20	20	1
B50	43.9	45.5	44.2	30	30	1
B51	45.0	46.2	45.3	15	25	1
B52	49	49	49	40	10	1

Table B.3. The experimental data: moisture content (X), basic density (ρ_s), initial temperature (T_i), water temperature (T_4), wood type and heating time.

Blocks	Heating Time [s]	T_i [°C]	T_4 [°C]	ρ_s [kg·m^{-3}]	X [kg·kg^{-1}]	Wood Type[a]
Block 1	8754	9.0	60.0	398.0	1.46	SW
Block 2	10582	8.7	60.1	397.3	1.57	SW
Block 3	9687	2.9	59.9	372.1	1.38	SW
Block 4	8774	3.0	70.0	413.4	1.58	SW
Block 5	7154	4.9	70.0	414.9	1.51	SW
Block 6	7593	3.1	59.9	375.9	1.31	SW
Block 7	8110	3.7	50.0	413.9	1.60	SW
Block 8	7258	2.7	50.0	375.7	1.35	SW
Block 9	7900	5.1	59.9	414.9	1.09	SW
Block 10	7193	3.6	59.9	376.7	1.04	SW
Block 11	4192	16.8	59.9	390.2	0.40	HW
Block 12	4161	17.9	60.0	399.7	0.40	HW
Block 13	3488	14.4	69.8	440.6	0.37	HW
Block 14	3751	14.6	69.6	420.3	0.41	HW
Block 15	3177	16.1	69.7	411.2	0.42	HW
Block 17	3262	14.4	69.8	378.2	0.42	HW
Block 18	3336	15.1	69.8	365.5	0.46	HW
Block 19	3317	12.4	59.8	418.5	0.39	HW
Block 20	3879	13.7	59.9	396.2	0.40	HW
Block 21	6006	14.2	59.9	384.6	0.41	HW
Block 22	3618	15.3	60.0	368.8	0.44	HW
Block 23	4165	16.3	60.0	350.8	0.54	HW
Block 24	2964	18.7	64.8	401.8	0.33	HW
Block 25	3618	16.4	50.0	359.5	0.45	HW
Block 26	4451	18.0	50.0	378.6	0.40	HW
Block 27	4032	15.1	69.8	385.0	0.43	HW

Block 28	5621	16.8	69.9	376.5	0.43	HW
Block 29	5832	13.5	69.9	401.7	1.55	SW
Block 30	6539	4.7	69.9	416.9	1.49	SW
Block 31	6358	12.7	79.4	419.7	1.55	SW
Block 32	5417	17.6	69.8	407.9	1.52	SW
Block 33	8725	3.1	69.9	396.9	1.49	SW
Block 34	9226	3.3	69.8	398.3	1.58	SW
Block 35	3382	11.8	59.8	394.0	1.52	SW
Block 36	3685	15.7	59.9	399.1	1.56	SW
Block 37	7901	14.1	59.9	402.8	1.54	SW
Block 38	3960	4.6	59.9	404.0	1.61	SW
Block 39	6196	14.8	59.9	369.8	1.78	SW
Block 40	6889	18.8	60.0	368.4	1.73	SW
Block 41	8522	2.7	59.9	387.9	1.75	SW
Block 42	5690	3.0	59.9	371.2	1.48	SW
Block 43	5393	12.3	70.0	397.6	1.48	SW
Block 44	6010	3.1	69.7	397.9	1.70	SW
Block 45	7226	2.5	60.0	420.5	1.64	SW
Block 46	7224	2.4	60.0	418.9	1.66	SW
Block 47	7101	2.1	59.9	424.9	1.63	SW
Block 48	7274	3.5	70.0	416.7	1.60	SW
Block 49	5346	5.2	70.1	337.0	0.65	HW
Block 50	5480	4.3	60.0	323.5	0.50	HW
Block 51	6335	3.8	60.1	419.0	0.47	HW
Block 52	5352	2.6	59.8	341.8	0.63	HW

[a] SW and HW denote sapwood and heartwood, respectively.

Table B.4. Coordinates of Temperature Probes.

Blocks	T_1[a]			T_2[a]			T_3[a]		
	x_1	y_1	z_1	x_2	y_2	z_2	x_3	y_3	z_3
Block 1	20.0	52.0	84.0	26.0	26.0	26.0	48.5	58.8	49.4
Block 2	20.0	52.0	94.0	26.0	26.0	26.0	64.9	44.6	45.2
Block 3	20.0	51.6	83.2	25.4	25.4	25.4	48.9	70.0	59.6
Block 4	10.0	51.7	88.3	26.4	26.4	26.4	57.8	47.3	68.4
Block 5	15.0	51.5	88.1	25.0	25.0	25.0	55.3	55.6	51.5
Block 6	10.0	51.5	93.0	27.2	27.2	27.2	47.1	56.4	65.0
Block 7	30.0	51.8	78.7	26.5	26.5	26.5	69.4	68.8	59.3
Block 8	30.0	51.8	93.7	25.8	25.8	25.8	49.3	59.3	49.3
Block 9	35.0	51.4	92.8	25.4	25.4	25.4	65.6	66.2	65.6
Block 10	35.0	51.4	92.9	25.7	25.7	25.7	64.8	64.3	63.7
Block 11	31.8	31.8	31.8	20.4	20.4	20.4	92.4	51.2	20.0
Block 12	31.2	31.2	31.2	20.7	20.7	20.7	91.9	51.0	20.0
Block 13	49.5	50.1	47.7	19.8	19.8	19.8	92.6	51.3	10.0
Block 14	49.2	49.2	49.2	19.9	19.9	19.9	92.7	51.3	10.0
Block 15	41.4	41.4	41.4	21.2	21.2	21.2	62.6	51.3	40.0
Block 17	48.2	48.1	48.4	18.3	18.3	18.3	82.6	51.3	30.0
Block 18	48.4	48.5	48.3	21.3	21.3	21.3	82.6	51.3	30.0
Block 19	41.1	41.1	41.2	19.7	19.7	19.7	82.4	51.2	20.0
Block 20	41.3	41.2	41.9	21.3	21.3	21.3	92.7	51.4	10.0
Block 21	49.0	49.0	49.0	18.1	18.1	18.1	77.7	51.4	15.0
Block 22	49.4	49.4	49.4	21.3	21.3	21.3	77.6	51.3	15.0
Block 23	41.4	41.4	41.4	19.8	19.8	19.8	82.7	51.4	20.0
Block 24	40.8	40.8	40.8	21.2	21.2	21.2	82.7	51.3	20.0
Block 25	44.5	44.5	44.5	18.7	18.7	18.7	72.5	51.3	15.0
Block 26	44.9	45.5	45.5	20.7	20.7	20.7	72.6	51.3	15.0
Block 27	44.8	44.7	44.3	18.4	18.4	18.4	82.8	51.4	20.0

Block 28	44.9	44.4	44.1	21.7	21.7	21.7	82.7	51.4	20.0
Block 29	53.8	52.9	52.9	20.7	20.7	20.7	86.5	53.2	35.0
Block 30	56.1	54.8	54.8	20.2	20.2	20.2	86.8	53.4	35.0
Block 31	49.5	49.3	50.2	20.3	20.3	20.3	76.5	53.3	10.0
Block 32	48.5	48.9	48.3	20.5	20.5	20.5	76.6	53.3	10.0
Block 33	40.6	40.3	39.3	30.9	30.9	30.9	81.5	53.3	28.0
Block 34	38.9	38.6	37.4	30.9	30.9	30.9	79.2	52.9	13.0
Block 35	49.4	49.5	49.5	14.9	14.9	14.9	76.4	53.2	15.0
Block 36	48.5	48.9	50.0	15.0	15.0	15.0	76.5	53.3	15.0
Block 37	49.2	49.3	49.3	14.6	14.6	14.6	76.5	53.3	15.0
Block 38	49.0	49.1	48.8	14.7	14.7	14.7	76.4	53.2	15.0
Block 39	25.5	51.4	90.3	23.7	23.7	23.7	43.5	43.1	44.7
Block 40	31.1	32.0	32.8	23.8	23.8	23.8	77.3	51.4	12.5
Block 41	33.8	33.4	32.8	23.8	23.8	23.8	77.2	51.6	13.0
Block 42	34.7	33.3	33.0	24.2	24.2	24.2	77.5	51.7	13.0
Block 43	20.6	21.2	21.5	24.3	24.3	24.3	68.2	46.6	25.0
Block 44	44.0	47.5	47.4	24.3	24.3	24.3	82.6	51.3	20.0
Block 45	20.0	52.2	84.5	25.9	25.9	25.9	36.4	35.6	35.9
Block 46	30.0	52.1	74.3	26.1	26.1	26.1	57.5	56.4	56.4
Block 47	15.0	52.1	79.2	26.2	26.2	26.2	63.8	63.3	62.9
Block 48	40.0	52.3	94.6	25.9	25.9	25.9	51.9	52.1	52.3
Block 49	20.0	50.5	81.0	27.8	27.8	27.8	59.1	59.2	63.6
Block 50	30.0	50.0	70.0	27.7	27.7	27.7	62.7	61.1	62.4
Block 51	15.0	50.5	76.0	27.9	27.9	27.9	62.5	61.3	62.2
Block 52	40.0	50.1	90.1	28.0	28.0	28.0	58.2	58.2	58.2

[a] All values are in millimetres.

B.2 Reference Errors

Table B.5. The reference error: The difference between the experimental temperatures and estimated by the CFD models based on Pang et al.'s and Nijdam et al.'s equations.

Blocks	Pang et al.			Nijdam et al.		
	T_1 [°C]	T_2 [°C]	T_3 [°C]	T_1 [°C]	T_2 [°C]	T_3 [°C]
Blocks 1	-3.7	-5.5	-3.6	2.6	2.0	2.6
Blocks 2	3.6	-6.2	-5.7	6.6	1.7	-2.4
Blocks 3	-4.1	4.1	-4.8	3.1	9.1	3.0
Blocks 4	-2.2	-0.7	1.6	4.6	8.3	6.7
Blocks 5	3.3	-2.2	-0.7	8.5	6.2	5.6
Blocks 6	-3.9	-2.4	-4.9	2.0	6.0	-1.3
Blocks 7	3.6	2.8	-0.7	10.6	9.4	7.1
Blocks 8	-5.3	-5.0	-4.3	2.1	2.7	0.9
Blocks 9	1.9	2.7	-1.3	8.8	8.8	3.0
Blocks 10	-3.8	-3.2	-7.3	4.6	4.8	-3.4
Blocks 11	6.5	-3.2	3.5	11.1	5.8	10.5
Blocks 12	6.1	-4.8	1.2	10.5	3.2	8.1
Blocks 13	4.7	2.1	11.4	10.9	9.6	17.8
Blocks 14	7.9	1.5	11.7	13.7	10.7	17.6
Blocks 15	2.2	2.4	2.0	11.6	11.7	11.4
Blocks 17	5.7	1.1	3.4	14.6	9.2	12.6
Blocks 18	6.2	2.3	3.1	14.3	10.9	12.1
Blocks 19	2.8	-3.5	2.5	10.5	5.3	10.6
Blocks 20	5.2	-2.4	4.8	10.1	6.8	9.8
Blocks 21	-1.2	-2.9	2.3	8.1	6.2	9.5
Blocks 22	1.3	-1.8	4.4	-8.9	-12.0	-3.9
Blocks 23	-0.8	-3.0	3.6	5.8	4.1	9.5
Blocks 24	6.9	2.0	3.3	14.9	10.9	11.9
Blocks 25	-1.7	-1.9	2.9	4.8	4.1	7.6
Blocks 26	-0.5	-1.9	4.0	6.1	4.3	8.2

Blocks 27	4.9	-2.0	3.3	13.6	8.3	12.2
Blocks 28	8.1	-3.0	6.5	16.0	8.9	14.6
Blocks 29	7.3	3.1	-0.6	13.6	9.0	5.8
Blocks 30	1.8	-4.3	-2.3	8.5	3.4	6.0
Blocks 31	1.7	-3.1	2.8	7.6	3.1	6.7
Blocks 32	1.1	-2.6	2.0	6.0	2.9	4.9
Blocks 33	4.4	-2.3	1.4	12.1	7.5	9.7
Blocks 34	10.3	1.3	1.4	18.4	10.2	5.2
Blocks 35	-2.7	-5.2	-3.6	3.1	1.2	3.5
Blocks 36	2.2	0.5	-0.6	7.3	5.1	5.2
Blocks 37	-2.3	-3.1	-1.7	3.2	2.6	4.8
Blocks 38	2.1	-3.2	-2.2	8.7	3.8	6.1
Blocks 39	-1.9	-1.9	-3.7	3.8	3.7	0.6
Blocks 40	-2.1	-1.9	-0.9	3.0	3.0	2.6
Blocks 41	0.9	1.4	-2.3	8.5	9.3	3.8
Blocks 42	1.1	-1.7	-4.3	7.5	6.5	1.4
Blocks 43	-3.0	-5.1	-4.0	4.3	1.9	3.7
Blocks 44	2.0	2.4	1.3	8.6	10.9	7.8
Blocks 45	-2.0	-2.0	-3.7	6.3	6.9	4.6
Blocks 46	0.9	0.5	-1.0	8.5	8.7	8.2
Blocks 47	-1.3	1.5	1.2	5.5	9.9	9.9
Blocks 48	-3.5	-2.2	-2.3	6.4	7.0	2.3
Blocks 49	-3.1	5.6	4.0	7.7	14.8	11.4
Blocks 50	4.7	1.6	0.9	13.4	10.5	9.2
Blocks 51	2.8	-2.2	-2.8	10.2	8.2	6.6
Blocks 52	3.4	4.1	0.8	12.1	13.0	5.1

Appendix C

C.1 Electrical Conductivity of Other Species

Electrical conductivity of *E. nitens*, *E. globoidea*, *P. menziesii*, and *S. sempervirens*, were studied. *E. globoidea* was grown in Marlborough, New Zealand, while the other species were grown in Owen River forest. Diameters of the logs, out of which samples were cut, was less than 200 mm, and the logs' lengths were around 1.5 m long, except for the *E. globoidea* samples that had been cut to 100 mm length. Once being cut, the logs from Owen River forest were delivered within a couple of days, but the offcuts of *E. globoidea* were delivered within 2-3 weeks. Once delivered to the university, all the samples were stored inside a freezer at -20°C, before being cut into cubes as described in Chapter 5. However, unlike the longer logs, the short *E. globoidea* sections were cut with a band saw. This method was less accurate in producing cubes of uniform dimension due to the lack of stability of the cutting blade that led to many rejected cubes. As a result, the number of samples for *E. globoidea* is the lowest among the tested specimens (Table C.1). Furthermore,

Table C.1. The basic density (BD) and moisture content (MC) of *E. nitens*, *E. globoidea*, *P. menziesii* and *S. sempervirens*.

Species	Wood Types	BD [$kg \cdot m^{-3}$]	MC [%]	Number of Samples [a] (Directions)
P. menziesii	Heartwood	407±13	48.4±0.9	8(L)
P. menziesii	Sapwood	449±22	143±13	12(L) + 8(R) + 8(T)
E. globoidea	Heartwood	668±34	79±7	7(L)
E. globoidea	Sapwood	675±92	84±24	4(L)
E. nitens	Sapwood	416±11	132±15	8(L)
S. sempervirens	Heartwood	385±16	183±8	8(L)
S. sempervirens	Sapwood	310±13	256±14	8(L) + 8(R) + 8(T)
S. sempervirens	Transitional	316±5	145±5	8(L)

[a] L, R, and T denote the longitudinal, radial, and tangential directions, respectively.

the blade of the band saw left a rough conducting surface, to which the gold leaves were poorly attached. Electrical conductivity was measured every 10°C from room temperature of around 23°C to 90°C, following the method described in Chapter 5. *E. globoidea*, *P. menziesii*, and *S. sempervirens* had heartwood sections (Figure C.1); electrical conductivity of those heartwood

zones were determined in this study. However, heartwood of *E. nitens* was unobservable by visual means and hence it was considered undeveloped. In addition, the *S. sempervirens* log had a transitional zone, the electrical conductivity of which was also assessed. Due to the relatively small size of the heartwood and transitional zones, the samples from those zones were tested only in the longitudinal direction. The moisture content and basic density of all samples based on wood type and species are summarised in Table C.1.

Results and Discussion

All the samples showed a positive correlation between electrical conductivity and temperature (Figure C.2). The sapwood was the most conductive zone, where the highest electrical conductivity was in the longitudinal direction. On the other hand, the heartwood of each species was the least conductive. The difference between heartwood and sapwood electrical conductivities was more pronounced in *S. sempervirens* and *P. menziesii*, where high electrical conductivity of sapwood can be explained by the higher moisture content. In *S. sempervirens* and *P. menziesii*, at saturation, most of sapwood's cavities are filled with sap. Connected with each other, these cavities conduct electric current and make sapwood more conductive than heartwood. Cavities of heartwood contain less sap and much more air and vapour. The latter are less conductive than sap and hence they create obstacles for conduction of electrical charge, making the heartwood less conductive. Therefore, it can be concluded that the fewer the cavities filled with air and vapour, the higher the electrical conductivity of wood.

P. menziesii's heartwood, with the moisture content of 48.4±0.9%, was relatively non-conductive. Its mean electrical conductivity was around 0.001 $S \cdot m^{-1}$ at 24.6°C and increased by a factor of 3.5 at 90°C. Sapwood electrical conductivity increased by a factor of 3.7, rising from about 0.019 $S \cdot m^{-1}$ at room temperature to 0.07 $S \cdot m^{-1}$ at 90°C. Thus, the ratio of sapwood's electrical conductivity to heartwood's conductivity stayed constant during the heating and was approximately 20.

In *S. sempervirens*, this ratio was close to 2, as heartwood was nearly as electrically conductive as sapwood. According to Stamm (1929), electrical conductivity of *S. sempervirens* heartwood and sapwood are comparable, and at near room temperature and at 180% moisture content, they are around 0.015 $S \cdot m^{-1}$. In this research, the mean electrical conductivity of heartwood was around 0.014 $S \cdot m^{-1}$ at 183%; however, its sapwood's electrical conductivity was approximately

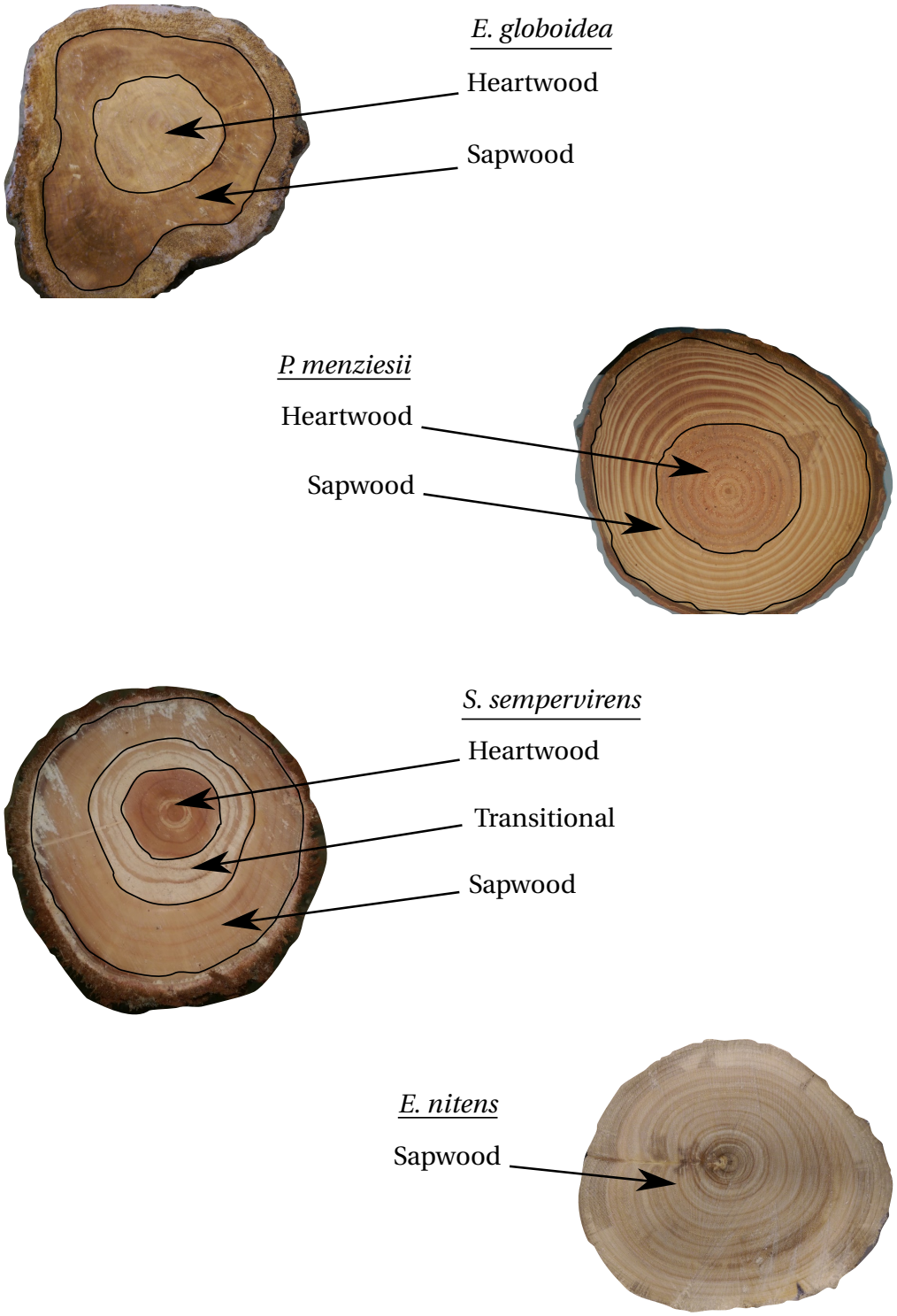

Figure C.1. The cross sections of *E. globoidea, P. menziesii, S. sempervirens,* and *E. nitens. Note:* The black contour lines show the actual wood zones.

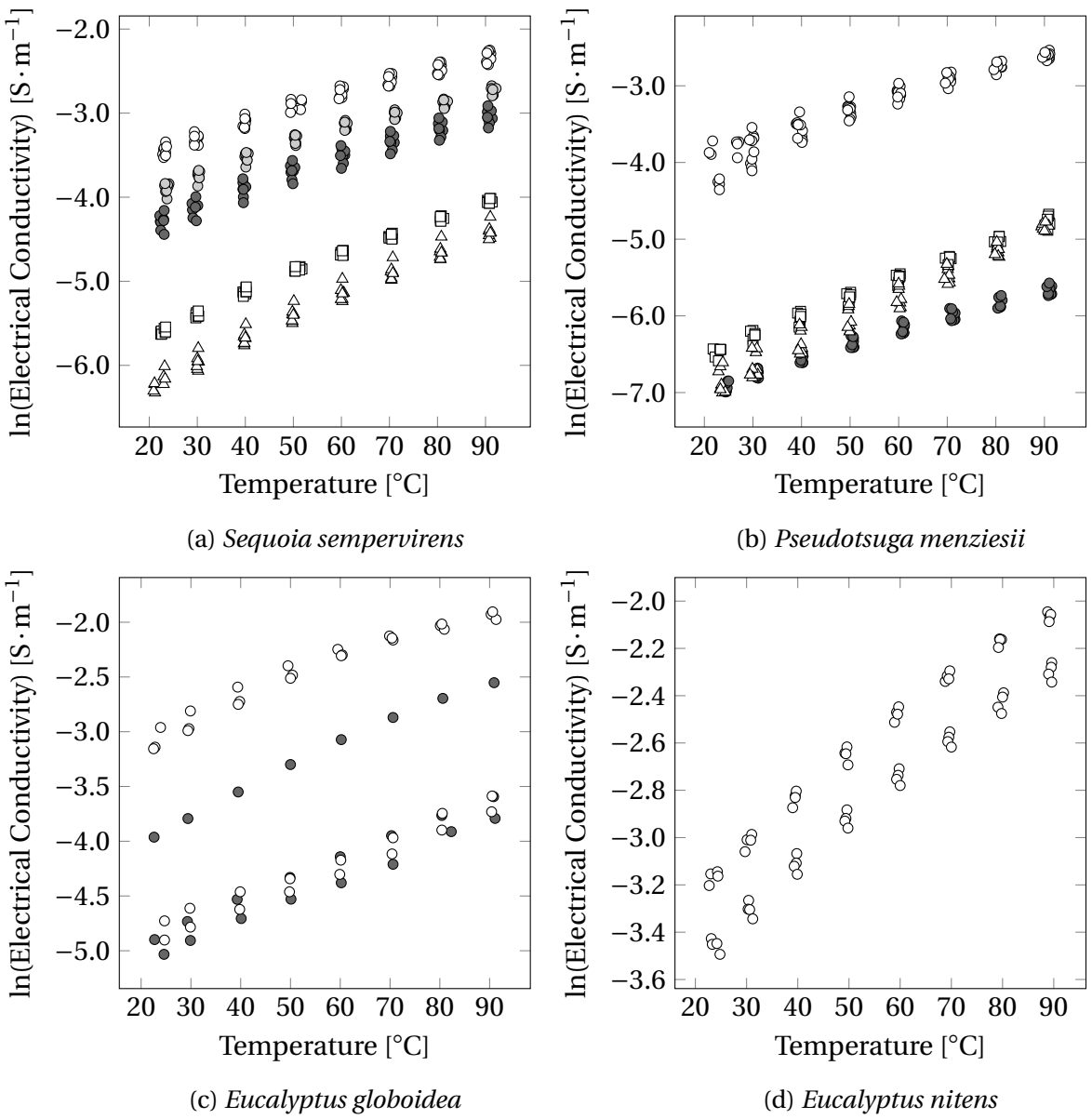

(a) *Sequoia sempervirens*

(b) *Pseudotsuga menziesii*

(c) *Eucalyptus globoidea*

(d) *Eucalyptus nitens*

Figure C.2. The effect of temperature on the natural logarithm of the electrical conductivity of (a) *S. sempervirens*, (b) *P. menziesii*, (c) *E. globoidea*, and (d) *E. nitens*. The white, light grey, and dark grey colours denote the sapwood, transitional, and heartwood zones, respectively. The circular, square, and triangular scatter represent the longitudinal, radial, and tangential directions, respectively. *Note:* The electrical conductivity measurements affected by the electrode corrosion are not included in this graph.

0.032 $S \cdot m^{-1}$, at 256% moisture content. Furthermore, electrical conductivity of the transitional zone was higher than the heartwood. At room temperature, it was 0.020 $S \cdot m^{-1}$ despite the moisture content being around 145%. Thus, the results indicate there is an additional parameter (or parameters) in *S. sempervirens's* transitional zone that affects electrical conductivity, making it more conductive than heartwood with a higher moisture content. Future research needs to be done involving different *S. sempervirens* trees of various ages to identify that parameter.

The heartwood of *E. globoidea* was relatively conductive. The ratio of sapwood's mean electrical

conductivity to heartwood's was around 7 at room temperature and approximately 6 at around 90°C. Thus, despite the comparable moisture contents of the sapwood and heartwood, the mechanism of electrical conductivity in these zones is different. Additionally, some drop of electrical conductivity was observed while testing *E. globoidea*, which happened due to the corrosion of the electrodes, described in Chapter 5. In general, the data showed high variation in electrical conductivity. That might be linked to drying of the samples prior to testing. *E. globoidea* was delivered as relatively short offcuts; these offcuts could have dried much faster than the logs of other specimens. Therefore, future study is required, with a larger data set based on samples that are cut from longer, freshly sawn logs.

The sapwood of *E. nitens*, with an average moisture content of 132%, showed the mean electrical conductivity of 0.037 $S \cdot m^{-1}$ at room temperature and 0.114 $S \cdot m^{-1}$ at around 90°C. In Figure C.2d, two groups of data were observed, where one of them was noticeably more conductive than the other. The variation was potentially caused by formation of heartwood, which began to form in the log (around 12 years old) but was invisible during the visual inspection. White et al. (1998) detected heartwood formation in 6 year old *E. nitens* by measuring pH, using dimethyl yellow. According to Walker (2006), the green moisture contents of *E. nitens*' sapwood and heartwood are 125% and 115%, respectively. The mean moisture content of four *E. nitens* samples, with lower electrical conductivity, was 118%, while the mean moisture content of the other four samples was 146.5% (Figure C.3). To check this hypothesis, samples from an older tree of *E. nitens*, with the fully developed heartwood zone, need to be tested in the future research.

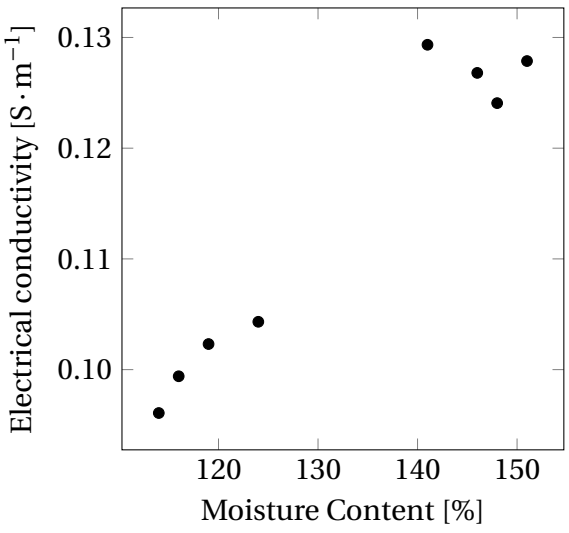

Figure C.3. The effect of moisture content on *E. nitens* sapwood's electrical conductivity at 90°C.

C.2 Conductivity of Dry Patches Inside *P. radiata*

Many dry patches were found in a log cut from a *P. radiata* tree from Owen River forest. Nine cubes, with a different extent of dryness, were selected to determined moisture content (Figure C.4). The moisture content and basic density of each cube were measured and summarized

Figure C.4. The dry patches in the cubes, which were cut from a *P. radiata* tree from Owen River forest. The four cubes on the right were used to determine electrical conductivity.

in Table C.2. On a three centimetre scale, the moisture content within the log varied from almost 200 to 30%. Electrical conductivity of the selected cubes was measured from 20 to 90°C (Figure C.5). The electrical conductivity of Cube 1, with 195% moisture content, was similar to those observed in *Sets 1-3* (Section 5.3.2). At about room temperature, the conductivity of Cube 9, with 30% moisture content, was 0.001 $S \cdot m^{-1}$. This is similar to the electrical conductivity of the heartwood boards (0.001-0.002 $S \cdot m^{-1}$), described in Section 3.3.2. The conductivities of Cubes 4 and 7 were comparable and were higher than that of Cube 9. Hence, the larger the size of dry patches, the lower the conductivity.

Table C.2. Moisture content and basic density of the *P. radiata* cubes with the dry patches.

Cube No.	MC [%]	BD [kg·m^{-3}]
Cube 1	195	358
Cube 2	198	342
Cube 3	153	358
Cube 4	115	364
Cube 5	107	363
Cube 6	99	365
Cube 7	96	359
Cube 8	50	363
Cube 9	30	364

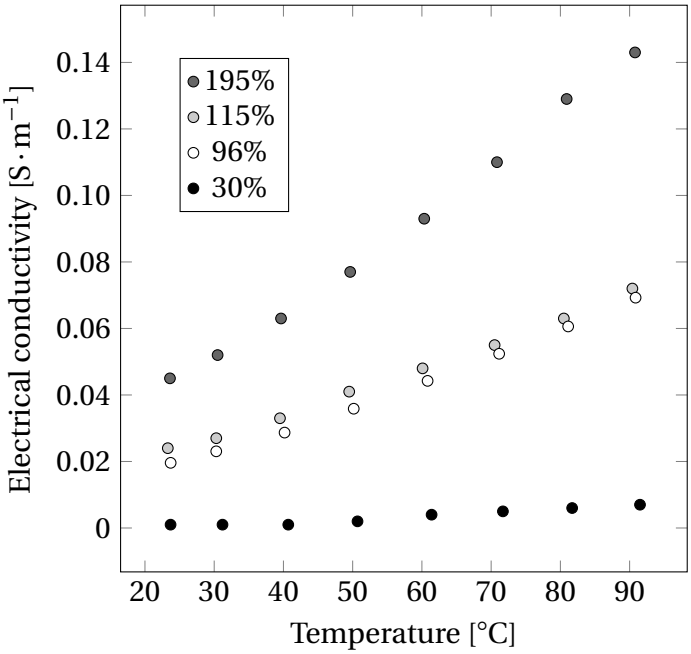

Figure C.5. Effect of temperature on electrical conductivity of *P. radiata* cubes, with dry patches, in the longitudinal direction.

These results showed the importance of treating green logs by the Joule heating effect within a relatively short time after a harvest, as large dry patches inside a log will cause non-uniform Joule heating, extending the duration of equilibration (relaxation). The process of heating industrial logs, relaxation, and excitation is described in Chapter 7.

C.3 Importance of Low Contact Resistance

Electrical conductivity can be derived from Equation 2.8 as:

$$\sigma = \frac{l}{RA}. \tag{C.1}$$

To calculate it, the cross-sectional area of a conductor (A), through which an electric current flows, must be known. The cross-sectional area depends on the shape and the structure of the conductor. The latter can affect the conduction of electric current, reducing the active conducting area of the actual cross-sectional surface. Figure C.6 shows a schematic diagram of two extreme cases: a good isotropic conductor and a poor anisotropic conductor, both with two electrode arrangements, a point contact and a surface contact. At the point contact in a good isotropic conductor (Figure C.6a), an electric current almost instantaneously spreads over the contact surface and flows through the conductor's volume due to the high isotropic electrical conductivity. In this case, the active conducting area is equal to the actual cross-sectional area of the conductor, and a fully-covered face contact does not significantly improve the active conducting area of a good isotropic conductor (Figure C.6b). Such behaviour is common to metals such as copper which require a single contact point to conduct the current through the whole volume. On the other hand, in the point-contact case in a poorly conducting anisotropic material, an electric current flows preferentially in the most conductive direction. Therefore, in Figure C.6c, where the conductivity in the Y direction is significantly lower than in the X direction, the electric current will not spread over the contact surface, reducing the active conducting area. A surface contact electrode can enlarge the conducting area if each point on the conductor's surface is attached to the electrode as shown in Figure C.6d.

Contact between two materials (a conductor and electrodes) may not be ideal, as a contact interface contains voids. The size of the voids depends on the roughness of the contacting materials. Filled with air, these voids increase contact resistance and hence measurements underestimate the electrical conductivity of an anisotropic conductor. To reduce the error, the contact surface needs to be improved using a material that will fill voids and will conduct electric current to each point on a contact surface. The higher the conductivity of this material, the lower the error of measured conductivity.

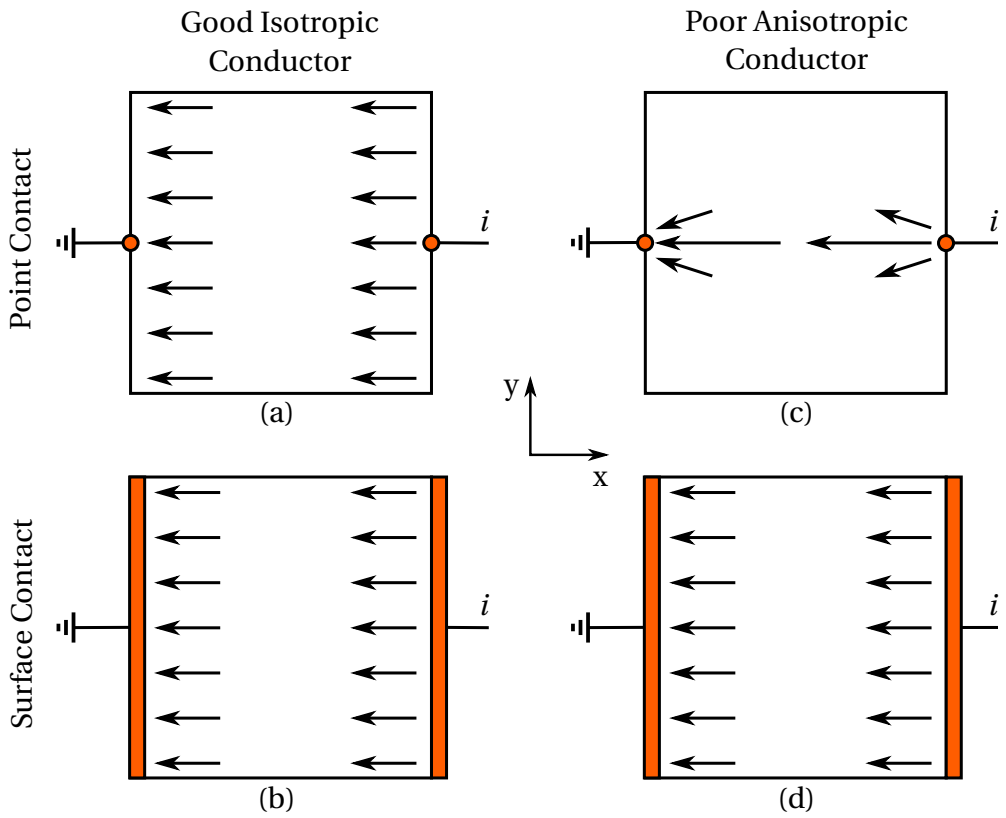

Figure C.6. The schematic diagram of the conduction of electric current (i) in good isotropic and poor anisotropic conductors, with point and surface contacts. *Note*: The length of arrows schematically shows the magnitude and direction of the electric current. Electrical conductivity of the anisotropic conductor in the Y direction was assumed to be significantly lower than in the X direction.

In this study, the effect of a bad contact is demonstrated on resistors of 50, 330, 550, and 3300 Ω soldered to two copper plates as shown in Figure C.7a. The plates played the role of a

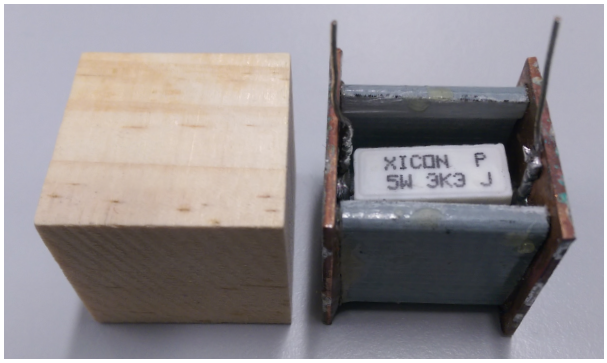

(a)

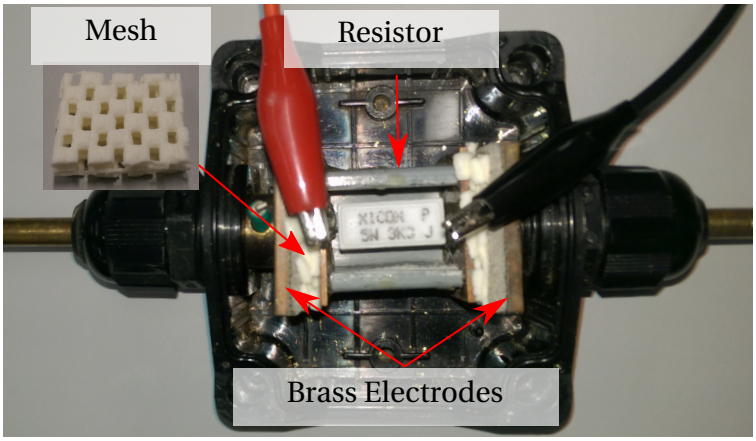

(b)

Figure C.7. The contact resistance testing: (a) the resistor of 3300 Ω, soldered to the copper plates, imitated the shape of the wood cube (the fibreglass walls between the copper plates provided a electrically insulated structural support), and (b) the complete assembly with the crocodile clips connected to the point contacts between the resistor and the copper plates.

surface contact similar to one face of a *P. radiata* cube. However, unlike a cube of wood, the point contacts between the resistor and the internal sides of the copper plates allowed measurement of the voltage across the resistor, using crocodile clips connected to pins as shown in Figure C.7b. The resistor, with the soldered plates, was inserted between the brass electrodes covered with a silver foam. An insulating mesh, consisting of three layers of a closed cell foam with holes, was inserted into the space between the contacting surfaces. The holes in the layers were aligned, imitating roughness of a contact surface. Three layers of the mesh prevented a direct contact between the resistor and the silver foam, representing a case of very poor contact. To improve the contact, those holes in the mesh were filled with a conductive gel.

Using the resistor of 330 Ω, two cases were studied: with low conductive and high conductive gels. In the first experiment, the holes in the mesh were filled with a low conductive gel, the conductivity of which was around 0.4 $S \cdot m^{-1}$. A sinusoidal voltage of 50 V at 400 Hz was applied to the brass electrodes by an electric source, Chroma 61504. Three parameters were recorded: electric current flowing through the whole assembly, the voltage across the resistor and the voltage across the whole assembly. Knowing these parameters, the resistance of the assembly and of the resistor was calculated. The measurement was repeated five times. Thereafter, the experiment was performed with the high conductive gel, saturated with sodium chloride. The obtained resistances were compared by calculating an error as:

$$Error = \frac{|R_a - R_r|}{R_r} \cdot 100\%, \tag{C.2}$$

where R_a is the resistance of the assembly, and R_r is the resistance of the resistor (Table C.3). The

Table C.3. The mean resistance values measured in the contact resistance test.

Resistors	Gel[a]	R_a [Ω]	R_r [Ω]	Errors [%]
50	HC	57.97 (SD = 0.04)	51.9 (SD = 0.1)	11.6
330	LC	895 (SD = 35)	325 (SD = 1)	175.9
330	HC	352 (SD = 1)	328.3 (SD = 0.5)	7.3
550	HC	574.5 (SD = 0.3)	556.2 (SD = 0.1)	3.3
3300	HC	3268 (SD = 2)	3230 (SD = 3)	1.2

[a] LC and HC denote the low conductive and high conductive gels, respectively.
[b] The indices a and r indicate the whole assembly and the resistor, respectively.

resistance of the assembly dropped from 895 to 352 Ω, once the low conductive gel was replaced by the high conductive gel. The gels affected the precision of measurements; the standard deviation decreased from 35 Ω, 4% of the measured value, to 1 Ω, 0.3% of the measured value, using the low and high conductive gels, respectively. The high conductive gel reduced the contact resistance and decreased the error from 176% to 7.3%. In addition, using the high conductive gel, it was found that the higher the resistance of the resistor, the less significant the contact resistance. The errors for the resistors of 50, 550, and 3300 Ω were 11.5, 3.2 and 1.2%, respectively. Thus, contact resistance significantly affects short samples with a large cross-sectional area such as cubes rather than long samples with a relatively small cross-sectional area such as export size logs.

Thereafter, the effect of temperature on contact resistance was assessed. The 50 Ω resistor

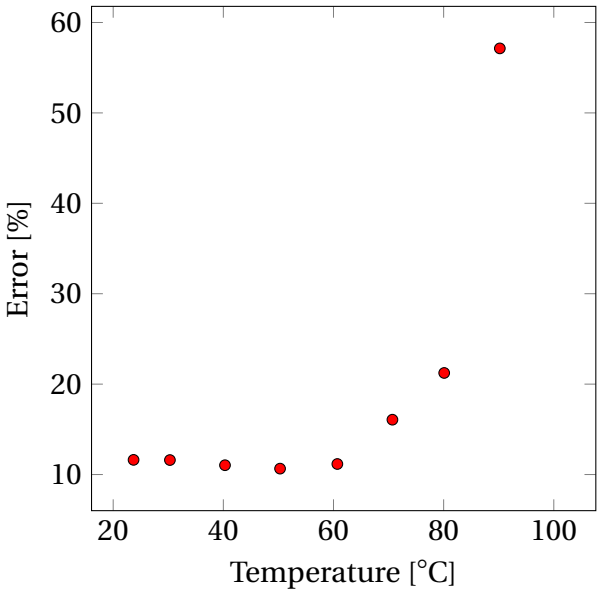

Figure C.8. The effect of temperature on the error of resistance measurement.

was chosen for this test; as it showed the highest effect of the contact resistance. The plastic box with the resistor was left inside an oven. To measure the voltage across the resistor, the box's lid was removed. The temperature inside the oven increased every 10°C from room temperature, about 23°C, up to 90°C. Figure C.8 shows the effect of temperature on the error, calculated using equation C.2. The initial error of 11.6%, measured at 23°C, slightly decreased to 10.6%, at 50°C. However, the error increased to 16.1%, at 70°C, and was equal to 57.1%, at 90°C. The initial negative trend, the decrease of error from 23 to 50°C, was potentially caused by the improvement of the gel's conductivity. The rise of temperature increased the mobility of ions in the gel and hence its conductivity, consequently decreasing the contact resistance. As a result, the error of measurement decreased. The positive trend, the error rise between 60 and 90°C, was potentially caused by drying of the gel, as the box was open, to measure the voltage across the resistor, that allowed the water in the gel to evaporate. Without water, the mobility of ions decreased, consequently reducing the conductivity of the gel and increasing the contact resistance.

C.4 Effect of High Conductive Gel on Electrical Conductivity of *P. radiata* Cubes

C.4.1 Electrical Conductivity of Cubes

The high conductive gel showed significant reduction of contact resistance and a consequent decrease of the measurement error in the measurements, in comparison to the low conductive gel. Therefore, this gel was used to measure *P. radiata's* electrical conductivity in the three principal directions: longitudinal, tangential, and radial. The method and sample preparation in this test was identical to those described in Section 5.2.

Cubes were cut out of several green *P. radiata* beams, provided by the McVicar Timber sawmill, Christchurch, New Zealand. Only the cubes with straight grain were selected in this study. The total number of cubes was 240 (80 cubes in each principal direction). The mean moisture content and basic density of the cubes were 164% (SD = 33%) and 387 $\mathrm{kg \cdot m^{-3}}$ (SD = 31 $\mathrm{kg \cdot m^{-3}}$), respectively.

Figure C.9 shows the effect of temperature on electrical conductivity of green sapwood of *P. radiata* in three principal directions, using the high conductive gel at the contact interface. The average electrical conductivities measured in the longitudinal, radial, and tangential direction at 20°C were 0.043 $\mathrm{S \cdot m^{-1}}$, 0.0045 $\mathrm{S \cdot m^{-1}}$, and 0.0018 $\mathrm{S \cdot m^{-1}}$, respectively. At 90°C, the conductivity increased up to 1.078 $\mathrm{S \cdot m^{-1}}$ in the longitudinal direction, 0.05 $\mathrm{S \cdot m^{-1}}$ in the radial direction, and 0.047 $\mathrm{S \cdot m^{-1}}$ in the tangential direction. Therefore, the average increase of electrical conductivity was about 25 times in the longitudinal and tangential directions, and 11 times in the radial direction.

Figure C.10 shows the natural logarithm of electrical conductivity of sapwood cubes and four sapwood boards in the temperature range from 20 to 60°C. The latter conductivity was determined in the board experiment, described in Chapter 3. At 20°C, the average electrical conductivity of the cubes and boards was 0.043 $\mathrm{S \cdot m^{-1}}$ and 0.035 $\mathrm{S \cdot m^{-1}}$, respectively. However, at 60°C, the average electrical conductivities of the cubes and boards were 0.64 $\mathrm{S \cdot m^{-1}}$ and 0.08 $\mathrm{S \cdot m^{-1}}$. Thus, the ratio between the average cubes' and boards' conductivities increased from 1.2 to 8. The conductivity of cubes was enhanced by an unknown parameter. The increase

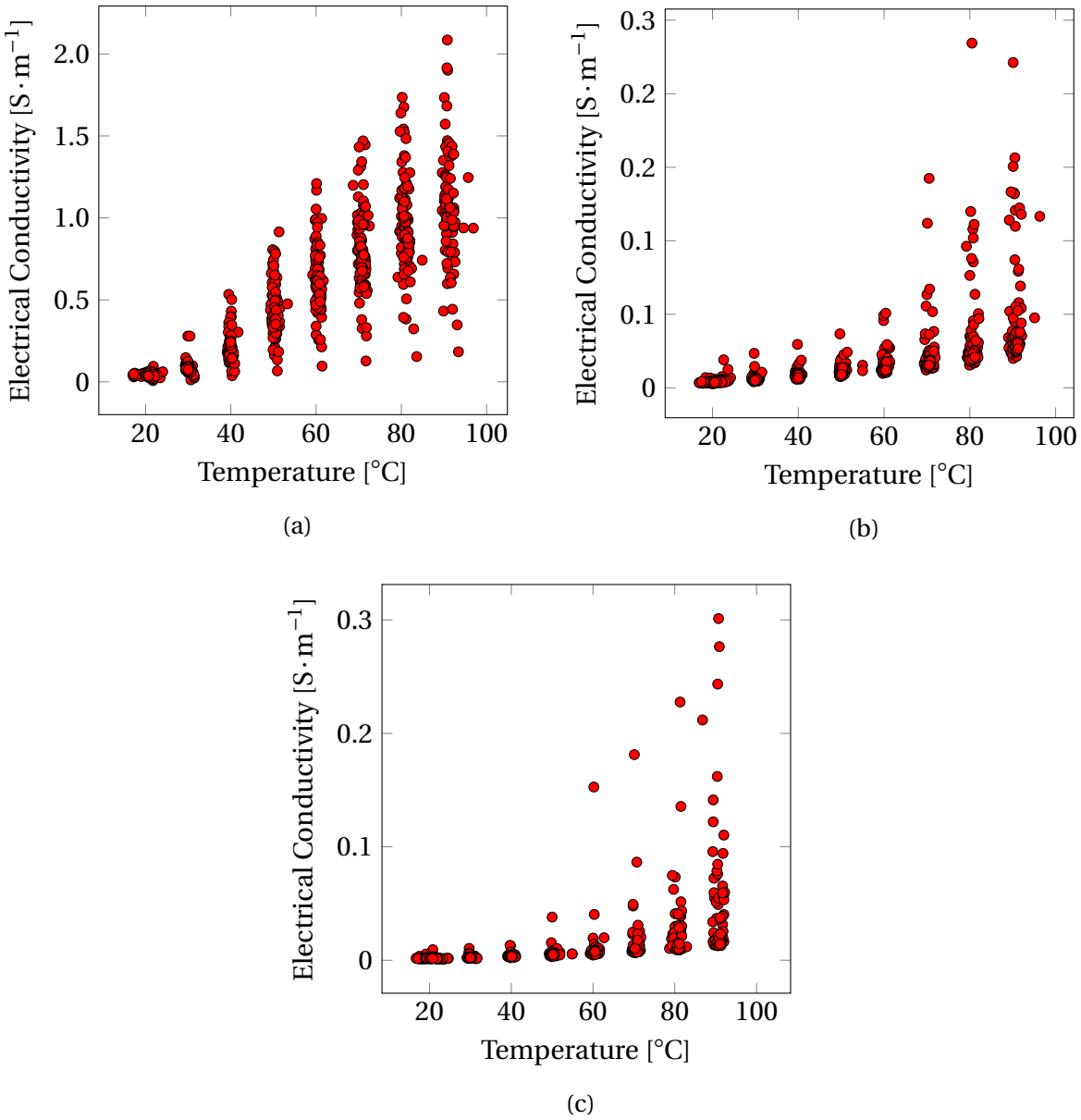

Figure C.9. The effect of temperature on the electrical conductivity of *P. radiata* sapwood in the (a) longitudinal, (b) radial, and (c) tangential directions, using the high conductive gel.

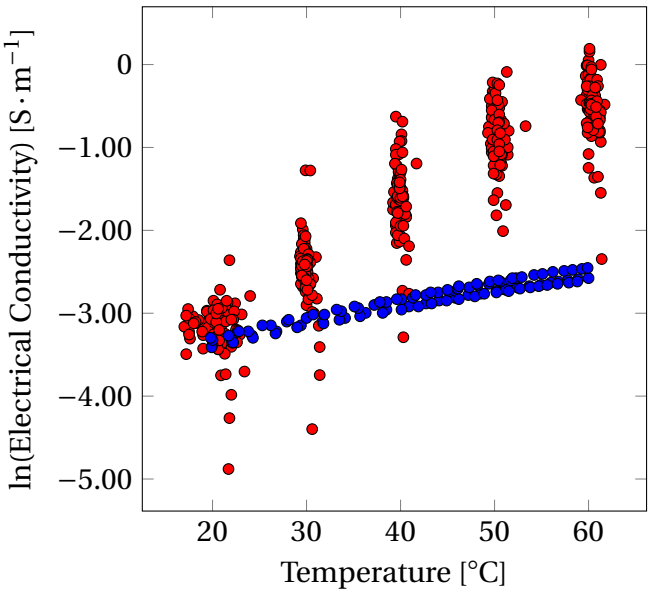

Figure C.10. The effect of temperature on the natural logarithm of electrical conductivity of green *P. radiata* sapwood in the longitudinal direction, measured using the high conductive gel. The blue and red circles represent the results from the board and cube experiments, with the high conductive gel, respectively.

of data-spread with temperature meant that the unknown parameter had a different effect on each cube. That led to a hypothesis of penetration of the sodium chloride from the gel into the cubes. The sodium chloride penetration, however, was less pronounced in the boards due to the longer length of the boards, 500 mm. This hypothesis was tested in Section C.4.2.

C.4.2 Electrical Conductivity of Water Soluble Extractives

The method described in this section (C.4.2) and Section C.5 is based on the work done by Fischer (2014). To test the hypothesis of sodium chloride penetration, electrical conductivity values of aqueous solutions of water soluble extractives from treated and untreated wood were compared. The wood from the cubes that had been in contact with the gel was called treated, while the untreated wood was taken from a fresh green *P. radiata* top log. If sodium chloride penetrated into the cubes, electrical conductivity of the extracted solutions from the treated wood would be higher than that of the untreated wood. In this experiment, three samples of the treated wood were studied; each sample consisted of three randomly selected oven-dry cubes that had been used to measure electrical conductivity in the same grain direction. The extraction was performed using an accelerated solvent extraction (ASE) system, Dionex ASE 350. The main advantage of the ASE technique is a relatively short extraction time (Richter et al., 1996).

Sample Preparation

Initially, 5 mm of the cubes' contact faces were trimmed, as they were in contact with the gel. Then, the cubes were chipped into chips of 5 mm cross-sectional thickness as shown in Figure C.11a, using a chisel and mallet. Afterwards, the chips were milled in a Wiley mill,

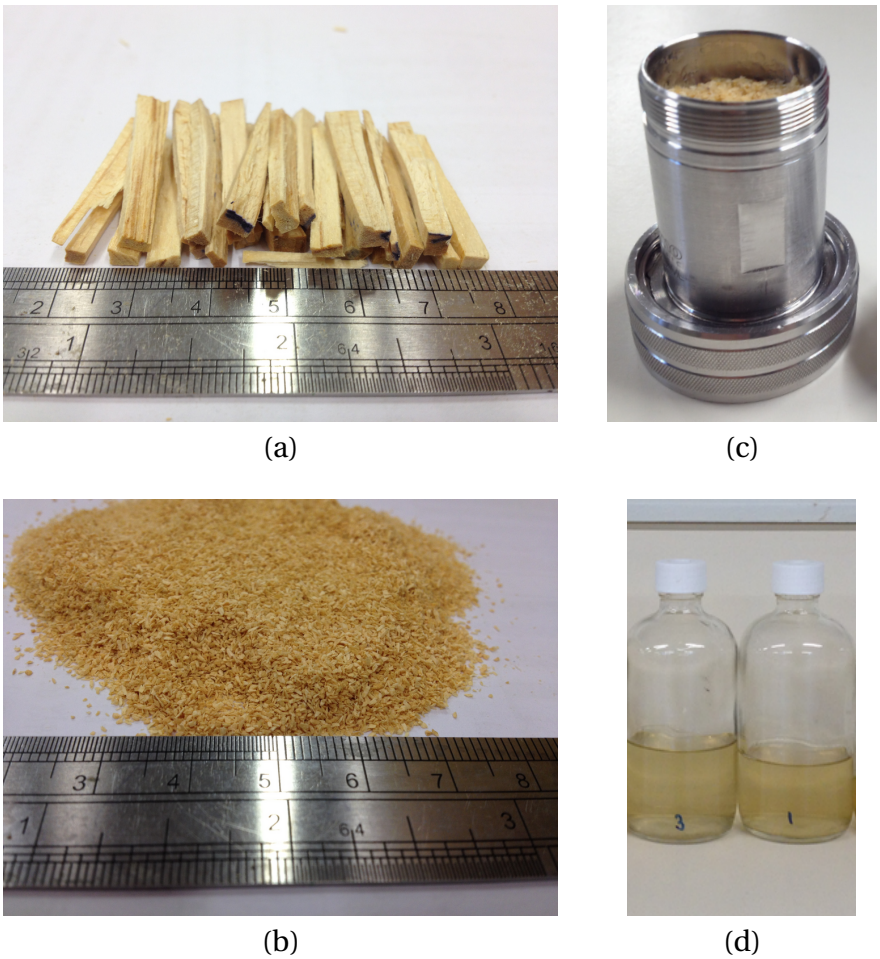

(a) (c)

(b) (d)

Figure C.11. The sample preparation for the extraction test, with (a) the chipped and (b) milled wood, (c) the stainless steel cell, and (d) the extracted solutions.

equipped with a 2 mm sieve (Figure C.11b). As the untreated wood samples were cut from green wood, they had been dried inside an oven at 105°C until its mass stopped changing. Thereafter, the untreated samples were chipped and milled. To avoid cross-contamination between the samples, the mill was air blasted prior to milling another sample.

Experimental Procedure

The milled wood was loaded into 37 mL stainless steel cells as shown in Figure C.11c. The net mass of wood inside the cells was 5.00 g, measured at low relative humidity condition. The extraction was done in two cycles using deionized water, with the resistivity of 18 MΩ·cm, as a solvent. During each cycle the cells had been kept at 90°C and 10.34 MPa for 15 minutes. Then,

the cells were rinsed with deionized water, 25% of the cells volume. After the second rinse, the cells had been purged with nitrogen for 60 seconds.

The solutions of water soluble extractives had different volumes (Figure C.11d). To compare the collected solutions, they were standardised to the same volume of 100 mL, using deionised water. The temperature compensated conductivity was measured by setting the temperature compensation coefficient of 2.21 $\% \cdot {}^{\circ}C^{-1}$ in a conductivity meter, YSI EcoSense EC300. The value of temperature compensation coefficient was determined experimentally, as described in Appendix C.5.

Results

The results showed that electrical conductivities of the extracted solutions from the cubes used for the longitudinal, tangential, and radial directions were 1.907, 1.244, and 1.107 $mS \cdot cm^{-1}$, respectively. The conductivity of the extractives' solution from the untreated wood was 0.2 $mS \cdot cm^{-1}$. Such difference between the treated and untreated wood, more than 5 times for the radial and tangential directions and almost 10 times for the longitudinal direction, indicates that sodium chloride penetrated into the treated wood. The penetration was the highest in the longitudinal direction due to axially located tracheids. The penetration in the tangential direction was slightly higher than that in the radial direction. This can be explained by orientation of pits. Located on radial cell walls, pits conduct sap tangentially and hence diffusion of salt from the gel was higher in the tangential direction. In addition, the rate of diffusion of water molecules through the cell walls increases with temperature (Langrish and Walker, 2006). Thus, at room temperature diffusion is slow and hence the cubes' electrical conductivity is similar to the flat-boards' conductivity (Figure C.10); however, the higher the temperature, the more significant the difference between the cubes and the boards. Other parameters that caused the difference between the cubes and the boards were: duration of the experiments, length of the samples, and contact surface area.

Conclusion

Although the high conductive gel decreases contact resistance, it cannot be used to determine electrical conductivity of cubes. The sodium chloride contained in the gel penetrates into wood tissue. Hence, to avoid the effect of penetration either the sample size must be increased, or a different contact material such as a metal should be used. Unlike ions, which penetrate into wood, electrons will stay within the metal's volume and will not enhance wood's electrical

conductivity.

C.5 Temperature Compensation Coefficient

During the extraction test, a pressurized cell was heated up to 90°C and hence the temperature of the collected solution was close to that temperature. However, the solutions extracted earlier cooled to a room temperature of about 25°C. As conductivity of solutions depends on temperature, all the values had to be standardised to the same temperature, e.g. 25°C, for comparison. Generally, conductivity meters have a temperature compensation mode that allows to compensate the effect of temperature using a temperature compensation coefficient. However, this coefficient is solution dependent and must be obtained experimentally.

C.5.1 Calibration of Electrical Conductivity Meter

Initially, the electrical moisture meter was calibrated using two standard aqueous solutions of 30 and 1000 ppm of sodium chloride, with the respective conductivities of 64 and 1990 $\mu S \cdot cm^{-1}$ at 25°C (Invensys Foxboro, 2015). These standard solutions, poured into 100 mL graduated cylinders, were left in a water bath at 25°C to equilibrate. Once the temperature of the solutions reached 25°C, the measured conductivities in the conductivity meter were manually adjusted to the respective values. Thereafter, conductivity of each solution was measured several times to ensure that deviation of the result was insignificant and lay within the accuracy range of the meter. For the electrical conductivity ranges of 0.0 to 499.9 $\mu S \cdot cm^{-1}$ and of 500 to 4999 $\mu S \cdot cm^{-1}$, the accuracy of the meter was ±1% of reading plus 2 $\mu S \cdot cm^{-1}$ and ±1% of reading plus 5 $\mu S \cdot cm^{-1}$, respectively (YSI Inc., 2008).

C.5.2 Estimating Temperature Compensation Coefficient

Theory

Once the meter was calibrated, it was used to determine the temperature compensation coefficient, calculated as:

$$\lambda = \frac{\sigma - \sigma_{\text{Ref}}}{\sigma_{\text{Ref}}(T - T_{\text{Ref}})} \cdot 100\%, \tag{C.3}$$

where λ is the temperature compensation coefficient [$\% \cdot °C^{-1}$], σ is the electrical conductivity of the solution [$mS \cdot cm^{-1}$], σ_{Ref} is the electrical conductivity at reference temperature [$mS \cdot cm^{-1}$], T is the temperature [°C], and T_{Ref} is the reference temperature, equal to 25°C. If electrical conductivity is linearly dependent on temperature, then Equation C.3 can be rewritten as:

$$\lambda = \frac{\theta}{\sigma_{Ref}} \cdot 100\%, \tag{C.4}$$

where θ is the regression slope, determined by measuring electrical conductivity at different temperatures.

Experimental Part

Several randomly selected cubes, being used in the electrical conductivity experiments with the high conductive gel, were milled. Then, all milled wood was thoroughly mixed and extracted as described in Section C.4. The collected solution was heated in a 100 mL graduated cylinder inside a water bath to 25, 30 and 40°C, measuring electrical conductivity at each temperature. Three repeated measurements were performed (Table C.4). Plotting the obtained results (Figure C.12),

Table C.4. Electrical conductivity of water soluble extractives measured in triplicate at three temperatures.

	T1	T2	T3
T [°C]	25.0	30.0	40.0
	25.0	30.0	40.0
	25.0	30.0	40.0
μ_T [°C]	25.0	30.0	40.0
SD_T [°C]	± 0.0	± 0.0	± 0.0
σ [$mS \cdot cm^{-1}$]	2.524	2.800	3.361
	2.526	2.797	3.364
	2.529	2.799	3.364
μ_σ [$mS \cdot cm^{-1}$]	2.526	2.799	3.363
SD [$mS \cdot cm^{-1}$]	± 0.003	± 0.002	± 0.002

the temperature compensation coefficient was calculated as:

$$\lambda = \frac{0.0559 \ mS \cdot cm^{-1} \cdot °C^{-1}}{2.526 \ mS \cdot cm^{-1}} \cdot 100\% = 2.21 \ \% \cdot °C^{-1}, \tag{C.5}$$

where the value at denominator, 2.526 $mS \cdot cm^{-1}$, is the mean electrical conductivity of the solution at 25°C.

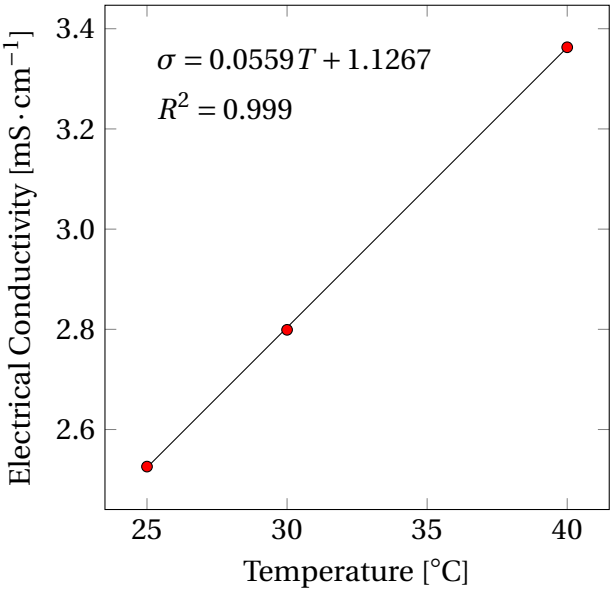

Figure C.12. The effect of temperature on the mean electrical conductivity of the extracted solution from the cubes, being in contact with the high conductive gel.

C.6 Mesh and Time-Step Independence Study

In this study four mesh resolutions were investigated: (1) 1000 mesh elements, in a $10 \times 10 \times 10$ array; (2) 8000 mesh elements, in a $20 \times 20 \times 20$ array; (3) 64000 mesh elements, in a $40 \times 40 \times 40$ array; (4) and 512000 elements, in a $80 \times 80 \times 80$ array. Four simulation runs, one per mesh, were performed using 1000 time steps. The predicted temperatures, measured in the centre of the cube's geometry, were compared at each time-step using the following equation:

$$\delta = \left| T - T_{f.m.} \right|, \tag{C.6}$$

where $T_{f.m.}$ is the temperature determined using the finest mesh of 512,000 mesh elements [°C]. Afterwards the average error over 1000 time-steps was calculated as:

$$\mu_\delta = \frac{\sum_{n=1}^{n} Error_n}{n}, \tag{C.7}$$

where μ_δ is the average of the errors calculated over all time-steps [°C], and n is the number of the time-steps. Figure C.13a shows the effect of the mesh refinement on the average error, where

the resolution of 64,000 mesh elements provides a mesh independent solution. In the time-step

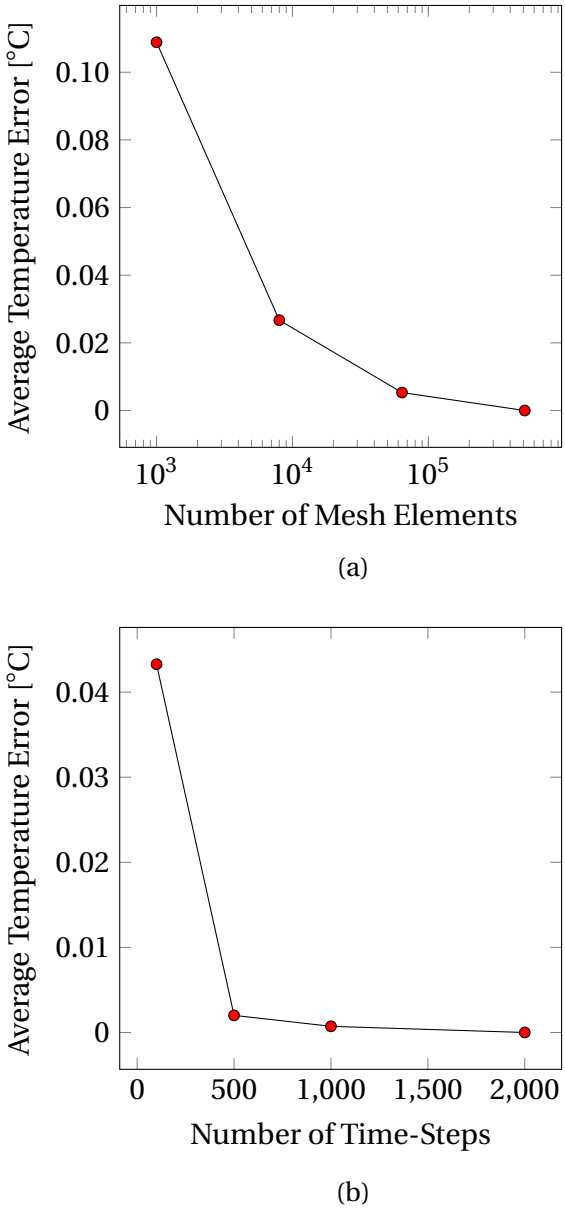

Figure C.13. The dependence of error on the number of the mesh elements (a) and the number of time-steps (b).

independence study the mesh of 64,000 mesh elements was used. The simulations were done with 100, 500, 1000, and 2000 time-steps. The computational error was calculated as:

$$\delta = |T - T_{2000}|, \tag{C.8}$$

where T_{2000} is the temperature determined using 2000 time-steps. The average error, calculated using equation C.7, changed insignificantly from 500 to 2000 time-steps and hence 500 time-steps provided a time-step-independent transient result.

Appendix D

D.1 Mesh and Time-Step Independence Studies

Case 1

In this case, the mesh was made of rectangular hexahedrons with a mesh spacing - the side to side distance - the same in all directions. The computational and analytical solutions were compared based on a relative error, calculated using the following equation:

$$\delta = \frac{|T_c - T_a|}{T_a} \times 100\%, \tag{D.1}$$

where δ is the error [%]; and T_c and T_a are the temperature values calculated using the CFD model and analytical solution, respectively [°C]. Figure D.1 shows the dependence of the relative error on the mesh spacing and time-step. The mesh spacing and the time-step did not affect,

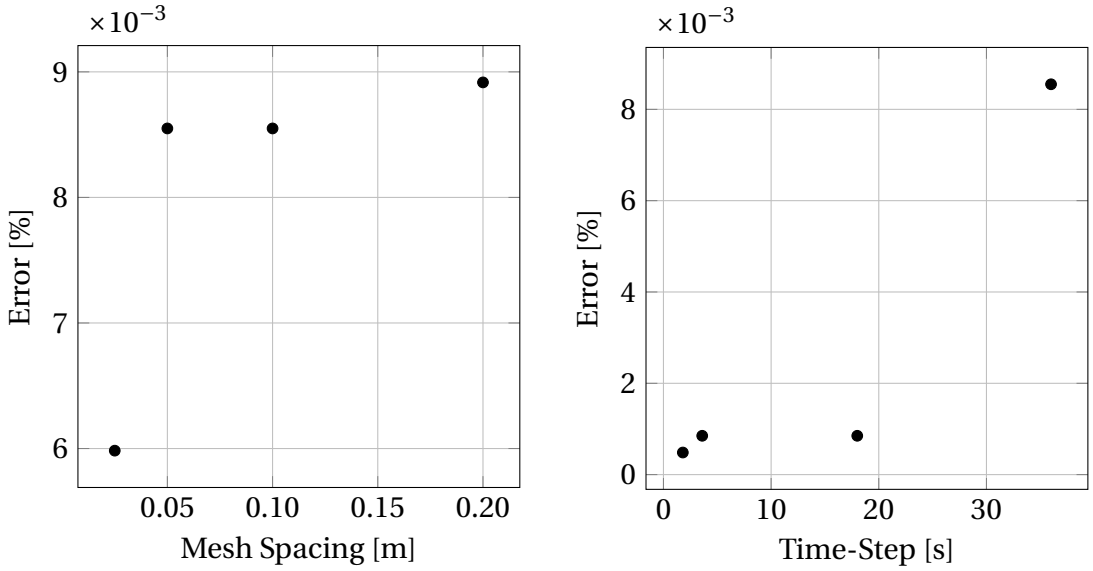

Figure D.1. The relative errors between the analytically and numerically predicted temperature values over the range of (a) mesh spacings and (b) time-steps in the solution of constant heat generation problem at $t = 3600$ s.

significantly, computational error in *Case 1*. Hence, to reduce the calculation time of the final simulation, the following resolutions were selected: the mesh-spacing of 0.05 m, equal to 20

mesh elements per direction or 8,000 mesh elements in total, and the time-step of 18 s.

Case 2

The CFD model was verified using the known analytical solution of 1D transient heat conduction within the slab with an internal heat source. The average relative error was calculated as follows:

$$\delta = \frac{\sum_{i=1}^{N} \frac{|T_{c(i)} - T_{a(i)}|}{T_{a(i)}}}{N} \times 100\%, \tag{D.2}$$

where N is the number of temperature points aligned along the direction of heat diffusion and calculated using the analytical solution. The mesh and time-step independence study was performed in all three directions (Figure D.2). The mesh spacings and time-steps that provided a mesh and time-step independent solution are shown in Table D.1.

Table D.1. The final mesh spacings and time-steps selected for *Case 2*.

Direction	Mesh Spacing [m]	Time-Step [s]
X	$2.5 \cdot 10^{-4}$ m	20 s
Y	$2.5 \cdot 10^{-3}$ m	20 s
Z	0.01 m	8 s

Case 3

In this case, three cubes were connected using ideal thermal contacts at the interfaces between the cubes. That means the temperature at both sides of interface should be the same. However, the interfaces can cause numerical problems such as temperature discontinuities, if not meshed properly (Figure D.3). Those discontinuities depend on mesh spacing, where the denser the mesh or the smaller the mesh spacing, the lower the discontinuity. Figure D.4 shows effect of different mesh spacings and time-steps on the discontinuity. The optimum mesh spacing and time-step were $6.25 \cdot 10^{-4}$ m and 20 s, respectively. The final temperature profile (Figure 6.20a), generated using the optimal mesh spacing and time-step, did not show discontinuity, meaning that temperature at both sides of interface was the same.

Case 4

These verification cases were done in steady-state and hence a time-step independence study was omitted. Furthermore, due to the non-realistic conditions of *Sub-case 4.1* - the grounded

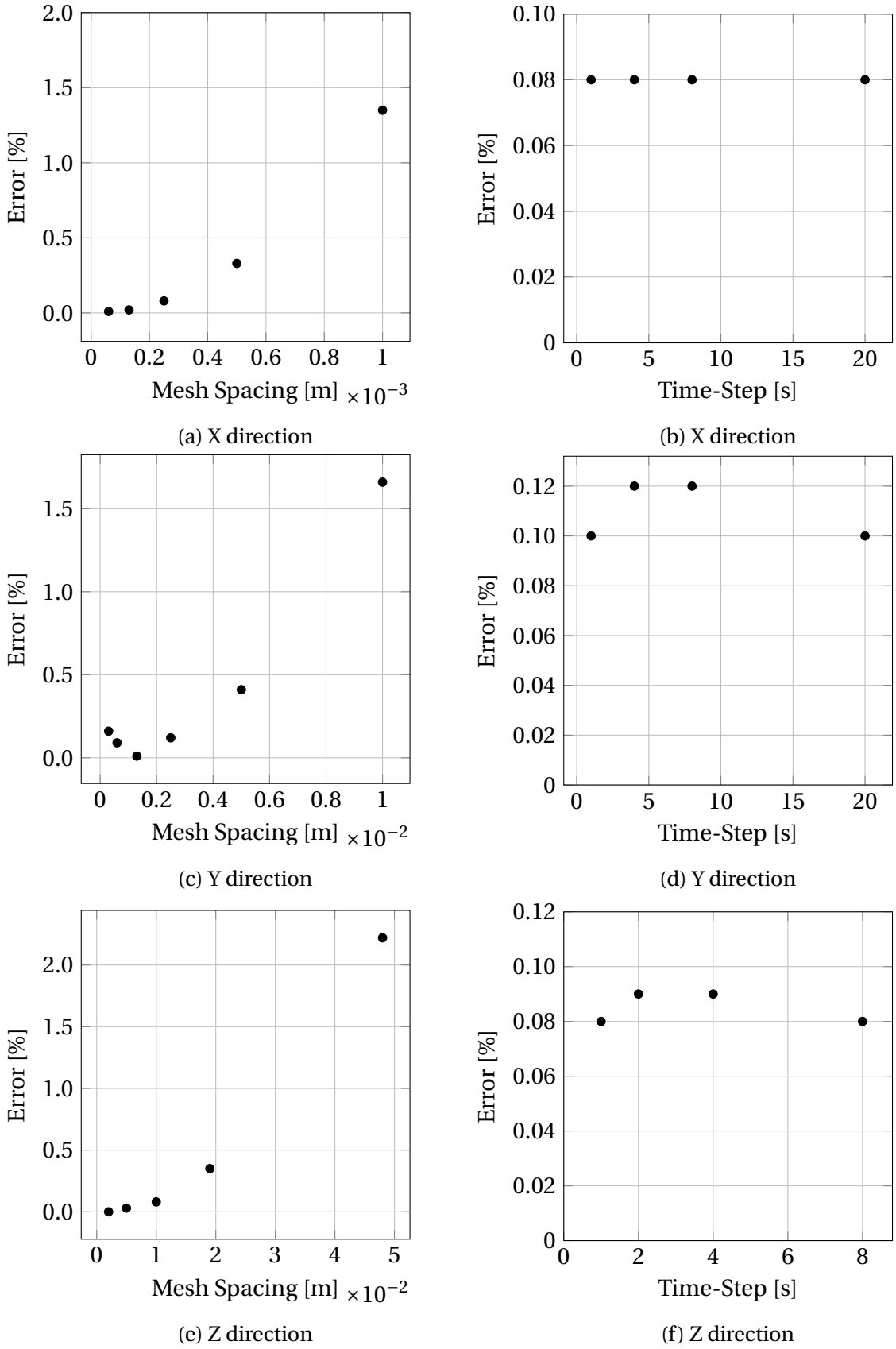

(a) X direction

(b) X direction

(c) Y direction

(d) Y direction

(e) Z direction

(f) Z direction

Figure D.2. The effects of mesh spacing (*left*) and time-steps (*right*) on the relative error in *Case 2*. *Note:* The rows of the figures from the *top* to *bottom*: the 1st, 2nd, and 3rd simulation, respectively.

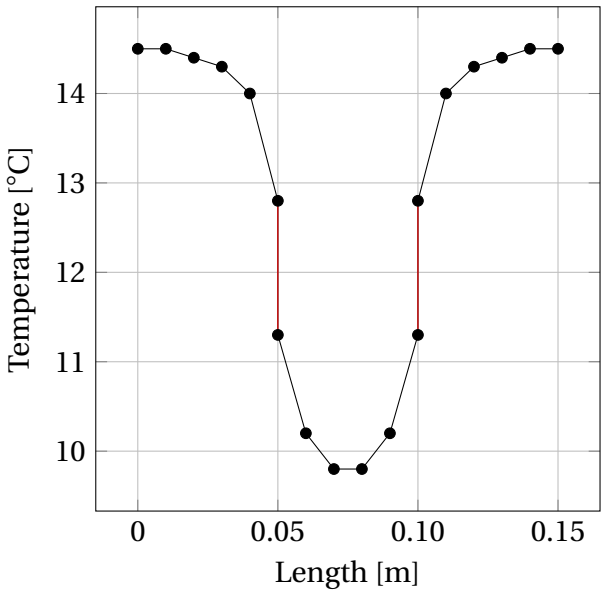

Figure D.3. The temperature profile, estimated after 1000 s of heating, in three cubes assembly, where the red lines show the discontinuity of temperature across the interfaces.

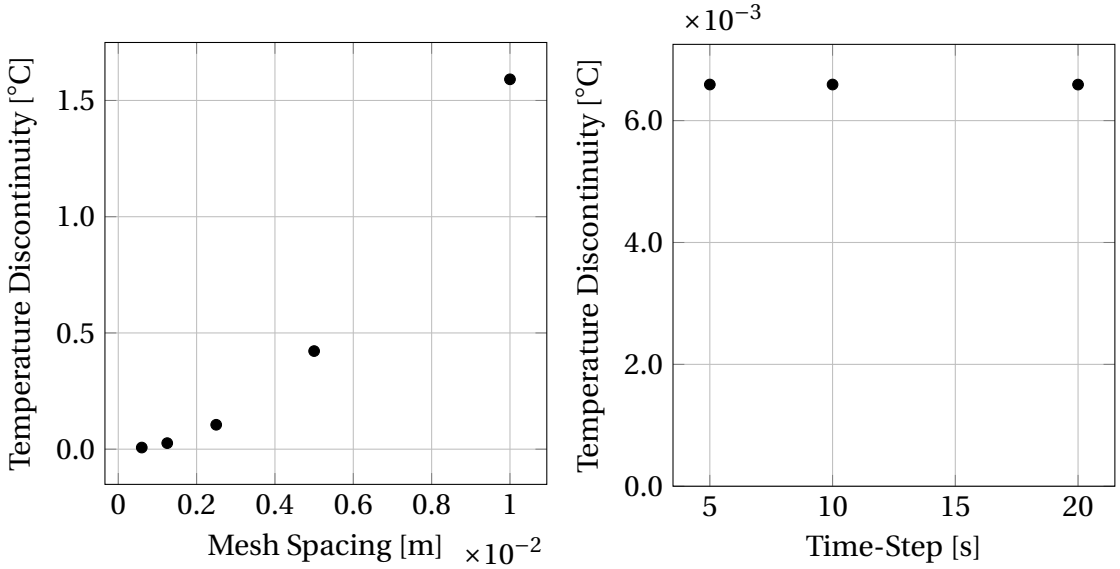

Figure D.4. The effect of (a) mesh spacing and (b) time-step on temperature discontinuity of *Case 3*.

faces had a high voltage edge, and the high voltage face had two grounded edges - this case was considered entirely qualitative. Thus, a mesh independence study has not been done for *Sub-case 4.1*.

In the mesh independence study of *Sub-case 4.2*, current flowed through the truncated cone from the high- to low-voltage sides. Ideally, the magnitude of the current values on each side should be the same, to satisfy charge conservation; however, in computational modelling, those values depend on the mesh resolution. Therefore, the error was calculated based on the

percentage error of the value of electric current as:

$$\delta = \frac{|I_{LV} - I_{HV}|}{I_{HV}} \times 100\%, \tag{D.3}$$

where δ is the error [%], I_{HV} and I_{LV} is the electric current flowing through the high- and low-voltage faces [A], respectively. Three mesh resolutions were used in this study: coarse, medium, and fine, with the total number of mesh elements of 30,400, 243,200, and 1,945,600, respectively. The number of mesh elements increased by two times per direction, or by eight times in total, for each consecutive resolution. The study consisted of six mesh independence tests: one for each of the scenarios and one for the additional isotropic case, as shown in Figure D.5. The error decreased to nearly 1% in most of the scenarios, except Scenario 3, where the error was approximately 30% using the finest possible mesh.

In Scenario 3, the axial electrical conductivity was 100 times higher than that in the radial and tangential directions. In theory, under these conditions, the equipotential lines had to lie along the cone's axis. Figure 6.23c shows that the model produced a qualitatively correct solution and that the physics of Scenario 3 were correctly simulated. Therefore, the error was potentially caused by the insufficient number of mesh elements. Future work with bigger computing power should be done to test this assumption.

Case 5

As the simulated problem does not have a simple analytical solution, and De Alwis and Fryer (1992) have not provided information about their mesh and time-step independence study. It was decided to calculate a maximum error value of temperature based on the results obtained using the highest available mesh and time-step resolution, as they theoretically provided the most accurate results. Overall, in this verification, three mesh and time-step resolutions were used (Table D.2) The error was calculated for cold and hot spots within the assembly (Figure D.6).

Table D.2. The resolution of mesh and time-steps for *Case 5*.

Resolution	Number of Mesh Elements	Number of Time-Steps
1	23,040	1000
2	184,320	2000
3	1,474,560	4000

As the problem is transient, the error was calculated at each of 1000 time-steps in the mesh

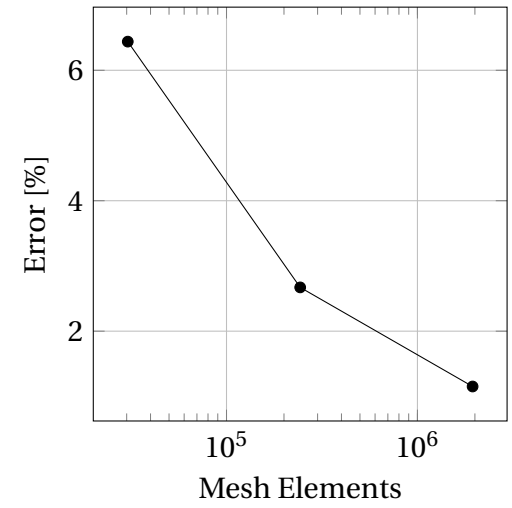

(a) Scenario 1

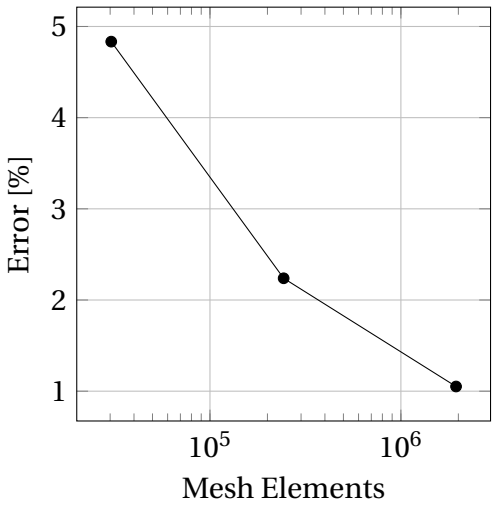

(b) Scenario 2

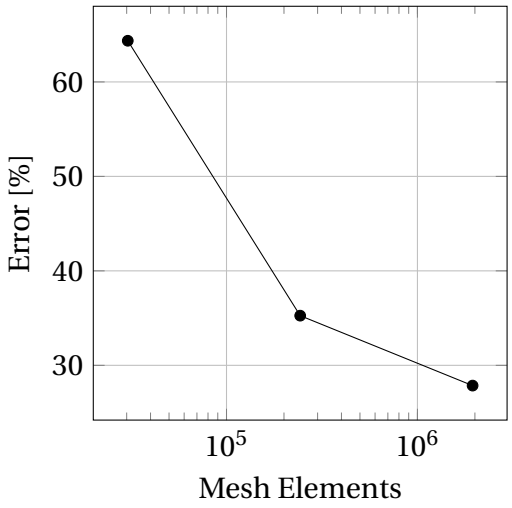

(c) Scenario 3

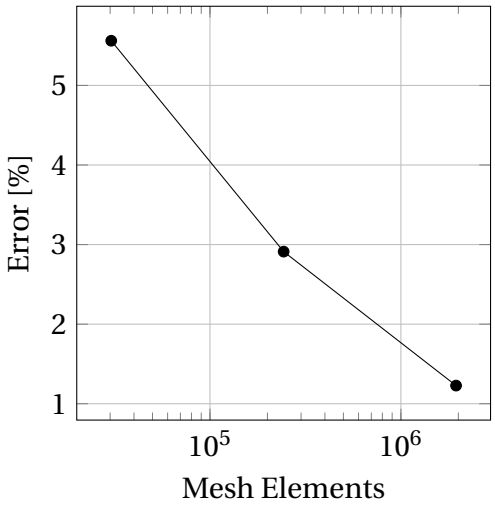

(d) Scenario 4

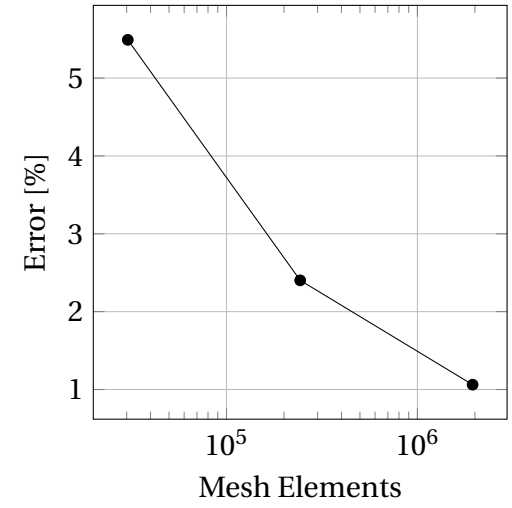

(e) Scenario 5

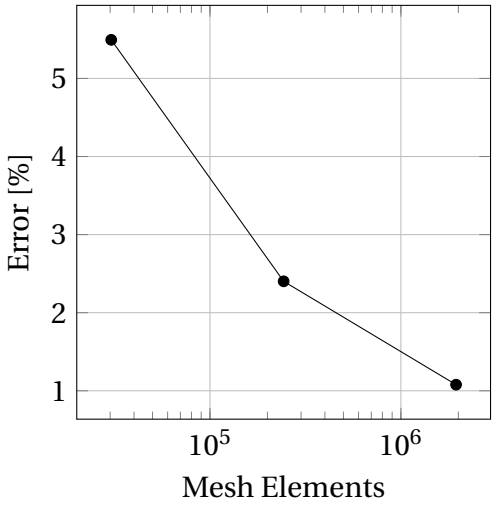

(f) Isotropic

Figure D.5. The effects of the mesh resolution on the relative error in the *Case 4.2* verification.

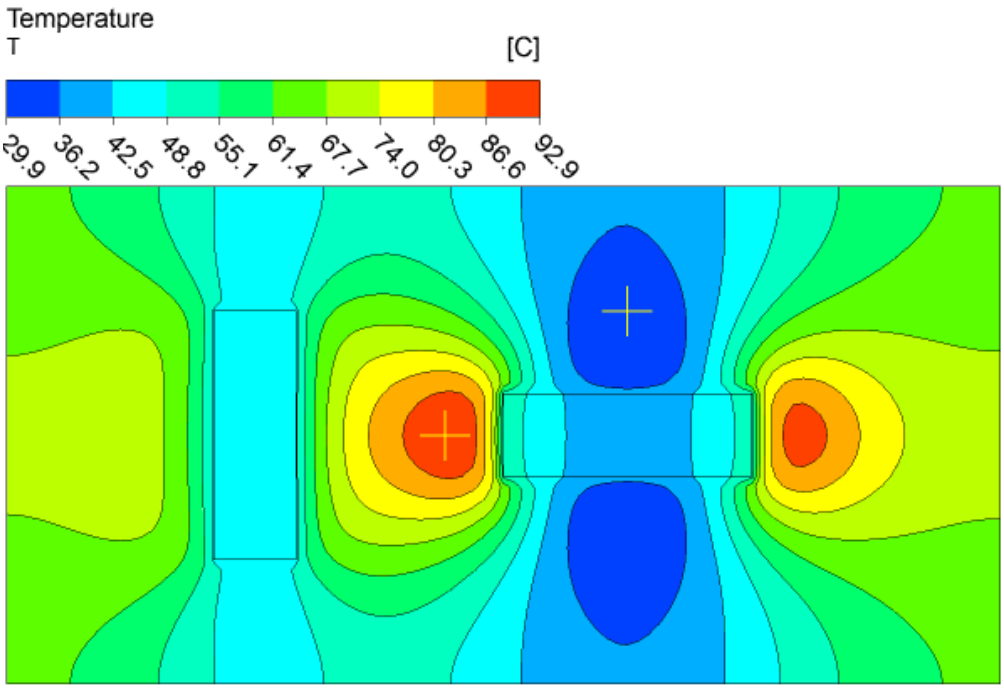

(a) Iron Blocks

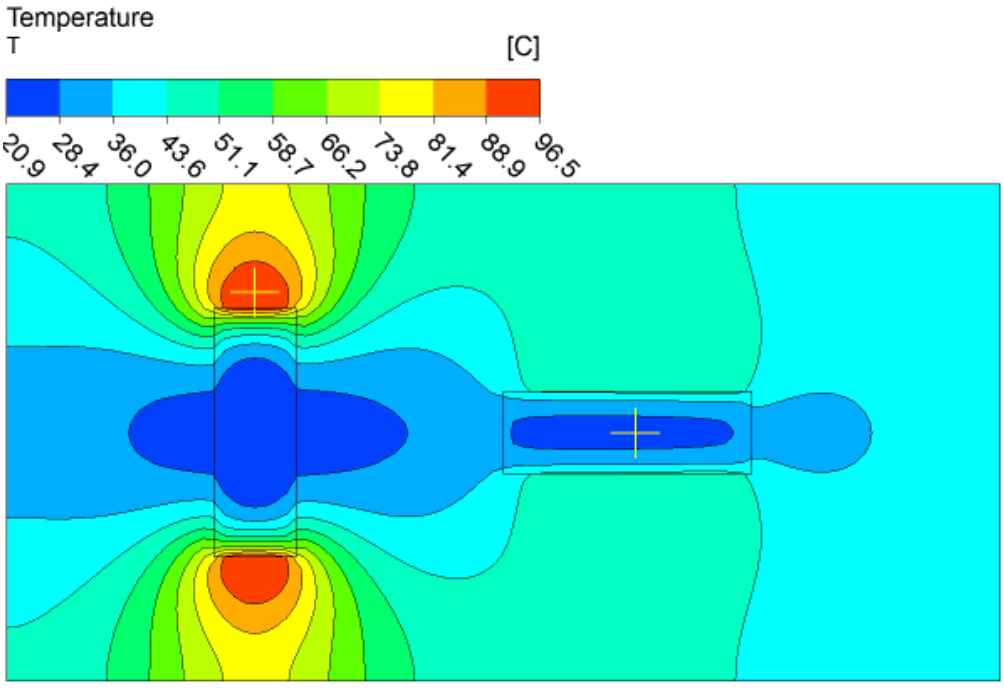

(b) Wood Blocks

Figure D.6. The position of the points (the yellow crosses) at which temperature was recorded for the mesh and time-step independence study.

independence study, and the maximum error value was selected; mathematically, that can be written as:

$$\delta = max\left(\frac{\left|T_{m.i.} - T_{f.m.}\right|}{T_{f.m.}} \cdot 100\%\right), \tag{D.4}$$

where $T_{m.i.}$ and $T_{f.m.}$ are the temperatures calculated in the cases with the tested mesh and with the finest mesh, respectively. After the mesh independence study being done with 1000 time-steps, the time-step independence study was done with the selected mesh of 184,320 elements. The effect of mesh and time-step resolution on the computational error is shown in Figure D.7.

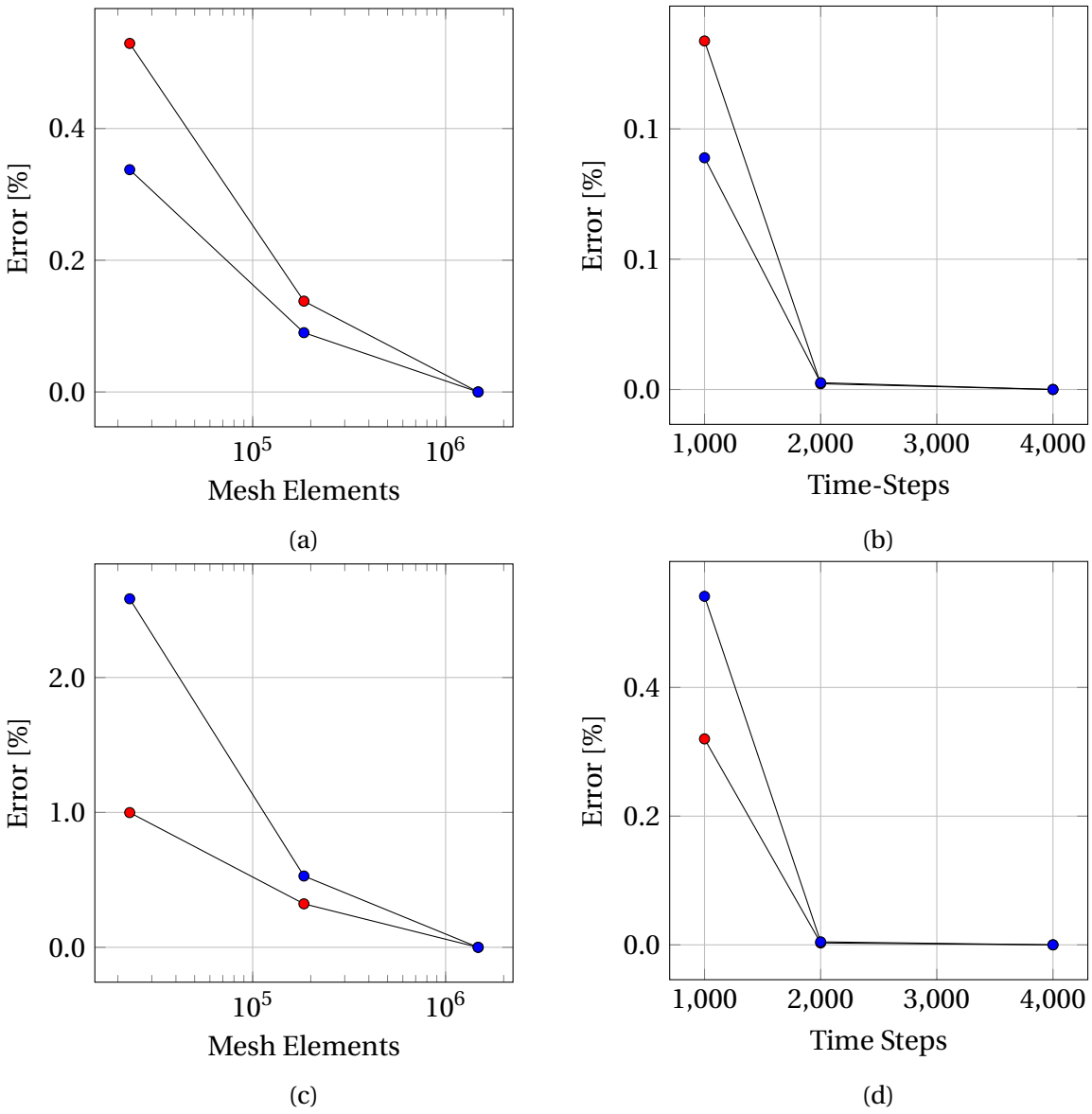

Figure D.7. The effects of the mesh and time-step resolution on the relative error in the *Case 5* verification. *Note:* The red and blue circles denote temperature points located in the hot and cold spots, respectively. The top and bottom rows of the figures represent results based on the scenarios with iron and wood blocks, respectively.

D.2 Additional CCL Codes for ANSYS CFX to Set Anisotropic Electrical Conductivity in Cartesian Coordinates

Listing D.1. The code to set the anisotropic electrical conductivity in ANSYS CFX-Solver

```
RULES:
  SINGLETON: ELECTRICAL CONDUCTIVITY
    Description = Hold the details for an advanced description of \
    Electrical Conductivity.
    Solver Name = CONELEC
    Context Rule = Option
    Essential Parameter List = Option
    Allowed Option List = \
      Value, \
      Orthotropic Cartesian Components
    CONTEXT: Value
      Essential Parameter List = \
      Electrical Conductivity
    END
    CONTEXT: Orthotropic Cartesian Components
      Essential Parameter List = \
      Electrical Conductivity X Component, \
      Electrical Conductivity Y Component, \
      Electrical Conductivity Z Component
    END
  END
  PARAMETER: Electrical Conductivity X Component
    Parameter Type      = Real
    Quantity Type       = Electrical Conductivity
    Dynamic Reread Item = Yes
    Solver Name         = CONELEC-11
```

```
27       Group Membership    = ORTTEN2, CONELEC, 1
28    END
29    PARAMETER: Electrical Conductivity Y Component
30       Parameter Type      = Real
31       Quantity Type       = Electrical Conductivity
32       Dynamic Reread Item = Yes
33       Solver Name         = CONELEC-22
34       Group Membership    = ORTTEN2, CONELEC, 2
35    END
36    PARAMETER: Electrical Conductivity Z Component
37       Parameter Type      = Real
38       Quantity Type       = Electrical Conductivity
39       Dynamic Reread Item = Yes
40       Solver Name         = CONELEC-33
41       Group Membership    = ORTTEN2, CONELEC, 3
42    END
43 END
```

Listing D.2. The code to set values of anisotropic electrical conductivity

```
LIBRARY:
   MATERIAL: Solid
      Material Description = Solid (Solid)
      Material Group = User
      Option = Pure Substance
      Thermodynamic State = Solid
      PROPERTIES:
         &replace ELECTRICAL CONDUCTIVITY:
            Option = Orthotropic Cartesian Components
            Electrical Conductivity X Component = 0 [S m^-1]
            # value for the X direction
            Electrical Conductivity Y Component = 0 [S m^-1]
            # value for the Y direction
            Electrical Conductivity Z Component = 0.5 [S m^-1]
            # value for the Z direction
         END
      END
   END
END
```

D.3 Additional CCL Codes for ANSYS CFX to Set Anisotropic Electrical Conductivity in Cylindrical Coordinates

Listing D.3. The code to set the anisotropic electrical conductivity in ANSYS CFX-Solver

```
1  RULES:
2    SINGLETON: ELECTRICAL CONDUCTIVITY
3       Description = Hold the details for an advanced description of \
4       Electrical Conductivity.
5       Solver Name = CONELEC
6       Context Rule = Option
7       Essential Parameter List = Option
8       Allowed Option List = \
9          Value, \
10         Orthotropic Cylindrical Components
11      CONTEXT: Value
12         Essential Parameter List = \
13         Electrical Conductivity
14      END
15      CONTEXT: Orthotropic Cylindrical Components
16         Essential Parameter List = \
17         Electrical Conductivity r Component, \
18         Electrical Conductivity Theta Component, \
19         Electrical Conductivity Axial Component
20         Essential Child List = AXIS DEFINITION
21      END
22   END
23   PARAMETER: Electrical Conductivity r Component
24      Parameter Type      = Real
25      Quantity Type       = Electrical Conductivity
26      Dependency List     = ANY
```

```
27       Dynamic Reread Item = Yes
28       Solver Name         = CONELEC-11
29       Lower Bound         = 0 [S m^-1]
30       Group Membership    = ORTCYL2, CONELEC, 1
31    END
32    PARAMETER: Electrical Conductivity Theta Component
33       Parameter Type      = Real
34       Quantity Type       = Electrical Conductivity
35       Dependency List     = ANY
36       Dynamic Reread Item = Yes
37       Solver Name         = CONELEC-22
38       Lower Bound         = 0 [S m^-1]
39       Group Membership    = ORTCYL2, CONELEC, 2
40    END
41    PARAMETER: Electrical Conductivity Axial Component
42       Parameter Type      = Real
43       Quantity Type       = Electrical Conductivity
44       Dependency List     = ANY
45       Dynamic Reread Item = Yes
46       Solver Name         = CONELEC-33
47       Lower Bound         = 0 [S m^-1]
48       Group Membership    = ORTCYL2, CONELEC, 3
49    END
50 END
```

Listing D.4. The code to set values of anisotropic electrical conductivity

```
LIBRARY:
   MATERIAL: Solid
      Material Description = Solid (Solid)
      Material Group = User
      Option = Pure Substance
      Thermodynamic State = Solid
         PROPERTIES:
            &replace ELECTRICAL CONDUCTIVITY:
            Option = Orthotropic Cylindrical Components
            Electrical Conductivity r Component = 1 [S m^-1]
            # value for the radial direction
            Electrical Conductivity Theta Component = 1 [S m^-1]
            # value for the tangential direction
            Electrical Conductivity Axial Component = 1 [S m^-1]
            # value for the longitudinal direction
            AXIS DEFINITION:
               Option = Coordinate Axis
               Rotation Axis = Coord 0.3
               # rotation axis aligns with the Z direction
            END
         END
      END
   END
END
```

Appendix E

E.1 Discretization of 1D Heat Equation

Assuming a heat flow in the wood's radial direction, the 1D governing heat conduction equation with an internal heat source can be written as:

$$\frac{\partial \rho_g C_p T}{\partial t} = \frac{\partial}{\partial r}\left(k\frac{\partial T}{r}\right) + \bar{S}. \tag{E.1}$$

This equation can be integrated over a control volume (Figure E.1) and a time-step, which gives (Versteeg and Malalasekera, 2007):

$$\int_t^{t+\Delta t}\int_{\mathrm{CV}} \rho_g C_p \frac{\partial T}{\partial t}\,\mathrm{d}V\,\mathrm{d}t = \int_t^{t+\Delta t}\int_{\mathrm{CV}} \frac{\partial}{\partial r}\left(k\frac{\partial T}{r}\right)\mathrm{d}V\,\mathrm{d}t + \int_t^{t+\Delta t}\int_{\mathrm{CV}} \bar{S}\,\mathrm{d}V\,\mathrm{d}t \tag{E.2}$$

For a fully implicit scheme, the above equation can be re-written as (Versteeg and Malalasekera,

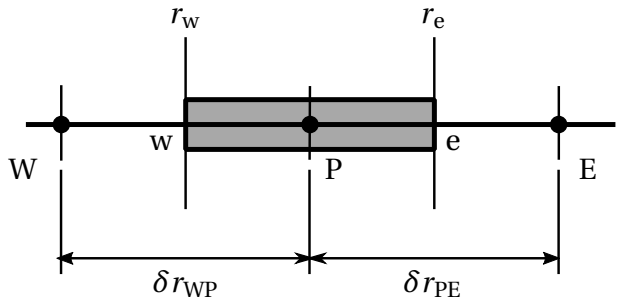

Figure E.1. One dimensional control volume (grey colour), with the node P in the centre. *Note:* w and e are the West and East sides of the control volume, respectively. δr_{WP} and δr_{PE} are the inter-node distances from node P to nodes W and E, respectively.

2007):

$$\rho_g C_p \left(\frac{T_{\mathrm{P}} - T_{\mathrm{P}}^0}{\Delta t}\right)\Delta V = \left(k_{\mathrm{e}} A_{\mathrm{e}} \frac{T_{\mathrm{E}} - T_{\mathrm{P}}}{\delta r_{\mathrm{PE}}}\right) - \left(k_{\mathrm{w}} A_{\mathrm{w}} \frac{T_{\mathrm{P}} - T_{\mathrm{W}}}{\delta r_{\mathrm{WP}}}\right) + \bar{S}\Delta V, \tag{E.3}$$

where T_{P}^0 is the "old", given temperature value of node P at time t; T_{P}, T_{E}, and T_{W} are the new temperature values of nodes P, E, and W at time $t + \Delta t$, respectively; $\bar{S}$ is the average source

strength; A_e and A_w are the face areas on the east (e) and west (w) sides of the control volume, respectively; and ΔV is the volume of the control volume. In this research, the nodes lay in the centre of control volumes, the same distance away from the sides w and e. As the problem is one dimensional, given in cylindrical coordinates (Figure E.2), the volume of control volume is equal to:

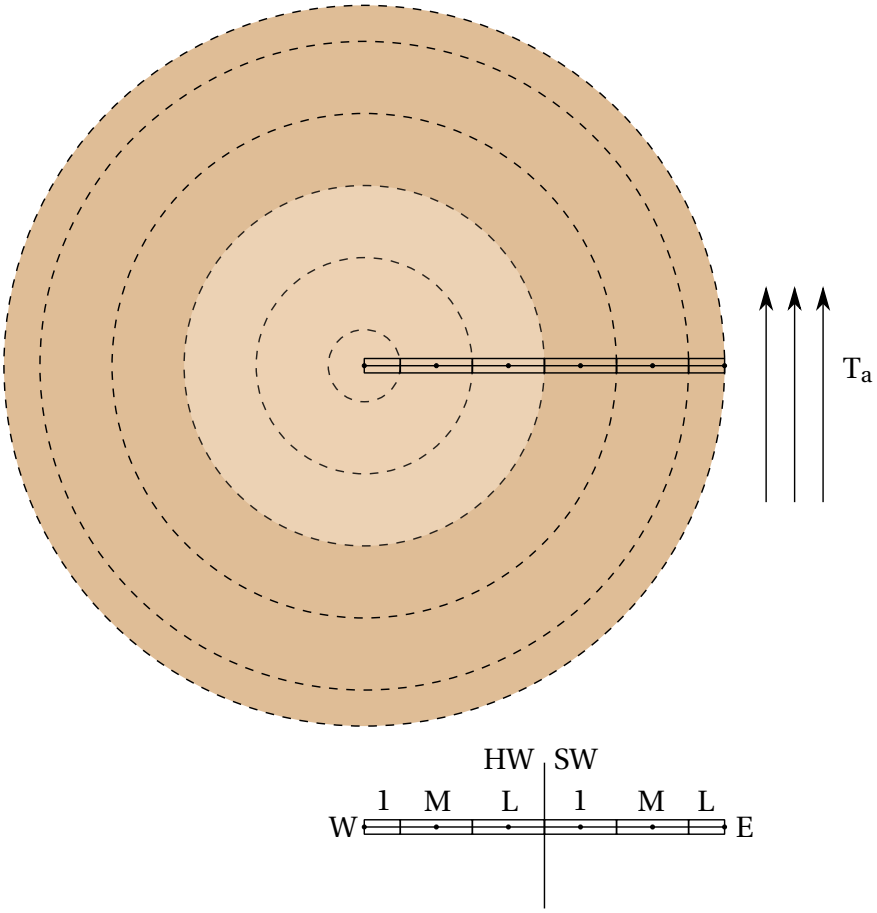

Figure E.2. The simplified 1D mesh in the log's geometry. *Note:* The control volumes 1, M, and L denote the first, middle, and last, respectively. HW is the heartwood and SW is the sapwood. The dashed lines shows the circumference, related to the face area of the control volumes (Equation E.5 and E.6). The number of control volumes is schematic and can vary by increasing the number of middle control volumes.

$$\Delta V = \pi(r_e^2 - r_w^2), \tag{E.4}$$

where r_e and r_w is the distance from the centre ($r = 0$) to the e and w sides of the control volume, respectively. The face area of the side e and w can be estimated as follows:

$$A_e = 2\pi r_e \tag{E.5}$$

and

$$A_{\mathrm{w}} = 2\pi r_{\mathrm{w}}, \tag{E.6}$$

respectively.

After rearranging Equation E.3 and dividing both sides by π, the discretised equation can be written in a common form as (Versteeg and Malalasekera, 2007):

$$a_P T_P = a_W T_W + a_E T_E + a_P^0 T_P^0 + S_u, \tag{E.7}$$

where

$$a_P = a_P^0 + a_W + a_E - S_P, \tag{E.8}$$

$$a_P^0 = \rho_g C_p \frac{\Delta V}{\Delta t}, \tag{E.9}$$

$$a_W = \frac{k_w A_w}{\delta r_{\mathrm{WP}}}, \tag{E.10}$$

and

$$a_E = \frac{k_e A_e}{\delta r_{\mathrm{PE}}}. \tag{E.11}$$

It should be noted that the source term was linearised as (Patankar, 1980):

$$\bar{S} = S_u + S_P T_P. \tag{E.12}$$

Finally, taking into account boundary conditions for each control volume in Figure E.2, the above coefficients can be summarized in Table E.1.

Table E.1. The discretization coefficients for the 1D model.

Wood Type	Node †	a_W	a_E	S_P	S_u
Heartwood	1	0	$\frac{k_e A_e}{\delta r_{\text{PE}}}$	0	$S\Delta V$
	M	$\frac{k_w A_w}{\delta r_{\text{WP}}}$	$\frac{k_e A_e}{\delta r_{\text{PE}}}$	0	$S\Delta V$
	L	$\frac{k_w A_w}{\delta r_{\text{WP}}}$	$\frac{k_e A_e}{\delta r_{\text{if}}}$ ††	0	$S\Delta V$
Sapwood	1	$\frac{k_w A_w}{\delta r_{\text{if}}}$ ††	$\frac{k_e A_e}{\delta r_{\text{PE}}}$	0	$S\Delta V$
	M	$\frac{k_w A_w}{\delta r_{\text{WP}}}$	$\frac{k_e A_e}{\delta r_{\text{PE}}}$	0	$S\Delta V$
	L	$\frac{k_w A_w}{\delta r_{\text{WP}}}$	0	$-A_e h$ †††	$S\Delta V + A_e h T_a$ †††

† For simplicity, the number of middle nodes (M) are assumed to be one. However, depending on the actual number of control volumes, the number of middle nodes may vary.
†† These coefficients are further discussed in Section E.1.1.
††† In the last control volume, $A_e = 2\pi r_L$, where r_L is the radius of the log.

E.1.1 Discretization of Interface

In this research, it was assumed that the interface between heartwood and sapwood is an ideal thermal contact, meaning that the heat flux on both sides of the interface is the same. For the last control volume of the heartwood (Figure E.3), the heat flux on the left side of the interface can be expressed as:

$$\boldsymbol{J}_h = k_P \frac{T_e - T_P}{\delta r_{e-}}, \tag{E.13}$$

where k_P is the thermal conductivity of the heartwood, T_e is the temperature at the interface, and δr_{e-} is the distance from the node P to the interface. The heat flux on the right side can be written as:

$$\boldsymbol{J}_h = k_E \frac{T_E - T_e}{\delta r_{e+}}, \tag{E.14}$$

where k_E is the thermal conductivity of the sapwood, T_e is the temperature at the interface, and δr_{e+} is the distance from the interface to the node E. Alternatively, the heat flux can be described as follows:

$$\boldsymbol{J}_h = k_e \frac{T_E - T_P}{\delta r_{\text{if}}}, \tag{E.15}$$

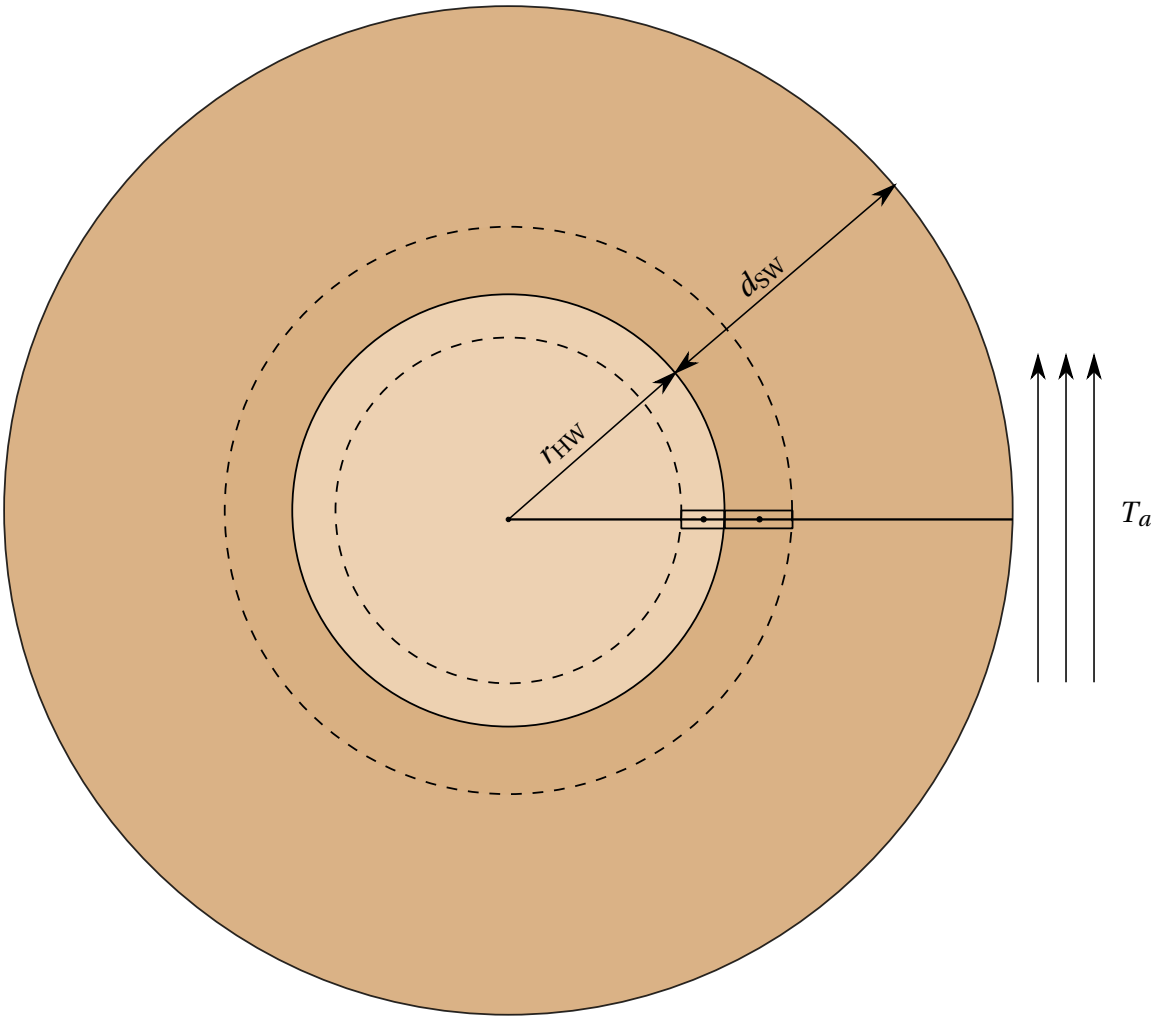

Last Control Volume (Heartwood)

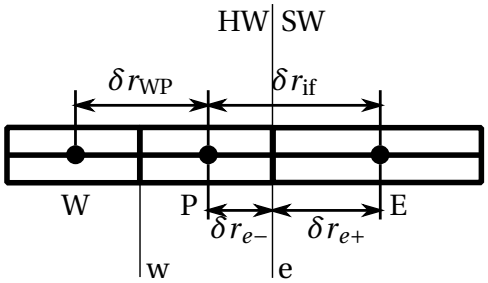

1st Control Volume (Sapwood)

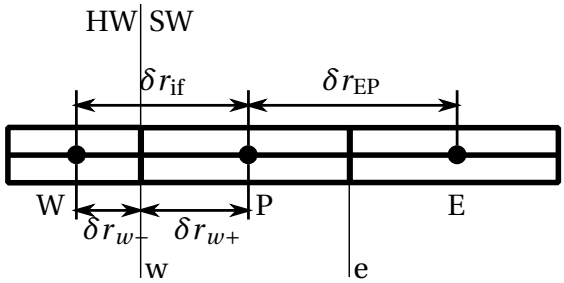

Figure E.3. The mesh at the interface between the sapwood and heartwood. *Note:* In logs, the sizes of heartwood and sapwood are often different; thus, assuming each domain was discretised into the same number of control volumes, the width of those control volumes will vary between heartwood and sapwood.

where k_e is the mean value of sapwood and heartwood thermal conductivities, and δr_{if} is the distance from the node P to the node E across the interface. According to Patankar (1980), using the arithmetic mean of the conductivities can provide an incorrect solution in composite materials. Instead, he suggests to use the harmonic mean of the conductivities to express k_e.

The calculation of k_e started by eliminating T_e from the Equations E.13 and E.14, which gives:

$$\boldsymbol{J}_h = \frac{k_E}{\delta r_{e+}} (T_E - T_P) \left(1 + \frac{k_E}{\delta r_{e+}} \frac{\delta r_{e-}}{k_P}\right)^{-1}. \tag{E.16}$$

Substituting $\boldsymbol{J}_h$ in Equation E.15 by Equation E.16, thermal conductivity at the interface can be written as:

$$k_e = \frac{k_E}{\delta r_{e+}} \delta r_{\text{if}} \left(1 + \frac{k_E}{\delta r_{e+}} \frac{\delta r_{e-}}{k_P}\right)^{-1}. \tag{E.17}$$

This can be simplified to:

$$k_e = \delta r_{\text{if}} \left(\frac{\delta r_{e+}}{k_E} + \frac{\delta r_{e-}}{k_P}\right)^{-1}. \tag{E.18}$$

Substituting k_e in the a_E coefficient of the last heartwood control volume in Table E.1 with the above equation, the a_E coefficient can be re-written as:

$$a_E = \left(\frac{\delta r_{e+}}{2 r_{\text{HW}} k_E} + \frac{\delta r_{e-}}{2 r_{\text{HW}} k_P}\right)^{-1}, \tag{E.19}$$

where r_{HW} is the radius of the heartwood.

Reciprocally, a_W coefficient in the the first sapwood control volume (Figure E.3) can be described as follows:

$$a_W = \left(\frac{\delta r_{w+}}{2 r_{\text{HW}} k_P} + \frac{\delta r_{w-}}{2 r_{\text{HW}} k_W}\right)^{-1}, \tag{E.20}$$

where k_P and k_W are the thermal conductivities of the sapwood and heartwood, respectively.

E.1.2 Calculation

Using values of the obtained coefficients in Equation E.7, the following set of equations can be formed:

$$\text{Heartwood Node 1st}: \quad a_P T_P - a_E T_E = a_P^0 T_P^0 + Su \tag{E.21}$$

$$\text{Heartwood Node M}: \quad a_P T_P - a_E T_E - a_W T_W = a_P^0 T_P^0 + Su \tag{E.22}$$

$$\text{Heartwood Node L}: \quad a_P T_P - a_E T_E - a_W T_W = a_P^0 T_P^0 + Su \tag{E.23}$$

$$\text{Sapwood Node 1st}: \quad a_P T_P - a_E T_E - a_W T_W = a_P^0 T_P^0 + Su \tag{E.24}$$

$$\text{Sapwood Node M}: \quad a_P T_P - a_E T_E - a_W T_W = a_P^0 T_P^0 + Su \tag{E.25}$$

$$\text{Sapwood Node L}: \quad a_P T_P - a_W T_W = a_P^0 T_P^0 + Su, \tag{E.26}$$

or, in a matrix form, they can be written as:

$$\begin{bmatrix} a_P & -a_E & 0 & 0 & 0 & 0 \\ -a_W & a_P & -a_E & 0 & 0 & 0 \\ 0 & -a_W & a_P & -a_E & 0 & 0 \\ 0 & 0 & -a_W & a_P & -a_E & 0 \\ 0 & 0 & 0 & -a_W & a_P & -a_E \\ 0 & 0 & 0 & 0 & -a_W & a_P \end{bmatrix} \begin{bmatrix} T_{1_{HW}} \\ T_{M_{HW}} \\ T_{L_{HW}} \\ T_{1_{SW}} \\ T_{M_{SW}} \\ T_{L_{SW}} \end{bmatrix} = \begin{bmatrix} T^0_{1_{HW}} + Su \\ T^0_{M_{HW}} + Su \\ T^0_{L_{HW}} + Su \\ T^0_{1_{SW}} + Su \\ T^0_{M_{SW}} + Su \\ T^0_{L_{SW}} + Su \end{bmatrix}, \tag{E.27}$$

where T^0 values are known from the initial conditions or from the previous time step. To solve this system of equations, the tri-diagonal matrix algorithm (TDMA) method (Versteeg and Malalasekera, 2007) was applied.

The S_u term takes into account the heat generation caused by the Joule heating effect and was calculated for each control volume as:

$$S_u = \left(\frac{U}{l}\right)^2 \sigma, \tag{E.28}$$

where U is the voltage, l is the length of the log, and σ is the local electrical conductivity at the node within the control volume. As mentioned in Section 7.2.4, the voltage distribution along the log has not been calculated in the 1D model and was assumed to be constant in the radial

direction. Therefore, the voltage at each control volume was the same. Although the model is one dimensional, to calculate power dissipation the geometry required specification of a length. Therefore, it was assumed that each control volume is a concentric ring, or annulus, as shown in Figure E.2, with the log's length. Electrical conductivity of the sapwood was assumed to be temperature dependent and was described by Equation 7.8, written as:

$$\sigma_L = \exp\left[-2.60 + 0.017(T-55) - 0.073\frac{(T-55)^2}{1000}\right]. \tag{E.29}$$

Knowing the log's initial temperature or the temperature of each control volume at the previous time-step, electrical conductivity was calculated at each control volume.

Thereafter, the electrical conductivity was used to estimate resistance of each control volume, described as:

$$R_{CV} = \frac{l_L}{\sigma_{CV} A}, \tag{E.30}$$

where R_{CV} is the resistance of the control volume; l_L is the length of the log; σ_{CV} is the electrical conductivity of the control volume; and A is the cross-sectional area, through which the electric current flows. In this 1D model, the cross-sectional area is equal to ΔV of the control volume, calculated in Section E.1. Knowing electrical resistance of each control volume, the total resistance was calculated as follows:

$$R_T = \left(\sum_{n=1}^{N_{CV}} \frac{1}{R_{CV_n}}\right)^{-1}, \tag{E.31}$$

where R_T is the total resistance of the sapwood, assumed to be equal to the log's resistance; and N_{CV} is the number of control volumes within sapwood. Thereafter, the total resistance was used in Equation 7.19, to calculate voltage as:

$$U = \sqrt{PR_T}. \tag{E.32}$$

This voltage was applied in Equation E.28, to calculate the S_u term that was further used in Equation E.27 to calculate new temperature values for the consequent time-step. The whole calculation process was repeated at each time-step until the final time-step was completed.

E.2 Electrical Data of Logs 2-5

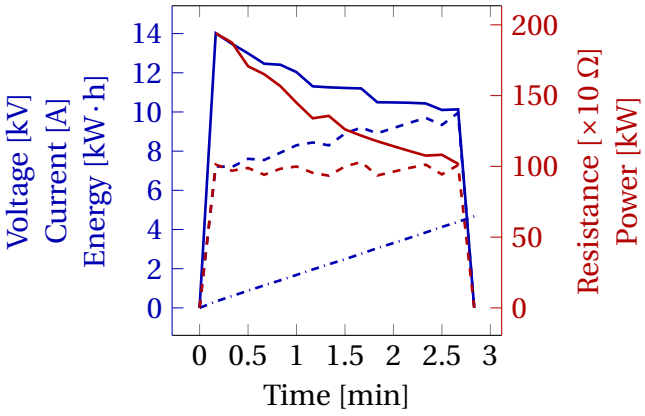

(a) First Excitation

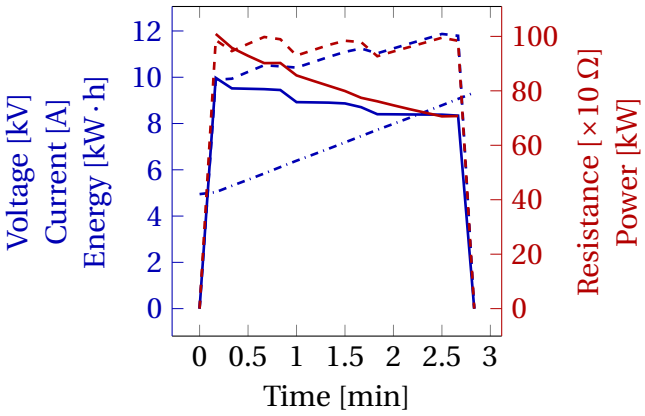

(b) Second Excitation

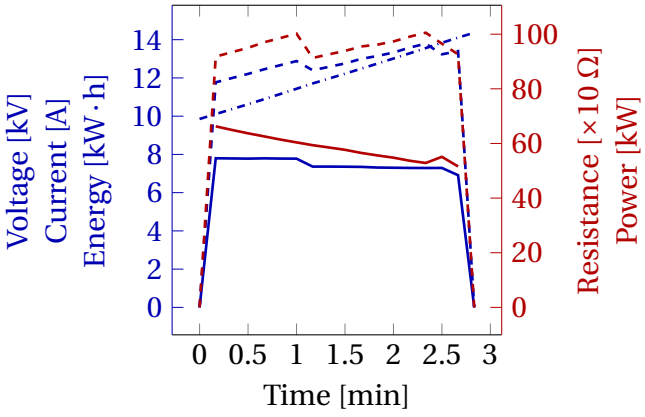

(c) Third Excitation

Figure E.4. The electrical data of Log 2. The blue solid, dashed, and dash-dotted lines denote the voltage, the current, and the energy, respectively. The red solid and dashed lines denote the electrical resistance and the power, respectively.

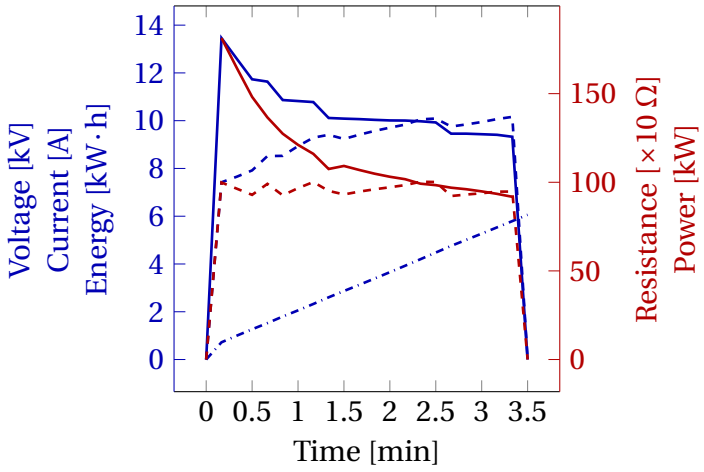

(a) First Excitation

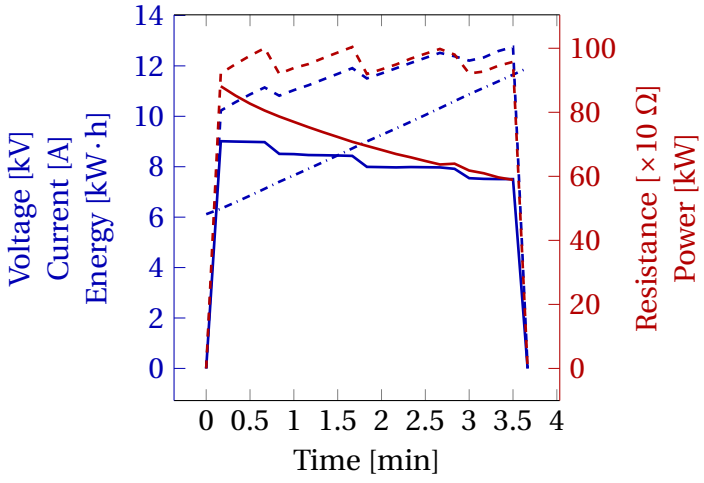

(b) Second Excitation

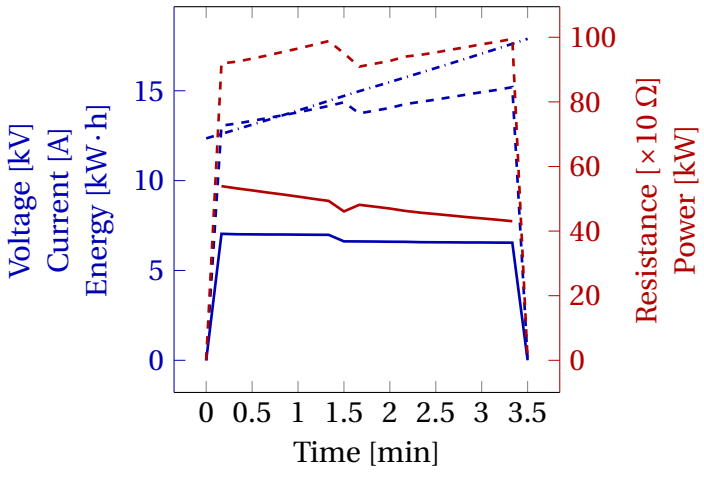

(c) Third Excitation

Figure E.5. The electrical data of Log 3. The blue solid, dashed, and dash-dotted lines denote the voltage, the current, and the energy, respectively. The red solid and dashed lines denote the electrical resistance and the power, respectively.

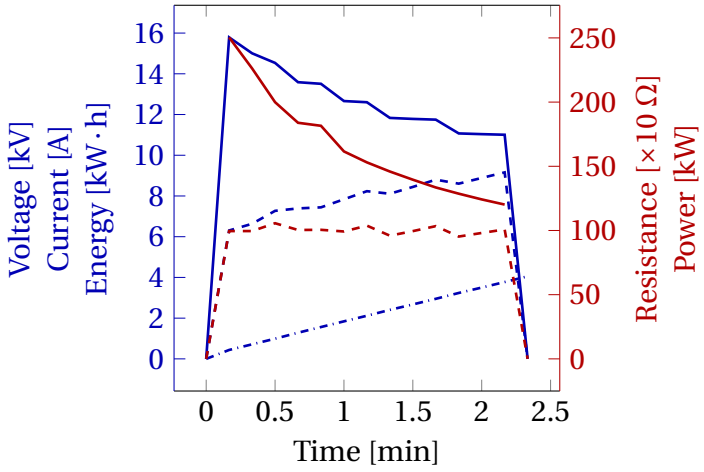

(a) First Excitation

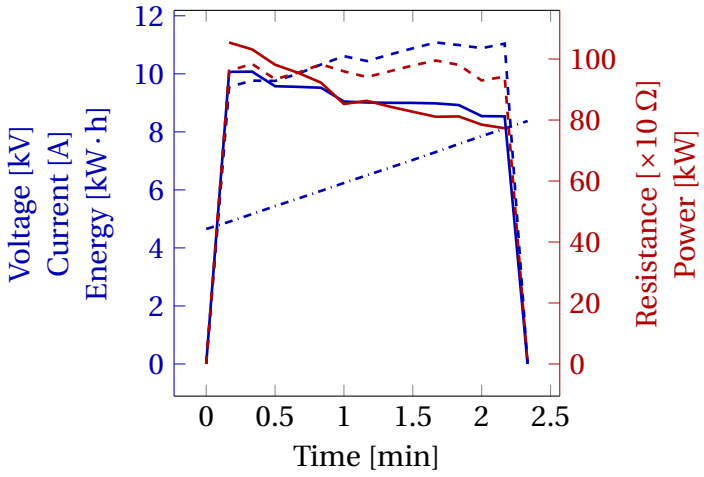

(b) Second Excitation

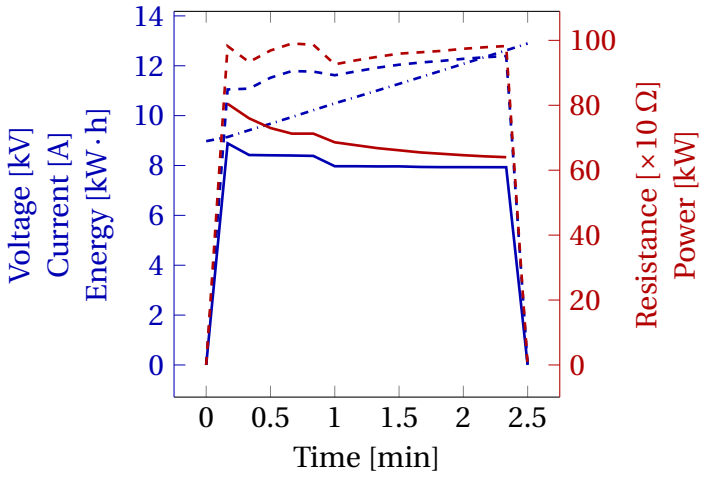

(c) Third Excitation

Figure E.6. The electrical data of Log 4. The blue solid, dashed, and dash-dotted lines denote the voltage, the current, and the energy, respectively. The red solid and dashed lines denote the electrical resistance and the power, respectively.

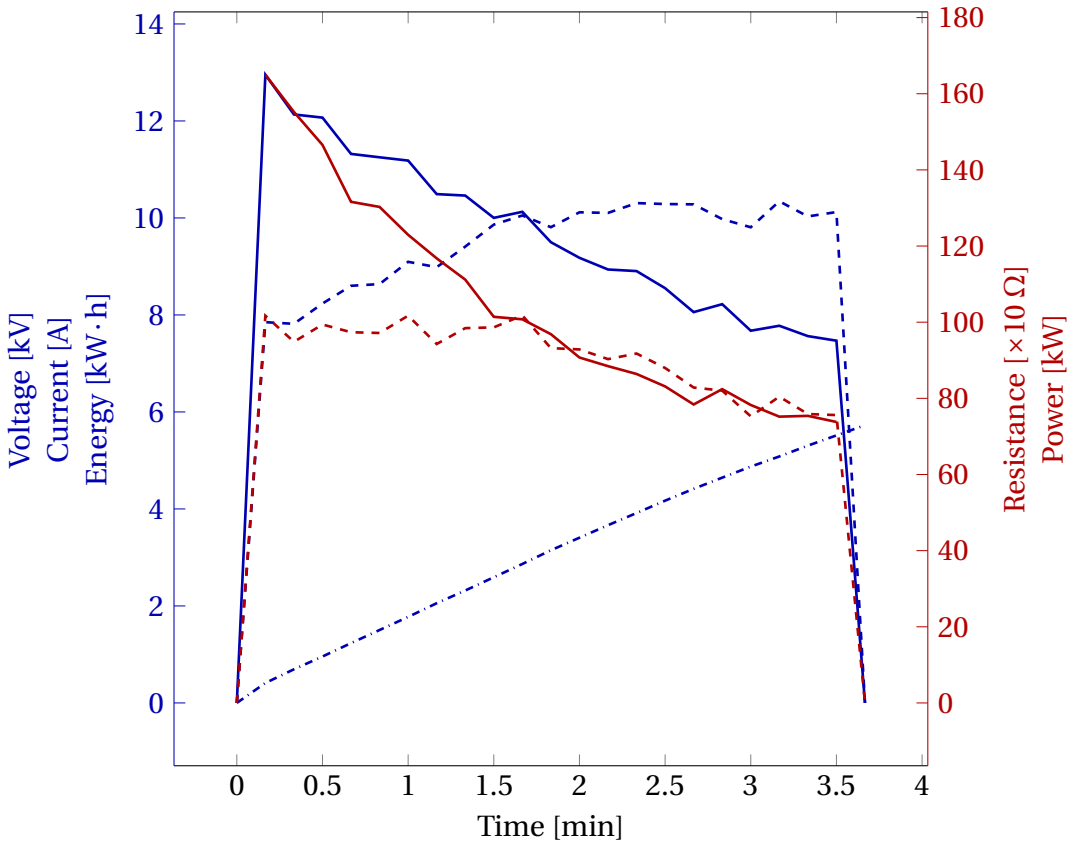

Figure E.7. The electrical data of Log 5 during the first excitation. The blue solid, dashed, and dash-dotted lines denote the voltage, the current, and the energy, respectively. The red solid and dashed lines denote the electrical resistance and the power, respectively. *Note:* After about 1.5 minutes at the first excitation of Log 5, the electric power decreased below the 100 kW limit, down to approximately 80 kW. This was caused by the arrangement of two transformers (each of 150 kVA) used in the experiments. When the log's resistance was above 1000 Ω, the transformers were in series, which doubled output voltage but kept the current limit at 10 A. Hence, when the resistance of Log 5 dropped below 1000 Ω and the electric current reached 10 A, the voltage decreased below 10 kV, reducing the electric power. During the relaxation period, the transformers were switched to parallel, which doubled the current and kept the electric power at 100 kW in the consequent excitations.

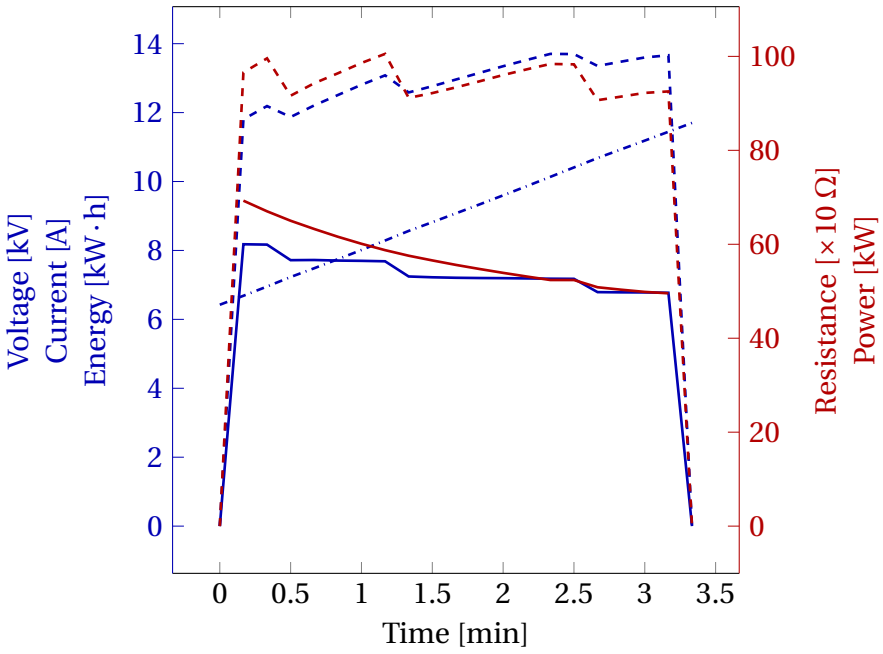

(a) Second Excitation

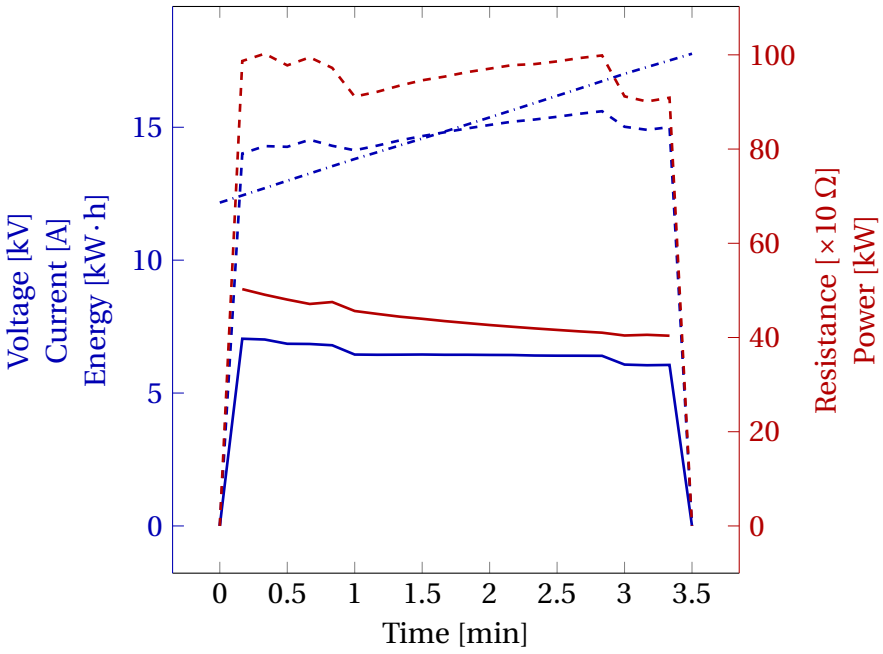

(b) Third Excitation

Figure E.8. The electrical data of Log 5 during the second and third excitations. The blue solid, dashed, and dash-dotted lines denote the voltage, the current, and the energy, respectively. The red solid and dashed lines denote the electrical resistance and the power, respectively.

E.3 Electrical Current Distribution of Logs 2-5

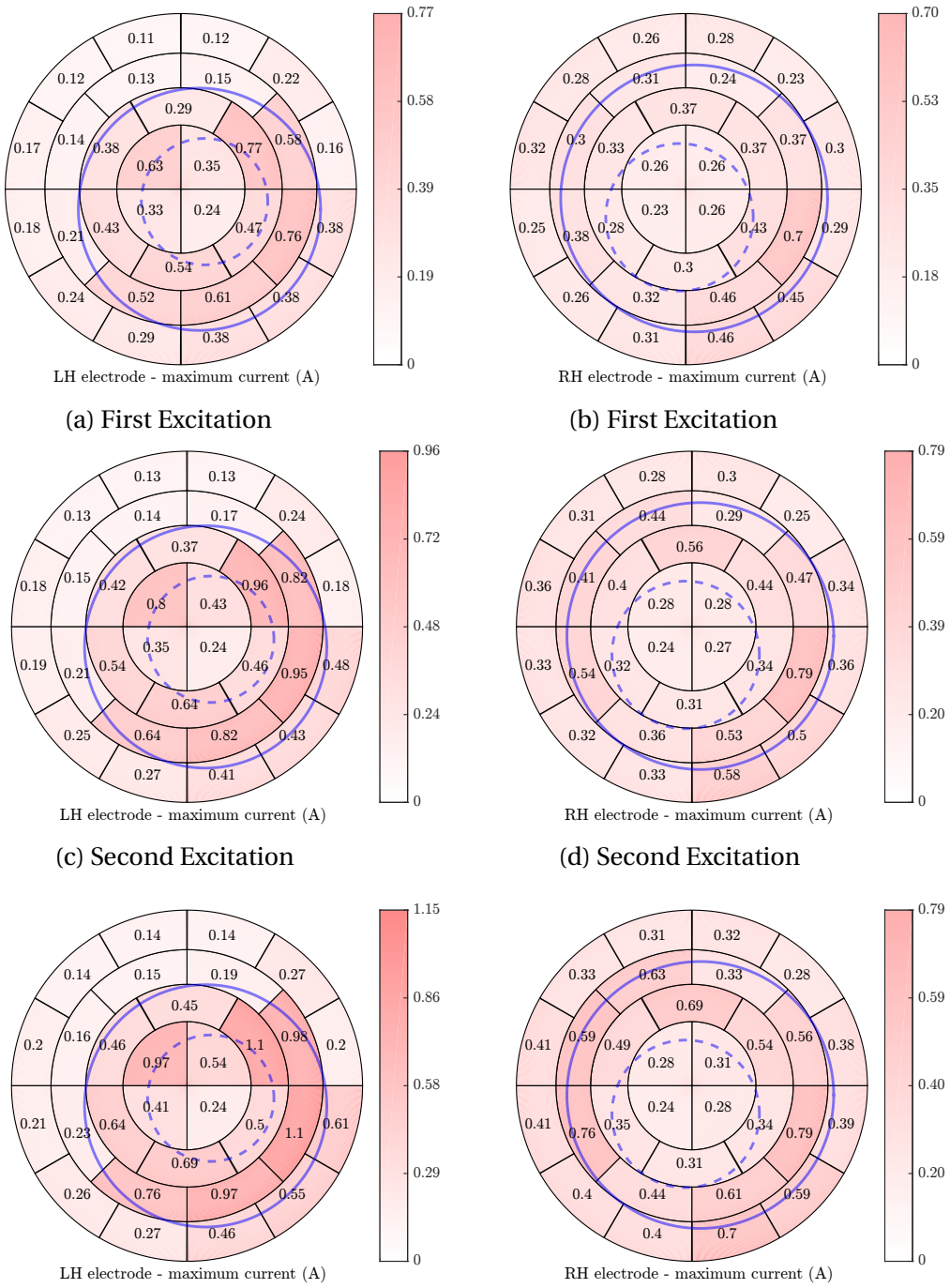

(a) First Excitation (b) First Excitation

(c) Second Excitation (d) Second Excitation

(e) Third Excitation (f) Third Excitation

Figure E.9. The current distribution at the left-hand electrode (LH) (*left*) and the right-hand electrode (RH) (*right*) of Log 2. *Note:* The blue solid and dashed lines denote approximately the size of the log and its heartwood. The values are in amperes.

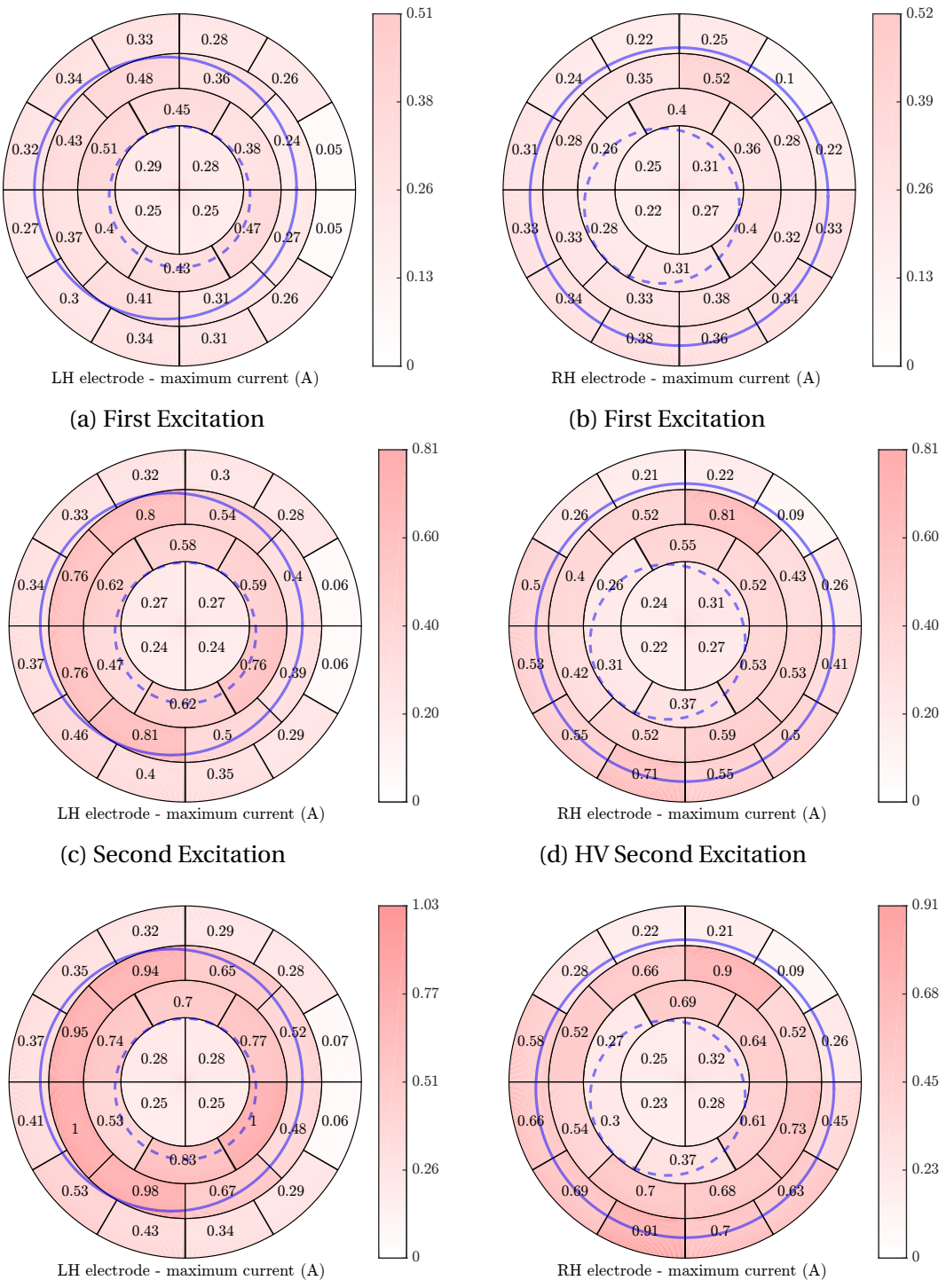

(a) First Excitation

(b) First Excitation

(c) Second Excitation

(d) HV Second Excitation

(e) Third Excitation

(f) Third Excitation

Figure E.10. The current distribution at the left-hand electrode (LH) (*left*) and the right-hand electrode (RH) (*right*) of Log 3. *Note:* The blue solid and dashed lines denote approximately the size of the log and its heartwood. The values are in amperes.

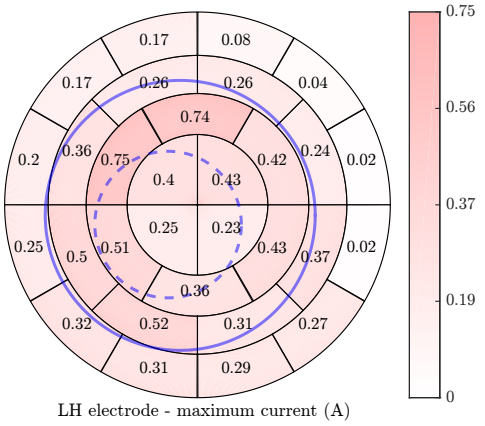

(a) First Excitation

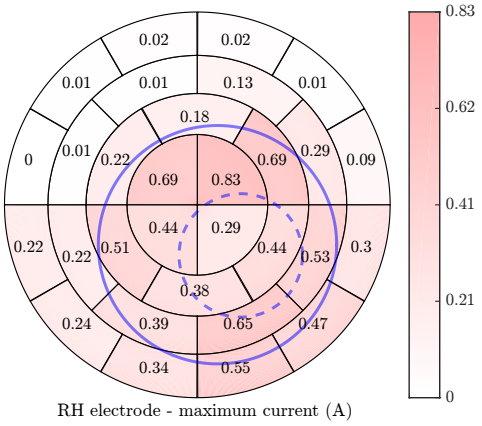

(b) First Excitation

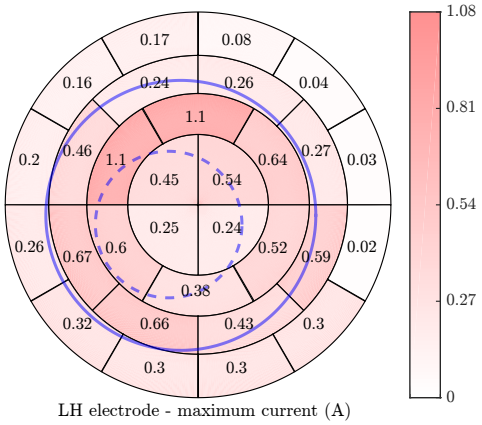

(c) Second Excitation

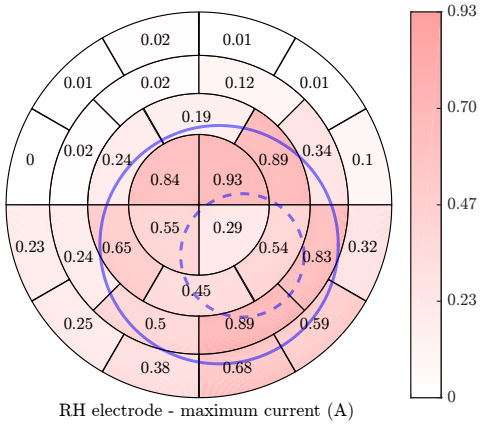

(d) Second Excitation

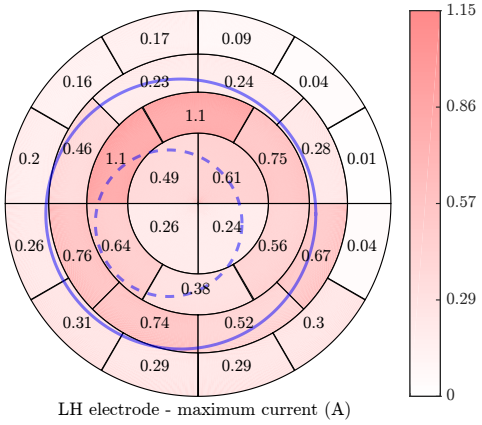

(e) Third Excitation

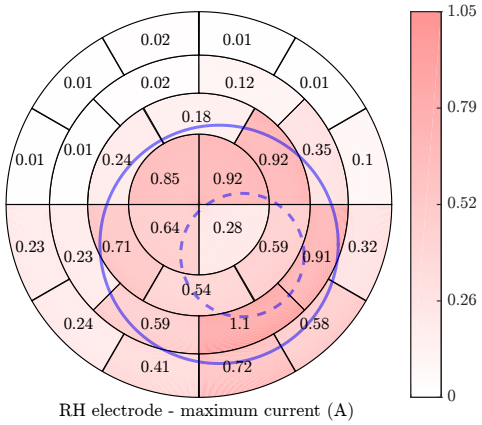

(f) Third Excitation

Figure E.11. The current distribution at the left-hand electrode (LH) (*left*) and the right-hand electrode (RH) (*right*) of Log 4. *Note:* The blue solid and dashed lines denote approximately the size of the log and its heartwood. The values are in amperes.

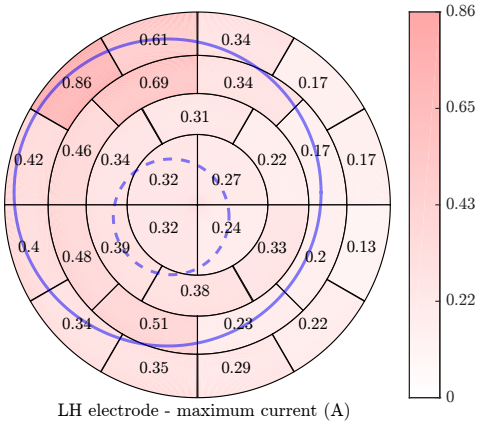

(a) First Excitation

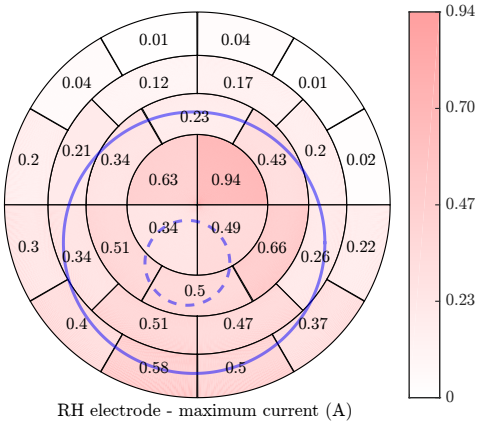

(b) First Excitation

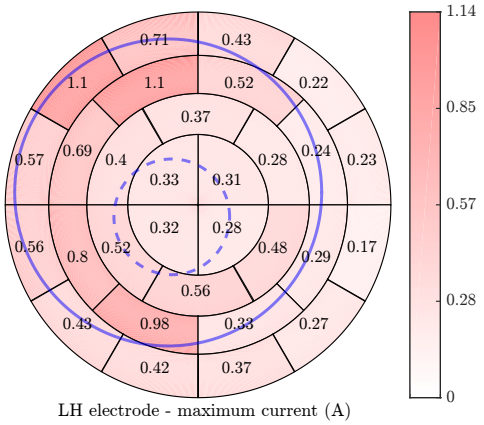

(c) Second Excitation

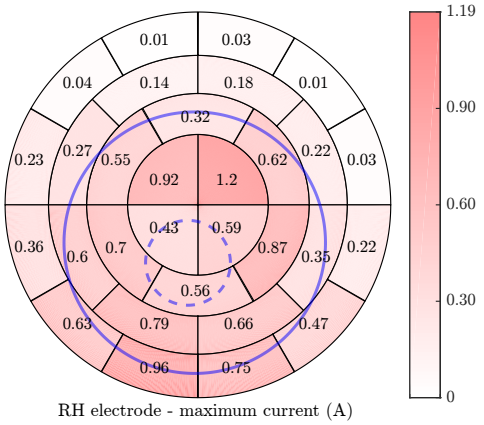

(d) Second Excitation

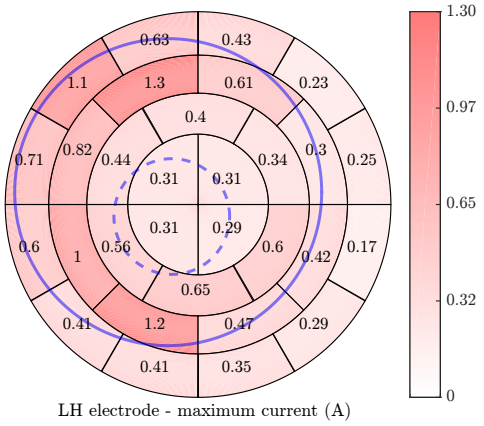

(e) Third Excitation

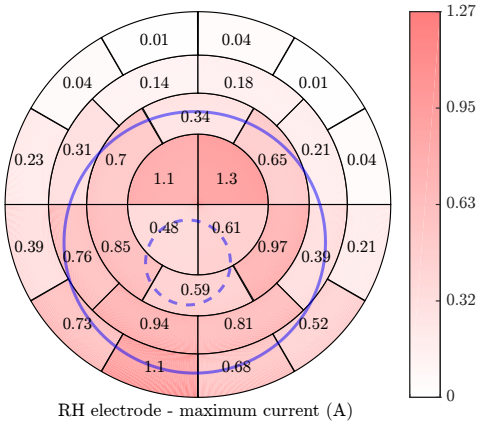

(f) Third Excitation

Figure E.12. The current distribution at the left-hand electrode (LH) (*left*) and the right-hand electrode (RH) (*right*) of Log 5. *Note:* The blue solid and dashed lines denote approximately the size of the log and its heartwood. The values are in amperes.

E.4 External Temperature of Logs 2-5

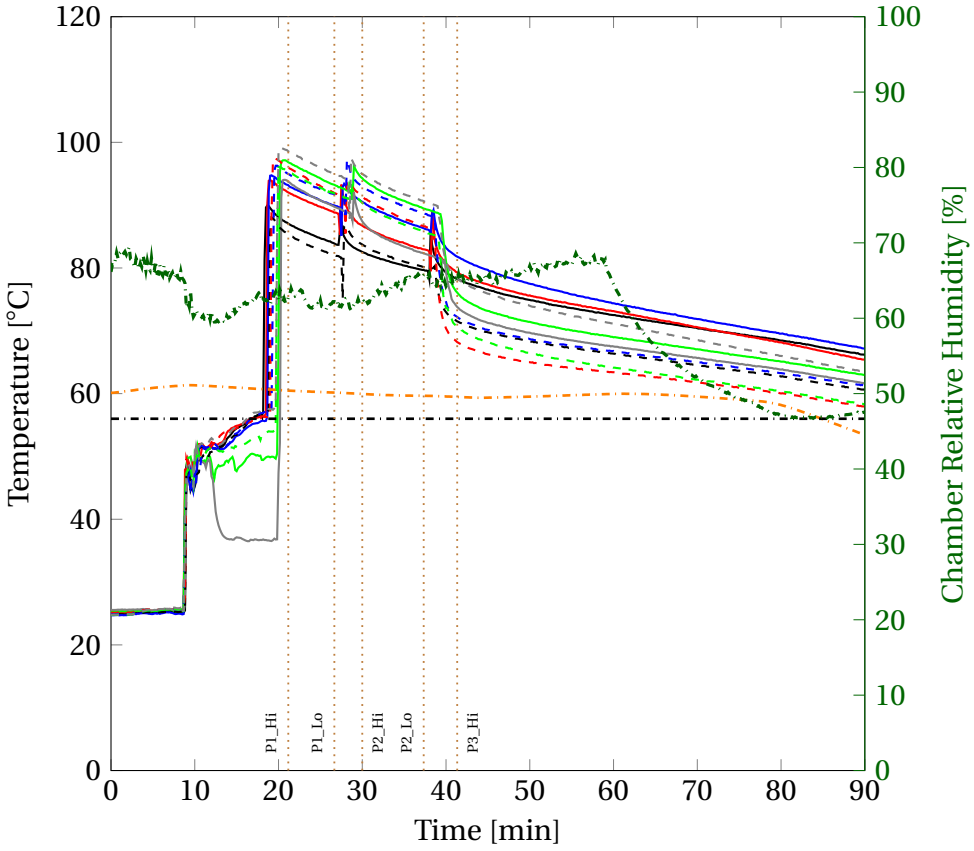

Figure E.13. The external temperature (32 mm depth) of Log 2 during the first 90 minutes after the last excitation ($t = 0$), measured by RTDs 1-10.The solid and dashed lines denote the temperature recorded by RTDs 1-5 and RTDs 6-10, respectively. The black and orange dash-dotted lines denote the ISPM15 temperature of 56°C and the chamber temperature, respectively. The dark green dash-dotted line represents the relative humidity in the chamber. *Note:* P1_Hi is the beginning of temperature recording at P1, P1_Lo is the end of temperature recording of temperature at P1. P2_Hi is the beginning of temperature recording at P2, P2_Lo is the end of temperature recording of temperature at P2. P3_Hi is the beginning of temperature recording at P3.

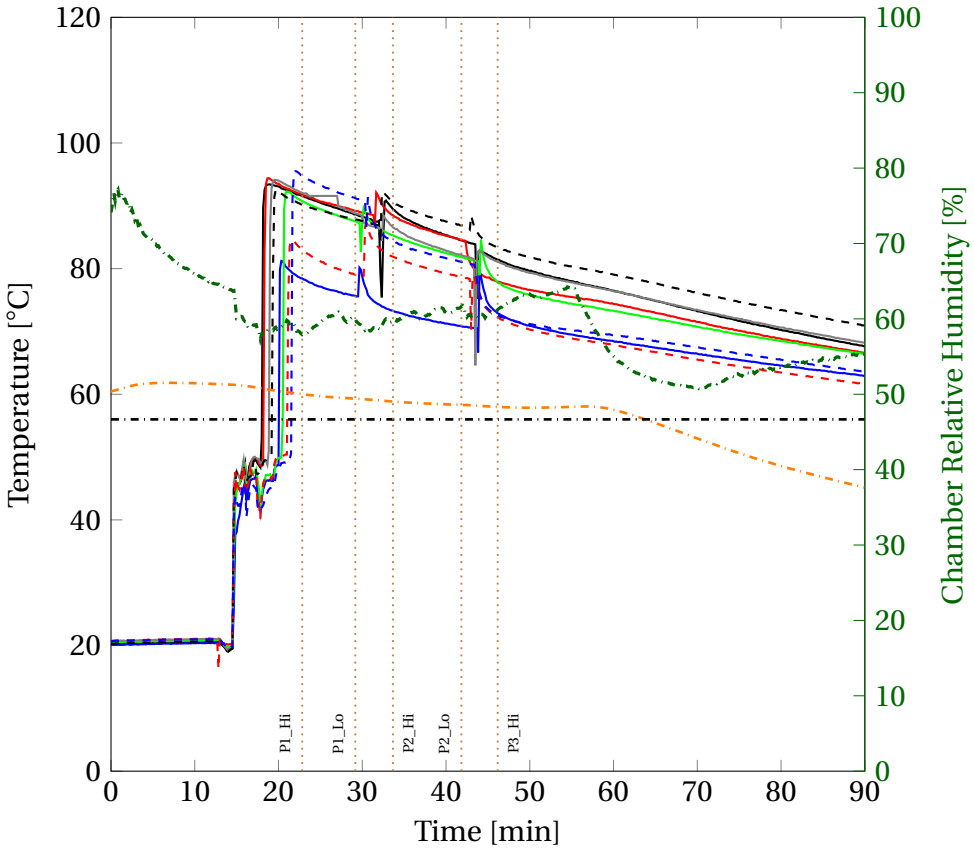

Figure E.14. The external temperature (32 mm depth) of Log 3 during the first 90 minutes after the last excitation ($t = 0$), measured by RTDs 1-10. The solid and dashed lines denote the temperature recorded by RTDs 1-5 and RTDs 6-10, respectively. The black and orange dash-dotted lines denote the ISPM15 temperature of 56°C and the chamber temperature, respectively. The dark green dash-dotted line represents the relative humidity in the chamber. *Note:* P1_Hi is the beginning of temperature recording at P1, P1_Lo is the end of temperature recording of temperature at P1. P2_Hi is the beginning of temperature recording at P2, P2_Lo is the end of temperature recording of temperature at P2. P3_Hi is the beginning of temperature recording at P3.

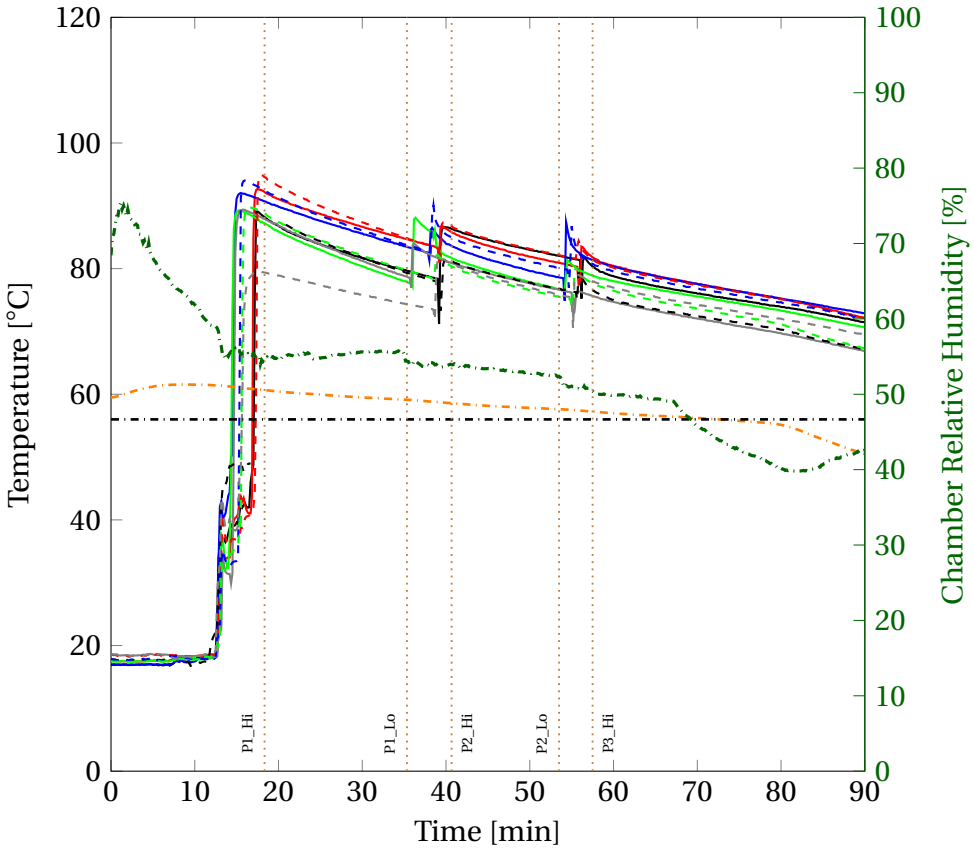

Figure E.15. The external temperature (32 mm depth) of Log 4 during the first 90 minutes after the last excitation ($t = 0$), measured by RTDs 1-10. The solid and dashed lines denote the temperature recorded by RTDs 1-5 and RTDs 6-10, respectively. The black and orange dash-dotted lines denote the ISPM15 temperature of 56°C and the chamber temperature, respectively. The dark green dash-dotted line represents the relative humidity in the chamber. *Note:* P1_Hi is the beginning of temperature recording at P1, P1_Lo is the end of temperature recording of temperature at P1. P2_Hi is the beginning of temperature recording at P2, P2_Lo is the end of temperature recording of temperature at P2. P3_Hi is the beginning of temperature recording at P3.

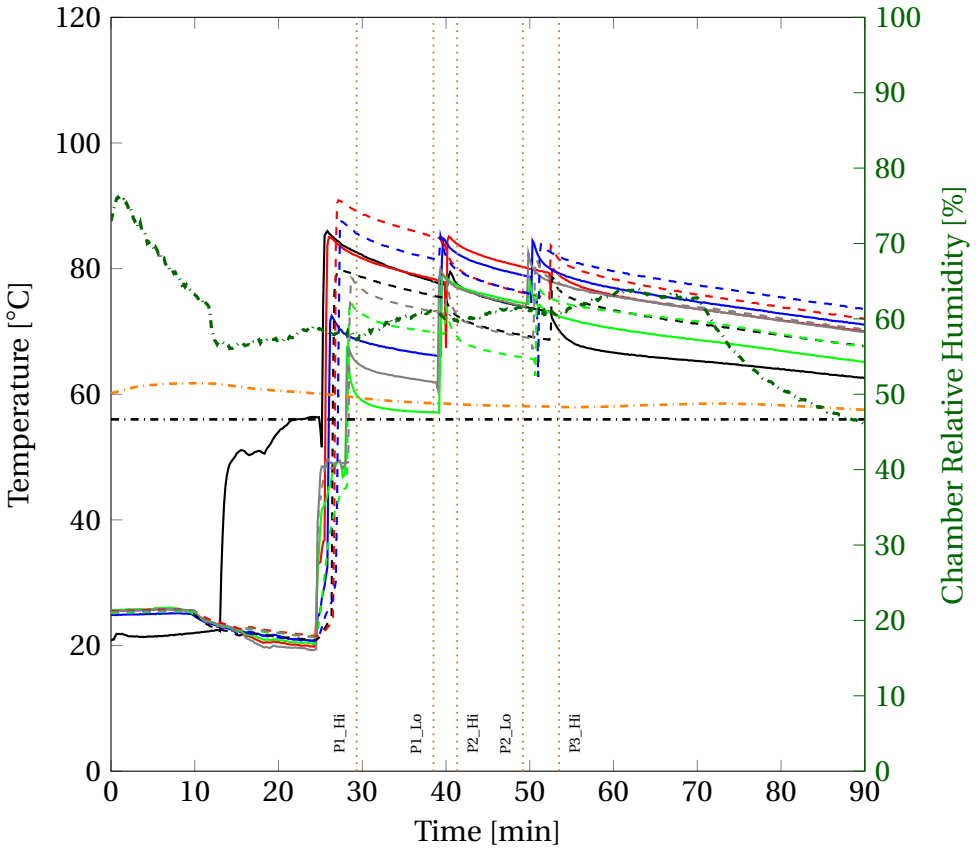

Figure E.16. The external temperature (32 mm depth) of Log 5 during the first 90 minutes after the last excitation ($t = 0$), measured by RTDs 1-10. The solid and dashed lines denote the temperature recorded by RTDs 1-5 and RTDs 6-10, respectively. The black and orange dash-dotted lines denote the ISPM15 temperature of 56°C and the chamber temperature, respectively. The dark green dash-dotted line represents the relative humidity in the chamber. *Note:* P1_Hi is the beginning of temperature recording at P1, P1_Lo is the end of temperature recording of temperature at P1. P2_Hi is the beginning of temperature recording at P2, P2_Lo is the end of temperature recording of temperature at P2. P3_Hi is the beginning of temperature recording at P3.

E.5 Internal Temperature of Logs 2-5

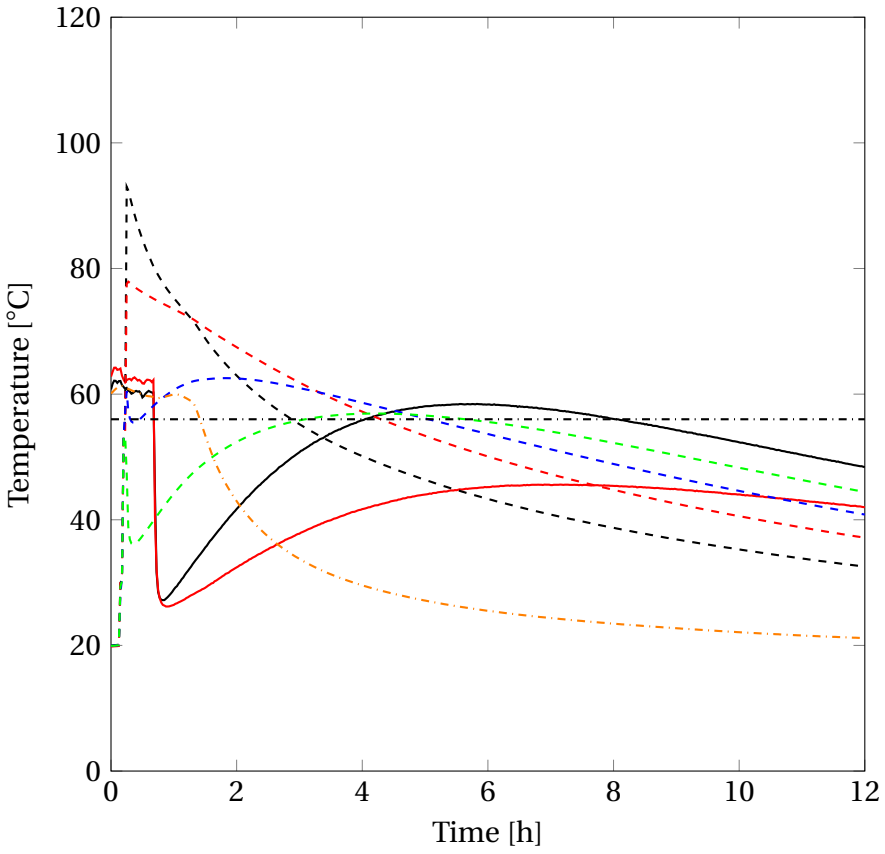

Figure E.17. The internal temperature of Log 2 during 12 hours of cooling, after the last excitation, measured by RTDs 11 and 12 (the black and red solid lines, respectively), and PTSs 1 (32 mm depth), 2 (62 mm depth), 3 (92 mm depth), and 4 (122 mm depth), shown as the black, red, blue, and green dashed lines, respectively. The black and orange dash-dotted lines denote ISPM15 temperature of 56°C and the chamber's temperature, respectively.

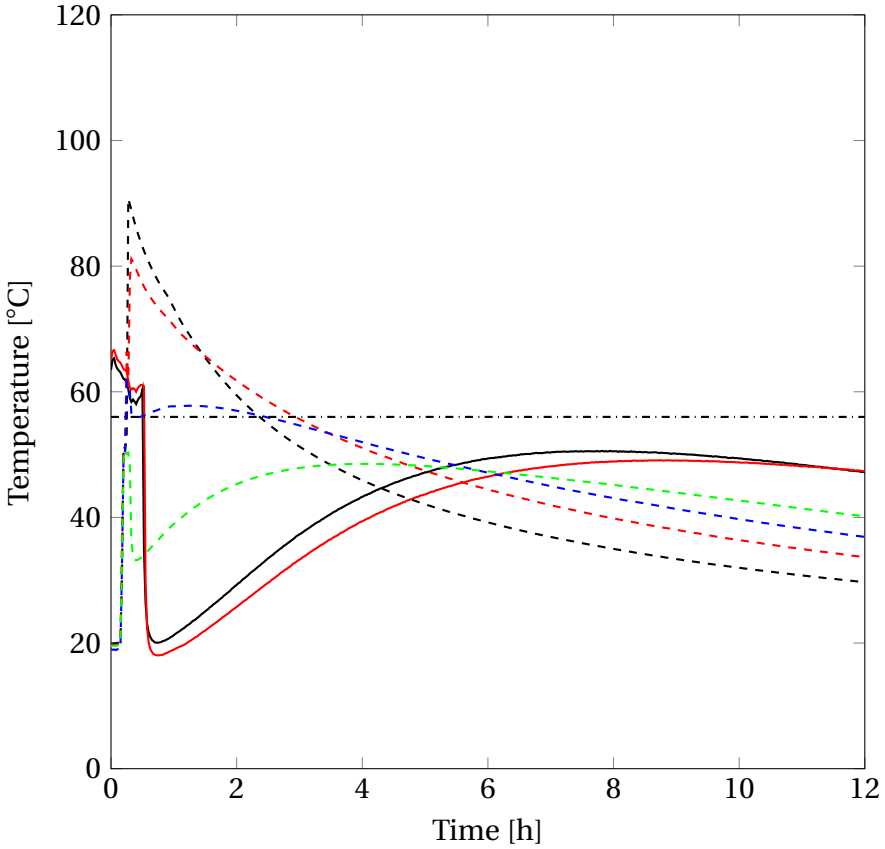

Figure E.18. The internal temperature of Log 3 during 12 hours of cooling, after the last excitation, measured by RTDs 11 and 12 (the black and red solid lines, respectively), and PTSs 1 (32 mm depth), 2 (62 mm depth), 3 (92 mm depth), and 4 (122 mm depth), shown as the black, red, blue, and green dashed lines, respectively. The black and orange dash-dotted lines denote ISPM15 temperature of 56°C and the chamber's temperature, respectively.

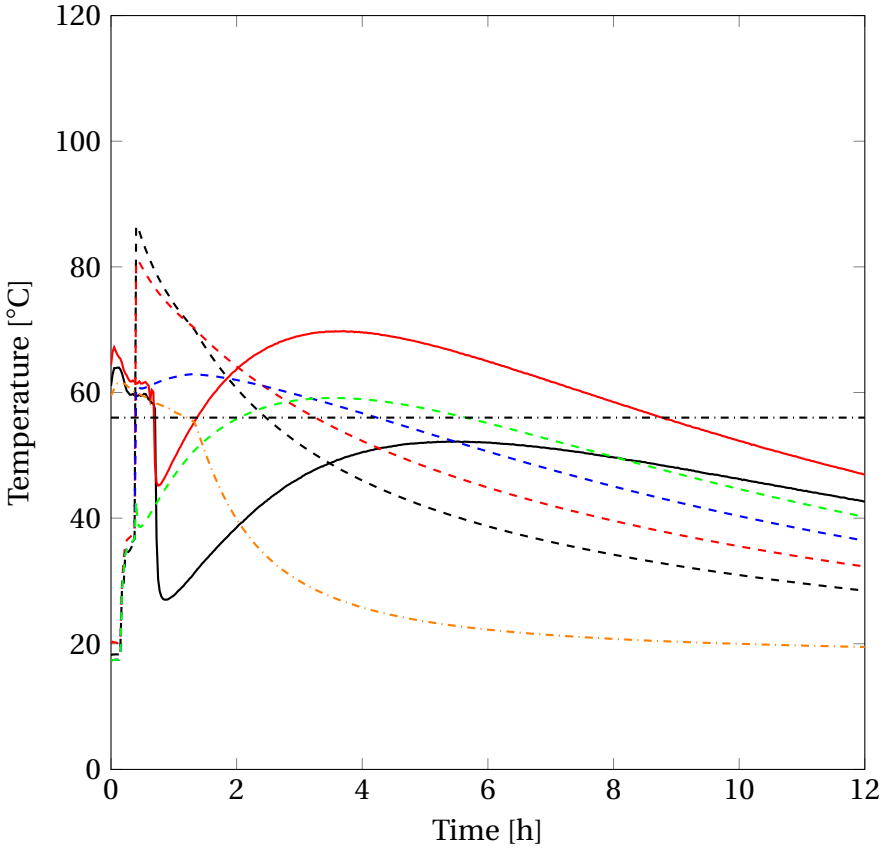

Figure E.19. The internal temperature of Log 4 during 12 hours of cooling, after the last excitation, measured by RTDs 11 and 12 (the black and red solid lines, respectively), and PTSs 1 (32 mm depth), 2 (62 mm depth), 3 (92 mm depth), and 4 (122 mm depth), shown as the black, red, blue, and green dashed lines, respectively. The black and orange dash-dotted lines denote ISPM15 temperature of 56°C and the chamber's temperature, respectively. *Note:* RTD 12 was inserted to the depth of 145 mm.

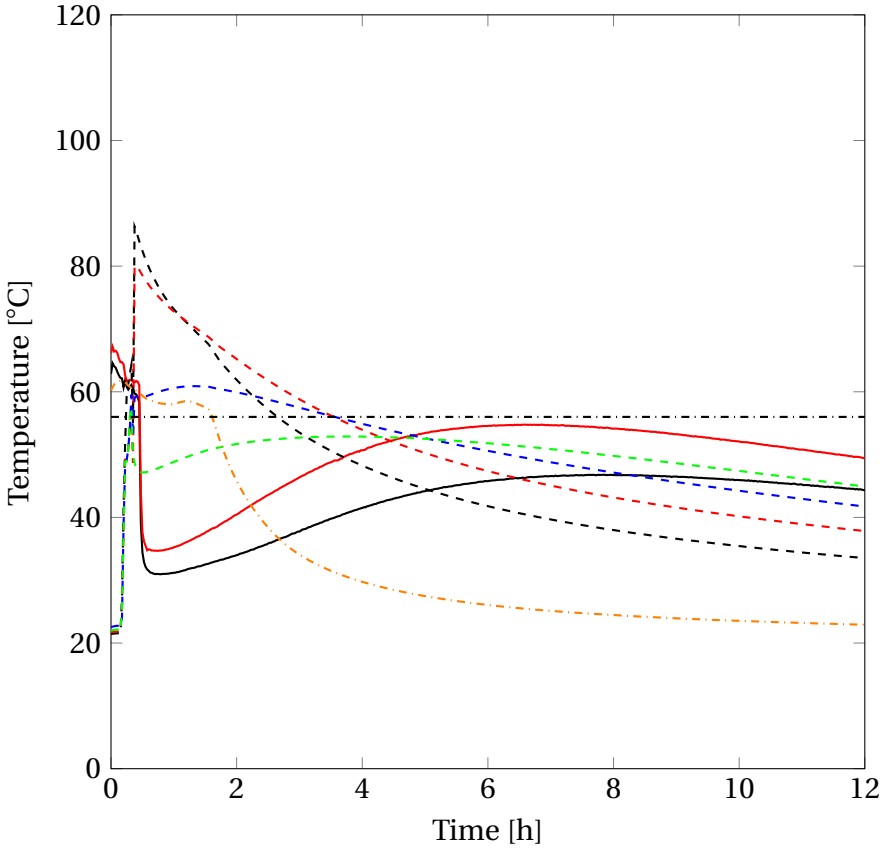

Figure E.20. The internal temperature of Log 5 during 12 hours of cooling, after the last excitation, measured by RTDs 11 and 12 (the black and red solid lines, respectively), and PTSs 1 (32 mm depth), 2 (62 mm depth), 3 (92 mm depth), and 4 (122 mm depth), shown as the black, red, blue, and green dashed lines, respectively. The black and orange dash-dotted lines denote ISPM15 temperature of 56°C and the chamber's temperature, respectively.

E.6 Predicted Temperature of Logs 1-5

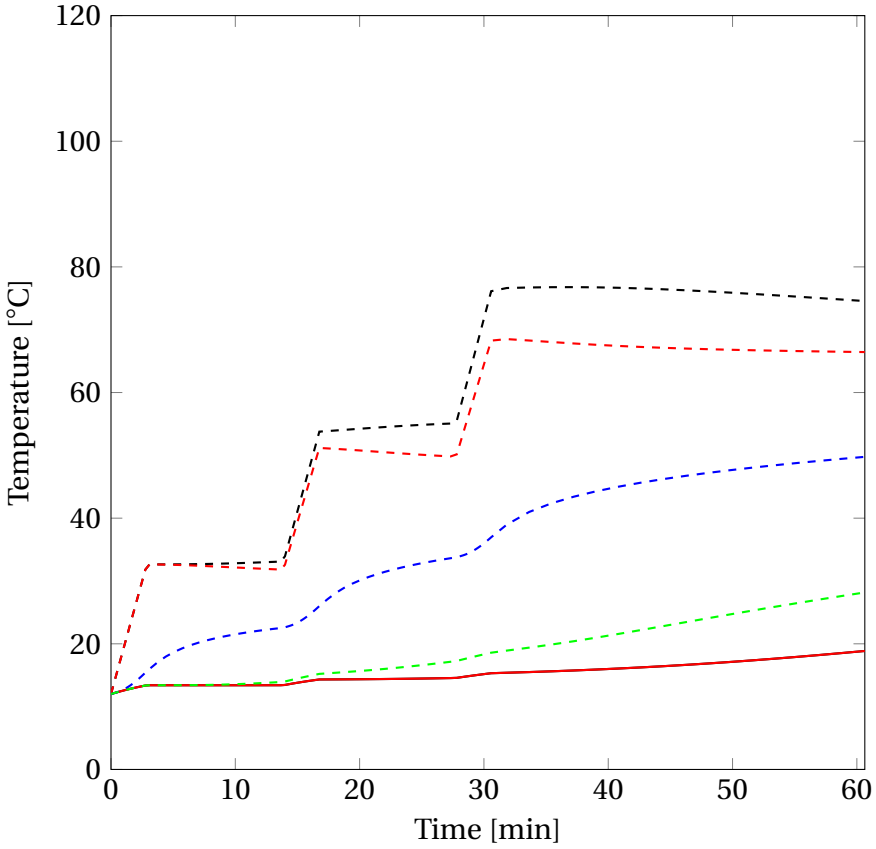

Figure E.21. The predicted temperature of Log 2. *Note:* The solid red and black lines denote RTDs 11 and 12, respectively, and the dashed black, red, blue, and green lines represent PTSs 1, 2, 3, and 4, respectively.

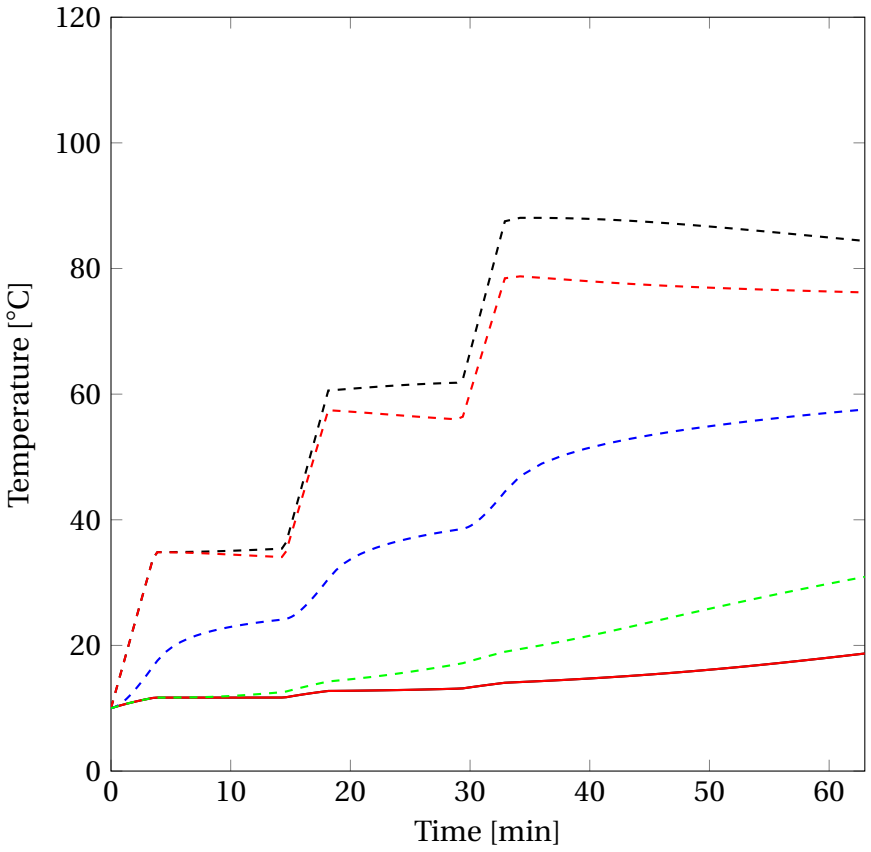

Figure E.22. The predicted temperature of Log 3. *Note:* The solid red and black lines denote RTDs 11 and 12, respectively, and the dashed black, red, blue, and green lines represent PTSs 1, 2, 3, and 4, respectively.

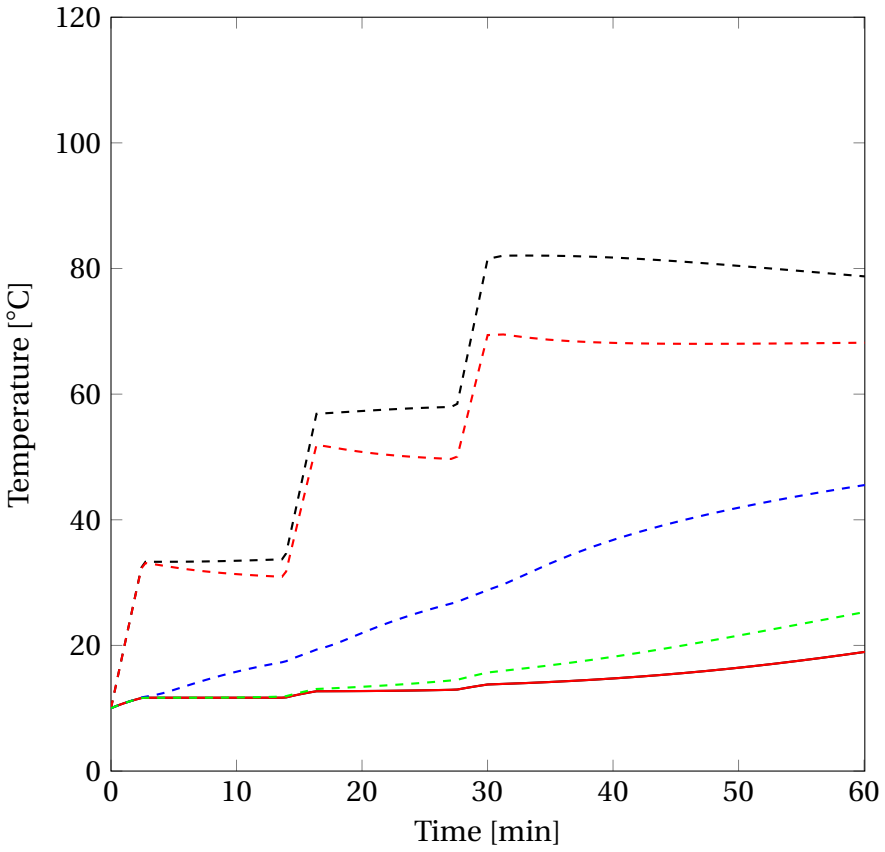

Figure E.23. The predicted temperature of Log 4. *Note:* The solid red and black lines denote RTDs 11 and 12, respectively, and the dashed black, red, blue, and green lines represent PTSs 1, 2, 3, and 4, respectively.

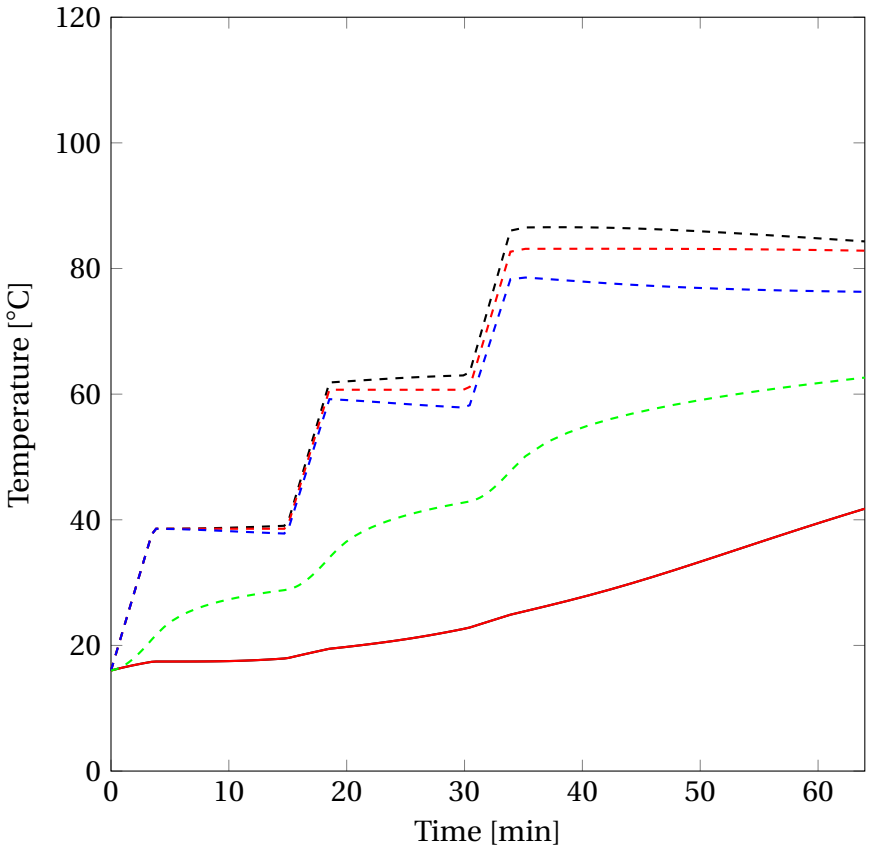

Figure E.24. The predicted temperature of Log 5. *Note:* The solid red and black lines denote RTDs 11 and 12, respectively, and the dashed black, red, blue, and green lines represent PTSs 1, 2, 3, and 4, respectively.

E.7 Predicted Temperature of Log 6

E.7.1 Methods for Log 6

Log 6 was tested much later than Logs 1-5 and hence it is only included in this appendix. Prior to the test, this log had been kept outside of the laboratory for 60 days, under tarpaulin. The log was tested following the methods described in Section 7.2. Its LED and SED were 392 and 372 mm, respectively, and the heartwood's LED and SED were 165 and 150 mm, respectively. The log's length was 3.3 m. The initial temperature was 15.5°C. Unlike Logs 1-5, Log 6 was weighed prior to the experiment (344 kg) and after the experiment, about 24 hours later, (329 kg). The total introduced energy was 18.6 kW·h. The transient moisture loss during the Joule treatment has been unknown.

Calculating Required Energy

To calculate the required energy for this log, it was assumed that the sapwood's moisture content and the basic density were 173% and 415 $kg \cdot m^{-3}$, respectively. This assumption was based on the moisture content and basic density of the cubes from *Set 1* used in the electrical conductivity experiment, described in Section 5.2.1. The heartwood's basic density and the moisture content were assumed to be 45% and 400 $kg \cdot m^{-3}$, respectively; the same values were used for Logs 1-5.

Using these basic densities and moisture contents, the mass of the log, of the sapwood and of the heartwood was calculated, using Equation 7.24, and was approximately equal to 393, 356, and 37 kg, respectively. Thereafter, the sapwood's moisture content was used to calculate the heat capacity (3148 $J \cdot kg^{-1} \cdot °C^{-1}$), using Equations 7.4. Knowing the sapwood mass and its heat capacity, the total required energy (18.6 kW·h) was determined using Equation 7.23.

Real Moisture Content

The calculated mass of the log was approximately 15% higher than the real mass determined prior to the experiment. This error increased the total required energy, causing unnecessary overheating and enlarging the difference between the experimental and predicted temperatures. As the total log mass was calculated based on the assumed moisture contents and basic densities, the error was hidden within the assumed values. However, basic density is independent of moisture content and shrinkage and hence the basic densities did not affect the error. Furthermore,

since heartwood was located in the centre of the log, its moisture content was assumed to be constant and its mass of 37 kg was potentially equal to the real mass of the heartwood. Thus, the only remaining cause of the error was linked to the sapwood's overestimated moisture content of about 170%.

Thus, the real sapwood mass was calculated as:

$$m_{SW_{exp}} = m_{L_{exp}} - m_{HW_{exp}}, \tag{E.33}$$

where $m_{SW_{exp}}$ is the experimental sapwood mass; $m_{L_{exp}}$ is the experimental log mass, determined as the average value of two mass values obtained before and after the experiment, respectively; and $m_{HW_{exp}}$ is the experimental heartwood mass, equal to 37 kg. Hence the real sapwood mass was approximately 300 kg, which is 56kg lower than initially calculated. Using the real sapwood mass in the following equation:

$$X_{SW_{exp}} = \frac{m_{SW_{exp}}}{\rho_{s_{SW}} V_{g_{SW}}} - 1, \tag{E.34}$$

the fitted sapwood moisture content ($X_{SW_{exp}}$) of 1.3 (or 130%) was calculated. If this moisture content was used to calculate the sapwood heat capacity and the required energy, they would be equal to 2954 $J \cdot kg^{-1} \cdot °C^{-1}$ and 14.6 $kW \cdot h$, respectively. Hence, in the experiment, extra 4 $kW \cdot h$ of energy was introduced to Log 6. In this appendix, using the sapwood moisture content of 170% and 130%, two cases of the experimental heating were simulated using the 1D model. The results were compared with experimental temperature of Log 6.

E.7.2 Results for Log 6

The total energy of 18.6 $kW \cdot h$ was split into three excitation (Figure E.25). Figures E.26 and E.27 show temperature profiles measured by RTDs 1-10 and PTSs 1-4, respectively. The calculated temperature of two simulated cases are shown in Figure E.28a. Using fitted moisture content, the predicted temperature at the 32 mm depth increased from about 78°C to 94°C. The temperatures determined at other depths are summarised in Table E.2. Overall, at the end of the final excitation, the sapwood temperature calculated using 130% moisture content was about 15°C higher than that determined with 170% moisture content (Figure E.28b). The predicted heartwood temperatures were comparable. In addition, following the method discussed in

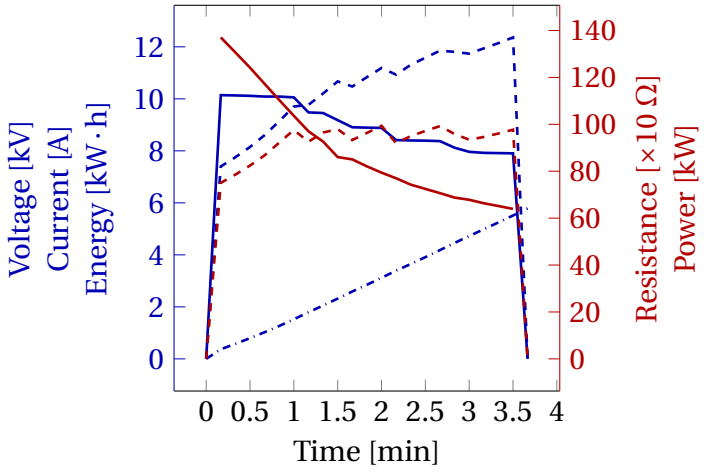

(a) First Excitation

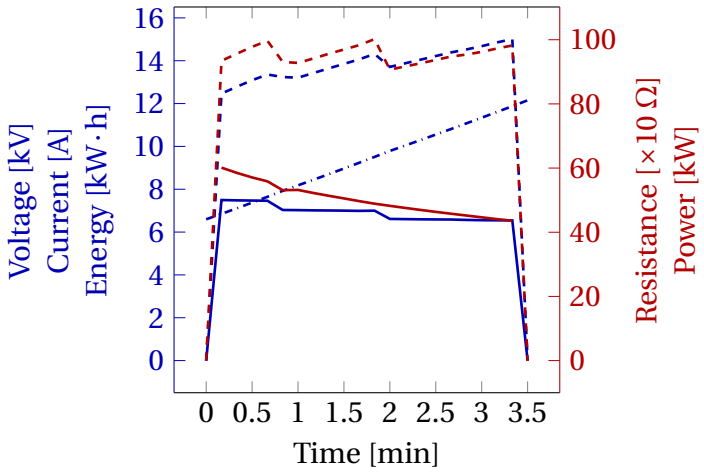

(b) Second Excitation

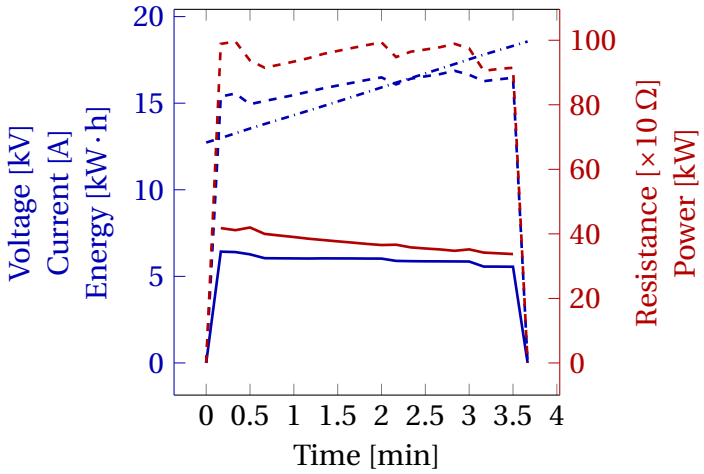

(c) Third Excitation

Figure E.25. The electrical data of Log 6. The blue solid, dashed, and dash-dotted lines denote the voltage, the current, and the energy, respectively. The red solid and dashed lines denote the electrical resistance and the power, respectively.

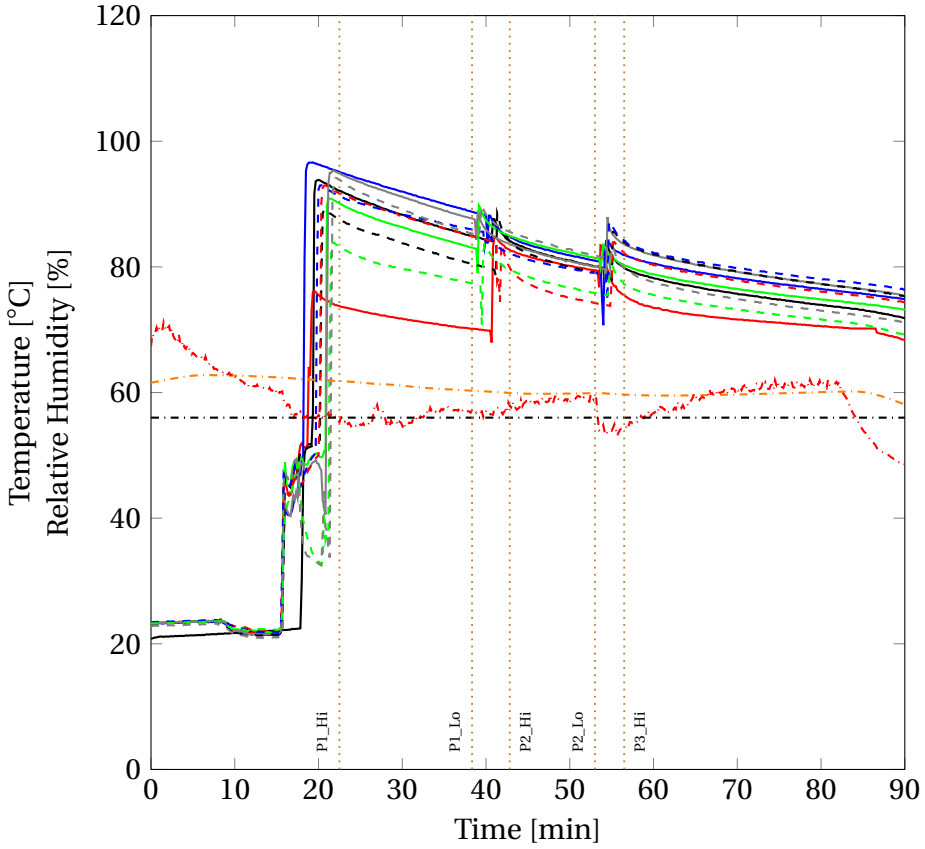

Figure E.26. The external temperature (32 mm depth) of Log 6 during the first 90 minutes after the last excitation ($t = 0$), measured by RTDs 1-10. The solid and dashed lines denote the temperature recorded by RTDs 1-5 and RTDs 6-10, respectively. The black, orange, and red dash-dotted lines denote the ISPM15 temperature of 56°C, the temperature and relative humidity of the chamber, respectively. *Note:* P1_Hi is the beginning of temperature recording at P1, P1_Lo is the end of temperature recording of temperature at P1. P2_Hi is the beginning of temperature recording at P2, P2_Lo is the end of temperature recording of temperature at P2. P3_Hi is the beginning of temperature recording at P3.

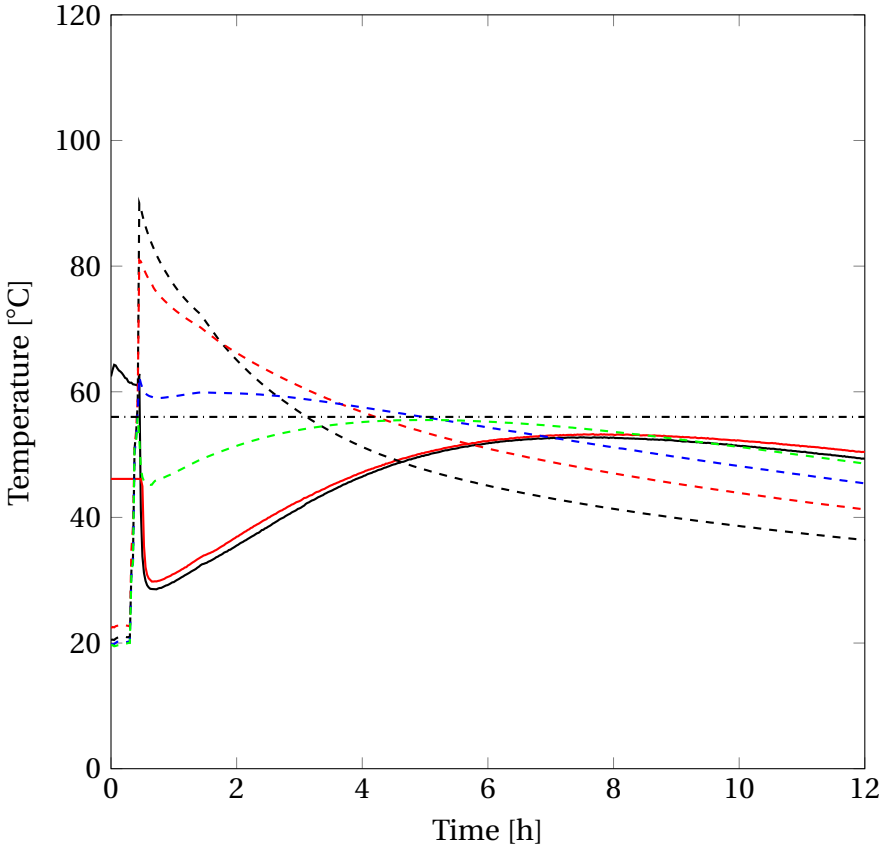

Figure E.27. The internal temperature of Log 6 during 12 hours of cooling, after the last excitation, measured by RTDs 11 and 12 (the black and red solid lines, respectively), and PTSs 1 (32 mm depth), 2 (62 mm depth), 3 (92 mm depth), and 4 (122 mm depth), shown as the black, red, blue, and green dashed lines, respectively. The black and orange dash-dotted lines denote ISPM15 temperature of 56°C and the chamber's temperature, respectively.

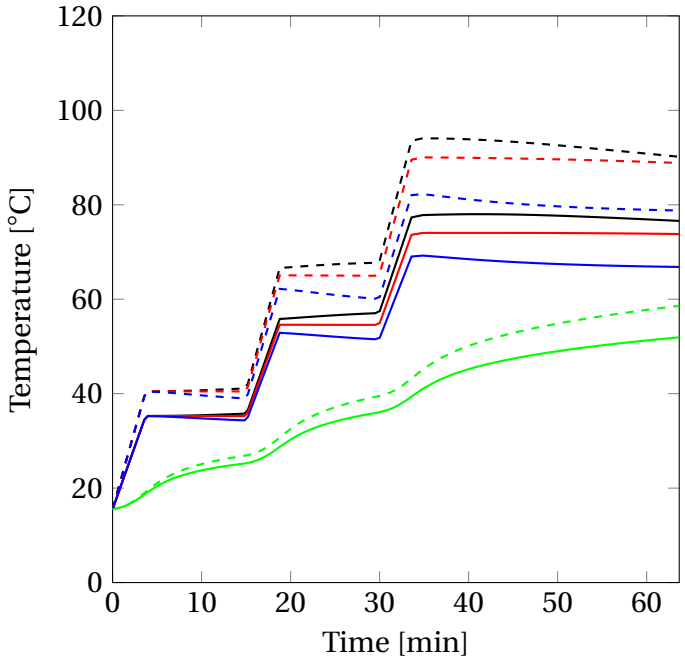

(a)

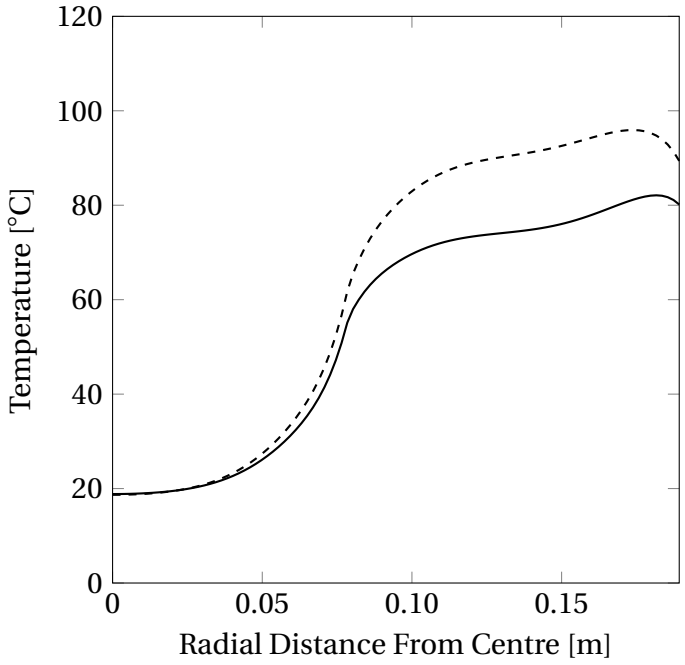

(b)

Figure E.28. The predicted temperature of Log 6 calculated using the sapwood moisture contents of 170% (solid lines) and of 130% (dashed lines): (a) the transient temperature change at different depths and (b) the radial temperature profile. *Note:* In (a), the black, red, blue, and green lines represent PTSs 1 (32 mm depth), 2 (62 mm depth), 3 (92 mm depth), and 4 (122 mm depth), respectively.

Table E.2. The experimental and predicted temperature values measured at the different depths after the third (final) excitation of Log 6.

Logs	Temperature [°C]			
	32 mm [a]	62 mm	92 mm	122 mm
Experimental Data	89±6	81	62	45
Fitted MC (130%)	94	90	82	43
Non-fitted MC (170%)	78	74	69	39

[a] The temperature of the logs at the 32 mm depth is shown as the average value with the standard deviation (±), based on the results obtained from RTDs 1-10 (at P1) and PTS 1.

Section 7.2, the experimental total and local resistances were estimated (Figures E.29a and b).

The obtained results show a more accurate prediction of the log's temperature and the total resistance. Hence, knowing real moisture content of sapwood, which can be readily estimated by mass measurement, helps to avoid logs' over-heating by accurately calculating the required amount of energy.

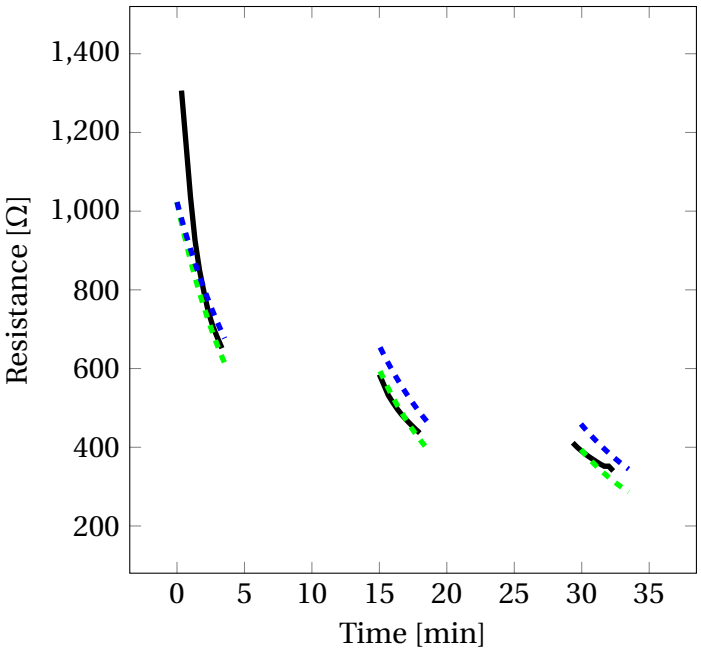

(a) Total Resistance

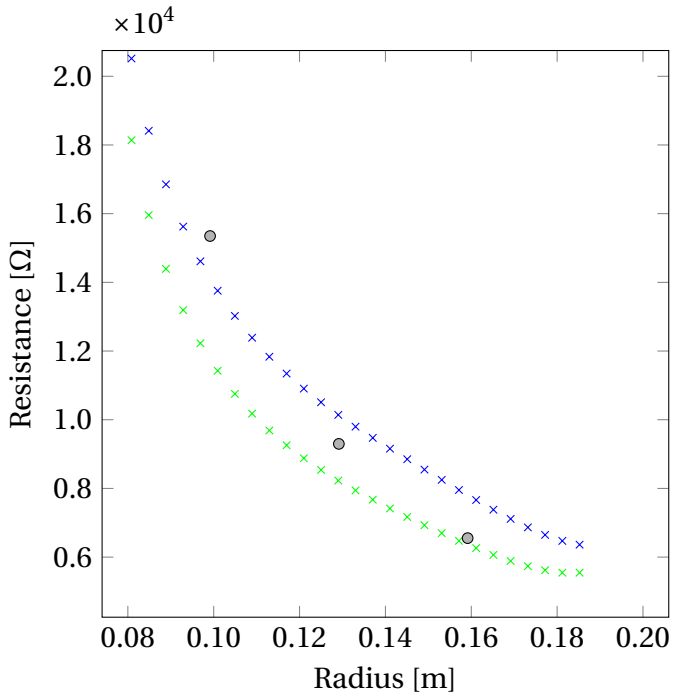

(b) Local Resistance

Figure E.29. Log 6: (a) the total electrical resistance and (b) the local resistance. *Note:* The blue and green colours denote the values calculated using the sapwood moisture contents of 170% and of 130%, respectively. The black line and the grey circles represent the experimental total and local resistances, respectively.

E.8 Experimental Data vs Model: Total Resistance

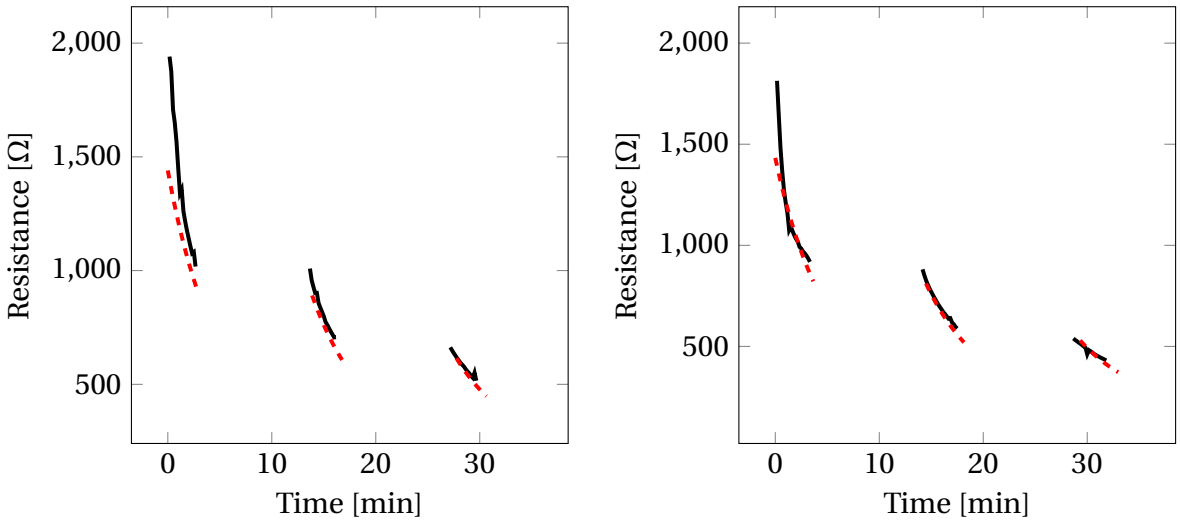

(a) Log 2

(b) Log 3

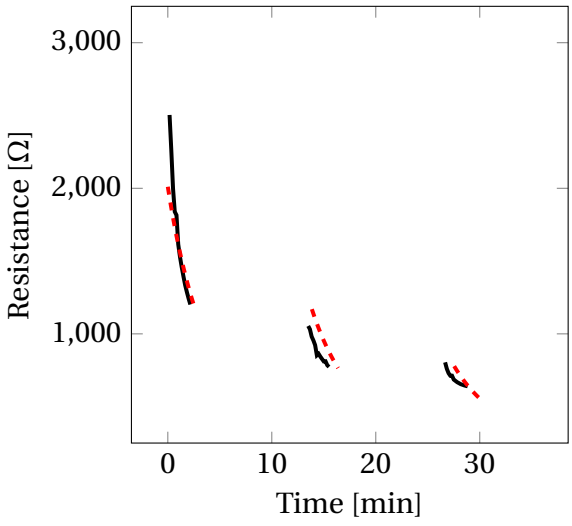

(c) Log 4

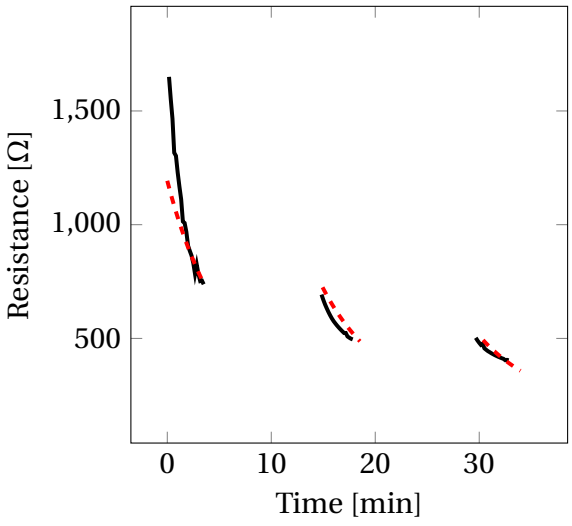

(d) Log 5

Figure E.30. The total electrical experimental resistance (black solid lines) and the predicted total resistance of Logs 2-5 (dashed red lines).

E.9 Experimental Data vs Model: Local Resistance

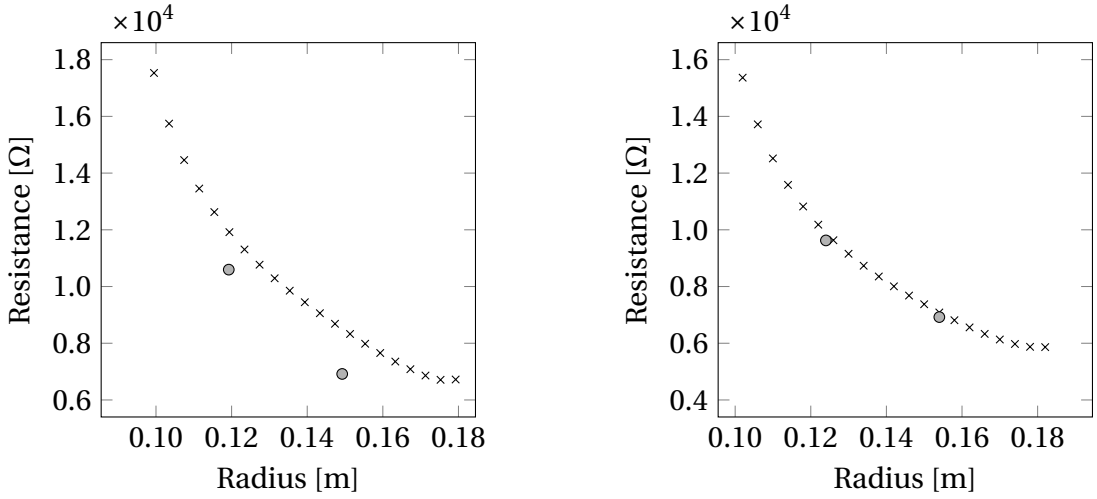

(a) Log 2

(b) Log 3

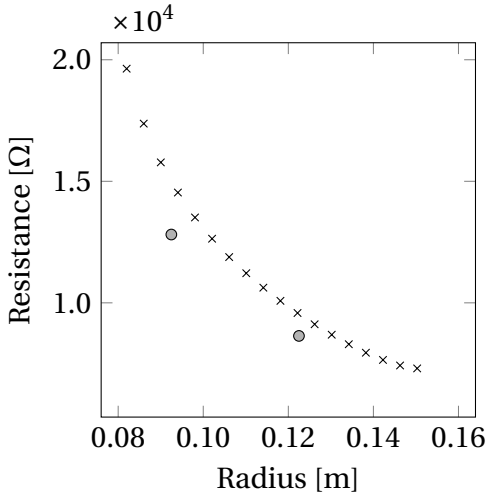

(c) Log 4

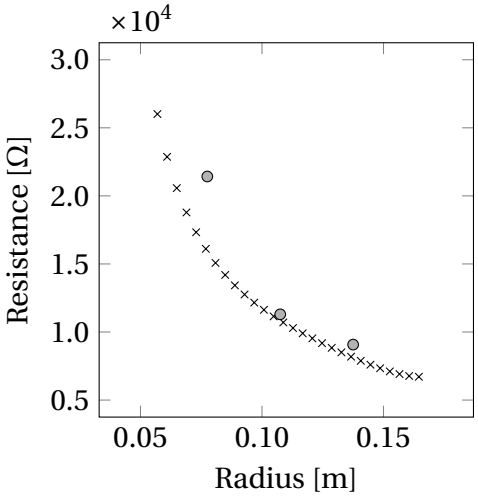

(d) Log 5

Figure E.31. The local resistance calculated based on the experimental temperatures recorded within the sapwood of Logs 2-5 (dots) and the predicted local resistance (crosses), at the end of the last excitation.

E.10 Current Distribution of Logs 1-5

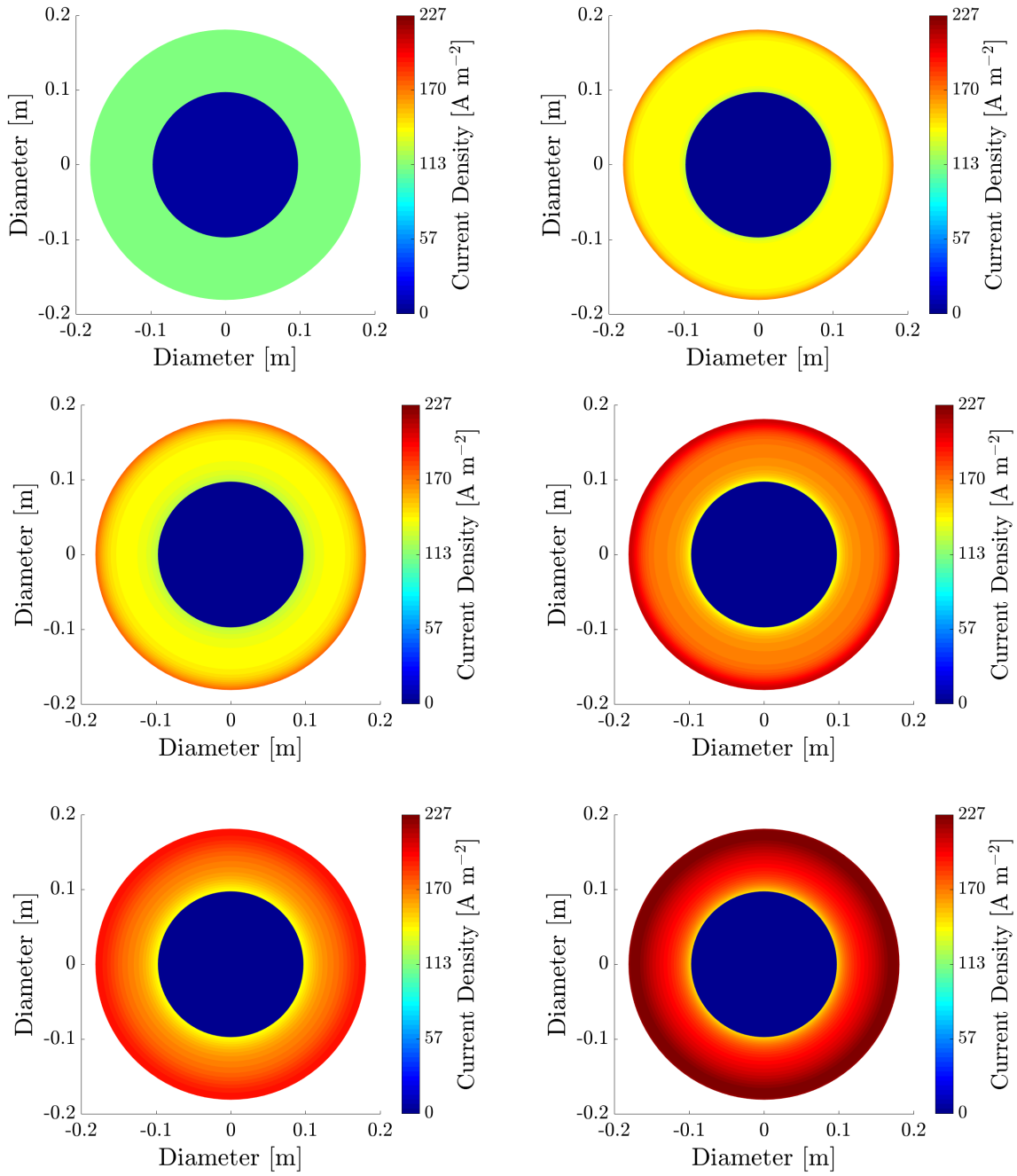

Figure E.32. The predicted current density distribution within Log 2 at the beginning (*left*) and the end (*right*) of each excitation. The top, middle, and bottom figures are the results from the 1st, 2nd, and 3rd excitation, respectively.

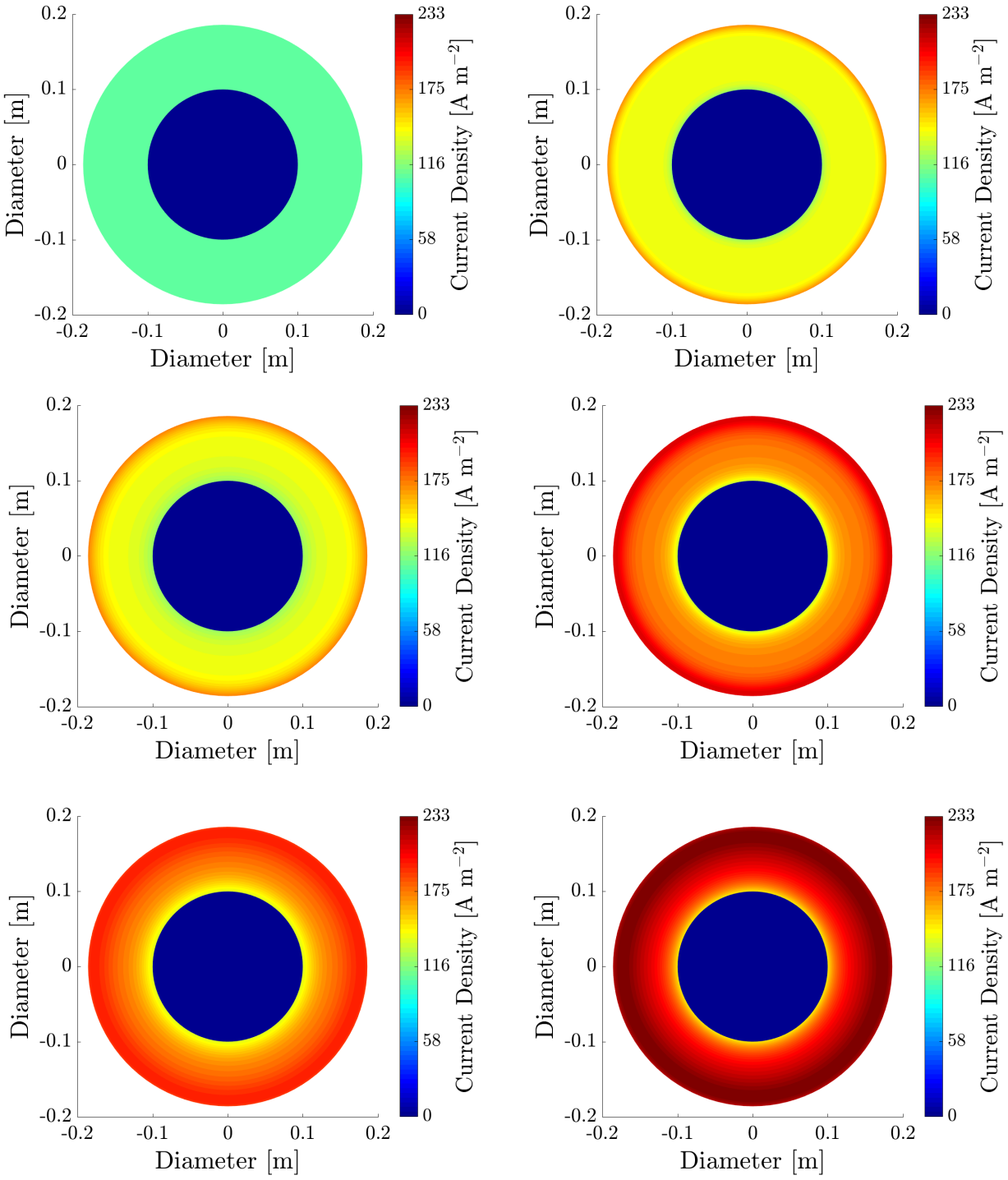

Figure E.33. The predicted current density distribution within Log 3 at the beginning (*left*) and the end (*right*) of each excitation. The top, middle, and bottom figures are the results from the 1st, 2nd, and 3rd excitation, respectively.

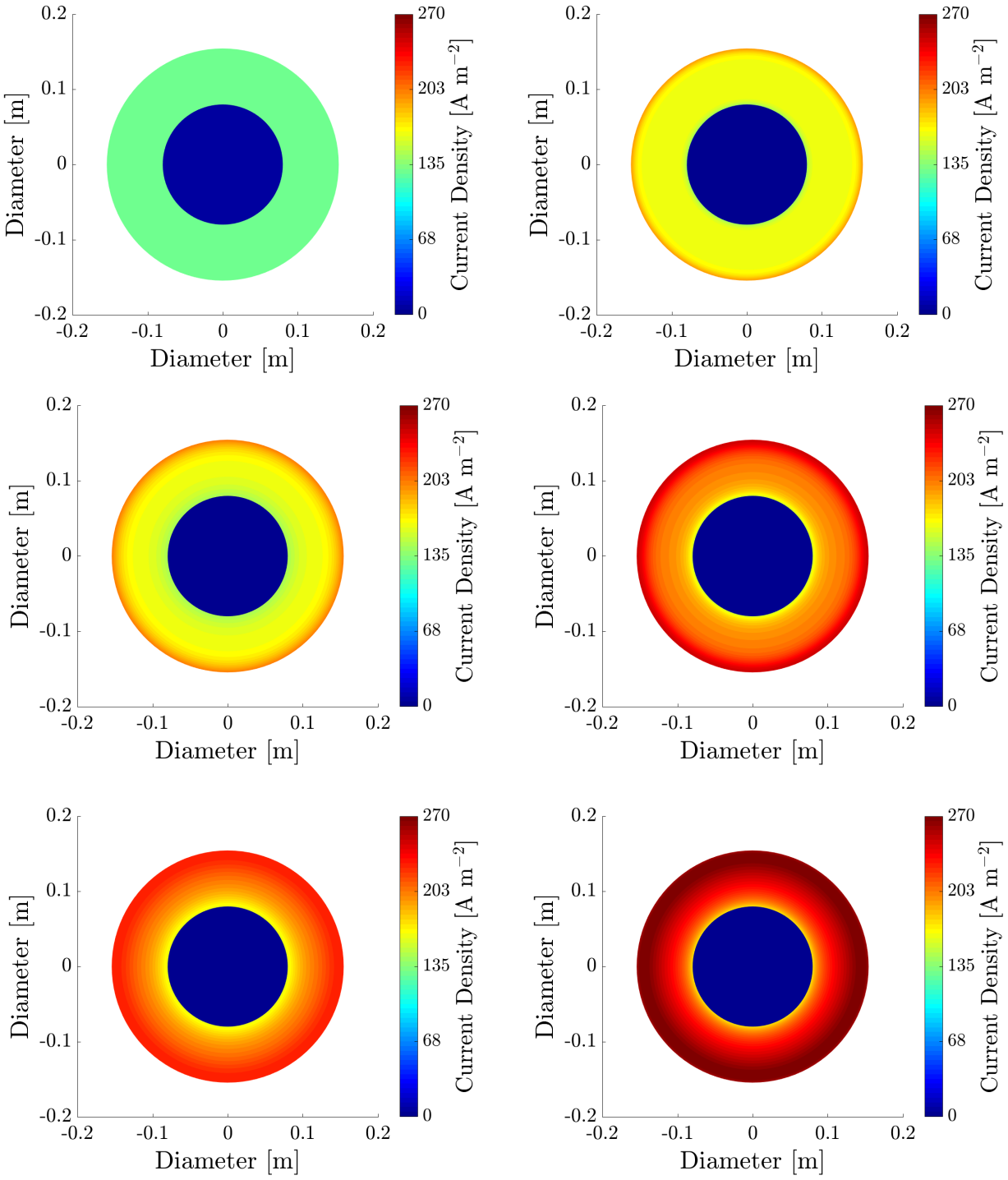

Figure E.34. The predicted current density distribution within Log 4 at the beginning (*left*) and the end (*right*) of each excitation. The top, middle, and bottom figures are the results from the 1st, 2nd, and 3rd excitation, respectively.

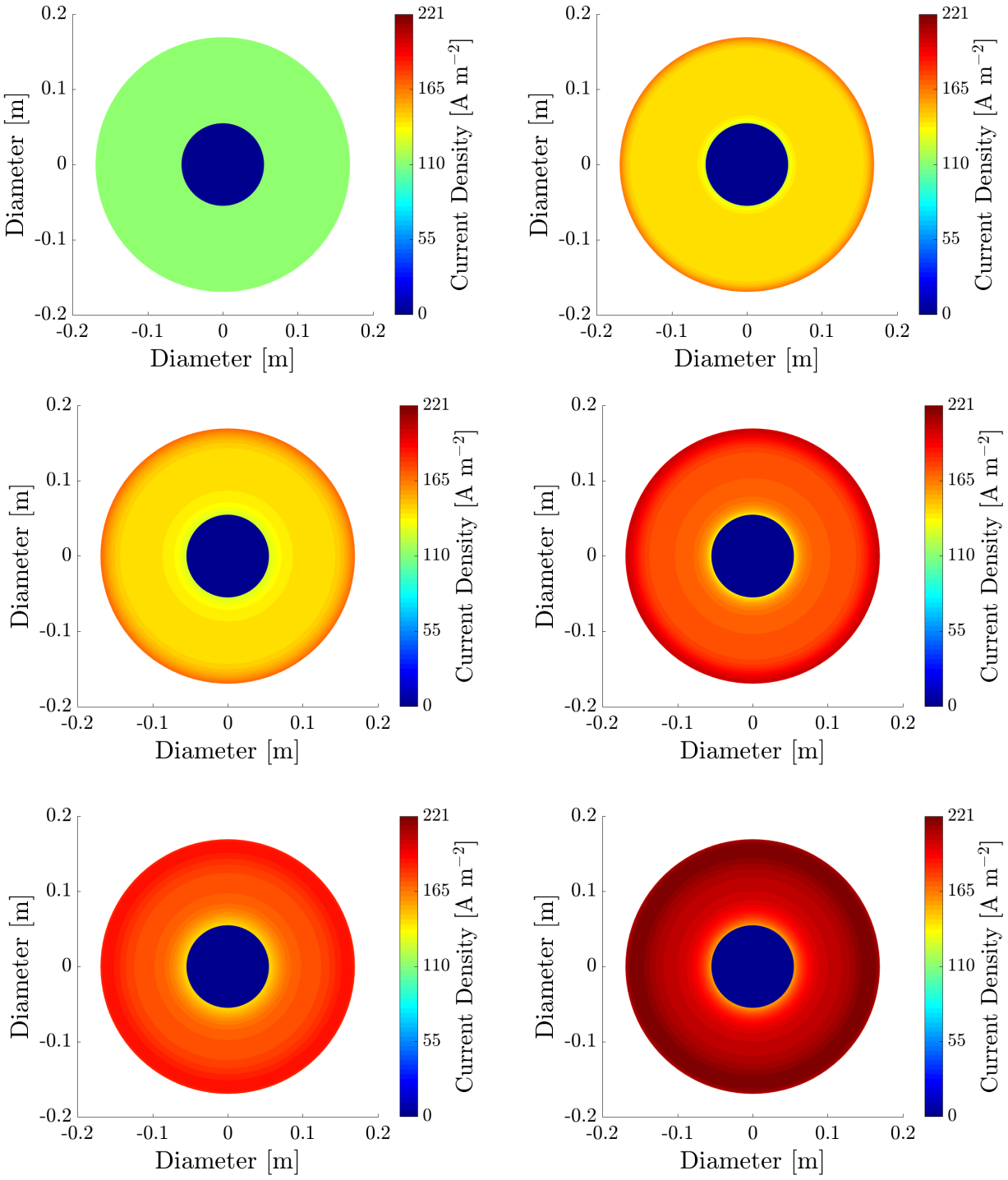

Figure E.35. The predicted current density distribution within Log 5 at the beginning (*left*) and the end (*right*) of each excitation. The top, middle, and bottom figures are the results from the 1st, 2nd, and 3rd excitation, respectively.

E.11 Temp Distribution of Logs 1-5

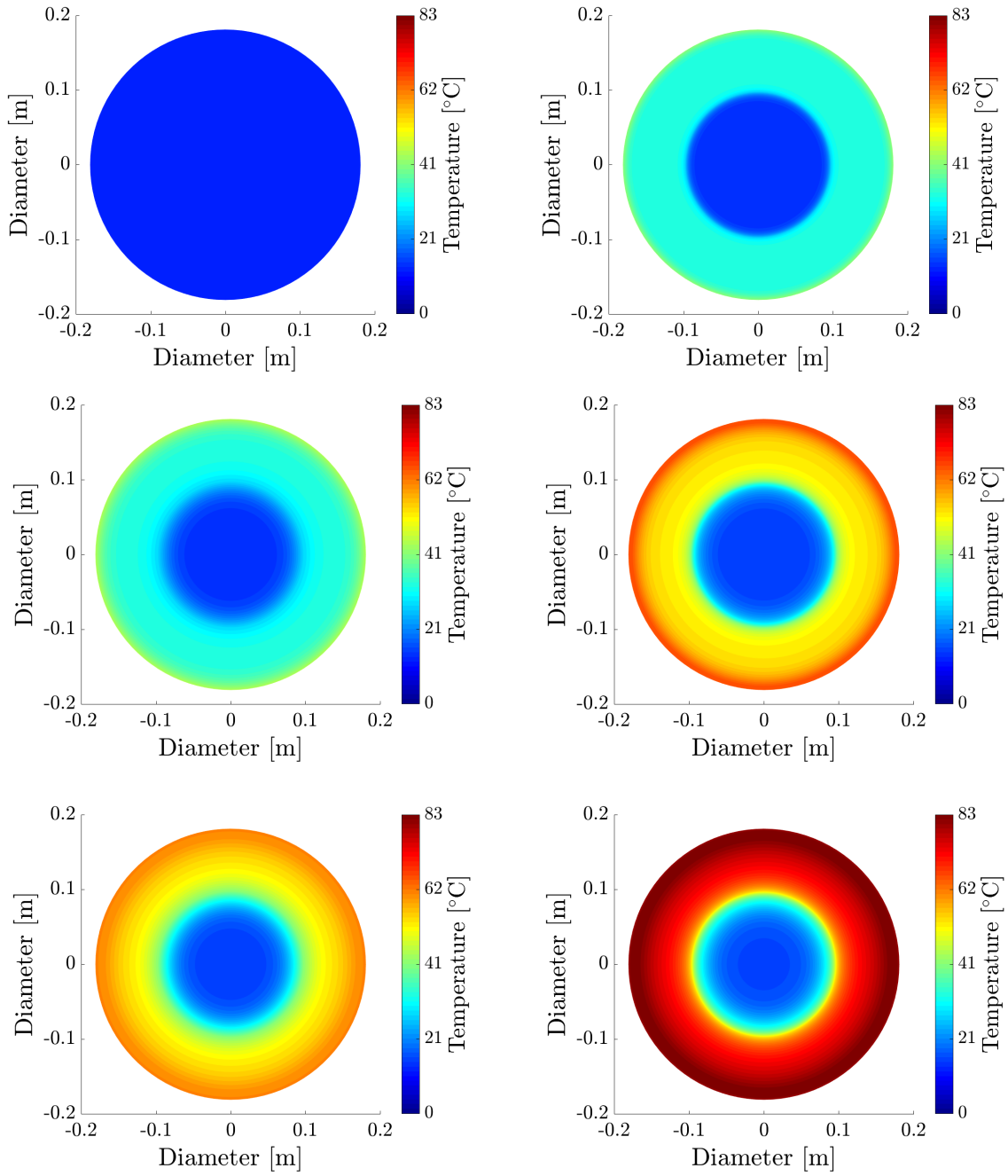

Figure E.36. The predicted temperature distribution within Log 2 at the beginning (*left*) and the end (*right*) of each excitation. The top, middle, and bottom figures are the results from the 1st, 2nd, and 3rd excitation, respectively.

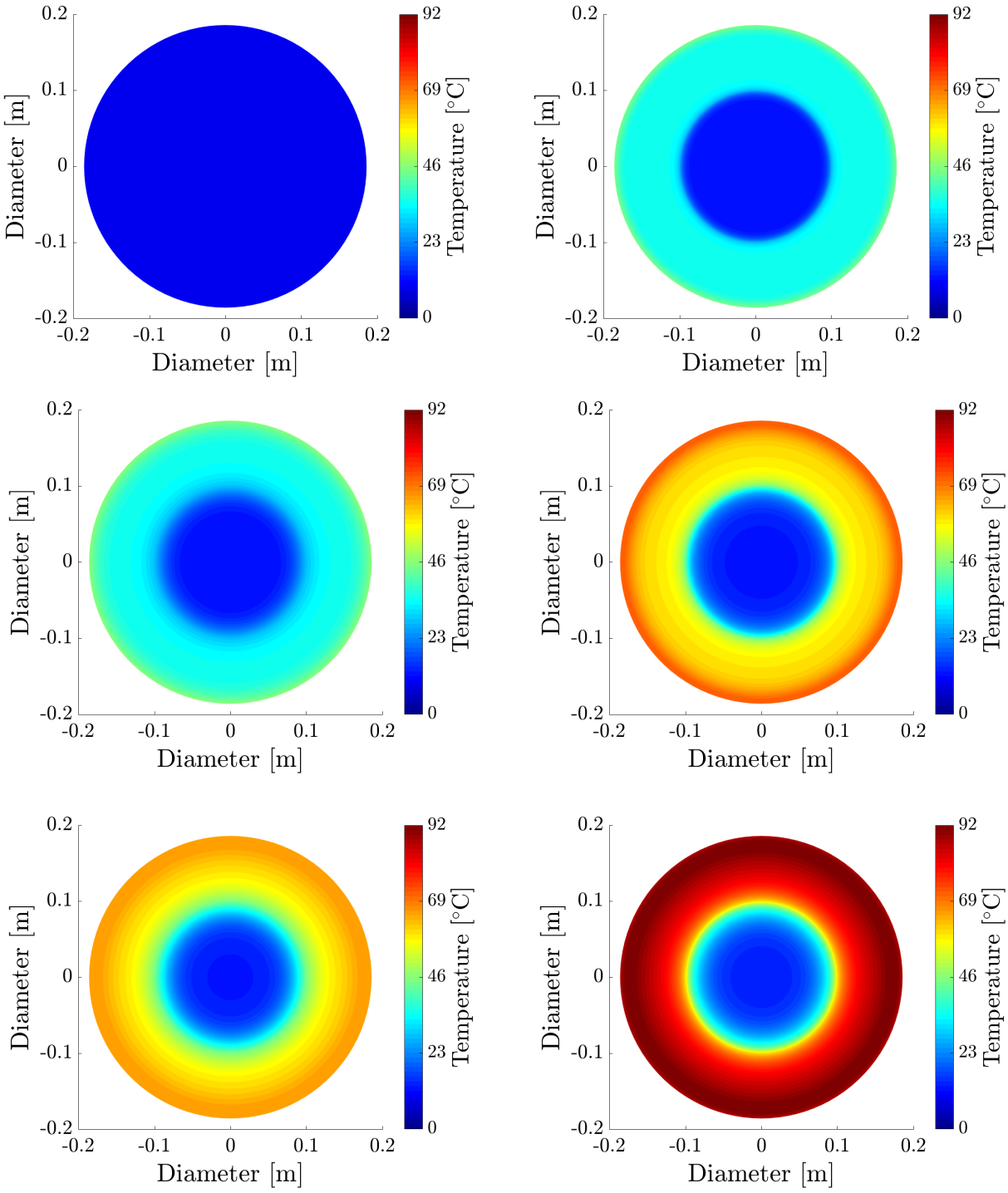

Figure E.37. The predicted temperature distribution within Log 3 at the beginning (*left*) and the end (*right*) of each excitation. The top, middle, and bottom figures are the results from the 1st, 2nd, and 3rd excitation, respectively.

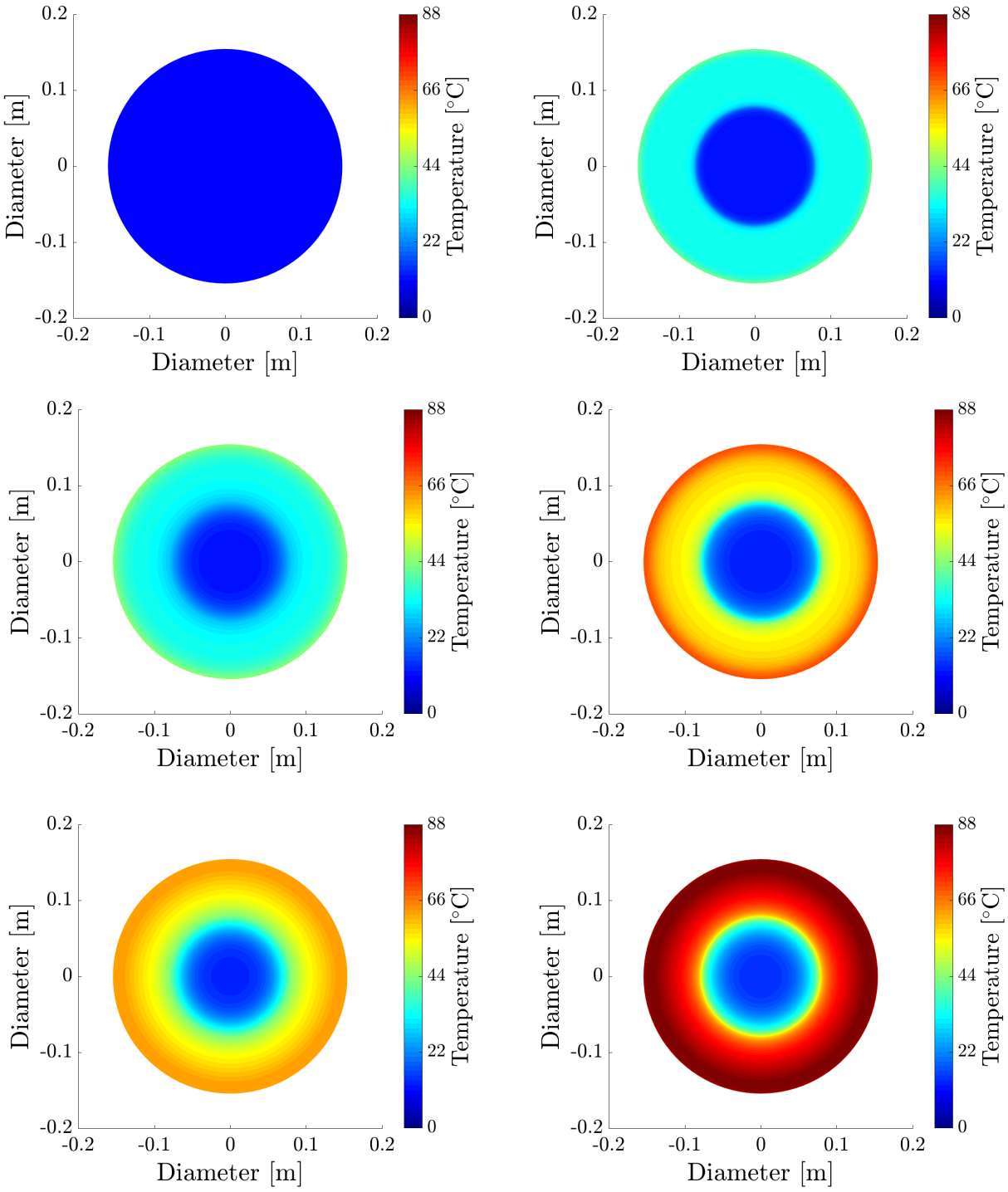

Figure E.38. The predicted temperature distribution within Log 4 at the beginning (*left*) and the end (*right*) of each excitation. The top, middle, and bottom figures are the results from the 1st, 2nd, and 3rd excitation, respectively.

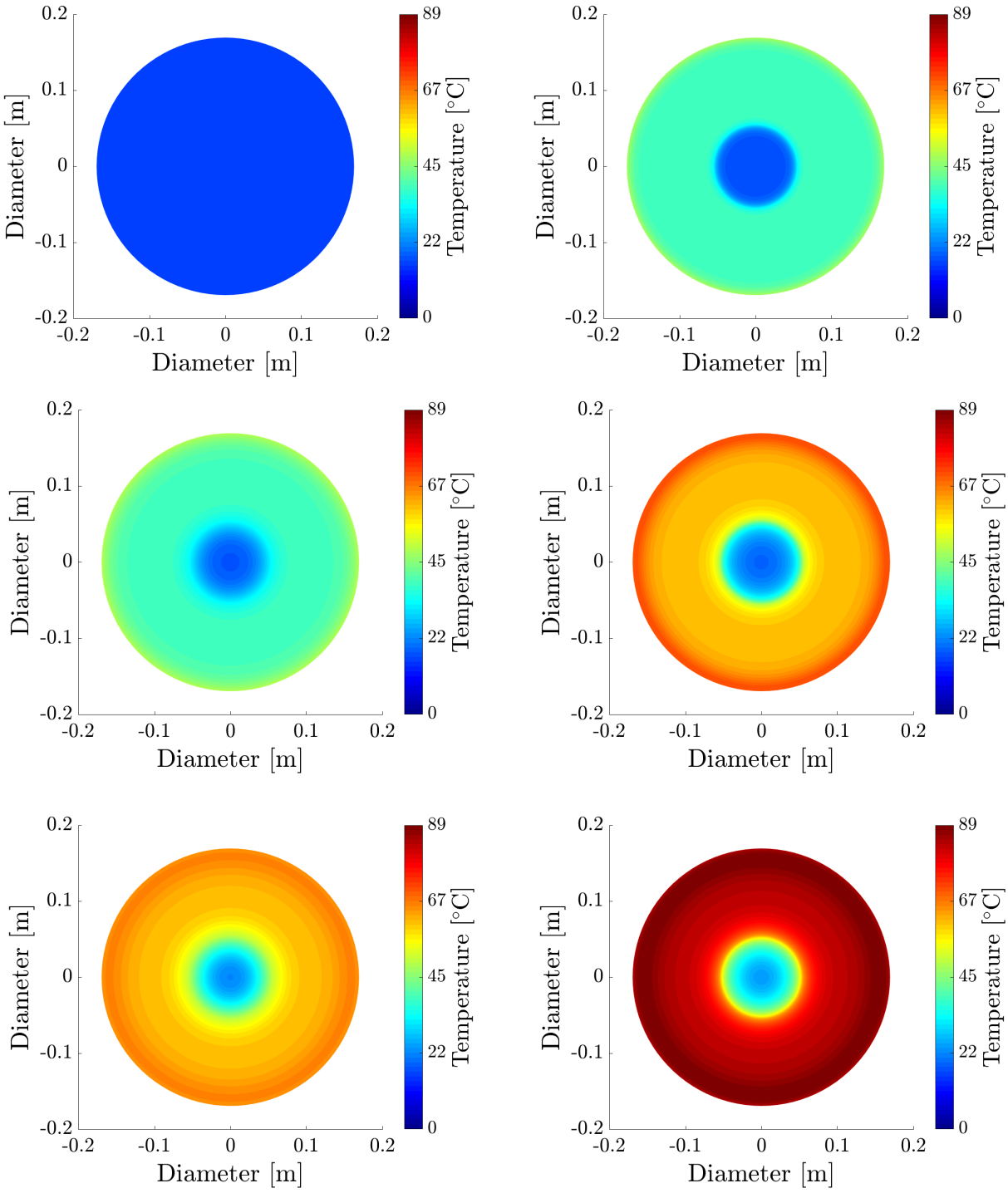

Figure E.39. The predicted temperature distribution within Log 1 at the beginning (*left*) and the end (*right*) of each excitation. The top, middle, and bottom figures are the results from the 1st, 2nd, and 3rd excitation, respectively.

E.12 Energy Calculation of Logs 1-5

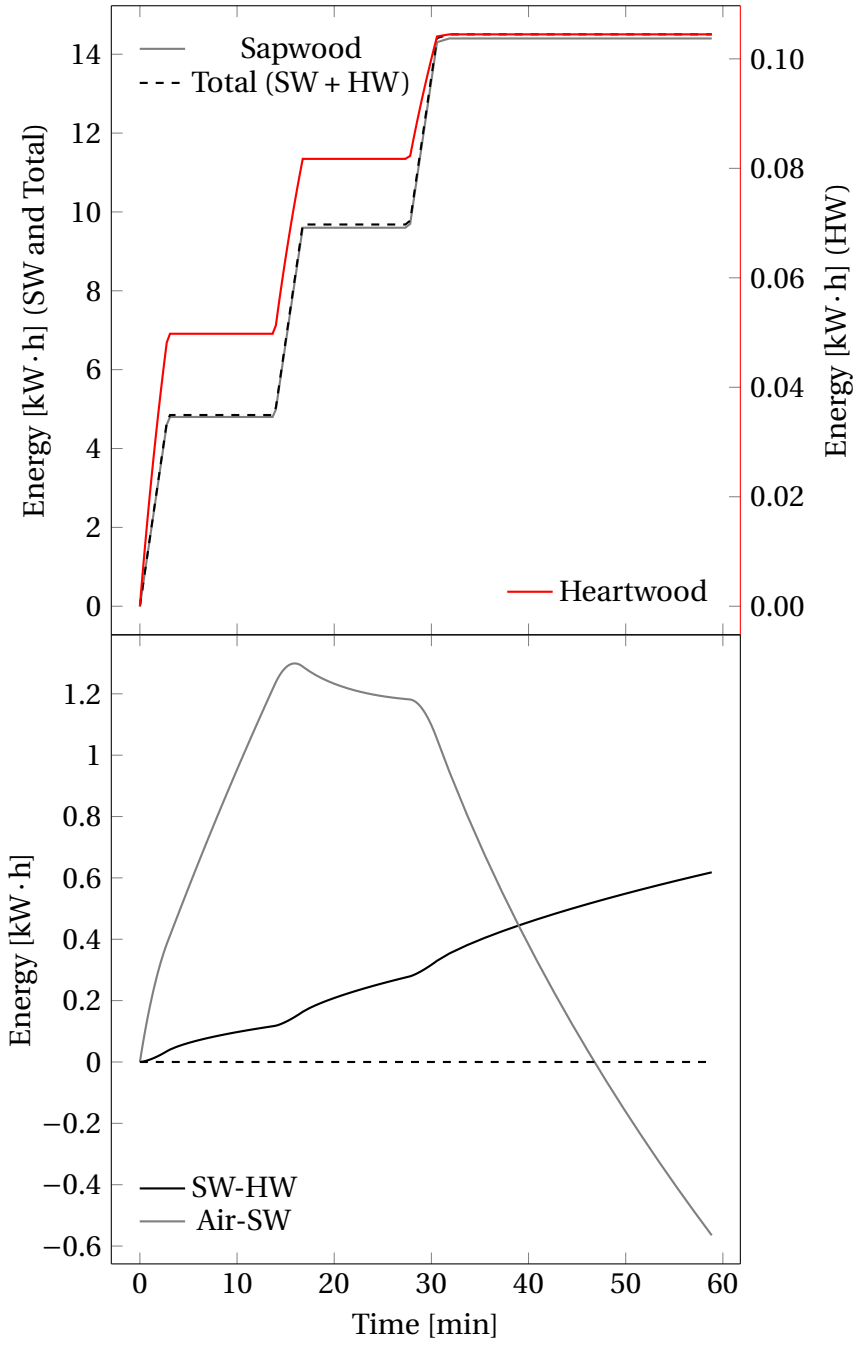

Figure E.40. The amount of energy generated within Log 2 due to the Joule heating effect (*top*), within the heartwood and the sapwood. The heat diffusion (*bottom*) between the surrounding air and the sapwood, Air-SW, and heat conduction from the sapwood to the heartwood, SW-HW.

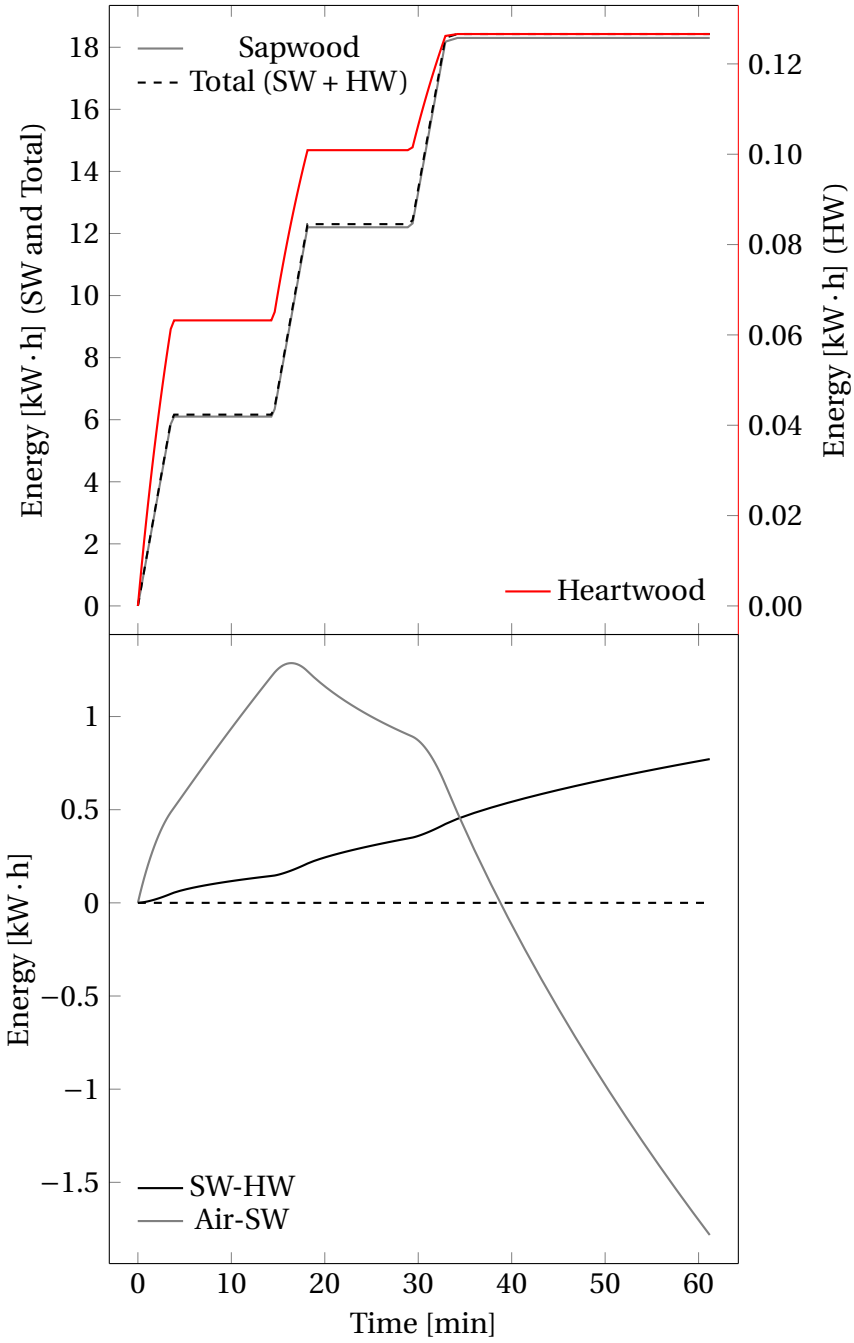

Figure E.41. The amount of energy generated within Log 3 due to the Joule heating effect (*top*), within the heartwood and the sapwood. The heat diffusion (*bottom*) between the surrounding air and the sapwood, Air-SW, and heat conduction from the sapwood to the heartwood, SW-HW.

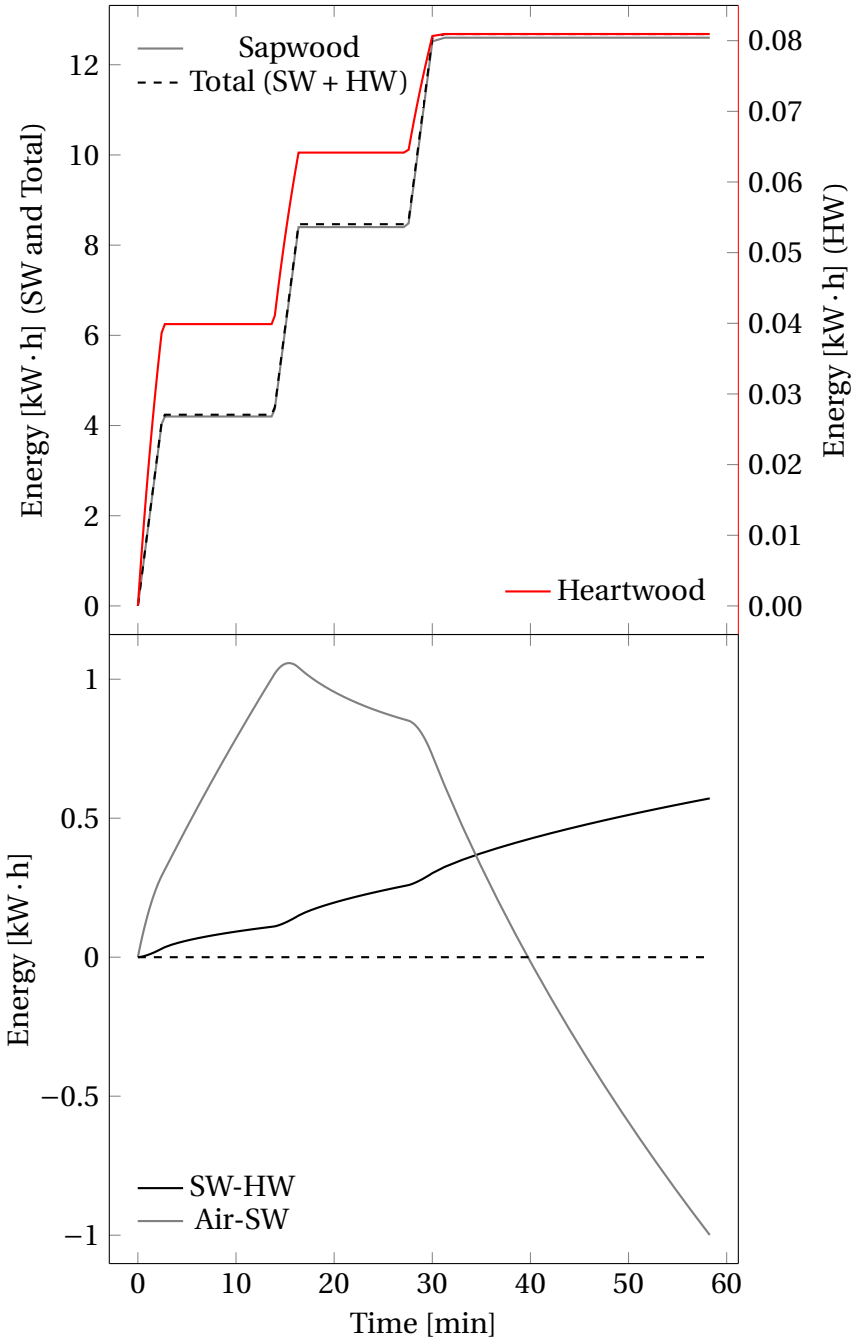

Figure E.42. The amount of energy generated within Log 4 due to the Joule heating effect (*top*), within the heartwood and the sapwood. The heat diffusion (*bottom*) between the surrounding air and the sapwood, Air-SW, and heat conduction from the sapwood to the heartwood, SW-HW.

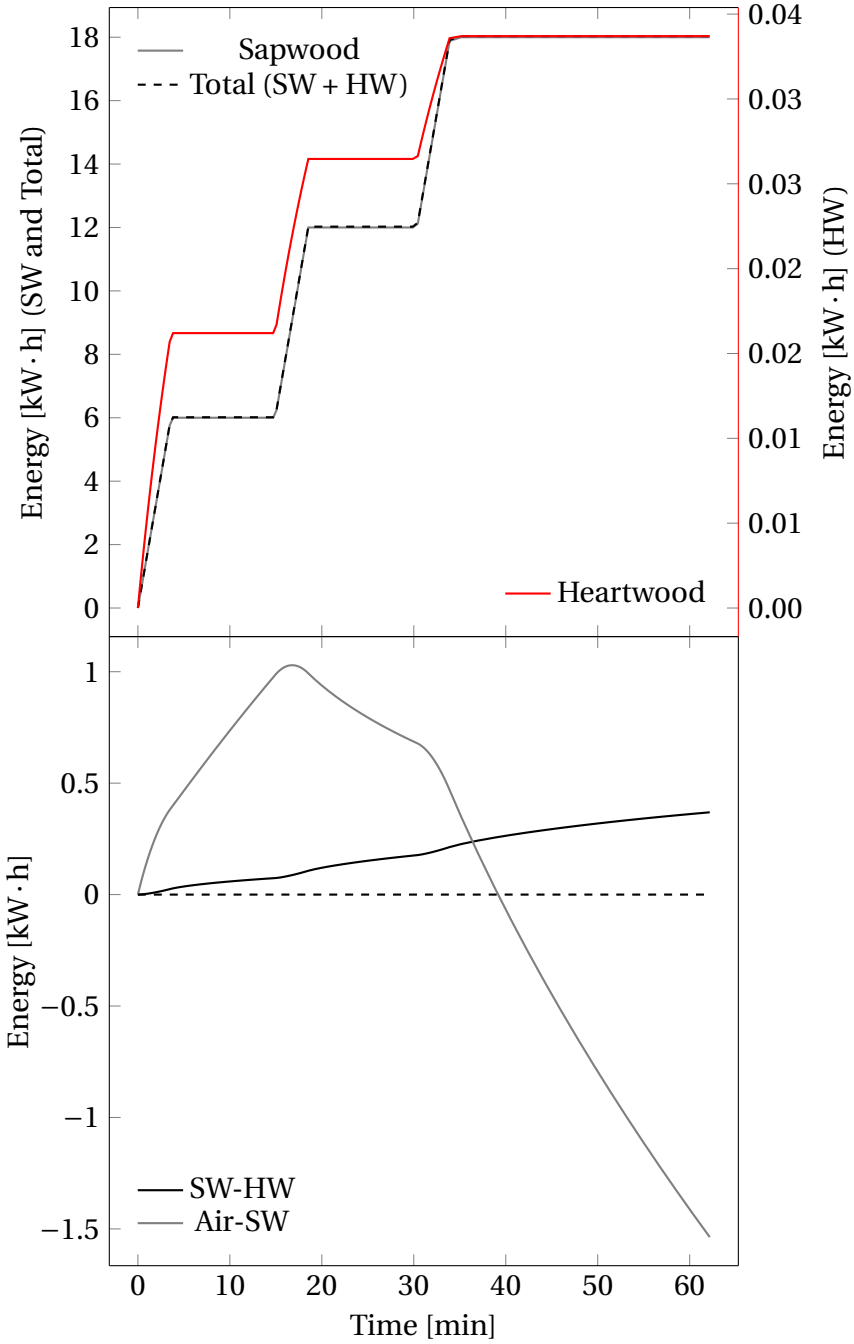

Figure E.43. The amount of energy generated within Log 5 due to the Joule heating effect (*top*), within the heartwood and the sapwood. The heat diffusion (*bottom*) between the surrounding air and the sapwood, Air-SW, and heat conduction from the sapwood to the heartwood, SW-HW.

Appendix F

F.1 Temperature Distribution Within Knot-Heating Model

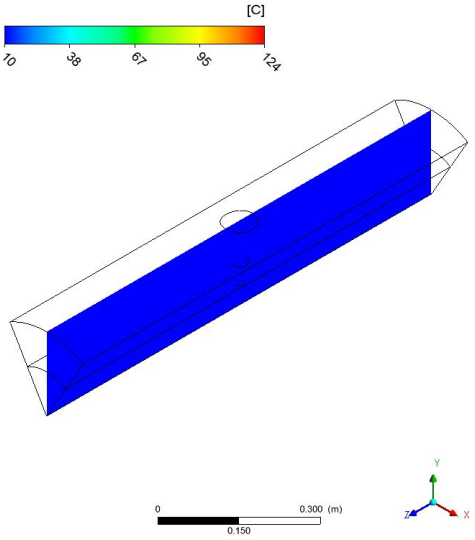

(a) Isometric View

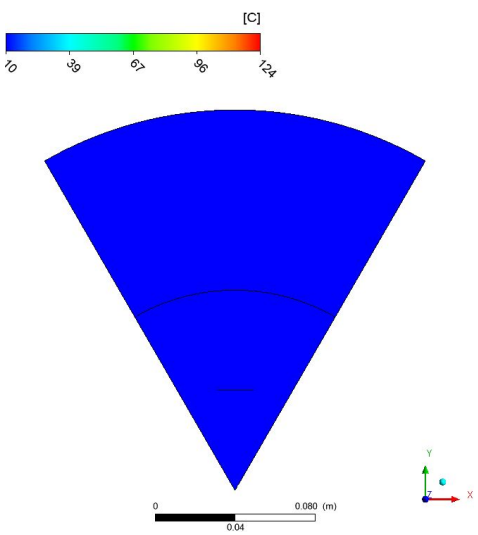

(b) Middle Cross-Sectional Cut

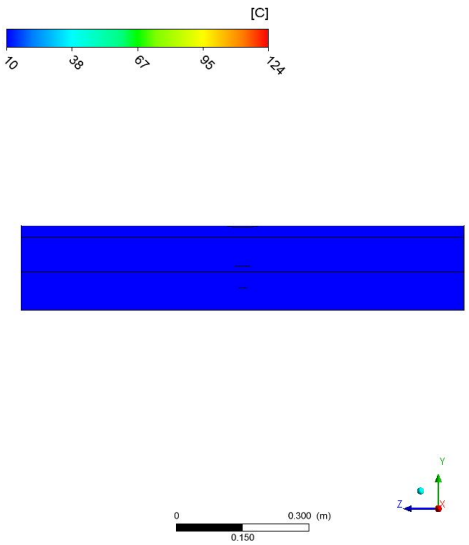

(c) Central Cut

Figure F.1. The temperature distribution within the log prior to the treatment.

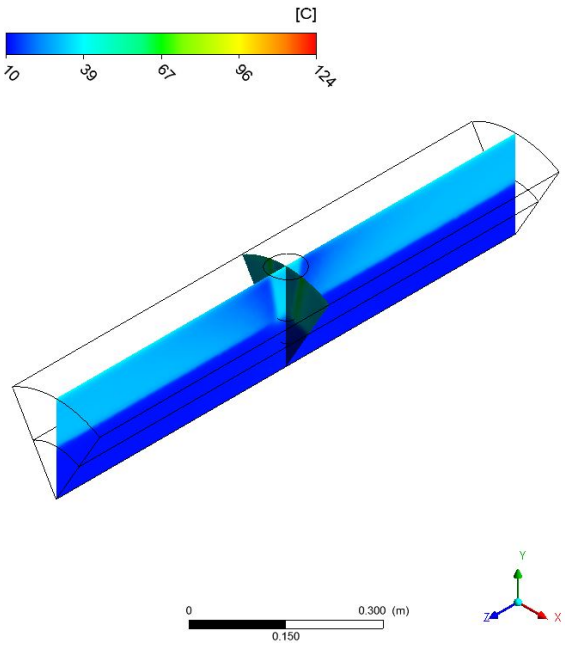

(a) Isometric View

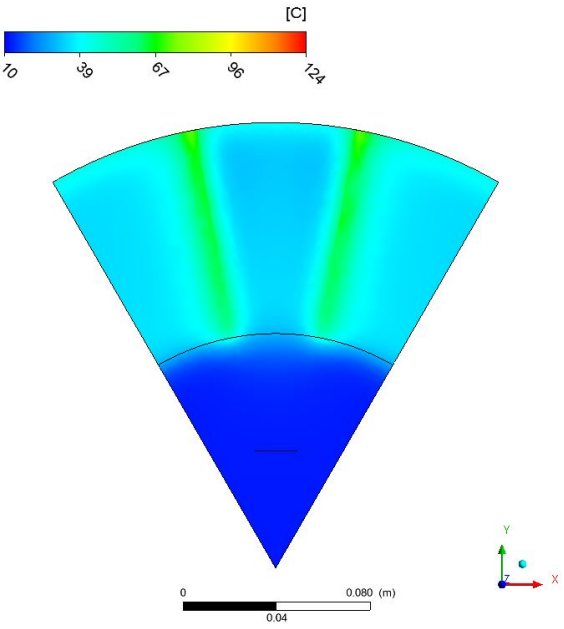

(b) Middle Cross-Sectional Cut

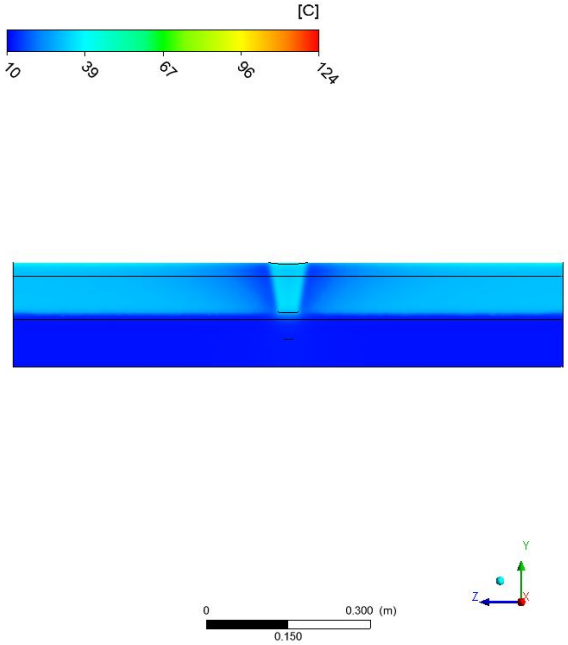

(c) Central Cut

Figure F.2. The temperature distribution within the log at the end of the 1st excitation.

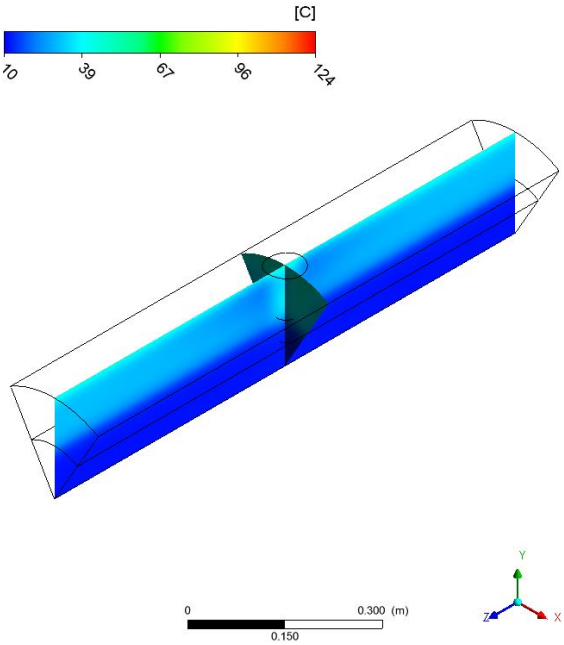

(a) Isometric View

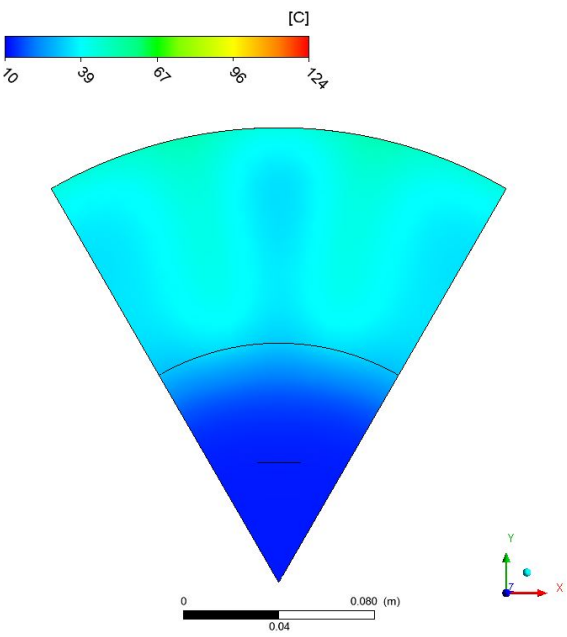

(b) Middle Cross-Sectional Cut

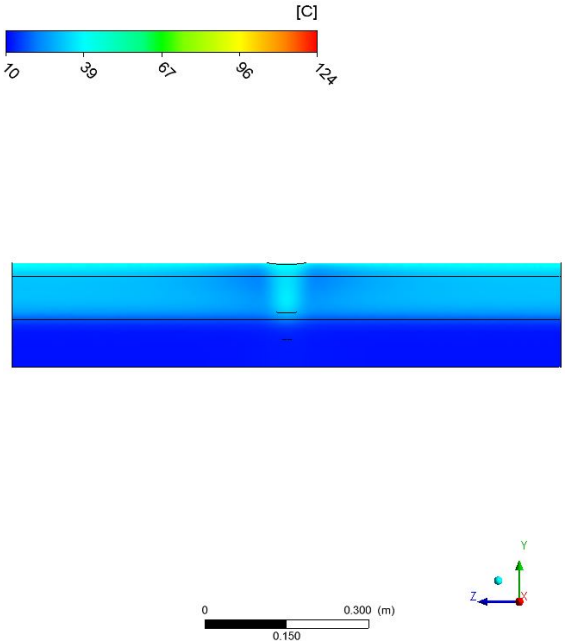

(c) Central Cut

Figure F.3. The temperature distribution within the log at the beginning of the 2nd excitation.

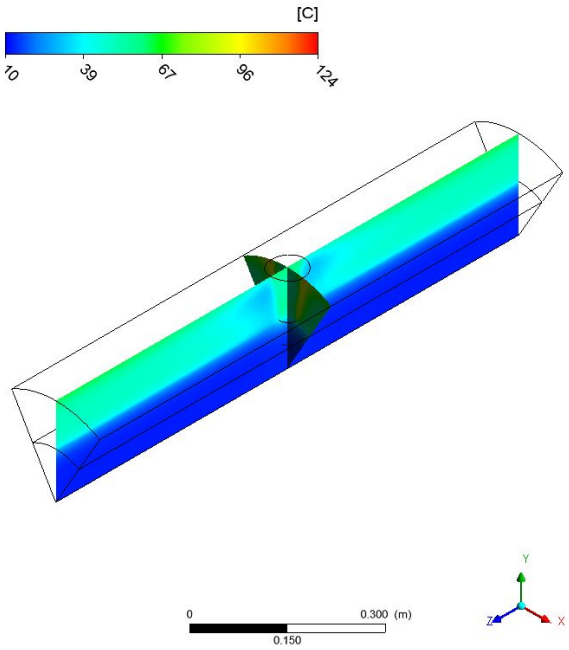

(a) Isometric View

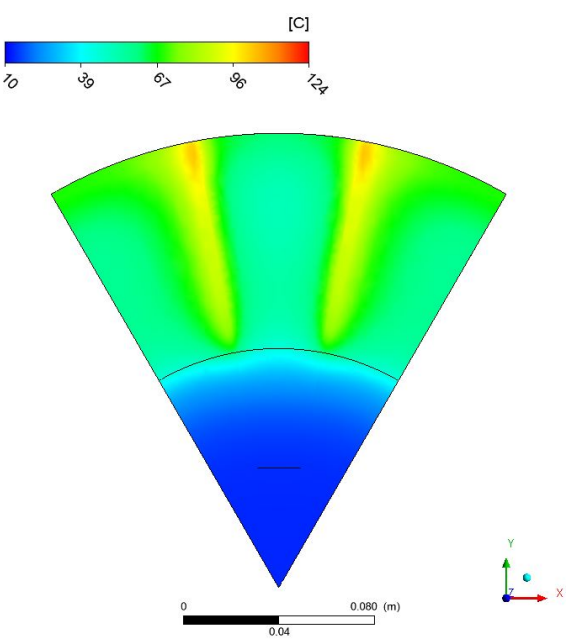

(b) Middle Cross-Sectional Cut

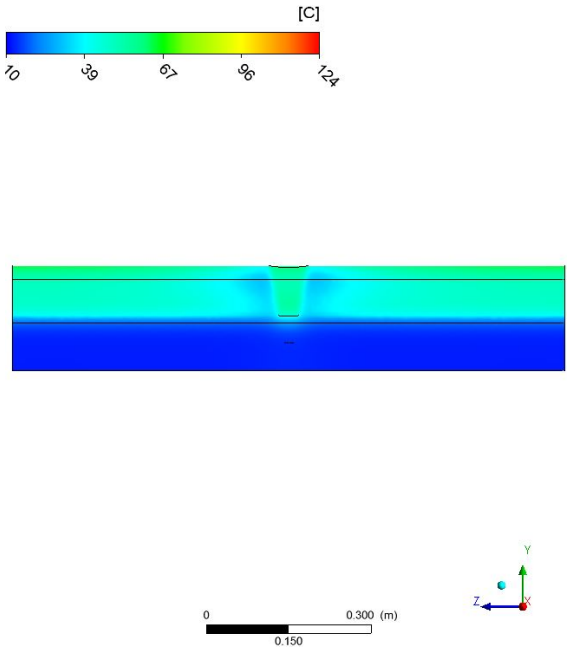

(c) Central Cut

Figure F.4. The temperature distribution within the log at the end of the 2nd excitation.

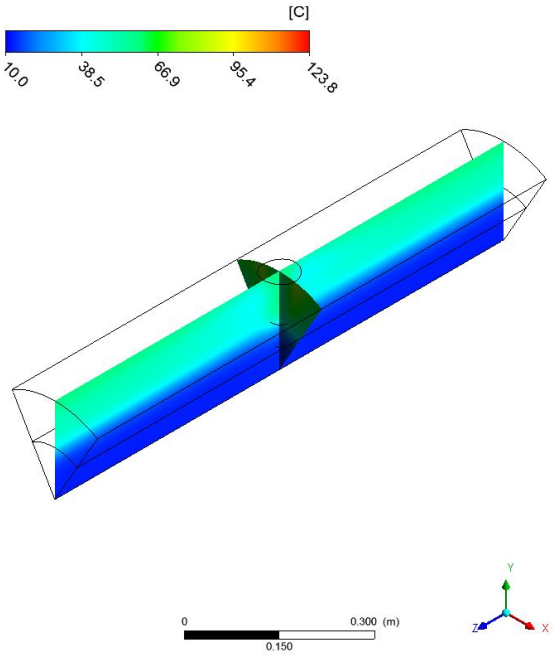

(a) Isometric View

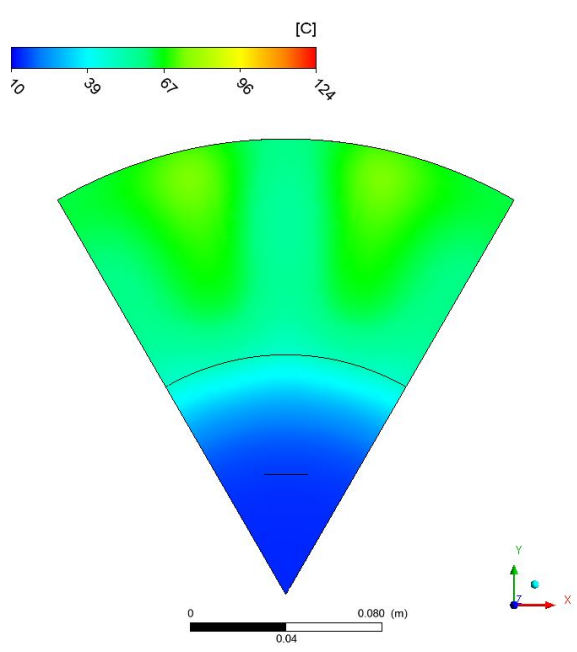

(b) Middle Cross-Sectional Cut

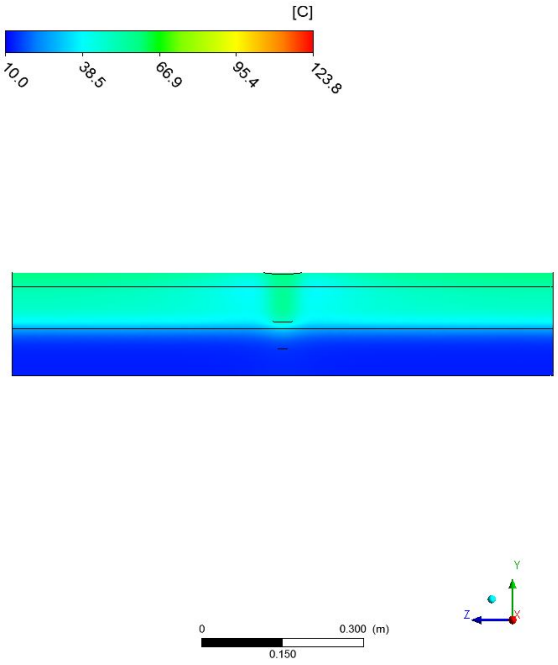

(c) Central Cut

Figure F.5. The temperature distribution within the log at the beginning of the 3rd excitation.

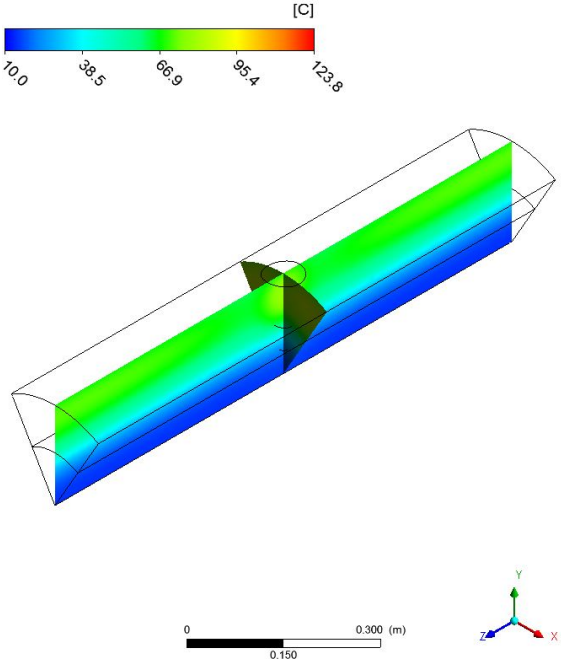

(a) Isometric View

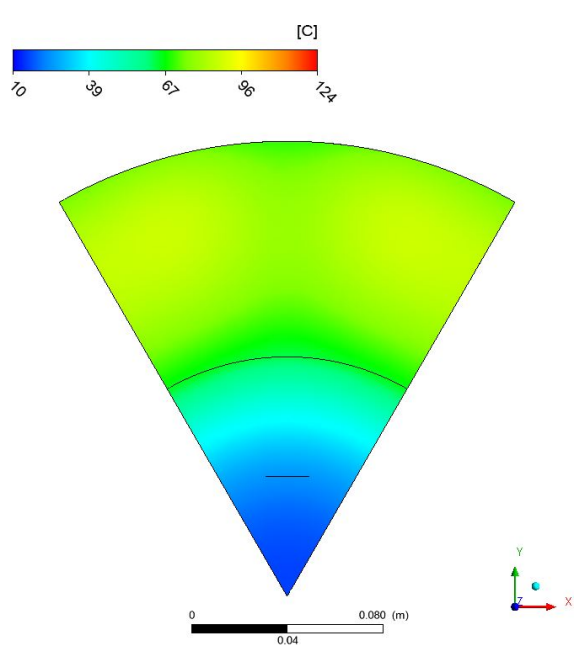

(b) Middle Cross-Sectional Cut

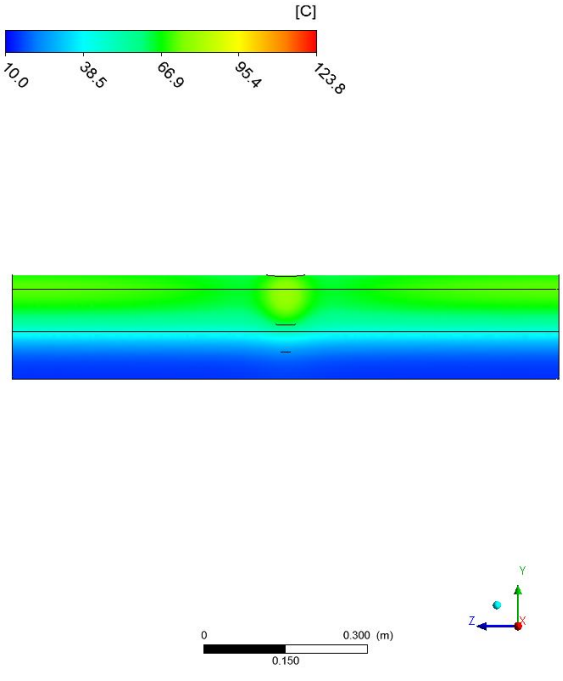

(c) Central Cut

Figure F.6. The temperature distribution within the log after the 30 minute equilibration period.